Geomechanical Characterization of Coal for CBM Reservoir Engineering

by

Nathan Deisman

A thesis submitted in partial fulfillment of the requirements for the degree of

Doctor of Philosophy

in

Geotechnical Engineering

Department of Civil and Environmental Engineering
University of Alberta

Abstract

The Government of Canada's Clean Coal and CO_2 Capture and Storage Strategic Plan identifies key knowledge gaps that need to be addressed for post capture injection of CO_2, long term reliability of CO_2 containment, and monitoring of sequestered CO_2. The geomechanical responses of the CO_2 host coalseam formation have been labelled as 'high' priorities according to the needs of the injection and reliability R&D streams and activities table. Currently, there is not a systematic method to understand the hydro-geomechanical state of the coalseam reservoir, in response to engineering activities. Therefore, a hydro-geomechanical workflow for the characterization of coal for coalseam reservoir engineering was developed utilizing the Geological Strength Index (GSI) to aid in the understanding of mechanical and flow processes during the engineering life cycle of a coalseam from methane extraction through to CO_2 injection and long-term containment.

The workflow starts with the collection of coal from the field and then branches into two integrated streams: field and laboratory testing. The original GSI chart from Hoek was re-worked for the application to core and circular wellbores for reservoir engineering applications. It was determined that GSI could be applied to the coal core and also be estimated from wellbore formation image logs. In situ field testing included the development of a new downhole tool for measuring permeability over a short interval. The laboratory testing component required the development of two triaxial cells and systems. The first cell and system (CFC) was designed for the collection of coal fines during coal failure with results used to assess coal fracture plugging during drilling/production. The second triaxial cell and system (LPG) was used for long term testing of coal with independent axial and

radial stresses and could measure axial and radial stress, permeability to gas/water, gas sorption behaviours, and sonic P and S wave velocities.

The two triaxial systems were used to test coal specimens obtained from three open pit mine sites: Cardinal River, Elkview and Greenhills in Alberta. The testing results showed that coal behaviour, specifically: strength, Young's modulus, P and S wave velocity, and methane sorption are stress dependent. The laboratory specimens were assigned a GSI value and a technique was developed to back calculate the intact Hoek Brown parameters from the strength envelopes. It was found that using an a_{RM} of 0.4 in the Hoek Brown criterion provided the best results. Hoek and Diederichs Young's modulus reduction ratio was used to model the measured Young's modulus and included a new disturbance factor function. The disturbance factor was developed as a function of effective stress and a joint stiffness factor and fit the observed laboratory results very well. Several permeability measurements were completed at different anisotropic stress states. The permeability measurements were modeled with a newly developed dynamic permeability model which includes GSI and the disturbance factor function. This model fit the results from this work, as well as work from previous researchers, very well.

The use of GSI in the dynamic permeability model created a consistent link for the hydro-geomechanical characterization of coalseam reservoirs workflow. The characterization approach was applied to two scenarios: borehole stability and field scale coupled reservoir geomechanical flow. The borehole stability modeling demonstrated that using GSI can help optimize the borehole diameter and provide insight in the selection of liner design. Field scale modeling illustrated that a variable GSI through the reservoir impacts the production characteristics of the reservoir.

Preface

A majority of this thesis has been published in Journals or Conferences. Four Journal papers were published with Dr. Thomas Gentzis of CDX Canada (now defunct), who I worked closely with as part of my NSERC Industrial Postgraduate Scholarship. I was responsible for the engineering analysis and Dr Gentzis was responsible for data acquisition (through the company) and the inclusion of some of the geological aspects. In the thesis presented here, the majority of Dr Gentzis geological work has been removed except where it was necessary to provide a brief context to the application.

Gentzis, T., Deisman, N., and Chalaturnyk, R.J. 2007. *Geomechanical properties and permeability of coals from the Foothills and Mountain regions of western Canada*. International Journal of Coal Geology. 69 153-164.

Deisman, N., Gentzis, T., and Chalaturnyk, R.J. 2008. *Unconventional geomechanical testing on coal for coalbed reservoir well design: The Alberta Foothills and Plains.* International Journal of Coal Geology. 75 15-26.

Gentzis, T., Deisman, N., Chalaturnyk, R.J. 2009. *A method to predict geomechanical properties and model well stability in horizontal boreholes*. International Journal of Coal Geology. 78 149-160.

Gentzis, T., Deisman, N., and Chalaturnyk, R.J. 2009. *Effect of drilling fluids on coal permeability: Impact on horizontal wellbore stability.* International Journal of Coal Geology. 78 177-191.

Two additional papers are in preparation with Ryan Campbell and Claudio Virues from Nexen-CNOOC. Mr. Campbell and Mr. Virues were both responsible for data collection through Nexen-CNOOC and I was responsible for the engineering analysis.

Deisman N, RJ Chalaturnyk, R Campbell, and C Virues. 2015. Borehole stability analysis using results from full field reservoir geomechanics simulation: a CBM case history. Presented at the 49th US Rock Mechanics/Geomechanics Symposium in San Francisco, USA. 28 June – 1 July, 2015. Paper 15-751.

Deisman N, RJ Chalaturnyk, R Campbell, and C Virues. 2015.Reservoir characterization and coupled reservoir-geomechanical simulation of CBM using GSI – Case Studies. Presented at the SPE/CSUR Unconventional Resource Conference in Calgary, Canada. 20-22 October 2015. Paper SPE 175903-MS.

Over the period of 2006 to 2009, I worked with Itasca Consulting group where I helped develop the “Synthetic Rock Mass” approach to simulation of rock masses. I worked closely with Dr Mas Ivars during this period on the fundamental coding, verification and applications to coal work on the SRM concept, which resulted in three publication papers from the period of 2006-2008. Dr. Pierce was responsible for the editing of the work and the original concept and Dr Darcel was responsible for the generation of a coal specific discrete fracture network.

Deisman, N., Chalaturnyk, R.J., Mas Ivars, D., and Darcel, C. 2008. *Geomechanical characterization of coalseam reservoirs for continuum modeling: the SRM approach.* Asia Pacific Coalbed Methane Symposium, Sept 22-24 2008, Brisbane, Australia. Paper 03.

Deisman, N., Mas Ivars, D., and Pierce, M. 2008. *PFC2D Smooth joint contact model numerical experiments.* The 61st Canadian Geotechnical Conference held in Edmonton, Canada. Sept 21-24, 2008. (GeoEdmonton '08), Paper 83, Edmonton, Canada.

Deisman, N., Chalaturnyk, R.J., Mas Ivars, D., and Darcel, C. 2010. *Empirical and numerical approaches for geomechanical characterization of coalseam reservoirs.* International Journal of Coal Geology. 82 (2010) 204-212.

From 2010 to 2011, I worked for Opsens Solutions Inc as an employee on the development of a downhole tool to measure vertical permeability of the annular cement and rock formation. The period resulted in successful development of the tool and field deployment. I was responsible for the overall development of the tool with Hal Soderberg and Peter Lang directly supervising the project for Opsens Inc. The tool development and application was published in the following journal.

Deisman N, H Soderberg, P Lang, and RJ Chalaturnyk. 2013. *Cased wellbore tools for sampling and in situ testing of cement/formation flow properties.* International Journal of Greenhouse Gas Control. 16 S62-S69.

The final collaborative work was with Dr. Mehdi Khajeh, who was a colleague during his Ph D work. In this publication, Dr. Khajeh was responsible for the geostatistical modelling for input into the coupled reservoir geomechanical simulator that I developed.

Deisman N, M Khajeh, and RJ Chalaturnyk. 2013. Using geological strength index (GSI) to model uncertainty in rock mass properties of coal for CBM/ECBM reservoir geomechanics. International Journal of Coal Geology. 112 76-86.

Dedicated to those people who are unable to pursue a formal education.

Acknowledgements

The author would like to thank:

First my Mom Wanda, Dad Wally, and Brother Quentin.

Second to Jade Vo for all her love and support.

Third to my supervisor Prof Richard Chalaturnyk for his guidance and trust.

Fourth to Tanya Schulz who dedicated much time to editing this work.

Then comes everyone else who has helped me with this work through the years. In no order at all:

Salina Yong, Jamie Jimenez, Prof C. Derek Martin, Gonzalo Zambrano, Hal Soderberg, Steve Gamble, Jakob Brandl, Wayne Jamieson, Neil Schmiechel, Darren Miller, Thomas Gentzis, Professor Charles Fairhurst, Ed Dzik, Matt Pierce, David Potyondy, Deigo Mas Ivars, Alma Ornes Ines, Santiago Paz, Ahmad Al-Sayeed, Gilbert Wong, Tennille Mares, Fagang Gu, Seungjoo Lee, Nicholas Beier, Peter Lang, Magnus Friis, Hector Aguilar, Olle Lagerquist, Prof Dave Sego, Prof Tim Joseph, Prof John McLennan, Prof Chris Hawkes, Anna Ho, Denis Pone, Graham Price, Janetlee Banister, Doug Bearinger, Phebe Chung, Kip Pratt, Ken Leung, Prof Don Scott, Sally Petaske, and Hope Walls.

Table of Contents

List of Tables

List of Symbols

(Units: L = length, M = mass, T = time)

Symbol	Roman Symbols Name	Units
A	Cross sectional area	L^2
C_{eff}	Effective bulk rock compressibility	$M^{-1}LT^2$
C_f	Fluid compressibility	$M^{-1}LT^2$
C_s	Mineral compressibility	$M^{-1}LT^2$
C_w	Water compressibility	$M^{-1}LT^2$
D	Hoek-Brown disturbance factor	
E_D	Dynamic Young’s modulus	$ML^{-1}T^{-2}$
E	Young’s modulus of intact rock	$ML^{-1}T^{-}$
E_i	Young’s modulus of intact rock	$ML^{-1}T^{-2}$
E_{RM}	Young’s modulus of rock mass	$ML^{-1}T^{-2}$
E_{RR}	Young`s modulus reduction ratio	
E_{RR0}	Maximum modulus reduction ratio	
E_{RR1}	Minimum modulus reduction ratio	
E_S	Static Young’s modulus	$ML^{-1}T^{-2}$
E_x	Static Young’s modulus in x direction	$ML^{-1}T^{-2}$
E_y	Static Young’s modulus in y direction	$ML^{-1}T^{-2}$
E_z	Static Young’s modulus in z direction	$ML^{-1}T^{-2}$
G	Shear modulus	$ML^{-1}T^{-2}$
G_D	Dynamic Shear modulus	$ML^{-1}T^{-2}$
G_i	Intact Shear modulus	$ML^{-1}T^{-2}$
G_{RM}	Shear modulus of rock mass	$ML^{-1}T^{-2}$
G_{RR}	Shear modulus reduction ratio	
GSI	Geological Strength Index	
GSIi	Fictional Geological Strength Index in i direction	
J_2	Octahedral shear stress	$ML^{-1}T^{-2}$
K_D	Dynamic bulk modulus	$ML^{-1}T^{-2}$
K_0	Ratio of maximum horizontal effective stress to vertical effective stress	
L	Length	L
$L_{RM,i}$	Length of rock mass in direction i	L
$N(h)$	Number of pairs separated by distance h	
P	Pressure	$ML^{-1}T^{-2}$
P_d	Downstream pressure	$ML^{-1}T^{-2}$
P_o	Initial pressure	$ML^{-1}T^{-2}$
P_{LS}	Langmuir strain gas pressure	$ML^{-1}T^{-2}$
P_u	Upstream pressure	$ML^{-1}T^{-2}$
Q	Flow rate	L^3T^{-1}
Res	Resolution	
R_{max}	Maximum particle radius	L
R_{min}	Minimum particle radius	L
S_d	Downstream specific storage	L^2
S_0	Ratio of effective minimum horizontal stress to effective vertical stress	
S_s	Specific storage	$M^{-1}LT^2$
S_u	Upstream specific storage	L^2
T	Temperature	
V_p	Normal wave velocity	LT^{-1}
V_s	Shear wave velocity	LT^{-1}
Z	Height	L
a_{RM}	Rock mass value of Hoek-Brown failure envelope fitting parameter	

b_i	Initial fracture aperture in the direction i	L
$b_{i,n}$		
c'	Cohesion	$ML^{-1}T^{-2}$
d	Depth	L
dP	Change in pore pressure	$ML^{-1}T^{-2}$
d_{ij}	Dilation angle I due to strain in j	
h	Disturbance factor fitting parameter	$M^{-1}LT^{2}$
k	Permeability	L^2
k_i	Permeability along the joint in the i plane	L^2
k'_i	Updated permeability along the joint in the i plane due to change in aperture	L^2
k'_{ii}	Permeability in any direction ii at any effective stress state	L^2
k_{ii}	Permeability in the rock mass in the ii direction	L^2
m_i	Intact Hoek-Brown failure envelope parameter	
m_{RM}	Rock mass Hoek-Brown failure envelope parameter	
n_c	Normal to interface contact	
n_j	unit vector normal to joint plane	
p'	Mean effective stress	$ML^{-1}T^{-2}$
q	Shear stress	$ML^{-1}T^{-2}$
s_i	Fracture spacing in direction i	L
s_{RM}	Rock mass Hoek-Brown failure envelope parameter	
T	Time	T
t_j	Perpendicular to joint plane normal vector	
u_i	Initial pore pressure	$ML^{-1}T^{-2}$
u_f	Pore pressure at failure	$ML^{-1}T^{-2}$
z(u)	Random variable at location u	
z(u+h)	Random variable at location u+h	

Greek Symbols

Σ	Summation
α	Dimensionless time variable
β	Dimensionless upstream storage variable
δ	Differential delta operator
Δ	Change in …
$\varepsilon_{E,i}$	Elastic strain due to changes in effective stress
ε_{GC}	Strain due to changes in gas content
$\varepsilon_{L,max}$	Langmuir strain
ε_{ii}	Normal strain
ε_{ij}	Shear strain
$\varepsilon_{I,ii}$	Normal strain of the intact rock
$\varepsilon_{I,ij}$	Shear strain of the intact rock
$\varepsilon_{RM,ii}$	Normal strain of the rock mass
$\varepsilon_{RM,ii}$	Shear strain of the rock mass
ϕ	Friction angle
ϕ_m	Roots for the solution of the pressure transient equation
η	Porosity
$\eta_{f,i}$	Porosity of joint in direction i
$\eta_{f,T}$	Total fracture porosity
$\eta'_{f,T}$	Updated total fracture porosity

$\eta'_{f,i}$	Updated porosity of joint in direction i	
γ	Dimensionless downstream storage variable	
$\gamma(h)$	Experimentally calculated semivariogram for lag distance	
θ_p	Dip angle	
μ	Dynamic viscosity	$ML^{-1}T^{-1}$
ν	Poisson's ratio	
ν_D	Dynamic Poisson's ratio	
ν_S	Static Poisson's ratio	
ρ	Density	ML^{-3}
σ	Total stress	$ML^{-1}T^{-2}$
σ'	Effective stress	$ML^{-1}T^{-2}$
σ_1'	Major principle effective stress	$ML^{-1}T^{-2}$
σ_3'	Minor principle effective stress	$ML^{-1}T^{-2}$
σ_a'	Axial effective stress	$ML^{-1}T^{-2}$
$\sigma_{a,i}$	Initial axial effective stress	$ML^{-1}T^{-2}$
$\sigma_{a,f}$	Axial effective stress at failure	$ML^{-1}T^{-2}$
σ_c'	Confining effective stress	$ML^{-1}T^{-2}$
σ_{ci}	Intact compressive strength	$ML^{-1}T^{-2}$
$\sigma_{c,i}$	Initial confining effective stress	$ML^{-1}T^{-2}$
$\sigma_{c,f}$	Confining effective stress at failure	$ML^{-1}T^{-2}$
σ_H	Maximum horizontal total stress	$ML^{-1}T^{-2}$
σ_h	Minimum horizontal total stress	$ML^{-1}T^{-2}$
σ'_H	Maximum horizontal stress	$ML^{-1}T^{-2}$
σ'_h	Minimum horizontal stress	$ML^{-1}T^{-2}$
σ_{ii}	Normal stress in the intact matrix in the ii direction	$ML^{-1}T^{-2}$
σ_{ij}	Shear stress in the intact matrix in the ij direction	$ML^{-1}T^{-2}$
σ_m'	Mean effective stress	$ML^{-1}T^{-2}$
$\sigma_{RM,i}$	Normal stress in the rock mass in the i direction	$ML^{-1}T^{-2}$
$\sigma_{RM,ij}$	Shear stress in the rock mass in the i direction	$ML^{-1}T^{-2}$
σ_v	Vertical total stress	$ML^{-1}T^{-2}$
σ'_v	Vertical stress	$ML^{-1}T^{-2}$
σ_{xx}'	Effective stress in the xx direction	$ML^{-1}T^{-2}$
σ_{xy}	Shear stress in the xy direction	$ML^{-1}T^{-2}$
σ_{yy}'	Effective stress in the yy direction	$ML^{-1}T^{-2}$
σ_{yz}	Shear stress in the yz direction	$ML^{-1}T^{-2}$
σ_{zz}'	Effective stress in the zz direction	$ML^{-1}T^{-2}$
σ_{xz}	Shear stress in the xz direction	$ML^{-1}T^{-2}$
τ	Shear stress in Mohr-Coulomb failure criterion	$ML^{-1}T^{-2}$
τ_{oct}	Octahedral shear stress	$ML^{-1}T^{-2}$

1 Introduction

Coal is a term used for a mineral consisting of fossilized carbon with organic matter greater than 50% (Levine 2006) and therefore coal is a generic term similar to “soil” or “rock”. Coal is the most abundant fossil fuel in the world, with reserve estimates of more than one trillion tonnes (World Coal Organization). Historically, coal in and of itself was considered a primary energy source, mined and combusted to produce heat energy. Methane gas, created during the coal formation process, is released during coal extraction in both surface and underground mining. It mixes with air and is highly explosive at concentrations of 5 to 15 percent. As a result, particularly in underground mines with poor ventilation, explosions and outbursts have occurred causing extensive damage and significant loss of life. While venting of gases prior to mining has been carried out since the 19^{th} century, only relatively recently (over the last 40 years), have more significant efforts been made to capture methane.

Natural gas is classified as conventional or unconventional, differentiated by the manner and ease of extraction and costs. Conventional natural gas is comprised of 70 to 90 percent methane (with the rest being made up of ethane, propane, butanes, pentanes and higher molecular weight hydrocarbons, elemental sulphur, and sometimes helium and nitrogen). Coal seam gas is classified as unconventional natural gas and is typically comprised of more than 90 percent methane (CH_4). As energy demands have increased, coal seam gas is now considered a valuable energy resource. Accordingly, this has led to commercial coal seam gas, or more commonly termed coalbed methane (CBM) recovery and recovery of methane from deep unmineable coal seams (Flores, 1994).

Conventional natural gas reserves in Canada are declining (CAPP 2013) while demand continues to increase as a function of economic and population growth. Associated with these increases in energy demands, are increases in Greenhouse Gas Emissions (NEB 2007a). The Government of Canada is committed to reducing Canadian GHG emissions through a regulatory framework (Environment Canada 2013). MacLeod et al. (2000) identified unconventional gas (CBM included) “will be required to meet Canadian demand," potentially making up "65 percent of the supply by 2025." CBM reserves in Canada have been identified in British Columbia, Saskatchewan, Nova Scotia, with the largest reserves located in Alberta (NEB 2007b).

Gunter et al. (1997) estimated that there are 5.7 to 85.0 trillion cubic meters (200–3000 Tft^3) of CBM in the Alberta Basin as well as the potential to store 10 trillion cubic meters (20 giga-tonnes) CO_2 in those coal seams. Therefore, coal seam reservoirs in Alberta may provide an opportunity to address both issues of meeting future energy demands and reducing GHG emissions through CBM and enhanced coalbed methane (ECBM) operations through injection of CO_2 to displace methane with the CO_2 remaining in place.

1.1 CBM in Alberta

CBM in Alberta has been identified as a major resource that can add to Canada's energy economy by filling part of the gap left by declining conventional gas reserves. In Alberta, the CBM industry has gone from relatively little activity prior to 2003 (less than 100 wells drilled per year), to more than 18 000 total wells as of 2012 being drilled for CBM wells (some wells are comingled gas wells). The coal seams in Alberta are divided into roughly three groups: the Horseshoe Canyon and Belly River, the Mannville, and the Mountains (Luscar and Kootenay). Figure 1 shows the plan view locations of the coal formations with the number of wells per township being drilled or recompleted for CBM production. The majority of the Mannville CBM wells are located in a single area to the northwest of Edmonton, whereas the wells in Horseshoe Canyon and Belly River formation are located in the region termed the Calgary Edmonton corridor. Several reports were used to compile a summary of these coalseam gas reserves and associated production challenges as provided in Table 1 (AER ST98 2009, AER ST98 2013, Beaton et al. 2006, Langenberg et al. 2006).

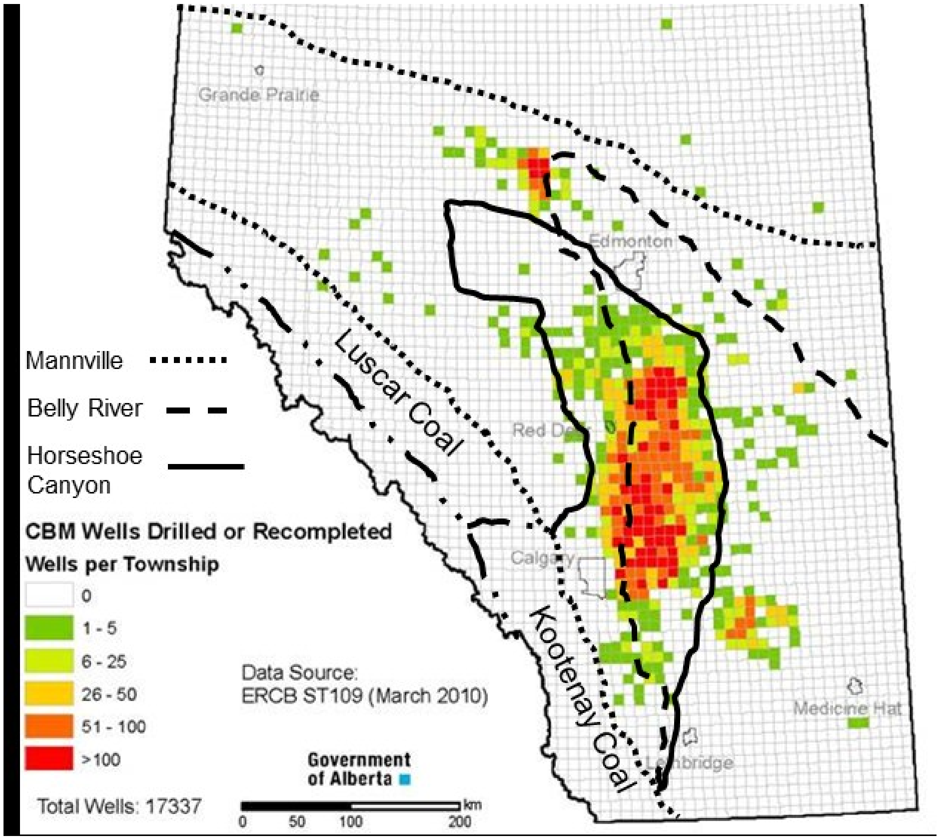

Figure 1. Overlay of the CBM activity on the coal formations in Alberta (modified from Alberta Environment, 2013).

Table 1. A summary of coalseam reservoir formations in Alberta.

Formation	Horseshoe Canyon and Belly River	Mannville	Foothills Coal and Kootenay Mountains
Depth (m)	200 to 800	800 to1400	1000 (shallow) to 2500 (deep)
Description	Many thinly stacked 0.1 to 1 m thick	3 or more 0.5 to 4 m thick	single seams 1 to 15 m, cumulative thickness to 50 m
Original Gas in Place (Gm^3)	234	67.9	873
Producible Reserves (Gm^3)	72.1	28.5	n/a
Recovery Factor %	31	42	n/a
Wells pre 2002	<1000	<50 /pre 2002	n/a
Wells as of 2012	>18000	>750	n/a
Cumulative Gas Produced	37.9	5.9	n/a
Production Challenges		dewatering low permeability	low permeability complex stress field

1.1.1 Vertical and Horizontal Well Production

In the Horseshoe Canyon and Belly River coal formation, vertical wells are used exclusively. Because the coals are thinly stacked with higher permeability, a vertical well is drilled and then completed and fracture stimulated (frac'd) using nitrogen (N_2) in multiple horizons. Although vertical wells are not contacting as much of a single seam, the wells are generally shallower and therefore less expensive and can be economical at lower production rates

In the Mannville coals, production rates in vertical wells rates are typically less than 3000 m^3/day. However, some successful horizontal wells have gas production rates greater than 12,000 m^3/day. Based on historic data, economic viability of methane extraction from the Mannville Formation is believed to be possible only through the drilling of horizontal wells, which provide greater connectivity to the coal reservoir surface (Gentzis et al., 2009). Horizontal wells have been used extensively in the United States for CBM development. Transfer of technologies from the USA to the Mannville Formation in the Alberta Basin has not been as successful as originally expected. In the Foothills and Mountains regions, only vertical wells have been used to access the coal formations, with no commercial success.

1.2 ECBM and CO_2 Storage

Major publicly funded research efforts have focused on the use of Mannville coal seams for CO_2 storage. Enhanced CBM (ECBM) technologies in association with CO_2 storage have been identified as a potential method to overcome the low production due to low permeability in the Mannville Formation coals (Gunter et al., 1997). Although there is a potential to store large amounts of CO_2 in the Alberta Basin, there has been only one pilot test with published results (Mavor et al., 2004). With the use of a single well as an injector and producer, it is difficult to determine if the injection of CO_2 or flue gas (N_2 plus CO_2) could provide a value added option to CO_2 storage, or if ECBM is a viable option to increase the economics in the Mannville Formation. There has been no research done on the potential to store CO_2 in Foothills or Mountains coals.

1.3 Statement of Problem

The primary factors constraining the CBM extraction are cost and level of technology currently available as well as a poor level of understanding of CBM reservoir behaviour (Rice and Paul, 1995). Economically viable production strategies (vertical wells with N_2) for the Horseshoe Canyon and Belly River have been identified and the methane resource is being recovered (47.8% remaining), even if the recovery factor is lower (31%) than the deeper Mannville coal (42%). In the Mannville coal, low permeability reduces production rates as well as decreasing injectivity for ECBM and CO_2 storage. These same problems would be magnified in the Foothills and Mountain coals as a result of the complex stress fields present in those locations.

As demands for energy increase the associated challenges and risks of producing energy from unconventional sources needs to be understood. The preferential sorption of CO_2 over CH_4 on coal, has made enhanced coal seam gas recovery an attractive value added option for potential coal seam sequestration operations (Gunter et al. 1997), and requires an understanding of the storage formation behaviour.

The Government of Canada's Clean Coal and CO_2 Capture and Storage strategic plan identifies key knowledge gaps that need to be addressed for post capture injection of CO_2, long term reliability of CO_2 containment, and monitoring of injected CO_2. The geomechanical responses of the CO_2 host coal seam formation and integrity of the wellbore have been labelled as 'high' priorities. However, as carbon trading and carbon taxes are not part of the world economy to date, there is no economic incentive for energy companies to developed coal seam reservoir characterization models outside the scope of primary production schemes. Therefore it is beneficial that any developed characterization methodology remains within 'the primary purpose of reservoir engineering [which] is to optimize economic recovery of hydrocarbons from the reservoir … by optimizing completion design… [and by] … optimizing well spacing" (Gas Research Institute Reservoir Engineering, 1995).

Currently there is no systematic method to understand the hydro-geomechanical state of the coal seam reservoir before CO_2 injection begins or even before primary CBM production begins. Therefore, there is a need to not only identify the controlling hydro-geomechanical processes in coal during the CBM, ECBM, and CO_2 storage life cycle, but there is a critical need to characterize and link these processes for use in simulations for performance and risk assessment. Understanding the hydro-geomechanical processes associated with borehole failure, permeability changes, and caprock damage during primary CBM, enhanced CBM (ECBM), and CO_2 storage reservoir lifecycle activities provides insight into the planned CBM project. Therefore, characterizing the hydro-geomechanical behavior (strength, deformation, and permeability change) of the coal seam is fundamentally important to the development of a CBM reservoir for each of these uses.

1.4 Objective and Scope

The objective of this thesis was to create an integrated approach to hydro-geomechanical characterization for coal seam reservoirs in the context of primary CBM production, with the foresight for applications to ECBM and CO_2 storage. This was accomplished by modifying an existing characterization coalseam reservoir workflow by identifying areas where geomechanical advancements can be included, as indicated in Figure 2. Additional discussion is provided in Chapter 2.

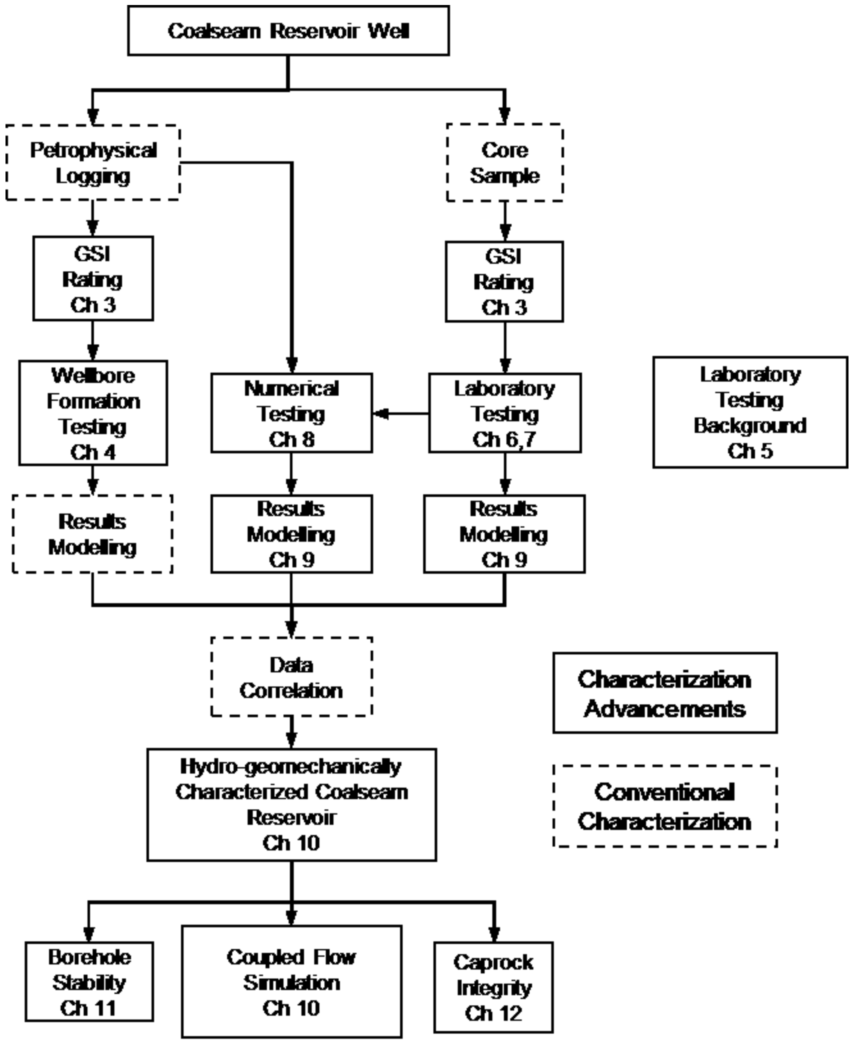

Figure 2. Hydro-geomechanical coalseam reservoir characterization workflow showing locations of advancement and associated chapters of discussion.

Once the characterization methodology was created, laboratory, numerical, and field tools for testing inside of the framework were developed and applied. The results from the testing were used along with the geological strength index (GSI - a geomechanical characterization index) to link the geomechanical behaviour to flow behaviour. The hydro-geomechanical characterization methodology is then demonstrated with reservoir engineering examples. The research program can be summarized as:

1. Characterization Framework Development.
2. Laboratory apparatus and wellbore tool development.

3. Laboratory testing for mechanical, flow, and gas sorption on coal samples under multiple effective stresses.

4. Investigation into numerical experiments using a particle flow code to aid in scaling between laboratory and field scale.

5. Theoretical hydro-geomechanical relationship development linking strain to change in permeability.

6. Reservoir engineering applications including: borehole stability, coupled reservoir geomechanical modelling for flow, and caprock integrity.

1.5 Organization of Thesis

The structure of this thesis was completed in paper format and those papers have been presented or published in the greater academic community, as follow:

- seven published in International Journals, six presented and published in peer reviewed conferences
- two currently being submitted for publication.

Four Journal papers were published with Dr. Thomas Gentzis of CDX Canada (now defunct), who I worked closely with as part of my NSERC Industrial Postgraduate Scholarship. A list of these publications is provided in Section 1.6. The manuscripts have been deconstructed to flow together as chapters, which also serve to remove redundancies from each manuscript.

In the greater context, the manuscripts fall within four categories: Methodology, Testing Tools, Results, and Applications.

The work completed in 'Chapter 2 – Hydro-Geomechanical Workflow' deals with the overall Characterization Methodology by introducing a framework for the integrated hydro-geomechanical characterization of a coal seam reservoir. The remainder of the work presented in this thesis fits inside of that framework. 'Chapter 3 – Rock Mass Classification and the Geological Strength Index' reviews rock mass classification systems and focuses on the Geological Strength Index, which is a key linking component of the characterization integration. 'Chapter 4 – Wellbore Formation Testing' discusses a downhole wellbore formation permeability measuring system and a tool for formation sampling. A general review of coal seams for coalbed methane production is provided in ‘Chapter 5 – Laboratory Testing of coalseam reservoirs’. ‘Chapter 6 – Laboratory Apparatus’ details the laboratory triaxial cell design, a flow system, and a loading system testing of coal for coalseam reservoir applications. ‘Chapter 7 – Laboratory Testing Program and Results’ presents experimental mechanical deformation, strength, and flow testing program and the raw results. ‘Chapter 8 – Numerical Testing – The Synthetic Rock Mass’ discusses numerical characterization experiments using a particle flow code and the results and the application of that work into the overall methodology. ‘Chapter 9 – Data Analysis and Modeling’ develops models based on the laboratory and numerical results and determines how well each set of data fits certain models.

The remaining chapters deal with the application of the characterization workflow to CBM and CO_2 storage applications.

‘Chapter 10 – Applications: Characterization and Reservoir Geomechanical Simulation of CNOOC Nexen’s CBM field for coal stability and production’ uses coupled simulation and numerical simulation along with data from the operator to investigate field issues related to geomechanical. ‘Chapter 11 – Applications: Borehole Modeling’ demonstrates the use hydro-geomechanically characterized reservoir for borehole stability and flow modeling. ‘Chapter 12 – Applications: Coupled Flow Modeling for Caprock Integrity during CBM and CO_2 storage’ then demonstrates the use of those approaches in field scale production modelling and associated CO_2 storage scenarios including caprock integrity. ‘Chapter 13 – Conclusions and Recommendations’ provides overall conclusions and recommendations for future investigations.

1.6 List of Publications

Deisman N, and Chalaturnyk RJ. 2008. *A methodology for hydrogeomechanical characterization of coalseam reservoirs.* The 61st Canadian Geotechnical Conference held in Edmonton, Canada. Sept 21-24, 2008. (GeoEdmonton ’08), Paper 82, Edmonton, Canada.

Deisman N, D Mas Ivars and M Pierce.2008. *PFC2D Smooth joint contact model numerical experiments.* The 61st Canadian Geotechnical Conference held in Edmonton, Canada. Sept 21-24, 2008. (GeoEdmonton ’08), Paper 83, Edmonton, Canada.

Deisman N, RJ Chalaturnyk, D Mas Ivars and C Darcel. 2008. *Geomechanical characterization of coalseam reservoirs for continuum modeling: the SRM approach.* Asia Pacific Coalbed Methane Symposium, Sept 22-24 2008, Brisbane, Australia. Paper 03.

Deisman N and RJ Chalaturnyk. 2008. *Hydrogeomechanical characterization and behaviour of coalseam reservoirs: Theoretical development.* Asia Pacific Coalbed Methane Symposium, Sept 22-24 2008, Brisbane, Australia. Paper 02.

Deisman N, T Gentzis and RJ Chalaturnyk. 2008. *Unconventional geomechanical testing on coal for coalbed reservoir well design: The Alberta Foothills and Plains.* International Journal of Coal Geology. 75 (2008) 15-26.

Deisman N, RJ Chalaturnyk, D Mas Ivars and C Darcel. 2010. *Empirical and numerical approaches for geomechanical characterization of coalseam reservoirs.* International Journal of Coal Geology. 82 (2010) 204-212.

Deisman N, P Lang and RJ Chalaturnyk. 2011. *A Hydromechanical Testing Facility for Tight Reservoirs.* Presented at the 45th US Rock Mechanics / Geomechanics Symposium held in San Francisco, CA, June 26–29, 2011. ARMA 11-538.

Deisman N, H Soderberg, P Lang, and RJ Chalaturnyk. 2013. *Cased wellbore tools for sampling and in situ testing of cement/formation flow properties.* N International Journal of Greenhouse Gas Control. 16 (2013) S62-S69.

Deisman N, M Khajeh, and RJ Chalaturnyk. 2013. *Using geological strength index (GSI) to model uncertainty in rock mass properties of coal for CBM/ECBM reservoir geomechanics.* International Journal of Coal Geology. 112 (2013) 76-86.

Deisman N, RJ Chalaturnyk, R Campbell, and C Virues. 2015. *Borehole stability analysis using results from full field reservoir geomechanics simulation: a CBM case history*. Presented at the 49th US Rock Mechanics/Geomechanics Symposium in San Francisco, USA. 28 June – 1 July, 2015. Paper 15-751.

Deisman N, RJ Chalaturnyk, R Campbell, and C Virues. 2015.*Reservoir characterization and coupled reservoir-geomechanical simulation of CBM using GSI – Case Studies.* Presented at the SPE/CSUR Unconventional Resource Conference in Calgary, Canada. 20-22 October 2015. Paper SPE 175903-MS.

Mas Ivars D, N Deisman, M Pierce and C Fairhurst. 2007. *The Synthetic Rock Mass approach – A step forward in the characterization of jointed rock masses.* The Second Half Century of Rock Mechanics, The 11th Congress of the International Society for Rock Mechanics, 2007.

Gentzis T, N Deisman, and RJ Chalaturnyk. 2007. *Geomechanical properties and permeability of coals from the Foothills and Mountain regions of western Canada.* International Journal of Coal Geology. 69 (2007) 153-164.

Gentzis T, N Deisman, RJ Chalaturnyk. 2009. *A method to predict geomechanical properties and model well stability in horizontal boreholes*. International Journal of Coal Geology. 78 (2009) 149-160.

Gentzis T, N Deisman, and RJ Chalaturnyk. 2009. *Effect of drilling fluids on coal permeability: Impact on horizontal wellbore stability.* International Journal of Coal Geology. 78 (2009) 177-191.

2 Hydro-Geomechanical Characterization Workflow

2.1 Introduction

Current field practices for CBM reservoir characterization present difficulties in obtaining relevant geomechanical data for full resource assessment and production forecasting. Core samples are usually extracted and partitioned by cutting lengthwise for geological interpretation ("slabbed") and are then used in canister desorption testing, crushed for sorption isotherm measurements, and analysed and burned for composition and rank measurements. These practices determine the gas desorption time, the sorption isotherms, as well as conventional information on coal composition if the coal is to be used as fuel (limitations of desorption testing). However, determining the composition and rank gives at best qualitative relationships with coalseam reservoir engineering properties. The aim of coalseam reservoir characterization is to gather sufficient information to aid in extracting in situ methane (or injecting and storing CO_2) from the coalseam.

Levine (2006) summarizes a conventional coalseam reservoir characterization program with four integrated steps, as follows:

- Planning
- Field Procedures
- Desorption Testing
- Compositional Analysis and Characterization

The program planning stage includes identifying the geological and engineering needs, selection of sampling intervals, and the type of sampling (core and/or drill bit cuttings). Testing requirements are identified to measure the requisite properties. The second step includes the onsite procedures, including: specimen selection, identification, and labelling. The third step is the desorption testing including determination of gas isotherms and gas composition. The fourth step would be compositional analysis and characterization including: compositional analysis (determining coal composition through burning), sample characterization (fracture and maceral analysis), sample processing (grinding, cutting, splitting), and sample storage. A standard downhole wellbore injection fall off or build up test provides bulk formation permeability and reservoir pressure. These steps provide standard coalseam reservoir flow properties for modelling including: in situ gas content, gas desorption time, sorption isotherms, bulk permeability, and initial reservoir pressure.

The influence of stress/strain and gas content/composition on the flow behaviour of coal has been well documented but current standard characterization methods do not account for testing under these in situ conditions, therefore the reservoir is not systematically characterized under simulated *in situ* conditions. New approaches for coalseam reservoir characterization through inclusion of hydro-geomechanical behaviour must fit with current characterization practices until advances become accepted in the CBM industry. Therefore, the objective of this chapter is to present a coalseam reservoir characterization workflow, while not deviating substantially from current practices, to obtain flow, mechanical, and hydro-geomechanical coal behaviour under in situ reservoir conditions. This includes laboratory, numerical, and field testing for: flow, deformation, strength, changes in permeability with strain, gas sorption times under stress, and gas isotherms under stress.

2.2 Coalseam Reservoir Characterization Considering Geomechanics

A proposed coalseam reservoir hydro-geomechanical workflow is presented in Figure 3. It incorporates standard practices and includes advancements for hydro-geomechanical characterization. The workflow begins with a well being drilled and core taken from the formation above and below the reservoir, with the knowledge that formations above and below may influence the behaviour of the coalseam, particularly if the coalseam is to be used for CO_2 storage. The workflow splits into two branches: in situ formation testing and core sampling.

In situ formation testing includes petrophysical logging and interpretation and wellbore horizontal and vertical flow testing. Core samples are classified using the Geological Strength Index (GSI) Rock Mass Classification approach, where provisions are made for partially retrieved or fragmented core. Samples are taken from the core and used for reservoir, geomechanical, and hydro-geomechanical testing. Results from the in situ formation testing and core sampling/testing are fed into numerical testing procedures, such as the SRM (Mas Ivars et al 2011), to help correlate the scale gap between in situ and the laboratory. All of the results are used to select and fit theoretical models for reservoir scale work and required engineering applications. Each of the steps in the work flow are addressed in general in this section and then covered in detail, including literature reviews, in the remainder of this thesis.

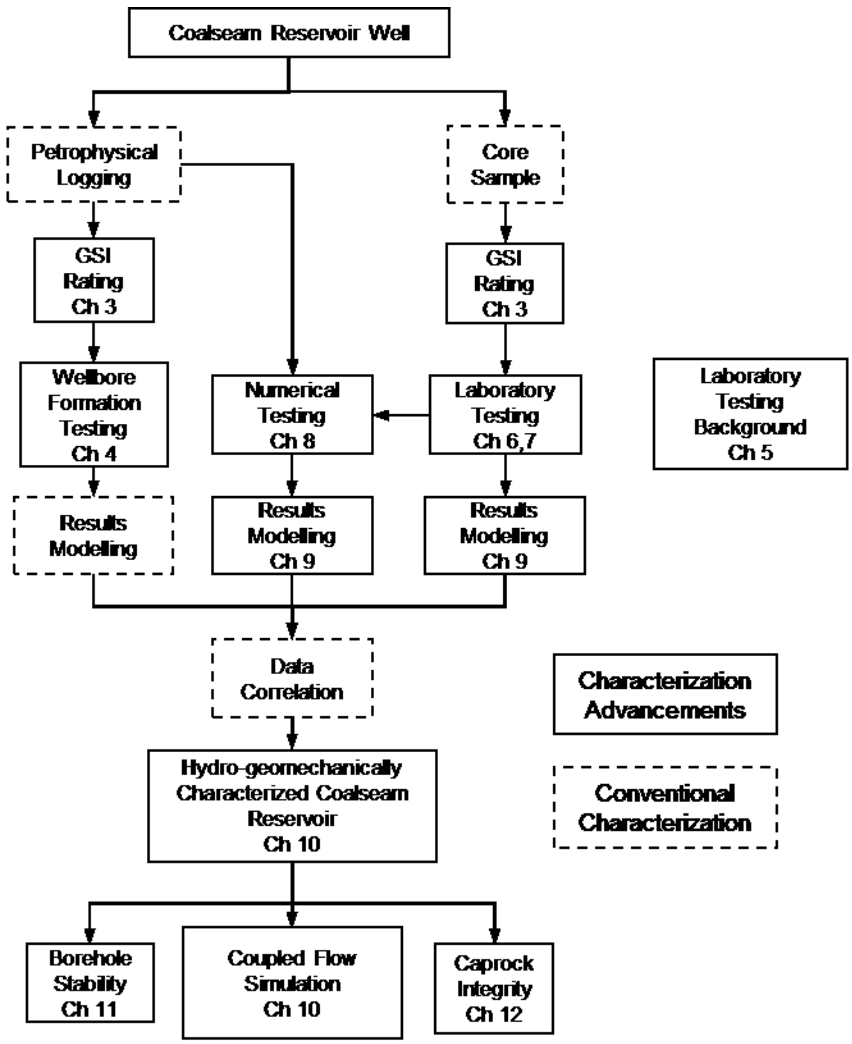

Figure 3. Coalseam reservoir hydro-geomechanical workflow with the dashed boxes representing areas where additions outside of standard characterization are included.

2.2.1 Coalseam Sampling

Obtaining high quality core samples is difficult due to coal's friable nature (Zheng et al., 1991). Characterization using drill bit cuttings is only useful for determining geology or crushed coal sorption isotherms (Levine 2006). Several types of coring options are available. Conventional drill string retrieved core may take too long to return to surface and gas will likely have desorbed. For coalbed methane reservoir continuous wireline core (carried in PVC tubing), pressure core (retrieved under pressure), and sidewall cores may be the best option. Gel cores, which coat the coal with a preservation gel may work if the gel used does not damage the coal.

Once the core has arrived on surface, the core needs to be cleaned, logged, and photographed quickly, then sealed and preserved appropriately. The logging process includes the assignment of an upper and lower Geological Strength Index (GSI) as described in the following subsection. Small pieces of fragment core may be extracted for conventional desorption and gas content testing. Large intact core samples should be preserved for full diameter hydro-geomechanical testing.

Methods to preserve core may include one or more of the following; depending on the length of storage time, required testing, and condition of core.

- Mechanical stabilization
- Heat-sealable plastic laminates
- PVDC (plastic) wraps
- Sealing in disposable inner barrels, liners or tubes.

If the coal is to be left in a liner tube, the tube should be sealed in order to prevent gas and water movement. If the core is portioned on site, the core should be wrapped tightly with PVDC or placed in heat-sealed laminates. Subsequently, the wrapped samples are mechanically stabilized by wrapping and sealing with a high strength tape.

2.2.2 Geological Strength Index

The majority of coal seam properties are dependent on the structure of the coal and require intact core samples with fractures. In most cases the portion of the coalseam recovered for flow or mechanical testing is intact, where the highly fractured, more permeable component of the coalseam is recovered as rubble. Therefore, tested core may not be large enough or contain enough discontinuities to represent the behaviour of coal at the required engineering scales (Bieniawski and Van Heerden, 1975) and recovered and laboratory tested core most likely:

- underestimates in situ permeability
- overestimates in situ strength
- underestimates in situ deformation, and
- insufficiently represents dynamic reservoir permeability.

Therefore, the characterization workflow integrates an empirical Rock Mass Classification (RMC) system to address the influence of fractures on rock mass behaviours. RMC systems are developed to account for the influence of fractures on rock engineering design (Milne et al., 1998) and the Geological Strength Index (GSI) RMC system visually evaluates the rock mass and was developed to work with the laboratory tested rock mass strength (Hoek, 1997) and more recently Young's modulus (Hoek and Deideriechs 2006). An in-depth discussion of GSI is presented in Chapter 3.

2.2.3 Laboratory Testing

Coring programs are expensive and subsampling coal core to create specimens for testing is very difficult, therefore as much information as possible should be gleaned from a single core sample. The goals of laboratory testing programs are to provide relevant data with respect to optimizing coalseam reservoir engineering design, specifically to maximize methane recovery and / or injection of CO_2. There are several laboratory tests available to characterize the flow, mechanical, and hydro-geomechanical properties of coal. Therefore, destructive tests such as triaxial testing, which provide simple strength and deformation behaviour, may not be the most relevant. As well, testing should be done at as close to in situ reservoir conditions as possible.

On site canister desorption testing using a mobile laboratory should be used to determine the total gas content of the coalseam as well as desorption time characteristics. However, only rubalized sections of the core should be used and intact core specimens should be saved for testing which requires larger specimens such as mechanical, flow, and hydro-geomechanical testing. Rubalized zones may also be used for crushed sorption isotherms with the foresight that these isotherms may not represent in situ behaviour.

Cylindrical intact specimens should be prepared from core samples observing ISRM triaxial testing standards however cylindrical specimens which do not meet length requirements may still be used for anything but strength testing. To glean the most information from the specimen, deformation testing using both static and dynamic methods should be completed at multiple effective stresses and gas pressures with a realistic stress path and gas pressures (an example testing program is discussed later).

2.2.4 Well Logging

Downhole well logging includes the conventional petrophysical reservoir evaluation logging to determine coal seam locations. Additionally, industry standard logs useful for hydro-geomechanical characterization are: density, sonic, and formation micro imaging (FMI). The density and sonic logs are used to interpret in situ dynamic deformation properties. If a multiple pole sonic logging tool is used, the formation modulus anisotropy may be determined from the results. This anisotropy in coal may be due to the orientation of the face and butt cleats, and therefore the directional permeability may also be qualitatively interpreted from the modulus results. FMI logging creates a continuous 360 degree borehole image of the formation and can be run in a vertical or horizontal well. FMI logging can be used to interpret fracture spacings and orientations in locations where core was and was not obtained and results may be used to supplement the assignment GSI throughout the full coalseam.

2.2.5 Wellbore Formation Testing

Industry standard well tests are used to determine reservoir pressure and reservoir permeability through pressure build up and draw down tests. Although coalseam reservoirs are known to have anisotropic permeability, determining these values from a single well is not possible. Typically a single value or horizontal and vertical permeability are reported. For thick coal seams a vertical interference test may be done inside of the coalseam if the test assembly is able to capture only the coal interval. In a vertical interference test, three packers are set and fluid is injected between the top and middle packer and the response measured between the middle and bottom packer. The interference test data along with standard buildup/draw down tests would provide at least bulk vertical and bulk horizontal permeability.

2.2.6 Numerical Testing

To aid in filling the void where mechanical data for coal testing does not exist, a numerical testing approach termed the Synthetic Rock Mass (SRM) technique is applied (Pierce et al. 2007). An SRM is two or three dimensional and simulates rock as an assembly of bonded spheres (intact rock) with an embedded discrete network of disc-shaped flaws (fractures). The full or partial coalseam, including zones where no core was recovered, is created with intact strength and modulus from laboratory testing and FMI logging to populate a fracture network. The SRM is then used for coalseam characterization by virtually testing multiple scales (core to the full seam) of calibrated coal containing multiple impersistent fractures. Estimates of rock mass strength and deformation behaviour are extracted from these tests.

2.2.7 Data Correlation

Once all of the testing has been completed, the data must be put together in a systematic approach. The goal of data correlation inside of the coalseam reservoir characterization workflow is to scale the collected properties and data to something that can be applied at the field scale by finding the so called representative element of volume (REV) where the sample size increases and the properties remain constant (if this exists) (Min et al, 2004).

Relationships may be created for:

- Laboratory to field strength;
- Laboratory to field modulus using static and dynamic information;
- Relationships between crushed coal and intact sorption isotherms;
- Stress/strain dependent permeability;
- Stress dependent gas isotherms; and/ore
- Stress dependent desorption times.

2.3 Hydro-Geomechanically Characterized Reservoir

After the data has been collected and correlated, a consistent characterized reservoir model may be developed. Integration of the geological strength index into dynamic permeability models is useful to help understand how pressure, flow, gas contents and effective stress changes throughout the reservoir. If the workflow remains consistent over several wells, a geostatisically populated model may be created for multiple simulations. Once a model is created, there will be sufficient information for studies on: standard flow modeling, well placement, coupled reservoir geomechanics, borehole stability, borehole flow, and caprock integrity.

2.4 Conclusions

A methodology to characterize the mechanical and hydro-geomechanical properties of a coalseam reservoir has been presented. The importance of testing for reservoir properties at reservoir conditions is discussed especially when testing for behaviours which may be stress sensitive. The Geological Strength Index and Numerical testing is presented to help with consistent approaches to scale the strength and deformation properties from a laboratory scale and borehole scales to required coalseam engineering scales. The remainder of this thesis goes into detail on each of the coalseam reservoir characterization workflow sections.

3 Geological Strength Index Rating

3.1 Background – Rock Mass Classification

Intact core coal samples may be acquired by core sampling and used in laboratory testing to obtain coalseam properties. The properties obtained from the mechanical testing will not be representative of the heavily fractured scale behaviour of the coalseam, and therefore will need to be adjusted for use in modelling of full scale operations. This chapter briefly reviews the Rock Mass Classification (RMC) concept, the Hoek-Brown (HB) failure criterion, Young's modulus reduction ratio, the Geological Strength Index (GSI) into the three previous, and the integration of GSI into the hydro-geomechanical characterization of coal for coalseam reservoirs.

Over the past century RMC methods have been used to group rock masses (RM) and empirically account for their mechanical behaviour, for the purpose of creating design charts and estimating mechanical properties for analytical or numerical design analysis (Tzamos and Sofianos 2007; Milne et al. 1998). Several RMC systems have been developed to characterize a RM and some common classifications are the: Rock Mass Rating System (RMR), Rock Quality Designation (RQD), Norwegian Geotechnical Institutes Q system, and GSI. The Hydro-geomechanical Workflow for Coalseam reservoir characterization uses GSI due to its ability to scale from intact (laboratory scale) to field scale.

GSI was first introduced by Hoek (1994) and is used to scale the intact strength of a rock to *in situ* RM properties for direct use in the HB failure criterion (Hoek and Marinos 2007). More recently, relationships between laboratory and field measured Young's modulus have been developed using GSI (Hoek and Diederichs 2006). Figure 4 illustrates where GSI fits into the hydrogeomechanical workflow for coalseam reservoirs. Classifying the coalseam based on an established RMC system – GSI – is key to maintaining consistent hydrogeomechanical indexing throughout the workflow across an entire coalseam reservoir. This chapter reviews the development of GSI and how it was developed to be linked strongly to engineering applications where properties of strength and deformation are required. The remainder of this chapter is organized as follows: the Hoek-Brown failure criteria, GSI, applications to coal, GSI's relation to strength and deformation, and Hoek-Brown and Young's modulus parameter determinations (coal specimens, optimization, and the disturbance factor).

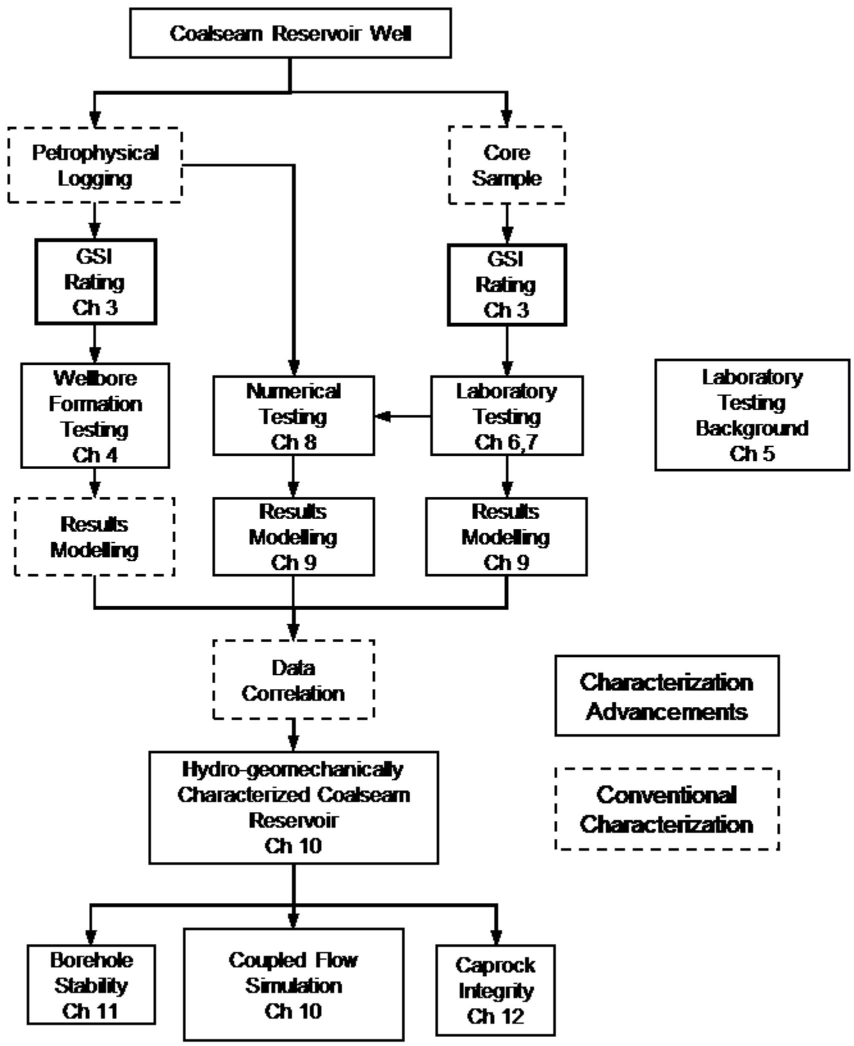

Figure 4. The overall location of GSI into the hydrogeomechanical workflow for coalseam reservoir characterization.

3.2 Hoek-Brown (HB) Failure Criteria

The original HB failure criterion was developed in 1980 to integrate simple geological observations using RMR into a strength criterion for engineering design of tunnels. The criterion focused on being unrelated to scale and copied a formulation developed for concrete in 1936 (Hoek and Marinos 2007). The formulation was created by curve fitting results from a large number of triaxial tests on hard rock and used three parameters: m, s and the intact unconfined compressive strength (σ_{ci}). The criterion assumed that in the field, the rock mass would be confined and could be treated as isotropic due to chaotic fracture pattern and no preferred failure direction. Formal relationships between the rock mass and the intact HB parameters measured in the laboratory were developed using RMR.

Although the original criterion was developed for a confined rock mass, it was being used extensively for slope stability analysis if rock. HB was not developed for this purpose; therefore there was the need to define separate relationships for determining m and s for undisturbed and disturbed rock masses. HB was also being used in very low quality rock masses and the finite tensile strength predicted by the original HB criterion was optimistic. Therefore the exponential variable '*a*' parameter was introduced to replace the original 0.5 exponent by Shah (Hoek and Marinos 2007). HB was then determined to be too conservative and the generalized HB criterion was developed to better fit rock masses with zero tensile strength. Additionally the use of RMR was found lacking in low stress regions. This was the motivation for developing the Geological Strength Index (GSI), which ranges from 100 for intact rock masses to 5 for extremely poor quality RMs (discussed below). All of these modifications result in the currently used version published in 2002 (Hoek et al. 2002) which contains relationships between *m, s, a* and GSI and the disturbance factor D. Douglas (2002) provides several alternate equations for m_{RM}, s_{RM}, and a_{RM} based on statistical fitting of laboratory tests on sandstone, noting that a_{RM} may vary from 0 to 0.9 based on his data analysis.

The disturbance factor is associated with the degree of excavation damage or stress relief and ranges from 0.0 (no damage) to 1.0 (extensive damage/stress relief). The HB parameters σ_{ci}, m_i, s_i, and a , where the latter are determined from curve fitting laboratory triaxial test data to Eq 1 which assumes that sample is intact and undisturbed (GSI = 100 and D = 0). Once measured and curve fitted, the intact HB parameters can be adjusted to the rock mass using GSI and D through Eq 2, Eq 3, and Eq 4; and then incorporated back into Eq 1 for field scale applications. A plot of the influence of GSI and *D* on the overall HB failure envelope is illustrated graphically in Figure 5.

$$\sigma_1' = \sigma_3' + \sigma_{ci}\left(\frac{m_{RM}\sigma_3'}{\sigma_{ci}} + s_{RM}\right)^{a_{RM}} \tag{1}$$

$$m_{RM} = m_i \exp\left[(GSI - 100)/(28 - 14D)\right] \tag{2}$$

$$s_{RM} = s_i \exp\left[(GSI - 100)/(9 - 3D)\right] \tag{3}$$

$$a_{RM} = \frac{1}{2} + \frac{1}{6}\left[\exp(-\frac{GSI}{15}) - \exp(-\frac{20}{3})\right] \tag{4}$$

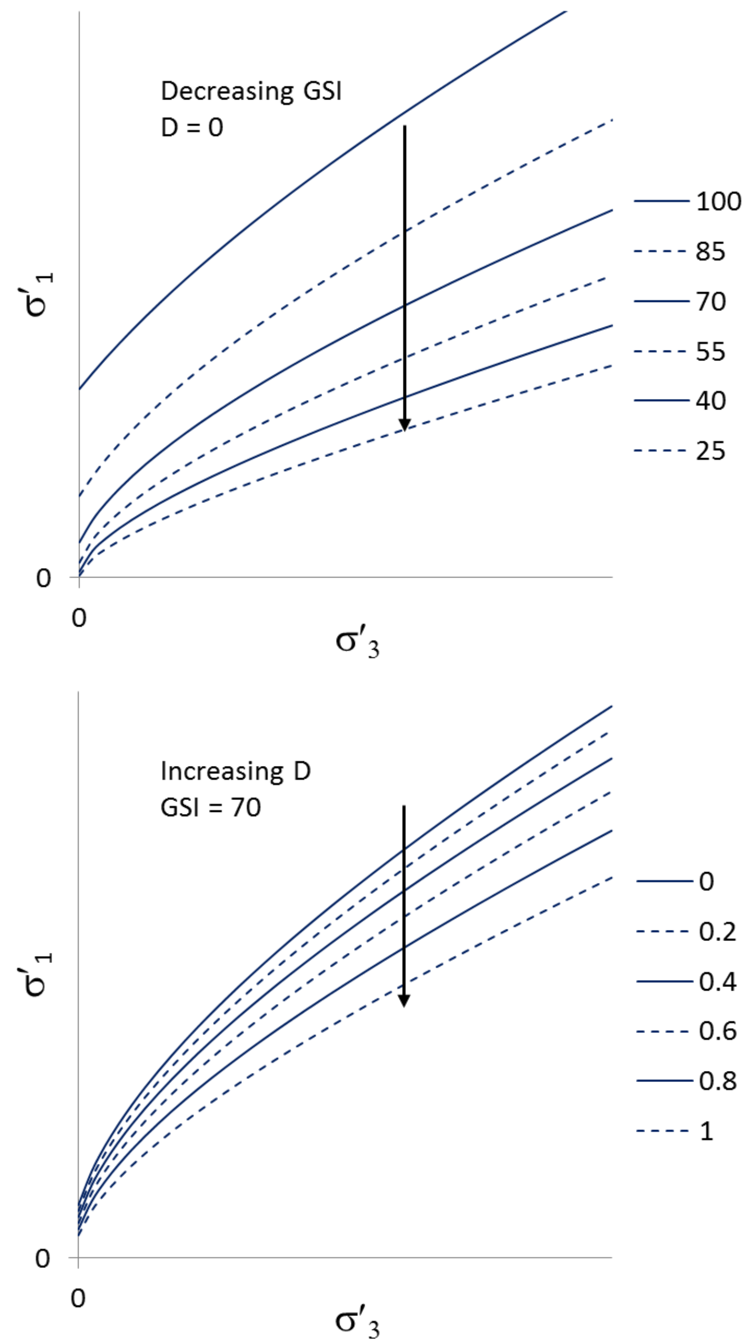

Figure 5. The Hoek Brown failure criteria showing the influence of GSI and D.

The Young's modulus of a rock mass (E_{RM}) is function of the modulus of the intact rock (E_i) and of the fracture spacing and fracture stiffness (Barton et al 1985). Data from numerous field and laboratory tests on Young's modulus led to the relationship by Hoek and Diederichs (2006) between GSI, D and a Young's modulus reduction ratio (E_{RR}). The relationship is presented in 5 and plotted in Figure 6.

$$E_{RR} = \frac{E_{RM}}{E_i} = 0.02 + \frac{1 - D/2}{1 + \exp[(60 + 15D - GSI)/11]} \quad 5$$

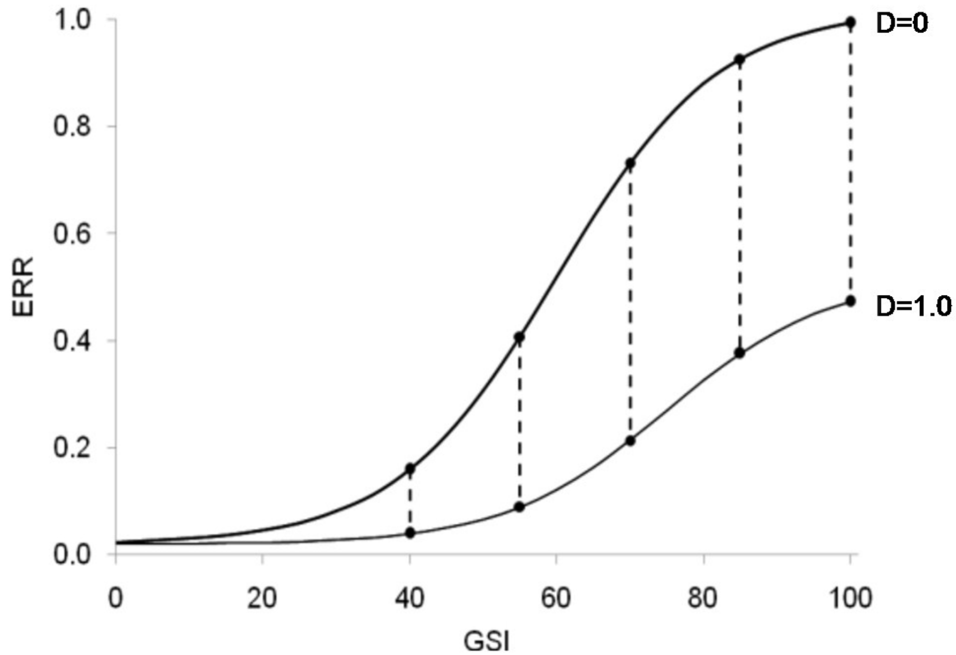

Figure 6. Young's modulus reduction ratio function (Eq 5) using *GSI* and *D*.

3.3 Geological Strength Index

The overarching concept of the GSI is to relate the scale of the discontinuities to the scale of the excavation. For example, keeping the rock mass fracture density fixed, as the size of the excavation increases, the overall strength of the rock mass relative to the excavation decreases and conversely, as the size of the excavation decreases, the relative strength of the rock mass increases. These are two examples of changing the excavation size based on a fixed rock mass fracture density. The second approach would be to keep the excavation size constant while varying the rock mass fracture density (i.e. more fracture in the rock, the rock strength decreases).

GSI was first introduced by Hoek (1994) as a method to scale rock properties derived from testing intact rock to *in situ* rock mass properties through visual comparisons of structure (fracture density and blockiness) and fracture surface conditions. The index was developed based on two general RM concepts:

- Strength of the RM depends on intact properties and freedom of intact rock to move; and
- Freedom of intact rock to move is a function of shape and surface properties.

Figure 7 is taken from Hoek's original publication on GSI indicating when and where the HB failure envelope should and should not be used. The fracture density from the original diagram has been scaled to diameter of the excavation to give a frame of reference for determining the relative scale of GSI to the excavation. If the excavation induced damage parameter *D* can be estimated, it should be accounted for and not confused when determining the *in situ* GSI. Misinterpretation of poorly controlled excavations may reduce GSI by as much as 10 points (Hoek and Marinos 2007).

GSI may be determined visually from surface outcrops, excavation faces, or core logging. If a fragmented core zone is recovered, the material should be used as a basis for estimating GSI (Hoek 1994). Figure 8 shows the original GSI selection chart with its two selection criteria columns: joint (fracture) blockiness and joint (fracture) surface conditions. The blockiness column moves from intact or massive to sheared or laminated. The fracture surface conditions progresses from rough or unweathered to slickenside with soft infilling. Once the blockiness and fracture surface conditions are determined for the RM zone, then a single GSI range is selected from the chart for that RM zone. It is recommended by Hoek (1994) that a GSI range (i.e. 70-75) is more appropriate and reasonable than a single value. Figure 8 includes the fracture density patterns from the original Figure 7 diagram and estimates where the GSI value may fall based on ideal fracture surface conditions.

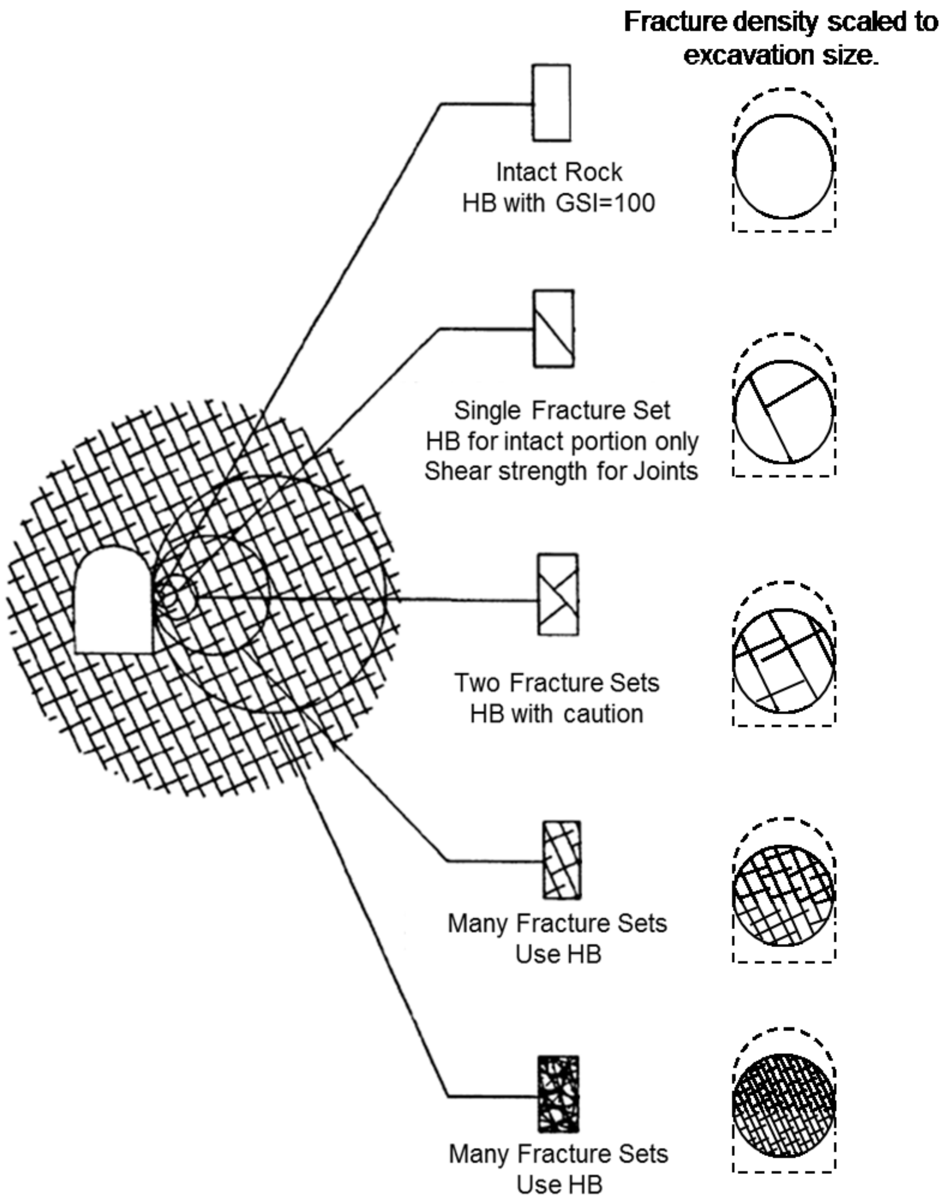

Figure 7. Original scale guidelines for using the Hoek-Brown failure criteria (modified from Hoek 1994).

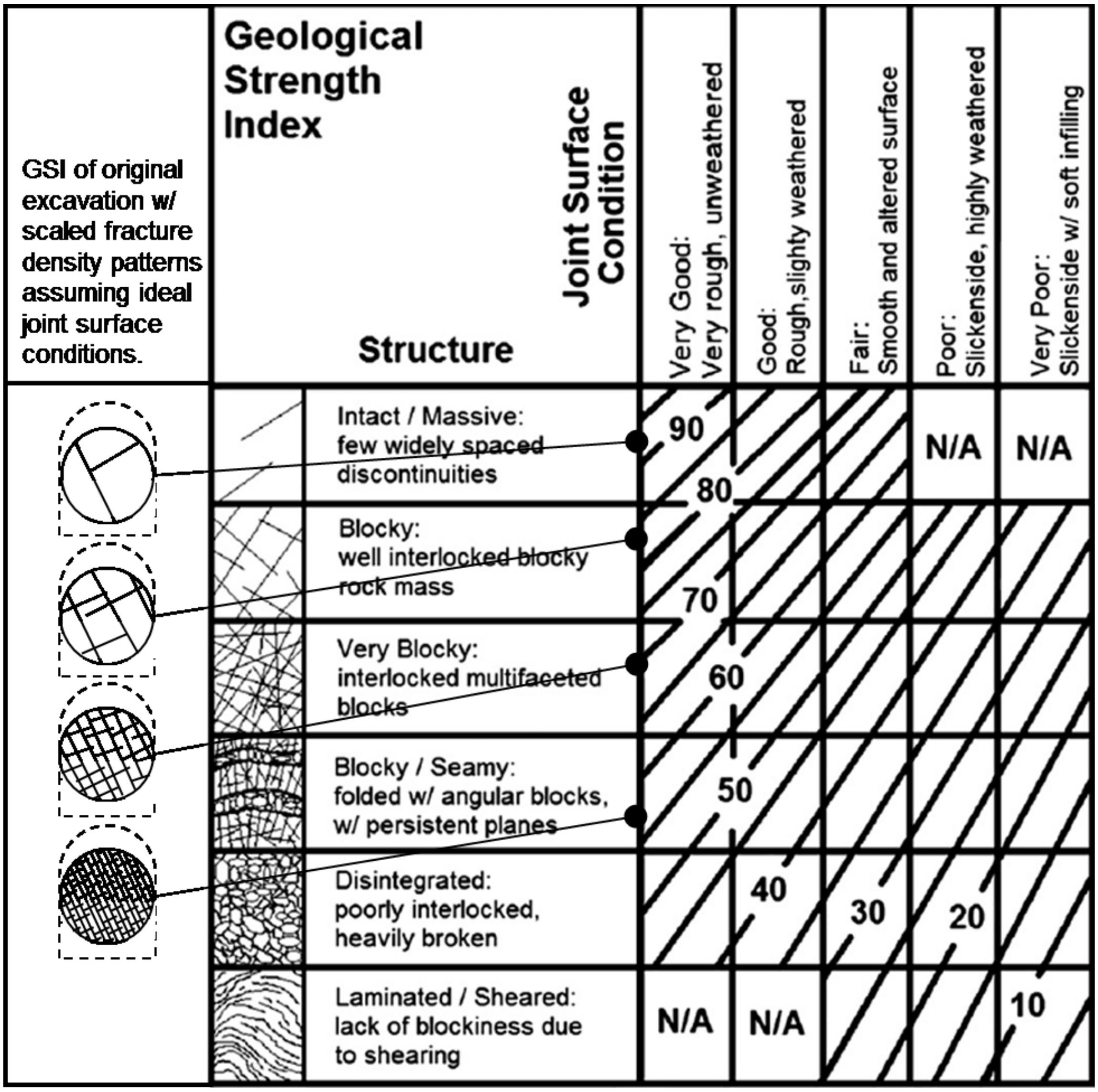

Figure 8. The original fracture density diagram by Hoek scaled to the excavation diameter and the associated value of GSI assuming ideal joint conditions (adapted from Hoek 1994).

3.4 Application to Coal

To date only one researcher has used HB to determine rock mass strength for coal pillar design (Medhurst 1996; Medhurst and Brown 1997). They developed the parameters by testing approximately 60 specimens with diameters ranging from 61 mm to 303 mm. The authors made no attempt to assign GSI to the coal and preferred to use the current Australian system of coal classification (Brightness Profiles) to attempt to match to HB failure envelopes. HB failure envelopes were fit to each of the specimen sizes, with the results for samples of the same brightness rating summarized in Table 2. Their results have shown the applicability of a general form of the HB failure criterion for coal, however, the a parameter which is usually set to 0.5, ranged between 0.5 and 0.65, with 0.65 giving the best overall fit (Medhurst and Brown, 1998). Additionally, results obtained from extensive HB analysis on all types of rock indicate that the parameter 'a_{RM}' may vary between 0.2 and 0.95 (Douglas, 2002).

Table 2. The summary of Hoek Brown parameters m, s, and a from the coal testing program executed by Medhurst and Brown 1997 using an intact UCS of 32.7 MPa.

Diameter mm	M	s	A	Sum of Squares
61	19.4	1	0.5	177
101	13.3	0.555	0.5	26
146	10.0	0.236	0.5	23
300	5.7	0.184	0.6	-
Mass	2.6	0.052	0.65	-

Although coal is often assumed and as idealized as a structured rock mass, photographs of coal by Massarotto et al. (2003) show that in some cases coal may have sufficiently random fractures to warrant it being classified as isotropic (Figure 9). Additionally, Hoek and Brown (1997) site the work of Medhurst and Brown (1997) and make no comments on the inapplicability of HB to coal. They comment that HB should only be used when there are sufficiently closely spaced discontinuities as to create isotropic failure in the rock mass. Saroglou et al (2004) completed studies on highly anisotropic Athens schist stating that the HB criterion could be applicable to anisotropic material. They determined the strength of the schist in several directions and stated that results in the direction that created the lowest strength should be used to determine the HB parameters.

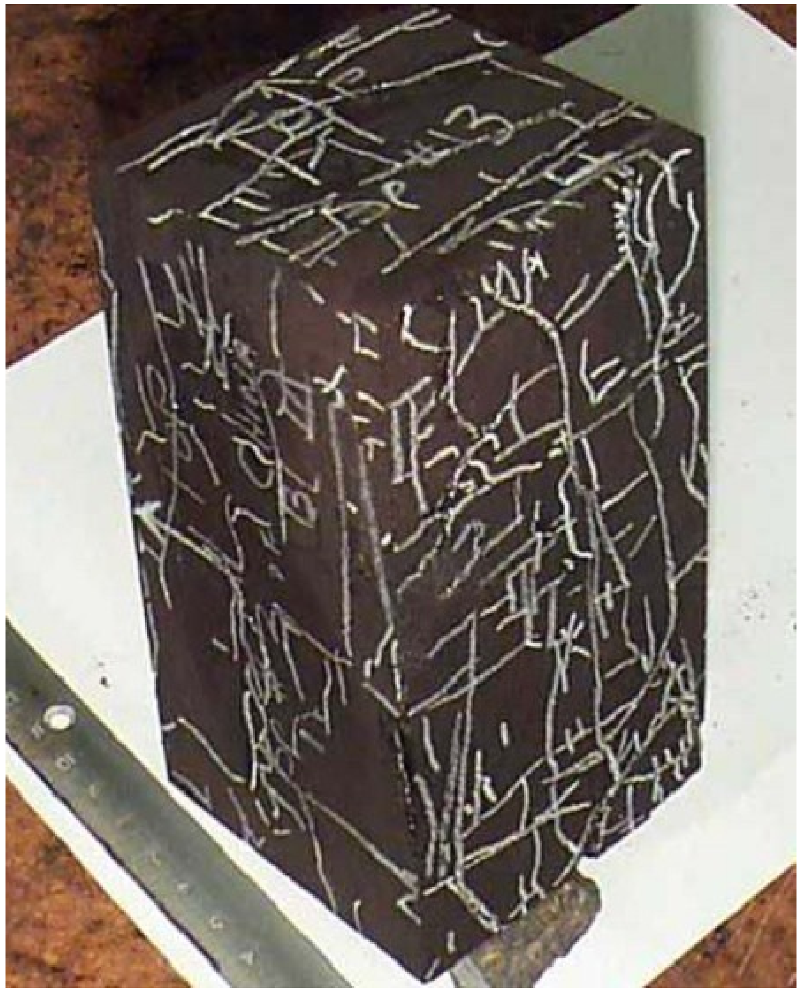

Figure 9. Outline of fractures inside of a coal seam (from Massarotto et al 2003).

The original H–B envelopes used by Medhurst and Brown (1998) shown in Table 2, are reproduced as solid lines in Figure 10. The original degradation of the failure envelope with increase in sample size was matched by varying the HB input parameters σ_{ci}, m, and s, and not through *GSI* relationships. In the smallest sample, diameter equal to 61 mm, face cleats and butt cleats were present (also true for the remaining samples), therefore the smallest sample failure envelope is not representative of the intact coal strength, or intact coal strength HB parameters required for Eq 1, Eq 2, Eq 3, and Eq 4.

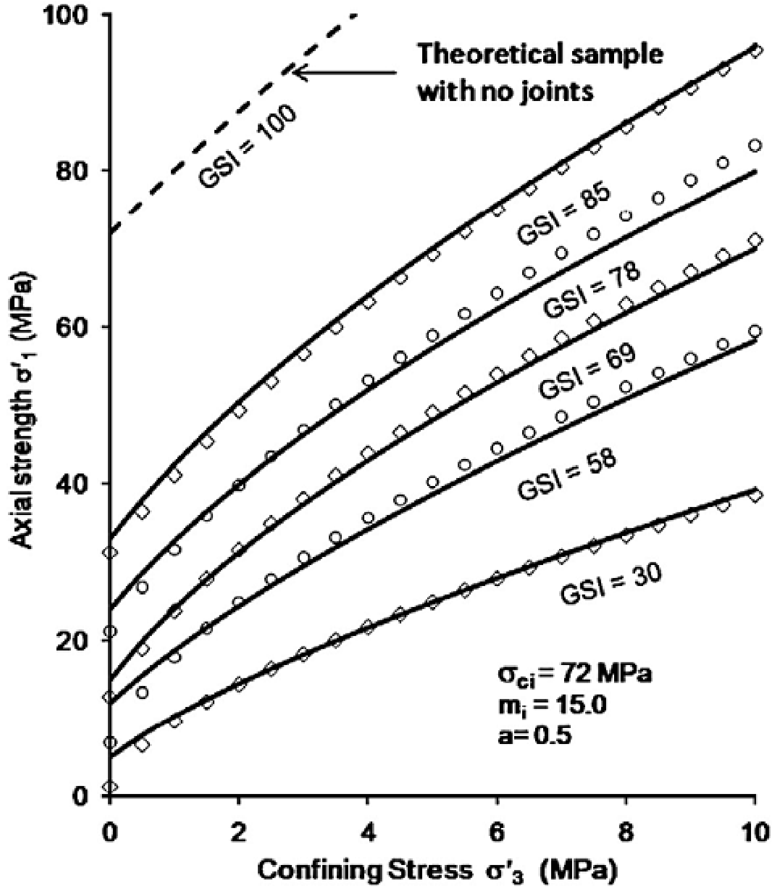

Figure 10. Results from matching coal core strength using *GSI* (open boxes) to data presented by Medhurst and Brown (1998) (solid lines).

Based on the reported major and minor fracture spacings for the 41 61 mm diameter samples (Medhurst, 1996), an averaged reported face and butt cleat spacings, (4 +/−3) mm and (17 +/−3) mm respectively, were used to draw a theoretical cross section of an average 61 mm diameter coal sample cleat structure. (It must be noted that without a detailed picture or joint analyses, that the reconstructed cross section is only a best estimate. In the original work, cleat trace lengths or relative orientations were not reported, therefore it is assumed that all joints are perpendicular, and butt cleats terminate on face cleats.)

The theoretical sample was then used to compare to the *GSI* estimation chart presented by Marinos et al. (2006) by reducing it to the scaling to that of the illustrated joint structure, thus removing the dimensionality (Figure 11). The joint structure falls between the two top illustrations and the joint surfaces are assumed to be in the 'good' category. Therefore, an estimate of *GSI* = 85 was assigned to the 61 mm samples, and the intact properties were back calculated by setting $GSI = 100$, resulting intact properties of $\sigma_{ci} = 72$ MPa, $m_i = 15$, and s = 1 (Figure 11). The remainder of the results was fitted by adjusted *GSI* until the two curves reasonably matched for each of the larger samples. When fitting the larger 141 mm and 300 mm curve data, as well as the rock mass estimate, the H–B curves did not match well in the low confinement (1.5 MPa) region, and the formulations suggested by Douglas (2002) may provide a better fit.

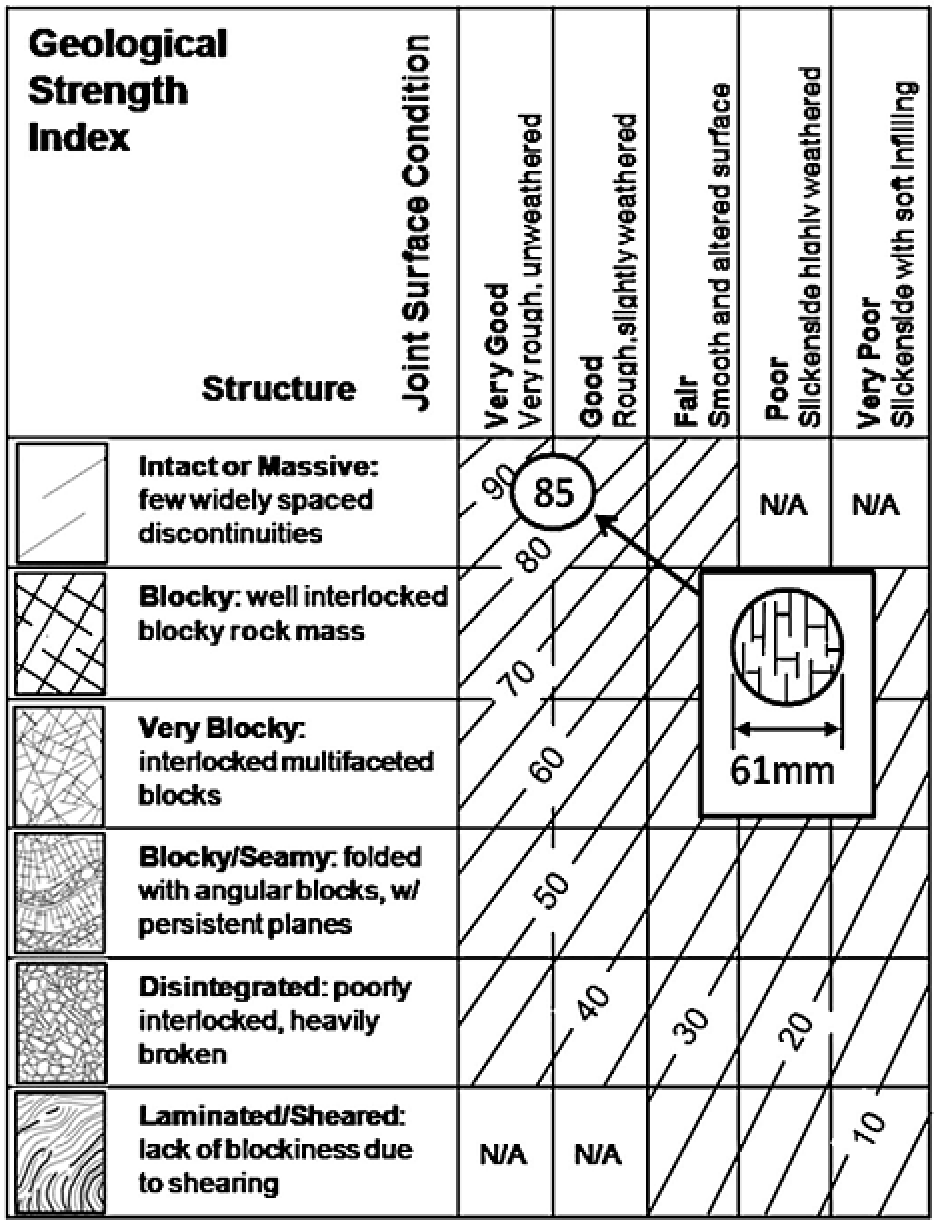

Figure 11. Theoretical reconstructed sample (inset) and the selected value of *GSI* (chart adapted from Marinos et al. (2006)).

3.5 Determination of HB and Modulus Reduction Parameters

The measurement of the intact rock strength is critical for the application of the HB criterion (Hoek and Marinos 2007). Obtaining coal core samples which contain no fractures is difficult and therefore intact HB parameters may not be directly obtained. However it is possible to obtain samples which are intact and contain fractures (Figure 9). One solution is to subsample the retrieved core to a size that does not contain fractures. An alternative technique proposed in this thesis is to use laboratory samples, which contain fracturing; then assign GSI to the core specimen tested in the laboratory and back calculate the intact HB values. This procedure assumes that throughout the section of coal tested, the coal has single intact σ_{ci}, m_i, s_i and a HB parameters, which is also the case for testing any other intact rock to determine any mechanical property. However there is generally variability in testing results of any geomaterial. A similar approach can be used when calculating the intact Young's modulus from specimens which contain fractures. This section describes the procedures to back calculate intact HB and Ei parameters from core specimens. Two fictitious data sets are used as examples here and the techniques are used in the laboratory data analysis later in this thesis.

3.5.1 Specimens

The procedure begins with identifying and selecting coal specimens that all have the same GSI rating. As noted above, GSI may be obtained from core logging. Hoek (1994) notes that the use of HB criterion is only valid for GSI values less than roughly 85 or intact rock (Figure 7 and Figure 8). Therefore, when selecting specimens to be tested for strength, the core should have GSI values less than 85 or be intact. The scale of the problem must also be taken into account to assign GSI. In this case, because the core is tested using a triaxial test, GSI is selected based on the diameter of the core, which means the fracture pattern observed in the core can be directly matched to the GSI chart. A minimum number of three specimens must be tested to fit the HB criterion and all of the specimens must have the same GSI range. A disturbance factor of 0 should be assigned to the core, and a technique for determining disturbance factor is discussed in the determination of the E_i. More samples create be more statistically representative of HB parameters.

3.5.2 HB Parameter Optimization

Once the core specimens are chosen and prepared, a range of minimum effective stresses should be selected that represent the range expected in the field. The test results are then optimized using the Levenberg-Marquardt (L-M) method (Press et al 1999). Based on the formulation of HB with GSI and *D*, the only two parameters that are unknown are σ_{ci} and m_i.

The complete HB fit optimization procedure is illustrated in Figure 12, and described as follows:

1. Estimate initial HB parameters σ_{ci} and m_i.

2. Calculate m_{RM} using Eq 2. GSI has already been determined and the parameters a_{RM} and s_{RM} are constant.

3. Calculate the sum of the squares residual (SSR) for the current iteration *n* using 6, where σ'_1 is the value predicted by Eq 1 and y_1 is the laboratory result. If SSR too large or σ_{ci} and m_i are not constant, continue to step 4. Otherwise stop and the HB parameters have been determined to a satisfactory value.

4. Solve the L-M routine for non-linear regression and return to step 2.

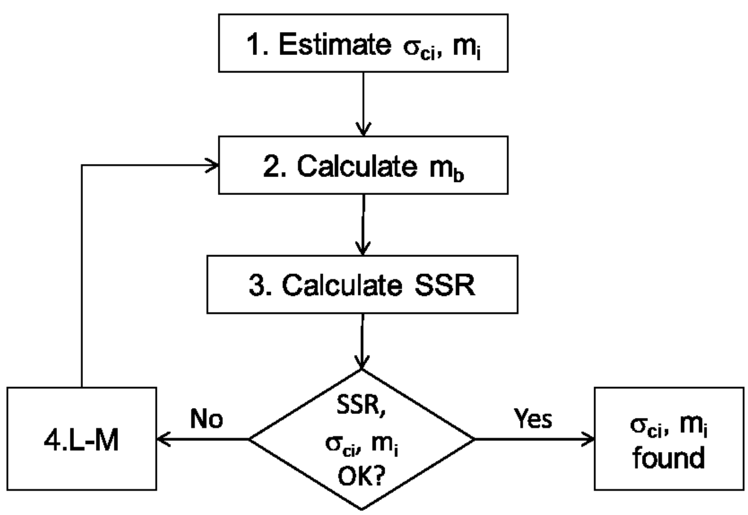

Figure 12. Flow chart for fitting of HB parameters on coal samples which contain fractures.

$$SSR^{n} = \sum(\sigma_1' - y_1)^2 \qquad 6$$

$$\begin{bmatrix} \sigma_{ci} \\ m_{RM} \end{bmatrix}^{n+1} = \begin{bmatrix} \sigma_{ci} \\ m_{RM} \end{bmatrix}^{n} + \begin{bmatrix} \partial\sigma_{ci} \\ \partial m_{RM} \end{bmatrix}^{n} \qquad 7$$

Where the last term in Eq 7 is calculate through Eq 8:

$$\begin{bmatrix} \partial\sigma_{ci} \\ \partial m_{RM} \end{bmatrix}^{n} = \begin{bmatrix} \left(\sum \frac{\partial\sigma_1'}{\partial\sigma_{ci}}\right)^2 + 1 & \left(\sum \frac{\partial\sigma_1'}{\partial\sigma_{ci}} \frac{\partial\sigma_1'}{\partial m_{RM}}\right) \\ \left(\sum \frac{\partial\sigma_1'}{\partial\sigma_{ci}} \frac{\partial\sigma_1'}{\partial m_{RM}}\right) & \left(\sum \frac{\partial\sigma_1'}{\partial m_{RM}}\right)^2 + 1 \end{bmatrix}^{-1} \begin{bmatrix} -\sum \frac{\partial\sigma_1'}{\partial\sigma_{ci}}(\sigma_1' - y1) \\ -\sum \frac{\partial\sigma_1'}{\partial m_{RM}}(\sigma_1' - y1) \end{bmatrix} \qquad 8$$

where the partial derivatives of HB with respect to the variables σ_{ci} and m_i shown in Eq 8 are given by Eq 9 and Eq 10:

$$\frac{\partial\sigma_1'}{\partial\sigma_{ci}} = \left(\frac{m_{RM}\sigma_3'}{\sigma_{ci}} + s_{RM}\right)^{a_{RM}} + \left(\frac{m_{RM}\sigma_3'}{\sigma^2{}_{ci}} + s_{RM}\right)\left[a_{RM}\sigma_{ci}\left(\frac{m_{RM}\sigma_3'}{\sigma_{ci}} + s_{RM}\right)^{a_{RM}-1}\right] \qquad 9$$

$$\frac{\partial\sigma_1'}{\partial m_{RM}} = \left(\frac{\sigma_3'}{\sigma_{ci}} + s_{RM}\right)\left[a_{RM}\sigma_{ci}\left(\frac{m_{RM}\sigma_3'}{\sigma_{ci}} + s_{RM}\right)^{a_{RM}-1}\right] \qquad 10$$

An example of the process is shown here from triaxial testing on coal. Results from Medhurst (1997) testing on the 16DU seam where the average face cleat and butt cleat spacing for the three specimens 61.2 mm specimens where the most similar (Table 3). The fracture spacings were used to estimate a GSI value of 85±2.5. The initial estimates for σ_{ci} and m_i were 20 MPa and 29.5 respectively. The final values for σ_{ci} and m_i were: 17.0 MPa and 32.4 for GSI of 85, 16.6 MPa and 29.1for GSI of 87.5, and 18.2 MPa and 34.0 for GSI of 82.5 (Figure 13). It was determined for this set of data that even though SRR was relatively constant after 25 iterations, the HB parameters σ_{ci} and m_i were not stable until 200 iterations of the regression, therefore focus should remain on the convergence of the HB variables and not the SRR (Figure 14).

Table 3. Results from triaxial testing on coal on 61.2mm diameter coal samples from the 16DU seam.

Depth	Face cleat Spacing	Butt Cleat Spacing	Confining Stress	Young's Modulus	Axial Stress at Failure	GSI Range
(m)	(cm)	(cm)	(MPa)	(MPa)	(MPa)	
101.16	3.5	10	0.2	2490	11.57	85 ± 2.5
101.21	3.5	11	2.0	3230	25.68	
100.88	4	7.5	5.0	4310	47.98	

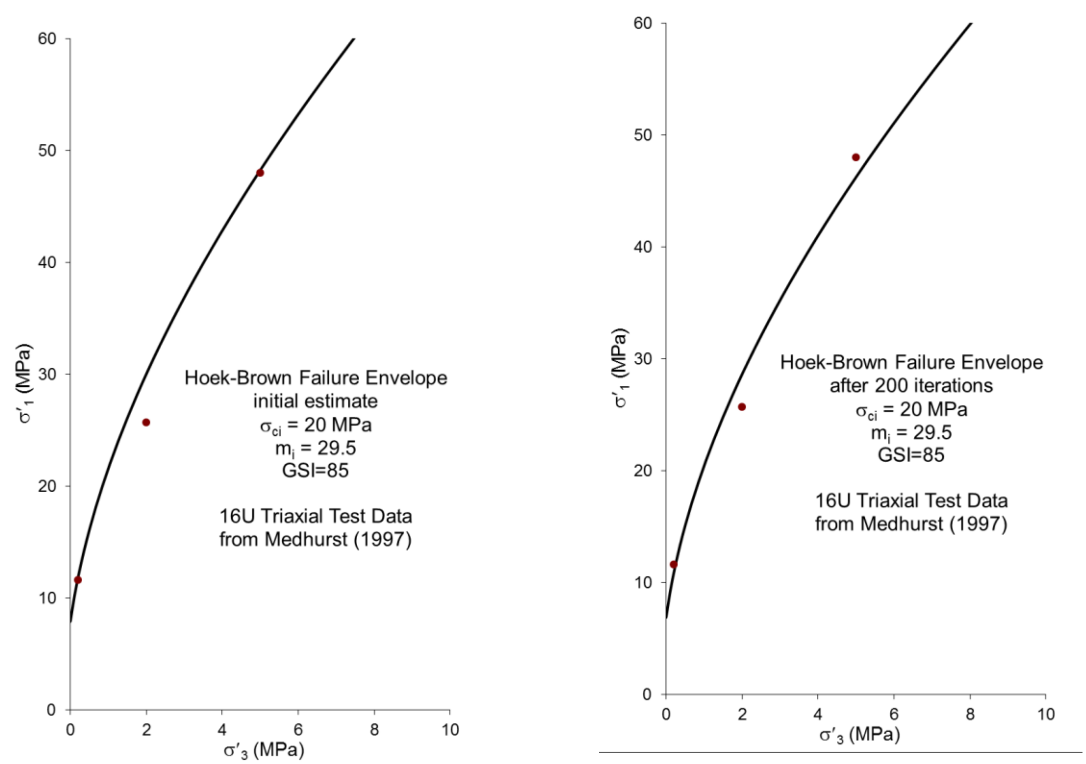

Figure 13. Example of the Levenberg-Marquardt non-linear regression analysis for fitting the HB failure criterion with to the fictions data set where GSI was 85 giving σ_{ci} and m_i of 17.0 MPa and 32.4 respectively.

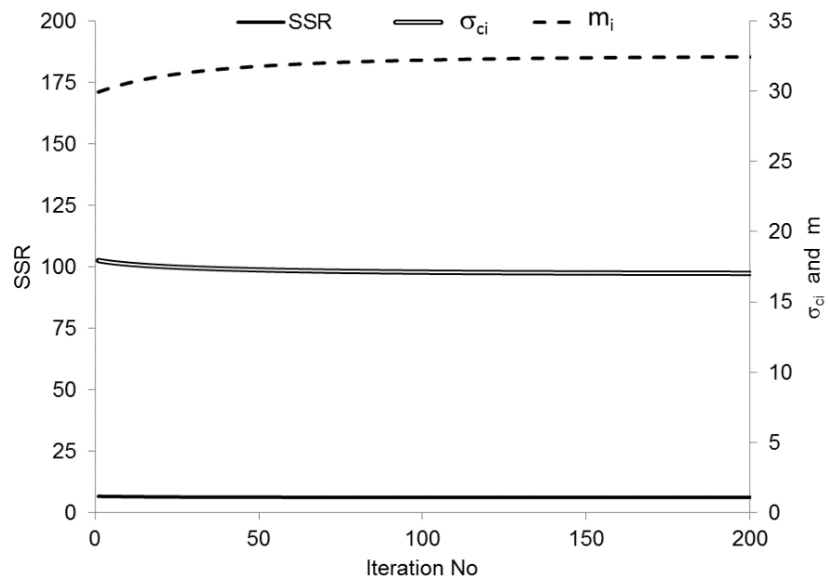

Figure 14. HB parameter stabilization of σ_{ci} and m_i for 200 iterations and the relation to SRR.

3.5.3 Young's Modulus Reduction Ratio and the Disturbance Factor

The Young's modulus of a rock mass is a function of the modulus of the intact rock and of fracture density and stiffness. Based on this observation, Hoek and Diederichs proposed their function for Young's modulus reduction ratio (Eq 5). The *D* parameter was introduced as a method, to characterize the disturbance of the rock mass due to the excavation method which could be blast damage or stress relaxation. *D* ranges from 0.0 to 1.0 for undisturbed to highly undisturbed rock masses. Hoek and Diederichs (2006) give guidance on the selection of *D* stating that *D*, of the rock mass will decrease moving away from the excavation face. It is suggested here that increasing distance from the excavation face is related to the minimum effective stress (σ'_3) and therefore a function can be created to relate *D* to σ'_3.

The E_{RR} function states that for a fixed value of GSI, the reduction in Young's modulus is the greatest when the disturbance is a maximum (*D* = 1.0) and the reduction in Young's modulus is the least when the disturbance is a minimum (*D* = 0). The boundaries of a function which relates σ'_3 to *D* can be established assuming that the maximum disturbance (*D* = 1.0) occurs when σ'_3 is 0 and the minimum disturbance (*D* = 0) occurs at the value of σ'_3 where Young's modulus is constant. With these two points set as the boundaries, the values of E_{RR} can be used to establish D as some function of σ'_3. This function may take any shape, and two functions are discussed below. The first function is based on laboratory coal data from Medhurst (1997) and the second is based on the theorectical coal relationship used by Gu and Chalaturnyk (2010).

The first model assumes that D varies exponentially with confining stress and is dependent on a fitting factor h_1 (Eq 11). The h_1 value is used to fit the Young's modulus data as a function of confining stress. Medhurst (1997) tested 61 samples for strength and not specifically for modulus, therefore, the samples which were from the same depth, same seam, and had the same fracture spacings were selected for modelling (Table 3).

$$D = \exp\left(-\sigma'_3 / h_1\right) \qquad 11$$

A similar linear regression scheme used in fitting the HB parameters may be used here, although the partial derivative of E_{RM} with respect to h_1 is more difficult, therefore varying E_i and h by hand with an SRR calculation may provide a sufficient fit for engineering purposes. The fitting method works well by plotting Eq 12 and first estimating E_i and then adjusting h_1 to minimize SSR. The result from this data set is an E_i of 5900 MPa and h_1 of 6.3 MPa (Figure 15).

$$E_{RM} = E_i\left[0.02 + \frac{1-\exp\left(-\sigma'_3 / h_1\right)/2}{1+\exp\left[\left(60+15\exp\left(-\sigma'_3 / h_1\right)-GSI\right)/11\right]}\right] \qquad 12$$

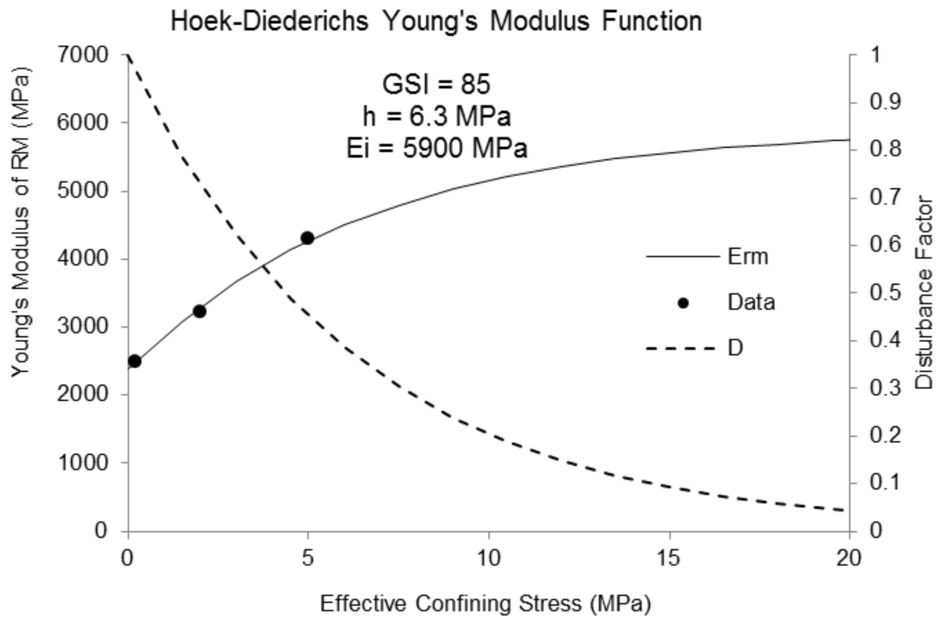

Figure 15. Medhurst (1997) triaxial test results modelled with the Young's modulus as a function of GSI (Eq 12) and the disturbance factor function (Eq 11).

The second case uses Gu and Chalaturnyk's (2010) theorectical relationship equivalent continuum concept (Eq 13) and an aperture update model to define the change in stiffness with changes in normal stress (Eq 14). The equivalent continuum concept assumes that all fractures are equally spaced, have the same joint aperture and the same joint stiffness. The inputs for the model are taken from Gu and Chalaturnyk (2006) and plotted in Figure 16, where: s is fracture spacing (20 mm), initial aperture (30μm), $K^o{}_n$ is initial fracture stiffness (28.8 GPa/m), $\Delta\sigma'_n$ is change in effective normal stress, and u_{max} is the maximum aperture closure (75%).

$$\frac{1}{E_{RM}} = \frac{1}{E_i} + \frac{1}{s \cdot K_n} \tag{13}$$

$$K_n = \frac{K_n^o}{\left[1 - \left(\frac{\Delta\sigma'_n}{K_n u_{\max}}\right)\right]^2} \tag{14}$$

The second function for D (Eq 15) and the rock mass Young's modulus (Eq 16). The shape of the second function is parabolic with three fitting factors: D_{Max}, h_2, and c. The values of the function were determined by plotting the results from the equivalent continuum model and setting up an SSR between Eq 16 and the equivalent continuum. The first step is to determine GSI. Then E_{RM} where the apertures have reached maximum closure in the equivalent continuum model is determined, which is equivalent to $D = 0$. The next step is to fit D_{Max}, which determines the maximum amount of disturbance. Finally h_2 is determined, which is σ'_3 where the E_{RM} is a maximum and constant. The exponent c is then used to fit the shape of the curve. Following this procedure for this model fit, the final values for this case are: E_{RM} = 1011 MPa, GSI = 75, D_{max} = 0.8, h_2 = 0.32 MPa, and c = 2.5. These values give an SSR of 708 which provides a reasonable fit for engineering purposes and is illustrated in Figure 16.

$$D = \begin{cases} D_{Max} - \left(\sigma'_3 / h_2\right)^c, \mathit{if}\ D > 0 \\ 0, \mathit{if}\ D \le 0 \end{cases} \tag{15}$$

$$E_{RM} = \begin{cases} E_i \left[0.02 + \dfrac{1 - \left(D_{Max} - \left(\sigma'_3 / h\right)^2\right)/2}{1 + \exp\left[\left(60 + 15\left(D_{Max} - \left(\sigma'_3 / h\right)^2\right) - GSI\right)/11\right]} \right], \mathit{if}\ D > 0 \\ E_i \left[0.02 + \dfrac{1}{1 + \exp\left[(60 - GSI)/11\right]} \right], \mathit{if}\ D \le 0 \end{cases} \tag{16}$$

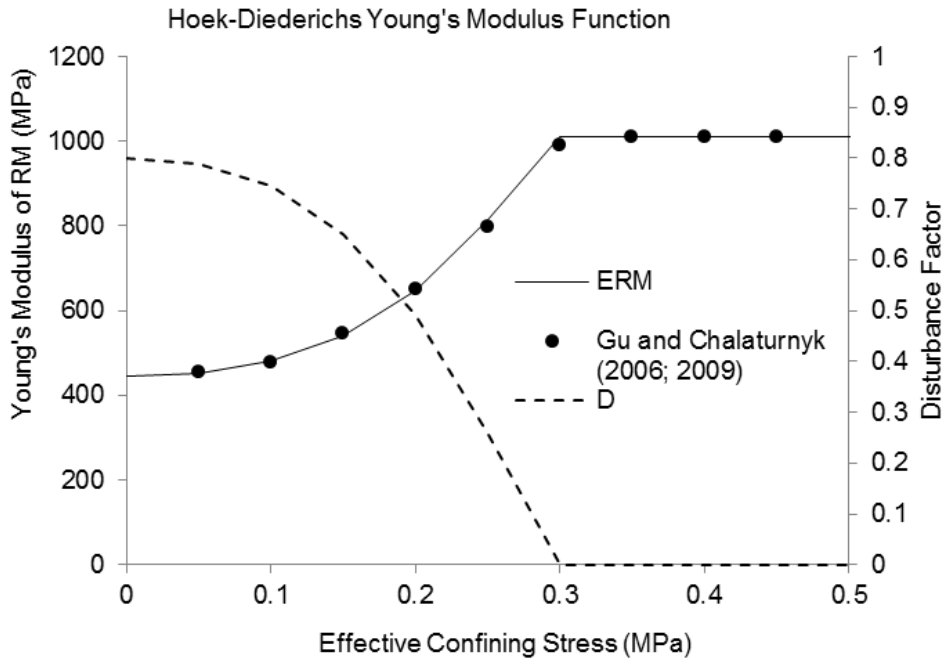

Figure 16. Gu and Chalaturnyk (2009) equivalent continuum function plotted with Eq 16 using the *D* function given by Eq 15 with GSI of 75.

3.6 Conclusions

The application of GSI to coal seam reservoirs and a visual representation of scale for coal seam reservoir characterization have been discussed. Techniques to determine intact Hoek-Brown parameters and Young's modulus values from fractured coal samples through laboratory testing have been introduced. The origins of the empirically developed Hoek Brown failure envelope and the inclusion of the Geological strength index have been reported. Approaches using a specimen scale GSI and back calculated the intact compressive strength and HB m_i parameters using the Levenberg-Marquardt regression approach are shown. Additionally the Young's modulus reduction ratio function developed by Hoek and Diederichs with the inclusion of GSI and *D* has been reviewed. Two relationships for *D* as a function of the minimum effective stress have been developed, with procedures to find fitting parameters. The two models for *D* as a function of the minimum effective stress potentially bracket the function shape where the first model is concave down and the second model is concave up until a maximum E_{RM} is reached at *D* equals zero. There may be other examples for other types of rock, or types of coal, but in these two cases these functions appear to work reasonably well.

4 Wellbore Formation Testing

This chapter addresses the development of two wellbore tools for downhole horizontal and vertical permeability testing and wellbore casing/cement sampling and their applications to coalseam reservoir characterization. Figure 3 illustrates where the wellbore formation testing tools fit into the overall characterization program. The permeability testing pressure transient testing (PTT) tool was designed with Opsens Solutions Inc. and the casing/cement sampling (CemCore) tool Penetrators Canada Inc., in conjunction with Opsens Solutions Inc. Both tools were developed to characterize wellbore cements for CO_2 storage applications. The tools were deployed in May 2011 to characterize a well in the Weyburn field set for abandoned which was exposed to CO_2 for the International Energy Agency Green House Gas (IEAGHG) Weyburn–Midale CO_2 Monitoring and Storage Project and a complete review of the wellbore testing program can be found in Hawkes and Gardner (2013).

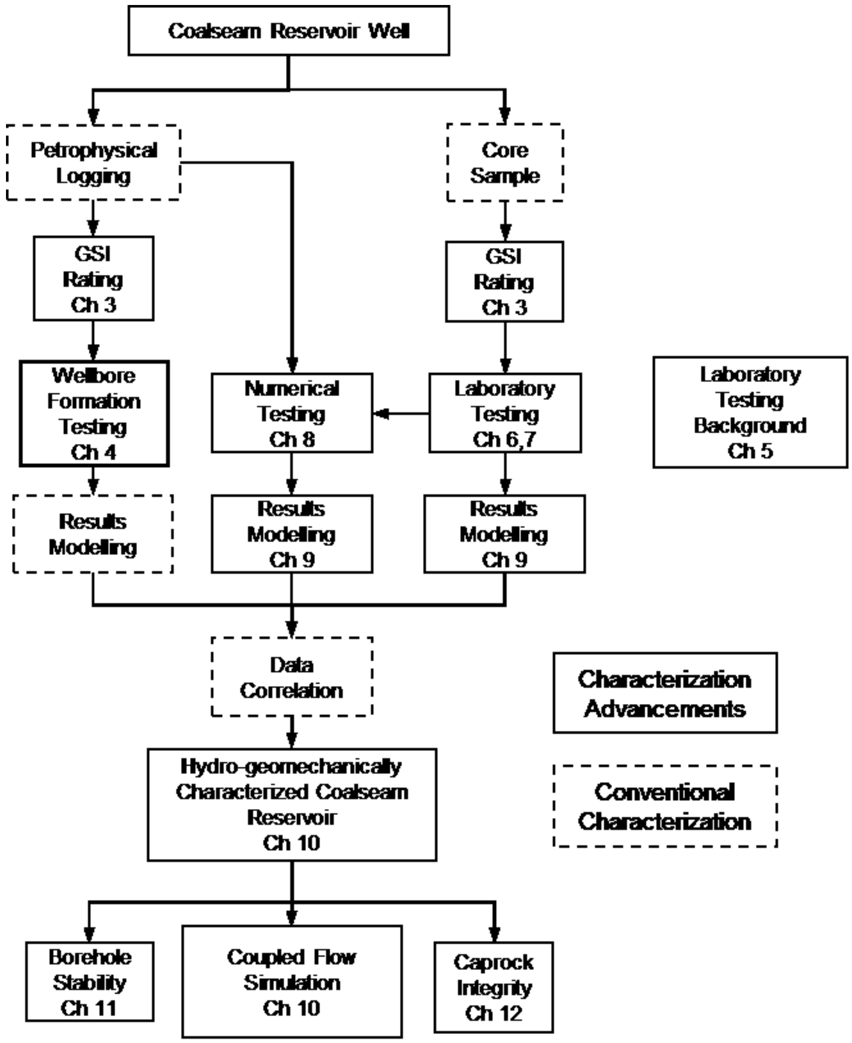

Figure 17. Coalseam reservoir hydro-geomechanical workflow showing where wellbore tools fits into the overall characterization approach.

Previous wellbore testing by Crow et al. (2010) used a wireline-deployed packer system to conduct a vertical interference test over a 3.35 m interval in a 177.8 mm diameter and 1575.5 m deep 30-year-old CO_2 production well. Their program also collected several 22 mm diameter cement samples. The PTT and CemCore tools were designed for a 139.7 mm diameter wellbore. The PTT tool is carried on coiled tubing with internal fluid and instrument cables and is capable of testing a formation interval 0.5-3.68m thick at depths up to 1600m. The CemCore tool is based on an existing wellbore tool perforation tool which can be deployed on coiled tubing or drill pipe with no current depth limit.

Although the tools were designed for a specific CO_2 wellbore program, each tool was built with sufficient flexibility to allow for use in other downhole applications. When doing injection/falloff testing in a cased well, there are two systems that are being tested: the formation and the cement. The CemCore tool allows for retrieval of intact wellbore cement samples which may be tested directly in the laboratory, thereby determining and removing the unknown cement permeability. The development, deployment, and solutions from the data obtained by the tools are described below.

4.1 Pressure Transient Test Tool Design

The PTT tool was designed to isolate two separated sets of holes (pseudo slots) drilled through the well casing and cement once the tool was lowered to the desired depth on coiled tubing. A fluid pulse would be applied to the top hole set, pass down the tubing, and into the top slot. The pulse would then be transmitted through the cement/formation interfaces and response measured in the bottom hole set. This pulse testing concept was based on pressure transient testing across a cylindrical laboratory specimen (Hsieh et al., 1981; Neuzil et al., 1981). The distance between the two pseudo slots and hole sizes are required inputs for design, so numerical simulations were used to provide required information.

Numerical Modelling for Design

Numerical modelling of the near well area fluid flow through the pseudo slots was used to understand pressure responses in the lower slot due to pressure changes in the upper slot. The results aided in the development of the PTT tool configuration including: interval spacing, slot/hole spacing and sizes, and effects of different applied pressure pulse wave forms. The first set of simulations was completed by Ornes and Chalaturnyk (2008) in a wellbore in permeable sands using Comsol 3.2 (Comsol Inc., 2006). Results aided in understanding of pressure wave forms and system responses including constant pressure, sinusoidal pulses, and square pulses.

A second set of simulations, building on this initial work but focused on the wellbore investigated in this program, was completed by research collaborators at the University of Saskatchewan using Comsol 3.5 (Comsol Inc., 2008). From an operational perspective, the downhole tool employed to cut holes in the casing performed optimally using a 16 mm drill bit. Accordingly, this dimension was input to the model and the number of holes needed to effectively simulate a slot in the casing was determined. The results showed that 16–20 holes constrained to a 152.4 mm vertical spacing would emulate a slot, thus creating effective flow into the formation. A minimal vertical distance between the two slots was ideal. This dimension was, however, constrained by the initial tool design that was being conducted in parallel to the modeling. The minimum packer length possible was 457 mm, which created a maximum distance between the two slots of 3.68 m. This dimension was used for modelling input and indicated that simulated tests results were acceptable for interpretation.

A third study was completed by Itasca Consultants AB (Sweden) using FLAC3d (Itasca Consulting Group Limited, 2011) to understand the potential of coupled flow geomechanical effects of the pressure pulse. In addition, the study sought verification of the second study results by using a different simulation code, the design criteria generated by the previous two studies (Figure 18), and the previous results were confirmed.

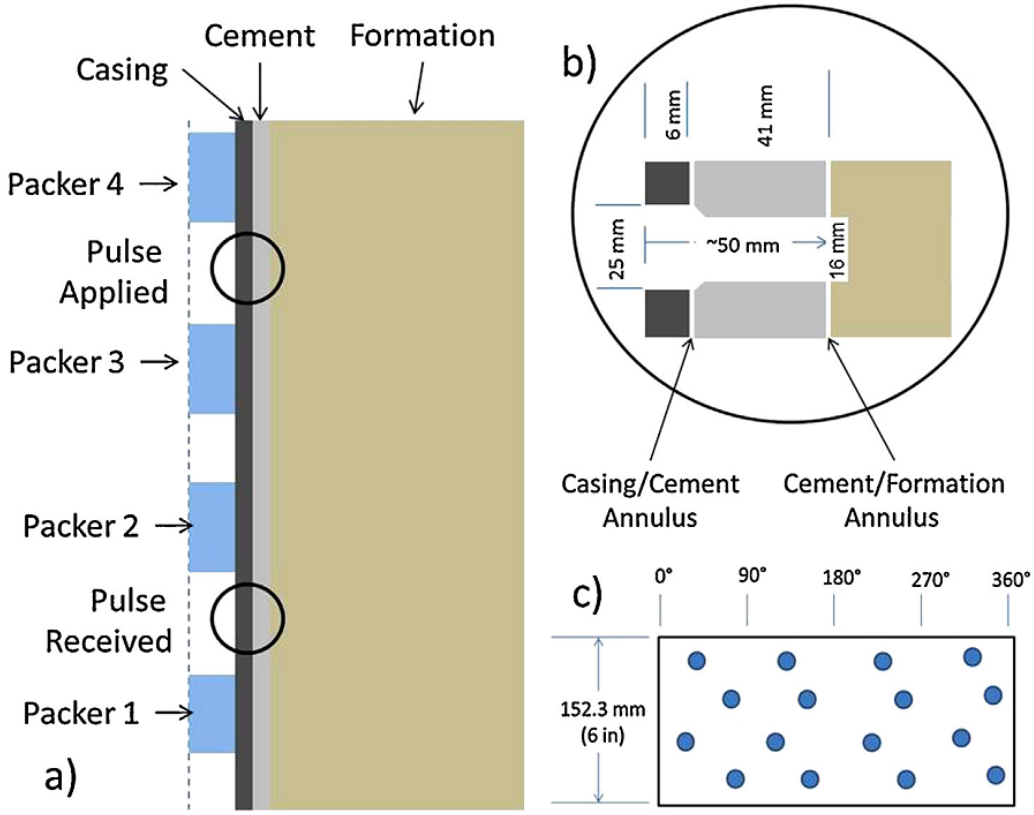

Figure 18. The wellbore model design (a) used to determine the vertical slot distances between applied and received pulse. A sectional view of the interface between the casing, cement, and formation as well as the hole penetration depth is shown in (b) and the

“unrolled” pattern of holes drilled around the inside of the casing to simulate a slot is shown in (c).

Initial Tool Design

The Vattenfall Quadruple Packer Tool (VQPT) provided some of the initial design concepts for the PTT (Ask et al., 2009). The VQSP was designed for measuring stress (up to 68 MPa) during hydraulic fracturing in small 76 mm boreholes in conjunction with measuring formation permeability through single-port injection leak-off testing.

With initial parameters determined from numerical modelling (and input from other researchers and industry), the final concept for PTT tool design was developed. The initial design consisted of a three packer system to isolate the top and bottom hole sets with a third packer in the middle to separate the two slots (Figure 19a). A pressure and temperature sensor (P/T) would be placed in the top and bottom interval to measure the applied and received pulses. This design, however, offered no on-site ability to interpret pulse bypass if the central packer did not create an effective seal, so a four-packer design was selected with a central P/T sensor to monitor fluid bypass (Figure 19b). This four-packer design also allowed for increased measurement sensitivity by reducing the volume of fluid in the receiver section of the tool.

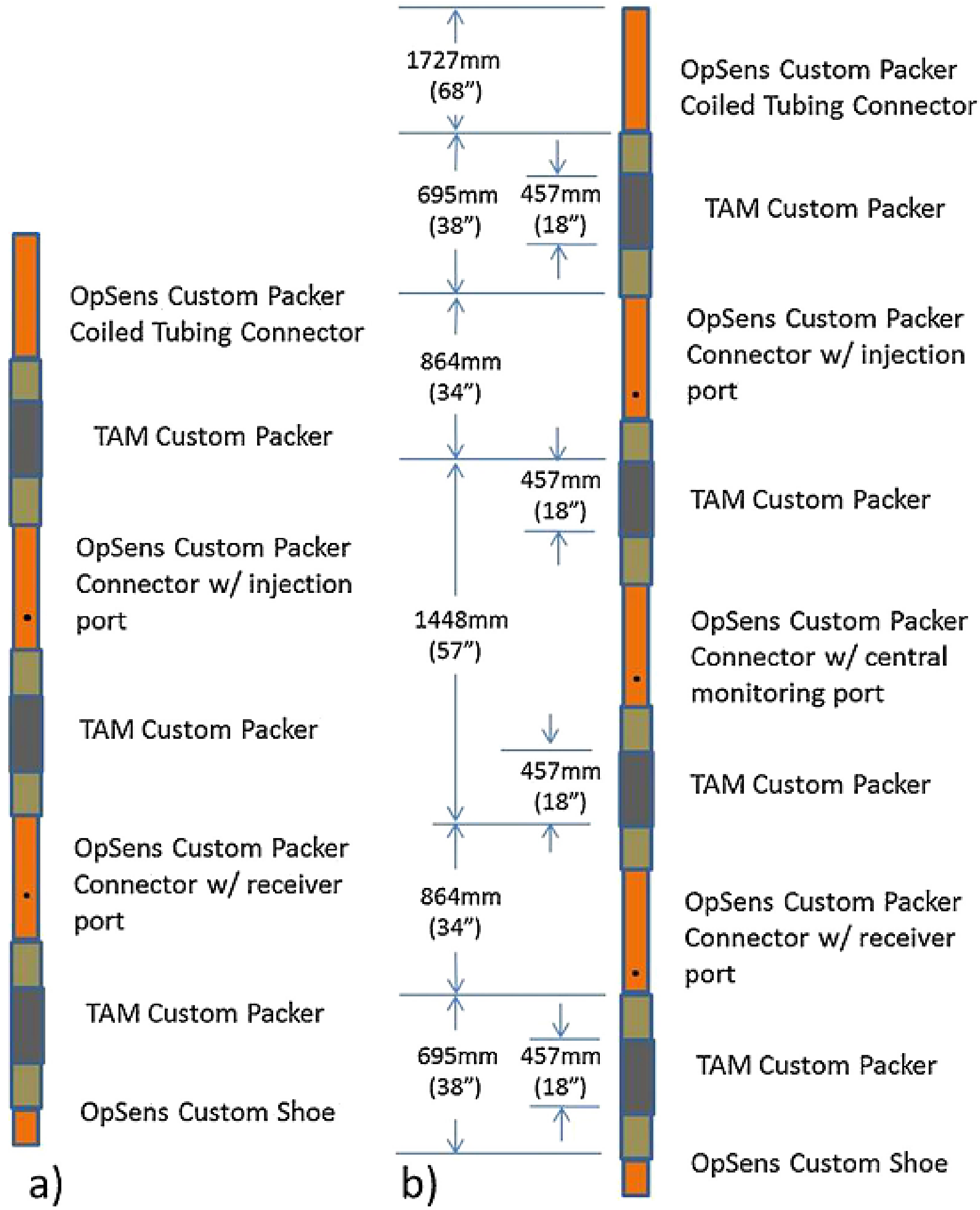

Figure 19. (a) Initial three packer design using TAM custom packers and custom packer connections. (b) The final four-packer design, with a central monitoring port.

Final Tool Design

The final PTT design consists of four inflatable packers, eight P/T sensors, and injection, receiver and monitoring ports (Figure 20). The PTT tool is connected to coiled tubing, which contains four packer control lines and two signal conductor lines, and transmits the fluid pulse to the formation.

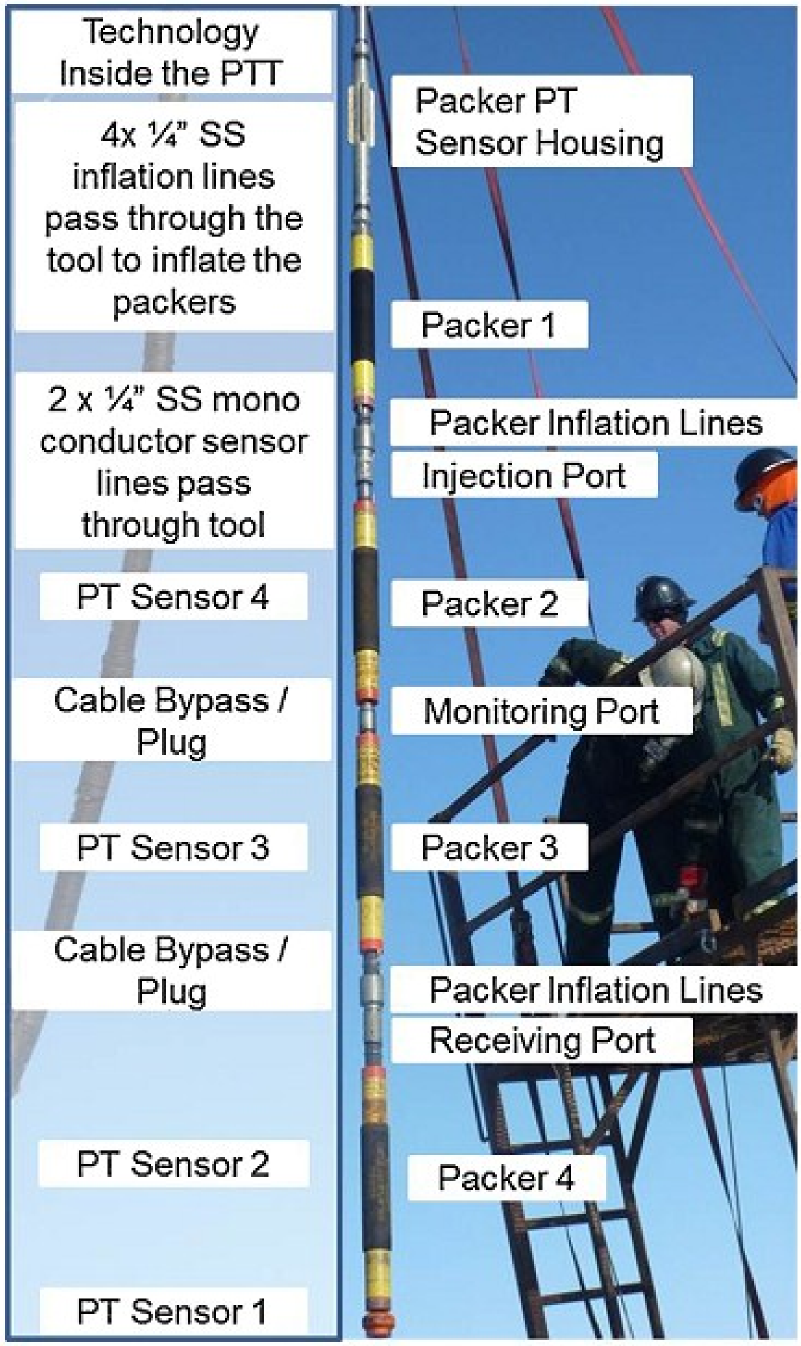

Figure 20. The complete PTT tool showing the internal instrumentation, the packers, and receiving ports.

The packers are individually controlled by four 6.35 mm diameter stainless steel 117 MPa packer inflation lines inside a 1600 m long and 38 mm diameter coiled tube. The packers were custom built by TAM International to meet the length requirements of the PTT tool. Each packer consists of a solid mandrel and an inflation element rated for 6894 kPa differential pressure. The inflation element is 114 mm in diameter and 457.2 mm in length, which is the also the length of the sealing surface minus a minor amount required for packer expansion. The final length of the tool is 6.3 mm.

The packers were inflated with nitrogen gas through a port on the outside of the mandrel. All the packer inflation lines run through the interior of the tool and, as a result, a crossover sub was designed to transition lines from inside to outside at each packer (Figure 21).

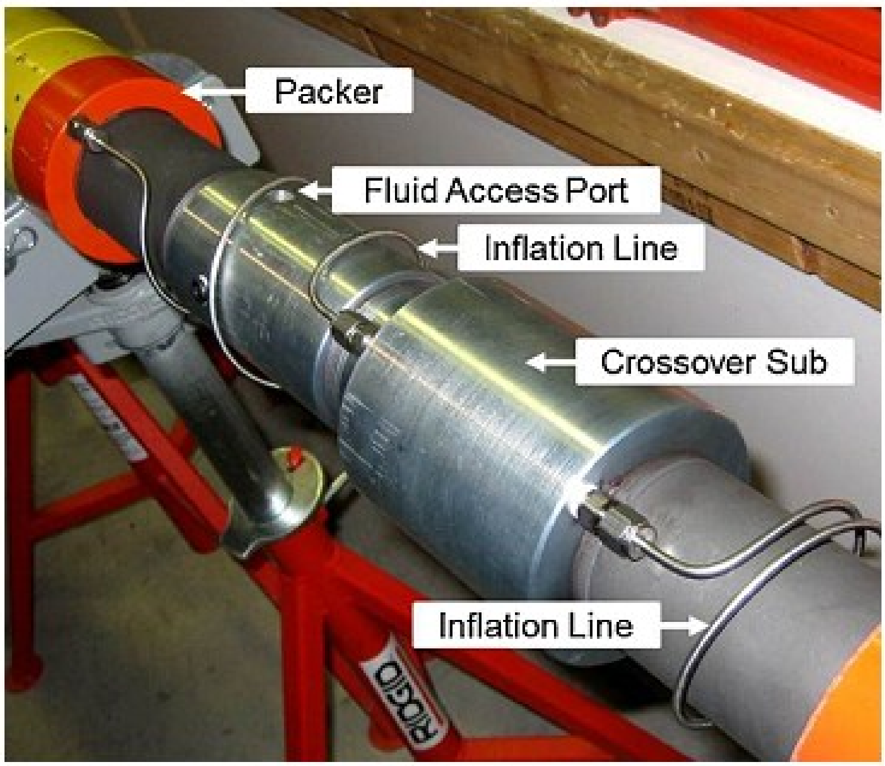

Figure 21. Inflation line crossover and connection to packers

The inflation lines are sealed on the outside of the crossover sub using bored-through Swagelok fittings and connected to the packer mandrel using Swagelok connectors. The individual packer inflation P/T sensors were positioned inside the tool, eliminating the requirement of calculating the actual in situ pressure from surface measurements. Discrete downhole sensors were included to identify issues with packer sealing by comparing uphole pressures on the control board with downhole pressures measured by the sensors. The four-packer P/T signals were transmitted via the first mono conductor signal line.

On the inside of the tool, several plugs were required to create isolated zones for pressure transient testing. As a result, each of the individual inflation lines passed through these plugs via Conax sealed connectors (Figure 22). A Conax connector is a compression fitting that, when torqued, creates a seal by compressing a rubber (or graphite) element around the stainless steel line. At each stage of the PTT assembly, all inflation connections were pressure tested using helium gas. Packer pressure and temperature sensor assembly was tested using nitrogen gas at pressures greater than the anticipated bottom-of-hole test conditions. The internal plug and National Pipe Thread (NPT) tapered thread sub to packer transition seals were tested by filling and pressurizing the tool to 6.89 MPa with water.

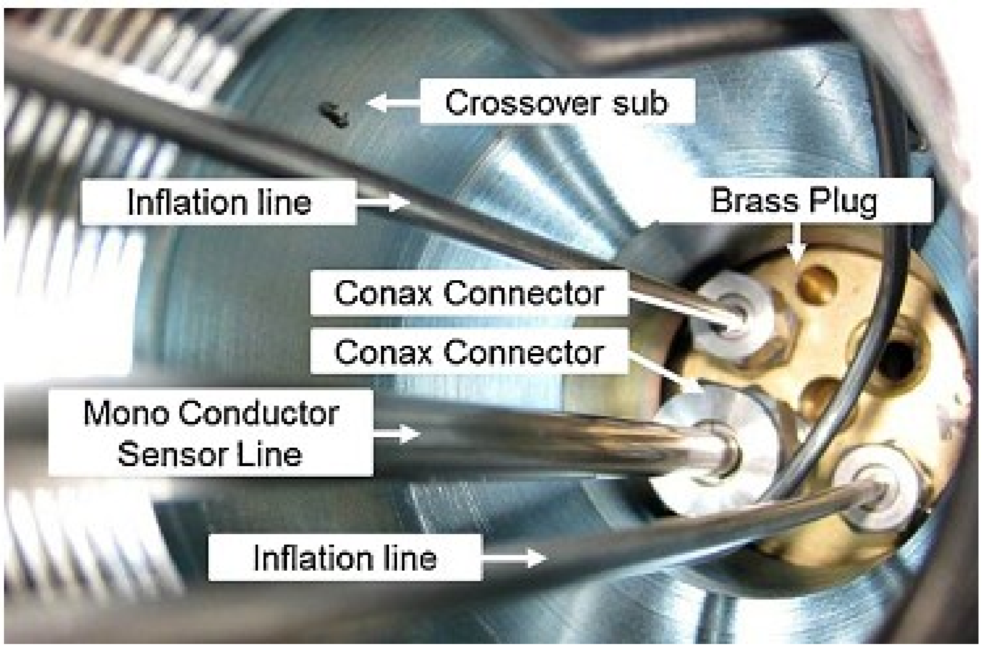

Figure 22. Inside the packer inflation crossover sub showing mono conductor line, two packer inflation lines, isolation plug, and three Conax connectors.

Sensor System

The PTT tool is designed to monitor pressure and temperature at the point of fluid delivery and reception rather than through a bypass line with the sensors located above the tool. The pressure and temperature sensors were supplied by Canada Tech (Permanent Tool Piezo 20.7 MPa at 125 °C). A sensor was placed between packers 3 and 4, which is where the fluid pressure pulse is delivered from surface to the pseudo slot (Figure 23). The pressure pulse is then expected to migrate through the near-well area (most importantly, the cement-filled annulus and its interface with casing and rock), and received at the sensor between packers 1 and 2. The sensor between packers 2 and 3 was included to monitor leakage past either of the seals created by packers 2 or 3. A sensor was also placed below packer 1 to monitor pressure and temperature changes below the tool.

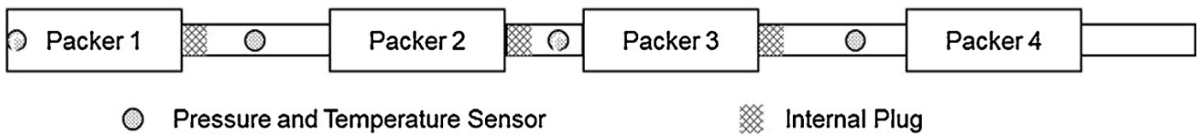

Figure 23. Location of pressure and temperature sensors within the PTT tool.

The signals for the four P/T pulse sensors are transmitted via the second mono conductor line which passes through the entire length of the tool (Figure 24) and to surface. During PTT tool construction, each of the sensor connections was tested with pressurized helium. The Conax fitting seals were checked during the internal pressurization of the tool test.

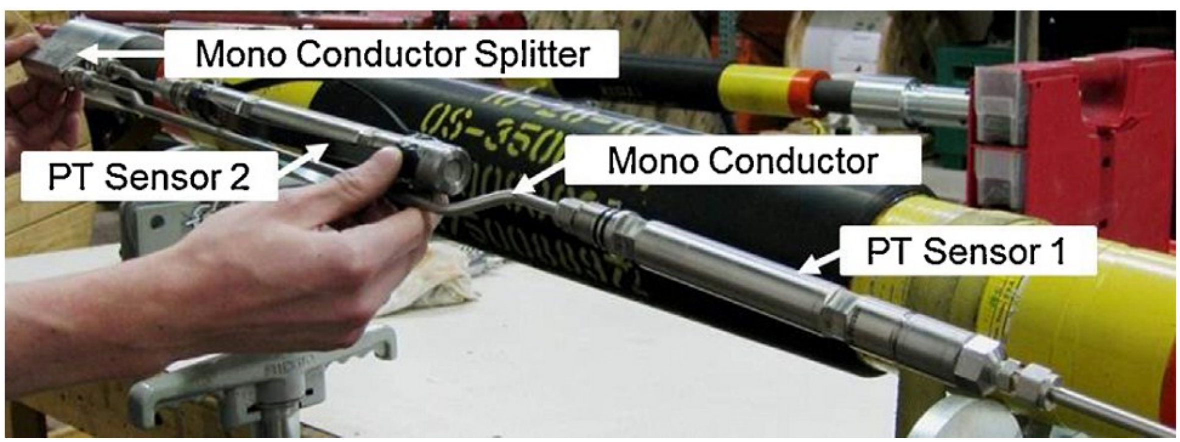

Figure 24. The sensor configuration within the PTT tool showing two sensors, mono conductor cable, and the mono conductor splitter.

Coil and Spool

The PTT tool is connected to the 38 mm diameter coiled tubing on site with a coil-to-tool connector. The connector allows the four packer inflation and two instrumentation lines which control and monitor the PTT tool to connect at a single point. Six set screws are used to create minor indentations in each of the control and monitoring lines, thus preventing translation and rotation of each line. The connector is also used to attach a long stabbing bar that is required to pass the coil through the coiled tubing injector head (“stabbing the coil”). Once the coil is stabbed, the stabbing bar is removed, the tool control lines connected, and then the tool is coupled to the coiled tubing. The coil also conveys the fluid pulse to the delivery port. At surface, all the stainless steel lines exit the coil through a custom built ‘showerhead’ bypass with sealable Conax connectors (Figure 25).

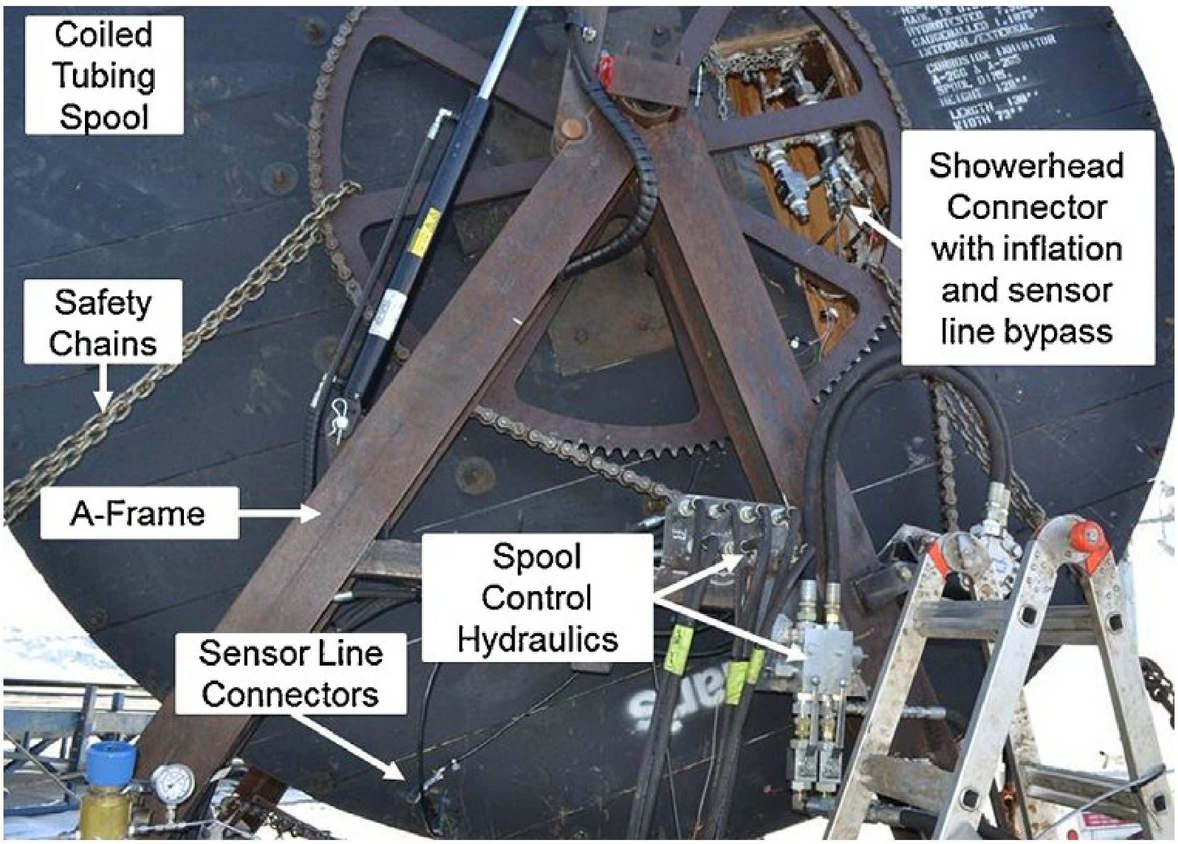

Figure 25. Custom coil power spooler with sensor and inflation line feed through connections.

The PTT tool is lowered to depth on the coiled tubing which is spooled onto a custom stand-alone power spooler designed and built by Balanced Energy Oilfield Services (Figure 25). On the uphole end of the coiled tubing, a window was cut into the side of the spool to allow access to the stainless steel lines. On the end of the coil, a pass-through sealed connector was designed to allow the 6.35 mm lines to pass out of the coil while still being able to maintain pressure inside the coil. This was accomplished by custom building a three-port ‘showerhead’ adapter that connected to the coil and (Figure 25). Custom coil power spooler with sensor and inflation line feed through connections had room for three dual 6.35 mm Conax connectors (Figure 25). All of the connections were tested to pressures between 20 and 31 MPa. In addition to having the three-port adapter connected to the uphole end of the coil, a tee with a bypass valve and pressure delivery port was connected. The bypass valve is required to saturate the entire system by reverse circulation of the well (i.e., pushing fluid down the casing and up the tool). The uphole fittings are 25.4 mm and the entire assembly was connected to the coil by a Swagelok fitting.

Surface Connections

Once outside the coil, all lines are connected from the spool to the transient control unit (TCU). The mono conductor lines are sealed and connected to a water proof military bayonet connector and then to a single soft-sided line, which is in turn connected to the TCU bulkhead connector. The inflation lines are connected to valves on the spool and then to the TCU bulkhead connector. The TCU is designed to contain all of the data acquisition systems, the pressure control using regulators for the packers, the pressure pumps for the test (including fluid reservoirs), and a work bench and tools. All control and monitoring lines are connected to the TCU through the bulkhead and then to the control board, pump, and data acquisition systems.

To control and monitor the PTT tool once at depth, the TCU was designed with a high pressure control and monitoring manifold and a data acquisition system (Figure 26). Once the tool is at depth, the entire testing routine, including packer inflation and pressure for testing, is controlled inside the TCU. Water pressure is delivered to the upper zone by connecting two Teledyne-Isco 500D pumps to the coiled tubing and operating the pumps in continuous flow mode at predetermined rates (25.9 MPa and 200 mL/min).

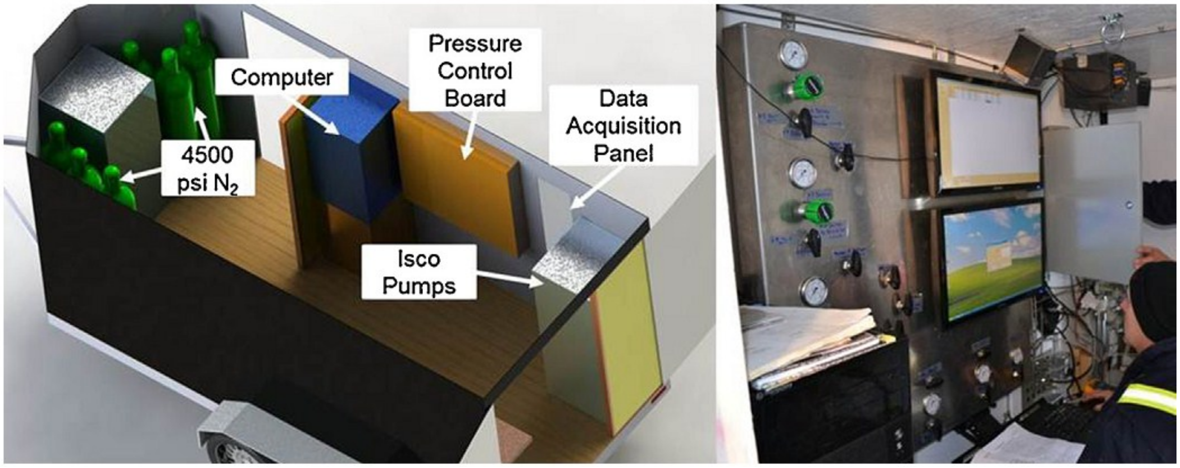

Figure 26. The transient control unit with high pressure nitrogen, pressure control board, Isco pumps, and data acquisition panel.

The packer pressure control board is used to individually regulate packer pressures. The main nitrogen pressure inlet was formed by connecting three 31.0 MPa bottles in series with an additional three-bottle series for reserve. This main source was regulated down to 20.7 MPa and fed into the board. The nitrogen was then delivered to each individual packer inflation regulator. There is a provision to equalize all of the packers or, if required, packers 1/4 and/or packers 2/3. Once nitrogen is delivered for inflation, a single valve enables pressure to be locked in to the packers. There is also an option to vent all nitrogen at any point during the testing procedure. The pressure control board was tested and rated to 31 MPa.

The packer and pressure sensors are monitored by two Canada Tech Dinline II surface assembly control boards. The control boards are linked to the data acquisition computer that records data, controls acquisition rates, and plots data in real time during testing.

Tool Compliance Testing

One of the inputs required to interpret PTT test results is compressibility or compliance of the tool itself. The entire system was, therefore, tested on surface in a 139.7 mm diameter and 8 m long J-55 grade (380 MPa burst pressure) oilfield casing cell. Three ports were drilled into the wall of the casing at the open packer intervals and NPT tapped for valves and fittings. At each end of the casing, caps were screwed on with one cap containing custom Swagelok and Conax feed-through ports tapped for sensor, inflation, and water lines (Figure 27).

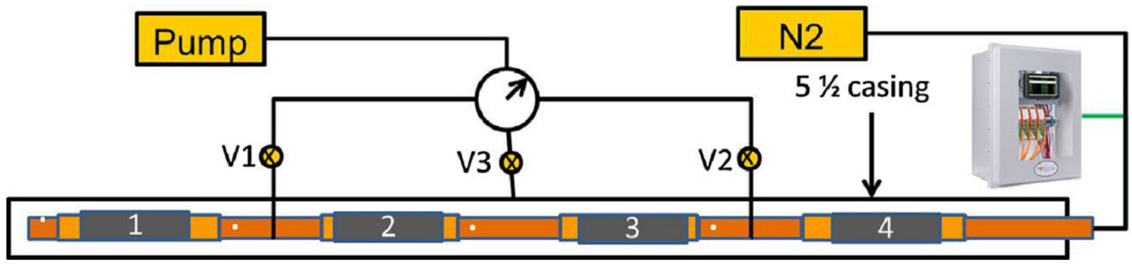

Figure 27. Initial test set up of PTT tool in cell with pump and sensors attached.

The PTT tool was placed into position and the six control lines for the sensors and packers were fed though the end cap, sealing the tool in the casing. The sensor lines were connected to the control panel and the water line was connected to one of the 500D Isco pumps. The packer inflation lines were connected to the TCU control board, and nitrogen was used to inflate the packers. The second Isco pump was connected to three ports that were pre-drilled in the casing and were positioned between the packers on the tool.

The casing, PTT tool, and pump lines were filled with water and all the air was removed from the system. During the first stage of the testing, the fluid in the casing and tool was pressured to 5000 kPa and then the packers were inflated to 4000 kPa above the fluid pressure and held at that pressure. The interval between packer 1 and 2 was isolated using two-way valves and then pressurized above the initial fluid pressure in two steps: 500 kPa and 1.0 MPa. The change in pump fluid volume was measured for each of these stages. The packer interval 2–3 was isolated and then the pressure increase sequence repeated. The changes in volume and pressure were used to calculate the compliance of the tool at each average pressure. After each 1–2 and 2–3 stage test stage, the initial fluid pressure was increased by 3.0 MPa and the test was repeated. This testing sequence continued to 21.0 MPa.

4.2 Cement Coring Tool

The design of the cement coring (CemCore) tool was based on modifications of the existing Penetrators MaxPERF tool. The purpose of the tool was to retrieve cement (and possibly formation) samples in a 139.7 mm diameter cased wellbore. The standard

MaxPERF tool operates by first perpendicularly milling through the casing to expose the cement. The milling extends slightly into the cement and creates a 45°chamfer. The tool changes from the milling bit to the drilling shaft by pulsing fluid pressures, thus indexing the tool and positioning a 2 m long flexible drill shaft over the milled hole. Hydraulic fluid pressure drives an internal motor that rotates the drill shaft into the formation perpendicular to the wellbore.

4.2.1 Design

The CemCore tool uses the same milling technology, but with a modified drilling section, by attaching a coring bit and shortening the drill stem. This modified drill stem is used to drill into the formation and retrieve a cement sample. The sample is retained by being 'press fit' into the core barrel and then retracted into the tool body. The coring barrel is a modified cement diamond cutting coring barrel with a 9.5 mm internal diameter. The maximum rigid end length of the drill stem (without completely re-engineering the MaxPERF tool) was constrained by the 90° corner section that transitions the drill from parallel to the tool body to perpendicular to the tool body. After a slight modification to the transition section, the maximum length that is able to move around the corner is 34.9 mm. The coring barrel was cut this length with 24.9 mm of the length required for threading and connecting to the drill stem. This limitation, caused by not redesigning the existing MAXPerf tool, only allowed for a coring length of 10.3 mm (Figure 28). As a result, the entire cement annular thickness of 41 mm in this field test well was not able to be collected.

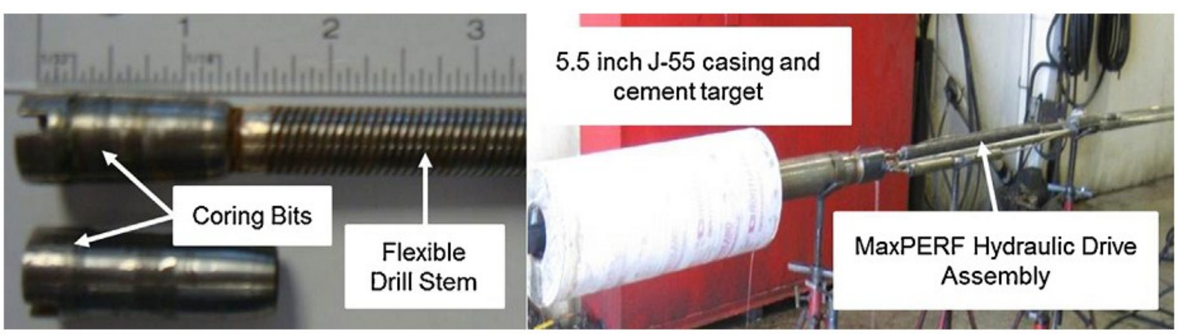

Figure 28. Sample target with a 139.7 mm (5.5 in.) diameter J-55 casing and oilfield cement in a 305 mm (12 in.) diameter sonotube.

4.2.2 Testing

A sample target was prepared with a 139.7 m diameter J-55 casing and conventional oilfield cement inside a 305 mm diameter sonotube. The flexible shaft with the core barrel was attached to the tool and the target was placed over the milling and drilling section of the tool. The tool was then operated as per normal field procedures. During testing, several attempts were made to gauge the correct length of the drill shaft to optimize the press fit of the core into the core barrel. A longer shaft would force the core into an already full barrel, which may damage the integrity of the core.

During each of the sonotube target tests, the tool was able to retrieve cement samples. The samples were tightly compressed into the barrel as per design criteria. The holes cut in the side of the casing from the milling and coring bit were clean without burs or obstructions (Figure 29). The retrieved samples were 9.5 mm in diameter, with lengths close to 10.3 mm.

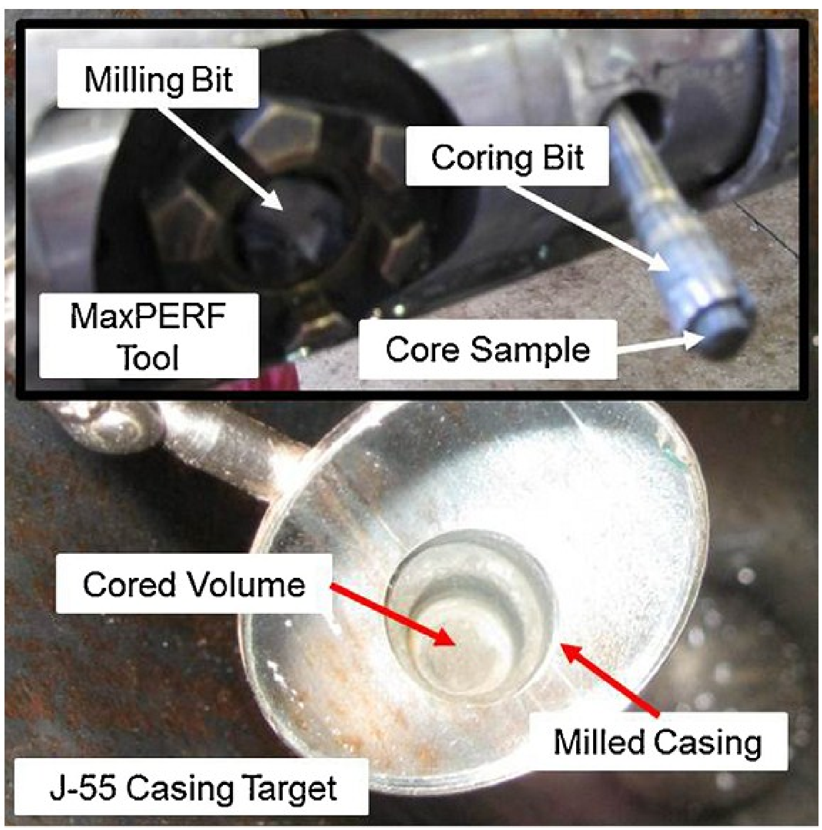

Figure 29. Successful retrieval of 9.5 mm diameter core from sample target showing cleanly milled casing and sampled volume.

4.2.3 Deployment

The PTT and CemCore tools were successfully deployed as part of a 28-day testing program in March, 2011. The PTT tool was run three times to depths between 1.3 km and 1.4 km, where only one of the tests was successful. There were several issues with the packer sealing elements, which failed during two of the tests.

The CemCore tool operated without issue and was able to obtain four core samples in five runs (Figure 30). Images retrieved from a downhole camera showed a cleanly milled casing cut similar to that in the uphole testing (Figure 30). Successful retrieval of a 9.5 mm diameter cement sample from 1310 m TVD 139.7 mm cased well using the CemCore tool to that in the uphole testing. The one attempt that failed was due to an operator tool depth issue where the tool landed over a casing collar where milling was not possible since the steel is significantly thicker at the collar. After each run, the core barrel bit was unthreaded from the drill string and stored for transport with the core remaining in the barrel. A new core barrel was attached to the drill stem and prepared for the next run. The casing/cement/formation samples collected with the CemCore tool are planned to be used for geochemical and petrophysical testing and analysis.

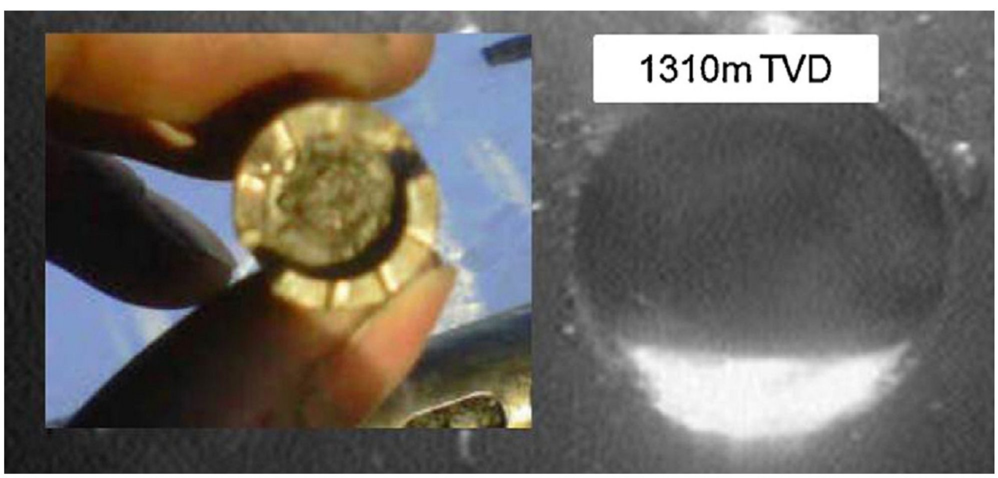

Figure 30. Successful retrieval of a 9.5 mm diameter cement sample from 1310 m TVD 139.7 mm cased well using the CemCore tool.

4.3 Data Analysis

Several established techniques are available to analyze the pressure response of a fluid injection into a coalseam reservoir (Seidle et al. 1991). The approach used by Hawkes and Gardner (2013) for a caprock material used inverse numerical modelling to analyze the results (Figure 31) the Weyburn well test. Their procedure used CMG's IMEX flow simulator and with the main assumptions noted as:

- The problem is axisymmetric;
- Each of the casing perforations zones were modelled as a single fracture;
- The space between the formation and casing is modelled a single unit element; and
- Tool and formation are saturated with the same fluid.

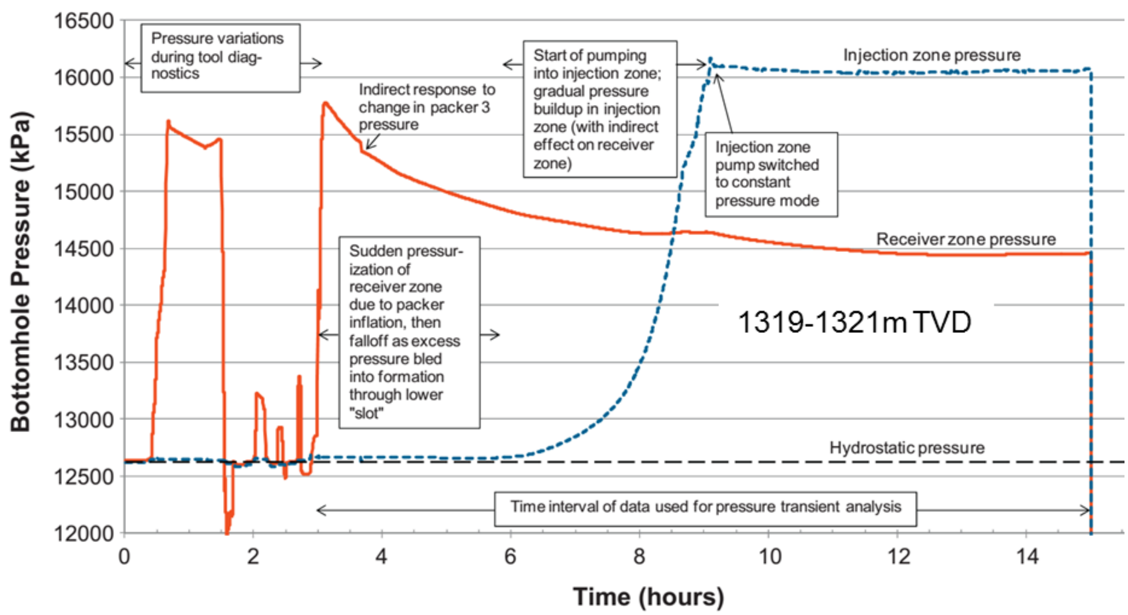

Figure 31. Data analysis by Hawkes and Gardner from the downhole pressure injection test using the PTT tool at 1320m (adapted from Hawkes and Gardner, 2013).

Hawkes and Gardner's approach to modelling the response of the PPT tool by using a parametric analysis based on seven unknown inputs: formation and cement vertical and horizontal permeability, formation compressibility, cement and formation porosity. Their modelling results fit reasonably well, and are shown in Figure 32.

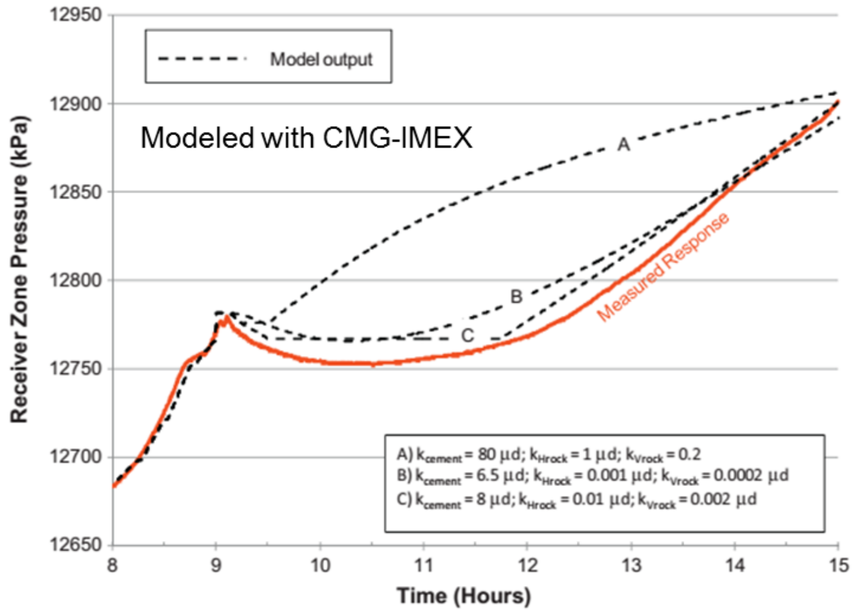

Figure 32. CMG-IMEX model of measured pressure response from of PTT tool at 1321m TVD (adapted from Hawkes and Gardner, 2013).

In this field trial example the cement plugs from the CemCore tool coring were not taken from the same zone as the drilled slot for injection or receiving of fluid pressures. In a new well however, an injection testing procedure for formation evaluation should drill one plug (or several if feasible) and use that plug to determine horizontal cement permeability and porosity, reducing the number of unknowns from seven to five. The in situ wellbore cement permeability may also be isotropic, which could lead to the removal of one more unknown, however more work is required to understand this, or determine if anisotropic cement permeability influences results greatly. In the case demonstrated by Hawkes and Gardner, the central receiver of the PTT tool was used to monitor fluid bypass and was not in contact with the formation. If the coal formation is thick enough (>1.5m), both the middle and bottom pressure receivers could be used to monitor the fluid injection pressure response, providing more data for analysis from the same test.

4.4 Conclusions

Two wellbore tools have been developed and successfully deployed in a CO_2 wellbore integrity project in the IEAGHG Weyburn–Midale CO_2 Monitoring and Storage Project. The PTT tool was designed to measure wellbore cement permeability for deployment inside a 139.7 mm diameter wellbore, where the CemCore tool was designed to run in the same wellbore diameter to collect sidewall cement core samples. The tools were built with sufficient flexibility to be deployed in any type of reservoir material to conduction injection testing over a short interval (0.5m to 3.8m), which is ideal for the thin seams typically encountered in coalseam reservoirs.

The PTT tool has a four packer system with internal pressure and temperature sensors that are conveyed on coiled tubing. The four PTT packers are capable of 6.895 MPa differential pressure and are independently controlled. The sensor and packer pressure lines are contained inside a 1600 m coiled tubing spool, which is mounted on a custom built stand-alone spool and operated by a conventional coiled tubing rig. The PTT tool is controlled and data acquired through the TCU, which houses the packer pressure control board, data acquisition system, and pumps that transmit the transient pulse downhole to the tool. The PTT tool was deployed once successfully, with two failed attempts due to defective packers.

The CemCore tool is designed to operate inside a 139.7 mm diameter cased wellbore and has been modified from the existing MaxPERF technology developed by Penetrators. The tool is able to successfully collect 9.5 mm diameter and 10.3 mm long plug samples by milling through the wellbore casing and then positioning cement and formation from depth (1310 m) during field operations. The CemCore tool was deployed five times to successfully retrieve four cement core samples. The failed attempt was due to operator error and not tool failure.

An example of data analysis from a single wellbore test is provided which was analysed using inverse modelling with CMG's IMEX. Suggestions for improvement of results analyze have been provided including the sampling of the new wellbore cement from the same zone that is that being used for the slot drilling. The cement samples could be analyzed in the laboratory for permeability and porosity, providing input for inverse modelling of results.

5 Laboratory Testing of Coalseam Reservoirs

5.1 Background

This chapter addresses the previous work investigating the behaviour of coal at the laboratory scale and where laboratory testing fits into the overall hydro-geomechanical characterization program (Figure 33). A review of the literature indicates a large amount of laboratory testing has been completed on the mechanical behaviour, flow properties, and desorption characteristics of coal. The majority of the mechanical testing of strength and deformation is completed for the coal mining industry, whereas work on flow properties, including permeability and desorption isotherms, has been carried out for both the mining industry and oil and gas industry. Very little work has been completed that tests coal for both flow and mechanical properties, or how mechanical properties influence the reservoir properties of coal. This chapter provides a background of coalseam reservoir behaviour including: genesis (including lithotypes, macerals, and rank), reservoir (gas storage and transport), geomechanics (deformation, velocity, strength), and hydro-geomechanics (stress-permeability-composition, stress-relative permeability, gas content/composition-volumetric strain-stress). The chapter then concludes with not the short comings of previous research, but how each of the discoveries and contributions of coal behaviour can be integrated into a single testing program that fits into the overall hydrogeomechanical characterization workflow.

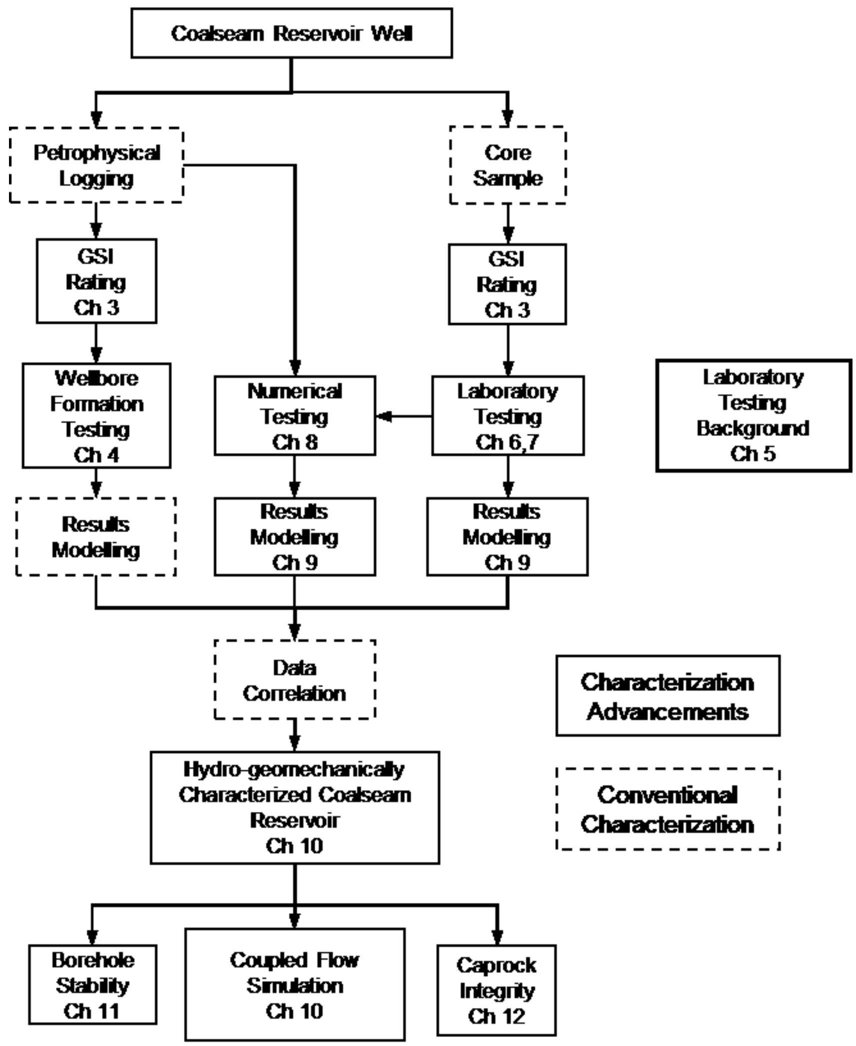

Figure 33. Coalseam reservoir hydro-geomechanical workflow showing where laboratory testing fits in the characterization workflow.

5.2 Coal Genesis

Coal and coal seam formations originate through a thermogenic process termed coalification, in which plant material degrades diagenetically and metamorphically, resulting in two products: coal, and methane gas (Berkowitz, 1993). Coal begins as peat, which forms in swampy mires, containing trees, plants, and other vegetation as well as inorganic material. Mires may contain as many as 76 of naturally occurring elements (Schweinfurth 2009). The major organic compounds in mires are carbon, hydrogen, oxygen, nitrogen, and sulfur.

Through geologic time, thermogenic degradation occurs as temperature and stress levels rise with increasing depth of burial, thus increasing the carbon and gas content of the coal (coalification). Macroscopically, coal has four distinct bands types, or lithotypes, and microscopically, coal can be divided into maceral groups (analogous to mineral types) (Berkowitz, 1993). In the coalseam, naturally existing fractures, or cleats, most likely form from shrinkage, stress relief and extensional strain of the coal matrix during coalification (Labauch et al., 1998).

5.2.1 Coal Rank

A major factor in determining coal quality is rank. Rank refers to steps of coalification where with stress and temperature, the buried mire transitions to carbon rich hardened geo-material. Descriptive terms for the thermal maturity of coal in rank and ascending order are: peat, brown coal/lignite, sub-bituminous coal, bituminous coal, and anthracite. Each rank may be further subdivided, with rank being determined by the percentage of dry ash free carbon and the calorific value in BTU (Figure 34). Generally, the methane sorption capacity of coal increases with increasing rank, and can be second order polynomial with a minimum at high volatile A (Laxminararyana and Crosdale 1999). However, there are no firm correlations between coal rank and flow and mechanical properties, only very general relationships (discussed further below).

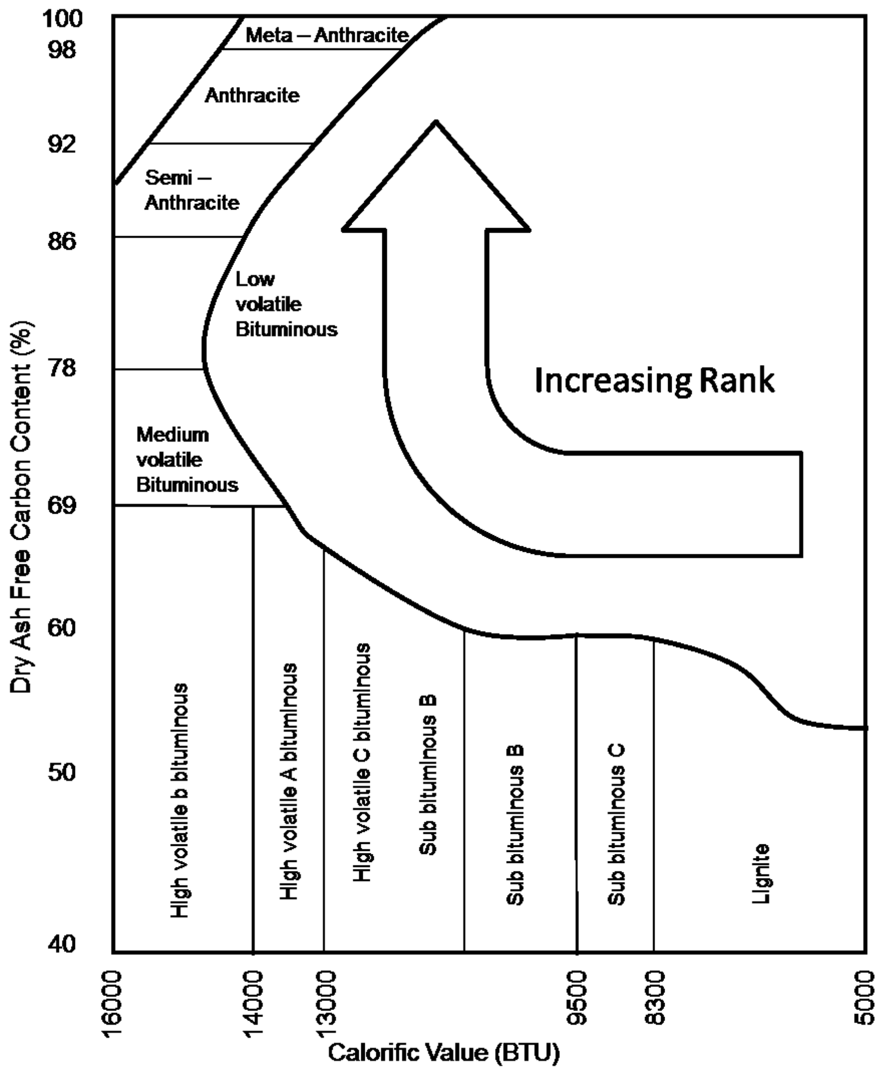

Figure 34. The coal rank classification system (adapted from Schweinfurth 2009).

5.2.2 Coal Lithotypes

Bituminous coals often have well defined stratigraphic bright or dull material banding. The bands are divided into two dull lithotypes durain and fusain, and two bright lithotypes clarian and vitrain. Durain has a dull grainy texture, fusain has a dull, fibrous charcoal texture, clarian has a bright satiny texture and is brittle and vitrain has a bright, black glassy texture and is brittle (Berkowitz, 1993). Based on the relative amount of lithotypes, a bituminous coal may be classified as bright, bright banded, dull banded or dull.

5.2.3 Coal Macerals

Macerals are the name of the particles of organic matter in coal remaining from plants such as roots, spores, seeds and may be useful in determining coal quality. Macerals have three main subdivisions: vitrinite, liptinite, and inertinite. Liptinite and inertinite are broken down into further subdivisions. Coals can range in maceral composition depending on the plant matter contained in the mire.

5.3 Coal as Methane Reservoir

Coal is a discontinuous, heterogeneous, and anisotropic organic material in which the majority of the contained natural gas is adsorbed in the intact sections (matrix) of coal and not in the pore space. Coal seam reservoirs are typically ranked as sub-bituminous and higher and can be described as dual porosity matrix–joint systems, where fluid is transported from the matrix, through the fracture network to the wellbore (Rodgers, 1994). Coalseam reservoirs differ from conventional natural gas reservoirs in that the reservoir rock is not only the trapping mechanism, but also the gas source rock. Due to the sedimentary geological processes of coal genesis, small, semi-regular, orthogonal fracture patterns (cleats) are created, usually perpendicular to the bedding planes. In the Alberta Plains coals, these fractures are aligned with major and minor principal horizontal stresses. The more continuous fracture pattern, called "face cleats," are aligned parallel to the major horizontal principal stress direction, whereas the less continuous fractures termed "butt cleats" are aligned parallel to the minor horizontal principal stress direction. This fracture system creates mechanical and flow anisotropy within the CBM reservoir. The permeability, assumed only in the fractures, has been shown to be dependent on effective stress and gas content. As the volume of gas and type (methane, CO_2, etc) in the coal changes, the coal swells or shrinks (Patching, 1965; Levine, 1996). For reservoir engineering applications, coalseam reservoirs are complex with many interacting behaviours, each being difficult or time consuming to isolate, and each impacting reservoir design and performance.

5.3.1 Gas Storage

In a coalseam reservoir, the micropore diameters range from 0.5 to 5 nm in which the gas is stored through sorption in a condensed or liquid-like phase on the coal surface following a non-linear pore pressure volume relationship, typically represented by a Langmuir isotherm model (Yee et al 1993). Increases in moisture content, mineral matter and temperature have a negative effect on the volumes of gas a coal can store and there is little or no direct relation between gas sorption and coal rank (Azmi et al. 2005; Bustin and Clarkson, 1998). Crosdale et al. (1998) found that maceral composition affects both sorption and desorption properties of coals where vitrinite rich coals usually have greater capacity than inertinite rich coals. This is only a generalization, and variation in sorption capacity is also related to pore surface structure development, particularly the micropores.

Coal gas volumes, represented as moles of gas per mass of rock, are obtained by placing extracted core samples into sealed canisters and measuring gas volumes and desorption times. Sorption isotherms are determined by finely grinding coal into particles less than 0.5 mm diameter, placing the particles into a sealed vessel, injecting gas, and measuring increases in gas volumes with pressure. Karacan and Okandan (2001) demonstrated that different coal structures and lithotypes have different sorption capacity and different rate of release behaviours, and therefore, using crushed coal samples to determine these parameters would at best lead to some average of the desorption behaviours and may not be representative of actual in situ behaviour. Bell et al. (1986) investigated both sorption and desorption in a low to medium volatile bituminous coal from the Black Warrior Basin in Alabama, and looked at pressure equilibrium relationships. They determined that there is a hysteresis effect, where the curves for sorption were not as nonlinear as those for desorption. This has implications for reservoir performance if sorption isotherms were used to predict desorption behaviour.

Mazumder et at. (2006) completed preferential gas sorption experiments on high volatile bituminous coal taken from a block sample from the Silesia mine in Poland using flue gas (CO_2+CH_4+N_2) and pure CO_2. The core samples were cut in three, oven dried at 40°C for two weeks at 30kPa (4.35 psi), and then subjected to double distilled water for 3 hours at 30°C prior to testing. They showed that CO_2 is by far the preferred adsorption gas, with CH_4 second, and N_2 having little absorption. However, subjecting coal to these conditions of drying and then water saturation causes structural damage to the coal, possibly creating new pore spaces for gas to reach (St. George and Barakat 2001).

5.3.2 Gas Transport

Due to the sedimentary geological processes of coal genesis, small, semi-regular orthogonal fracture patterns are created, usually perpendicular to the bedding planes. This fracture system creates anisotropic permeability within the CBM reservoir. The permeability parallel to the face cleats may be much larger (up to 17 times) than the permeability parallel to the butt cleats (Li and Shimada 2004). Gamson et al. (1993) summarized the process step model for gas transport during production as illustrated in Figure 35 and described as follows:

1. After a decrease in fracture pressure due to initial production of gas contained in the cleats, gas molecules desorb from the micropore surface of the matrix.
2. Once in a free gas form, molecules will diffuse through the matrix from areas of high gas concentration to low gas concentration.
3. Then gas molecules enter the cleat system and flow to the well under Darcy Flow.

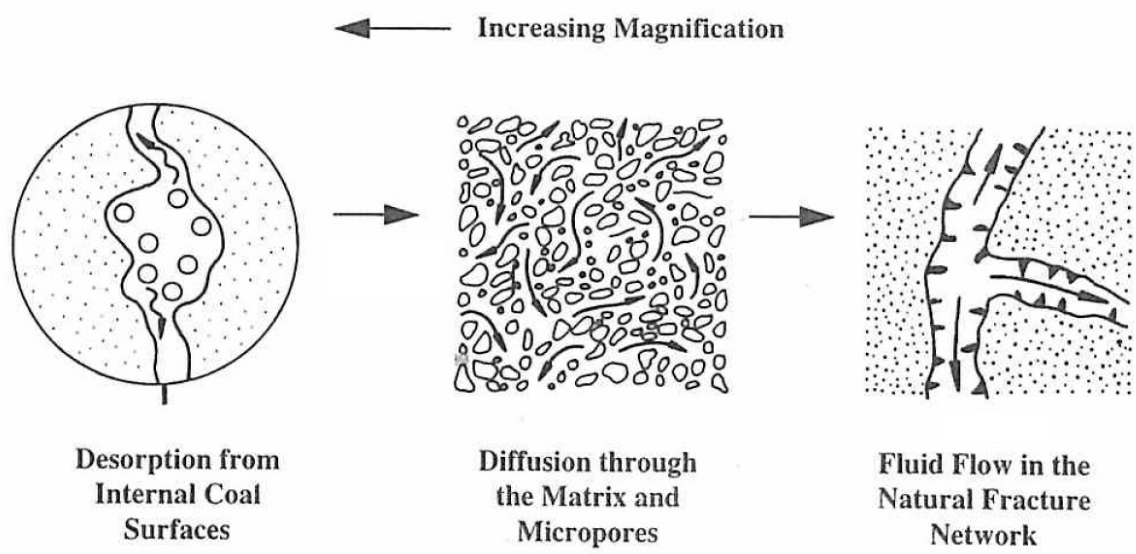

Figure 35. Idealized gas transport model of gas desorption to diffusion through the coal matrix to flow into the cleat system (adapted from Gamson et al., 1993).

Therefore, in a CBM reservoir, the production of methane (or injection of CO_2) may be constrained by limitations in permeability or limitations in diffusivity (Gunter et al., 1997). If coal is water-saturated, water is "pumped off", creating a pressure gradient between the matrix and cleats releasing the gas as well as reducing the water saturation allowing gas to flow. A fictitious desorption isotherm from an under saturated reservoir is provided as an example, where the formation pressure would need to be reduced before methane gas can be desorbed from the coal (Figure 36).

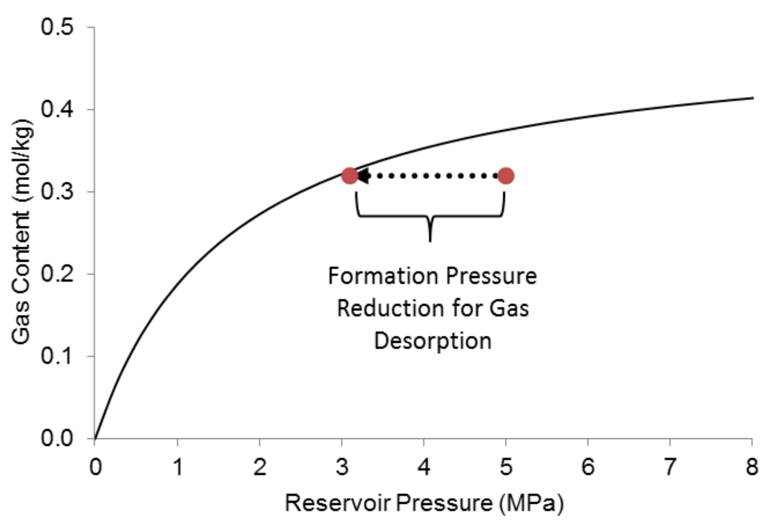

Figure 36. Example of an under saturated coalbed methane reservoir where the reservoir pressure would need to be reduced before gas desorption.

5.4 Coal Geomechanics

Geomechanically, the fracture–matrix system has a primary influence on the mechanical behaviour of the coal. The mechanical behavior of coal has been widely studied for pillar design in coal mining and is therefore specific to those engineering design issues (Medhurst and Brown, 1997). Underground *in situ* testing showed the influence of sample size on strength (Bieniawski, 1964). Large compression testing on simulated boreholes illustrated time dependent anisotropic strength and anisotropic deformation properties of coal (Kaiser and Morgenstern, 1981). The degree of jointing in coal influences the strength and deformation behavior of the coal mass. However, the difficulty in coalseams comes when attempts are made at assessment of the intact properties of coal due to the dense fracturing. Most tested samples contain fracture spacings less than the diameter of the specimen being tested (Medhurst 1997) which must be accounted for when determining the engineering behaviour of the coal mass. The following subsections discuss work completed by previous researchers on the static deformation, compressional and shear wave velocities, and strength of coal.

5.4.1 Deformation

Coal exhibits non-linear, scale dependent deformation behavior typical of rock masses. Experiments by Medhurst and Brown (1998) on coal from the Moura mine in Queensland, Australia studied the effects of sample diameter on Young's modulus and Poisson's ratio. They tested samples from 63mm to 300mm in diameter. For both parameters, results were very scattered however, the general trend shows that as the sample diameter increases, the values of Young's modulus and Poisson's ratio are less scattered. Young's modulus decreases with increasing diameter (Figure 37) and for Poisson's ratio, there is no appropriate scale relationship (Figure 38). Medhurst and Brown (1998) also investigated the influence of confinement stress on volumetric strain increase during triaxial compression. As confining stress increased, the mode of failure changed from axial splitting to shear plane formation and the amount of dilation decreased (Figure 39). Kaiser and Morgenstern (1981) and Szwilski (1984) both used coal blocks with boreholes to study the deformation behaviour of coal. Kaiser and Morgenstern used a 610 mm sub-bituminous coal block from Wabamun district with a 120 mm borehole, while Szwilski used a 305 mm coal cube (no information on rank/location) with a 38.1 mm borehole. They showed Young's modulus increased as the load increased and Young's modulus was anisotropic and coal creeps. The Young's modulus was lowest in the direction of the bedding planes, and highest in the direction perpendicular to the butt cleats, although it was difficult to differentiate between face cleats and butt cleat directions.

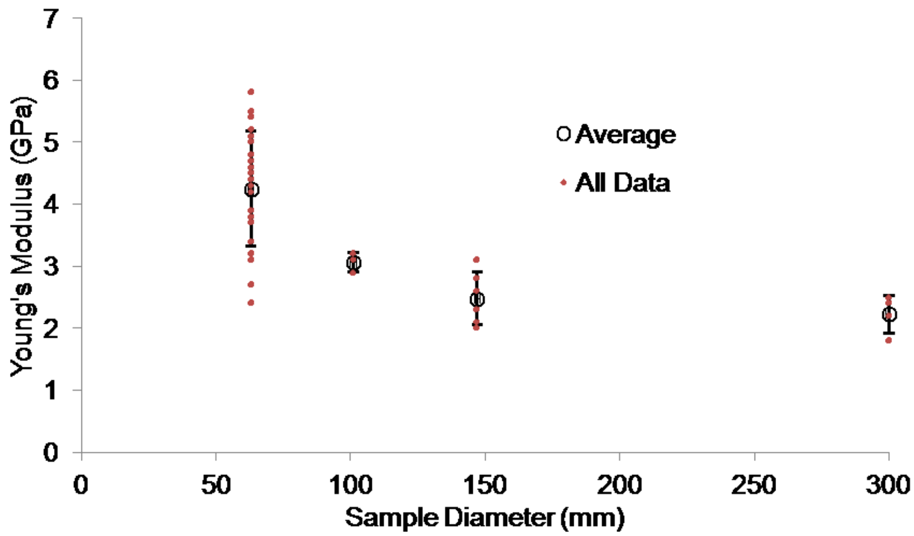

Figure 37. Influence of sample size on the Young's modulus (modified from Medhurst and Brown, 1998).

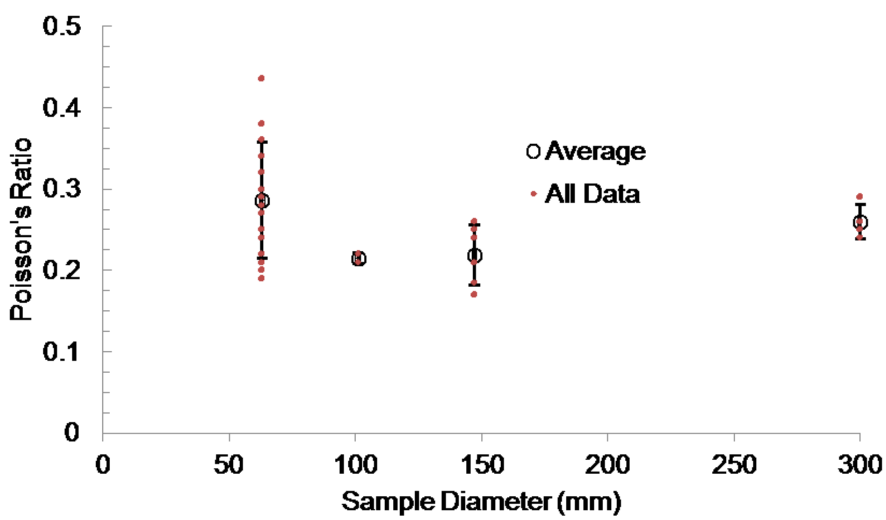

Figure 38. Influence of sample size on the Poisson's Ratio (modified from Medhurst and Brown, 1998).

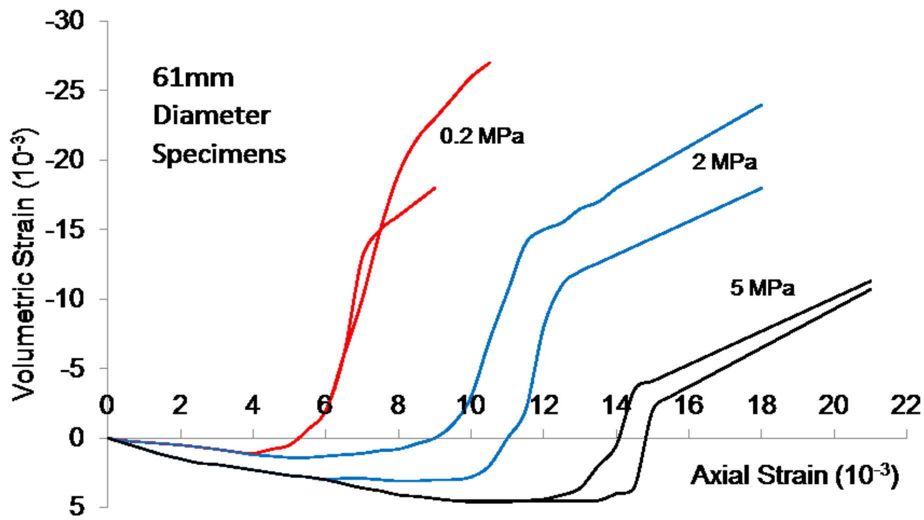

Figure 39. Volumetric strain with variable confinement (modified from Medhurst and Brown, 1998).

5.4.2 Compressional Wave Velocity

Several researchers have conducted studies on coal using ultrasonic compressional (P) velocity measurements on Bituminous coal from Japan and the United States of America (Inouye, 1951) and Schuylers et al (1958) which showed the dependence of velocity on carbon content. The most recent examples are Khandelwal and Singh (2009) who measured compressional wave velocities in 12 samples attempting to correlate P-waves to: UCS, tensile strength, shear strength, density, Young's modulus and Poisson's ratio, Very good correlations for each of the samples were obtained. Pan et al (2013) related UCS and Young's modulus to coal rank, compressional velocity and maceral composition. They conclude that when applying previous correlations to different coals the correlations do not work, and P-Wave to mechanical properties correlations are coal dependent. Cai et al (2014) investigated permeability changes in coal while CT scanning and measuring P-wave evolution under axial loading. They show decreases in P-wave velocity with increased fracturing.

5.4.3 Strength

Bieniawski (1964) conducted unconfined compressive tests UCS tests on South African Witbank mine coal cube specimens ranging from 20 mm to 1500 mm. His results showed coal is UCS is scale dependent, decreasing with increasing size (Figure 40). Swziliski (1984) (same coal he used in deformation testing) showed strength anisotropy by testing cores taken in three perpendicular directions from coal blocks. Definite anisotropy is observed with confinement less than 1.4MPa. At stresses greater than 1.4 MPa, the strength of the coal samples converged (Figure 41). Medhurst and Brown (1998) completed several triaxial tests on cylindrical specimens to evaluate the influence of size and brightness on mechanical properties. The study used 61mm to 300mm diameter specimens, tested under triaxial stress conditions with varying confining stress, ranging from 0 to 10 MPa. As the sample sizes increased, the strength decreased (Figure 42). Their results also concluded that the variability in strength of the coal samples was related to sample size. There was no apparent relationship between strength and brightness.

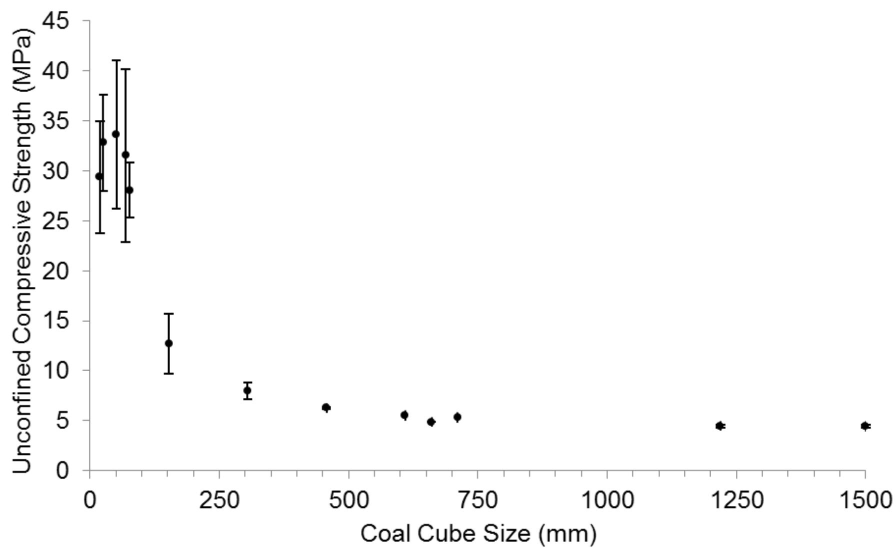

Figure 40. Results from coal cube block testing on strength decreases as sample size increase (modified from Bieniawski 1964).

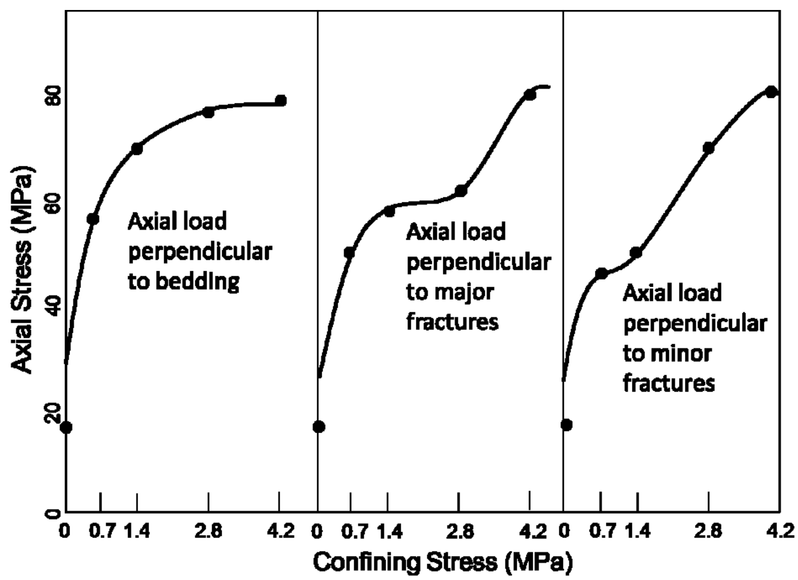

Figure 41. Anisotropic strength increase with confining stress increase (modified from Szwiliski 1984).

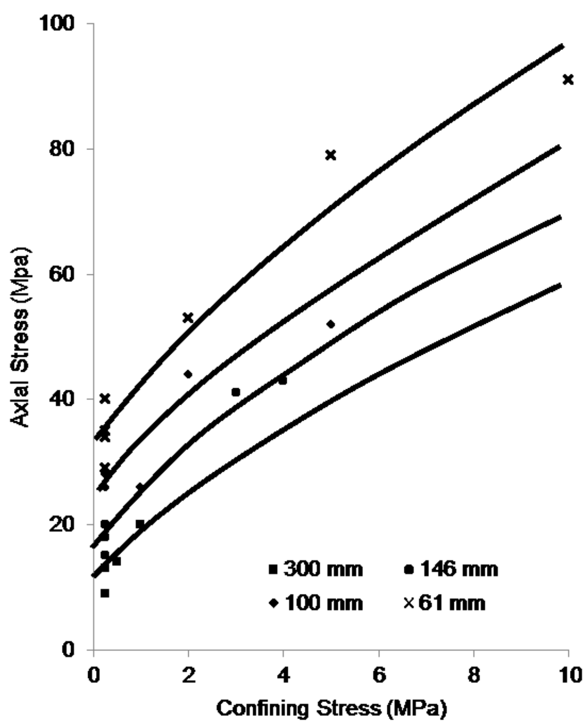

Figure 42. Effects of scale and confining stress on the strength of coal (modified from Medhurst and Brown, 1997).

Moisture Content

Hawkes (2007) reported a series of triaxial tests results that showed water saturation decreases the strength of coal (Figure 43). Therefore, testing mechanical properties of coal after air drying can lead to overly optimistic strength results. St. George and Barakat (2001) stated that drying the coal at elevated temperatures during sample preparation created internal damage in the coal sample that subsequently affected mechanical properties of the coal and its sorption characteristics.

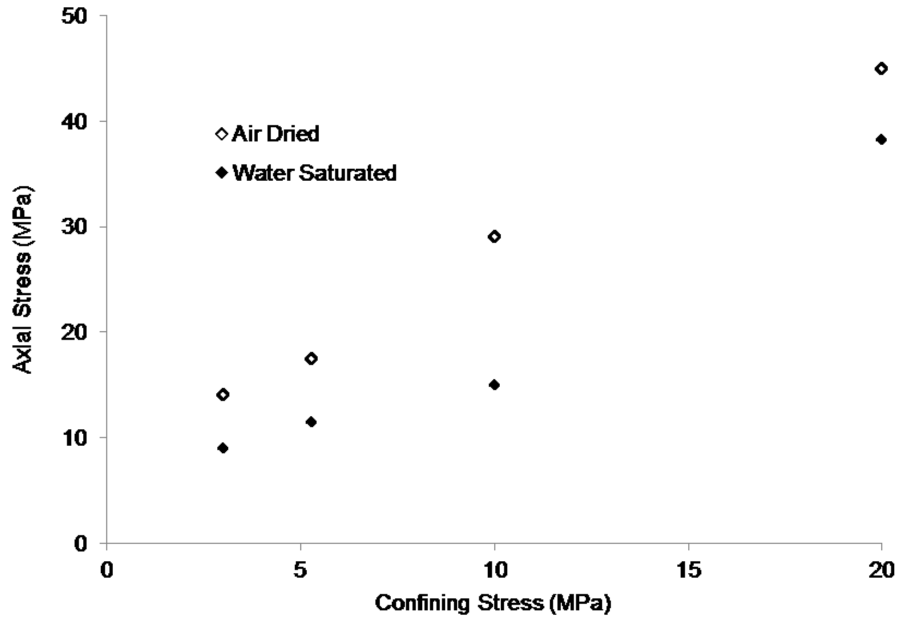

Figure 43. Influence of moisture content on triaxial strength (modified from Hawkes, 2007).

Rank Dependence

Historically, the most common strength index test for coal used in mining is the Hardgrove Grindability Index (HGI). HGI measures the ease at which coal can be pulverized. A sample of coal is inserted into the machine and a series of steel balls apply a grinding action for a set period of time. Coal fragmentation is then measured to determine the “grindability” of the coal. Recent work has attempted to link the Hardgrove index to rank, and then rank to UCS (Palmer et al., 2005) (Figure 44). A second plot of the same relation was completed previously by Szwilski (1984) contradicting any apparent correlation and demonstrating only a very scattered correlation and a general trend (Figure 44). Additionally, Hawkes (2007) commented on the relation between rank and UCS, stating that carbon content (related to rank) does not solely determine the UCS of coal and that the relationship may not be true for all coals (German coals with the same rank were weaker). Therefore, these types of correlations may be useful for a first approach to obtain strength data.

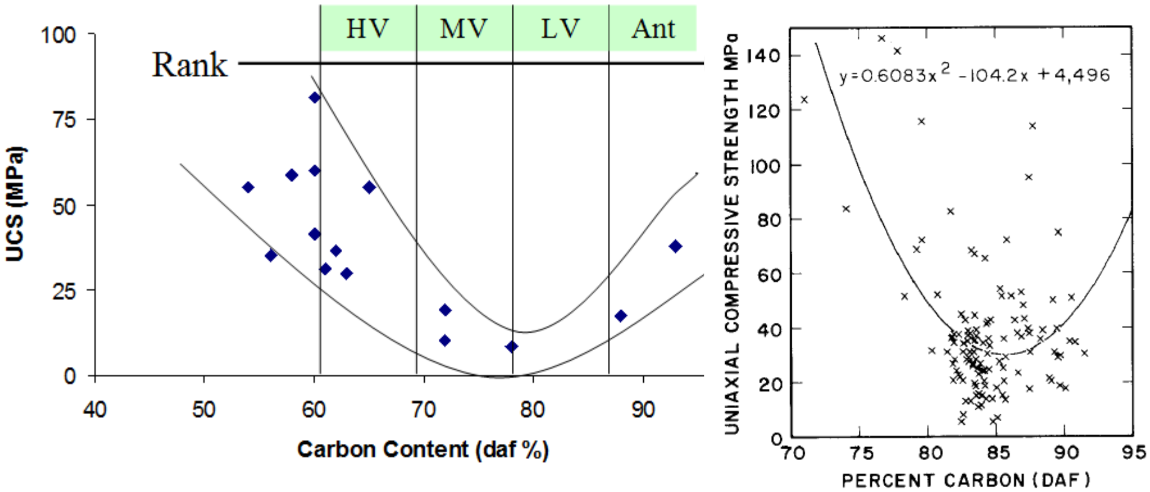

Figure 44. (Left) Relation of rank of coal to the *UCS* (adapted from Palmer et al, 2005) and (Right) the relation of carbon content to UCS by Szwilski (1985).

5.5 Coal Hydro-geomechanics

Coal seam reservoirs are described as dual porosity matrix-cleat systems, where during production, gas desorbs from matrix micropore surfaces, is transported through the matrix to the cleat and bedding plane network and then to the well. As shown by numerical simulation results, production and/or injection processes lead to changes in effective stress. These lead to changes in permeability in the reservoir, which in turn influence production and injection rates (Gu and Chalaturnyk, 2006). The following subsections discuss work completed by previous researchers on the permeability, relative permeability, and gas sorption and the associated influences of geomechanics.

5.5.1 Effective Stress and Permeability

Several researchers over the past 60 years have conducted laboratory experiments with the aim of understanding the effects of changes of effective stress on the permeability of coal. A general conclusion is that an increase in mean effective stress creates an exponential decrease in permeability. Most of the experiments were completed under increasing or decreasing isotropic stress conditions, and permeability is generally measured in one direction, perpendicular to the bedding plane. For permeability, an increase in isotropic effective stress may not translate to an equal reduction in directional permeability. Some researchers have recognized this and have made attempts to investigate anisotropic stress change and directional permeability (discussed below).

Jones et al. (2002) conducted experiments on reservoir rock (not coal) to demonstrate the effect of the stress path on changes in reservoir permeability. They conducted single phase and two phase (oil and water) permeability tests while changing both the confining stress and the axial stress, until failure. Results indicated that changes in permeability are not only dependent on the mean stress, but also on the deviatoric stress. Therefore, simply relating permeability to changes in mean effective stress may not capture permeability behaviour.

Isotropic Stress

Patching (1965) showed the decrease in permeability by increases in isotropic effective stress and noted that changes in permeability and the concurrent deformation associated with isotropic stress increase are also time dependent. Many researchers have completed similar studies of isotropic stress or confining and deviator stress showing similar inverse effective stress permeability relationships (Pomeroy and Robinson 1967; Bustin 1997; Li and Shimada 2004; Pan et al 2010). Results from tests on 13 different specimens for permeability with changing effective isotropic stress tests are shown in Figure 45 (Somerton et al 1975).

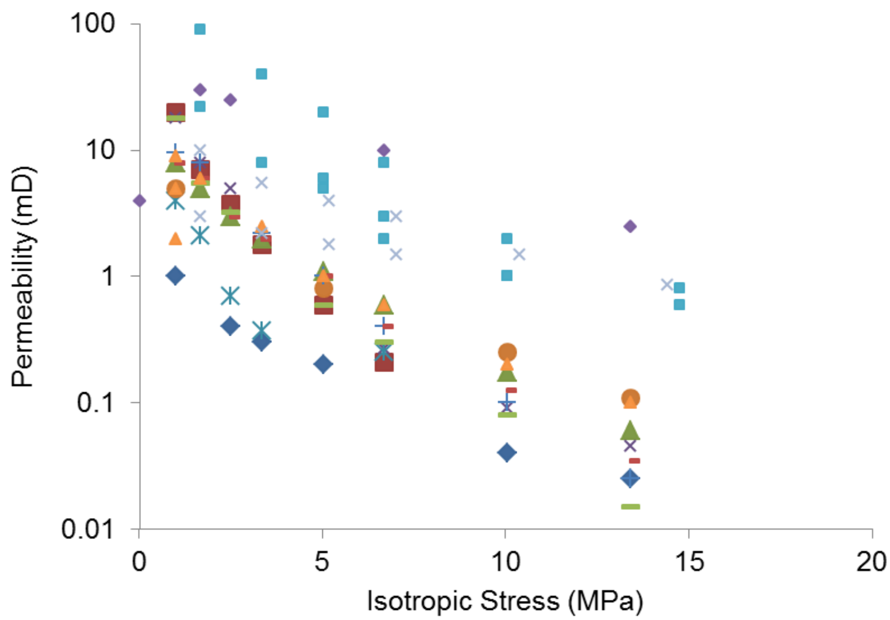

Figure 45. Changes in coal permeability with isotropic effective stress (data from Somerton et al 1975).

Li and Shimada (2004) used sub bituminous cylindrical samples from the Kushiro coalfield in Japan mine investigation to examine permeability anisotropy. They cylindrically cored in three directions, obtaining three core specimens and applied an increasing isotropic stress while measuring permeability. They determined that there was significant anisotropy until an isotropic stress of 16 MPa was reached. At that point, permeability in the three directions converged, although they did not test at higher isotropic stresses (Figure 46).

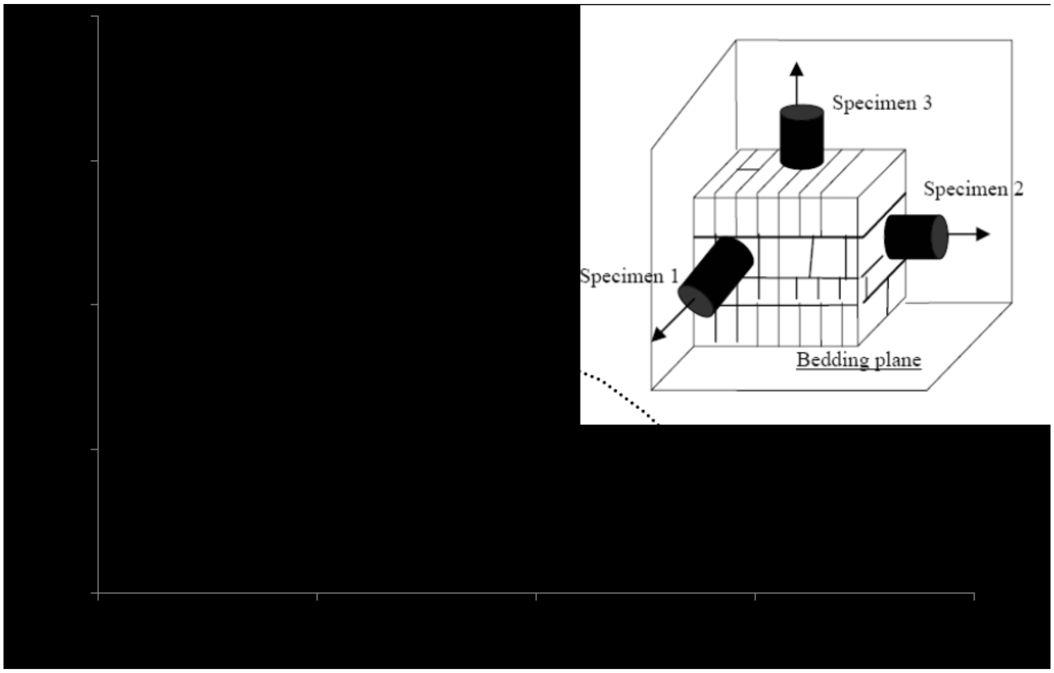

Figure 46. Results for changes in directional permeability with increases in effective stress (modified from Li and Shimada 2004).

Harpalani (2006) found that increasing effective horizontal stress while maintaining pore pressure resulted in decreasing permeability while using different gases (CO_2, CH_4, N_2+CO_2) as pore fluids (Figure 47). The results follow the expected trend of an exponential decrease in permeability with increase in horizontal effective stress.

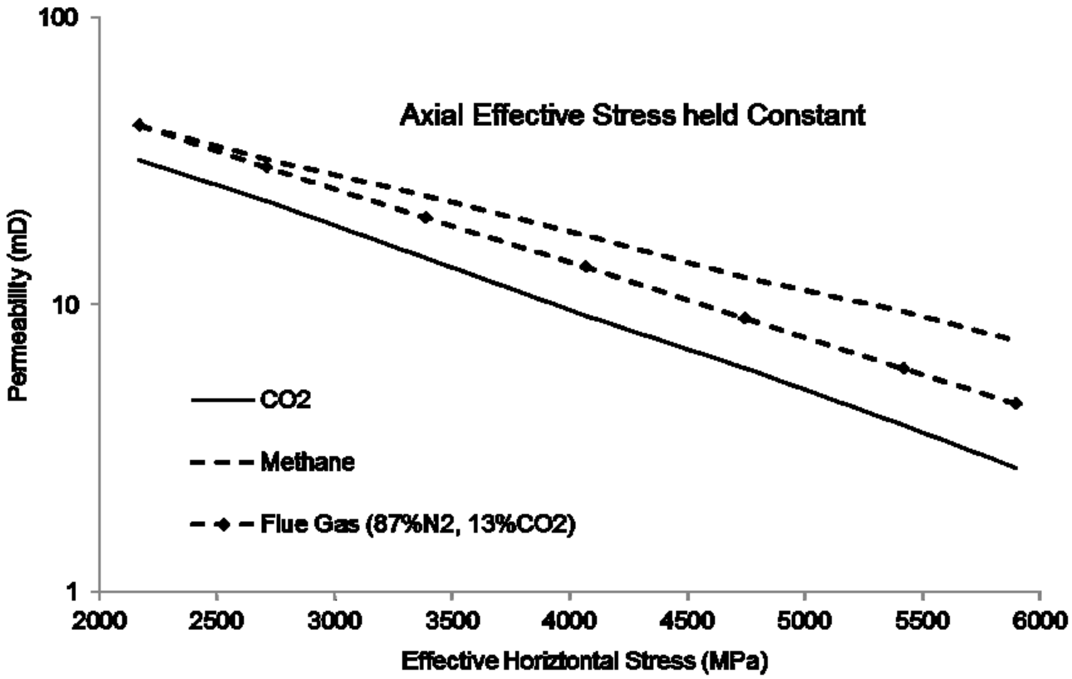

Figure 47. Changes in permeability with increases in effective horizontal stress (Harpalani, 2006).

Massarotto et al (2003) conducted a series of coal permeability measurements using a “True Triaxial Cell Permeameter” on coal from the TaoYuan mine in Sunan Basin China and the Bowen Basin mine in Australia. A true triaxial cell or polyaxial cell uses cubic or parallelepiped shaped samples and applies stress in all three directions. The cell also has the ability to flow fluids in three directions during testing. Figure 48 shows the results of the testing, with the x-axis plotting the effective stress parallel to the direction of flow (σ_{nz}), divided by the effective mean stress (σ_{an}). Their results indicated that the direction of the applied stress has a strong effective on the directional permeability of the coal showing that when the direction of the principal stress plane is perpendicular to the flow direction, permeability increases. This indicates that there may be increases in permeability due to dilation. The mechanical properties of the samples were not reported.

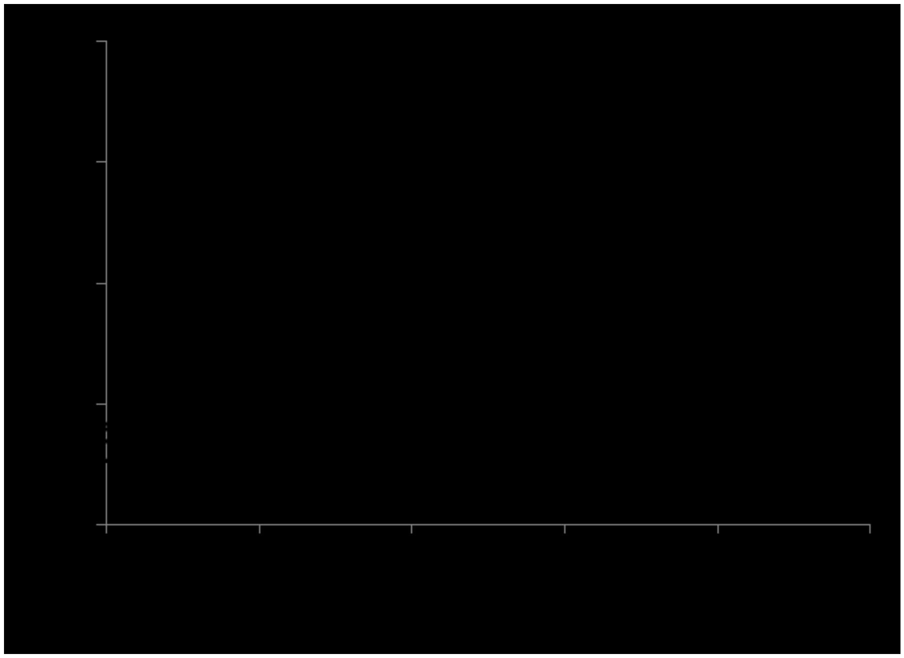

Figure 48. Results from polyaxial permeability tests showing stress permeability changes from (modified from Massarotto et al 2003).

Permeability and Composition

Clarkson and Bustin (1998) investigated the permeability of high and medium volatile bituminous coal. They associated permeability with lithotype and found that permeability decreased in order of: bright coal (4.1md), banded coal (0.79md), fibrous coal (0.5md), banded dull coal (0.14md), and dull coal (0.016md). Bright coal has the highest permeability due to the degree of cleating, while dull coals have lower permeability as cleating is less prevalent (Figure 49). However, it is interesting to note that a single permeability is most likely an incorrect assumption in a coal seam, and some combination of the permeability of each lithotype in the reservoir may be required for more accurate modelling results.

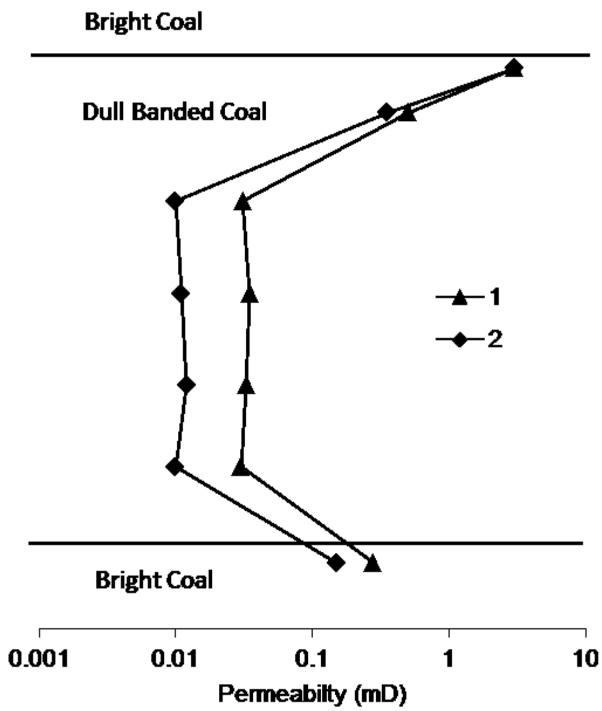

Figure 49. Permeability variation with degree of banding in coal seam (from Clarkson and Bustin, 1997).

Bustin (1997) investigated the effects of coal macerals on permeability stress sensitivity using a series of Upper Permian high-volatile to low-volatile bituminous bright and dull banded coal specimens from the Sydney Basin, Australia. Specimen maceral composition varied from predominately vitrinite for the bright banded coals to inertinite for the dull banded coals. Samples with the greatest change in permeability were thinly and discontinuously banded and Bustin suggests that for low permeability coals, bright coal may have higher matrix Young's modulus and cleat stiffness than dull coals. This was consistent with Gu and Chalaturnyk (2003) who demonstrated through numerical simulation that one of the greatest influences of changes in permeability is cleat stiffness. Additionally, Bustin (1997) completed in situ permeability tests on the same coalseam that the coal samples were collected. In each case, the in situ permeability was one order of magnitude higher than the laboratory specimen. Additionally, they note relative change in situ permeability changes matched that seen in the laboratory.

Aperture Closure

Walsh (1981) stated that permeability of a fracture decreases under increasing stress due to two factors. First, aperture decreases under increasing compression, thus decreasing permeability. Second, apertures are not smooth plates, but undulating and sometimes rough surfaces. As the number of points of contact between the surfaces increase and the area of contact increases, therefore, the tortuosity of the flow path also increases. Both effects create changes in permeability. Detournay (1998) conducted a series of experiments on single fractures in simulated rock to help understand changes in permeability with changes in stress. Commonly in CBM reservoir geomechanics, the cubic law for fracture flow is assumed to relate changes in stress to changes in permeability. Detournay found that the cubic law holds only if an initial aperture is defined as the reference condition for the flow. He also found that the joint deformation became more nonlinear as the load was increased, and the assumed linear relation between flow and pressure for increased effective stress did not hold. This suggests that although a linear relation may hold for certain cases, at effective stress increases beyond a certain magnitude, the cubic law may not provide an appropriate estimate of the change in permeability.

The Klinkenberg Effect

Harpalani and Chen (1993) discuss the concept of gas slippage known as the Klinkenberg effect. For fluid flow at constant effective stress, the permeability of the material is assumed independent of pore pressure. However, for gas at low pressure (less than 1.7 MPa), the permeability of the material is not independent of the gas pressure and a corrected permeability is required. If the flow paths are on the same order as the gas molecules (~10 nm), the gas molecules interact with flow surfaces, creating an additional contribution to Darcy flow. The value of the Klinkenberg coefficient is different for each flowing gas and may have a large influence on permeability in the later stages of reservoir depletion when pressures are low.

5.5.2 Effective Stress Relative Permeability

Dabbous et al. (1976) was the first and only researcher to date to complete experiments investigating the effects of effective stress on relative permeability in coal. The results showed that capillary pressure curves and relative permeability curves are strongly dependent on effective stress (Figure 50). The researchers used the results to calculate relative permeability and showed that as stress decreases more gas will flow at higher water saturations.

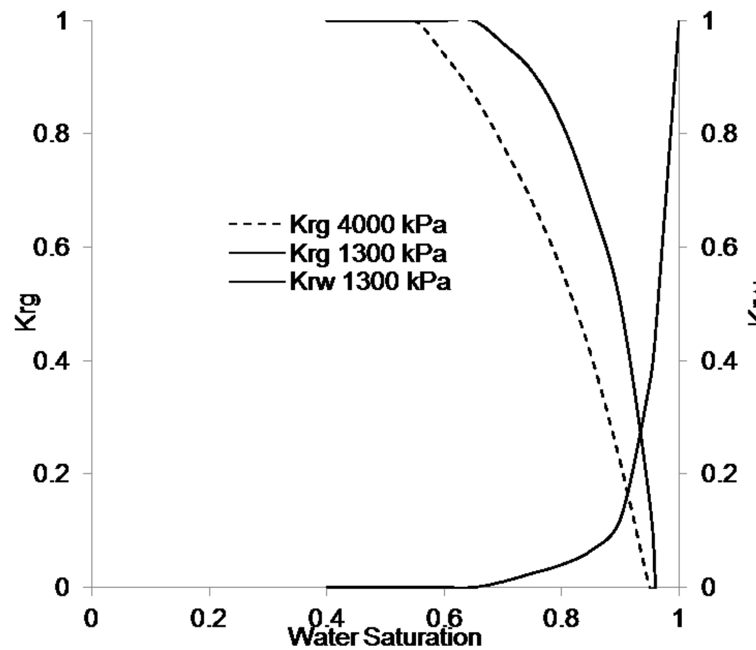

Figure 50. Relative permeability with changes in isotropic stress (modified from Dabbous et al 1976).

5.5.3 Deformation Due to gas Content/Composition

Coal is an organic material, where the surface area of the pores interacts (adsorption) with the contained fluid (water, CO_2, CH_4, etc.) and this interaction causes volumetric changes within the coal (Mitra et al., 2008). Patching (1965) found that different gas pore pressures caused coal samples to change in volume (swell/shrink). Mazumder et al (2006) provides a summary of previously measured linear volumetric strain with changes in gas content. Cui and Bustin (2005) found that volumetric strain to gas volume sorbed in the coal is nonlinear relationship (Figure 51).

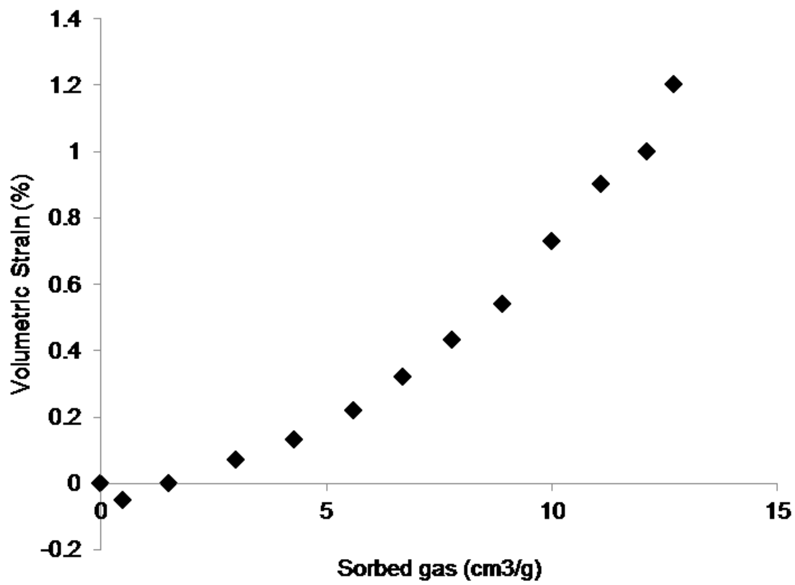

Figure 51. Volumetric strain versus gas volume for coal (adapted from Cui and Bustin 2005).

Seidle and Huitt (1995) completed swelling strain experiments on coal by fixing strain gauges to the samples in major fracture (face cleat), minor fracture (butt cleat) and vertical directions and then subjecting the coal to CH_4 gas pressure at zero effective stress. Their results showed that strain is related to gas content and not gas pressure (results not shown here), and that strain is anisotropic as illustrated in Figure 52. Karacan (2007) also compiled available results on the swelling behaviour of coal and summarized that coals possess anisotropic strain behavior due to gas sorption and the strain rate is greater perpendicular to the bedding plane compared to parallel to the bedding plane.

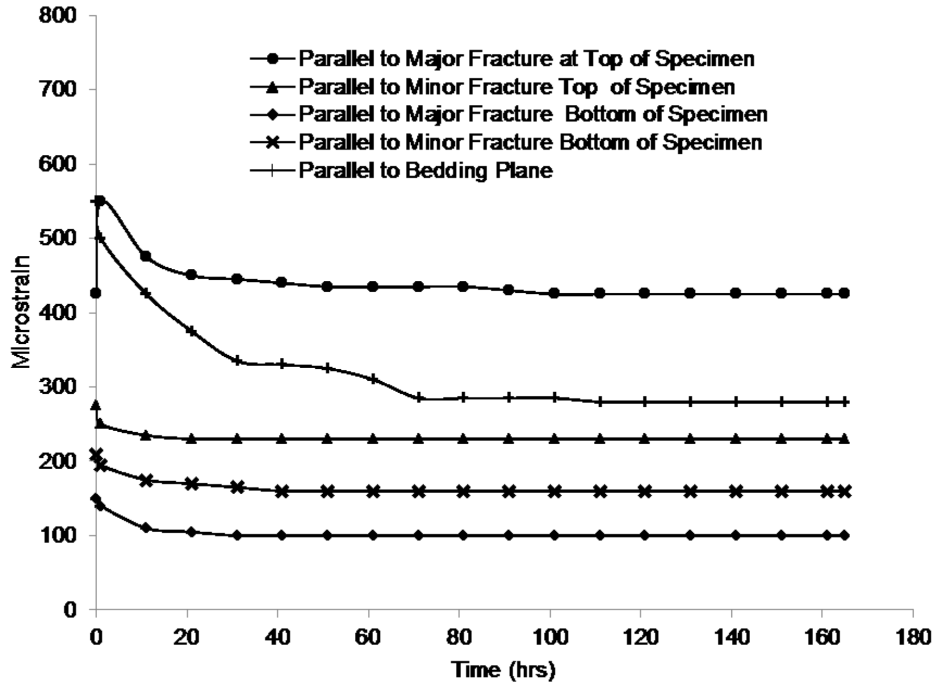

Figure 52. Results of swelling tests performed by Seidle and Huitt (1995) showing strain anisotropy during gas adsorption.

St. George and Barakat (2001) stated that volumetric shrinkage associated with gas desorption has a large influence on the stress field which is important for changes in permeability and also strength of the coal seam. They completed experiments on sub bituminous B coal specimens from the Ohai mine in South Island, New Zealand using three different gas types and measured the overalls shrinkage associated with each gas (Figure 53). Harpalani (2006) completed similar experiments (shown in Figure 53 also), and found that, for Southern Illinois coal, there was a negative volumetric strain when a flue gas was used to displace methane (the sample shrunk when the initial gas saturation was methane). Siemons et al. (2004) and Busch et al. (2005) showed that for some basins, CO_2 may be preferentially sorbed over methane and that each coal basin may need to be investigated individually. Robertson and Christiansen (2007) showed that modelling of laboratory results for swelling due to CO_2 injection in coal under stress improved if a term accounting for the effective stress were included.

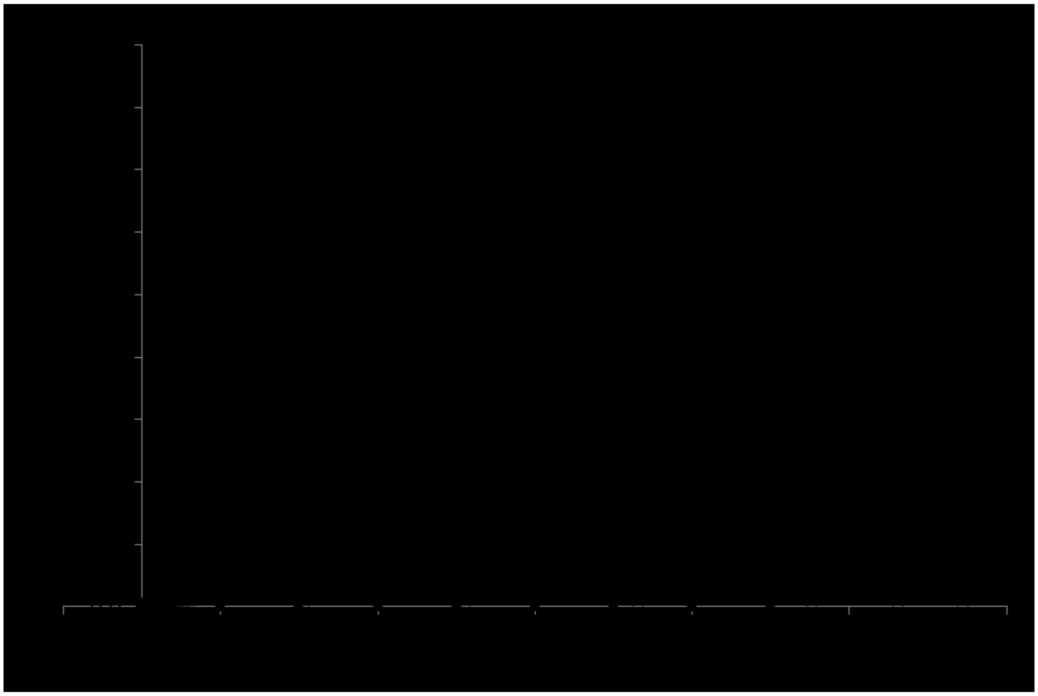

Figure 53. Gas pressure versus volumetric strain for four different gas types (modified from St. George and Barakat 2001 and Harpalani 2006).

Harpalani (2006) found that increasing pore pressure while maintaining effective stress conditions increased permeability on an Illinois coal (Figure 54). The expected result was that due to coal swelling, as gas pressure increased, the fractures would close. Harpalani suggests there is strong interplay between effective stress and sorption induced swelling. Karacan (2007) presented work from a very sophisticated triaxial testing system which took x-ray computed tomography scans of a single Bituminous coal specimen from the Pittsburgh DECS12 seam and subjected it to variable pressures of CO_2 gas while under constant effective isotropic stress of 1.36 MPa. With this technique he was able to monitor swelling within individual macerals and determine the internal swelling of the coal sample due to CO_2 exposure. His results showed that although volumetric strain can be measured on the outside of the specimen to get bulk volumetric strain behaviour, the internal mechanics of swelling are extremely complex and dependent on maceral type. For the coal specimen at CO_2 pressure of 4.0 MPa, the vitrinite increased in volume by 12.5-18% where the clays and inertinite compressed by 10-17%. Therefore, even though the volumetric strain measured by external gauges indicate a small amount of strain which is thought to reduce overall flow apertures, the effect of volumetric strain may create large internal strains which, are practically, un-measurable. Pone et al. (2009) used a confined coal sample and continuous CT scanning to identify that volumetric strain under CO_2 saturation was localized and lithotype dependent, confirming Karacan's results.

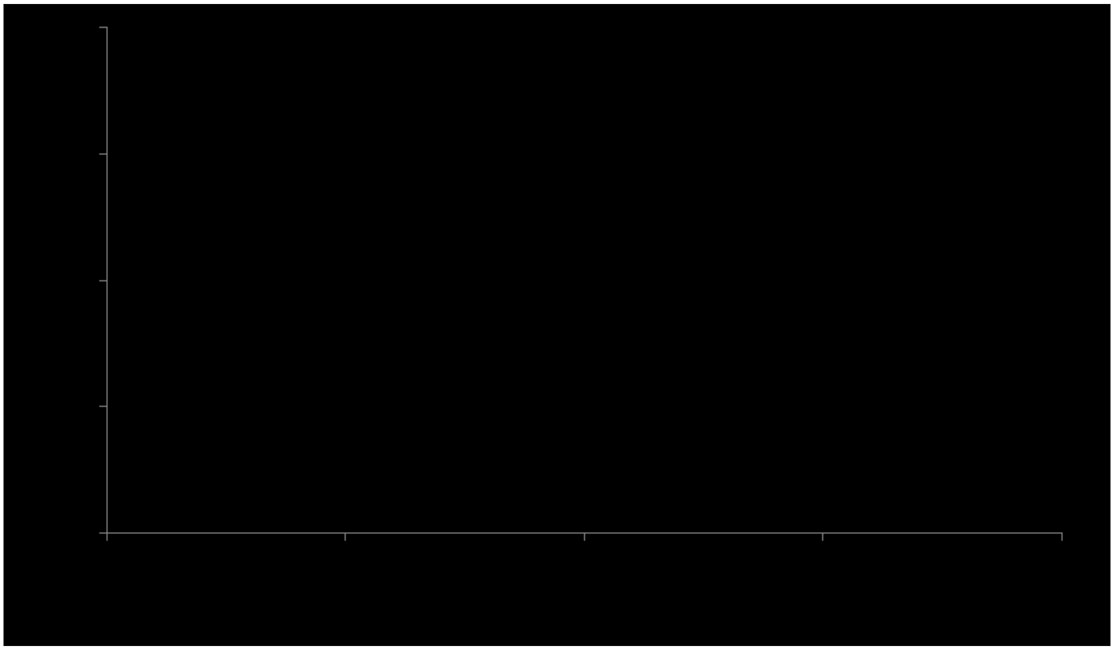

Figure 54. Results from increasing the mean gas pressure while maintaining a constant effective stress (adapted from Harpalani, 2006).

5.5.4 Influence of Stress on Gas Content and Swelling

Industry practice in measuring gas diffusion times and CBM volumes is completed by extracting coal core and placing it in a canister at zero effective stress. This method of measuring gas diffusion times is not representative of *in situ* reservoir conditions. As well, standard practice for measuring isotherms is to crush a coal sample to 74 micron and subject the sample to increases in gas pressure while measuring the changes in gas volume, also not representative of in situ processes. Sabir (2004) compared the CO_2 isotherm results for an intact coal sample subjected to an isotropic confining stress and afterwards, crushed the sample to industry standards and measured the CO_2 isotherm again. He found that the intact sample subjected to stress had a consistently lower gas sorption value for each pressure (i.e. a lower isotherm). As well, Hol et al. (2010) investigated the effects of loading on a crushed coal sample, demonstrating that the applied stress reduced the sorption capacity of coal during CO_2 flooding. Sabir`s work was completed to demonstrate the importance of measuring isotherms under in situ conditions, and therefore the work completed by Hol et al may be speculative as to actual in situ behaviours.

5.6 Summary

This chapter concludes with not the short comings of previous research, but how each of the discoveries and contributions of coal behaviour could be integrated into a single testing program. Previous coal testing programs have revealed several interesting behaviours. However academic laboratory testing programs are generally limited to isolating and determining singular items, interactions, or behaviours, and therefore are not generally combined to get an overall behaviour of the coal at several conditions. The strength and deformation behaviour are dependent on: effective stress, scale or fracture density, moisture content (strength only), and rank (loosely correlated to strength only). The permeability is: anisotropic, effective stress dependent and related to fracture density and the relative permeability is also effective stress dependent. Additionally, coal exhibits anisotropic nonlinear strain behaviour when exposed to gas and changes with: gas composition, gas pressure, effective stress state, and maceral type.

Obtaining core for a sampling program can be capital intensive and collecting intact (non-rubleized) coal may be difficult no matter the cost due to the fractured nature of coal. Therefore, a test should be developed to gather the most data from single coal specimen as possible. This test should be related to: static and dynamic anisotropic deformation, the effects of stress on permeability, effects of gas pressure/composition on strain, which are all non-destructive tests and could be executed on a single specimen. The strength of the coal may also be determined however destructive tests should be planned carefully. The following chapter presents a testing apparatus and program which is designed to gather the maximum amount of data on in situ coal behaviour from a single specimen.

6 Laboratory Apparatus

This chapter of the thesis deals exclusively with the design and construction of two testing systems used for the hydro-geomechanical characterization of coal (Figure 55). The first system was developed to determine strength, deformation, and permeability properties and evaluate coal fines generation after specimen failure. The second system was developed to measure strength, deformation and permeability properties, gas sorption characteristics, and compressional (P) and shear (S) wave velocities. Subsequent chapters describe the testing programs and present results. In addition, the results from the testing are used as field scale numerical modelling inputs.

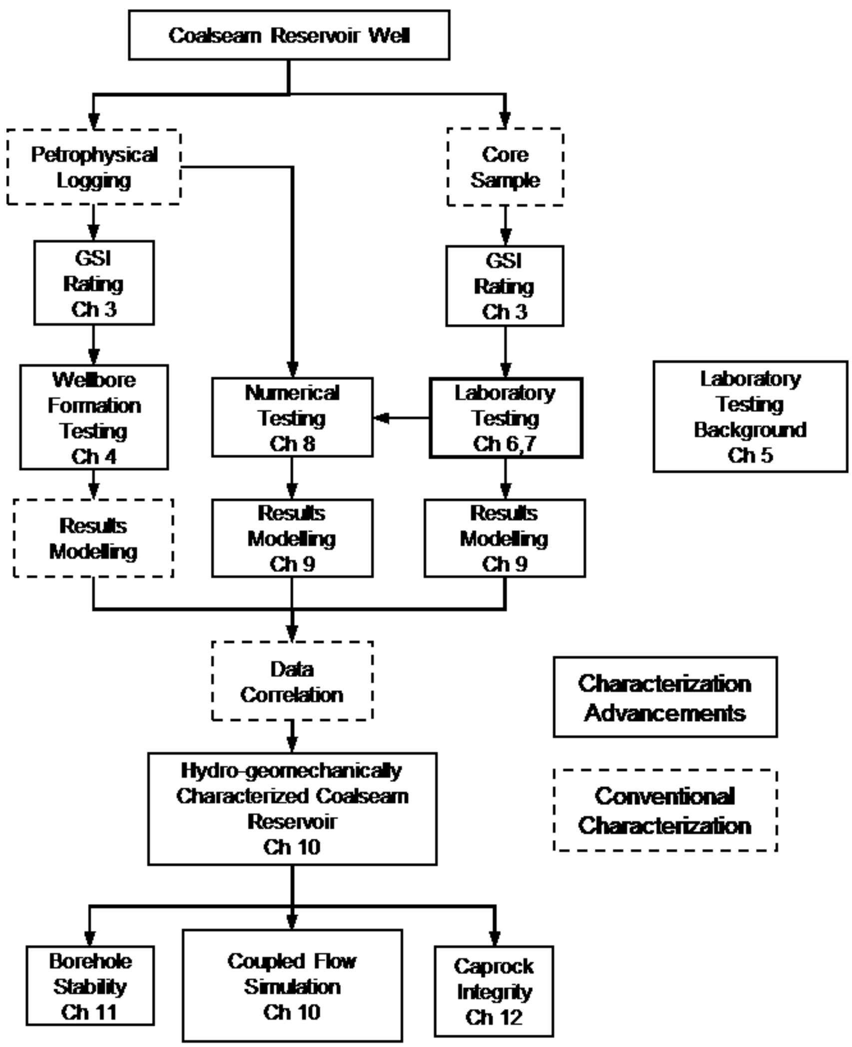

Figure 55. Coalseam reservoir hydro-geomechanical workflow showing where laboratory testing fits in the characterization workflow.

6.1 Testing Considerations

Taking into account the reservoir conditions in the Alberta Basin and the previously observed behavior of coal, laboratory testing apparatus were designed to measure the behaviour and properties of coal specimens throughout the majority of the coalseam reservoir life cycle conditions. These conditions include the use of CO_2 and gases other than CH_4 as a potential pore fluid for enhanced CBM (ECBM) and CO_2 storage. Additionally, as a well is drilled into a coalseam, coal fines or fragments are created which may cause plugging of fractures and correspondingly decrease production or plug downhole pumps. Industry had identified this as a critical issue. Considerations to produce and measure fines are included here.

The following design criteria (in no particular order) for a testing cell were deemed critical by Ho (2002) in her work on developing experimental methodologies to investigate transport processes in reservoir cap rocks. Enhancements to Ho's work considered in this thesis are included in items (14-16).

- Saturation of compatible pore fluids;
- Minimized specimen disturbance;
- Production and injection pore fluid scenarios;
- Accuracy over a wide range of stress, pressures, and temperature;
- Isotropic in situ stress conditions: isotropic;
- Multiple core types and sizes;
- Gas impermeable membrane or gas insoluble cell fluids;
- Improved upper and lower platen sealing mechanisms;
- Internal axial and radial measurements;
- Test adsorption and diffusion ;
- Test permeability;
- Test strength and deformation;

- P and S wave velocity under reservoir conditions;

Enhancements to the requirements outlined above included in this thesis are:

- Ability to apply independent axial and confining stresses;
- Capture of fines production after coal failure; and
- Testing of relative permeability.

To fulfill the requirements of the testing program two separate systems were developed. The first system, the Coal Fines Capture (CFC) apparatus, was a relatively simple design which addressed items 11, 12, and 15. The second system, the Low Permeability Gas (LPG) system, was more complex, and addressed all of the items except the capture of fines after failure (Item 15).

6.2 Coal Fines Capture Apparatus

A triaxial cell capable of independently applying axial and confining stresses to the specimen and capturing coal fines creation during testing was developed (Figure 56). Modifications to an existing cell (rated to 25 MPa confining pressure) were made to accommodate the capture of coal fines during testing. The 25 MPa maximum confining stress applied by the cell is sufficient to mimic the stress conditions in the near wellbore area (1-2 borehole radius) where the greatest deviatoric stress occurs (addressed in detail in the following chapter). The bottom platen was machined with a slot to simulate a horizontal well liner and allowed collection of coal fines. This allowed the flow of coal fines and fragments generated in the specimen during testing to exit and be collected in a downstream accumulator. One flow line into the top platen and one flow line into the bottom platen were used to apply upstream and downstream pore pressure. An Isco pump was used to control the top pore pressure and a Quizix® QL 700 pump was used to control the bottom pore pressure. One Teledyne ISCO® 500D (Isco 500D) was used to control the confining stress. A 400 kN load frame instrumented with a strain gauge on one of the columns and controlled with an Teledyne ISCO® 260D (Isco 260D) pump was used to apply the reaction force to the cell's axial ram. Vertical displacements of the specimen were measured with an external LVDT (linear variable displacement transducer).

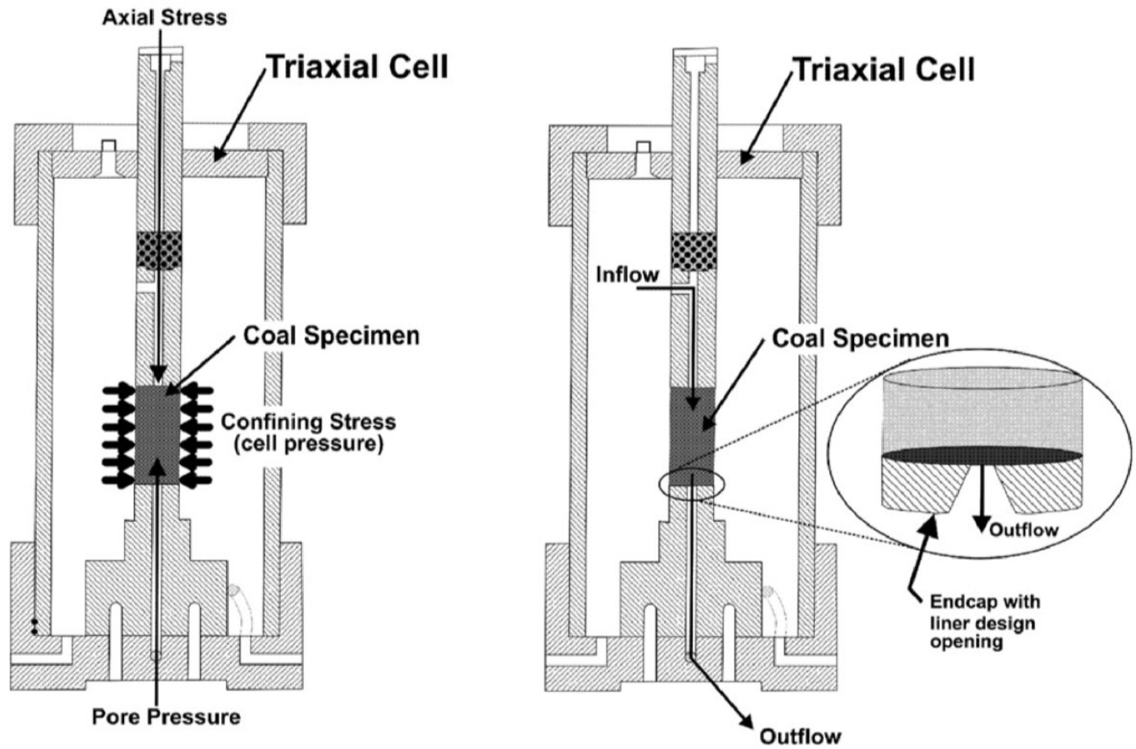

Figure 56. Coal fines collection (CFC) traixial cell for independent application of axial and confining stresses with a slotted endcap for solids flow production testing.

6.3 Low Permeability Gas Apparatus

Bachu (2007) completed a scoping analysis of the coal formations in the Alberta Basin outlining criteria for CO_2 storage. The analysis indicated that depths (d) should be between 300 to 900 m taking into account the injectivity (permeability and thickness) of the coal and CO_2 sorption isotherms. Additionally, current CBM production depths are 1500 m in the Mannville formation in Alberta. Using this depth range (300-1500m), the vertical (σ_v), maximum (σ_H) and minimum (σ_h) horizontal total stresses, pore pressure (u) and temperature (T) can be estimated to give a range of possible reservoir conditions (Table 4). The ratio (K_0) of effective maximum horizontal stress (σ'_H) to effective vertical stress (σ'_v) was estimated to be 1.1. The effective minimum horizontal stress (σ'_h) to effective vertical stress ratio (S_0) was estimated to be 0.5, however this may vary for each formation considered (Bell and Bachu, 2003). The geothermal gradient in the Alberta Basin ranges from 30 to 70 °C/km (Ho, 2002). Along with CH_4, the deeper coal formations are often saline water saturated and salinities are likely spatially variable.

Table 4. Equations used to calculated reservoir conditions in the Alberta Basin to constrain the LPG testing apparatus.

	Units	Equation	Min (d=300m)	Max (d=1500m)
σ_v	(MPa)	$0.023(d)$	6.9	34.5
U	(MPa)	$0.00981(d)$	2.9	14.7
σ_H	(MPa)	$K_0(\sigma_v - u) + u$	7.3	36.5
σ_h	(MPa)	$S_0(\sigma_v - u) + u$	4.9	24.6
T	(°C)	30-70 °C/km	9	105

6.3.1 Deisman Cell 6500

The design of the Deisman triaxial cell (TDS 6500) (Figure 57) included the ability to measure axial and radial strain, *P* and *S* wave velocities, permeability and relative permeability. The cell was designed with a fluid displacement drainage profile, to mimic a reservoir gas cap enabling production and injection pore fluid replacements with two flow lines into the top and bottom platens. These features made it possible to saturate a core with a desired pore fluid, displace it completely from the bottom, and inject another into the bottom. As a result, CH_4 production, ECBM production, or CO_2 storage scenarios could be simulated.

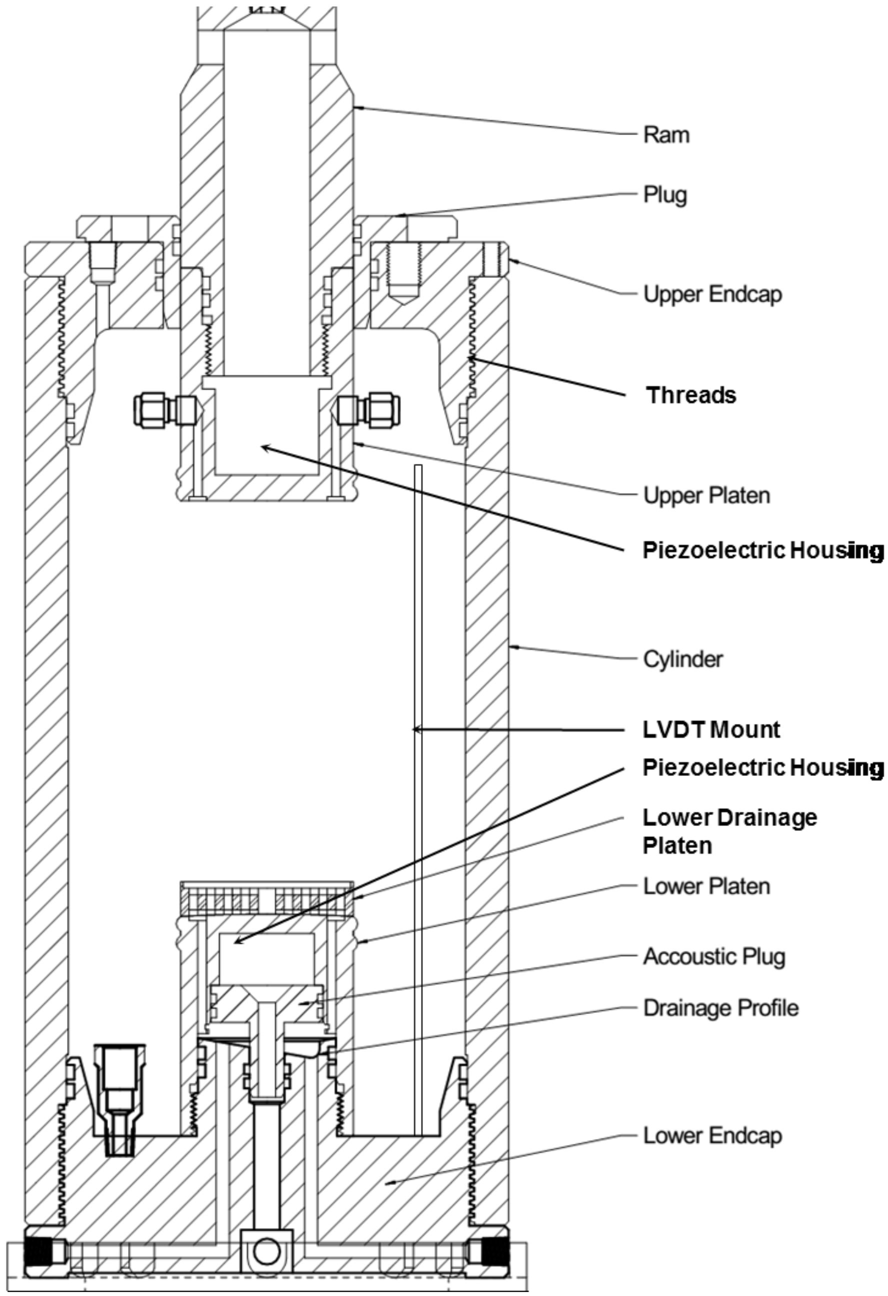

Figure 57. The Deisman cell with independent axial and radial stress, acoustic housing, drainage profile and two flow lines into the top and bottom platens.

Design parameters for the cell, based on an overall factor of safety of 4.0, are summarized in Table 5. The cell was designed to have maximum independent axial and radial operating stresses of 45 MPa, a maximum pore pressure of 20 MPa, and a maximum temperature of 60 °C. The 60 °C maximum operation pressure is below the maximum possible formation temperature of 120 °C at 1500m depth listed in Table 5 and was a design alteration that was dictated by flow system (as described in the Flow System subsection). The cylindrical cell has a 381 mm height and 171.5 mm outer diameter and all parts were constructed from AISI 4140 QT steel with a yield stress of 758 MPa (110 000 psi). All flow and cell pressure stainless steel tubing 6.35 mm lines enter through the cell base. The four flow lines (two for the top and two for the bottom platen) enter through the base and are connected once the specimen is in place. There are two top ports on the cell cap: one for a temperature probe and one used to aid in filling with cell fluid. The complete cell design and drawings are provided in Appendix A.

Table 5. Design parameters for the TDS triaxial cell.

Parameters	Metric Units	Imperial Units
Maximum Confining Pressure	45 MPa	6500 psi
Maximum Axial Stress		
Maximum Temperature	60 C	140 F
Maximum Pore Pressure	20 MPa	3000 psi
Maximum Specimen Height	127 mm	5.0 inches
Maximum Specimen Diameter	63.5 mm	2.5 inches

The bottom platen contains the drainage profile with an acoustic housing plug and stainless steel diffuser plate modelled after Butt (1999 and 2007). The diffuser plate was included to help distribute the pore fluid across the bottom of the specimen. The top platen threads onto the 63.5 mm outside diameter hollow axial ram, which passes through the plug in the upper end cap and contacts the load cell. To transmit the electrical instrumentation signals out of the cell, eight pin electrical seal connectors with ¼ inch NPT threaded steel housings were used (Green Tweed Oilfield Operations). The top and bottom platens contained P and S piezoelectric crystals for measurement of P and S wave velocities. Top and bottom platens contain rounded rings near the specimen which act to increase the stretch of the membrane to aid in sealing the specimen from the confining fluid. The specimen diameter is 63.5 mm, with a maximum height of 127 mm.

Cell Assembly

To minimize specimen disturbance while assembling the cell, an isolation support plate and top plug were designed (Figure 58). Once the specimen is placed between the upper and lower platens and sealed with a membrane, the cylinder and upper end cap are fastened to lower end cap. The upper end cap contains six bolt holes to fix the plug in place. The plug is placed over the ram, but not depressed into position. The ram is fixed to the upper end cap using the isolation plate and threaded support rods. The plug is then depressed or ratcheted into position. This helps to minimize disturbance during assembly. If the ram and top cap were not stabilized during assembly, there would be force acting on the specimen which may cause damage.

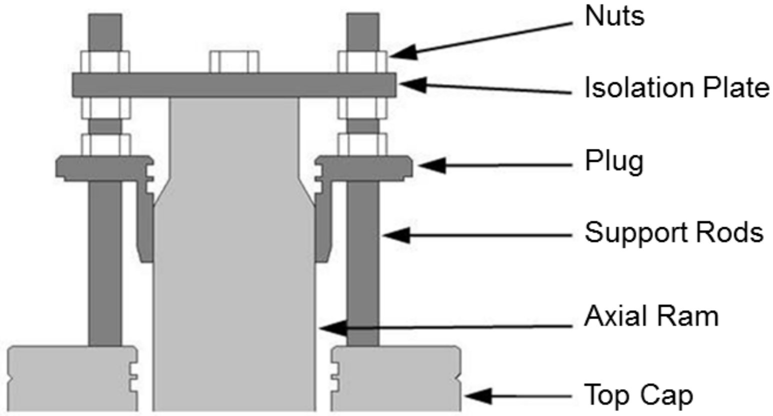

Figure 58. Support system used to minimize specimen disturbance during cell assembly.

Displacement Measurement

Three threaded holes at 120 degrees spacing around the inside of the base provide locations for internal threaded rods to run vertically beside the specimen. Up to three vertical linear variable differential transformers (LVDTs) are placed around the specimen to measure vertical displacement. Multiple internal vertical displacement measurements are key, as mounting an external LVDT on the axial ram to measure vertical displacement may lead to bulk results whereas internal gauges are mounted to measure deformations over the central 50% of the specimen (Figure 59) (Jimenez, 2006). Provisions are included to place up two rings of six LVDTs around the specimen to measure lateral displacements. Additionally, a circumferential chain with a spring loaded LVDT is used to measure change in specimen circumference.

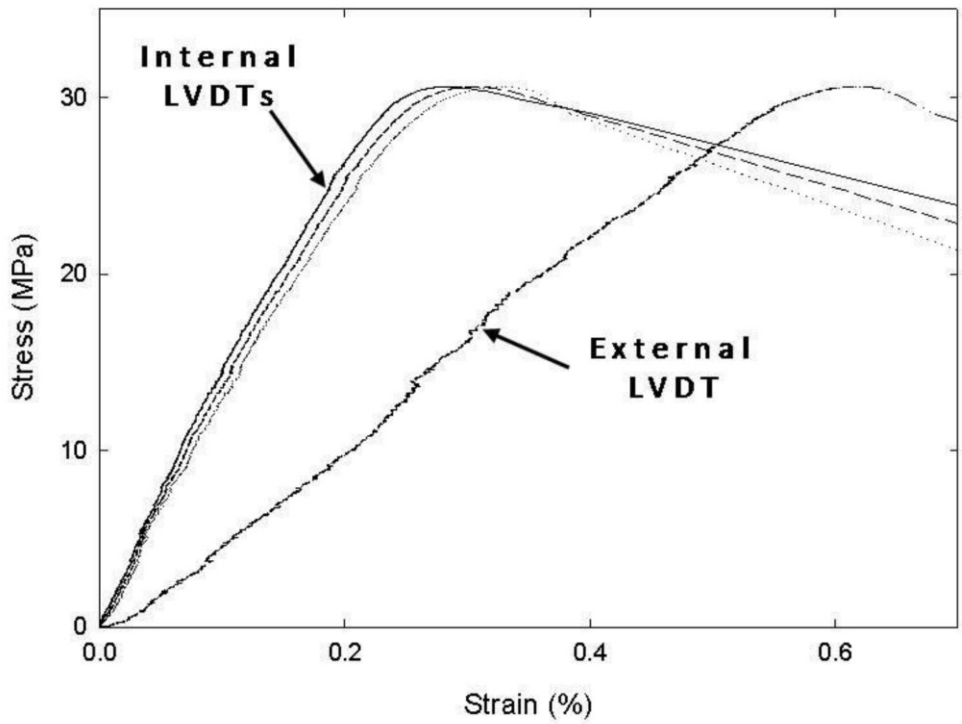

Figure 59. Internal LVDTs mounted on the middle 50% of the specimens verses external displacement measurements (adapted from Jimenez, 2006).

6.3.2 LPG Apparatus Design

To meet the pore fluid and pore fluid exchange design criteria, the system required a manifold to distribute multiple fluids as well as the ability to mix them during a test. Also an axial loading system (load frame), a hydraulic system for radial and axial stress control, a flow system for pore pressure and permeability measurement, a measurement/logging system, and a fluid sampling system were also included (Figure 60). Heat tracing on external lines and a large oven, containing the majority of the system, are used to raise and maintain the temperature.

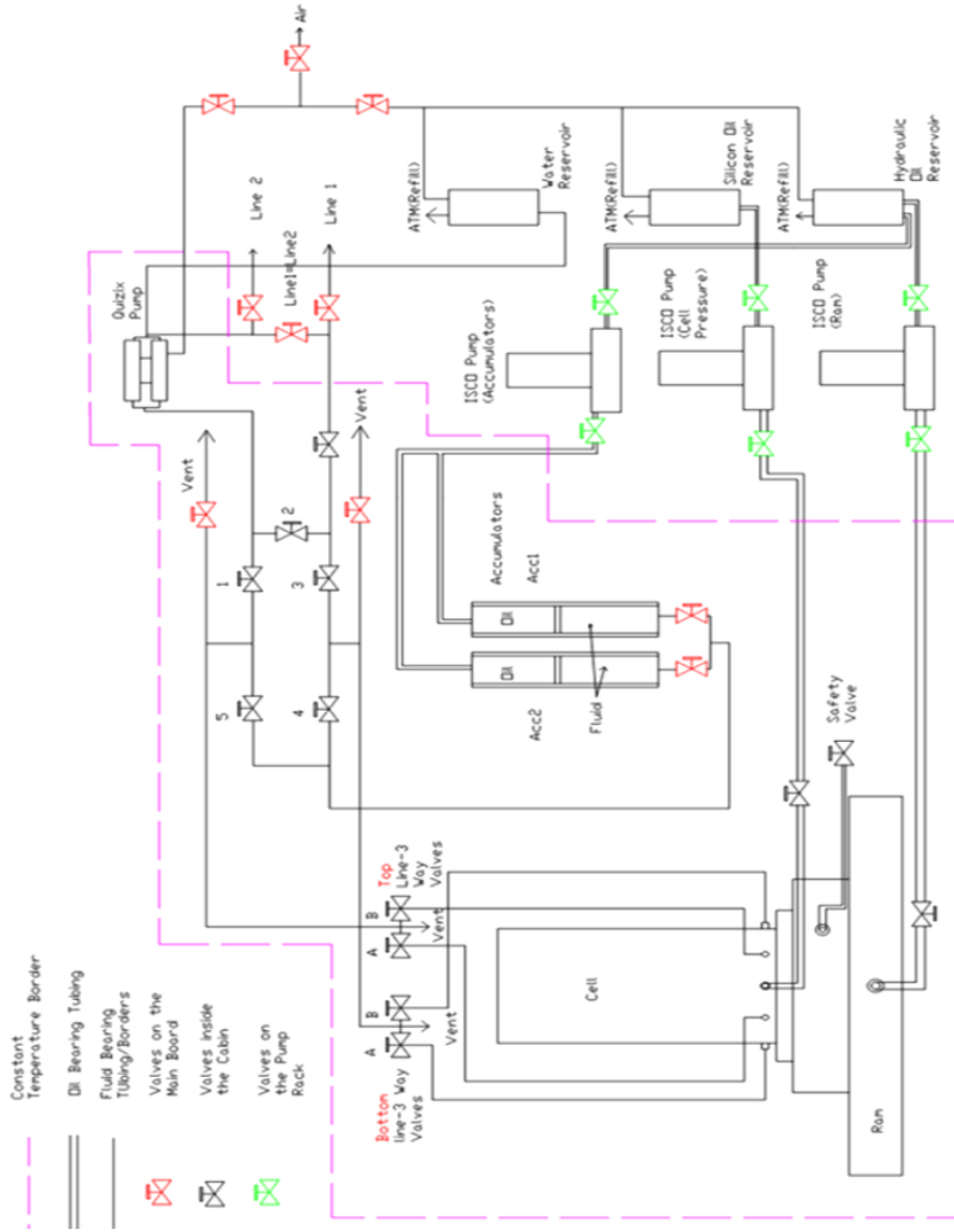

Figure 60. General layout for the Low Permeability Gas apparatus flow system.

Axial Force and Confining Fluid System

A low profile loading frame with a 228.6 mm diameter hydraulic piston connected to an external 45 MPa Jeffri syringe pump was used to apply an axial load in constant stress mode (Figure 61). The load is measured with a 200 kN external load cell fixed to the top load frame above the ram. The displacement of the ram is measured through an external LVDT. Radial stress is applied using non-conductive silicon oil pressurized by an Isco 260D outside of the oven and measured with a 20.7 MPa pressure transducer. The high precision/accuracy pump can operate in constant flow (0.01-107 ml/min) or pressure mode (max. 51.7 MPa). Tubing rated to 68.9 MPa and 6.35 mm fittings and valves rated to 41.4 MPa were used in the entire loading system with inline pressure relief valves set to 20 MPa for safety purposes.

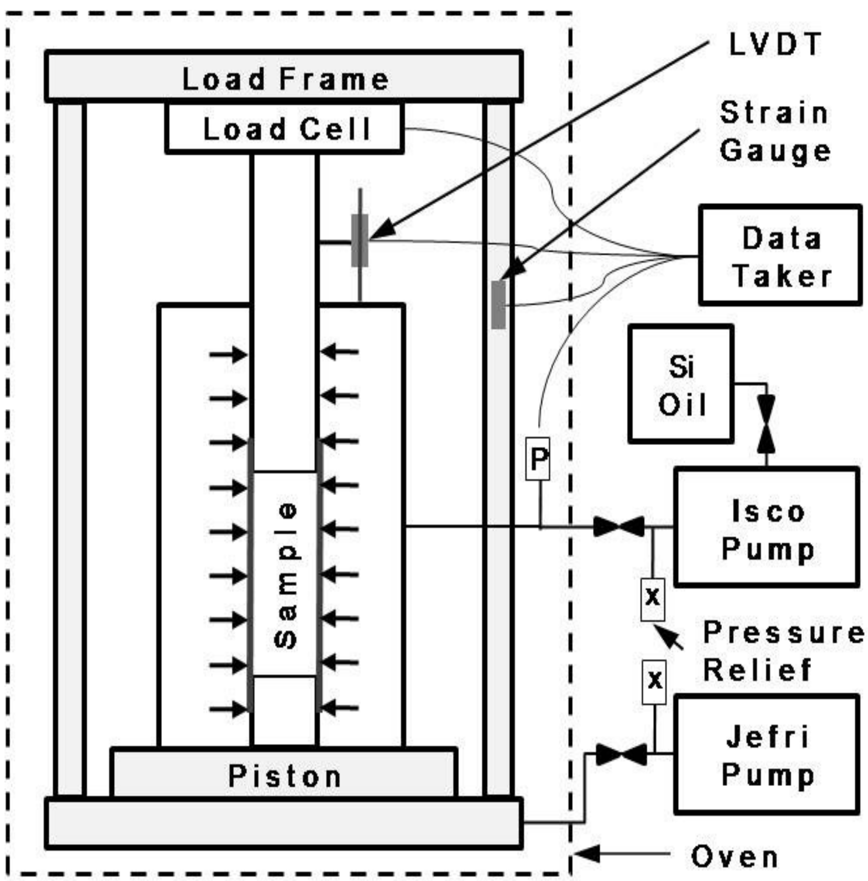

Figure 61. Schematic of the loading system contained inside of a medium temperature 60 °C oven.

Flow System

An external fluid mixing manifold with four gas inlets and one water inlet was designed with inlet pressure gauges and needle values. The mixing manifold has two output lines for gas and one output line for liquid to distribute fluid to “Line 1” and “Line 2” in the main flow system (“Line 2” can take fluid or gas) (see Figure 60). The three outlet flow lines are heat traced to bring fluid to test temperature, and then two lines (one gas, one water) are connected to an internal Quizix® pump. The remaining gas line connects to an internal switching system leading to the Quizix® pump or two reactors with internal pistons. Quizix® pump is a high precision and accuracy pump with two cylinders capable of operating as constant flow/pressure or independent pressure (34 MPa maximum) or flow mode with a minimum and maximum flow of (0.0001-34 ml/min), respectively. Each reactor has a volume of 2.31 L with maximum pressures of 68.9 MPa and are controlled together by a single Isco 260D pump with an inline relief valve set to 20 MPa. The Quizix® pump was mounted inside of the oven to minimize the fluctuations of gas properties during testing. This however, created a limitation with the operating temperatures as the Quizix® pump control electronics must remain below 60 °C.

Flow lines from the internal pump or reactors move through a switching system to direct fluid to the top or bottom of the specimen. Two flow lines with pressure and differential pressure transducer systems and temperature probes are connected to the top and bottom of the specimen, and are directed with three way valves and a vent pressure regulator (Figure 60). The vent pressure regulator allows for flushing of top and bottom flow lines, while maintaining specimen fluid pressure. The pressure transducer valves and vents inside of the oven are connected to an air actuated system to minimize temperature fluctuations cause by opening the oven door during testing and for quick release of fluid pressures for safety. Stainless steel tubing rated to 68.9 MPa with 6.35 mm outside diameter and 3.175 mm internal diameter stainless steel fittings rated to 41.4 MPa and valves were used throughout the flow system. Air actuated vents, pressure relief valves, and a vented gas water separator are placed in line for safety purposes.

Data Logging System

The readings of the load cell, cell pressure, top and bottom pressure, differential pressure, axial and radial strains, and temperature probes are logged and continuously displayed on a control board using a DataTaker® DT800 system. The calibrations were input directly into the DT800 system by translating the mV signals using the instrument calibration factors (including pressure transducers, LVDT's, temperature probes, and the load cell). The DT800 allows for 12 - 42 analog sensor channels, 16 digital channels, with internal data storage and high sampling rates. As well the Jefri and Isco pumps all have in-house designed software and control systems to set and log pressures and flow rates for secondary or back up data acquisition. The Quizix® pump control and data acquisition is supplied.

6.4 Testing Measurements

Several techniques have been developed to measure the sorption, permeability and relative permeability of materials. Each technique and its applicability depend on the properties of the material being tested. The CFC and LPG testing apparatus were each designed to be flexible enough to apply required measurement techniques. As well, the mechanical behavior of the specimen can be measured either using stress or strain loading increments.

6.4.1 Strength and Deformation

The CFC and LPG apparatus are both able to measure deformation and strength. Both systems use Isco syringe pumps to compress oil to displace a hydraulic piston, which then acts on the axial ram. Therefore, each system is capable of running in an axial stress mode only (i.e. not constant strain). Each system is also capable of applying variable radial (confining) stress through an Isco pump. The CFC and TDS 6500 cells each have ram designs that allow for independent application of axial and confining stress and are therefore capable of applying several stress paths, with the pure stress paths as follows and depicted on Figure 62:

- Loading Compression - increasing axial stress, constant confining stress;

- Loading Extension - constant axial stress, increasing confining stress;
- Unloading Compression - constant axial stress, decreasing confining stress;
- Unloading Extension – decreasing axial stress, constant confining stress.

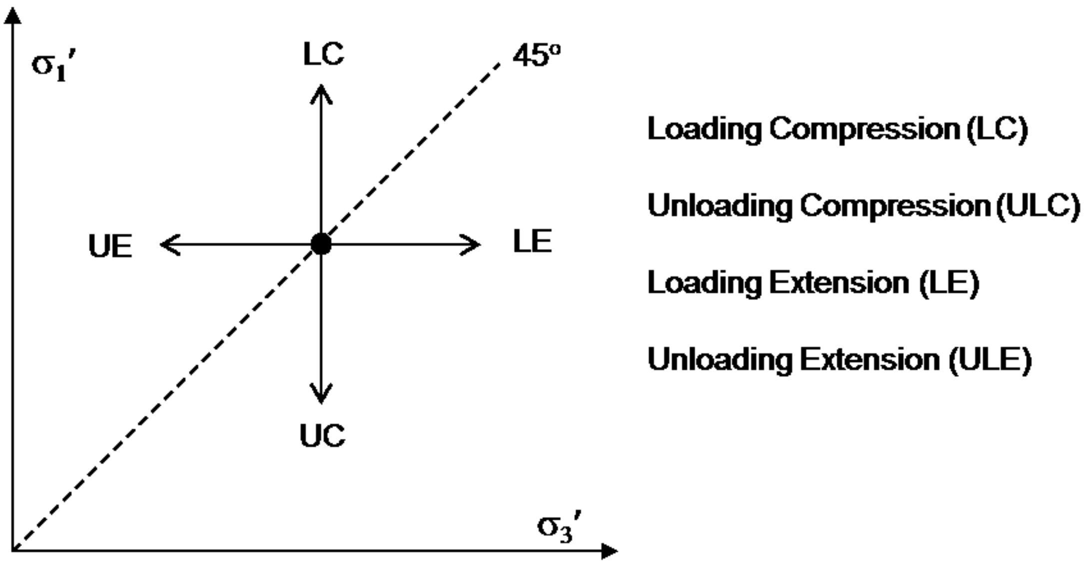

Figure 62. Pure loading and unloading stress paths plotted in effective stress space.

Additionally, the independent axial and radial control of stress allows for the testing of anisotropic deformation of the specimen. For example, if the radial stress is held constant while the axial stress is increased or decreased, the deformation characteristics in the axial direction can be determined. Then, if the axial stress is held constant and the radial stress is increased, the deformation characteristics of the specimen can be determined in the radial direction. This allows for an assessment of specimen anisotropy.

6.4.2 Coal Fragments and Fines

The generation of coal fragments and fines can be measured at two stages. First, during the application of the stress path, fluids may flow through the specimen into the accumulator, where coal fines could be collected. Secondly, after the specimen has been tested, the specimen can be removed and fines or fragments determined. At each stage of collection, the particle diameter distribution can be determined with a sieve analysis.

6.4.3 Sorption and Diffusion

Adsorption isotherms can be measured using either a volumetric or gravimetric technique (Bustin, 1999). The volumetric method measures the change in pressure as volume of gas is sorbed to the coal, where the gravimetric method is based on the change in mass of the specimen during pressure changes. The volumetric approach is preferred due to its simplicity. Diffusion properties can be measured in coal through a characteristic sorption time (τ), which is the time required to desorb 63.2% of the initial gas volume in the coal during a constant pressure gradient (Mavor, 1999).

6.4.4 Permeability

The flow through coal may be difficult to experimentally measure. Laboratory permeability may range from tens of mD to below μD depending on the stress level and number and distribution of fractures present. Several methods may be used to measure permeability (k) including constant flow, constant differential pressure, or transient pressure techniques. In each case, a reservoir is connected to the top and bottom of a specimen of length (L), area (A), and change in height (Z).

Constant Flow or Constant Differential Pressure

The constant flow approach applies a fluid with a density (ρ) and viscosity (μ), and a flow rate (Q) in one pump and records the pressure differential (dP) once stable, whereas the constant differential pressure rate applies differential pressure and records flow rate once stable. The data is then used to solve Darcy's equation (Eq 17) for permeability:

$$Q = \frac{kA}{\mu}\left(\rho g \frac{dZ}{dL} - \frac{dP}{dL}\right) \tag{17}$$

Transient Pulse Technique

The transient pulse technique was presented by Brace et al (1968) with a more complete analytical solution offered by Hsieh et al. (1981). The transient pulse technique applies a small increase in pressure in one of the reservoirs and monitors the pressure change with time in both reservoirs. The data is then used to match the one dimensional diffusion equation for permeability (Eq 18) and specimen specific storage (S_s) (Eq 19).

$$\frac{\partial^2 P}{\partial x^2} = \frac{\mu S_s}{k}\frac{\partial P}{\partial t} \qquad 18$$

$$S_s = \eta C_w + C_{eff} - (1+\eta) C_s \qquad 19$$

where C_w, C_{eff}, and C_s are the water compressibility, effective compressibility, and the solids compressibility.

The transient pressure decay is mathematically solution is describe by Eq 20 and Eq 21 where the specimen is connected to upstream and downstream reservoirs with associated upstream (S_u) and downstream (S_d) specific storages, at initial pressure P_o, where one reservoir is subjected to a sudden increase in fluid pressure ΔP (Figure 63) (Hsieh, 1981).

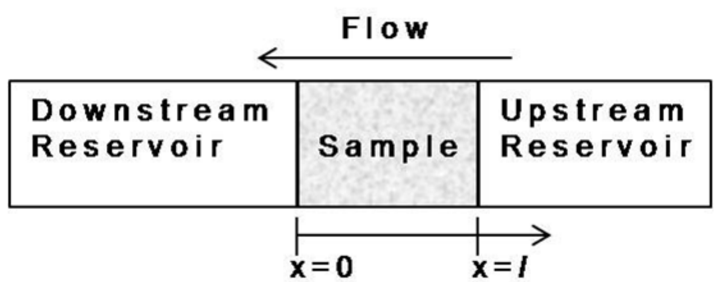

Figure 63. Transient pulse technique diagram for permeability measurement technique.

$$\frac{P_u - P_o}{\Delta P} = \frac{1}{1+\beta+\gamma} + 2\sum_{m=1}^{\infty} \frac{\exp(-\alpha\phi_m^2)(\beta+\gamma^2\phi_m^2/\beta)}{\left[\gamma^2\phi_m^4/\beta^2 + (\gamma^2\beta+\gamma^2+\gamma+\beta)\phi_m^2/\beta + (\beta^2+\gamma\beta+\beta)\right]} \qquad 20$$

$$\frac{P_o - P_d}{\Delta P} = \frac{1}{1+\beta+\gamma} + 2\sum_{m=1}^{\infty} \frac{\exp(-\alpha\phi_m^2)(\beta-\gamma^2\phi_m^2/\beta)}{\left[\gamma^2\phi_m^4/\beta^2 + (\gamma^2\beta+\gamma^2+\gamma+\beta)\phi_m^2/\beta + (\beta^2+\gamma\beta+\beta)\right]} \qquad 21$$

where ϕ_m are the roots of Eq 22:

$$\tan\phi_m = \frac{(1+\gamma)\phi_m}{\gamma{\phi_m}^2/\beta - \beta} \qquad 22$$

The solution contains a dimensionless variable α (Eq 23) and two dimensionless parameters β (Eq 24) and γ (Eq 25).

$$\alpha = \frac{kt}{\mu L^2 S_s} \qquad 23$$

$$\beta = \frac{S_s A L}{S_u} \qquad 24$$

$$\gamma = \frac{S_d}{S_u} \qquad 25$$

The dimensionless variable γ is easily measured however α and β are dependent on both the specific storage and the permeability of the specimen. Therefore, when matching the data obtained from the laboratory test to the predicted solution provided by Eq 20 and Eq 21 an iterative technique must be used. First, an estimate S_s is made to solve ϕ_m, where m=1 to 100 (Eq 22). ϕ_m is then used to solve S_s at t=0 (α=0) through Eq 20 and Eq 21 by iteration. The remainder of the solution is then matched for t>0 ($\alpha \neq 0$) by iterating the permeability in by Eq 20 and Eq 21. This technique was programmed in Visual Basic for use with Microsoft Excel® to automate the solution fitting and was found that 15 roots (Eq 22) are enough for a sufficient curve fit.

Four constants are required from the testing system as well as behaviour of the pore fluids (density and viscosity) for the solution to the equations. The constant are the upstream and downstream volume and compressive storage of the reservoirs, as summarized in Table 6. Only the LPG system was developed to allow the use of the transient pressure pulse technique and was measured for the required constants.

Table 6. Upstream and downstream volume and compressive storage of the LPG apparatus.

Constant	Unit	Upstream	Downstream
Volume	mL	54.312	35.46
Compressive Storage	m^2	2.281 $x10^{-10}$	1.489 $x10^{-10}$

6.4.5 Relative Permeability

Relative permeability measurements are made using either steady or unsteady state techniques (Hycal Energy Research Laboratories). In the steady state approach a mixture of two or more fluids is flowed through a specimen until equilibrium is achieved, computing the relative permeability from individual flow rates and phase pressures, and measuring saturation. The unsteady state method displaces a single fluid through a specimen, which is saturated with two fluids, with the injection fluid at the minimum or irreducible saturation. The pressure differential and production of the fluid is monitored and sampled throughout the injection period. Several approaches can be used to analyze the unsteady state data including the Buckley-Leverett displacement theory or through the use of reservoir simulation to history match (Mavor, 1999).

6.5 Initial Calibrations and Systems Check

The CFC system used a modified bottom platen to collect coal fines and fragments during testing. The system had already been in place and calibrated prior to the commencement of the coal fines generation testing, and therefore there were limited requirements to test or calibrate the system. However, there was a need to pressure the system to test for leaks around the slotted platen as well as in the fines collection accumulator.

The LPG system implemented three testing separate programs test the performance of the system and the TDS 6500 testing cell. The first 'no specimen' program for the TDS 6500 was used to calibrate the load cell to the internal cell pressure. This was done by simply increasing the cell pressure at 1 MPa increments to 45 MPa and then using the internal pressure to load cell reading to create the ram friction calibration, which was then programmed directly into the DT800. This was also useful to test all of the O-ring and Swaglok fitting seals.

The second program was to test only an aluminum specimen and proper specimen membranes to test the flow seals and fittings. As well, the *P* and *S* wave velocities were measured and agreed with theoretical values. Because gas diffusion properties are a required testing parameter, the aluminum specimen was wrapped with a thin lead sheet and the seams filled with silicon and allowed to dry before a latex membrane was placed over top. The third program used a shale specimen to measure permeability using the transient pulse technique.

6.5.1 LPG Apparatus - Shale Permeability Test

A preliminary shale specimen was used to test the performance of the LPG flow system and the ability to perform the transient pulse technique. The specimen length and diameter were 112.5 mm and 62.5 mm, respectively. A critical point in the test is the ability to keep a constant temperature throughout the testing. In the NREF 5-120 laboratory at the University of Alberta, temperatures may fluctuate four degrees throughout a 24 hour period. Therefore, the oven was raised to 25 °C, which is above the maximum measured laboratory temperature. The pore fluid used for the test was a brine solution of 3000 ppm NaCl. The initial effective confining stress on the specimen was 1 MPa. A pressure pulse of 110 kPa was applied by pressuring the Quisix pump and then opening the deliver valve. The size of the pulse is the instantaneous reading after valve opening and the volume of the upstream reservoir must include the volume of the Quisix pump chamber. The results of the test are shown in Figure 64. The normalized pressure pulse initially began at 0.96 and decayed in 50 seconds to 0.6. The results for the downstream pressure change can also be modeled, however only the top pulse decay is required to determine the permeability of the specimen (Jimenez, 2006).

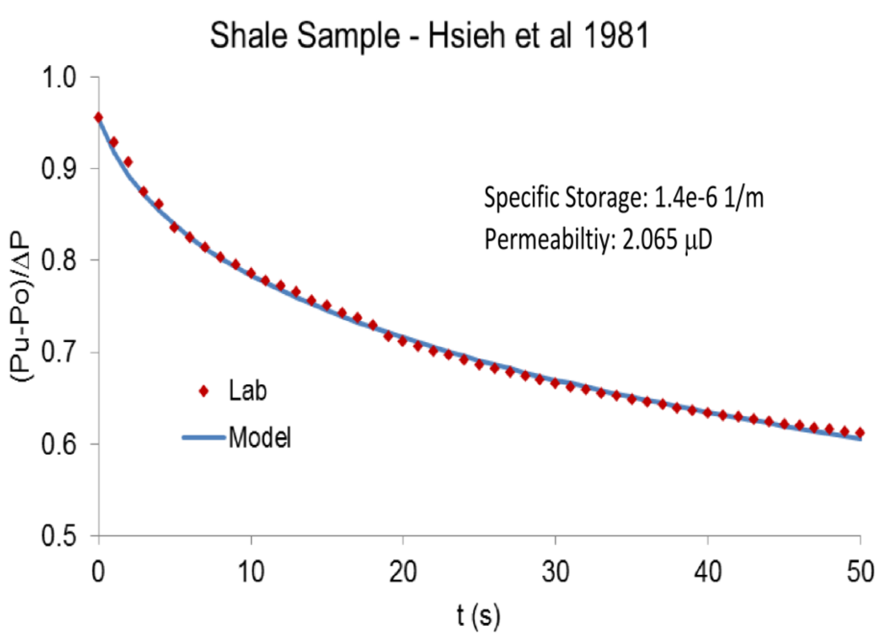

Figure 64. Demonstration of the transient pulse theory solution on a shale specimen in the LPG apparatus.

6.5.2 Modifications

Several issues arose during the calibration and systems check program. The first issue was the requirement for O-ring spacers under the bottom and top O-rings on the top cap and base respectively, which help seal the cell at higher pressures. This was due to a machine shop error where design tolerances were not respected. As well, phosphate coatings were applied to all of the surfaces of the cell to prevent corrosion as well as excessive wear. With a threaded screw cap cell design, the thread design and protection is important and mistreatment of the threads led to many assembly issues.

During the aluminum specimen testing, there was difficulty in creating a seal using a lead and latex wrap. The major issue was the rounded ring nearest the specimen on the top and bottom platen. These were removed leaving only one ring each on the top and bottom platen. As well, there was initially an arch on the top of the bottom platen for use with a shaped diffuser plate. This was modified to a flat platen with no diffuser plate to increase the P and S wave transmission through the specimen. Also, during deformation measurements from the two internal LVDTs, placed at 120 degrees separation around the specimen, were not vertical. Therefore, greater attention to installation is required.

6.6 Conclusions

The experimental capabilities developed at the University of Alberta to carry out hydromechanical characterization of coal and other geomaterials at medium temperatures (< 60 °C) are summarized. The apparatus meets several of the design criteria goals including: pore fluid saturation, minimized specimen disturbance, production/injection capabilities, representative stress conditions, internal measurements, and failure analysis.

The coal fines production apparatus is capable of measuring deformation, strength, permeability, and the generation of coal fines during and after the test. The cell associated with the system was designed with a slot in the lower platen and is capable of applying independent axial and radial. The low permeability gas apparatus contains a 45 MPa pressure, 60 °C temperature triaxial cell for hydromechanical testing capable of measuring diffusive properties, absolute and relative permeability, strength, deformation and compressional and shear wave velocities under independent axial and confining stresses and fluid saturation conditions. Several modifications to the initial design are discussed and some solutions provided. Results for measuring permeability on a shale specimen using the transient pulse technique were demonstrated. For both apparatus, techniques for measuring gas sorption isotherm, permeability, and relative permeability, coal fines sizes were briefly reviewed.

7 Laboratory Testing Program and Results

7.1 Introduction

This chapter details the three separate hydrogeomechanical laboratory testing programs carried out and the results developed for this research. The testing program used block samples and a brief description of the geology is provided for each block coal sample. Figure 65 illustrates where the laboratory testing appears in the overall program for hydrogeomechanical characterization of a coalseam reservoir.

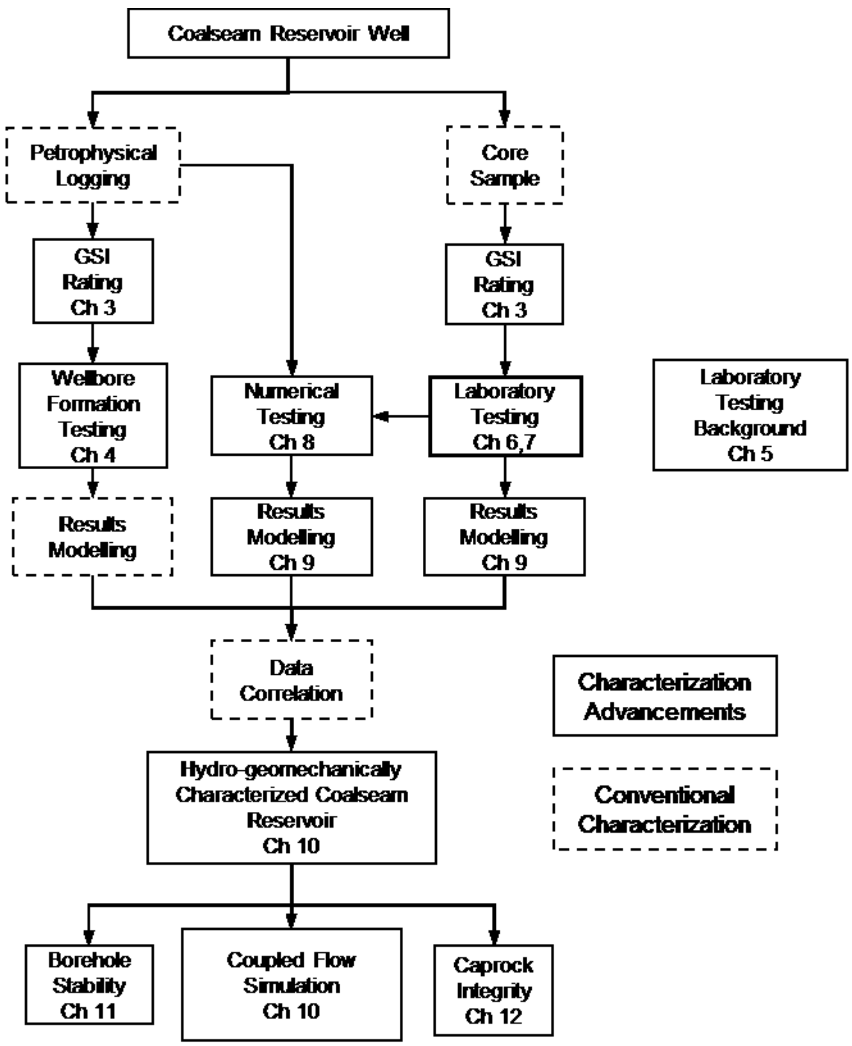

Figure 65. Coalseam reservoir hydro-geomechanical workflow showing where the laboratory testing fits into the overall characterization approach.

This chapter is structured as follows:

- A brief summary of the testing program is provided;
- Coal geology and specimen preparation/storage procedures are described;
- Testing procedures are described;
- An overview of the test evaluation equations is presented;
- Results from all tests are presented; and
- A summary of the chapter is provided.

7.2 Coal Testing Programs

Three separate but similar coal testing programs were conducted in this research program to investigate deformation, seismic wave velocity (velocity), strength, permeability, fragmentation (particle size), and methane sorption behaviour of coal. In the previous chapter, it was noted that several of these coal properties are related and therefore, the three testing programs were structured to investigate the interaction behaviours of these.

<u>Program 1: Conventional Triaxial Stress path with Velocity and Permeability (CT w/ V,P)</u>

The first testing program was comprised of several conventional triaxial tests with compressional (P) and shear (S) wave velocity measurements to calculate the dynamic Young's modulus and permeability. The testing was completed by a consulting company (TerraTek) with the processed data provided for analysis.

<u>Program 2: Unconventional Triaxial Stress path with Permeability and Particle Size (UT w/P,PS)</u>

In the second program, unconventional triaxial stress paths were followed with permeability measurements at various stress states along the stress path. During permeability testing, a production cell was used to attempt to capture coal fragments as the coal sample neared the failure envelope and post failure fragmentation measurements were also taken. This testing utilized the coal fines measurement (CFM) laboratory apparatus with the coal fines collection (CFC) triaxial cell at the University of Alberta.

<u>Program 3: Elastic Triaxial Stress path with Velocity and Methane Sorption (ET w/ V,G)</u>

The third and final testing program used a triaxial stress path that remained in the elastic range and measured velocity and gas sorption at several effective stress states. The program was completed at the University of Alberta and with the low permeability gas (LPG) apparatus with the Deisman Triaxial (TDS) cell.

All of the coal specimens tested were prepared from large block coal samples collected and preserved from three different open pit mine sites: Greenhills, Elkview, and Cardinal River. A summary of the each of the testing programs and data measured is provided in Table 7.

Table 7. Summary of the coal hydrogeomechanical testing programs.

Property	Symbol	Test Program		
		1	2	3
Radial Effective Stress	σ'_{xy}	x	x	x
Axial Effective Stress	σ'_z		x	x
Mean Effective Stress	σ'_m		x	x
Young's Modulus	E	x		x
Poisson's ratio	ν	x		x
Dynamic Modulus	E_D	x		x
Axial Effective Stress at Failure	σ'_f	x	x	
Particle Size Distribution	PS		x	
Permeability	K	x	x	
Gas Volume	V_g			x
Axial Strain	ε_z	x		x
Radial Strain	ε_{xy}, ε_r	x		x

7.3 Sample Description

7.3.1 Geology

Coal samples were collected from Southern Alberta/BC and Central Alberta open pit mines: Greenhills, Elkview, and Cardinal River. Each coal sample was collected in a large block and then sub samples were cored and specimens for each testing program were created. These locations were selected due to their active coalseam methane activity and their analogy to active coalseam methane production reservoirs.

Greenhills and Elkview

The Foothills and Mountains regions of SE British Columbia (Figure 66) have been the focus of exploration and exploitation of natural gas from coal (Chevron, Gulf, Norcen Energy have initiated CBM evaluation projects). Medium volatile bituminous ranked coal blocks were taken from the Greenhills (GH) mine from Seam 3, 7, and 10 and from the Elkview (ELK) mine from Seam 8 and Seam 10 in SE British Columbia. The coal used in this testing program was collected by an external consulting company (TerraTek) and there is no further information on the collection and transport of the coal block samples to the laboratory.

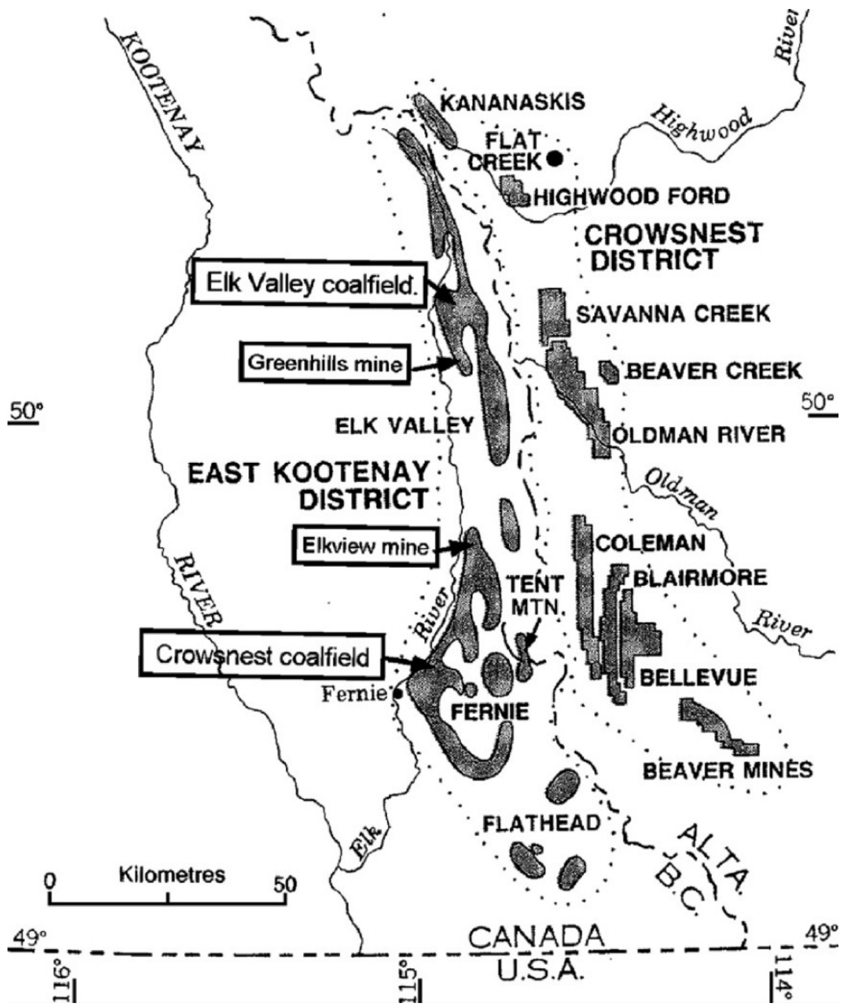

Figure 66. Mine areas of SE British Columbia / Alberta showing the Elkview and Greenhills mines (modified from Smith, 1989).

Cardinal River Coal

The coal samples were obtained from freshly-exposed areas of the Jewel Seam in the Cardinal River Mine (Figure 67), Alberta Mountains region, away from fold structures. At the sampling location, the rank of the Jewel Seam is medium volatile bituminous (Mean Maximum Reflectance is 1.3%) and the coal contains 70% vitrinite and 25% inertinite.

These samples were selected to provide qualitative information on horizontal well performance drilled in Foothills/Mountains coals and guidance on slotted wellbore liner design (slotted liners are used to filter coal fragments).

Figure 67. The location of the Cardinal River mine near Hinton, Alberta.

7.3.2 Coal Storage and Specimen Preparation

Large coal block samples were collected from the Greenhills, Elkview and Cardinal River coal mines. These blocks were then cylindrically cored to create specimens for testing. The CT w/ V,P program used coal from all three locations, whereas only coal from the Cardinal River mine was used for the two other programs.

Sample Collection and Storage

Several large coal blocks ranging in size from 0.5 m^3 to 1 m^3 were collected during winter conditions (~ -20°C). The samples, which had fallen from the freshly exposed face, were collected during two separate trips. The coal blocks were strapped onto pallets, covered by polyethylene sheeting and transported at the University of Alberta (duration 4 hours). Coals are sensitive to oxidation which alters coal properties (Robertson and Christiansen 2007), and because these samples were collected from a newly exposed coal face, the samples were immediately wrapped in several layers of plastic wrap upon arrival at the U of A. Once the samples were wrapped, the block samples were stored inside the moisture room for long term storage. The moisture room maintains a constant temperature of 6 C° and a constant humidity of 100%. This procedure was used to try to maintain the *in situ* moisture content of the samples. The coals were expected to have limited, if any, gas due to their shallow depth and recent surface mining activities. Therefore sealing the blocks to prevent gas migration was not attempted. Information on the collection and storage of the coal samples from the Greenhills Mine and Elkview mine was not available.

Conventional Triaxial with Velocity and Permeability Specimens

Vertical cylindrical cores (for triaxial tests) and horizontal cylindrical cores (for permeability tests) were cut from the Greenhills, Elkview, and Cardinal River mine coal blocks using water as a circulating/cooling fluid. Each sample was 37.5 mm in diameter and 75 mm in length. In a few instances, smaller samples were extracted from the blocks due to difficulties maintaining larger intact specimens. The ends of each core were surface-ground flat with a stationary belt sander and parallel to within a tolerance of ±400 μm), in accordance with International Society of Rock Mechanics (ISRM) standards. A summary of the density and dimensions of the prepared specimens is provided in Table 8.

Table 8. Summary the coal specimens prepared for the CT w/ V,P testing program.

Coal Seam	Sample ID	Bulk Density (kg/m^3)	Length (mm)	Diameter (mm)
Greenhills, Seam 3	GH3-1 GH3-2 GH3-3	1317 1318 1320		
	GH3-4	1369	44.8	37.9
Greenhills, Seam 7	GH7-1 GH7-2 GH7-3	1395 1281 1303		
	GH7-4	1312	46.9	38.4
Greenhills, Seam 10	GH10-2 GH10-3	1336 1328		
	GH10-4	1310	47.4	37.9
	GH10-5	1339		
Elkview, Seam 8	8UX-1 8UX-3 8UX-4 8UX-5	1324 1334 1309 1331	50.0	38.3
Elkview, Seam 10	ELK10-1 ELK10-3 ELK10-4	1448 1452 1456		
	ELK10-5	1485	19.5	37.9
Cardinal River	CR-2 CR-3 CR-4	1308 1334 1343		
	CR-5	1350	38.3	38.3

Unconventional Triaxial with Permeability and Particle Size

To create a specimen for testing, a large block sample from the Cardinal River Mine was removed from the moisture room and taken directly to a drill press coring room. The plastic wrap was removed from the sample and a wooden frame was built around the sample to minimize vibration while drilling. The bedding planes were orientated perpendicular to the core barrel to create cores. A 63.5 mm diameter core barrel with two slots in the side of the barrel was used. During coring of the block, air was used to circulate the drill cuttings and cool the cutting surface. A tremendous amount of coal fines are created during coring, which required the operators to wear goggles and respiratory protective equipment. As well, a large portable vacuum hood was placed over the drill press with another large vacuum hose placed directly at the face of the cutting barrel to collect the coal dust.

Several circular cores were attempted however a majority of these were broken or lost due to the friable nature of coal. Attempts were made to create test specimens from areas of the coal block which had higher fractures/cleats density, however, this was difficult and not possible. Therefore, the long drilled cores were only successful in areas that contained few large cleats. After core was created, it was removed from the core barrel and the ends were cut to create right cylinders using a diamond blade on a multi cutter equipped with air cooling and two vacuums. Once the specimens were prepared, they were wrapped in several layers of plastic wrap and stored for future use.

Elastic Triaxial with Velocity and Gas Content Specimen Preparation

The procedure described above was used to create a core specimen for this testing. However, due to many samples being destroyed, an exception to the length requirement was made. In this program, as the specimen was not to be taken to failure, the ISRM recommended 2:1 height to diameter ratio was not used (1.748). The specimen had almost no visible fractures (i.e specimen is intact) and therefore the fracture density was characterized by assigning a Geological Strength Index of 100 (Deisman et al., 2010). A summary of the specimen properties of the ET w/ V,G program are shown in Table 9.

Table 9. Properties of coal specimen used in ET w/ V,G.

Sample Location	Units	Cardinal River Mine (near Hinton, Alberta, Canada)
Coal Rank		Medium Volatile Bituminous
Mean Maximum Reflectance	%	1.3
Vitrinite/Inertinite	%	70/25
Diameter	mm	63.5
Height	mm	111
Density	kg/m^3	1435
Geological Strength Index		100

7.4 Testing Apparatus and Procedures

7.4.1 Conventional Triaxial Compression with Velocity and Permeability

Conventional triaxial compression tests were executed at multiple effective confining stresses to allow a strength envelope, Poisson's ratio, and Young's modulus for three coal types to be determined. In addition, velocity measurements were performed concurrently at five to seven separate stress states during testing and the dynamic mechanical properties were calculated. In addition to the mechanical tests, porosity and permeability to water were determined for one representative horizontal sample from each coal type.

Test Apparatus

All mechanical stress path tests were conducted using a servo-hydraulic controlled load frame with a triaxial testing cell, which subjected the specimens to the desired stress. Prior to triaxial testing, each test specimen was placed between two titanium platens containing ultrasonic transducers. A Teflon® sleeve was fit around the specimens and platens and the test specimen was then instrumented with an axial LVDT and radial cantilevers (strain gauges mounts on flexible cantilevers) for strain measurements and placed in the triaxial cell for testing. Axial strain, radial strain, and the axial stress were continuously recorded throughout the test using a digital data acquisition system. The P and S wave velocities were measured using 1 MHz piezoelectric crystals.

Test Procedures

The specimens were initially loaded to isotropic stress states of 0.2 MPa, 5 MPa, and 14 MPa, which were based on estimates of the *in situ* stress field. The block samples were obtained from for an area in SE British Columbia where the vertical stress gradient was estimated to be 25 kPa/m from bulk density logs and the maximum (26 kPa/m) and minimum (22 kPa/m) horizontal stress gradients were estimated based on geological structure and tectonic history. A formation pore pressure gradient of 10.4 kPa/m (slightly over pressured) was used based on measurements of gradients in nearby Elk Valley basin water wells (Harrison, 2002). Once the target isotropic stress state was reached, the deviator stress was then applied using a strain rate of $1\times10^{-5}\,s^{-1}$ until failure occurred and then continued past peak strength until residual strength could be measured (if possible).

Velocity

Five to seven ultrasonic velocity measurements were made during the triaxial compression tests; at the target isotropic stress states; and at several points during axial loading prior to failure, and at a residual stress condition (post-failure).

Porosity and Permeability

Total coal porosity, effective cleat porosity, and permeability to water measurements were made on samples drilled parallel to the bedding surfaces and in a location as to maximize the number of cleats intersected in each sample. The samples were end trimmed and the circumference of the sample was then encased in Teflon® heat shrink allowing for axial flow measurements. The specimen was placed in a rubber jacket with stainless steel platens, loaded into a hydrostatic pressure vessel, and had an isotropic stress of 3.45 MPa applied. The direct helium pore volume was measured in order to obtain total porosity. Water was then injected into each specimen at an upstream pressure of 414 kPa while maintaining a constant backpressure of 345 kPa, creating a differential pressure of 69 kPa. Fluid flow continued through the sample until steady state flow was achieved. Effective cleat porosity was calculated from the total amount of fluid injected and total amount of fluid expelled.

7.4.2 Unconventional Triaxial with Permeability and Particle Size

To address well placement and wellbore design issues, a testing program with the goal of providing qualitative and quantitative information was developed. The tests were designed to best emulate the key issues regarding wellbore stability, coal strength, permeability change and coal fines generation, each issue being fundamental to successful horizontal well planning. The testing included investigating coal strength, changes in permeability with changes in stress, creation and production of coal fines during testing, and examination of particle size distributions of failed coal. These investigations took place under non-trivial unconventional wellbore stress paths matched to stress field alterations simulated by a numerical 3D model of wellbore drilling.

Numerical Modelling Simulation of Borehole Stress Path

A reservoir material may undergo an infinite number of stress paths during exploitation, which may or may not reach the failure envelope. Figure 62 shows four 2D stress paths for which the initial stress state is isotropic. In Loading Compression (LC), which is the typical triaxial testing stress path, the axial stress is increased while the confining is held constant. Loading Extension (LE) entails the axial stress being held constant while the confining stress is increased. In the Unloading Compression (ULC), the axial stress is held constant while the confining stress is decreased. In Unloading Extension (ULE), the confining stress is held constant while the axial stress is decreased.

Figure 68. Pure loading and unloading stress paths plotted in σ'_x - σ'_z stress space.

The four stress paths described have one constant stress and one variable stress that can be easily applied in a triaxial system. In reality though, the stress path in a coal formation during drilling is more complex. To better understand the stress path the coal undergoes during drilling, an elastic uncoupled FLAC3D numerical simulation of an advancing horizontal wellbore was conducted in a manner similar to Corkum and Martin (2007). A coal reservoir at 1250 m was simulated with an anisotropic stress field, such as present in the Alberta Basin (Bell and Bachu, 2003). For this testing program, a borehole radius of 100 mm was selected and advanced perpendicular to the minimum horizontal stress plane.

Measurement points were placed along the entire borehole length at orientations of θ = 0 and θ = 90 degrees and at radial distances of R = 1.0r, 1.3r, 1.5r, and 2.0r (Figure 69) and a Hoek-Brown failure criterion was superimposed to provide an indication of potential failure points. The results of the numerical simulation indicate that coal with a 1.5m radius experiences an increase in mean stress regardless of radial orientation, and that this stress increase is inversely related to the distance from the borehole. As the borehole advances, a coal volume at $\theta = 0$ degrees follows an increase in isotropic stress, then a decrease in isotropic stress followed by ULC and LC stress path. At $\theta = 90$ degrees, a coal volume experiences an increase in isotropic stress, then a slight decrease and then a LE and ULE stress path.

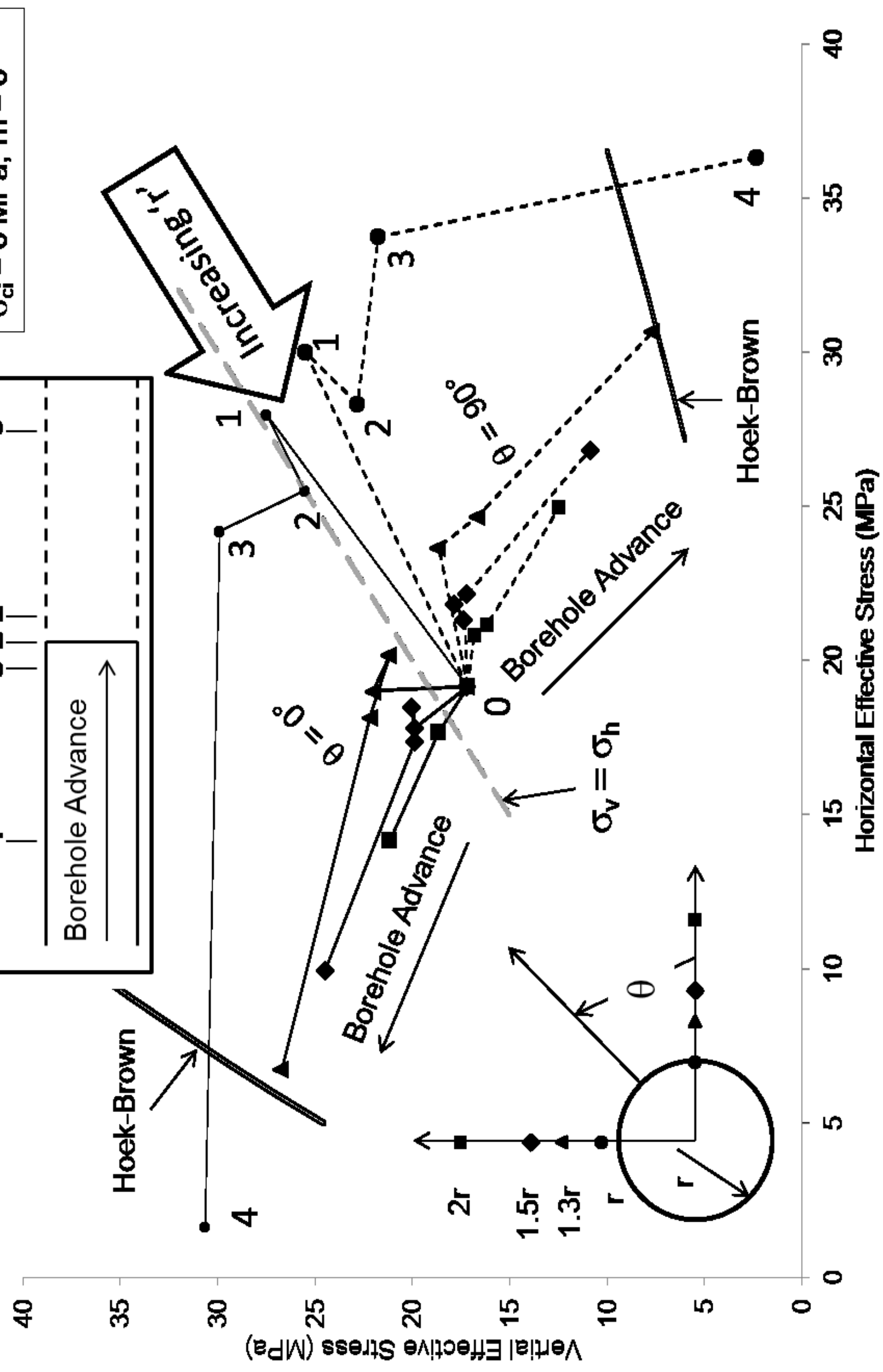

Figure 69. Numerical simulation of the near wellbore stress path around an advancing borehole for various radial distances away from the borehole.

Testing Apparatus

All unconventional stress path tests were conducted using the coal fines capture (CFC) testing apparatus. Each coal specimen was jacketed in a latex membrane and placed between the two stainless steel platens to isolate the specimen from the confining fluid. The CFC apparatus was able to independently control the axial and radial total stress while the pore pressure was controlled with an upstream and downstream pump. The top fluid pressure was controlled with a Teledyne ISCO pump and the bottom with a Quizix QL700 pump.

Testing Procedures

It was assumed that a yield zone will develop around the horizontal borehole and that a liner design must be sufficient to retain a mass of yielded coal. Consequently, the initial testing stages attempted to reproduce the development of this yielded zone using a realistic stress path. This was done in to more appropriately reflect coal fines generation and solids inflow through a slotted liner opening. To achieve this goal, simulated *in situ* disaggregation tests followed by solids flow tests were conducted.

Saturation

Samples requiring saturation were loaded to an initial isotropic total stress of 100 kPa, and then a simultaneous and equal isotropic total stress and pore pressure increase was applied until the pore pressure reached 1 MPa and the effective stress remained at 100 kPa. This condition was held for a minimum of 24 hours and until the pore pressure pump volumes were constant.

Testing Stress Paths

The testing stress paths were designed to examine compression and extension failure at several stress states in order to construct failure envelopes based on the numerical results above. Multiple stress paths were selected to find the compression and extension failure envelopes (UCS, LC, and LE). More complex stress paths were used upon confidence in the location of the compression and extension failure envelopes. During the unconventional stress path loadings, samples were taken to the calculated failure envelope then unloaded or moved along the failure envelope in order to assess the influence of pre-peak damage on fines generation.

Permeability and Solids Production Flow

Permeability and solid production tests were conducted at several locations along the stress path for selected samples by applying a pore pressure differential and collecting generated fines in a downstream accumulator. In each case, at the conclusion of the test, the cell was disassembled and the state of the coal specimen was assessed for damage and the sample and accumulator were investigated for coal fragments.

7.4.3 Elastic Triaxial with Velocity and Gas Sorption

This testing program measured the influence of methane gas content on P and S velocities at 1.1, 3.0 and 5.0 MPa constant effective stress, and the influence of effective stress on:

- Young`s modulus and P and S wave velocities;
- total gas content by testing coal at 0.0, 1.1, 3.0 and 5.0 MPa constant effective stress while incrementally increasing methane gas pressure from 0 to 8 MPa;
- swelling strain by testing coal at 1.1, 3.0 and 5.0 MPa constant effective stress while incrementally increasing methane gas pressure from 0 to 8 MPa.

Test Apparatus

A single coal specimen was tested in the Low Permeability Gas apparatus. The system was designed to measure axial and radial deformation, P and S wave velocities, and gas content and sorption time under independent axial and radial stress conditions at isothermal conditions between 25 and 60 Celsius. A triaxial cell with two internal vertical LVDTs and an internal radial LVDT displacement chain mounted at half the height of the specimen was used. The axial stress was applied with a load frame. The silicon oil confining fluid stress was pressurized and controlled with a second single Teledyne Isco 260D pump to provide radial stress. The top and bottom pore fluid pressure was controlled with a Quizix C-5200 pump. The Quizix pump, load frame, pressure transducers, and triaxial cell were all contained inside of an industrial oven. All of the pressure transducers, LVDTs, and the load cell data were logged by a Datataker DT800. The 63.5mm diameter triaxial cell platens had 100 kHz P and S piezoelectric crystals with voltages applied through two JSR Ultrasonic signal boxes and data collected through a timed JSR Ultrasonic Microsoft VBA program.

The circumference of the single coal specimen was wrapped twice with 2 mm thick lead sheeting, with the inner edge of the lead sheet being sealed against the coal with silicon caulking. The lead sheet extended 2 to 3 cm above and below the coal specimen. Two latex membranes were then placed around the mid height of the coal sample. The silicon caulking was then allowed to cure for 48 hours. Subsequently, the coal sample was placed between the top and bottom platen in the TDS cell and the latex membranes were unrolled over the platens to create a seal between the coal specimen and the confining fluid.

Test Procedures

The aim of the testing program was to measure the influence of methane gas content/pressure at constant effective stress on the mechanical properties including: effective stress-strain behaviour, sorption induced strain, and P and S wave velocities. First, the coal was tested at effective stresses between 1 to 9 MPa with no gas pressure. Then the coal was tested at effective stress states of 1.1 MPa and 3.0 MPa using Helium (He) and then Methane (CH_4) as pore fluids. After the effective stress testing was completed, the sample was removed and shipped to Trican Geological Solutions and the sorption isotherm for CH_4 was determined for the intact and crushed state at 0 MPa effective stress.

Stress Path

For each testing sequence, the coal was loaded by increasing the total axial and total radial stress in 100 kPa increments along a K_o loading path equal to 1.0, where K_o is defined as the effective horizontal (radial) stress divided by the effective vertical stress (Das, 2000). Once the total stresses reached the desired state, the pore pressure was increased to keep the previous effective stress state constant (using He or CH_4). An example of the stress state loading and resulting strain is depicted in Figure 70 and described as follows:

1. $\sigma_m=\sigma_m^0$ and $u=u^0$, then the isotropic mean stress is increased to $\sigma_m=\sigma_m^1$ (path 0-1), then;
2. the pore pressure is increased to $u=u^2$ (path 1-2). Therefore, after loading the effective stress is unchanged ($\sigma'^2=\sigma'^1$) and;
3. the resulting strain (path 2-3) is due only to changes in gas content, or swelling strain.

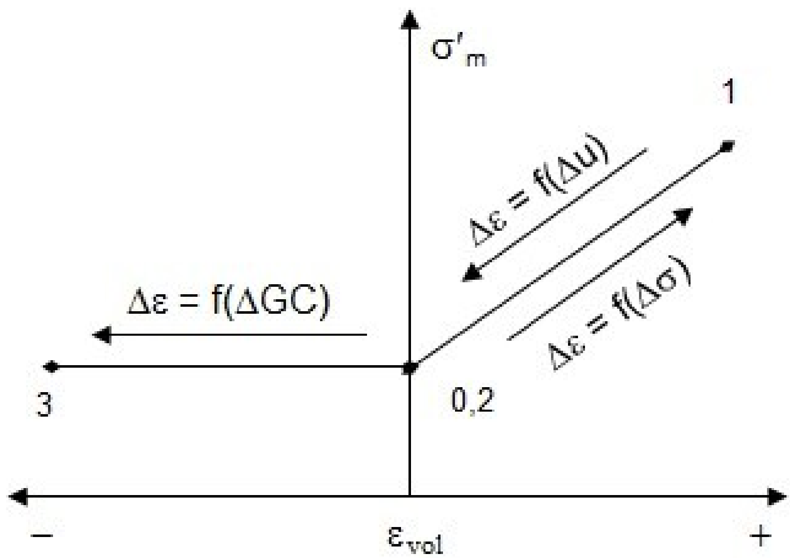

Figure 70. Example stress-strain path for changes in volumetric strain as a result of changes in total stress (0-1), pore pressure (1-2,) and gas content(2-3).

After the gas pressure increase, the effective isotropic stress state was held constant ($\sigma_{axial} = \sigma_{radial} = C_o$) for 48 hours, and then mechanical properties were tested by changing the axial or radial stress by a small amount ($\Delta\sigma$), and holding the opposite stress constant. After each stress increment was applied, the stress state was held for five minutes and the P and S waves were measured twice, with a one minute delay between the measurements. The strength of the specific coal specimen is unknown; however, previous testing by Deisman et al. (2008) on Cardinal River coal showed the Hoek-Brown parameters of: σ_{ci}=20.5 MPa, m_i=16.7, a=0.5, D=1 and therefore the stress perturbations were kept well below this envelope so as to not induce failure or fracturing. The full mechanical testing sequence is illustrated in Figure 71.

$\sigma_{axial} = C_o + \Delta\sigma$, Δt=5 min, P/S, Δt=1 min, P/S, $\sigma_{axial} = C_o - \Delta\sigma$

$\sigma_{axial} = C_o - \Delta\sigma$, Δt=5 min, P/S, Δt=1 min, P/S, $\sigma_{axial} = C_o + \Delta\sigma$

$\sigma_{radial} = C_o + \Delta\sigma$, Δt=5 min, P/S, Δt=1 min, P/S, $\sigma_{radial} = C_o - \Delta\sigma$

$\sigma_{radial} = C_o - \Delta\sigma$, Δt=5 min, P/S, Δt=1 min, P/S, $\sigma_{radial} = C_o + \Delta\sigma$

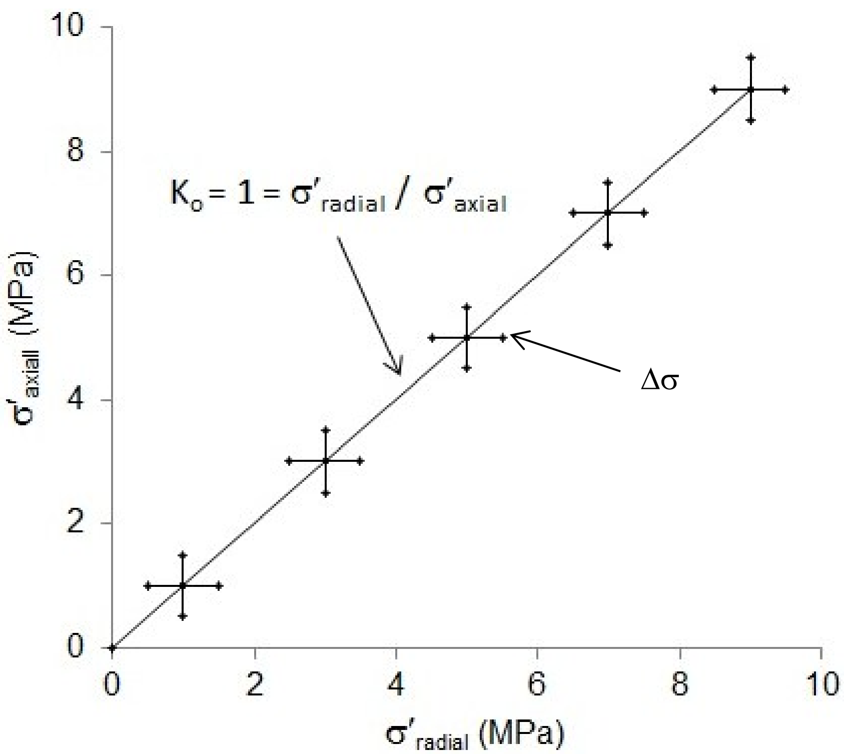

Figure 71. Example of effective stress path loading and stress path perturbations to test mechanical properties of coal.

7.5 Test Evaluation Equations

Several equations are required to evaluate the testing results for the mechanical deformation behaviour, Dynamic Young's modulus and Poisson's Ratio, permeability, and the gas sorption.

7.5.1 Stress-Strain Relationship

Two types of stress and strain analysis calculations are possible: large strain or small strain (engineering strain). Large strain calculations update the dimensions of the specimens as the specimen is being deformed where small strain calculations use the initial dimensions and assume the changes in dimensions are small. In this presented analysis work, engineering strain convention was used. Because the majority of geomechanical analysis and simulation software is formulated using this standard (although options to run simulation work in large strain exist). Therefore, the axial and radial strains and axial stress were calculated using the initial length and radius of the sample. The axial stress (σ_z) on the samples was determined by using the load cell force (F) and dividing by the cross sectional area (A) of each of the tested specimens.

The axial strain (ε_{zz}) is the change in original axial length (ΔL) divided by the original length (L). The radial strain (ε_{rr}) is the change in radius (Δr) divided by the original radius (r). The generalized Hooke`s Law relates changes in strain due to changes in effective stress for a linear elastic medium through a compliance tensor (S_{ijmn}), where effective stress is used to show that a change in either total stress or pore pressure can evoke a change in strain (Eq 26):

$$\Delta\varepsilon_{ij} = S_{ijmn}\Delta\sigma'_{mn} \ ; \left(\Delta\sigma'_{ij} = \Delta\sigma_{ij} - \delta_{ij}\Delta u\right) \qquad 26$$

The compliance tensor can be rewritten in right cylindrical coordinates and the matrix coefficients can be expressed in their more familiar engineering form. In the case where the axial and radial strain are the only strains measured, the highest level of anisotropy that can be measured is transverse isotropy, and if the Young`s modulus terms are equal ($E_z = E_r$), then the material is considered isotropic. If the triaxial cell sample is perturbed two times with different axial stress changes ($\Delta\sigma^1{}_z$, $\Delta\sigma^2{}_z$) and radial stress changes ($\Delta\sigma^1{}_r$, $\Delta\sigma^2{}_r$) in the material's elastic strain zone, then the resulting sample strains can be used to simultaneously solve the compliance tensor coefficients through (Mas Ivars et al 2011) (Eq 27):

$$\begin{pmatrix} \Delta\varepsilon^1_{rr} & \Delta\varepsilon^2_{rr} \\ \Delta\varepsilon^1_{zz} & \Delta\varepsilon^2_{zz} \end{pmatrix} = \begin{pmatrix} \dfrac{1}{E_r} & \dfrac{-\nu_{zr}}{E_z} \\ \dfrac{-\nu_{zr}}{E_r} & \dfrac{1}{E_z} \end{pmatrix} \begin{pmatrix} \Delta\sigma'^1_{rr} & \Delta\sigma'^2_{rr} \\ \Delta\sigma'^1_{zz} & \Delta\sigma'^2_{zz} \end{pmatrix} \qquad 27$$

For the first two testing programs, where the coal samples have been taken to failure under constant radial stress with a change in axial stress, the linear portions of the axial and radial strain curves can be used to solve the compliance tensor coefficients through (Eq 28):

$$\begin{pmatrix} \frac{1}{E_z} & \frac{-\nu_{zr}}{E_z} \end{pmatrix} = \begin{pmatrix} \Delta\sigma'_{zz} \\ \Delta\sigma'_{rr} \end{pmatrix}^{-1} \begin{pmatrix} \Delta\varepsilon_{zz} \\ \Delta\varepsilon_{rr} \end{pmatrix} \tag{28}$$

For the third testing program, where the coal has been kept in the elastic zone and changes in radial and axial stress have been applied in two separate steps, the linear portions of the resulting axial stress and strain curves can be used to solve the compliance tensor coefficients through (Eq 29):

$$\begin{pmatrix} \frac{1}{E_r} & \frac{-\nu_{zr}}{E_z} \\ \frac{-\nu_{zr}}{E_r} & \frac{1}{E_z} \end{pmatrix} = \begin{pmatrix} \Delta\sigma'^{1}_{rr} & \Delta\sigma'^{2}_{rr} \\ \Delta\sigma'^{1}_{zz} & \Delta\sigma'^{2}_{zz} \end{pmatrix}^{-1} \begin{pmatrix} \Delta\varepsilon^{1}_{rr} & \Delta\varepsilon^{2}_{rr} \\ \Delta\varepsilon^{1}_{zz} & \Delta\varepsilon^{2}_{zz} \end{pmatrix} \tag{29}$$

7.5.2 P and S wave Relationship

The P and S wave velocity were calculated by recording the wave initiation at the signal crystal and the arrival at the receiver crystal. The travel time measurements were stabilized prior to reading by programming the oscilloscope to display the average of 500 waves. Once the wave total arrival time (t_{total}) was determined (the wave travels from signal crystal, through platen, through coal, through platen, to receiver crystal), the platen face to face P and S wave arrival times were subtracted to give only the coal P and S wave travel time. This time was then divided by the length of the coal specimen to give the P wave velocity (V_p) and S (V_s) wave velocity. The complete process is the same for P and S wave and is simply (Eq 30):

$$V = \frac{\left(t_{total} - t_{face\ to\ face}\right)}{L} \tag{30}$$

Once the P and S wave velocities are calculated, they can be used, along with the coal density (ρ), to calculate dynamic Poisson's ratio (ν_D) (Eq 31) and Dynamic Young's modulus (E_D) (Eq 32):

$$\nu_D = \left[\left(\frac{V_p}{V_S}\right)^2 - 2\right] \Bigg/ 2\left[\left(\frac{V_p}{V_S}\right)^2 - 1\right] \tag{31}$$

$$E_D = V_S \rho \left[3\left(\frac{V_p}{V_S}\right)^2 - 4\right] \Bigg/ \left[\left(\frac{V_p}{V_S}\right)^2 - 1\right] \tag{32}$$

7.5.3 Water Permeability

The permeability characteristics of the samples in these testing programs were measured using water and a constant pressure gradient across the sample. The test can be set up two ways: set a pressure gradient ($\Delta P/L$) and wait for the flow rate to stabilize or set a flow rate and wait for the pressure gradient to stabilize. In either case, once a steady state (stable flow rate or stable differential pressure) has been established, a total flow volume was recorded over a period of time and used to calculate a fluid flow rate (Q). Darcy's law and the fluid viscosity (μ) were then used to calculate the intrinsic permeability (k) of the coal specimen (Eq 33):

$$k = \mu \frac{Q}{A} \frac{L}{\Delta P} \tag{33}$$

7.5.4 Gas Content Analysis

Gas content measurements on the coal specimen were made in the third testing program. To analyse the amount of gas sorption on the coal specimen a Pressure – Volume - Temperature mass balance technique demonstrated by Arri et al. (1992) was used. The total injected pump volume (v_{pump}) was measured, while the temperature (T) is constant and pressure in the pump and cell are equivalent. Volumes in the cell and flow lines (v_{cell}) were measured prior to testing and the volumes changes due to system compliance were negligible over the experimental pressure range. Therefore, the moles (n) of sorbed gas can be calculated and then divided by mass (m) of coal specimen to give (Eq 34):

$$\frac{n}{m} = \frac{P(v_{pump} - v_{cell})}{ZRT} \qquad 34$$

where R is the gas constant and Z is the gas compressibility factor obtained for each methane test pressure and temperature (T) using the Peng-Robinson equation (Peng and Robinson, 1976).

7.6 Testing Results

The results from each of the three testing programs have been grouped into fundamental results groups of:

1. Deformation
2. Velocity and Dynamic Modulus
3. Strength
4. Permeability
5. Gas Sorption and Swelling

All of the testing results have been either plotted or summarized in tables with only fundamental properties being extracted from the data where possible. The following chapters will be used to further model and explain the deviations from conventional results (ie the influence of effective stress on methane gas content isotherms).

7.6.1 Deformation Results

The first testing program CT w/ V,P was carried out on samples from the Greenhills, Elkview and Cardinal River Mines. Young's modulus was determined for each sample from the slope of the linear portions of the axial stress versus axial strain. The results are plotted in Figure 72 and presented in Table 10. Values for Young's modulus ranged from 1.12 GPa for the GH 3-3 sample with a 0.2 MPa confining stress, to 5.068 GPa for the ELK 10-1 sample with a 14.0 MPa confining stress. The results show the relationship between the increased confining stress and the change in Young's modulus. In each case, the slope of the Young's modulus versus confining stress curve shows a decrease with increasing confining stress.

Poisson’s ratio was also calculated from the testing program and the values are presented in Table 10. Values for the static Poisson's ratio ranged from 0.26 for the GH7-4 sample ($\sigma_r' = 0.2$ MPa) to 0.48 for the GH3-3 ($\sigma_r' = 0.2$ MPa) and there was no apparent trend between Poisson’s ratio and the radial confining stress.

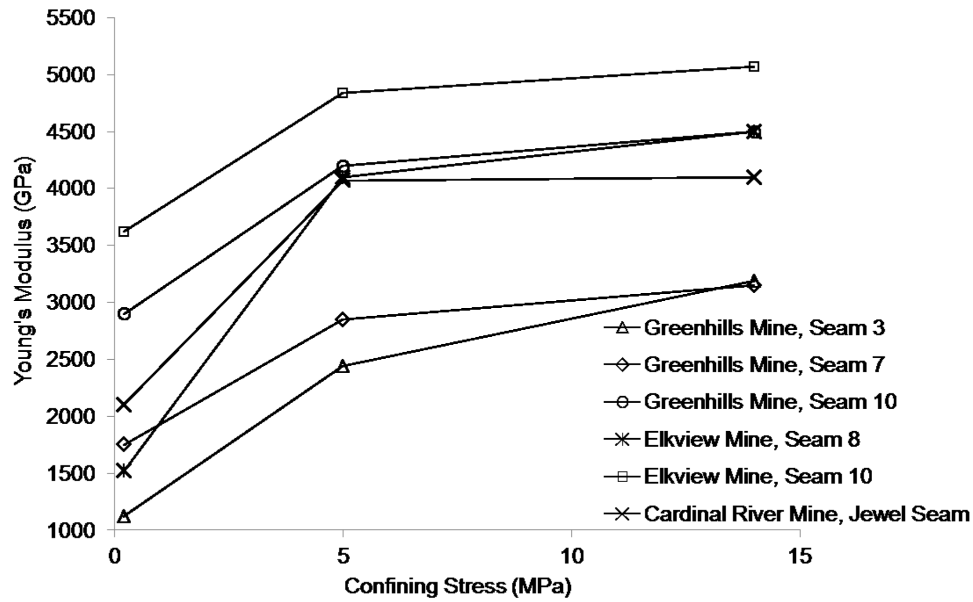

Figure 72. Influence of confining stress on Young’s’ modulus from CT w/ V,P.

Table 10. Summary of static mechanical properties determined from traixial compression testing.

Coal Seam	ID	σ'_r	E	ν
		(MPa)	(GPa)	()
Greenhills Mine, Seam 3	GH3-3	0.21	1.12	0.48
	GH3-2	5.0	2.44	0.30
	GH3-1	14.0	3.19	0.34
Greenhills Mine, Seam 7	GH7-4	0.21	1.75	0.26
	GH7-3	5.00	2.85	0.32
	GH7-2	14.0	3.15	0.35
Greenhills Mine, Seam 10	GH10-3	0.21	2.9	0.35
	GH10-2	5.00	4.2	0.38
	GH10-5	14.0	4.5	0.35
Elkview Mine, Seam 8	8UX-4	0.21	1.52	0.47
	8UX-3	5.00	4.19	0.34
	8UX-1	14.0	4.50	0.36
Elkview Mine, Seam 10	ELK 10-4	0.21	3.62	0.32
	ELK 10-3	5.00	4.84	0.28
	ELK 10-1	14.0	5.07	0.33
Cardinal River Mine, Jewel Seam	CR-4	0.21	2.10	0.28
	CR-3	5.0	4.07	0.33
	CR-2	14.0	4.10	0.34

The third testing program, ET w/ V,G, measured the Young's modulus at multiple effective stress states and methane gas contents. The first stage sequence was to determine the mechanical properties at effective stress states from 1.0 to 9.0 MPa with no pore pressure (no gas). Next, helium was used as a pore fluid and the effective stress state was held constant at 1.1 MPa, with the helium gas pressure was raised from 0 to 8 MPa while the P and S wave velocity were measured (two P and S wave measurements) at roughly 2 MPa intervals. The effective stress state was then increased to 3 MPa and the testing sequence repeated. Finally, the helium pore fluid was replaced with methane and the same testing sequence repeated. At each loading increment, the axial and radial stresses were changed to measure the mechanical constitutive properties of the coal. This sequence was repeated at an effective stress state of 5.0 MPa using methane only, however the P and S wave were not measured due to equipment problems.

In this testing program, Young's modulus was only measured for the zero pore pressure phase and the final 1.1, 3.0 and 5.0 MPa effective stress phases. The effective stress paths for each of these tests are shown Figure 73. As well, a Hoek-Brown failure envelop is superimposed on the stress path figure. The strength parameters for the envelope were estimated based on previous testing (discussed below) and were reduced to 40% of their values for illustrative purposes of the relation of the stress path to an estimated failure envelope. (Additionally, after testing the coal specimen was removed and there was no visible damage to the specimen). The axial strain data was measured with two internal LVDTs and one external LP and the radial deformation was measures with a radial chain LVDT. Unfortunately, the radial LVDT chain did not provide correct readings after analysis and one of the axial LVDTs also failed. However, the remaining axial LVDT and LP recorded almost identical displacement results, therefore giving confidence to the axial displacement measurements.

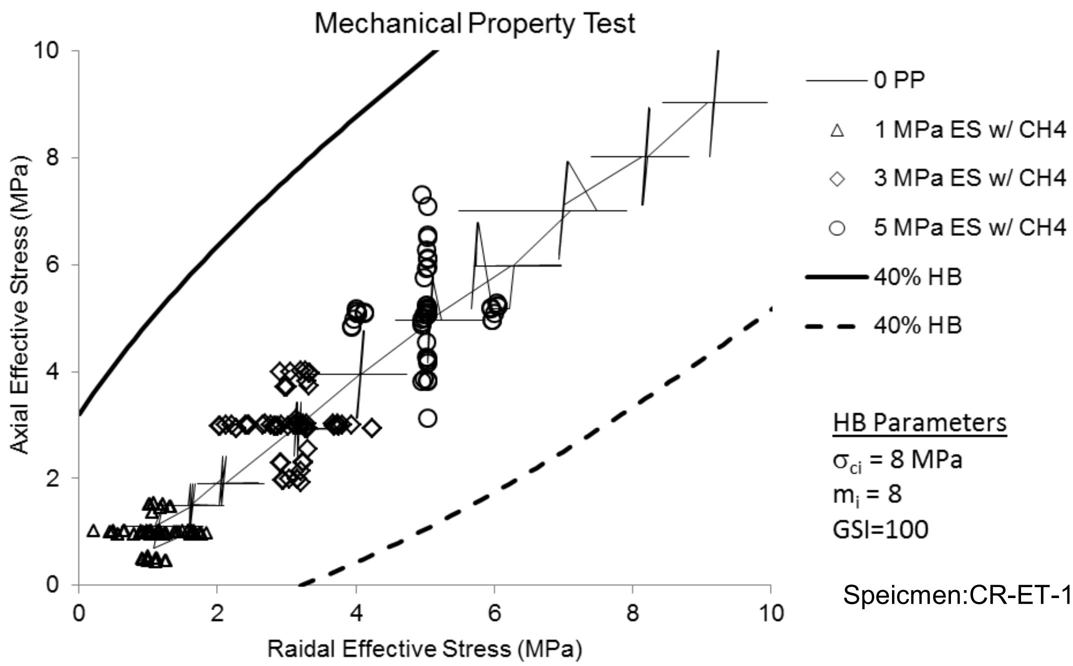

Figure 73. The effective stress loading path used to measure mechanical properties of coal. A 40% estimated Hoek-Brown Failure envelope is displayed to show the relation to failure of each stress perturbation.

The results from the ET w/ V,G testing show that, for the sample at zero pore pressure, the Young's modulus ranged from 5 GPa at 1.1 MPa isotropic effective stress up to 8.5 GPa at 9 MPa isotropic effective stress (Figure 74). For each isotropic effective stress testing point, the axial and radial stresses were cycled twice and both Modulus results are shown. The results from the constant effective stress tests using methane as a pore fluid are also shown and indicate that the Young`s modulus for these tests are within the same range as the values at zero pore pressure. For the tests at 1.1 MPa constant effective stress, the Young`s modulus ranges from 3.8 to 5.4 GPa, with the zero pore pressure test result being 5 GPa. The tests at 3 MPa constant effective stress are in the 6 to 8 GPa range, where the zero pore pressure tests results give a Young`s modulus of 6.5 GPa. The 5 MPa constant effective stress results show a Young`s modulus range between 5.8 GPa and 8 GPa, with the zero pore pressure result measured at 8 GPa. In all cases, the increase in radial effective stress – Axial Young`s modulus plot slope decreases as the radial effective stress increases.

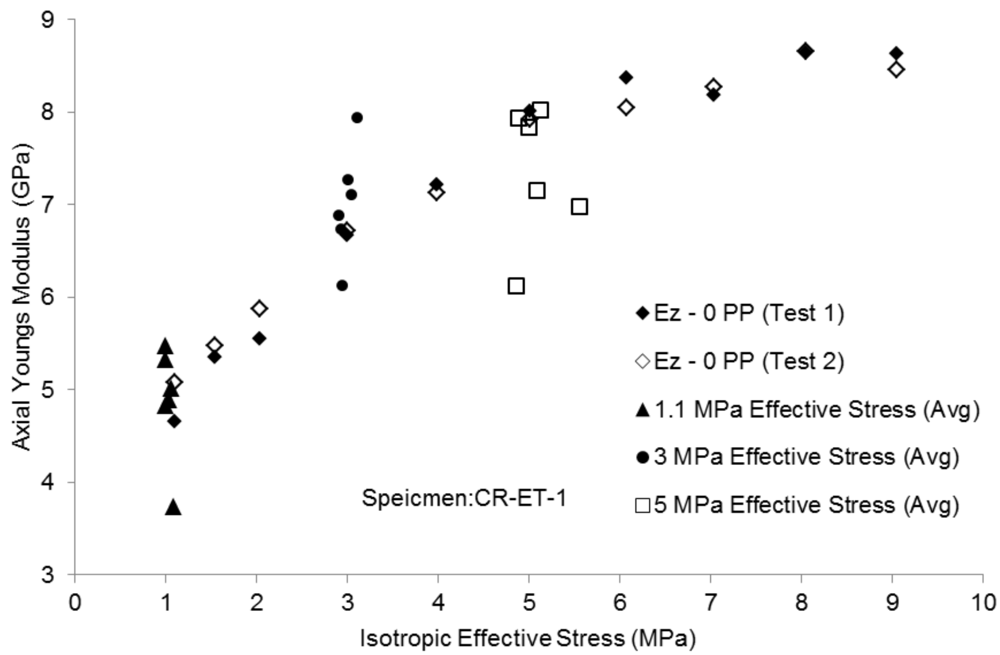

Figure 74. Static Axial Young's modulus as a function of mean effective stresses at zero pore pressure. Results from mechanical tests at 1.1 MPa, 3.0 MPa and 5.0 MPa effective stress and methane as a pore fluid are also shown.

Figure 75 more closely examines the results from the testing of Young`s modulus at constant effective stress with increasing the pore pressure. Results from the tests at 1.1 MPa, 3.0 MPa, and 5.0 MPa effective stress all show that as the gas pressure increases, there is no recognizable trend that can be attributed to the presence of methane gas. However, the results do show that Young`s modulus does vary above or below the average value measured at 1.1, 3.0, and 5.0 MPa effective stress with no pore pressure. The results for 5.0 MPa constant effective stress with show the greatest deviation, with the Young`s modulus measured as low at 6.2 GPa at 0.5 MPa gas pressure.

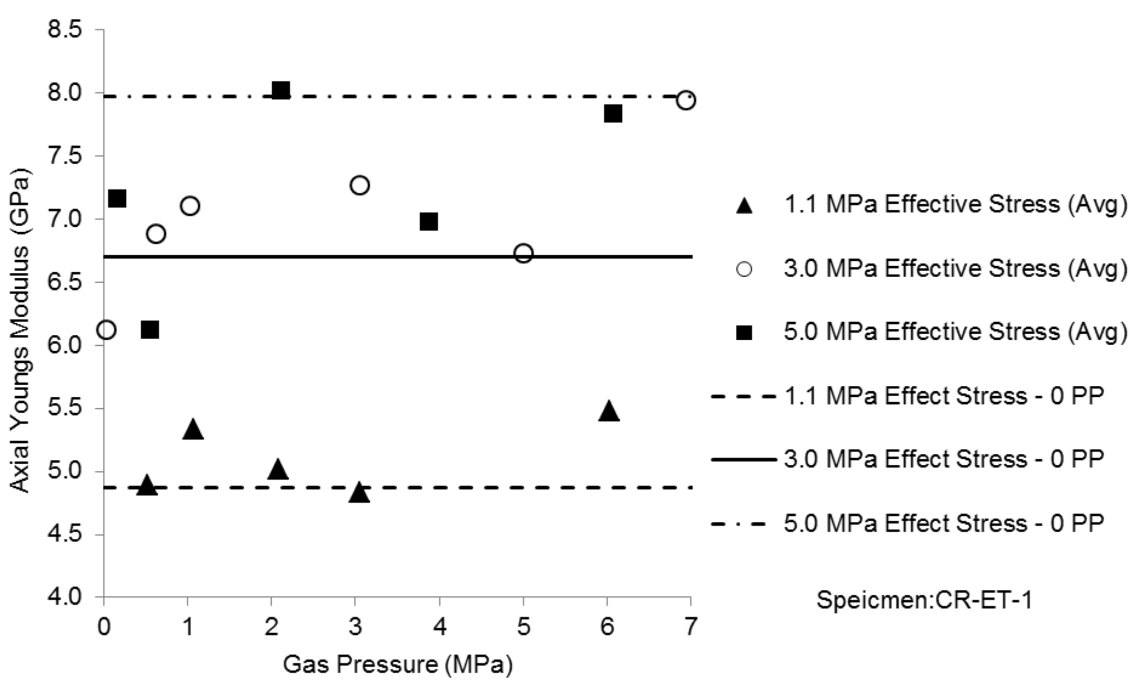

Figure 75. Changes in Young’s modulus with methane gas pressure at 1.1, 3.0 and 5.0 MPa constant effective stresses.

7.6.2 Velocity and Dynamic Modulus Results

Ultrasonic velocity measurements to determine the dynamic Young's modulus and dynamic Poisson's ratio were also completed for the CT w/ V,P program. In each of the cases, the dynamic Young's modulus increased as the mean effective stress increased. For the Greenhills Mine, Seam 10-2, the dynamic Young's modulus increased until the mean effective stress reached 8 MPa, and then began to level out and even decreased (Figure 76). The results for Greenhills Mine Seam 10-3 and 10-5 show the Dynamic Young`s modulus starting at roughly the same values (5 GPa) and continuing at this value over the axial stress range.

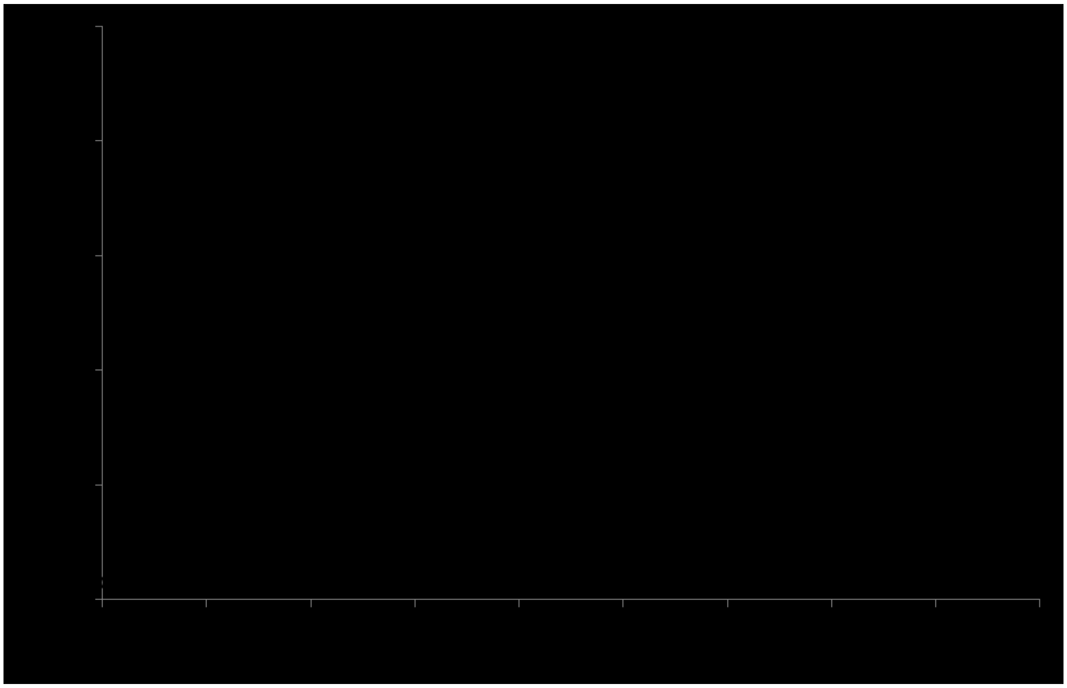

Figure 76. Dynamic Young's modulus from the Greenhills Mine, Seam 10 samples.

Velocity measurements were also completed for the ET w/ V,G testing at zero pore pressure and at 1.1 MPa and 3.0 MPa effective constant effective stress with increasing methane pore pressure tests. At each pore pressure value, the P and S waves were measured twice and results averaged. The tests at zero pore pressure show that as the mean effective stress is increased, both the V_p and V_s wave velocity increases (Figure 77). The V_p and V_s values start at 1.2 and 1.5 km/s respectively at 1.1 MPa mean effective stress and increase to 1.95 km/s and 1.35 km/s respectively at 9 MPa effective stress. The V_p/V_s ratio is also calculated and plotted in (Figure 77). Initially at 1.1 MPa effective stress, the ratio is 1.3 and increases until 3 MPa effective stress is reached, and then the ratio levels off, and does not increase further between the 3 MPa to 9 MPa effective stress range.

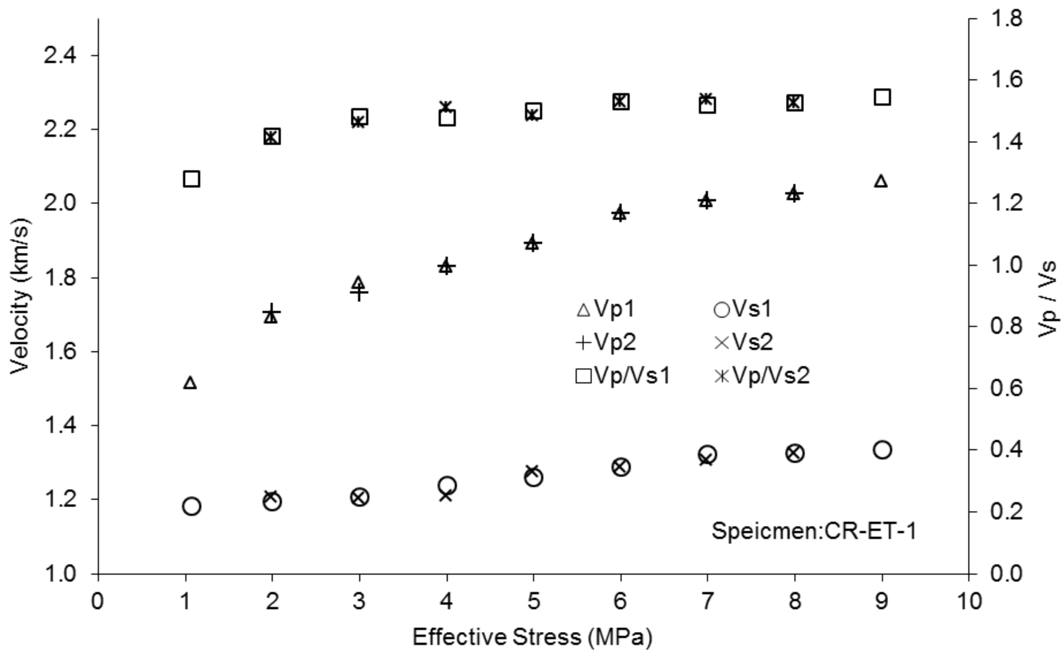

Figure 77. P and S wave velocities and Vp/Vs ratios at 0 pore pressure for the coal specimen.

The P and S wave velocities were also measured at 1.1 MPa and 3.0 MPa constant effective stress with both helium and methane pore fluid pressures ranging from 0 to 8 MPa. At each pore pressure value V_p and V_s were measured twice and results averaged and are plotted in Figure 78 for 1.1 MPa constant effective stress and Figure 79 for 3.0 MPa constant effective stress. V_p and V_s for methane gas at 1.1 MPa effective stress is greater than that measured using helium gas at the same pore pressures. As well, V_p and V_s with methane as the pore fluid at 1.1 MPa effective stress is greater than V_p and V_s with no pore fluid.

Once the effective stress increased to 3.0 MPa testing phase, V_p and V_s results with helium and methane as the pore fluid were much closer to each other and also to the results with no fluid pressure. For V_p, the measured velocities were only slightly higher than the velocities measured with helium as the pore fluid whereas V_s were very close to each other and also to the no pore pressure velocities for 3.0 MPa effective stress.

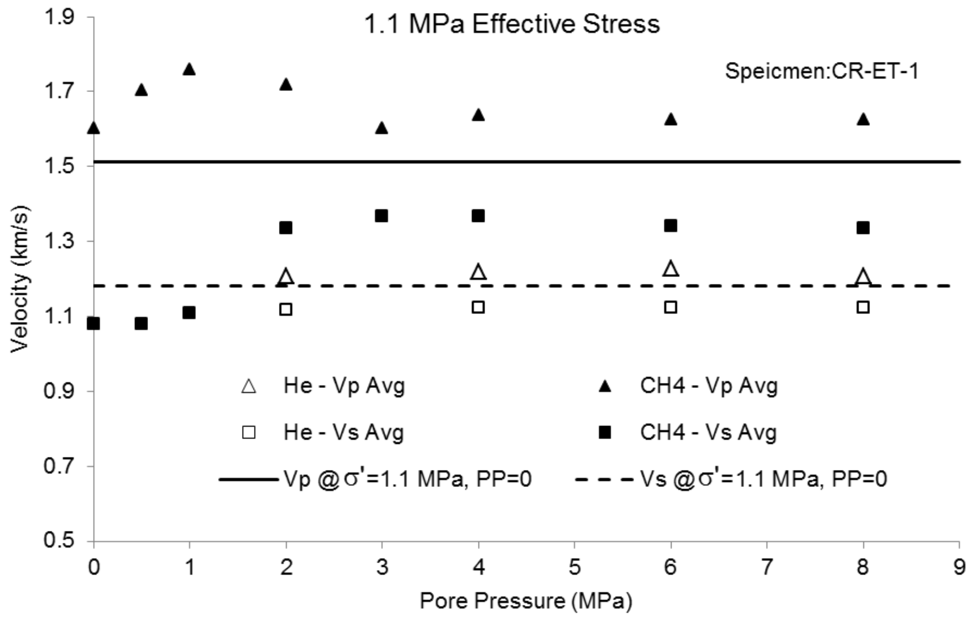

Figure 78. P and S Wave velocity at 1.1 MPa constant mean effective stress using helium and methane as pore fluids. The solid and dashed lines represent the V_p and V_s with no pore pressure at 1.1 MPa effective stress.

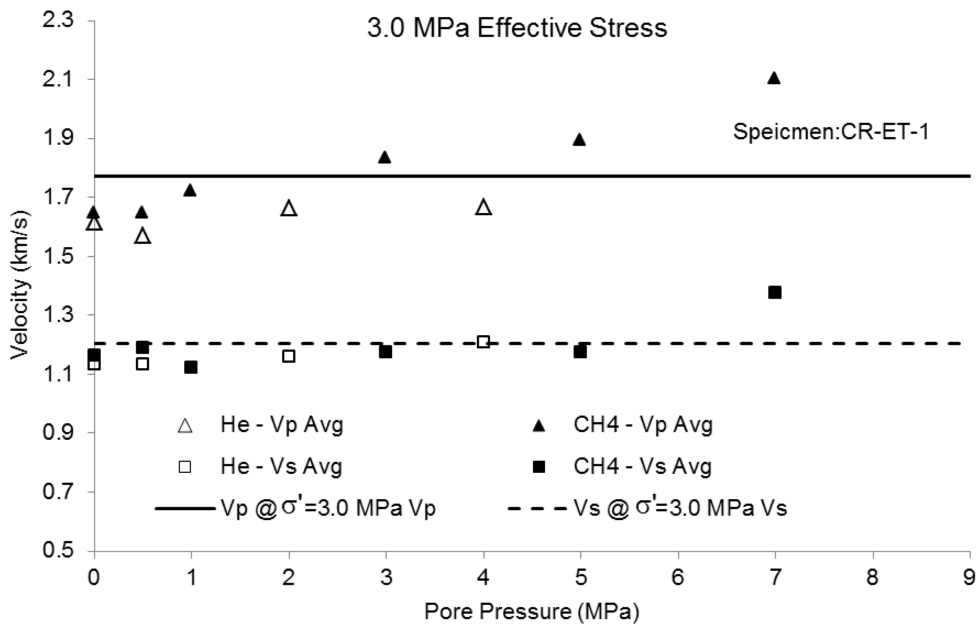

Figure 79. P and S Wave velocity at 3 MPa constant mean effective stress using helium and methane as pore fluids. The solid and dashed lines represent the V_p and V_s with no pore pressure at 3.3 MPa effective stress.

During the testing program, the total methane gas sorbed by the coal specimen was also measured at each point of the wave velocity test. In each case, V_p and V_s did not decrease with increasing gas content (Figure 80). The P and S wave velocities at 1.1 MPa constant effective stress were 1.6 km/s and 1.1 km/s respectively at no gas content. As the gas content of the sample increased to 0.13 mols/kg, the P and S waves both increased to their maximum values of 1.7 km/s and 1.35 km/s. At the final gas content of 0.31 mols/kg, the V_p had decreased to 1.6 km/s while V_s remained constant. The test at 3 MPa constant effective stress and zero gas content showed the V_p to be 1.65 km/s and the V_p to be 1.15 km/s. The velocities continued to increase as gas content increased to a maximum V_p of 2.1 km/s and an V_s of 1.35 km/s. When examining all the data for V_p and V_s with changes in gas content, it does not appear that gas content causes an observable pattern for either increases or decreases in V_p or V_s.

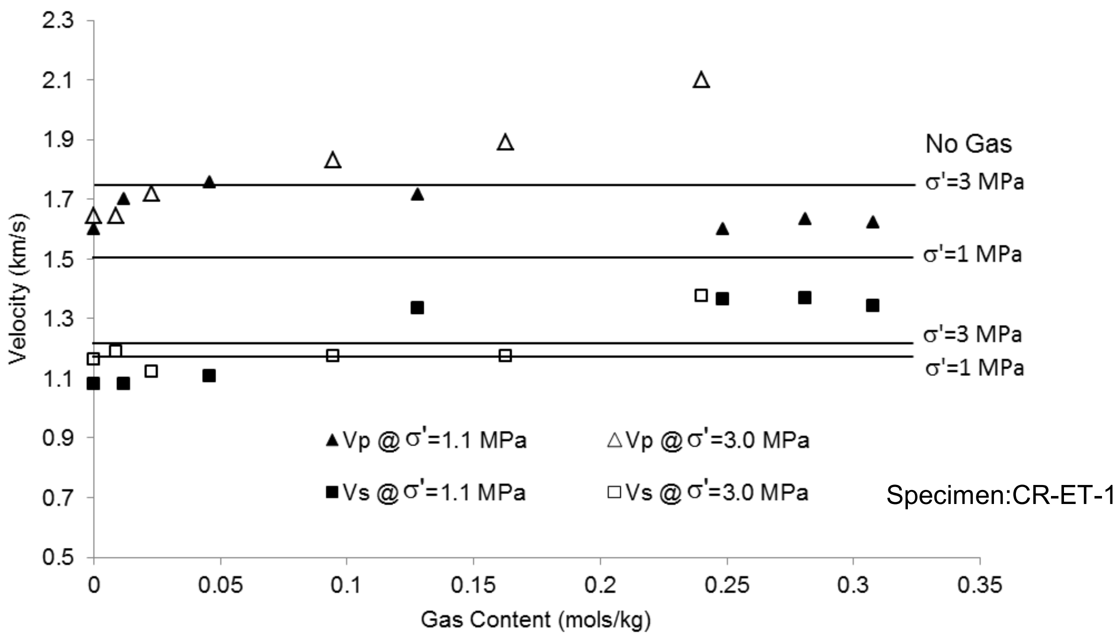

Figure 80. P and S wave velocity at 1.1 MPa and 3 MPa constant effective stresses with variable methane gas content for the same sample. The V_p and V_s lines measured with no gas are superimposed for reference.

In an attempt to determine the influence of shear stress on V_p and V_s, at each isotropic stress for the 1.1 MPa and 3.0 MPa effective stress test sequences, the axial stress was increased and then decreased, and then the radial stress was increased and then decreased. At each of these stress increments, V_p and V_s were measured. The increase or decrease in axial or radial stress was held for a maximum of 5 minutes and the whole testing sequence lasted no longer than 25 minutes, therefore it was assumed that there was no change in gas content due to changes in mean or deviator stress. V_p and V_s at the isotropic stress state was then subtracted to give a change in V_p (ΔV_p) and V_s (ΔV_s) at each of the changes in axial effective stress ($\Delta\sigma'_a$) and radial effective stresses ($\Delta\sigma'_r$). The ΔV_p with $\Delta\sigma'_a$ (Figure 81) and $\Delta\sigma'_r$ (Figure 82) results show that only the measurements from the 3.0 MPa constant effective stress test sequence had a reasonable trend. A linear function was fit to the results, and for ΔV_p with $\Delta\sigma'_a$, the R^2 was 0.07 for σ' = 1.1 MPa, and the R^2 was 0.73 for σ' = 3.0 MPa. For ΔV_p with $\Delta\sigma'_r$ the R^2 was 0.28 for σ' = 1.1 MPa, and the R^2 was 0.73 for σ' = 3.0 MPa.

The ΔV_s with $\Delta\sigma'_a$ (Figure 83) and $\Delta\sigma'_r$ (Figure 84) results show a very large data scatter. A linear function was fit to the data, and for ΔV_s with $\Delta\sigma'_a$, the R^2 was 0.03 for σ' = 1.1 MPa, and the R^2 was 0.14 for σ' = 3.0 MPa. For changes in V_s with changes in radial stress the R^2 was 0.03 for σ' = 1.1 MPa, and the R^2 was 0.02 for σ' = 3 MPa.

In each measurement case, the $\Delta\sigma'_a$ and $\Delta\sigma'_r$ was used to determine a ΔV_p. The maximum ΔV_p = 45 m/s at $\Delta\sigma'_a$ = 750 kPa, while the minimum ΔV_p = -150 m/s at $\Delta\sigma'_a$ = -750 kPa. The ΔV_p was much less dramatic when the radial stress was altered. For $\Delta\sigma'_r$ = 1.0 MPa the ΔV_p = 50 m/s and the minimum ΔV_p = -35 m/s at $\Delta\sigma'_r$ = -1000 kPa.

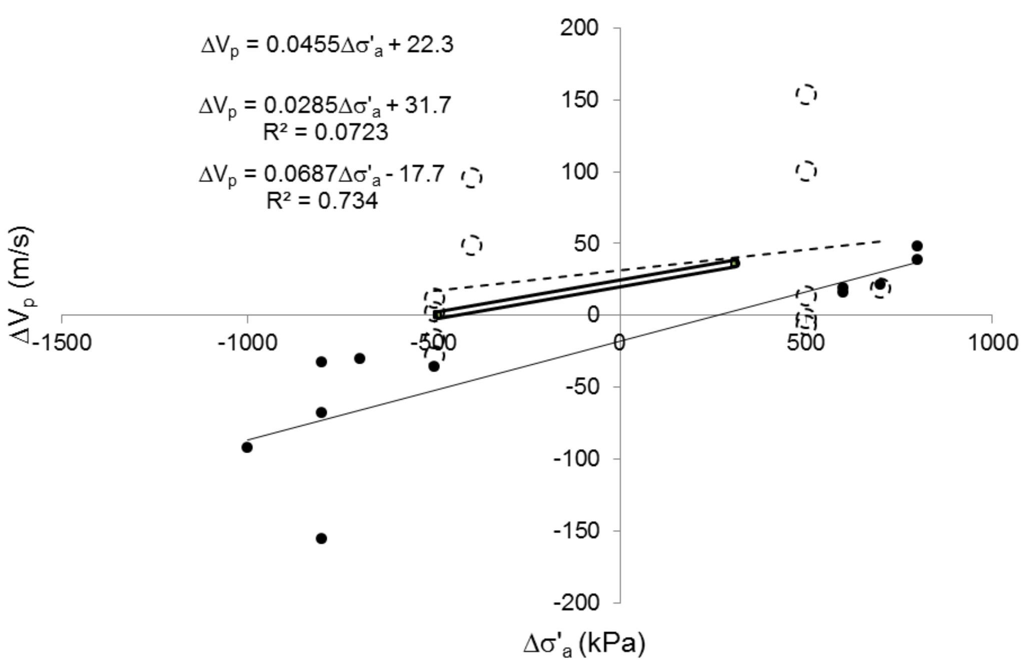

Figure 81. Change in P-wave velocity with change in axial stress at 1.1 MPa and 3 MPa effective stresses with methane gas pressures from 0 to 8 MPa.

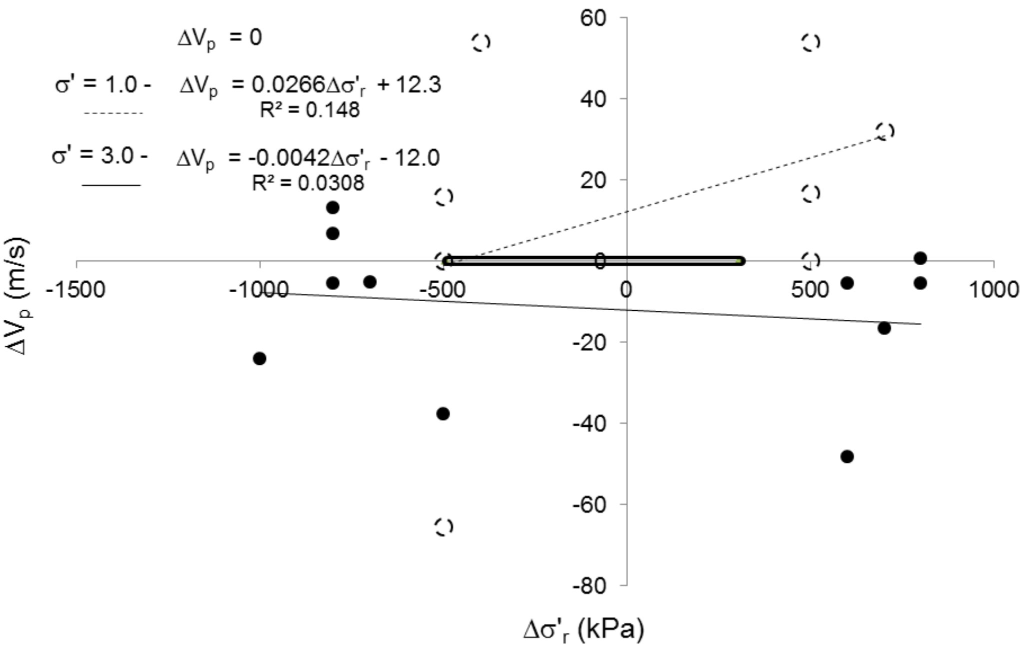

Figure 82. Change in P-wave velocity with change in radial stress at 1.1 MPa and 3.0 MPa effective stresses with methane gas pressures from 0 to 8 MPa.

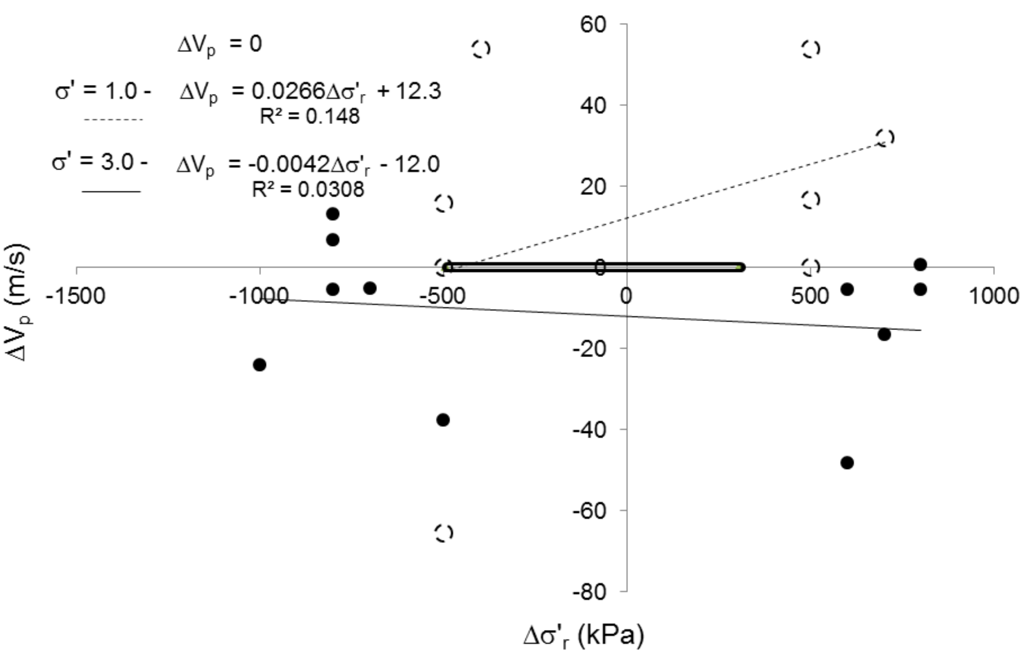

Figure 83. Change in S-wave velocity with change in axial stress at 1.1 MPa and 3.0 MPa effective stresses with methane gas pressures from 0 to 8 MPa.

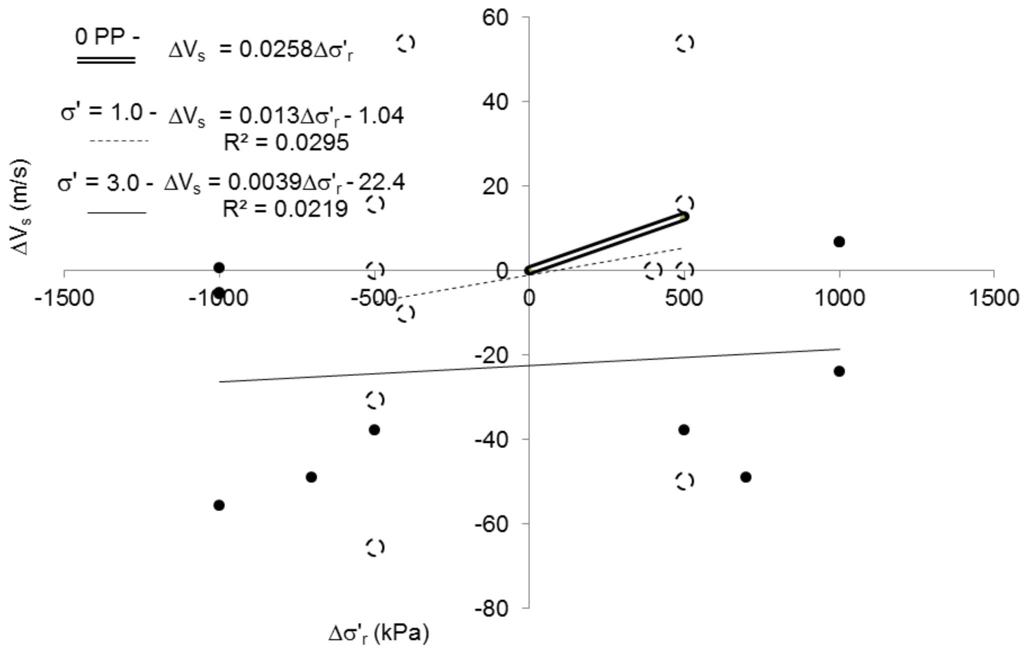

Figure 84. Change in S-wave velocity with change in radial stress for the same coal sample at 1.1 MPa and 3 MPa effective stresses with methane gas pressures from 0 to 8 MPa.

The Dynamic Young's modulus (E_D) measurements from the CR-ET-1 testing with no gas pressure were plotted against the measured Young's modulus from the same testing sequence, Figure 85. The results show that for a minimum E_D of 2.3 GPa, the corresponding E was 4.9 GPa, and for a maximum E_D of 4.1 GPa, the corresponding E was 4.12 GPa. The corresponding data between these two data points fell on an almost straight line. A linear relationship was plotted for the data with an R^2 value of 0.905.

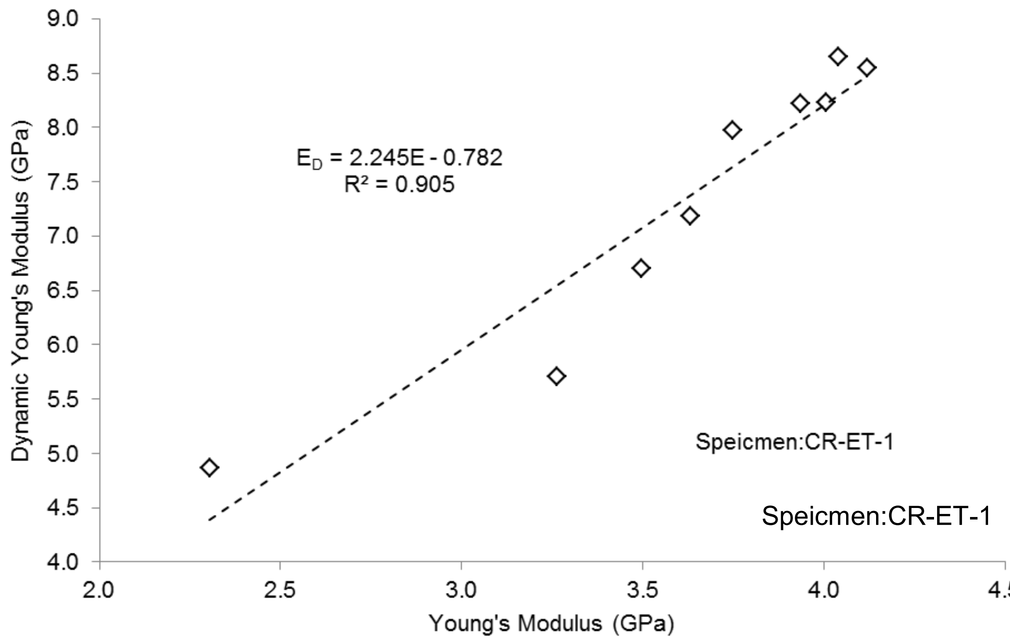

Figure 85. Static verses dynamic axial Young's modulus for the same coal specimen with increasing total stress.

The data from the ET w/ V,G was also plotted to determine the relationship between only the V_p and the Young's modulus for each of the zero pore pressure, 1.1 MPa constant effective stress and 3 MPa constant effective stress testing sequences. The test results are provided in Table 11 and illustrated in Figure 86 where a linear relationship was best fit to each of the test results.

Table 11. Tabulated values of P Wave velocity and Young's modulus for corresponding measurements at 1.1, 3.0 and 5.0 constant effective stress.

Measurement No.	1.1 MPa Effective Stress		3.0 MPa Effective Stress		5.0 MPa Effective Stress	
	P Wave	E	P Wave	E	P Wave	E
	km/s	GPa	km/s	GPa	km/s	GPa
1	1.51	4.87	1.70	4.89	1.65	6.12
2	1.70	5.71	1.76	5.33	1.65	6.88
3	1.77	6.70	1.72	5.01	1.72	7.11
4	1.83	7.18	1.60	4.83	1.83	7.27
5	1.89	7.97	1.63	3.74	1.89	6.73
6	1.97	8.21	1.62	5.48	2.10	7.94
7	2.01	8.23				
8	2.02	8.65				
9	2.06	8.54				

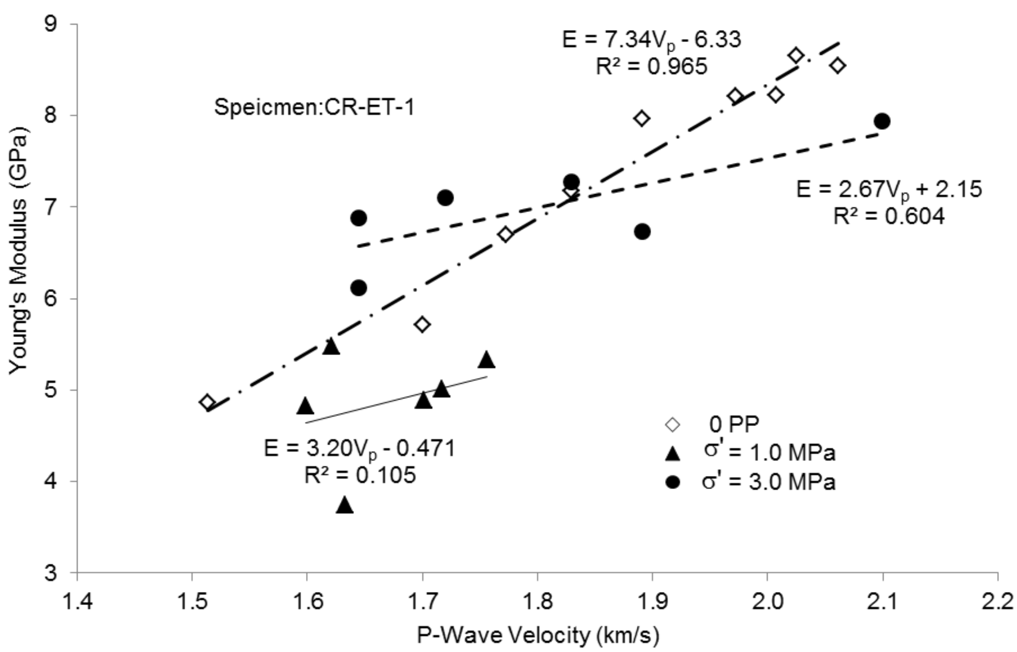

Figure 86. Relationship between P-wave velocity and static axial Young's modulus at multiple zero pore pressure. Results for 1.1 MPa and 3 MPa constant effective stress conditions with methane as the pore fluid are also illustrated.

The final plot created for the results from the ET w/ V,G was between methane gas pressure and the ratio of Dynamic Young's modulus to Young's modulus (Figure 87). The concept to plot the data in this manner was, if an operator knew the reservoir pressure, effective stress, and measured the Dynamic Young`s modulus, a more accurate Young`s modulus could be determined as compared to that shown in Figure 85.

The results from the 1.1 MPa test data show that, for pore pressure at 0.5 MPa, the resulting E_D to E ratio was 1.45 and as the methane pressure increased, the E_D to E ratio linearly decreased to 0.6 at 6 MPa methane pressure. The data from the 1.1 MPa and 3 MPa constant effective stress tests were plotted and show an excellent trend for the 3 MPa test case, whereas the 1.1 MPa test case shows scattered data. The results from the 3 MPa test data show that, for pore pressure at zero, the resulting E_D to E ratio was 0.88 and as the methane pressure increases, the E_D to E ratio also linearly increased to 1.2 at 7 MPa methane pressure.

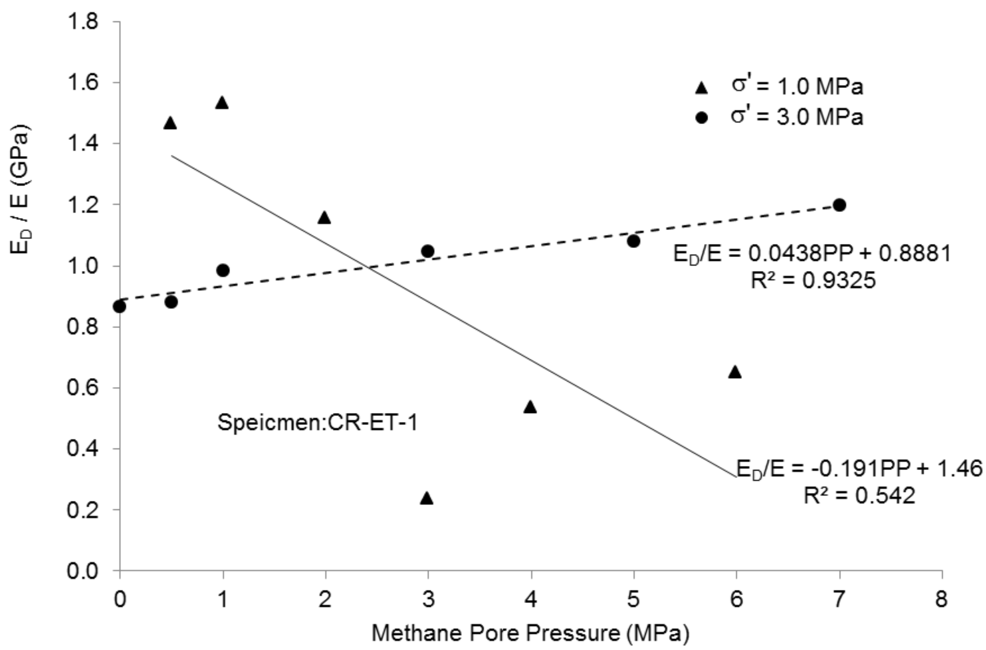

Figure 87. The relationship between pore pressure and the dynamic to static Young's modulus ratio for 1.1 and 3 MPa constant effective stress.

7.6.3 Strength Results

The strength results from the CT w/ V,P and the UT w/P,PS programs are presented here. In each case, the strength was a function of the minimum effective stress and showed a non-linear behaviour. Strength models are fit to the data in the following chapter.

Conventional Triaxial with Velocity and Permeability

A total of 18 strength tests were completed on samples from the 6 coal seams (3 tests per seam) at three effective confining stresses: 0.1, 5.0 and 14.0 MPa. In each test, the coal exhibited brittle failure along a distinct shear plane. The results from the triaxial testing on each of the specimens are shown in Figure 88 and provided in Table 12. The results show that the strength increase is not linearly proportional to the confining stress. All of the specimens tested showed this trend of non-linearity.

Table 12. Summary of static mechanical properties determined from traixial compression testing.

Coal Seam	Sample ID	Bulk Density	σ'_3	σ'_1 Peak	Residual Compressive Strength	E	ν
		kg/m^3	MPa	MPa	MPa	GPa	
Greenhills Mine, Seam 3	GH3-3	1320	0.21	8.6	5.6	1.12	0.48
	GH3-2	1318	5.0	37.2	28.0	2.44	0.30
	GH3-1	1317	14.0	58.6	48.1	3.19	0.34
Greenhills Mine, Seam 7	GH7-4	1312	0.21	21.9	7.1	1.75	0.26
	GH7-3	1303	5.00	49.7	24.7	2.85	0.32
	GH7-2	1281	14.0	68.2	44.8	3.15	0.35
Greenhills Mine, Seam 10	GH10-3	1328	0.21	14.3	4.1	2.9	0.35
	GH10-2	1336	5.00	56.7	27.3	4.2	0.38
	GH10-5	1339	14.0	80.8	47.4	4.5	0.35
Elkview Mine, Seam 8	8UX-4	1309	0.21	14.6	6.2	1.52	0.47
	8UX-3	1334	5.00	51.1	28.9	4.19	0.34
	8UX-1	1324	14.0	78.7	57.4	4.50	0.36
Elkview Mine, Seam 10	ELK 10-4	1456	0.21	19.7	11.2	3.62	0.32
	ELK 10-3	1452	5.00	55.1	27.9	4.84	0.28
	ELK 10-1	1448	14.0	64.7	45.6	5.07	0.33
Cardinal River Mine, Jewel Seam	CR-4	1343	0.21	19.3	5.5	2.10	0.28
	CR-3	1334	5.0	58.0	26.5	4.07	0.33
	CR-2	1308	14.0	66.5	22.4	4.10	0.34

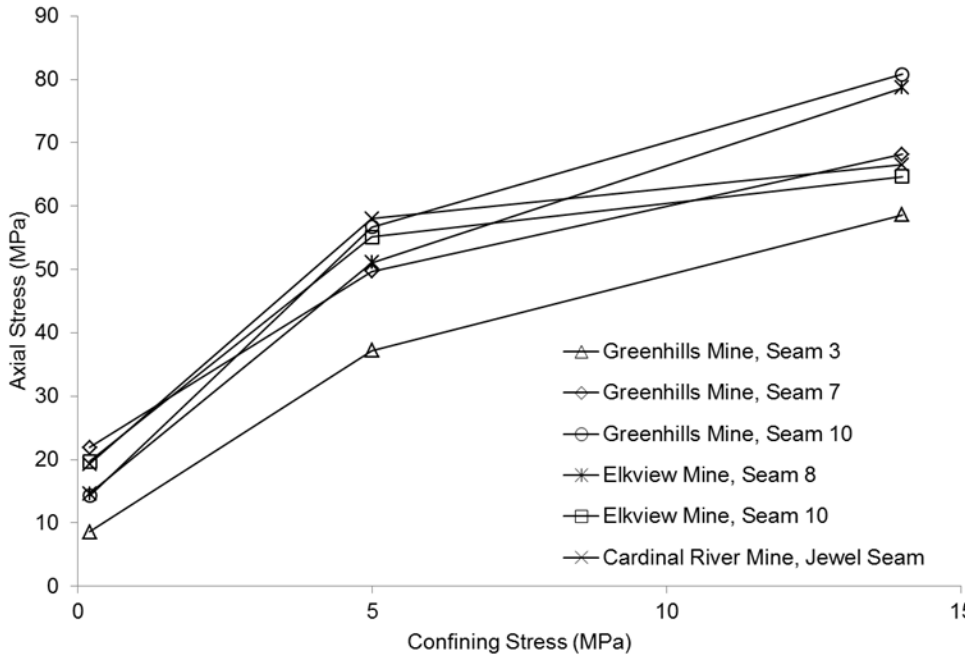

Figure 88. Strength results from the CT w/ V,P.

Unconventional Triaxial with Permeability and Particle Size

Initially, three loading compression (UA1, UA4, CE2), one ULC (CE5), and two loading extension (CE3, CE6) tests were completed to determine the location of the compression and extension failure envelopes. The failure envelopes were used to guide further tests for permeability changes with stress and coal particles generation near the failure envelope. The saturation isotropic stress state and pore pressures are provided in Table 13.

Table 13. Loading path for coal pre-testing saturation.

Sample Name	Pre-Saturation Stress (MPa)			Saturation Stress (MPa)		
	$\sigma_{c,i}$	$\sigma_{a,i}$	u	$\sigma_{c,f}$	$\sigma_{a,f}$	u
UA1-LC	n/a	n/a	n/a	n/a	n/a	n/a
UA2-LC-LE	n/a	n/a	n/a	n/a	n/a	n/a
CE2-LE	0.69	0.18	0.45	1.94	6.76	0.97
UA4-LC	0.25	0.68	0.01	1.30	1.48	1.0
UA5-LC	0.65	0.20	0.08	11.2	11.3	9.89
CE5-ULC	This sample was tested in Unconfined Compression					
CE1-LE/LC	0.27	0.21	0.47	1.98	8.79	1.02
UA3 LC/ULE	0.53	0.26	0.29	6.28	3.55	0.96
CE3-LE	0.51	0.43	0.19	2.00	1.90	1.0
CE4-LE	0.16	0.28	0.00	1.99	2.02	1.0
CE6-LE	0.75	0.15	0.18	4.97	5.46	0.97

Loading/Unloading Compression and Loading Extension

Several unconventional stress path tests were completed to determine both the compressional and extensional strength of the coal samples. The results are provided in Table 14 and illustrated in Figure 89.

Table 14. Peak strength results from unconventional stress path testing program.

Specimen	Test	σ'_r (MPa)	σ'_a (MPa)	u_f (MPa)
UA1	LC	0.0	8.2	0.0
CE2	LC	18.1	79.7	0.97
UA4	LC	1.0	13.3	1.0
UA5	ULC/LC	2.8	35.8	10.2
CE5	ULC	0.26	15.1	1.0
CE1	LC/LE/LC	19.9	92.0	0.99
UA3	LE/LC/ULE	20.4	3.3	1.0
CE3	LE	8.0	1.2	1.0
CE4-4	LE	24.0	4.3	1.0
CE4-8	LC	33.0	8.1	1.0
CE4-15	LC	32.9	14.8	1.0
CE6	LE	26.2	4.7	0.96

Initial Failure Envelope

The initial LC, LE, and ULC test results were used to create compression and extension failure envelopes for the second phase of the testing program. An arbitrary GSI = 85 and $D = 1.0$ were selected for each of the specimens in the compressive testing region. Using the best-fit approach outlined in Chapter 3, a compressive Hoek–Brown failure envelope was fit with 'intact' parameters of $\sigma_{ci} = 20.5$ MPa, $m_i = 16.7$ and $a = 0.5$. Assuming there is no anisotropy in the 'intact' sections of the coal, an extension envelope was fit using a $GSI = 55$ (Figure 89).

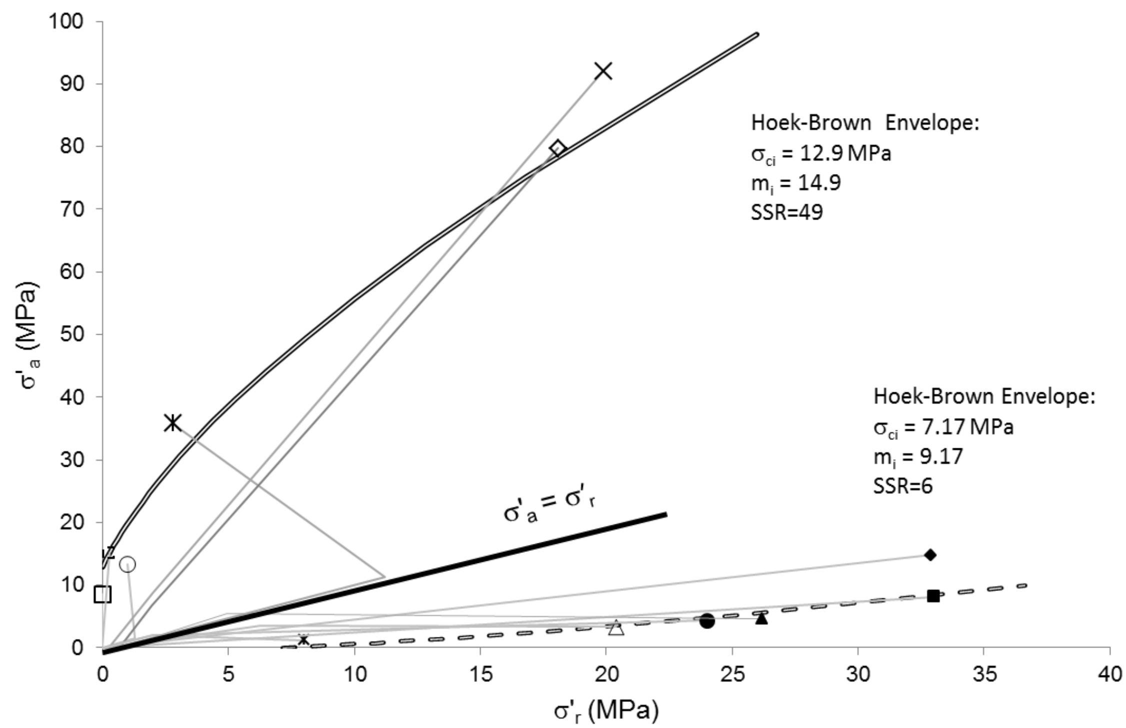

Figure 89. Initial extension and compression failure envelope from unconventional stress path testing program (see Table 14 for figure values).

Combined stress paths

Sample CE1 was saturated and loaded to an initial isotropic stress of 1.0 MPa. The sample was loaded in compression, then followed a loading extension path, then reversed along the loading extension path, and finally followed a compression loading stress path failing at σ'_r = 19.9 and σ'_a = 92.0 MPa (Figure 90).

Sample UA3 was saturated and loaded isotropically to 1 MPa, then followed an LE/LC/ULE/ULC testing path (Figure 90). After initial loading, the sample underwent extension to σ'_r = 20.3 and σ'_a = 11.4 MPa. The sample was then loaded in compression to σ'_r = 15.4 and σ'_a = 68.1 MPa and unloaded along the same stress path to the extensional failure envelope at σ'_r = 20.4 and σ'_a = 3.4 MPa. Once the stress reached the extensional failure envelope, the sample was unloaded along the extensional failure envelop to σ'_r = 1.5 and σ'_a = 12.0 MPa. Along the entire extension and compression stress path the sample did not fail.

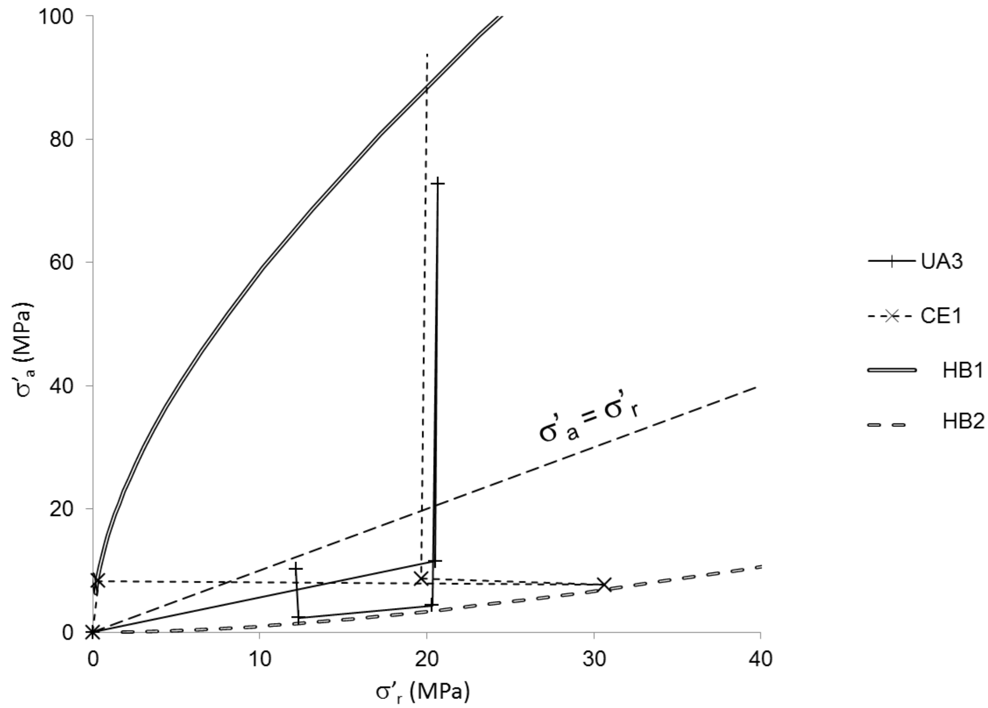

Figure 90. Loading compression and loading extension path of sample CE1 and UA3. Effective stress

7.6.4 Particle Size Distribution

Fines productions tests were conducted on samples CE1, CE4, CE6, UA3, and UA5 at multiple points throughout the testing stress paths. In all cases, coal fines were not produced as seen by examining the material collected in the accumulator. However, this does not mean that coal fines were not generated during testing, and possible damage as the coal sample neared its failure, fines may have been produced but were not able to flow through the cleats.

After completion of the loading compression tests on coal, the fragments were analyzed. There was no significant major or minor fracture plugging in specimen UA3 or CE1. Figure 91 shows the particle size distribution after the specimens were removed from the cell and the large intact core pieces separated from the fines distribution. Specimen CE3 had more than 96% of the created particles less than 19 mm and 6% greater than 0.43 mm. More than 76% of the particles generated from CE6 were larger than 19 mm, while 99% were greater than 0.43 mm. As well, several fines productions tests were conducted along the stress path for the UA3 specimen with no coal fines being produced.

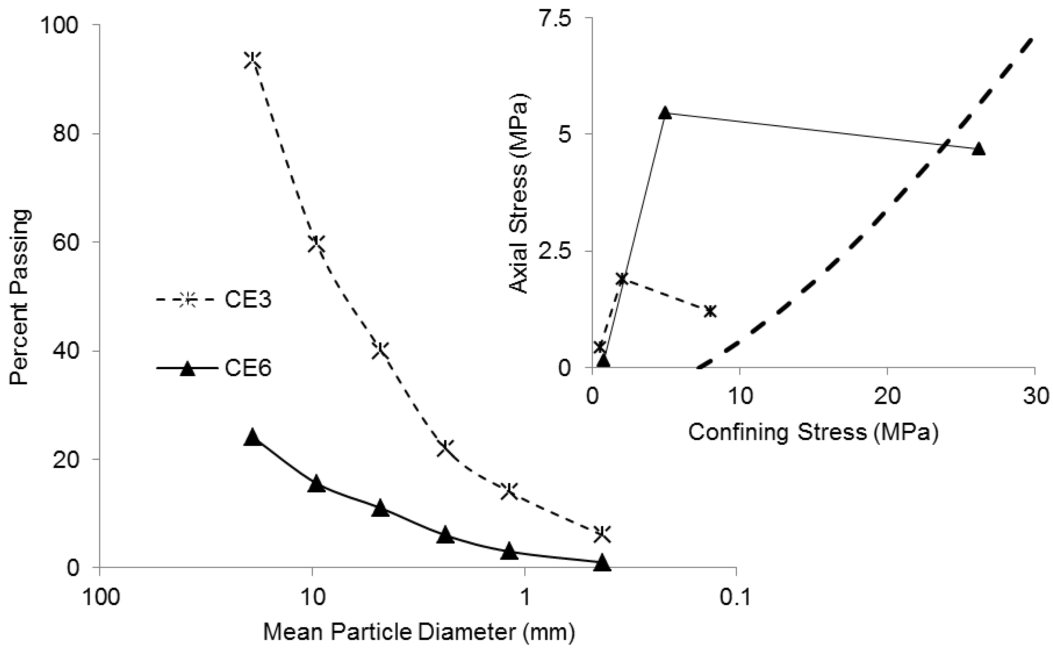

Figure 91. Particle size distribution for samples CE3 and CE6 after removal from triaxial cell.

7.6.5 Hydrogeomechanical results

Three samples (CE4, CE6 and UA5) were used to evaluate changes in permeability with stress as well as investigate the creation and production of coal fines as the stress state of the specimen approached the failure envelope. The stress paths, permeability measurement points, and corresponding permeability table are shown in Figure 92 with all of the testing values summarized in Table 15.

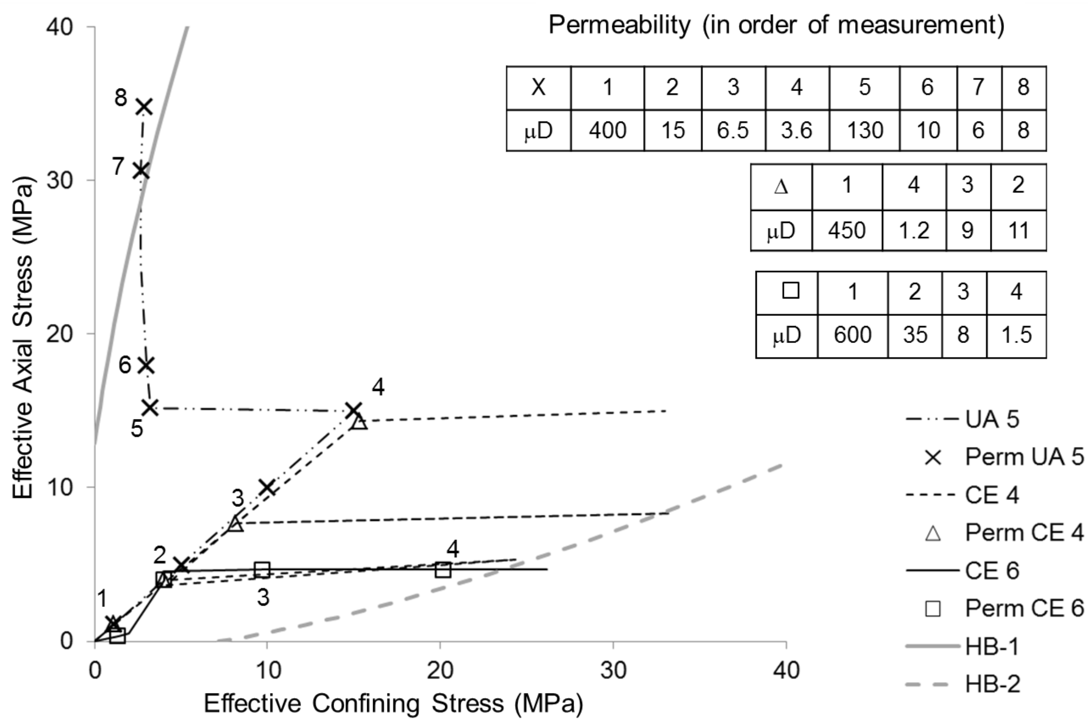

Figure 92. Stress with permeability measurements to water for samples UA5, CE4 and CE6.

Table 15. Results of permeability with changes in effective stress testing on coal block specimens.

Sample ID	Test	σ′$_1$	σ′$_3$	Permeability
		MPa	MPa	μD
CE4	Perm – 1	1.1	1.1	405
	Perm – 2	4	4	1.2
	Perm – 3	8.2	7.7	9
	Perm – 4	15.3	14.3	11
CE6	Perm – 1	1.3	0.3	600
	Perm – 2	4	4	35
	Perm – 3	9.7	4.7	8
	Perm – 4	20.2	4.7	1.5
UA5	Perm – 1	1.1	1.1	400
	Perm – 2	5	5	15
	Perm – 3	10	10	6.5
	Perm – 4	15	15	3.6
	Perm – 5	3.2	15.2	130
	Perm – 6	2.8	18.3	10
	Perm – 7	2.7	30.7	6
	Perm – 8	2.8	34.8	8

Sample CE4 was saturated and taken through a multi-stage extension stress path with permeability measurements and fines production tests at several isotropic stress states.

The sample was initially loaded isotropically to 1.1 MPa and a permeability of 450 μD was measured. An isotropic stress of 4.0 MPa was applied and the sample was loaded near the failure envelope to $\sigma'_r = 23.8$ and $\sigma'_a = 4.4$ MPa. Subsequently, the sample was unloaded along the same path (the return stress path data was not recorded) to an isotropic stress of 4.0MPa and a permeability of 1.2 μD was measured. The isotropic stress was then increased to 8.0 MPa and a stress cycle to $\sigma'_r = 32.7$ and $\sigma'_a = 8.0$ MPa (near the failure envelope) was applied and then reversed back to an isotropic stress of 8.0 MPa. A permeability of 9 μD was then measured. The isotropic stress was increased to 15 MPa, the sample followed an LE path to $\sigma'_r = 32.7$ and $\sigma'_a = 14.7$ MPa, which was not at the failure envelope, and then the stress was reversed along the same path. When the sample was returned to an isotropic stress of 15 MPa, the coal had a permeability of 11 μD. Along each of the extension stress paths the sample did not show any signs of failure and after each permeability test no coal fragments were produced.

Sample CE6 was used to both define the extension failure envelope and for permeability measurements. The sample had a permeability of 600 μD at an isotropic stress of $\sigma'_r = 0.3$ and $\sigma'_a = 1.3$ MPa. An isotropic stress of 4 MPa was then applied reducing the permeability to 35 μD. The sample was then subjected to a loading extension stress path, where $k = 8$ μD was measured at $\sigma'_r = 9.7$ and $\sigma'_a = 4.7$ MPa, then a $k = 1.5$ μD at $\sigma'_r = 20.2$ and $\sigma'_a = 4.7$ MPa, respectively.

Sample UA5 was saturated, incrementally isotropically loaded isotropically up to 15 MPa. Along the isotropic loading stress path permeabilities of 400, 15, 6.5, 3.6 μD were measured at 1, 5, 10, and 15 MPa, respectively. The sample was then unloaded towards the compression envelope to a stress state of $\sigma'_r = 3.2$ and $\sigma'_a = 15.3$ MPa where a permeability of 130 μD was measured. A loading compression path to failure was then applied and three permeability measurements along the failure stress path were made: $k = 10$ μD at $\sigma'_r = 2.8$ and $\sigma'_a = 18.3$ MPa, $k = 6$ μD at $\sigma'_r = 2.7$ and $\sigma'_a = 30.7$ MPa, and $k = 8$ μD at $\sigma'_r = 2.8$ and $\sigma'_a = 34.8$ MPa. After each permeability measurement no visible coal fines were present in the coal fines production cell.

7.6.6 Methane Gas Sorption and Swelling

In the ET w/V,S testing program, the methane content and axial strain occurring on the CR-ET-1 specimen at each gas pressure and constant effective stress were measured. This procedure was completed to investigate the influence of effective stress on gas sorption isotherms and axial swelling strain. The gas pressures were held at each increment for approximately 48 hours, allowing gas sorption to occur as listed in Table 16 and illustrated in Figure 93. After the testing under isotropic stress conditions was completed, the conventional sorption isotherms were tested in the intact and crushed by Trican Geological Solutions. The final sorption isotherms are shown in Figure 94.

Table 16. Methane gas pressures at each of the testing stages (all values in MPa).

Effective Stress	Pore Pressure Stage					
	1	2	3	4	5	6
1.1	0.5	1	2	3	4	6
3.0	0.5	1	3	5	7	
5.0	2	3	6.2	8.3		

For the test at 1.1 MPa constant effective stress, the gas pressure was increased incrementally and the specimen showed the greatest total gas sorbed at the 225 hour period where the final gas pressure was 6 MPa and the final gas content was 0.3 mols/kg. The gas pressure was reduced to zero and effective stress was reduced to 500 kPa and held for 150 hours, allowing the methane to desorb from the specimen. The effective stress was then increased to 3.0 MPa. The gas pressure was then incrementally increased until a final gas pressure of 7 MPa was reached after 250 hours. The final methane content at this pressure was 0.24 mols/kg. The gas pressure was again reduced to zero and the effective stress was held at 500 kPa for 6 weeks. The effective stress was then increased to 5.0 MPa and the gas pressure incrementally increased in stages to 8.3 MPa. The resulting gas content after 375 hours of testing was 0.2 mols/kg. In each case, the resulting final gas content was reduced as the effective stress state increased.

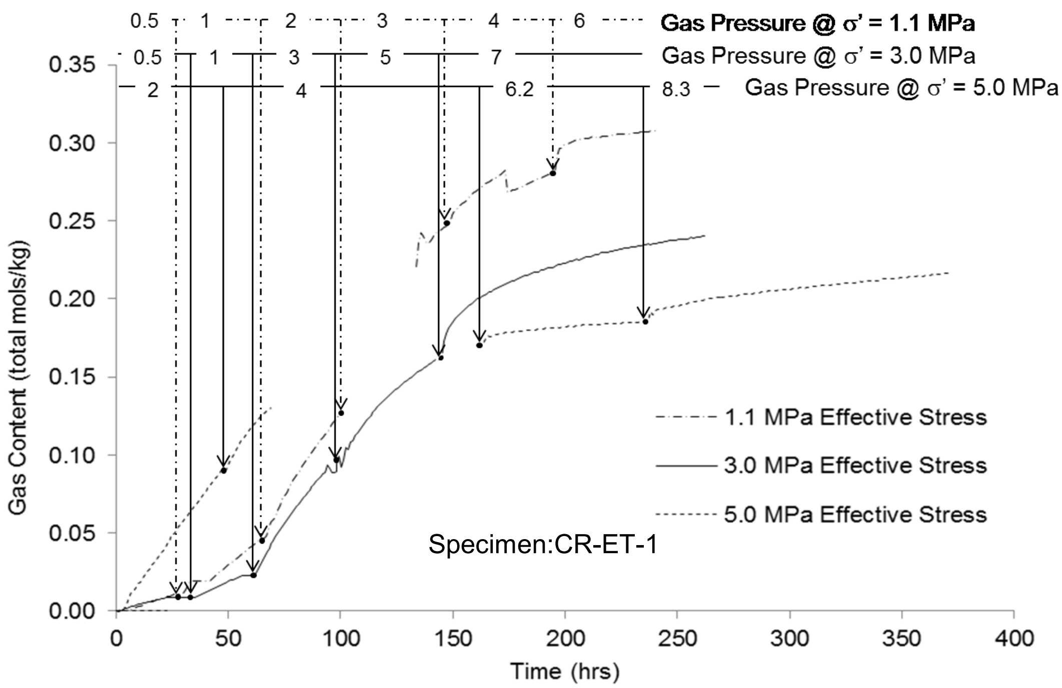

Figure 93. Methane gas sorption for each testing sequence at 1.1, 3 and 5 MPa effective stress. The gas pressure used for each pressure increment was variable and is shown in MPa at the top of the figure.

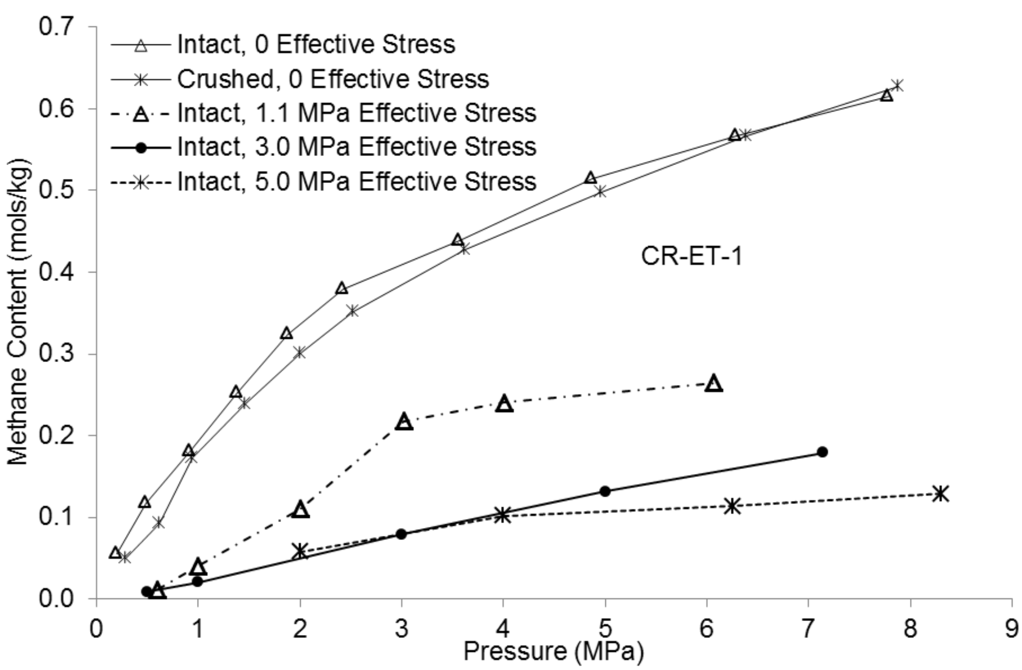

Figure 94. Isotherm for methane gas for intact coal at 0, 1.1, 3 and 5 MPa effective stress and crushed coal at 0 MPa effective stress all at 301.1 K.

For each of the constant effective stress tests on the CR-ET-1 specimen, the methane sorption was determined for each corresponding methane pressures (Table 17). The time for each gas pressure loading stage was different and equilibrium may not have been reached prior to the next gas content load. Therefore the gas content was determined at 30 hour mark for each stage.

The crushed and intact coal isotherms were very similar. The maximum sorbed gas was 0.62 mols/kg for the crushed coal specimen at 8.0 MPa gas pressure and zero effective stress. However, below 8.0 MPa gas pressure, the intact coal specimen had a higher gas content for corresponding pressures. The application of stress influenced the sorbed gas, were with 1.1 MPa constant effective stress, the maximum gas content was 0.26 mols/kg and at a gas pressure of 6.0 MPa. When the sample was loaded to 3.0 MPa and 5.0 MPa constant effective stress, resulting methane content was similar for gas pressures up to 4.0 MPa. The final sorbed gas content for the 3.0 MPa constant effective stress state at 7 MPa gas pressure was 0.18 mols/kg, while the 5.0 MPa constant effective state at 8.3 MPa gas pressure was 0.13 mols/kg.

Table 17. Results of gas sorption up to 8.3 MPa pressure and 1.1, 3 and 5 MPa constant effective stress states.

Specimen CT-CR-1	Total Stress	Gas Pressure	Gas Content	Axial Strain
Effective Stress (MPa)	MPa	MPa	mols/kg	
1.1	1.7	0.6	1.19×10^{-2}	-8.58×10^{-5}
	2.1	1.0	4.07×10^{-2}	-1.11×10^{-4}
	3.1	2.0	1.10×10^{-1}	-1.70×10^{-4}
	4.1	3.0	2.18×10^{-1}	-2.97×10^{-4}
	5.1	4.0	2.40×10^{-1}	-4.81×10^{-4}
	7.1	6.0	2.65×10^{-1}	-6.81×10^{-4}
3.0	3.5	0.5	8.80×10^{-3}	0.0×10^{-6}
	4.0	1.0	2.09×10^{-2}	-2.92×10^{-6}
	6.0	3.0	7.90×10^{-2}	-1.08×10^{-4}
	8.0	5.0	1.31×10^{-1}	-2.99×10^{-4}
	10.1	7.1	1.79×10^{-1}	-4.60×10^{-4}
5.0	7.0	2.0	5.76×10^{-2}	3.01×10^{-6}
	9.0	4.0	1.02×10^{-1}	-9.73×10^{-6}
	11.2	6.2	1.14×10^{-1}	-3.05×10^{-5}
	13.3	8.3	1.29×10^{-1}	-1.01×10^{-4}

7.6.7 Gas Content and Axial Strain

During the gas sorption stages of the ET w/V,S testing program, the axial strain was monitored to investigate the influence of effective stress on coal swelling due to gas sorption (Table 17). Each of the axial strain measurements was evaluated at 30 hours for equal comparison. The results showed that the maximum amount of swelling occurred for the sample at maintained at 1.1 MPa constant effective stress. The axial strain for this effective stress state was -6.8×10^{-4} (compression is positive) at 6 MPa gas pressure. After the specimen was unloaded to zero gas pressure and reloaded to 3 MPa effective stress, the specimen was exposed to 0.5 and then 1 MPa methane gas pressure. At these gas pressures, there was a much lower axial strain (close to 0). The specimen did not experience any axial expansion until 3 MPa methane pressure. The specimen reached a maximum axial expansion of -4.6×10^{-4} at 7.1 MPa gas pressure. The specimen was then unloaded to zero gas pressure and the gas allowed to desorb, then it was loaded back to 5.0 MPa effective stress. For this cycle, the axial swelling strain did not occur until a methane pressure of 4 MPa, and then increased and reached a maximum of -1.0×10^{-4} at 8.3 MPa methane pressure.

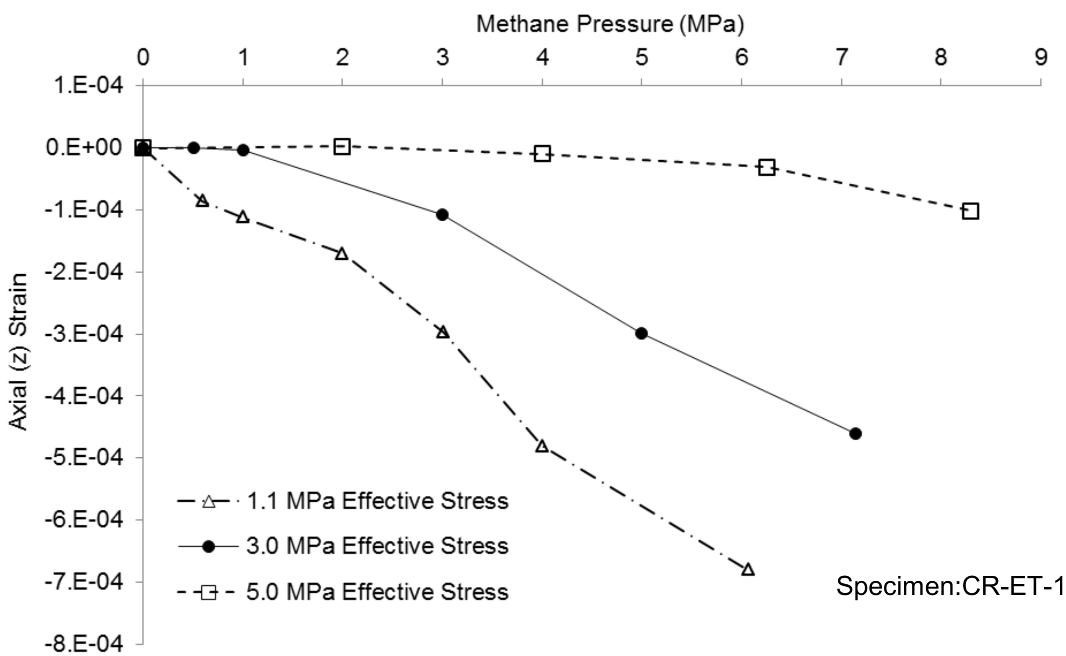

Figure 95. Axial swelling strain at 1.1, 3.0 and 5.0 MPa constant effective stress with increasing gas pressure.

The axial strain was also plotted against the sorbed methane at each effective stress state (Figure 96). The results showed that the maximum axial strain was -6.8×10^{-4} at 0.26 mols/kg and occurred for the 1.1 MPa constant effective stress state. The axial strain at the final methane content of 0.18 mols/kg for the 3.0 MPa effective stress state was -4.6×10^{-4}, and the axial strain at the final methane content of 0.13 mols/kg for the 5.0 MPa effective stress state was -1.0×10^{-4}.

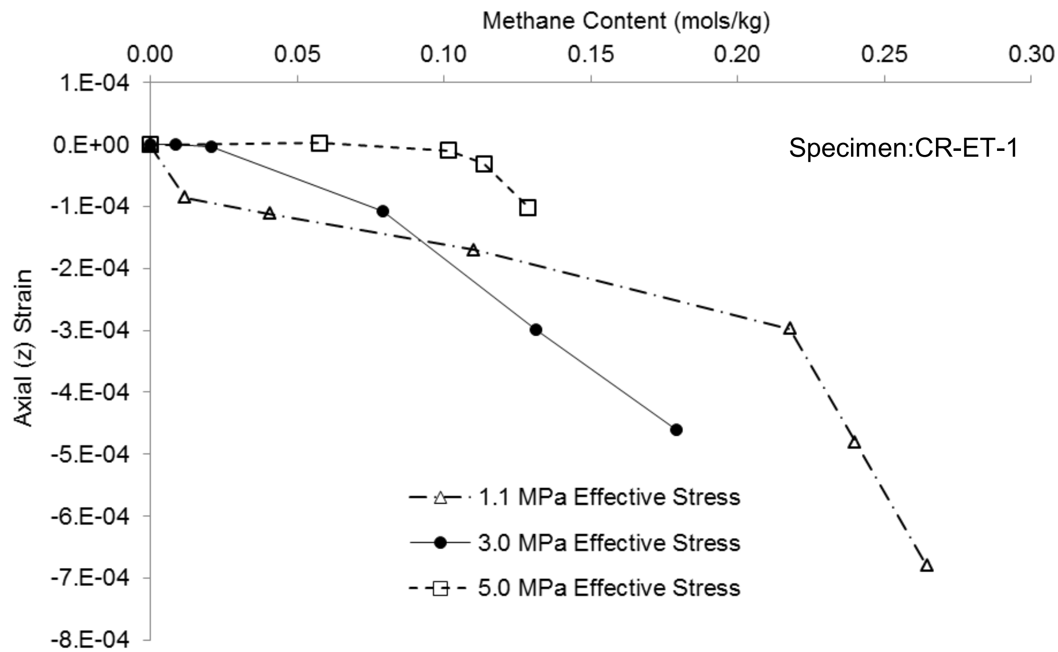

Figure 96. Axial swelling strain with changes in gas content at 1.1, 3.0 and 5.0 MPa constant effective stress.

7.7 Conclusions

The testing program in this thesis investigated the influence of effective stress and gas content on the mechanical, flow, velocity and sorption properties of coal. The coal was taken from several coal seams at three different coal mines: Cardinal River, Greenhills, and Elkview. The investigation was accomplished through three separate coal testing programs:

1. Conventional Triaxial Stress path with Velocity and Permeability (CT w/ V,P);
2. Unconventional Triaxial Stress path with Permeability and Particle Size (UT w/P,PS);

3. Elastic Triaxial Stress path with Velocity and Methane Sorption (ET w/ V,G).

The testing program specifically investigated the influence of effective stress on the following, and found:

1. Deformation: Increasing effective stress created a concave downward non-linear relationship between confining stress Young's modulus.
2. P and S wave velocity: Increasing effective stress created a concave downward non-linear relationship. Increasing gas content did not significantly influence the P or S wave velocity.
3. Strength: Increasing the confining stress created a concave down non-linear relationship.
4. Coal fines generation: During permeability testing during unconventional stress path testing, coal fines were not produced and collected in the accumulator however, fines may have been created not able to flow through the cleats.
5. Permeability: Several permeability tests were completed, showing that as the isotropic effective stress increased, the permeability decreased, however if an unconventional stress path was used, the permeability increased relative to the isotropic value.
6. Porosity: Effective cleat porosity ranged from 0.99% to 2.72% and has been shown difficult to measure due to the very small volume of cleats in a core sample. Cleat porosity of 1% has been used in the literature as a representative value of coals in the San Juan Basin, based on laboratory measurements (Harpalani and Chen, 1997).
7. Gas Content: The application of effective stress reduced the sorbed methane of the coal at equivalent gas pressures for increasing effective stress states.
8. Swelling Strain: The application of effective stress reduced the swelling strain experienced by the coal at equivalent gas pressures for increasing effective stress states.

8 Numerical Testing – The Synthetic Rock Mass

This chapter addresses the use of computer modelling of simulated rock masses to aid in the characterization and upscaling of coalseam properties from the laboratory to the field scale. Deformation and strength characteristics of coal laboratory specimens aid in predicting the mechanical response of a coalseam under operation conditions. Obtaining high quality samples of fractured coal is difficult, and laboratory strength and deformation results are often not representative of coalseam reservoir properties due to the scale effects caused by weak planes (cleating and bedding planes). When discussing wellbore stability in coalseams, Palmer et al. (2005) stated, "[f]or more reliable prediction of failure, a better way is to cut core from a well, and measuring rock strength directly … [h]owever, there is still an unsettled question of how best to scale core-scale [unconfined compressive strength] up to wellbore-scale or reservoir-scale." Numerical testing using the Synthetic Rock Mass (SRM) approach attempts to address the issue of scale dependence in coal geomechanical properties by numerically recreating both the intact coal and coal fracture network and then testing the coal mass at several scales, including the full coalseam.

Figure 97 illustrates where the numerical testing appears in the overall program for hydrogeomechanical characterization of a coalseam reservoir. This chapter is structured by providing background on the SRM, then testing the SRM concept against two dimensional laboratory results, and then using the SRM concept to characterize two fictional coal seams in three dimensions.

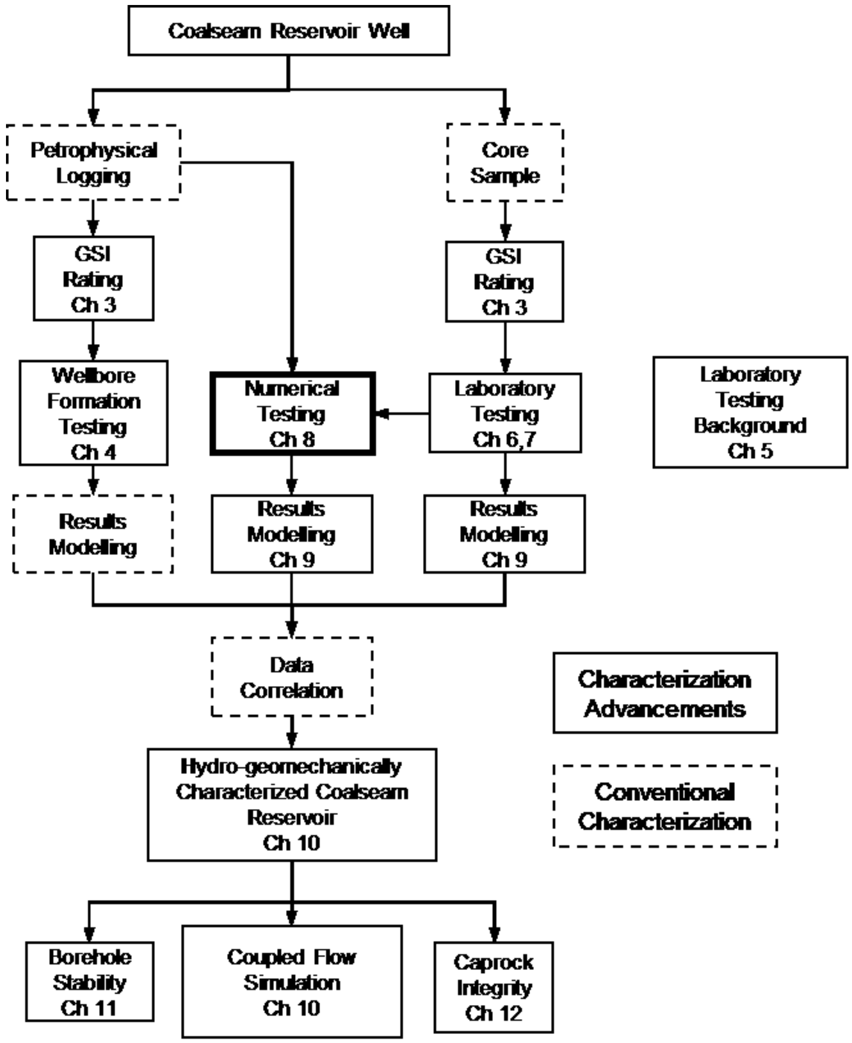

Figure 97. The coalseam hydro-geomechanical workflow illustrating where the numerical testing fits into the characterization workflow.

8.1 The Synthetic Rock Mass Approach

Given the difficulty of direct full-scale testing of a rock mass, reliance has been placed on empirical classification rules and systems derived from practical observations. Rock mass stiffness and strength typically decrease with an increase in scale, and is usually attributed to the presence of joints and discontinuities in the rock mass that are weaker than the intact rock.

Rock Mass Classification (RMC) systems were developed for use in Civil and Mining Engineering in response to the need for ways to 'rank' a specific rock mass, based in large part upon the joints and their weakening effect on the rock. By compiling histories of rock mass ranking relative to performance, it has been possible to develop relationships for quantitative prediction of rock mass strength and modulus. Despite the fact that RMC systems and relations are in widespread use in engineering design, their ability to consider strength anisotropy (resulting from the joint network) and strain softening/weakening behaviour remains limited. Another important limitation of such systems is the inherent uncertainty of extrapolation beyond the limits of the experience from which the rules have been derived. A comprehensive discussion on this matter can be found in Mas Ivars (2007).

The relatively recent development of numerical models based on particle mechanics and the advances in computer power allow detailed examination of the interaction between rock discontinuities and intact rock for a variety of cases and scales. It is now possible to simulate a rock mass and conduct ‘numerical experiments’ analogous in some respects to physical experiments, and thereby gain considerable insight into the nature of scale effects on the strength and constitutive behavior of rock masses.

Recently, a numerical technique termed the Synthetic Rock Mass (SRM) has been developed to model a large range of rock mass behaviours not possible through conventional laboratory testing or RMC systems (Pierce et al., 2007). The SRM technique uses numerical simulation methods based on particle mechanics and discrete fracture network modeling. Using geomechanical properties from core specimens along with knowledge of the fracture distribution from borehole imaging (FMI logs) and core logging, a rock mass (here a coal seam) can be numerically constructed at any volume.

The SRM technique provides the ability to conduct numerical experiments by combining two established simulation techniques: the Bonded Particle Model (BPM) and the Discrete Fracture Network (DFN) through the smooth joint (SJ) contact model (Pierce et al., 2007). The BPM uses a particle flow code (PFC) to assemble particles in 2D or 3D and then bond them together to simulate the mechanical behaviour of rock (Potyondy and Cundall, 2004). The DFN honours both the geometry and spatial distribution of the observed fracture pattern. The recent development of the SJ contact model allows for the insertion of the DFN into the BPM, creating the SRM (Potyondy 2008, Mas Ivars et al. 2008a).

The SRM concept allows for rock volumes at multiple scales containing thousands of non-persistent pre-existing joints to be subjected to any non-trivial stress path while extracting and/or monitoring a voluminous amount of information regarding the rock mass behaviour. The results can provide directional strength and deformation at multiple tested scales, which can then be used inside of continuum type software packages for engineering analysis. Other information that can be obtained from the SRM includes: brittleness, fragmentation, seismicity, and fracture aperture change (Mas Ivars et al., 2007).

8.1.1 Synthetic Rock Mass Construction and Testing

Information or input data for the SRM workflow are gathered in a manner similar to that of traditional RMC systems: core sampling, specimen testing, and detailed analysis of the fracture structure. Then samples are numerically reconstructed and tested at many desired scales and directions. The SRM is built and tested in three main steps (Figure 98):

1. Calibrate the BPM microproperties to the observed laboratory behaviours using the standard BPM procedures.
2. Create and calibrate a DFN using a DFN simulation program based on fracture data and insert the DFN into the BPM using the SJ contact model, thus creating the SRM.
3. Test the SRM using any method required to extract the necessary information from the SRM (i.e. Spherical Testing, Standard Suite, or any other method).

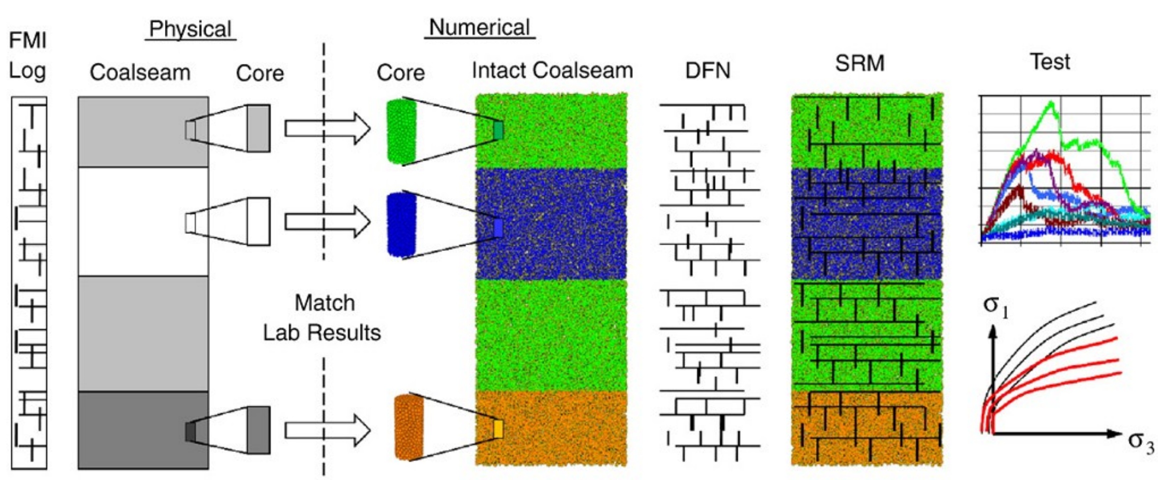

Figure 98. SRM workflow for geomechanical characterization of coal seam reservoirs.

The DFN and BPM can be created at any scale (limited only by computing RAM), making it possible to numerically generate and test SRM volumes of any size containing thousands of non-persistent joints. Unfortunately, PFC only runs on a single processor core, therefore the practicality of the numerical testing solution time must be taken into account.

Bonded Particle Model

Although Itasca's PFC is by definition, a particle flow code, a more accurate conceptual description would be a particle mechanics code (Itasca Consulting Group, 2007). PFC, through the BPM, has previously shown the ability to reproduce many features of intact and jointed rock behaviour, including: elasticity, fracturing, acoustic emissions, damage accumulation producing material anisotropy, hysteresis, dilation, post-peak softening and strength increase with confinement (Potyondy and Cundall, 2004; Cho et al., 2007; Hazzard and Young, 2000, 2002, 2004; Holt et al., 2005; Kulatilake et al., 2001; Park et al., 2004).

To create the BPM for SRM testing, a single small scale system may be built, and then using PFC's periodic space functions, replicated and pieced together perfectly to create very large simulation models. For example, a small 1m by 1m square could be built, and then the periodic space used to assemble the squares into a 10m by 10m section, greatly reducing the simulation construction time.

Smooth Joint Model

Joints in PFC have been previously modelled by identifying a joint plane and changing the properties of contacts between particles lying on either side of that plane. This technique created a joint plane with an unrealistically high joint friction angle due to the asperities on the joint. The SJ contact model was developed to remedy these shortcomings (Pierce et al., 2005) and is implemented in the SRM by changing the particle contact model wherever a joint intersects a contact.

While the BPM simulates the behaviour of a particle interface normal to the particle contact (n_c) (Figure 99), the SJ model allows for an interface in any desired orientation regardless of the local particle contact orientations. This allows two contact particles to displace relative to one another without having to honor local contact orientations, thereby eliminating the need for particles to "ride over" each other to accommodate relative shear displacement.

An SJ contact is shown in Figure 99 with the joint geometry consisting of surfaces 1 and 2 and a dip angle (θ_p). The joint plane orientation is defined by the unit-normal vector (n_j) and perpendicular vector (t_j). When the SJ model is assigned to the contact, ball1 and ball2 are associated with the appropriate joint surfaces. Normal and shear force and displacement are calculated relative to the SJ contact using Coulomb sliding with dilation and then mapped back to the ball1-ball2 contact to update the model (Itasca Consulting Group Inc., 2008).

The SJ model is defined in terms of conventional rock mechanics joint properties obtained from laboratory or field testing. Each joint can be assigned a friction coefficient (or angle), cohesion, tension, and shear and normal stiffness. The shear and normal force acting on the joint, as well as the normal and shear displacement, can be tracked during simulation.

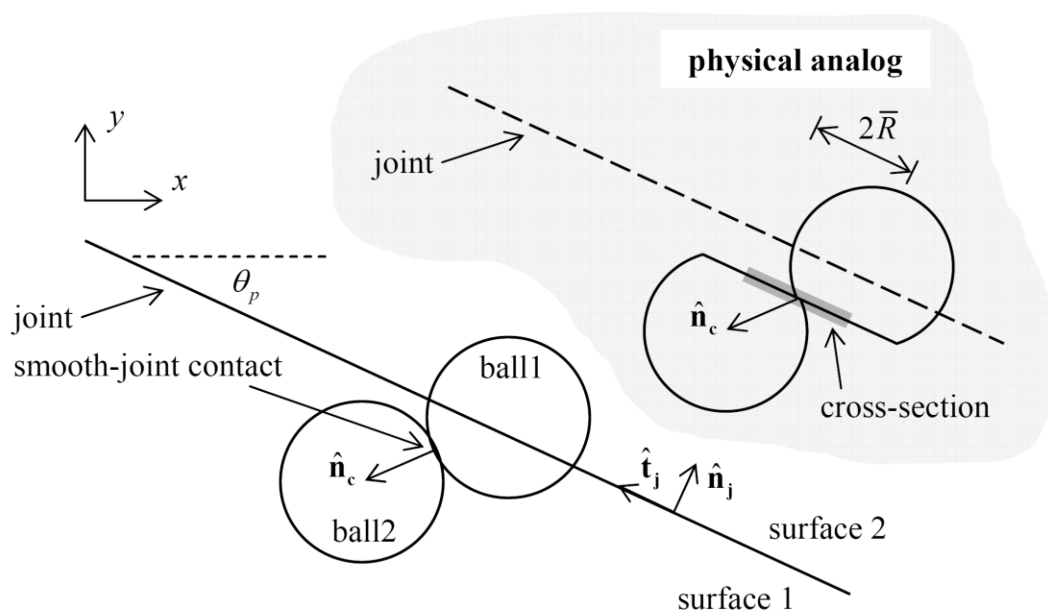

Figure 99. Smooth Joint contact model between ball1 and ball2. Surface 1 and surface 2 denote either side of the joint lying at a dip angle of θ_p (adapted from Itasca Consulting Group Inc., 2008).

Standard Suite of Tests

An SRM environment has been developed (Mas Ivars et al., 2008b) which includes three industry standard tests: direct tension, unconfined compressive strength (UCS), and triaxial compression. These tests are designed to provide measures of rock-mass tensile strength, *UCS*, and compressive strength at several minimum stress levels. Deformation parameters, including rock mass Young's modulus (E_{RM}) and rock mass Poisson's ratio (ν_{RM}), can also be measured in each test. These tests can be performed on SRM samples of different sizes in the three axial directions (x, y, z). In this manner, the so called "Standard Suite of Tests" environment allows for systematic rock-mass behavior characterization, capturing the effect of scale and anisotropy.

8.2 2D SRM Smooth Joint Contact Model Investigation

The first study was undertaken to assess the ability of the current SJ formulation in PFC2D to simulate crack initiation, propagation and coalescence. Results from several laboratory uniaxial compression tests on one, two and three small flaws embedded in rock-like material were simulated as well as the influence of strain rate and particle resolution on the fracturing behaviour.

Ideally, this work should be conducted in 2D and in 3D, however limited laboratory results on controlled materials with internal cracks were available. Additionally, mapping simulation results in PFC3D for bond breakages and fracture growth is very difficult. This 2D study is the first attempt for the SRM model verification to ensure that fracture growth and observed model strength are reasonable.

8.2.1 Numerical Simulations

A series of experimental results on simulated rock material containing one, two, and three initial fractures (flaws) orientated with different angles were selected from the literature for numerical simulation. These sets of experiments also used variable angles and distances between the flaws patterns, termed bridge angles and bridge distances. The selection criteria included documentation on intact strength, deformation properties, specimen and flaw geometries, photographs of fracturing, crack initiation angles, and crack initiation locations. The selected laboratory results were further divided into two sub groups: strong material containing one flaw and a weak material containing two and three flaws. These two materials enabled SJ testing in two significantly different materials and multiple internal flaw geometries.

For each of the models, the intact material was matched using a resolution of eight particles across the length of a single SJ, and then the SJ was inserted with reported properties (joint stiffness and friction angle). The physical and numerical results were qualitatively and quantitatively compared to reported fracture coalescence patterns and strength results.

Resolution

The number and size distribution of particles defining a BPM influence the macro properties of the model, which is why each BPM requires micro property calibration. Typically, an SRM simulation employs a "rule of thumb" of resolution (*Res*) of five to ten particles across the length (L) of a SJ inside of an SRM. The BPM is built with a user defined maximum and minimum particle radius. The minimum particle radius (R_{min}) and maximum to minimum particle size ratio (R_{max}/R_{min}) can be used to calculate the resolution (*Res*) Eq 35.

$$\mathrm{Re}s = (L/R_{\min})[1/(1 + R_{\max}/R_{\min})] \qquad 35$$

One Flaw

Wong and Einstein (2006) presented experimental results on single flaws with a length of 12.7 mm at multiple angles embedded in laboratory created gypsum specimen (Figure 100). The object of their study was to measure the distances and angles at which fractures initiated relative to the initial flaw tip as well as tensile wing crack initiation stress. The intact material had a height of 156 mm, width of 76 mm, and a thickness of 32 mm. These specimens had an intact *UCS* of 34.5 MPa, tensile strength of 3.2 MPa, Young's modulus of 5.96 GPa, and Poisson's ratio of 0.15.

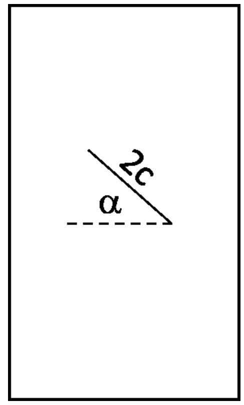

Test ID	α (°)
1-1	0
1-2	15
1-3	30
1-4	35
1-5	40
1-6	45
1-7	50
1-8	55
1-9	60
1-10	70
1-11	75

Figure 100. Specimen and flaw geometry for rock-like material containing a single embedded flaw (2c=12.7 mm).

Two and Three Flaws

Wong et al (2001) conducted similar laboratory experiments on simulated rock-like material containing two and three embedded flaws (also of length 2c=12.7 mm) (Figure 101, Figure 102). The intact material had a height of 120 mm, width of 60 mm, and a thickness of 25 mm with a *UCS* of 2.09 MPa, a tensile strength of 0.35 MPa, E of 330 MPa and Poisson's ratio of 0.19. The flaw bridge lengths (minimum distance between two flaws) for both the two and three flaw studies were held constant. In the case of the two flaw study, the flaw angle (α) and the bridge angle (β) were varied. In the three flaw study the flaw angle (α) and the second bridge angle (β_2) were varied, while the first bridge angle (β_1) was constant. Each of the orientations used flaws with a friction coefficient of 0.6 and 0.7.

The study measured the peak strength of the two and three flaw specimens with each flaw orientation and friction coefficient. The study also examined whether the crack coalescence was in shear, mixed (shear/tensile), or wing tensile mode.

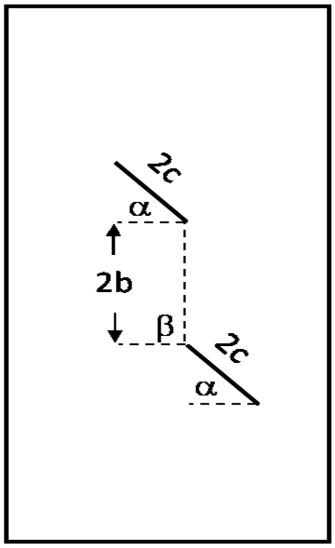

Test ID	α	β
	(°)	(°)
2-1	45	45
2-2	45	75
2-3	45	90
2-4	45	105
2-5	45	120
2-6	65	45
2-7	65	75
2-8	65	90
2-9	65	105
2-10	65	120

Figure 101. Specimen geometry for a simulated rock-like material containing two embedded flaws of length 2c = 12.7 mm and bridge length 2b = 20 mm. Each geometry was tested with flaws having a frictional coefficient of 0.6 and 0.7.

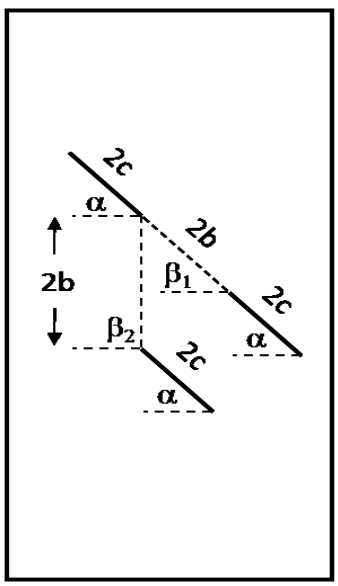

Test ID	α	β_1	β_2
	(°)	(°)	(°)
3-1	45	45	75
3-2	45	45	90
3-3	45	45	105
3-4	45	45	120
3-5	65	45	75
3-6	65	45	90
3-7	65	45	105
3-8	65	45	120

Figure 102. Specimen geometry for a simulated rock-like material containing three embedded flaws. Each geometry was tested with flaws having a frictional coefficient of 0.6 and 0.7.

Strain Rate

The BPM is generally calibrated in a simulated uniaxial, biaxial, Brazilian or direct tension environment. One of the critical parameters selected in the testing environment is the platen strain rate. The ISRM suggested strain rate for triaxial testing is much lower than that used in PFC due to the energy damping technique employed. This technique ensures that the results of a PFC simulation remain in a quasi-static condition, enabling strain rates that are much higher than the laboratory. Even with this technique and with the current processor speeds of 3.6 GHz for a reasonably sized BPM of 4000 particles, simulation times may exceed 24 hours.

Figure 103 shows the influence of strain rate on macroproperties values of the BPM. The SJ model crack initiation and coalescence may also be influenced by the strain rate, and thus the overall behaviour of the SRM. Simulations on selected specimens were conducted in an attempt to improve results and to investigate any behavioural changes caused by strain rate variation.

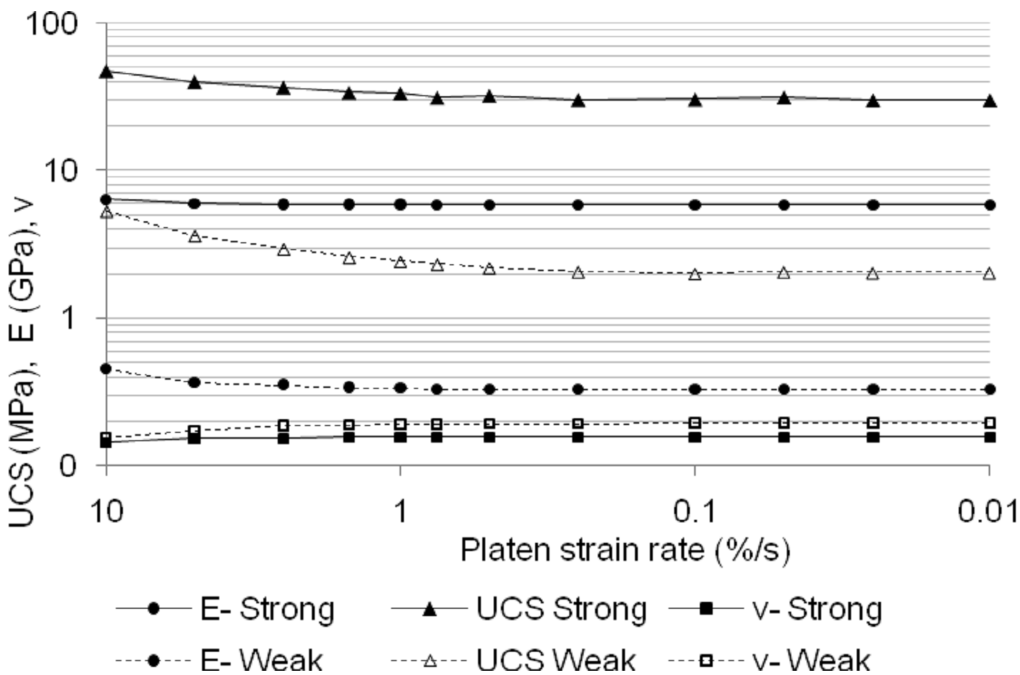

Figure 103. The influence of strain rate on compressive strength, Young's modulus and Poisson's ratio for weak and strong BPM samples under uniaxial compression.

8.2.2 Results

All of the numerical tests were completed using the *Augmented Fish Tank* which was developed to create, test and extract the properties of a PFC2D BPM. A parametric analysis code, the *Virtual Laboratory Assistant* (*VLA*) was developed to help easily create, test and extract the properties of multiple combinations of PFC2D BPM materials, specimens, and testing parameters.

Material Calibration

The BPM must first be calibrated to match the intact macroproperties of the laboratory specimens through selection and testing of BPM microproperties. When calibrating the BPM for SRM applications, only the *UCS*, Young's (*E*) modulus and Poisson's ratio (*v*) are matched, therefore, it was decided to also only use these values for calibration of the above materials.

The strong (one flaw) and weak (two and three flaw) simulated rock-like material microproperties are listed in Table 18. Several strain measurement techniques are possible inside of PFC. Here the *UCS* and *E* were calculated using wall based measurements and *v* was calculated using measurements based on gauge balls placed within the particle assembly. For each material, the particle size ratio was 1.66 and the particle friction coefficient was 2.5. Only parallel bonds were used to create the BPM with the normal and shear parallel bond strength standard deviations set to 22.5% of the mean values. The remainder of the BPM microproperties were set to the default values. A friction coefficient of 0.36 was used for the platens with a testing strain rate of 0.25%/s. The resulting BPM macroproperties are listed in Table 19.

Table 18. Microproperties of the strong and weak materials (P – Particle, B – Bond).

Sample	Total Particles	Minimum Particle Radius	Particle and Bond Modulus	Particle and Bond Stiffness Ratio	Bond Normal Strength	Bond Shear Strength
	(#)	μm	MPa		MPa	MPa
Strong	6043	564	4020	1.13	30.9	1.71
Weak	3747	564	235	1.62	30.9	1.71

Table 19. Resulting BPM macroproperties of the strong and weak materials.

Specimen		Young's Modulus	Poisson's Ratio	UCS	Direct Tension
		GPa		MPa	MPa
Strong	Physical	5.96	0.15	34.5	3.2
	BPM	5.97	0.15	34.9	7.4
Weak	Physical	0.330	0.19	2.09	0.35
	BPM	0.328	0.19	2.09	0.45

Smooth Joint Properties

The single flaw laboratory specimens were created by insertion of a thin metal sheet into the wet rock-like material and removal creating an aperture of 0.1 mm. The two and three flaw experiments used smooth and rough metal shims to create the flaws, while leaving them in during testing to create friction coefficients of 0.6 and 0.7 respectively.

The one flaw specimens were simulated with the SJ model friction coefficient set to zero with SJ normal and shear stiffness were set to 8.0 GPa/m. The two and three flaw specimens were simulated with SJ friction coefficients equal to those reported with SJ normal and shear stiffness of 10 GPa/m.

One Flaw Results

Figure 104 shows the results from the single flaw laboratory experiments with photographs and the corresponding SJ simulations. The simulation with the flaw orientated at $\alpha = 0°$ and $\alpha = 75°$ did not reasonably match the observed laboratory behaviour. The mode of crack initiation and propagation (tensile wing crack, shear, or tensile) was not compared to the laboratory results. The simulations at 30, 45, and 60 degrees did match the fracture patterns observed in the laboratory.

<table>
<tr><th>α (°)</th><th>Lab</th><th>PFC</th></tr>
<tr><td>0</td><td>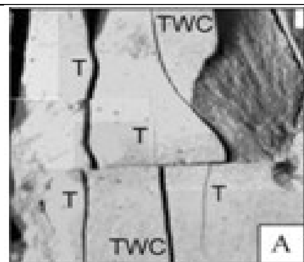
</td><td>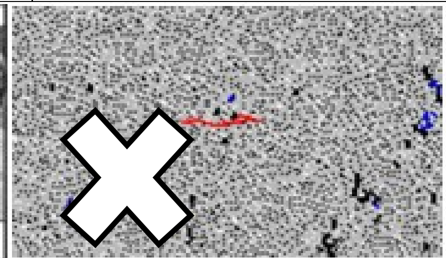</td></tr>
<tr><td>30</td><td>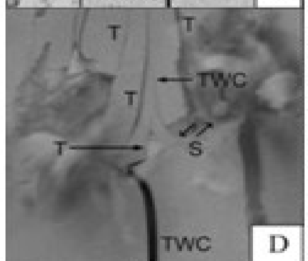
</td><td>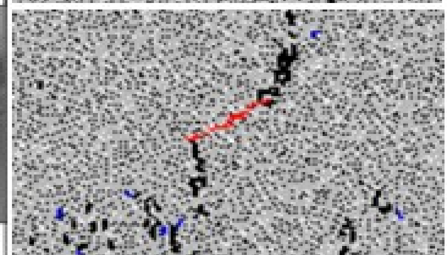</td></tr>
<tr><td>45</td><td>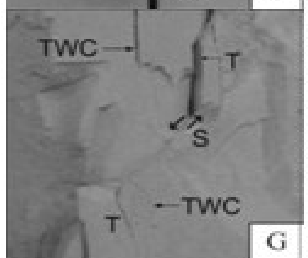
</td><td>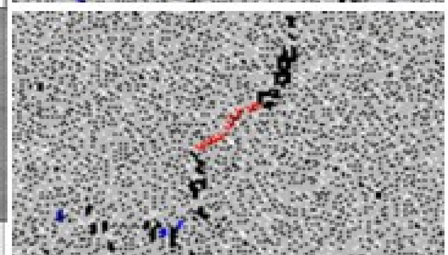</td></tr>
<tr><td>60</td><td>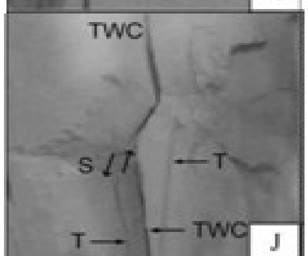
</td><td>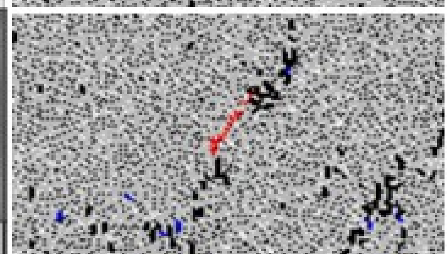</td></tr>
<tr><td>75</td><td>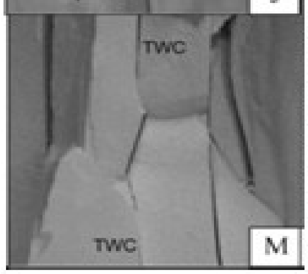
</td><td>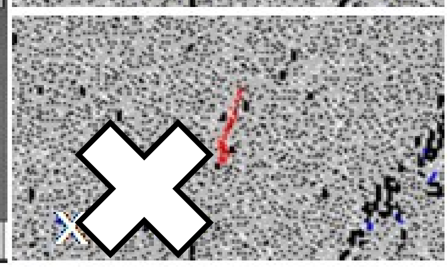</td></tr>
</table>

Figure 104. Results from SJ simulations on a single internal flaw compared with similar simulations conducted on laboratory specimens ('X' indicates no match). The red lines indicate the SJ model with tensile bond failure shown in black and shear failure shown in blue. (The letters in the laboratory photos are used by the authors of the laboratory study and not relevant here).

The laboratory experiments reported a series of measurements regarding the crack initiation distance from flaw tip and the angle of inclination of the crack relative to the flaw. Using only eight particles across the diameter of a flaw, crack initiation could only occur at four possible locations on either side of the joint, where d is measured from the flaw tip and $d \leq c$ (Figure 105). The angle of inclination of the crack is possible to measure, however it is a function of the BPM and not the crack initiation itself, and therefore not a good SJ performance indicator unless the resolution of the model is increased.

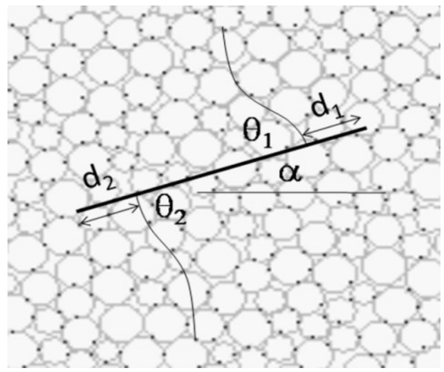

Figure 105. The measurement geometry for crack initiation from an internal flaw overlain on a BPM image. The crack initial distance (d_1 and d_2) are measured from the flaw tip.

Figure 106 shows the results for laboratory and PFC simulations for average crack initiation distance from flaw tip normalized to c. For flaw inclination angles between 30 and 45 degrees, the numerical results were consistently lower, although possible results were limited due to geometrical restraints of the BPM noted above.

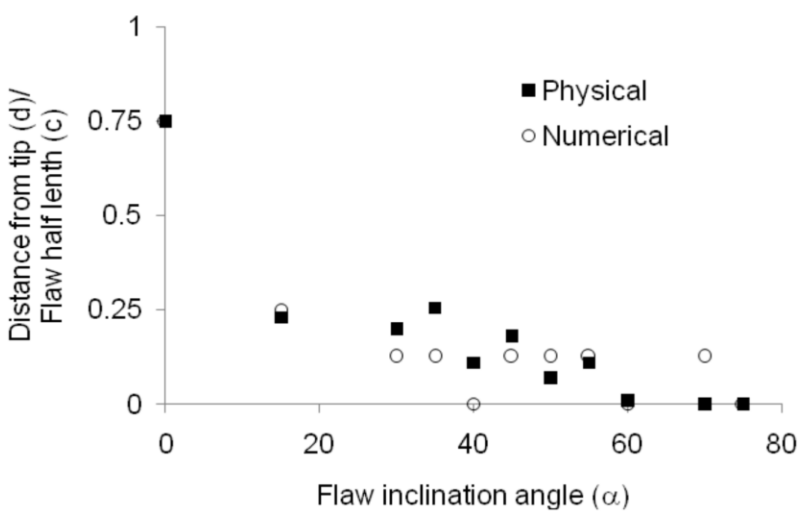

Figure 106. Measured crack initiation distances normalized to the flaw half-length with the PFC results separated into shear or tensile bond failure at crack initiation.

Two and Three Flaw Results

Figure 107 shows the qualitative comparison between the observed laboratory behaviours of specimens containing two internal flaws with μ = 0.6 and μ = 0.7. The results from simulations 2-4 and 2-9 with μ = 0.6 as well as 2-3 and 2-8 with μ = 0.6 and μ = 0.7 did not match the observed laboratory coalescence behaviours and they are not presented in the figure. The remainder of the simulations reasonably matched the observed behaviours.

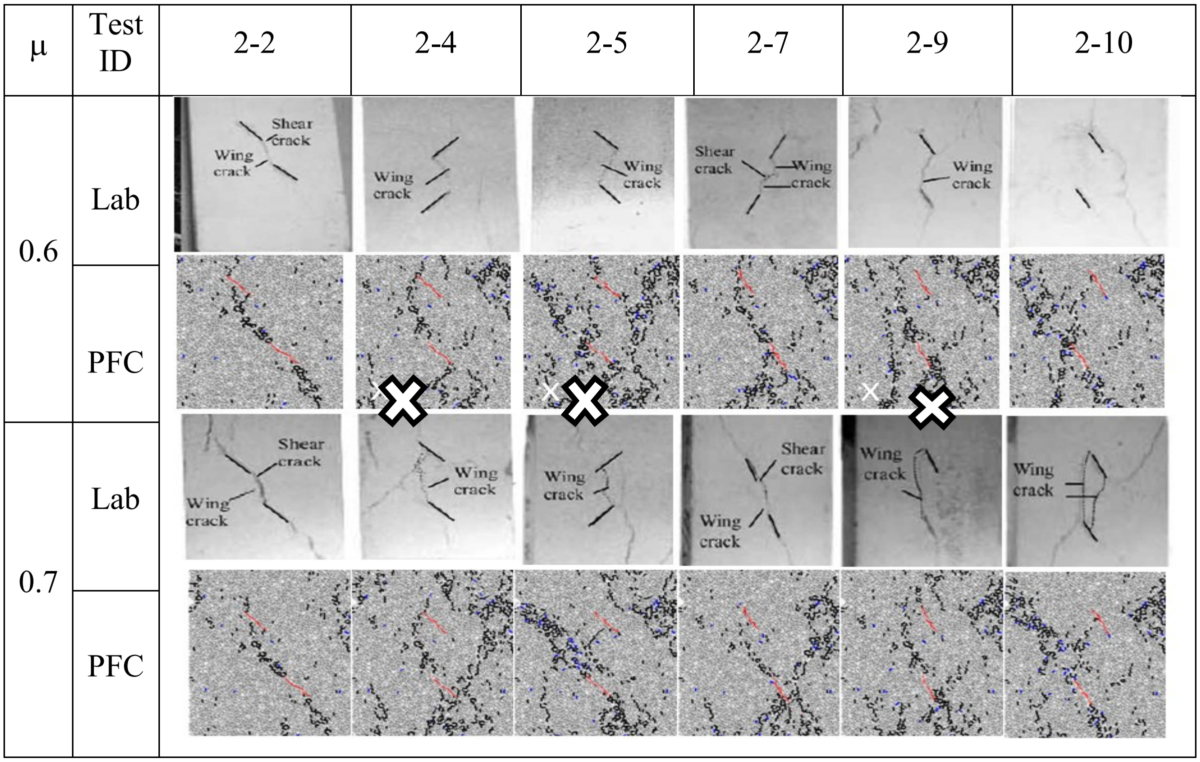

Figure 107. Laboratory and associated numerical simulation results on samples containing two internal flaws with friction coefficients of 0.6 and 0.7. Specimens with an ‘X’ did not match the observed laboratory results (SJ in Red and bond failure in black for tensile and blue for shear).

Figure 108 shows the qualitative results for laboratory and simulated three flaw specimens. Results for 3-3 and 3-4 with μ = 0.7, 3-7 with μ = 0.6 did not match the observed behaviour. The remainder of the simulations not shown did match the laboratory experiments. For specimen 3-3 it appears the wing crack from the bottom flaw will coalesce with the upper flaw however it does not coalesce, even as the sample is taken well into post peak strain.

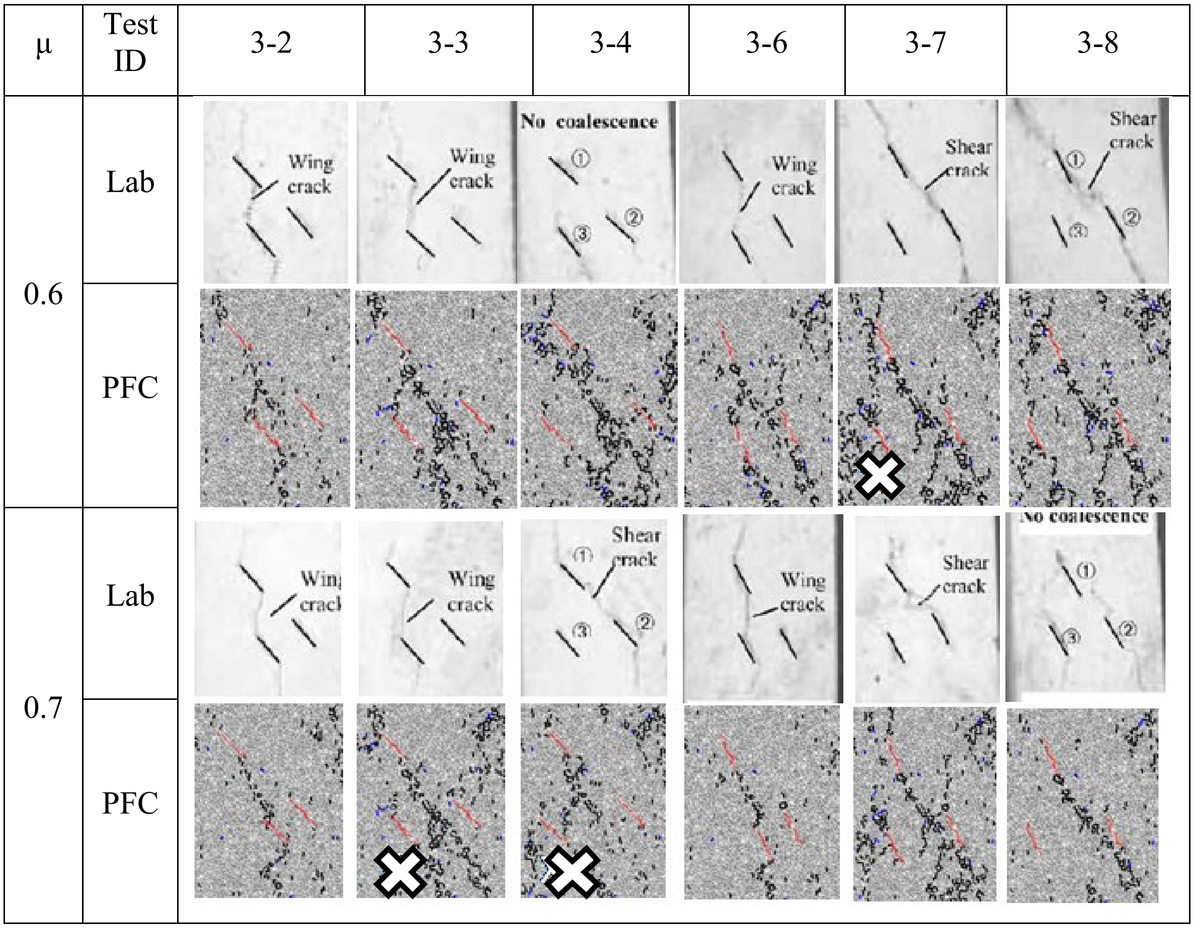

Figure 108. Laboratory and associated numerical simulation results on samples containing three internal flaws with friction coefficients of 0.6 and 0.7. Specimens with an 'X' did not match the observed laboratory results (SJ in Red and bond failure in black for tensile and blue for shear).

The strength results were also recorded for each of the simulations and compared against the reported laboratory values (Table 20). In each case the strength results from the PFC SJ simulations were significantly higher than the corresponding laboratory values. For the friction coefficients of 0.6 and 0.7, the strength was an average of 27% and 24% higher than observed in the laboratory.

Table 20. *UCS* results from laboratory and numerical simulations on specimens containing two and three internal flaws.

Test ID	Unconfined Compressive Strength (MPa)			
	μ=0.6		μ=0.7	
	Lab	PFC	Lab	PFC
2-1	1.67	2.00	1.88	2.07
2-2	1.59	1.91	1.80	1.99
2-3	1.59	1.81	1.57	1.87
2-4	1.88	2.06	1.84	2.07
2-5	1.64	1.99	1.73	2.04
2-6	1.42	1.96	1.44	1.96
2-7	1.45	2.01	1.49	2.00
2-8	1.49	1.97	1.48	1.97
2-9	1.51	2.05	1.52	2.06
2-10	1.46	2.00	1.48	2.00
3-1	1.59	1.90	1.73	2.03
3-2	1.57	1.97	1.73	2.04
3-3	1.60	1.93	1.61	2.03
3-4	1.69	1.97	1.70	2.03
3-5	1.43	2.01	1.58	1.93
3-6	1.42	1.93	1.52	2.07
3-7	1.51	2.01	1.62	2.00
3-8	1.51	2.00	1.58	2.02

Strain Rate Results

Simulations on specimens 1-11, 2-4, 3-7 with $\mu = 0.6$, and 2-3, 3-3 $\mu = 0.7$ (which did not match the observed lab results) were re-run using a range of strain rates as depicted in Figure 103 to investigate if flaw coalescence would be altered or produce a better match to laboratory observations. The intact BPM was not recalibrated to the macroproperties of the laboratory specimen in both the strong and weak cases. Nine different strain rates were used in the range of 0.025 to 5%/s.

Figure 109 shows the results from selected one, two and three flaw specimens. In each of the simulations, the strain rate influenced the number of failed bonds and the mode of bond failure (shear or tensile). As the strain rate was reduced, the number of total bonds and the number of bonds failed in shear were reduced. One, two and three flaw test results with the varied strain rates did not provide improvements in matching the observed laboratory behaviours. The crack initiation and distance of crack initiation from the flaw tip did not enhance the simulation results.

Test ID	Lab	PFC strain rate (%/s)					
		1.0	0.75	0.5	0.1	0.05	0.25
2-4 (μ=0.6)		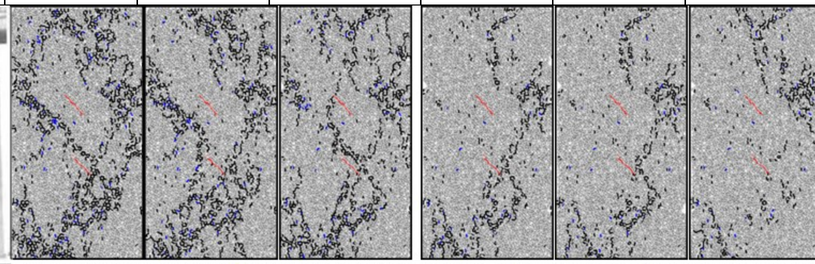					
3-3 (μ =0.7)		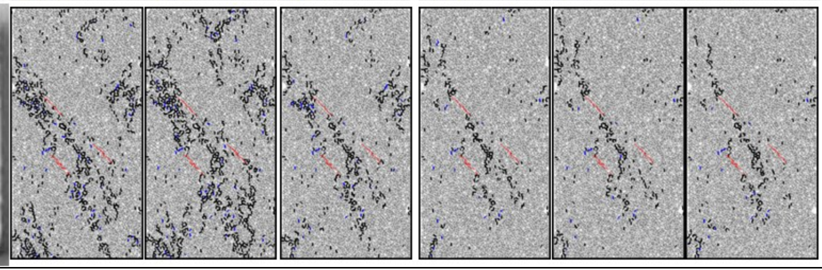					

Figure 109. Results from BPM specimens containing two and three internal flaws and failed using varying strain rates

8.2.3 Discussion

The numerical simulations on the behaviour of the SJ model versus observed laboratory behaviours produced, in general, acceptable visual pattern results, but not strength. The qualitative comparisons of crack initiation, propagation and coalescence versus those observed laboratory provided a 70% match . The strength results from the two and three flaw simulations continuously overestimated the measured laboratory results. The strain rate was shown to have an impact on failure of the samples, but only slightly altered the behaviour of the sample with regards to the SJ model.

Crack Initiation, Propagation, and Coalescence

For the one flaw, two flaw and three flaw numerical specimens, crack initiation, propagation and coalescence was simulated reasonably well. The single flaw laboratory results were able to match 80% of the observed fracture patterns. The two and three flaw results were able to match 65% and 81% of the observed fracture patterns, respectively.

The crack initiation distances measured from the flaw tip for the single flaw specimens also produced acceptable results. As the average measured normalized crack initiation distance was below 0.25, and in many of the cases, the results may have been constrained by the resolution of the simulated flaw. Therefore, if the crack initiated from the flaw at either the flaw tip, or one particle away from the flaw tip, the results can be considered successful. In all but two cases, the observed laboratory results did not match the crack initiation and failure.

The simulated two and three flaw specimens matched the observed laboratory flaw behaviour well. In the specimens 2-4, 2-5, 3-4, 3-7, the simulated behaviour did not match the laboratory behaviour, however the internal flaws did coalesce and influence the failure behaviour of the specimen. The cases which did not match adequately may be improved by altering the particle arrangements. Each simulation used the same initial sample to insert the SJ model.

Strength

The strength results of the two and three flaw simulations are consistently higher than those reported from the laboratory simulations. The crack initiation and propagation is a tensile failure process and the BPM is known to not properly reproduce *UCS* to tensile strength ratios when using circular (2D) or spherical (3D) particle shapes. The BPM was calibrated without tensile strength consideration. Then after calibration, the tensile strength was measured, resulting in a value 1.30 times greater than the laboratory specimens. The average strength of the simulated specimens was found to be 24 to 27% greater than the laboratory specimens. Insertion of two or three flaws did not change the strength, as is was the same as the intact specimen.

Crack initiation from a pre-existing internal flaw is predominantly tensile failure (Wong et al., 2001), and PFC does not simulate tensile to *UCS* strength ratios well. Recent work has demonstrated that changing the shapes of the particles to use “clumps” (Cho, 2008) better represents the tensile to *UCS* strength ratios observed in the laboratory. Clump material types are currently not capable of supporting the SJ model. Therefore, incorporating the SJ model into a clumped material with an improved tensile to *UCS* strength ratio, or if an improvement on the tensile-*UCS* strength ratio for the spherical BPM can be made, better results for the strength and perhaps the flaw behaviour may be observed.

Influence of Strain Rate

The strain rate of the numerical *UCS* test was shown to have an influence on the behaviour of the BPM with and without the SJ model. The reduction in strain rate on the BPM caused a decrease in the observed strength. This behaviour can be explained as an artefact of the dynamic nature of the PFC calculation method.

8.2.4 2D SRM Smooth Joint Conclusions

The SJ model has been shown to reasonably reproduce (within 74%) observed laboratory internal flaw behaviours of crack initiation, propagation and coalescence behaviours. This provides an increase in confidence that the SJ is behaving acceptably inside of the SRM. There is concern that the strength values reproduced in the experiments do not match laboratory behaviours, and that calibrating the BPM only to the *UCS*, *E* and ν may not be sufficient to capture observed material behaviours. Simulations using the SJ model within a BPM made up of non-spherical clumped shapes may improve the overall behaviour. With the fracturing in the 2D SRM behaving acceptably well, the modelling of coal was extended to 3D for coalseam geomechanical modeling.

8.3 3D Synthetic Rock Mass Modelling for Coalseam Geomechanical Characterization

Two separate example applications were selected to demonstrate techniques of geomechanical characterization of coal using the SRM. Literature results on strength data and deformation properties were used to calibrate the intact coal matrix, and a DFN created from the authors experience was used to create the coal SRM. The SRM was then subsampled and tested in three orthogonal directions.

8.3.1 Geomechanical Characterization

In the first case, laboratory results from three core specimens were used in the simulation of a coal seam with four distinct zones. The second case, the results of a single core specimen is used in a seam with one zone. In both cases a single DFN was generated to simulate the joint distributions (bedding plane, face and butt cleats).

Geomechanical Properties

Gentzis et al. (2007) obtained core samples from multiple coal seams and performed mechanical tests under various loading conditions to determine static and dynamic coal properties. Deisman and Chalaturnyk (2008) presented a methodology to obtain intact (no joints) mechanical properties from jointed specimens and applied it to this data set. Table 21 lists σ_{ci} and E_i results from the Greenhills (GH) Mine Seam 3, Seam 7 and Seam 10 which were selected for this study, along with calibrated BPM results.

Table 21. Mechanical properties of physical (P) and numerical (N) coal samples from Gentzis et al. (2007) and Deisman and Chalaturnyk (2008).

Coal	Type (P/N)	σ_{ci} (MPa)	E_i (MPa)	Poisson's ratio ()
Type 1	P	17.0	3440	0.48
	N	16.1	3296	0.33
Type 2	P	45.5	3400	0.26
	N	45.6	3380	0.26
Type 3	P	42.3	4920	0.35
	N	42.4	4940	0.29

Due to difficulties in obtaining larger core samples from conventional coring operations, it is assumed that only smaller core plug samples can be obtained with a diameter of 38.1 mm and heights of 76.2 mm. The intact values for *UCS* and modulus were used and intact BPM specimens were created with these dimensions. However, if specimens containing joints were tested, then specimens which contain joints can be simulated to calibrate the BPM. In this case, the intact core specimens were calibrated using a minimum particle size of 3.75 mm, a maximum to minimum particle ratio of 1.5. This results in specimen resolution of 4.0. The stiffness ratios for the bond and particle modulus were set equal, as well as the particle and bond normal and shear modulus. The particle bond mean normal and shear strength were set equal with a standard deviation of 20% of the mean. The particle friction coefficient was set to 0.5. The remaining BPM microproperties for each coal zone are listed in Table 22, and the resulting BPM macro properties are as listed in Table 21.

Table 22. PFC microproperties to create numerical coal samples. Bond normal and shear modulus and strength were equal. Particle and bond stiffness were equal.

Coal	Stiffness ratio (kn/ks)	Modulus (MPa)	Strength (MPa)
Type 1	5.0	5250	20.0
Type 2	2.1	3470	43.5
Type 3	3.5	6230	41.0

The joint properties used to simulate the DFN were produced from the authors experience in coal core and block sample examination. The joint spacings (*s*), dip (*D*) and dip direction (*DD*) of the bedding planes, face cleats and butt cleats are given in Table 23. The bedding plane, face cleats, and butt cleats are normal to y, x, and z direction, respectively, in the SRM. The DFN was simulated using a uniform distribution in a cube of 2 m side length giving a volume of 8 m^3, and producing 3.0×10^6 circular joints. The mean spacing of the joints was defined with an accuracy of approximately 10%.

Table 23. *s*, *D* and *DD* and standard deviation for both used in the DFN simulation.

Joint Name	s	D	DD	Std. Dev.
	(mm)	(°)	(°)	(°)
Bedding	50	0.0	0.0	5.0
Face	40	90.0	0.0	5.0
Butt	80	90.0	90.0	0

The required mechanical properties of the joints are normal and shear stiffness, friction and dilation angles. The joint shear and normal stiffness for the bedding planes, face and butt cleat were 40.0 GPa/m, joint friction was 25° and dilation angle was 5° (Gu and Chalaturnyk 2006).

In this example, a fictitious reservoir at a depth of 500 m with a hydrostatic reservoir pressure is simulated. Using a vertical total stress gradient of 0.022 MPa/m, this yields an initial reservoir vertical effective stress of 6.0 MPa. For simplicity, it is assumed that horizontal stresses are equal to the vertical stress and that the stress directions are perpendicular to the joint sets (bedding planes, face and butt cleats).

Case 1 – Multiple core samples

A theoretical coalseam is developed for simulation with four distinct zones containing three coal types with different mechanical properties and a total thickness of 1.0 m (Figure 110). It is assumed for simplicity that the same DFN is applicable for each of the zones and only the intact matrix properties of the coal seam vary.

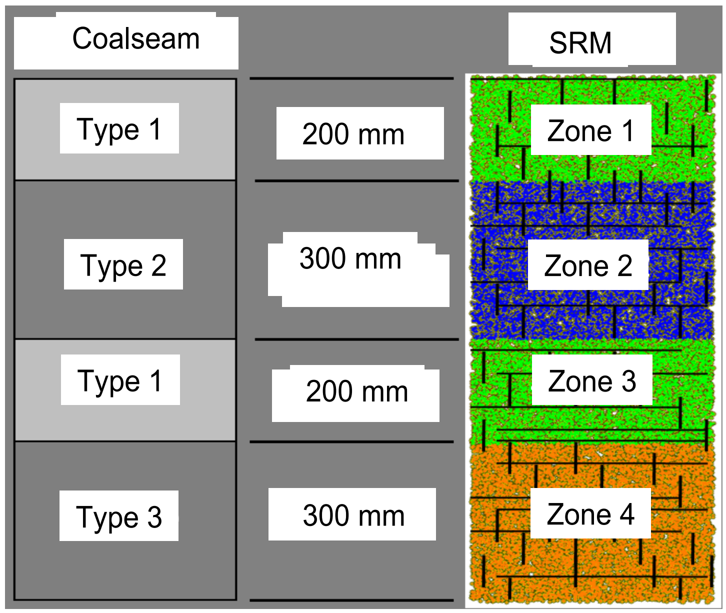

Figure 110. Theoretical coalseam with three coal types with different mechanical properties in four distinct zones.

The results from laboratory testing on each of the core samples are matched with the BPM (Table 21) and are used to reconstruct the full coalseam honouring the geometry of each of the zones. The calibrated material properties from each of the simulated cores (Table 22) are assigned to the particles contained in their respective zones. Because all of the particles are generated before the properties are assigned, there are no issues with artificial weak planes created by 'stacking' zones. The DFN is then inserted and joint mechanical properties assigned. The DFN is 'filtered' before insertion to remove joints which did not lie inside of the simulated area, greatly increasing SRM construction efficiency.

The sub specimens are sampled from the full coalseam SRM, and then the full SRM and sub specimens are tested. Borehole scale (height = 140 mm) and zone scale (height = 200, 300 mm) sub specimens were randomly vertically sampled from full SRM (Table 24).

All of the specimens were cylinders having a 2.5:1 height to width ratio. A number of large full coalseam specimens could also be sampled and tested, however for this example, only a single full coalseam SRM was tested.

Table 24. Number and dimensions of coalseam SRM sub samples specimens selected for testing. All specimens were cylinders having a height to width ratio of 2.5:1.

Height (mm)	Zone 1	Zone 2	Zone 3	Zone 4
300	0	2	0	2
200	2	0	2	0
140	4	4	4	4

Direct tension, *UCS*, and triaxial tests at multiple confining stresses were selected for simulation. The triaxial testing confining stresses were selected around the initial effective stress conditions of 6.0 MPa and were: 1.0, 2.5, 5.0, 7.5 and 10.0 MPa.

Case 2 – single sample

In the second case, the coalseam contains one distinct zone containing one coal of Type 1 with a total thickness of 1.0 m (Figure 110). This case could also represent an example where only one coal sample was obtained and tested. The DFN and joint properties used in case 1 are used here.

In this case, where only one coal material is used, the BPM is created using a periodic space approach (Itasca, 2007). First a periodic brick ('p-brick') is generated with certain dimensions, replicated, and then assembled to the final required dimensions. This greatly increases the BPM creation efficiency. The DFN is then filtered and inserted into the BPM, joint set properties assigned, thus creating the final full coalseam SRM.

The full SRM was sub sampled to created specimens in the x, y, and z direction (Figure 111) at three different scales (140, 500, and 1000 mm) to investigate the scale effects and geomechanical anisotropy of the coalseam (Figure 111). In this case the specimens selected were parallelepiped which allows for applying polyaxial (or true triaxial) stress conditions. Triaxial tests were run with confining stresses of 0.0, 1.0, 2.5, and 5.0 MPa respectively.

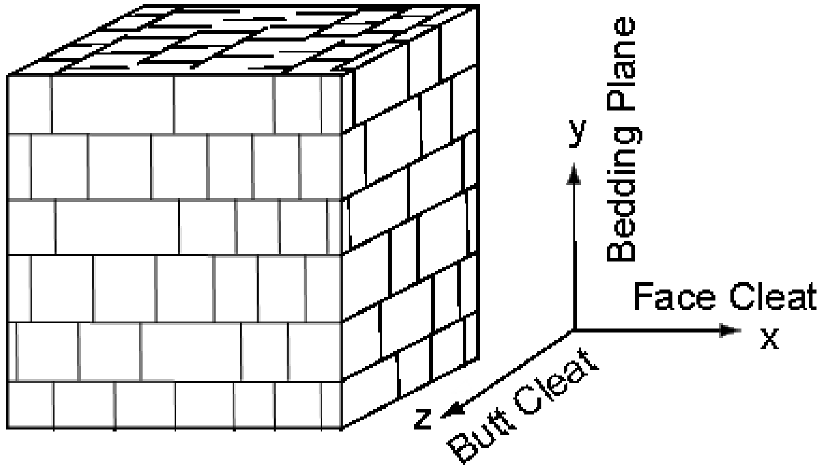

Figure 111. Theoretical coalseam with one zone showing the orientations the fractures for Case 2.

Table 25. Number and dimensions of coalseam SRM sub sampled specimens (height to width ratio of 2.5:1).

Height (mm)	x	y	z
1000	1	1	1
500	5	5	5
140	5	5	5

Results

The tests from both Case1 and Case2 demonstrate the ability of the SRM technique to capture the effects of sample scale, modulus anisotropy, and changes in strength and modulus due to changes in confining stress. Nonlinear strength behaviour as well as decreases in strength with increases in specimen size were also captured in Case 1 and Case 2.

Case 1 - Multiple Core Results

The numerical simulations were conducted on a 64-bit dual 3.4 GHz processor computer with 4 MB RAM to handle the model sizes. The simulations were set to run back to back with no break and were completed in approximately 25 days.

The results from tests on 140 mm, 200 mm, and 300 mm tests for Zone 1, 2, 3 and 4 are shown in Figure 112. As the specimen size increased, the E_{RM} decreased at each corresponding confining stress, and values were below the intact E_i at each simulation stress and simulation size. Similar results are shown for Zone 3, which used the same intact material properties, however E_{RM} did not change as the specimen sized increased. A decrease in E_{RM} with increase in size and an E_{RM} decrease below E_i also emerge from the SRM simulations.

All of the cases for the specimens tested from Zone 1 through Zone 4 show non-linear strength behaviour (Figure 112). In each test, the *UCS* of the samples is below the intact *UCS* (σ_{ci}). Zone 1 and Zone 3 had σ_{ci} equal to 17.0 MPa, while Zone 2 and Zone 4 had σ_{ci} of 45.5 MPa and 42.3 MPa, respectively. As the size of the specimen increases the strength of the specimen decreases in all the cases, except for Zone 4 where the strength of the 140 mm and 300 mm specimens are similar.

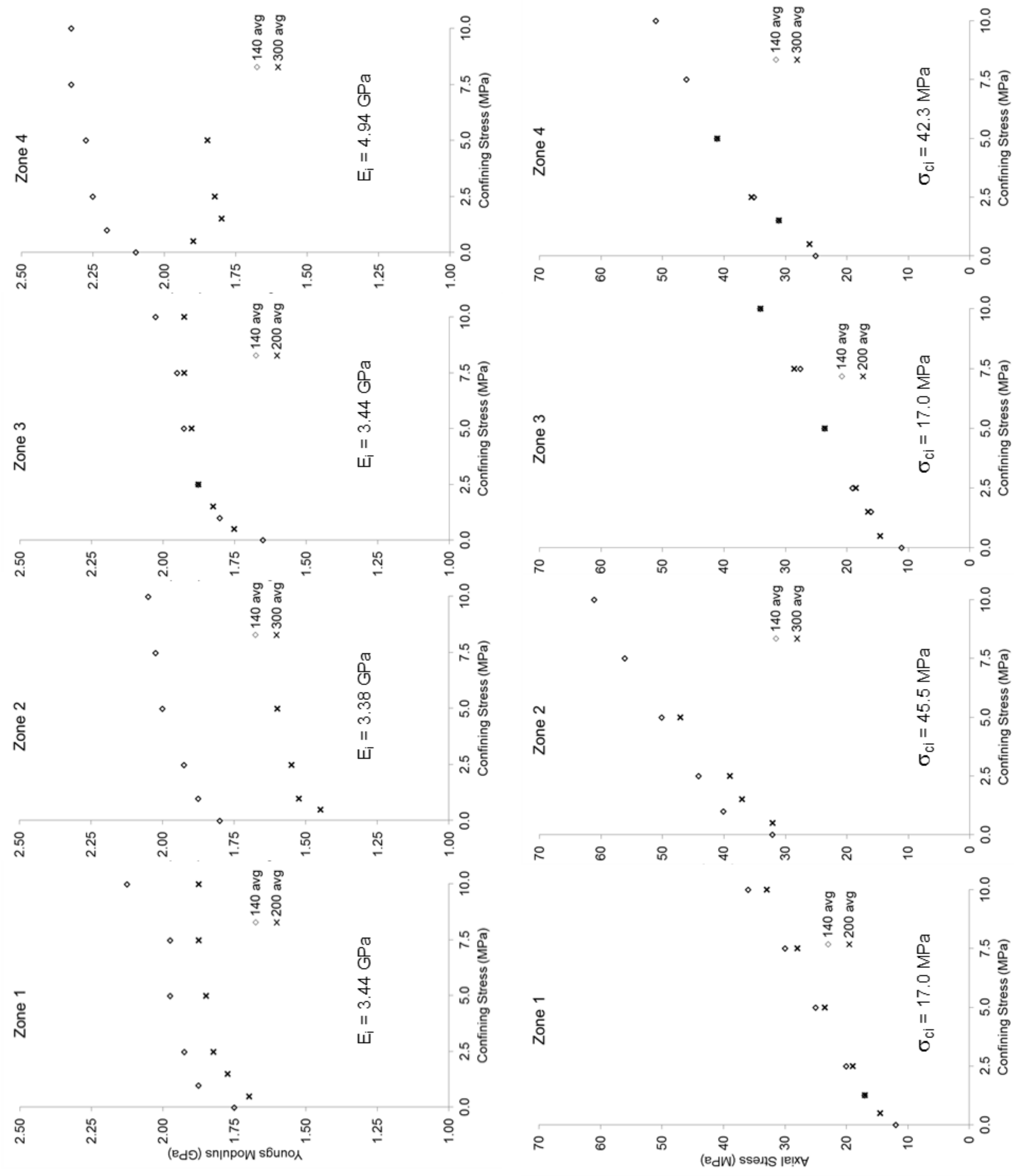

Figure 112. Young's modulus and axial strength for 140, 200 and 300 mm specimens tested in at multiple effective confining stresses.

Case 2 - Single Sample Results

The SRM simulations for the case of a single core sample are summarized in Figure 113. In each case, only the averages for each specimen size and direction are reported. The numerical simulations were conducted on a 32-bit Quad Core 2.4 GHz processor computer with 4 MB RAM, and a 32-bit Dual Core 2.6 GHz processor computer with 3 MB RAM. The simulations were run back to back with no downtime and were completed in 15 days. In general, the specimens simulated in the X, Y, and Z direction showed anisotropy in both strength and deformation. The simulations also captured the effects of increasing E_{RM} and strength with increasing confining stress, as well as decreasing E_{RM} and strength with increasing specimen size.

All of the results for deformation on specimens tested in the x, y, and z directions, the E_{RM} was below the E_i of 3440 MPa. The results for each direction show that as the confining stress increases, E_{RM} also increases, and that that E_{RM} decreases with increasing specimen size. Each of these simulated behaviours is similar to the presented from observed laboratory testing. The results from the 140 mm specimens and 500 mm specimens show that the E_{RM} decreased from the x, to z, and then to the y direction. For the 1000 mm specimens, the trend is similar, however the E_{RM} values begin to converge at 2.5 MPa of confining stress. These results are also similar to the results observed by Szwilski (1984).

The combined scale and directional results indicate that the SRM approach is able to reproduce anisotropic and scale dependent deformation behaviours exhibited by coal. The effects are captured due to the SRM's ability to represent coals unique joint fabric (three orthogonal joint sets, with butt cleats terminating generally on face cleats).

The average strength of the 140 mm, 500 mm, and 1000 mm specimens tested in the x, y, and z directions are summarized in Figure 113. In general, the strength of each specimen increased nonlinearly with increasing confining stress. The results, in general, also show that as the size of the specimen tested increases, the strength decreases. The exception to this is the specimens tested in the z direction, where the 140 mm and 500 mm specimens were reversed.

The strength of the specimens also changes with the direction of testing. Of the 140 mm samples, the strength decreased from y, to x, to the z directions. This trend changed for the 500 mm and 1000 mm specimens, where the strength decreased in the order of the z, y and x directions. The results show the SRM approach can simulate the scale effects on strength, as well as strength anisotropy, each caused by the intact matrix and joint fabric interaction.

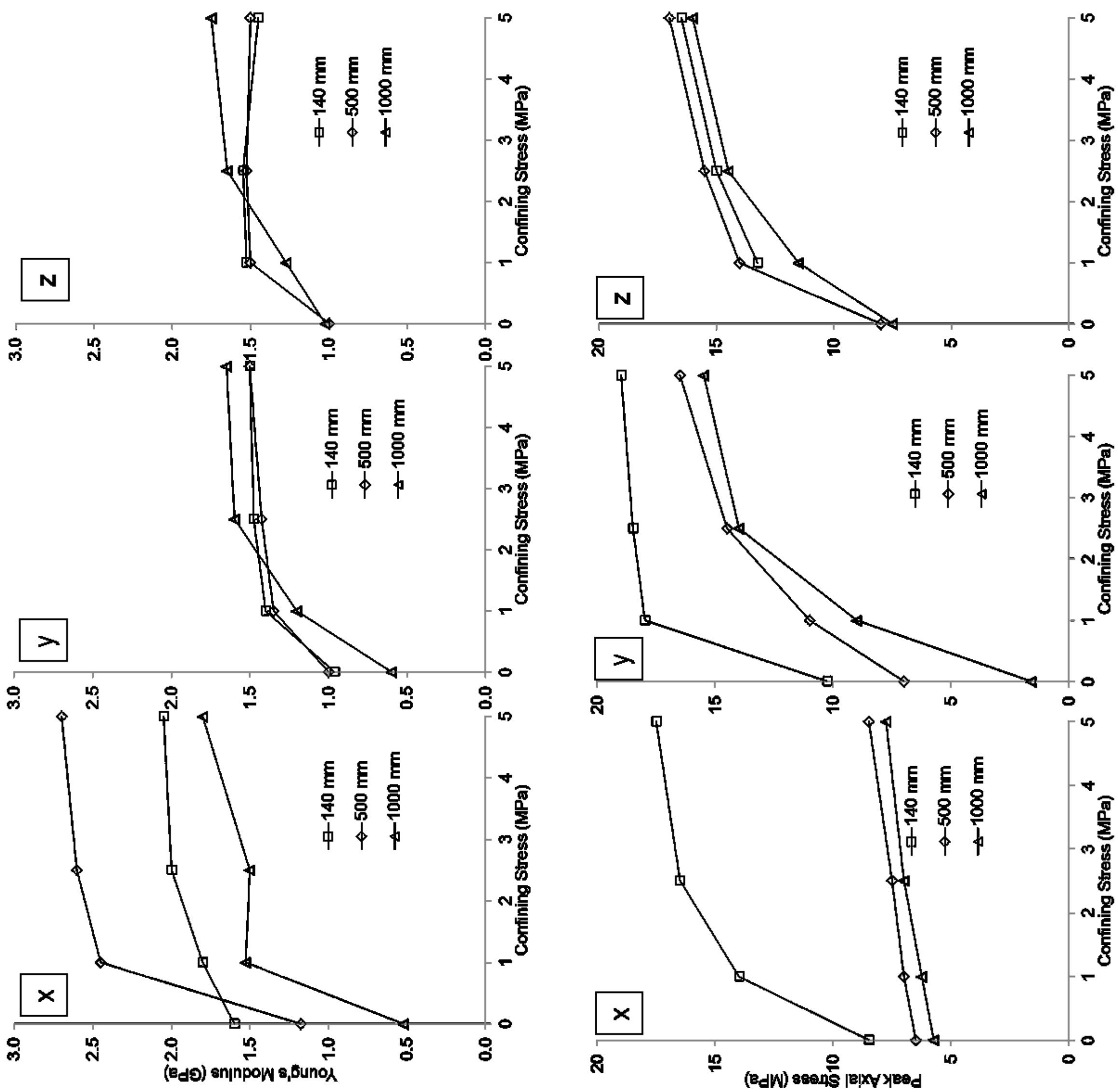

Figure 113. Young's modulus and peak axial strength versus confining stress for 140, 500 and 1000 mm specimens in the x, y and z directions.

8.3.2 Discussion

The SRM approach shows the ability to capture the scale effects and anisotropy created by the cleat and bedding planes. In Case 1, three material types were used to construct a coal seam. The SRM numerical tests simulated the nonlinear strength increase with increases in confining stress, as well as the effects of increasing the specimen sizes on strength. In Case 2, the ability of the SRM approach to capture the strength and deformation anisotropy was also shown. These geomechanical behaviours are well known for fractured rock masses. Values obtained from these SRM tests can be used to geomechanically characterize a coal seam for exploration and production applications.

Deformation

The Young's modulus of coal has been shown experimentally to decrease with increase in specimen size, increase with increasing confining stress, and be anisotropic. This scale effect is attributed to influences of the number of joints inside of the rock mass. With a constant joint density, if the size of the specimen is increased, the Young's modulus will decrease. The increase in Young's modulus due to increases in confining stress can be attributed to closure of joints and/or micro cracks, which in turn, causes the stiffness of the material to increase. The anisotropy of the Young's modulus is a function of the joint spacing and orientation. If the joint properties are equal, then the number of joints and their direction control the effects on deformation, where less joints in a direction will cause the rock mass to be stiffer in that direction. The SRM simulations were able to capture this behaviour well.

The scale effects on the E_{RM} are captured well by the SRM in each of the simulations from Case 1 and Case 2. The influence of the bedding planes and cleats reduce the E_i to an E_{RM}, for all of the simulations. The effects of increasing the confining stress were also captured well by the SRM. In each of the simulations the increase in confining stress created an increase in E_{RM} until the values reached a plateau. The anisotropy in the Young's modulus was also well represented by the SRM. The largest values of the Young's modulus shown in Figure 113 occurred in the x direction, which is the direction normal to the butt cleats. The modulus then reduced in order of decreasing joint spacing, from the bedding planes (y direction) to the face cleats (z direction). It is also noted that as the specimen size increased to 1000 mm, the E_{RM} values began to converge.

Strength

The strength of coal and of jointed rock masses is nonlinear and dependent on the confining stress. The strength is also dependent on the scale at which the material is tested and the scale of the application. As the scale of the specimen increases, the strength decreases. The strength of a rock mass can also be anisotropic.

Case 1 demonstrated the ability of the SRM to capture both the nonlinearity of the coal strength, and the influences of increasing scale. In each case, the *UCS* of the specimens from each of the zones was below that of the initial intact values. The strength also decreased with increasing specimen size.

Case 2 demonstrated the ability of the SRM to capture the scale effects shown in Case 1, but also the strength anisotropy created by the bedding planes and cleating. The strength increased in the direction normal to the butt cleat, bedding plane, and face cleat respectively in the 500 mm and 1000 mm specimens. This result may be due to the number and orientation of the bedding planes and cleats affecting the strength of the coal in those directions. The strength in the direction normal to the butt cleat (which is the least numerous and has the least influence on strength as they are parallel to the loading stress) would be the lowest. Therefore, the bedding planes and face cleats, which are perpendicular to the loading stress and more numerous, have a greater influence on the strength. The same theory can be applied to the remaining directions to explain the observed strength anisotropy.

An unexpected result was the altering of the strength anisotropy as the scale increased from 140 mm to 500 mm. In the 140 mm specimens, the strength increased in the order of Z, X, Y. In the 500 mm specimens, the order of the strength changed, increasing in the directions X, Y, Z. This result requires further investigation.

8.4 Conclusions

The Synthetic Rock Mass approach for geomechanical characterization of coalseam reservoirs has been demonstrated in this chapter. The first part of this chapter was to test the Smooth Joint model in two dimensions against observed laboratory tests on internal joints placed in simulated rock material. The second section of this chapter used the SRM approach in 3D to characterize a two fictional coalseams built from real laboratory data.

The SJ model has been shown to reasonably reproduce observed laboratory internal flaw behaviours including crack initiation, propagation and coalescence. This provides an increase in confidence that the SJ is behaving acceptably inside of the SRM. There is concern that the strength values reproduced in the experiments do not match laboratory behaviours, and that calibrating the BPM only to the *UCS*, *E* and ν may not be sufficient to capture observed material behaviours. Simulations using the SJ model within a BPM made up of non-spherical clumped shapes may also improve the overall behaviour and the SJ model should be adapted to work with these materials.

The SRM in three dimensions has been shown to be capable of estimating the strength and deformation of a simulated coal seam. Two cases have been demonstrated, incorporating different levels of input data and simulation procedures. Scale effects, anisotropy, and confining stress influences are captured well for the coal seam. The output from the SRM is intended to complement existing empirical techniques and to add information were data is lacking. The SRM output can be used to scale the strength and deformation properties of the coal seam to the desired size for the intended application, including bore stability analysis or reservoir geomechanics simulations. However, the SRM should be used only to supplement existing data and should be used with caution and not for design purpose.

Improvements to the SRM include better representation of the coal fracture network. Currently, the coal fracture network is represented as disks and not rectangular planes, as observed in the field. Additional work is in progress to assess the ability of the SRM to match laboratory test results for strength and deformation.

9 Data Analysis and Modeling

This chapter details the modelling of the hydrogeomechanical laboratory results from the previous chapter. The mechanical results, (strength and deformation) are modelled using the relationships derived in Chapter 3. The results for changes in permeability with stress (dynamic permeability) are modelled with a dynamic permeability model developed in this chapter. Figure 114 illustrates where the modelling of both laboratory testing and numerical testing fit into the overall program for hydrogeomechanical characterization of a coalseam reservoir.

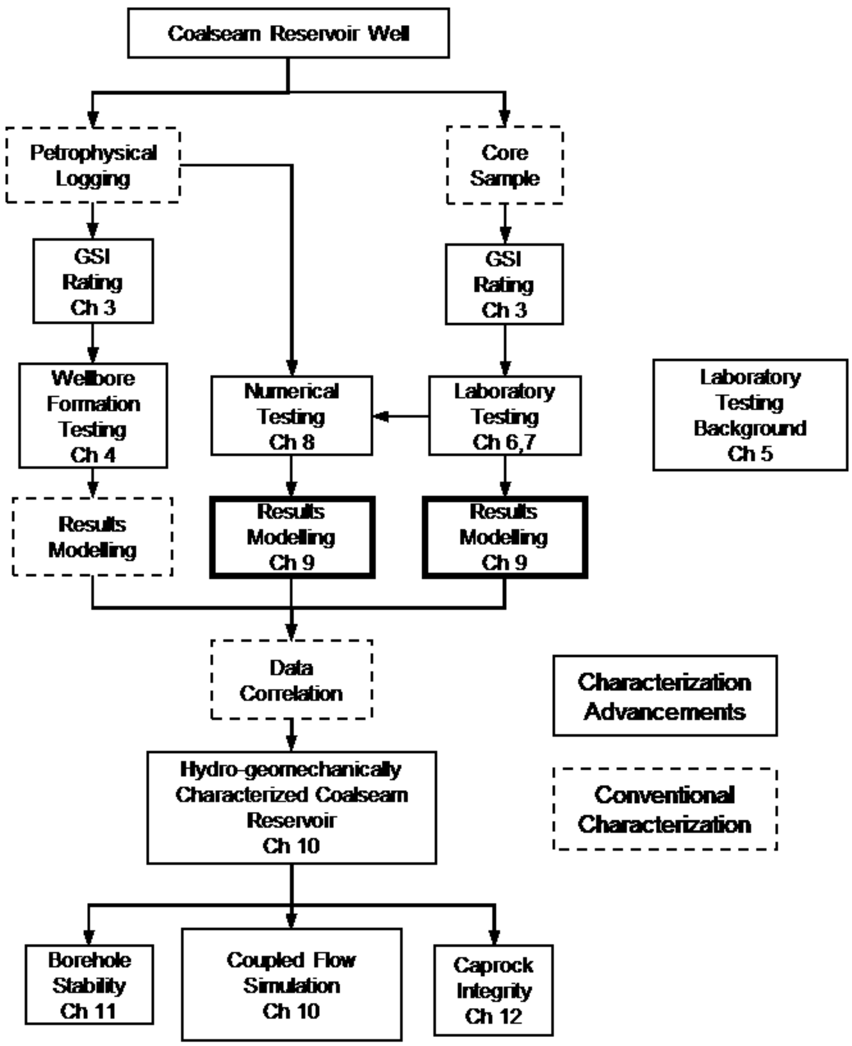

Figure 114. Coalseam reservoir hydro-geomechanical workflow showing where the laboratory testing fits into the overall characterization approach.

This chapter is divided into two main sections: Mechanical Modelling and Flow Modeling. In each section, a brief review of the models are presented, followed by model fitting, and then a discussion and specific conclusions on its applicability of the model to the data. The mechanical data modelling section investigates the strength and deformation (both from stress and sorption of methane) results from the coal laboratory and numerical testing programs. The flow modelling section examines the changes in permeability with stress and methane sorption results from the laboratory program. The dynamic permeability derivation is lengthy, therefore the complete derivation, parametric analysis, and applicability to previously published data are provided in Appendix B.

9.1 Hydro-Geomechanical Data Analysis and Modeling

The Hoek-Brown (HB) with the Geological Strength Index (GSI) and Mohr-Coulomb (MC) failure criterion were best fit to the laboratory and numerical strength testing results. The GSI dependent Hoek and Diederichs Young's modulus reduction ratio with the stress dependent *h* parameter model was best fit to the laboratory and numerical Synthetic Rock Mass (SRM) testing results. The methane sorption isotherms were also modelled using the Langmuir equation and two functions were developed that relate the Langmuir pressure and Langmuir methane volume to the isotropic effective stress.

9.1.1 Strength

Strength results from triaxial testing can be modelled in principal and shear stress space using multiple types of failure criterion. Figure 115 shows how a linear failure envelope can be fit at two different slopes and intercepts of the principal stress circles and how a non-linear envelop is able to capture the tangents of all principal stress circles. The most common linear strength envelop is the MC criterion, where the as most common non-linear envelop is the HB criterion.

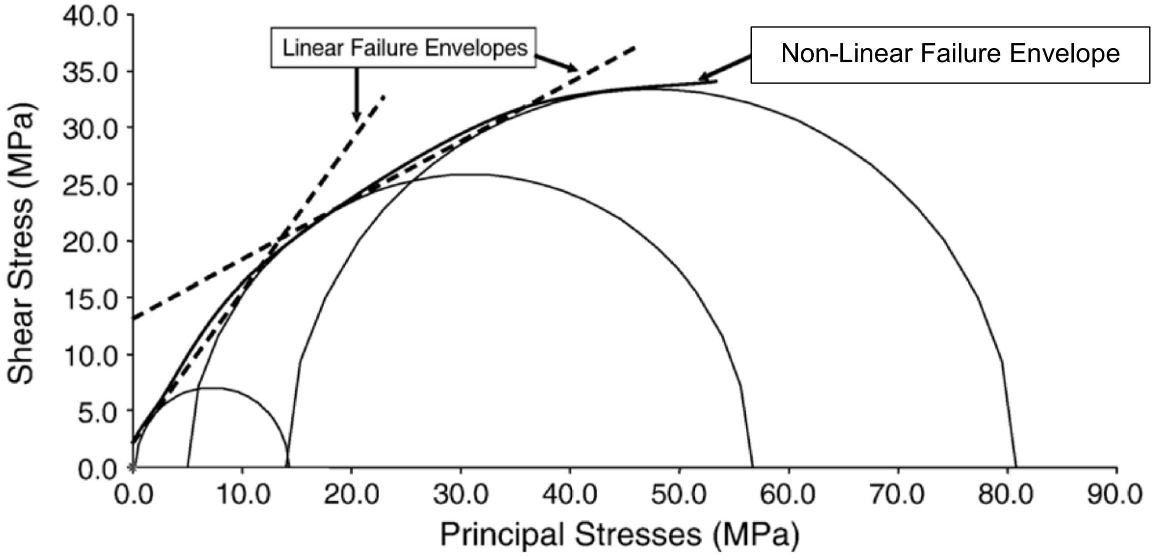

Figure 115. Three traixial test results from Greenhills Mine, Seam 10, plotted in Mohr space.

Most commonly, a Mohr–Coulomb (MC) failure envelope would be constructed based on results acquired from triaxial compression testing. A MC failure criterion is a linear locus drawn tangent to a series of Mohr's circles. The maximum effective stress (σ'_1) and the minimum effective stress (σ'_3) are plotted on the x-axis and shear stress (τ) is on the y-axis. A best fit line is constructed tangent to the circles to define a failure envelope, expressed as (36):

$$\tau = c' + (\sigma - u)\tan\phi \qquad 36$$

where: c' is the effective cohesion; ϕ is the angle of friction; σ_n is the normal stress on the failure plane; and u is the pore pressure at the time of failure. The MC envelop can be fit using the same Levenberg-Marquardt procedure used for HB best fit (Chapter 3).

The Hoek–Brown (HB) failure model was developed specifically to empirically capture the non-linear strength behaviour of rock and rock masses (Hoek et al., 2002). The HB failure model (37) and parameters (38, 39, 40) are determined from curve fitting maximum strength (σ'_1) results at various effective confining stresses (σ'_3) and can be adjusted for different fracture densities and fracture properties through *GSI* (Chapter 3).

$$\sigma_1' = \sigma_3' + \sigma_{ci}\left(\frac{m_{RM}\sigma_3'}{\sigma_{ci}} + s_{RM}\right)^{a_{RM}} \quad 37$$

$$m_{RM} = m_i \exp\left[(GSI - 100)/(28 - 14D)\right] \quad 38$$

$$s_{RM} = s_i \exp\left[(GSI - 100)/(9 - 3D)\right] \quad 39$$

$$a_{RM} = \frac{1}{2} + \frac{1}{6}\left[\exp(-\frac{GSI}{15}) - \exp(-\frac{20}{3})\right] \quad 40$$

Laboratory Strength Data

The strength results from "Conventional Triaxial Compression with Velocity and Permeability" (CT w/ V,P) and "Unconventional Triaxial Stress path with Permeability and Particle Size" (UT w/P,PS) were modeled. Each of the specimens had a *GSI* of 85 assigned. In the extensive work completed by Medhurst (1996) on Australian coal, $a_{RM} = 0.65$ provided the best fit, and not the calculated a_{RM} function prescribed in 4. In this modeling, a_{RM} between 0.3 and 0.7 was tested, and it was found that a value between 0.4 and 0.5 provided the best results. The *GSI* values were assigned based on experience of sampling coal blocks and pictures, documentation, or information on joint spacing for this program. Therefore, the data could have also been best fit with any reasonable *GSI* value. However, it is difficult to core and keep intact specimens with a core scale GSI less than, 80-85. The results from best fitting MC, HB $a_{RM} = 0.4$, and HB $a_{RM} = 0.5$ to the coal strength results are listed in Table 26.

Table 26. MC and HB parameters for coal specimens tested from the CT w/ V,P and the UT w/P,S testing programs. UT – C is compression and UT-E is extension envelopes.

Seam	MC Parameters			HB Parameters a_{RM} = 0.4				HB Parameters a_{RM} = 0.5			
	c MPa	ϕ	SSR	GSI	σ_{ci} MPa	m_i	SSR	GSI	σ_{ci} MPa	m_i	SSR
GH, S3	3.4	33.5	40	85	16.6	21.8	9	85	16.6	15.6	9.1
GH, S7	7.3	31.5	44	85	42.2	9.8	15	85	53.3	6.3	24
GH, S10	5.0	39.8	120	85	26.2	32.7	27	85	30.9	19.3	42
Elk, S8	5.4	35.6	65	85	25.0	31.3	7	85	30.4	17.4	14
Elk, S10	7.9	29.8	126	85	40.9	10.4	75	85	53.6	6.0	93
CR	8.0	30.8	161	85	39.8	12.4	97	85	53.6	6.7	120
UT – C	3.5	35.8	94	85	19.6	21.1	51	85	21.2	27.0	89
UT – E	1.9	33.8	15	55	19.6	21.1	9	55	21.2	27.0	41

The CT w/ V,P triaxial tests results are plotted in Figure 88, which shows the MC and HB with a_{RM} equal to 0.4 and 0.5, along with the SSR (measure of fit). In each case, the coal specimens non-linear strength behaviour is better captured with the HB envelope using a_{RM} = 0.4. In all cases, the HB strength model captured the behaviour of the coal during conventional triaxial testing better than the MC model.

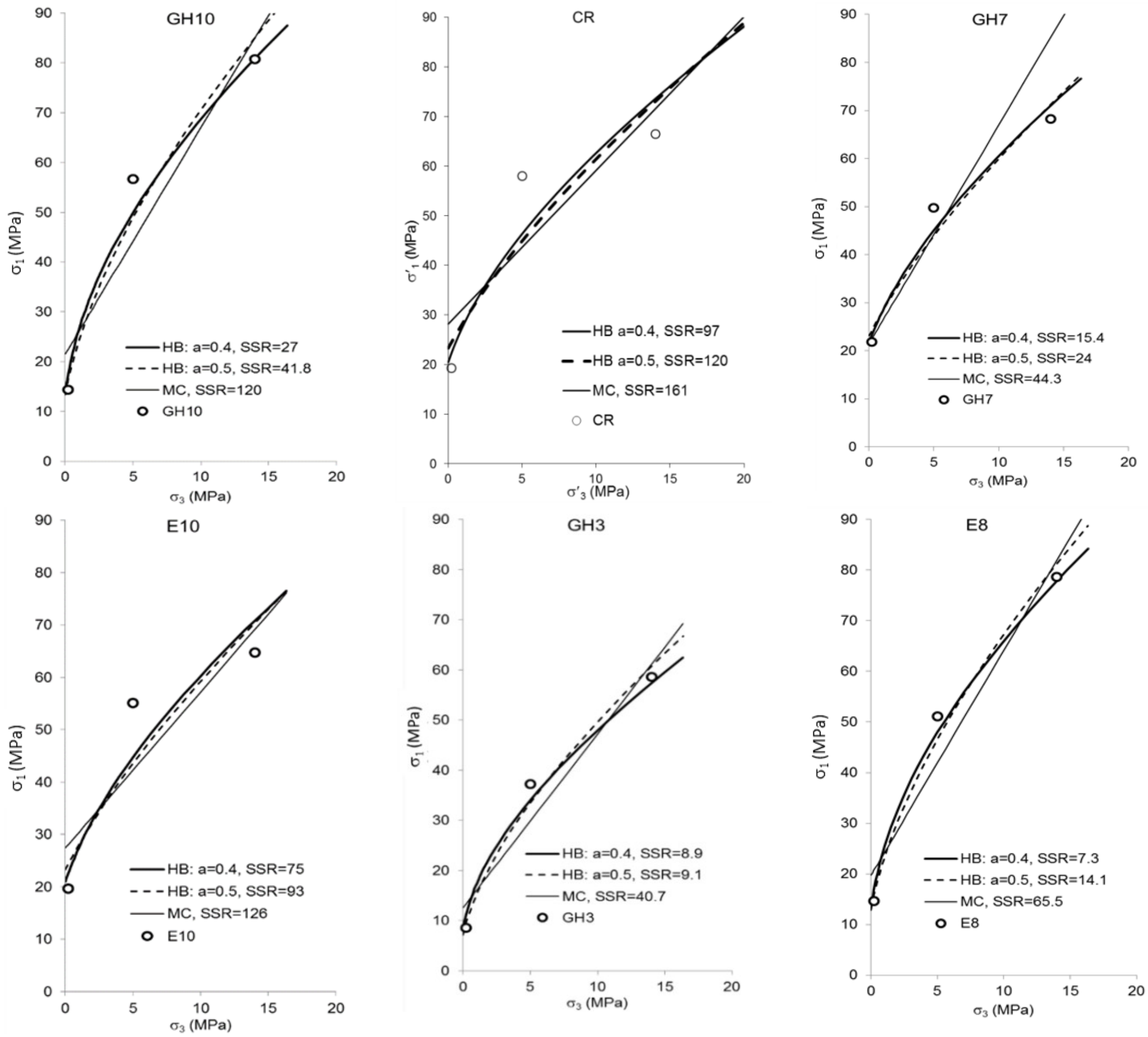

Figure 116. Strength results from the "Conventional Triaxial w/ Velocity and Permeability" testing on specimens from the Greenhills, Elkview, and Cardinal River mines.

The UT w/ P,PS results, best fit using the MC strength criterion, are plotted in Figure 117. The modelling fit found that ϕ values in compression (SSR = 91) and extension (SSR = 15) unloading and loading stress paths were almost identical (35.8° and 33.8°), and c values were 3.55 and 1.91 MPa, respectively.

For the HB modelling of the UT w/P,PS strength results, a_{RM} values were iterated between 0.3 and 0.7. Values between 0.4 and 0.5 provided the best fit, therefore in this modelling effort, only the results for a_{RM} = 0.4 and 0.5 are reported. The HB modelling with a_{RM} = 0.4 of UT w/ P,PS compression/extension loading and unloading results (Figure 118) gave σ_{ci} = 19.6 MPa and m_i = 21.1 with GSI = 85 resulting in an SSR = 51. The failure caused by the radial stress being a maximum was modelled by adjusting the GSI to 55, resulting in an SSR = 9. The modelling was repeated with a_{RM} = 0.5 (Figure 119) giving σ_{ci} = 21.2 MPa and m_i = 27 with GSI = 85, which gave an SSR = 89. The data where the radial stress was maximum was again modelled by adjusting GSI to 55, giving an SSR = 42.

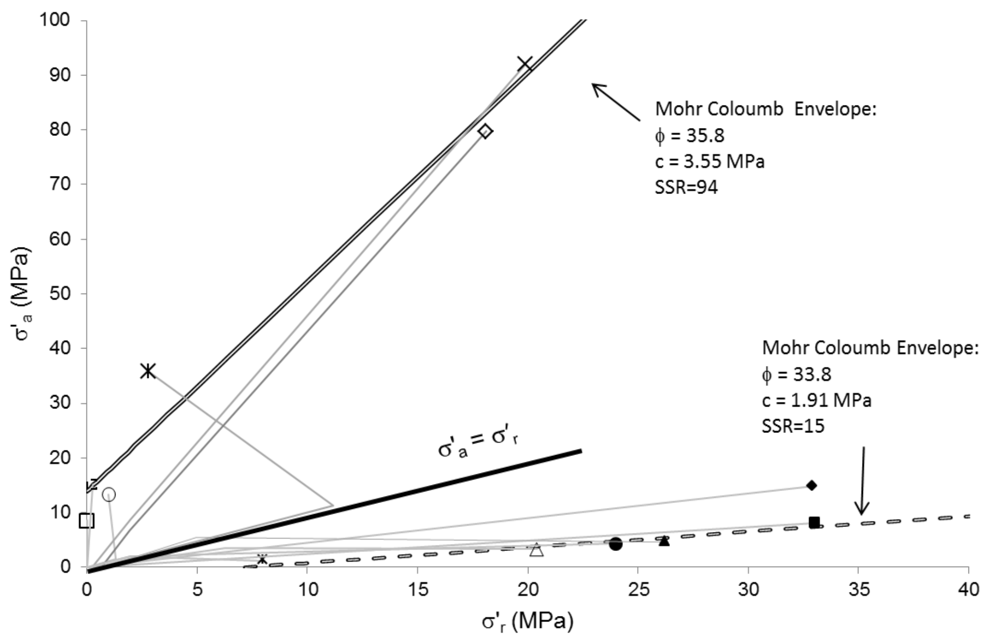

Figure 117. Best fit MC failure criterion for loading – unloading compression-extension tests on samples from coal block.

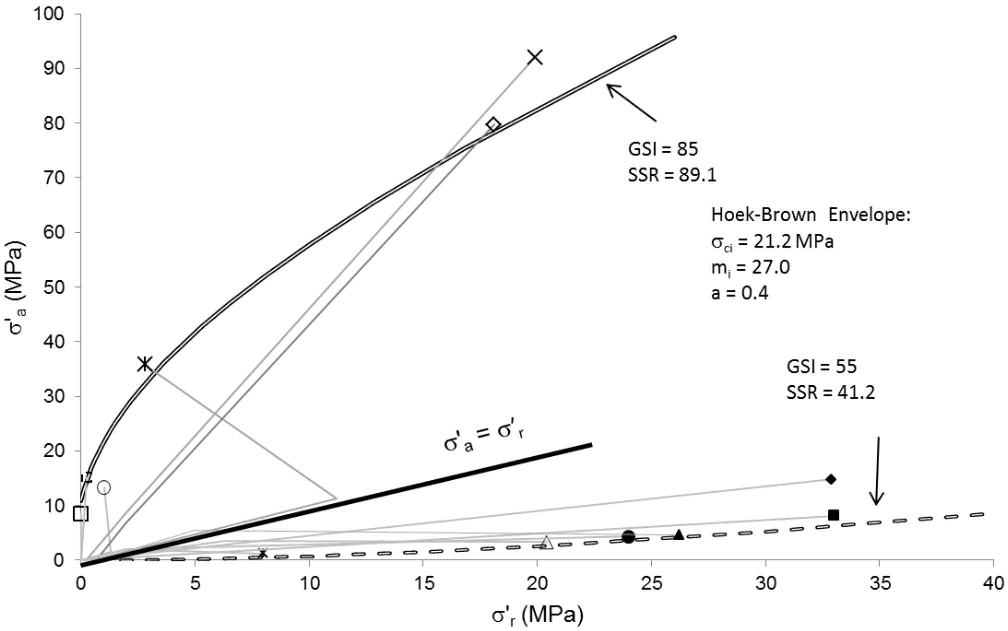

Figure 118. Best fit HB envelopes using $a_{RM} = 0.4$ for loading – unloading compression-extension tests on samples from coal block.

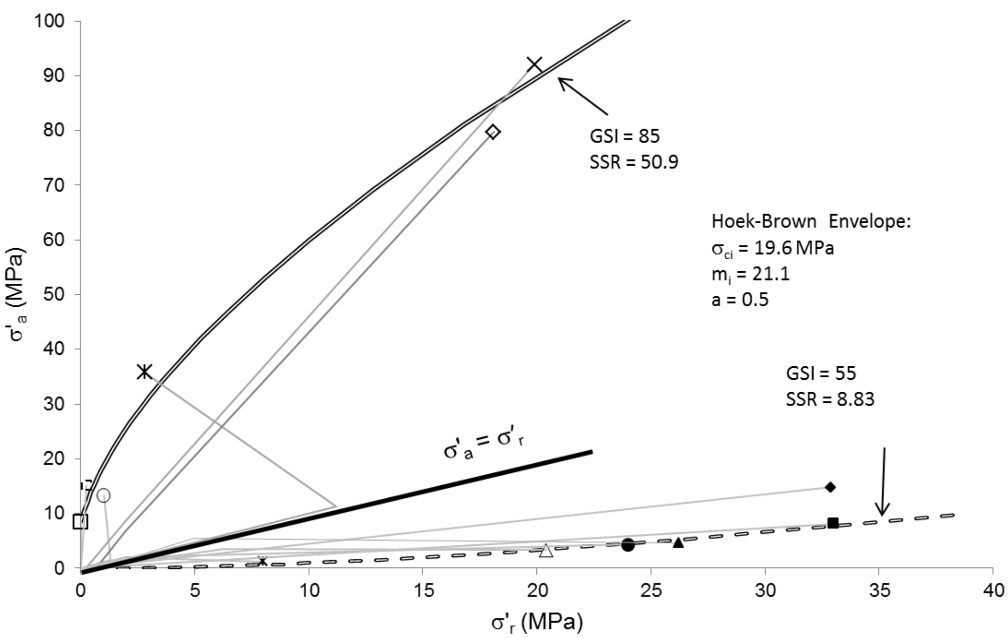

Figure 119. Best fit HB envelopes using $a_{RM} = 0.5$ for loading – unloading compression-extension tests on samples from coal block.

Laboratory Strength Discussion

In the unconventional stress path testing program (UT w/ P,PS), the HB model with $a_{RM} = 0.4$ also provided the best fit for the strength results. In this program the failure was induced by creating a stress field where the axial stress was the greatest at failure. The intact properties where then calculated from these data points, and then the GSI value reduced to fit the data where the radial stress was the maximum stress at failure.

The adjustment of the HB strength envelope for the axial and radial stress induced failure loading can be justified by assuming that the matrix of the coal was isotropic and homogeneous. Therefore, the difference in extension strength could be attributed to planes of weakness represented by assigning *GSI* = 85 to the envelope where the axial stress is maximum and a GSI = 55 for the case where the radial stress is maximum at failure. This is supported through visual evidence where maximum loading is in the direction of the more persistent bedding planes than face and butt cleating plan view. Using a *GSI* = 55 and the same intact strength properties, the extension failure envelope fit the measured data very well, as seen in (Figure 117). The assumption that the strength anisotropy of the coal is due entirely to the cleating and bedding planes most likely incorrect (due to the coalification process), however from an engineering perspective using a directional *GSI* accounts for the strength differences seen in this study and may be sufficient for design/forecasting work.

All of the measured strength was plotted against the predicted strength for each of the modelled strength data values using each of the strength models, and the non-linear coefficient of correlation was calculated (R^2) (Brown, 2001) (Figure 120). Calculated R^2 values were as follows: MC: $R^2 = 0.89$, HB $a_{RM} = 0.5$: $R^2 = 0.89$, HB $a_{RM} = 0.4$: $R^2 = 0.93$. It is the latter model provided the best fit.

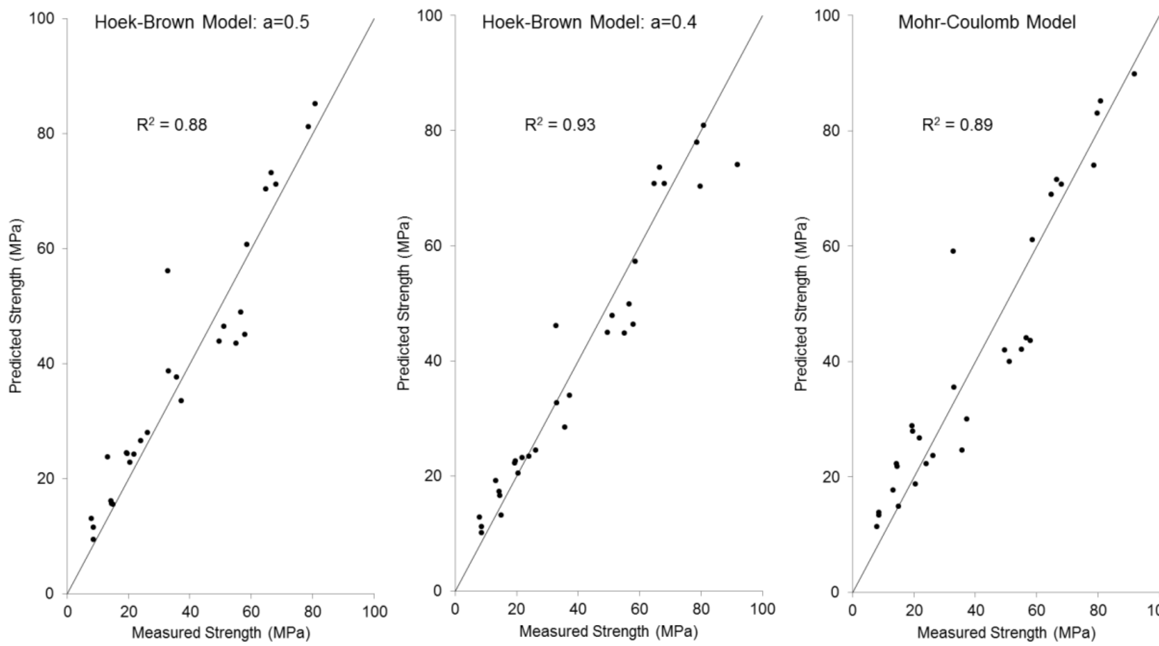

Figure 120. Best fit Mohr Coulomb, Hoek-Brown (a_{RM} = 0.4) and Hoek-Brown (a_{RM} = 0.5) predictions for laboratory tested strength results.

Numerical Strength Results

The SRM approach is a numerical technique using a bonded particle model and a DFN (Mas Ivars, 2011). The SRM was applied in this research to investigate the ability to simulate coal and was used in the "off the shelf" mode meaning:

- Joint stiffness was constant and not dependent on aperture or stress
- Matrix stiffness was constant and not dependent on stress

Three example coal volumes were created using the same DFN (Chapter 8). Each of the three coal volumes were sampled to create two coal specimens and then were simulated at different scales, and in different directions with the intact macro properties shown in Table 27. The testing results were modelled using two strength models: MC and HB.

Table 27. The macro properties used to represent the intact/matrix component of the SRM specimens.

Model	E (GPa)	σ_{ci} (MPa)	ν
C1-1, C1-3, C2	3.30	16.1	0.33
C1-2	3.38	45.6	0.26
C1-4	4.94	42.2	0.29

The MC, HB a_{RM}=0.4, and HB a_{RM}=0.5 failure criterions were best fit to each of the data sets created from the SRM specimens with the SSR shown for each of the model fits (Table 28). To fit the MC parameters, the c and ϕ were adjusted until the minimum SSR was determined. To fit the HB failure criterions, the intact UCS strength used to create the specimens was used for σ_{ci} in the HB failure criterion. The GSI was then adjusted to so the strength at zero confining stress was matched. The m_i value was then adjusted until the SSR was minimized for the $a_{RM} = 0.4$ and $a_{RM} = 0.5$ models. For the three specimens C2-500mm, C2-1000mm, C2-140mm, the MC and HB models could not fit the data, as the strength was shown to decrease with an increase in confining stress, therefore, a not applicable (NA) was assigned.

Table 28. MC and HB parameters for numerical SRM coal specimens using the intact values and GSI to reduce the strength.

Specimen	MC Parameters			HB Parameters							
				a_{RM} = 0.4				a_{RM} = 0.5			
	c (MPa)	ϕ	SSR	GSI	σ_{ci} (MPa)	m_i	SSR	GSI	σ_{ci} (MPa)	m_i	SSR
C1-1-140	4.44	22.9	1.8	93	16.1	5.6	2.3	95	16.1	3.75	2.7
C1-1-200	5.15	17.8	0.34	91			14.3	94			14
C1-2-140	10.8	27.2	10.9	92	45.6	6.4	29	93	45.6	5.5	51
C1-2-300	8.99	30.9	1.9	91			5.3	92			8.1
C1-3-140	4.29	21.2	2.7	91	16.1	4.9	4.6	93	16.1	3.5	5.8
C1-3-200	5.01	18.9	0.35	93			5	94			5.4
C1-4-140	8.67	25.2	5.4	88	42.3	4.8	9.1	91	42.3	3.7	8.7
C1-4-200	7.35	31.2	3.4	90			10	92			8.1
C2-140-x	4.24	13.3	60	86	16.1	3.6	16.6	89	16.1	2.4	17
C2-500-x	NA	NA	NA	NA			NA				NA
C2-100-x	NA	NA	NA	NA			NA				NA
C2-140-y	5.76	9.12	12	90		3.2	37	92		3	39
C2-500-y	3.13	16.7	2.9	81			6.4	85			8.1
C2-1000-y	1.43	26	13	70			18.2	77			20
C2-140-z	NA	NA	NA	86		2.6	NA	NA		2.5	NA
C2-50-z	4.16	12.4	6.4	85			16.7	87			21
C2-1000-z	3.47	13.2	3.2	82			8.6	86			9.8

The HB models were shown to fit the SRM data reasonably well. Additionally, all of the HB properties were adjusted (HB_{ALL}), except σ_{ci}, in an attempt to explore a better HB model fit to the SRM data. The first step was to adjust GSI fit the strength value at zero confining stress. The m_i and a_{RM} were then adjusted to create the best model fit. For the C2 specimens, the σ_{ci} and m_i were held constant and only GSI and a_{RM} were adjusted. The resulting HB parameters and the comparison to the best fit shown in Table 28 are provided in Table 29.

Table 29. Best fit HB parameters for numerical SRM coal specimens using only σ_{ci} as a fixed input and adjusting GSI, m_i, and a_{RM}

Specimen	Best Fit HB Parameters					
	GSI	σ_{ci} (MPa)	m_i	a_{RM}	SSR Best	SSR Best (Table 28)
C1-1-140	93	16.1	5.6	0.40	2.3	2.3
C1-1-200	91			0.30	3.8	14.3
C1-2-140	90	45.6	8	0.26	9	29
C1-2-300	85			0.24	3	5.3
C1-3-140	90	16.1	4.9	0.35	4.6	4.6
C1-3-200	93			0.33	2.7	5
C1-4-140	80	42.3	7.0	0.25	3.0	9.1
C1-4-140	78			0.22	3.5	10
C2-140-x	80	16.1	8	0.25	1.72	16.6
C2-500-x	NA			NA	NA	
C2-1000-x	NA			NA	NA	
C2-140-y	85			0.20	2.05	37
C2-500-y	50			0.15	0.844	6.4
C2-1000-y	25			0.15	1.18	18.2
C2-140-z	60			NA	NA	NA
C2-500-z	55			0.15	0.64	16.7
C2-1000-z	25			0.12	0.53	8.6

Numerical Strength Discussions

The MC model was able to better model the strength behaviour of the SRM results than the HB models, however the HB with a_{RM} equal to 0.4 or 0.5 fit the data sets very well. All of the measured SRM results were plotted against the predicted values for MC, HB a_{RM} = 0.4, HB a_{RM} = 0.5, and HB_{ALL} and the R^2 was determined. It was shown that the HB_{ALL} model was the best fit, however the increase in the models ability to predict the SRM results was very minimal overall. Therefore, it can be concluded that HB is able to predict the behaviour of the SRM very well.

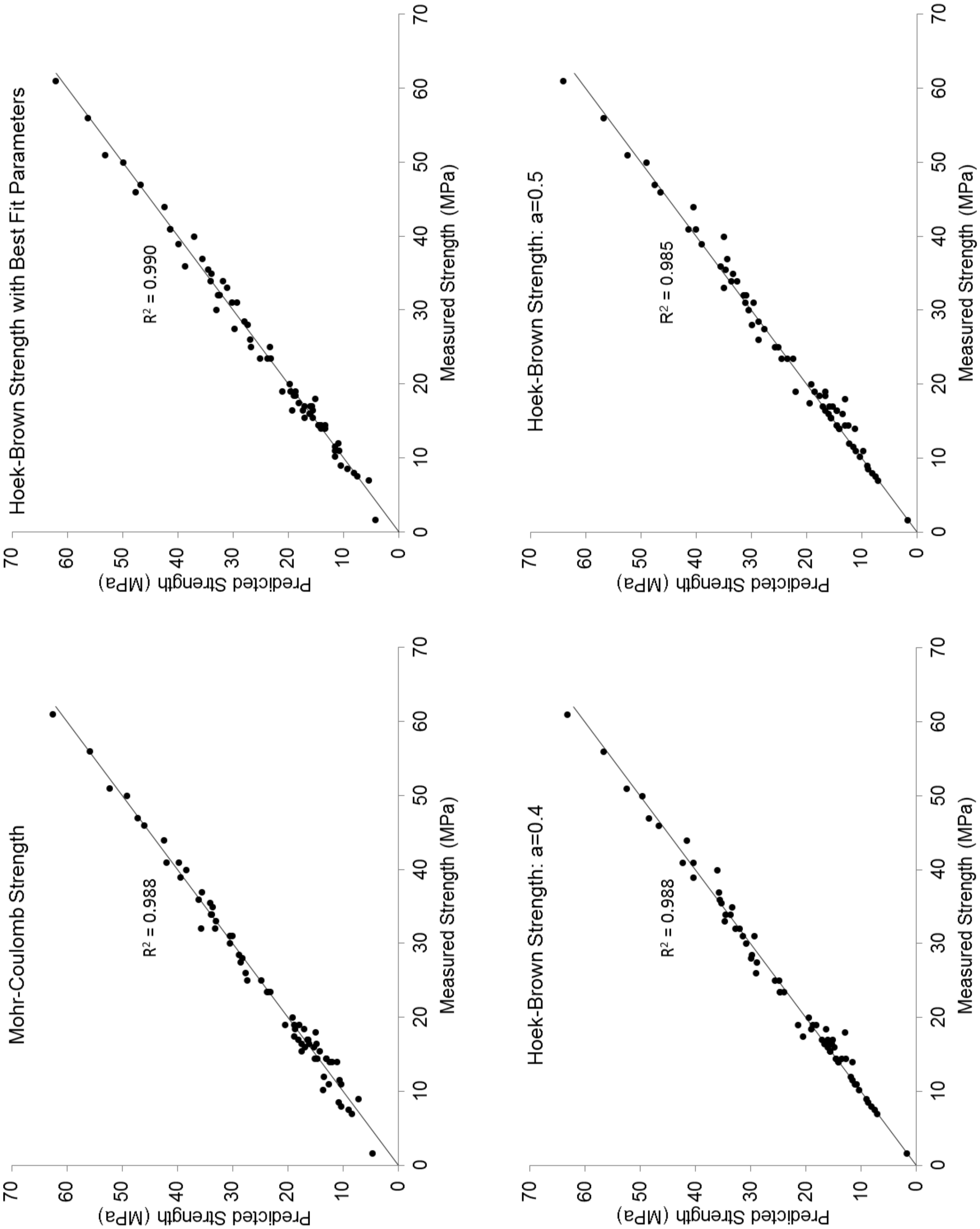

Figure 121. Best fit Mohr Coulomb, Hoek-Brown (varied inputs), Hoek-Brown (a=0.4) and Hoek-Brown (a_{RM} = 0.5) predictions for numerical SRM testing results.

A concerning SRM behaviour is the MC friction angles and HB m_i (somewhat analogous to the friction angle). The SRM friction angle was an average of 9.4 degrees less than the results from the laboratory testing on real coal specimens and m_i was an average of 13.1 units lower. It is well known that the PFC-BPM does not represent friction well (Cho et al, 2007); however, it was thought that the inclusion of fractures with the SRM model would better represent the friction angle shown of coal (and rock). The general behaviour from the SRM C2 y direction testing series does show expected behaviour, which is an increase in friction angle and a decrease in cohesion with increase in specimen size. However, the friction angle is still very low as the specimen size increases from 140 mm (9.1°), 500 mm (16.7°), and 1000 mm (26.0°).

The strength anisotropy can be compared in the C2-y and C2-z directions at the 500 mm and 1000 mm scales through GSI. The results showed that the GSI at each scale in the z direction was greater than in the y direction. This behaviour fits with the construction and testing of the models, where the more persistent bedding planes are aligned with the direction of loading (the normal of the bedding plane is perpendicular to the maximum stress plane). The z direction specimens have a higher strength in the z direction as for these specimens, the face and butt cleats planes are normal to the maximum stress plane. There were no data to compare the results from the x direction specimens.

The scale behaviour of the SRM models C1-1, C1-2, C1-3, C1-4 specimens was not expected. Each of these specimen sets (several specimens at each size, tested at multiple confining stresses) were tested at two scales, however, the results showed that the UCS of the smaller specimen was greater than that of the larger specimen. This is the opposite of what is expected from increasing the specimen size. However, the C2 specimen sets illustrated that as the specimen sizes increased, the strength decreased. Another concern with the SRM testing was the results showing the specimen strength decreasing with increasing confining stress (C2-500 mm-x, C2-1000mm-x, C2-140mm-y). Therefore, more investigation would be required to determine the departure from the 'scale effect' theory for these sets of specimens and into the cause of decreasing strength with increased confining stress.

Currently, the "off the shelf" SRM does not capture the behaviour of the coal well enough to provide confidence that it can sufficiently characterize the strength behaviour. Additions and improvements to the strength behaviour of the SRM could include:

- having the joints represented as impersistent rectangles and not disks; and
- addressing the cause of the low frictional behaviour.

9.1.2 Young's Modulus

The Hoek and Diederichs Young's modulus reduction ratio model with the stress dependent disturbance factor D is used to model the change in Young's modulus with change in confining stress (41). The model assumes that *D* varies exponentially with confining stress and is dependent on a fitting factor *h* (42).

$$E_{RM} = E_i\left[0.02 + \frac{1-\exp\left(-\sigma_3'/h_1\right)/2}{1+\exp\left[(60+15\exp\left(-\sigma_3'/h_1\right)-GSI)/11\right]}\right] \qquad 41$$

$$D = \exp\left(-\sigma_3'/h_1\right) \qquad 42$$

Laboratory Young's Modulus Data

Laboratory derived values for axial Young's modulus results were modelled with Eq 41, using *GSI* from the strength testing, except for the CR-ET-1 specimen, which used *GSI* = 95, which had no visible through going fractures. The Young's modulus model fitting, with E_i and *h,* are provided in Table 30. In each case, the model fits the data very well (R^2 > .85), except for the Greenhills – Seam 10 (R^2 = 0.512) and Elkview – Seam 8 (R^2 = -0.216) data. The CR-ET-1 single specimen stress dependent axial Young's modulus is shown in Figure 122 to illustrate the behaviour of the Young's modulus and the changes in the stress dependent disturbance factor. In addition, all of the data was plotted in Figure 123 showing the ability of the Young's Modulus reduction ratio model to predict the measured data, giving a R^2 = 0.969.

Table 30. Reported results for estimated *GSI*, back calculated intact modulus (E_i) and the parameter h.

Sample	GSI	Ei (GPa)	h (MPa^{-1})	R^2
GH3	85	3.3	4.0	0.961
GH7	85	4.2	8.1	0.842
GH10	85	5.4	4.0	0.512
E8	85	5.1	2.8	0.928
E10	85	5.6	2.0	-0.26
CR	85	4.5	1.9	0.985
CR-ET-1	95	8.6	2.9	0.940

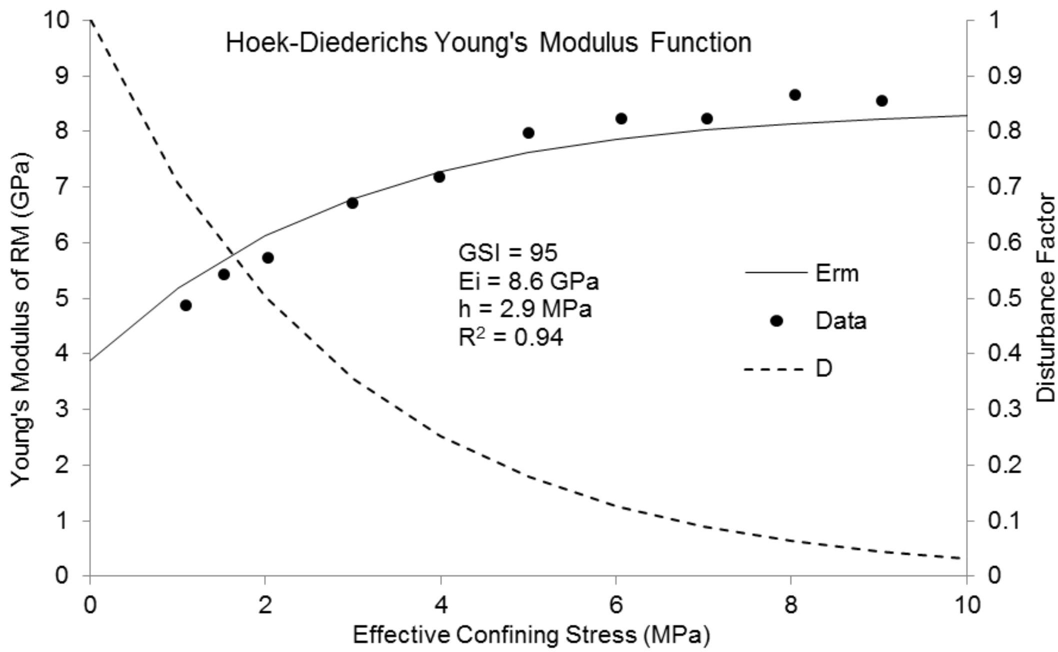

Figure 122. Static Axial Young's modulus for the CR-ET-1 specimen as a function of confining effective stress at zero pore pressure using the Hoek-Diederichs function with the 'h' parameter.

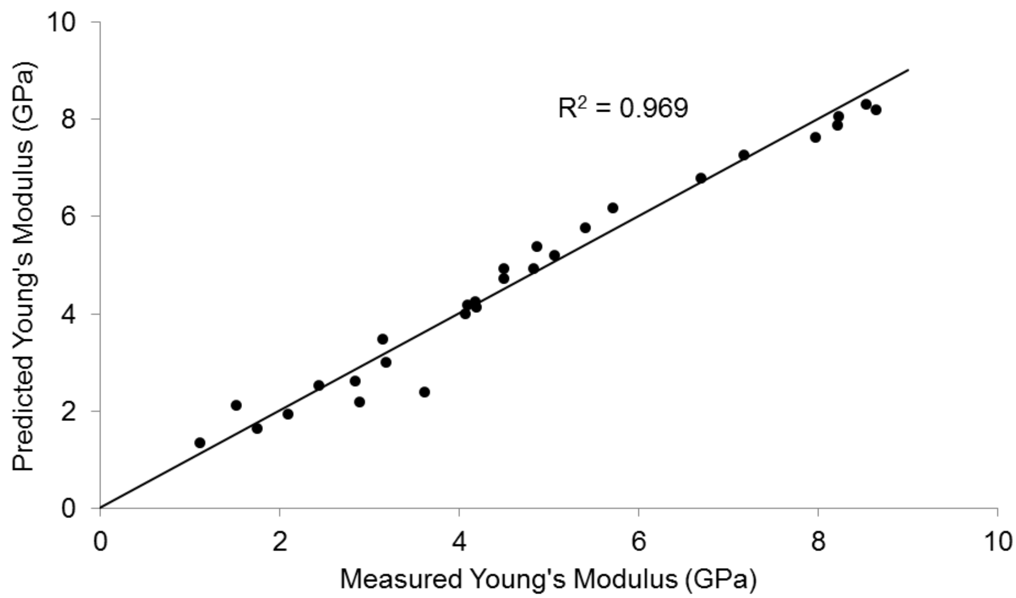

Figure 123. Measured verses predicted Axial Young's modulus for coal specimens as a function of mean effective stresses using the Hoek-Diederichs function with the 'h' parameter.

Laboratory Young's Modulus Discussion

Using this approach, determining *D* as a function of confining stress using the *h* factor, and then determining the intact Young's modulus of the coal showed good agreement with measured values. The resulting E_i determined from each of the experimental data sets were reasonable, falling between 3.3 and 8.6 GPa. All of the measured values from testing were within the boundaries of 2.2 to 6.0 GPa measured by Medhurst and Brown (1996) and 3.1 to 9.5 GPa measured by Szwilski (1984).

Using *GSI* = 85 for the all but one of the samples is suspect, as no photographs of the samples are available, however, the results were acceptable. With better characterization of the fracturing of the specimens prior to testing, a more realistic *GSI* could be assigned. This would provide a better evaluation of the functions used to determine E_i and if the D function using *h* is sufficient, or can be improved upon.

Numerical Young's Modulus Data

Several attempts were made to fit the Young's modulus reduction ratio function to the data generated from the SRM testing. The first attempt, Fit A, used *GSI* from the strength testing and the E_i from the BPM model that created the SRM specimens. The *h* value was then adjusted until the best fit was determined (in this case R^2 was used) and out of the 17 data sets, the R^2 was less than 0.61, indicating a very poor prediction (Table 31). In Fit B, the *GSI* and *h* were then allowed to be adjusted, keeping E_i from the BPM, which improved the fit of the model slightly. The final fitting attempt (Fit C), E_i, *GSI*, and *h* was adjusted to determine the best prediction of the Young's modulus reduction ratio function for the SRM data set, however R^2 was less than 0.76 for all cases (Table 32).

Table 31. Best fit Hoek and Diederichs Young's modulus reduction ratio equation using the E_i from the initial SRM calibartion and adjusting *h* (Fit A), and then adusting *h* and *GSI* (Fit B).

Specimen		E_i (GPa)	Fit w/ Strength GSI (Fit A)			Best Fit w/ Adjusted GSI (Case B)		
			GSI	h (MPa)	R^2	GSI	h (MPa)	R^2
Case 1-1	140	3.296	93	20	-3.07	100	18	-1.72
	200		91		-8.95	95		-8.68
Case 1-2	140	3.380	92	21	-9.37	100	23	-3.40
	300		91		-1.44	89		-0.96
Case 1-3	140	3.296	91	17.1	-2.97	100	22	-0.47
	200		93		-12.6	100		-7.63
Case 1-4	140	4.940	88	200	-13.3	91	93	0.63
	300		90		-20.0	83		-1.97
Case 2x	140		86	5.3	-1.50	100	10	0.53
	500		83		0.49	100		-0.01
	1000		65		0.28	75		0.58
Case 2y	140	3.296	90	15	-0.23	77	9	0.31
	500		81		0.61	80		0.42
	1000		71		-0.68	75		0.72
Case 2z	140		87	24	-9.95	90	55	-6.34
	500		85		0.34	85		0.25
	1000		83		0.09	85		0.32

Table 32. Best fit Hoek and Diederichs Young's modulus reduction ratio equation adjusting E_i, GSI, and h of SRM data (Fit C).

Specimen		Best Fit w/ Strength GSI and Adjusted Modulus (Fit C)			
		Ei (GPa)	GSI	h (MPa)	R^2
Case 1-1	140 mm	3.5	100	41	0.76
	200 mm		76		0.04
Case 1-2	140 mm	3.61	100	21	-5.51
	300 mm		60		0.75
Case 1-3	140 mm	3.1	100	21	0.03
	200 mm		100		-4.50
Case 1-4	140 mm	4.2	100	65	0.55
	300 mm		64		-1.26
Case 2x	140 mm	3.2	100	10	0.75
	500 mm		96		0.10
	1000 mm		60		0.30
Case 2y	140 mm	2.2	100	15	0.33
	500 mm		81		0.17
	1000 mm		70		0.18
Case 2z	140 mm	2.9	100	90	-1.50
	500 mm		70		0.10
	1000 mm		85		0.16

Numerical Young's Modulus Discussion

In all cases, the Young's modulus reduction ratio function did not predict the behaviour of the axial Young's modulus extracted from the SRM tests. The measured versus the function predicted values for each of the model fitting cases (A, B, and C) is shown in Figure 124. For model Fit A, the E_i derived from BPM models and the GSI from the strength modelling was used, however the function was not able predict the SRM response sufficiently, giving an overall $R^2 = 0.19$ for Case 1 and $R^2 = 0.59$ for Case 2. For model Fit B, GSI and h were adjusted, giving and overall $R^2 = 0.65$ and $R^2 = 0.69$ for Case 1 and Case 2 respectively. Finally, all of the inputs were allowed to be adjusted for Fit C, giving a Case 1 $R^2 = 0.8$ and Case 2 $R^2 = 0.63$.

In all cases, the SRM model did not show the expected confining stress dependent non-linear rock Young's modulus behaviour or the scale dependency exhibited in the laboratory or field. The Hoek and Diederichs Young's modulus reduction ratio function had been developed from many field tests of rock over a wide range of disturbances (D) and fracturing (GSI). This function was used to assess if the emergent SRM Rock mass Young's modulus was realistic. It would not be correct to assume the function represents reality however, it is expected that the SRM data should be captured by the function to a reasonable extent. For this set of tests, the SRM was not able to capture the expected non-linear behaviours.

From these sets of tests on coal, the "off the shelf" version of the SRM needs improvement to be able to supplement the characterization of coal outside of the sizes testable in the laboratory. Suggested improvements to the standard SRM model may include:

- non-linear joint behaviour; and
- non-linear intact matrix behaviour.

It should be noted that these improvement can be simply included through FISH coding, however, they are not a part of the standard model and require thorough testing.

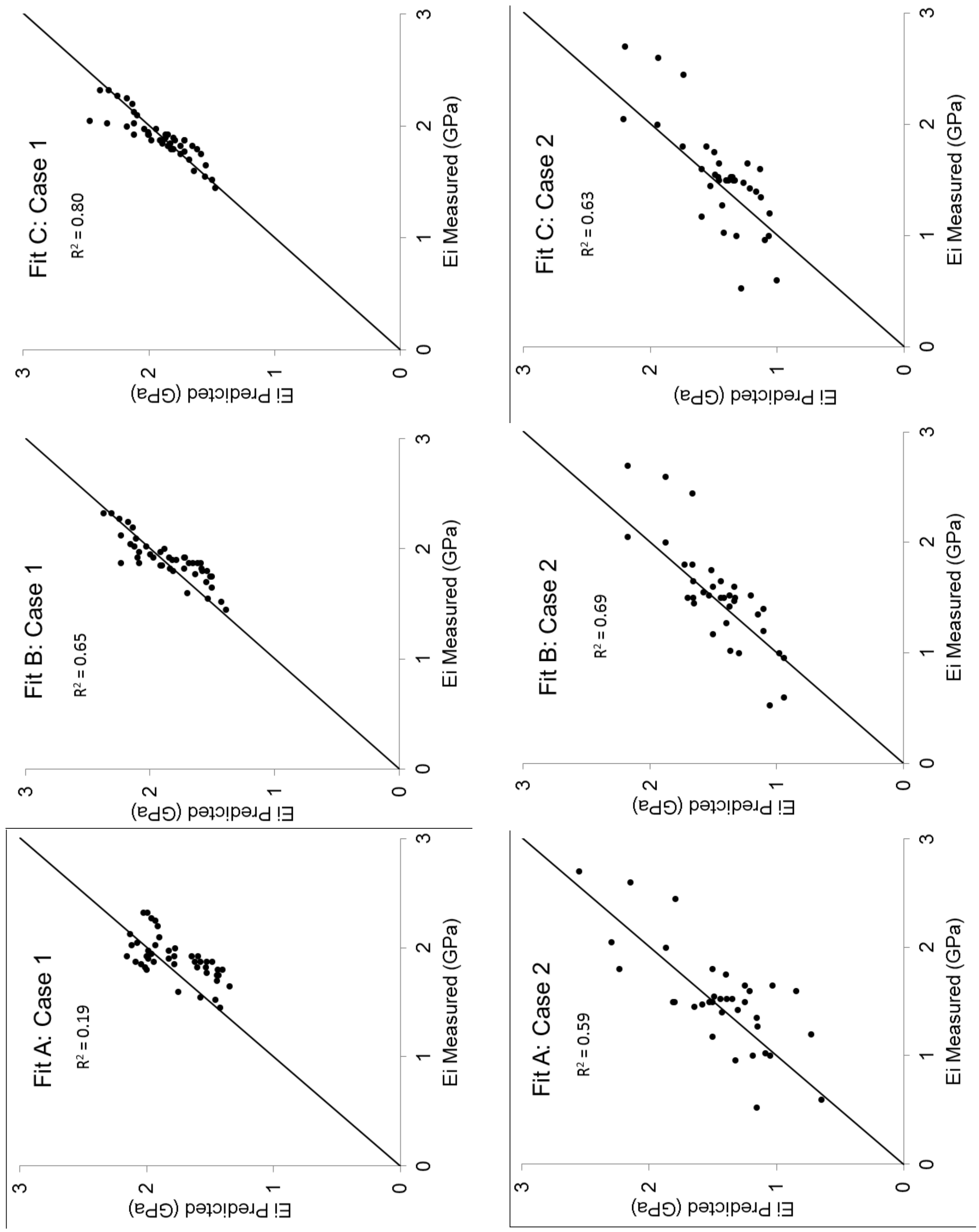

Figure 124. Measured versus predicted E_i results for SRM results modelled with the Young's modulus reduction ratio function with the disturbance factor h function.

9.1.3 Methane Sorption

Methane content was measured in an intact coal at four different effective stress conditions on the same sample during this testing program (1.1, 3.0, 5.0, 0.0 MPa).

Methane Sorption Data

The intact specimen sorption testing results at zero effective stress are reasonable when compared to other, as received coal specimens (not dry, ash free, measurements) (Bustin and Clarkson, 1998). The results indicate that as isotropic effective stress (σ'_{iso}) is increased, the total methane sorption at corresponding methane pressures is reduced (Figure 125).

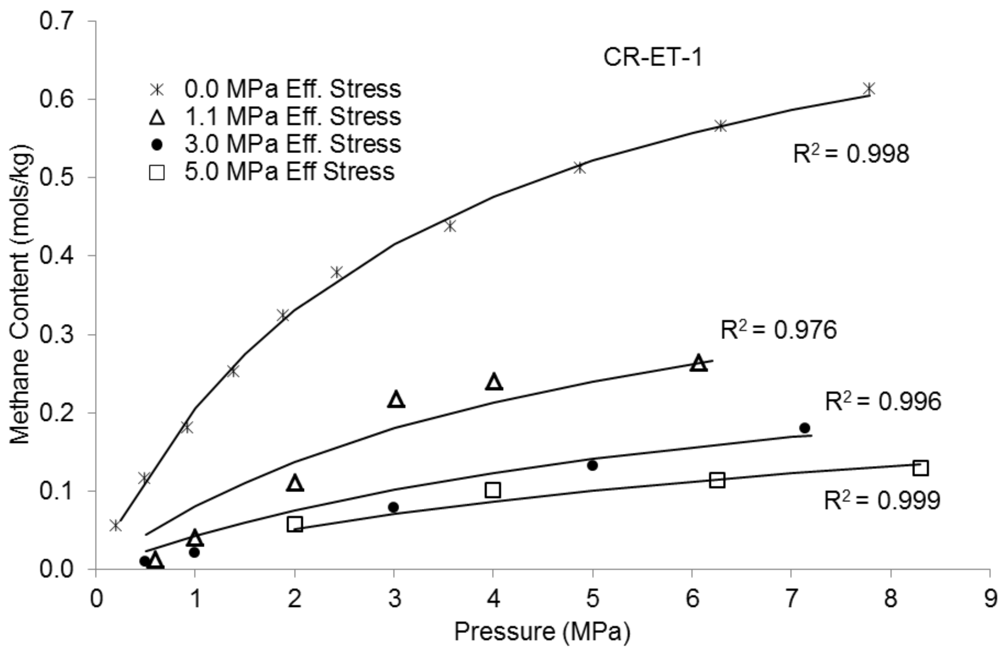

Figure 125. Isotherm for methane gas at 0, 1.1, 3 and 5 MPa effective stress at 301.1 K.

The sorbed methane volume (V_g) was modelled with the Langmuir equation (43), using the Langmuir Volume (V_L) and Langmuir Pressure (P_L).

$$V_g = \frac{V_L P}{P_L + P} \tag{43}$$

Table 33. Langmuir isotherm parameters for methane sorption on coal specimen CE-ET-1tested at σ'_{iso}: 0, 1.1, 3.0, and 5.0 MPa.

Parameter	Units	CR-ET-1 Specimen			
σ'_{iso}	MPa	0.0	1.1	3.0	5.0
V_L	mols/kg	0.848	0.408	0.340	0.280
P_L	MPa	3.12	5.0	7.1	9.0
R^2		0.998	0.976	0.996	0.999

Two functions were created in attempts to predict the influence of isotropic stress on the sorption of methane on an intact coal specimen. These functions were based simply on examining the data and determining functions that would fit the data for engineering purposes, and not to scientifically interpret the physical processes. The Langmuir volume as a function of σ'_{iso} (V'_L) uses the Langmuir volume determined at zero effective stress (V_L) as a starting point, and then subtracts a Langmuir equation involving a Langmuir effective stress to volume term (σ'_{L-V}), with stress units, and the σ'_{iso} (44). The Langmuir pressure as a function of σ'_{iso} (P_L) uses a linear relation, where the intercept is the P_L at zero effective stress and the slope is the Langmuir effective stress to pressure term (σ'_{L-P}) with stress units (45). The V'_L and P'_L functions are shown in Figure 126, where σ'_{L-V} = 1.848 MPa and σ'_{L-P} = 0.813 MPa.

$$V'_L = V_L\left(1 - \frac{\sigma'_{iso}}{\sigma_{L-V} + \sigma'_{iso}}\right) \qquad 44$$

$$P'_L = \frac{\sigma'_{iso}}{\sigma_{L-P}} + P_L \qquad 45$$

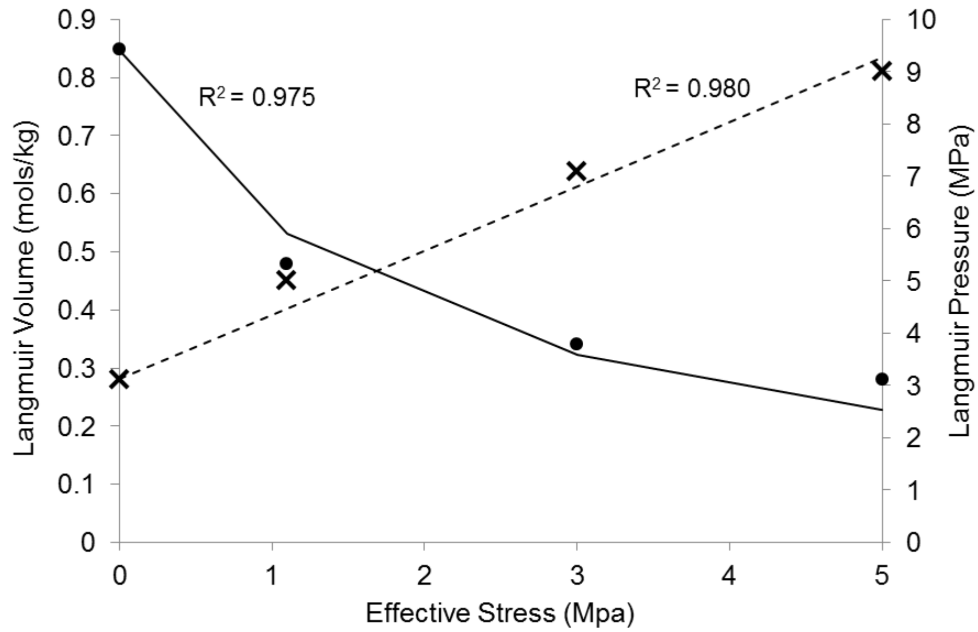

Figure 126. Best fit results from Figure 125 Langmuir volume and Langmuir pressures as a function of effective stress.

Methane Sorption Discussion

Isotropic stress reduced the sorption of methane onto the intact CR-ET-1 specimen. The fit of the Langmuir equations attempting to model the data did capture the shape of the methane sorption well except lower pressures for the 1.1 MPa effective stress condition (discussed below) (Figure 125).

Irving Langmuir (1918) developed his quantitative theory of adsorption by describing the adsorbent surface having elementary spaces which can adsorb a single molecule, and that those spaces are in a constant adsorption-evaporation (desorption) state. He described adsorption of gas onto a surface as dependent on the number of gas molecules striking the surface with time, which is directly related to pressure. Therefore, as the pressure increases, the number of molecule striking the surface increases, and more of elementary spaces are filled. From these assumptions, he was able to derive parameters which are now known as the Langmuir volume (maximum gas at infinite pressure) and the Langmuir pressure (pressure at which half the Langmuir volume can be adsorbed). Hol et al (2011) derived an addition to the original Langmuir theory, including an effective stress work term to explain desorption of CO_2 due to an applied stress. The theory explained that an increase in energy due to gas pressure is required to overcome the energy added to the coal by applied stress. This was to their experimental work on a single crushed coal specimen exposed to CO_2 and matched the data within reason.

From these two theories, the experimental measurement results shown in Figure 125 can be speculated. The decrease in V_L with increase in effective stress can simply be attributed to the compression of the specimen and the closing off the elementary adsorption spaces. The increase in P_L can be due to the additional work, in the form of pressure, required to overcome the energy supplied by the applied load. Much more work is required to examine these speculative conclusions, including long term testing to ensure equilibrium is reached at each effective stress state.

Simple functions attempting to model the influence of effective stress on V_L and P_L were developed and their ability to predict results is shown in Figure 127. The figure indicates that, if the initial values at $\sigma'_{iso} = 0$ are not included, the model does not perform well as the effective stress increases. Additionally, the functions were developed on the basis of a single coal specimen test over a small range of gas pressures. It can be seen from the results that σ'_{iso} does have an influence on the sorption of methane gas on coal. All of the methane gas contents were determined at the same time increment after methane pressure incrementing, therefore the σ'_{iso} does influence, at a minimum, the rate at which gas is sorbed on the coal. Further work would need to be completed to:

- have confidence in any relationship for σ'_{iso} influence on sorption,
- examine the actual physical processes occurring, and
- ensure specimens have reached equilibrium at each methane gas pressure.

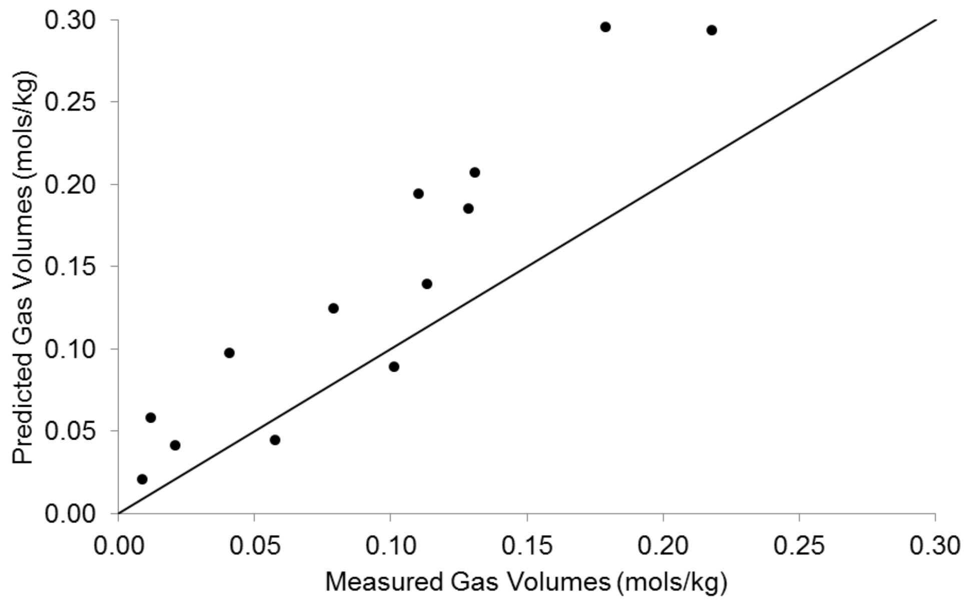

Figure 127. The predicted gas volumes using (44) and (45) versus measured gas volumes determined under σ'_{iso} = 1.1, 3.0 and 5.0 MPa (values measured at 0 MPa not measured).

9.1.4 Sorbed Gas and Mechanical Behaviour

The influence of sorbed methane gas on the mechanical behaviour is partitioned into the influence of sorption on volumetric strain and mechanical properties.

Sorption Induced Strain

Coal has been shown to increase in volume in response to increases in sorbed methane. Mazumder et al (2006b) summarized historical data published on the sorption strain coefficients (C_m) in coal developed for a Langmuir equation sorption strain model. Robertson and Christiansen (2007) reported methane sorption linear strains, showing linear strains coefficients for two coals of 0.93% and 0.77% measured at 26.7°C. For these reported measurements, the tests were completed at $\sigma' = 0$. Other researchers have studied methane sorption induced strain under stressed conditions (Mazumder et al 2006, Pone et al. 2009). In each of the experiments, the test conditions were not designed to specifically analyze the influence of stress on sorption induced volumetric strain. Hol et al (2010) did test the influence of applied stress on crushed coal, showing that applied stress does reduce CO_2 sorption induced expansion.

The experimental results showed the application of σ′$_{iso}$ reduced the total axial strain for similar changes in methane gas pressure (Figure 128). The results also illustrate that the σ′$_{iso}$ supressed the initiation of axial strain. The sorption strain data for each effective stress state did not follow the observed Langmuir equation shapes shown in the literature. As well, equilibrium may not have been reached at each gas pressure prior to increasing to the next pressure increment. Hol et al (2011) has derived an theory for this phenomenon in terms of work required to overcome the effects of an applied stress at the grain to grain contact level on a crushed coal specimen in terms of an stressed to unstressed swelling strain coefficient based on: the partial molecular absorbed volume of the gas, the Boltzmann constant, and temperature. This theory was not applied as further long term testing should be conducted to examine the final sorption strain at each methane pressure for each effective stress state.

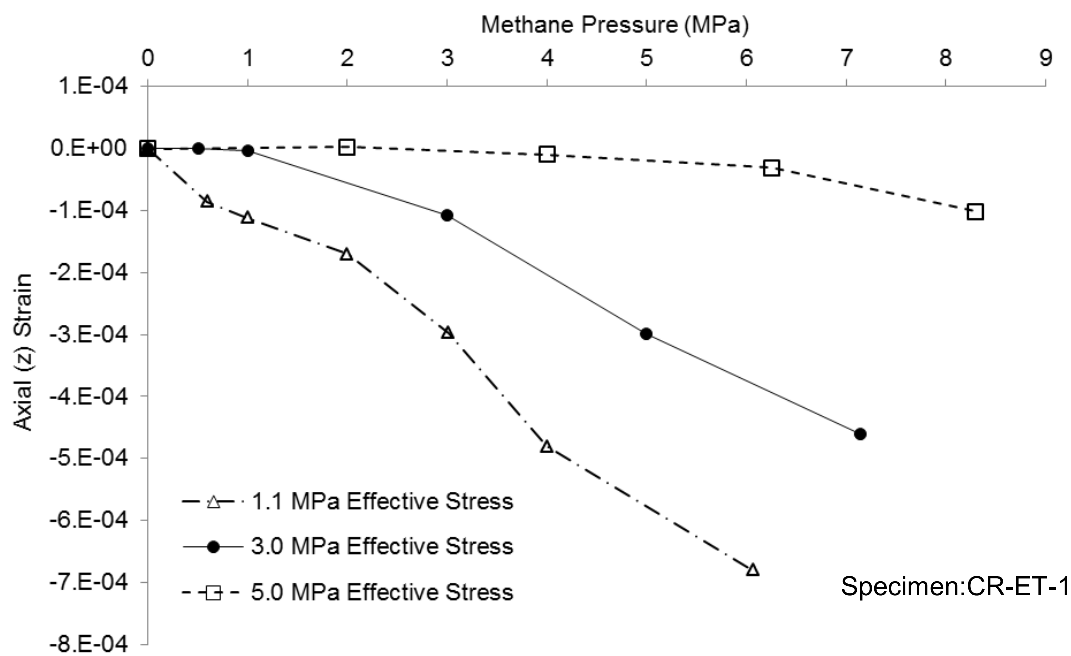

Figure 128. Axial swelling strain at 1.1, 3.0 and 5.0 MPa constant effective stress with increasing gas pressure.

Influence of Sorbed Gas on Coal Modulus

Results from the tests at different constant σ′$_{iso}$ states indicate that as the gas pressure increases, there is no recognizable trend that can be attributed to the presence of sorbed methane gas (Figure 129). The measured Young's modulus with methane pressure fluctuated above and below results with no methane pressure. Again, one of the issues in the experimental procedure is to ensure equilibrium is reached at each applied gas pressure. Therefore, further testing should be completed to determine if Young's modulus is influenced by methane gas sorption.

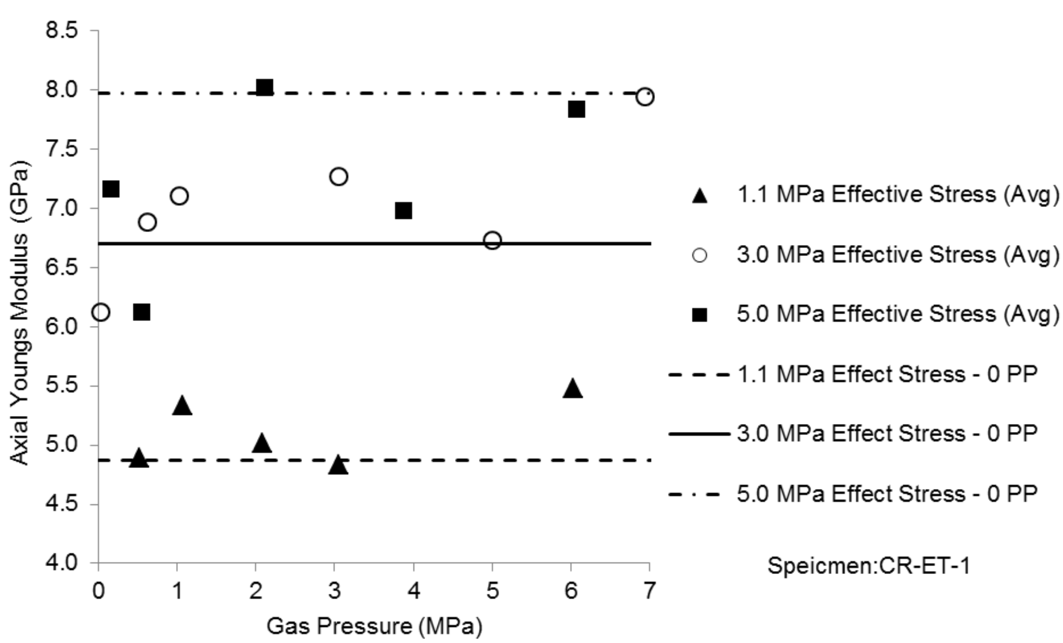

Figure 129. Changes in Young's modulus with CH_4 pressure at σ'_{iso} = 1.1, 3.0 and 5.0 MPa.

9.2 Flow Data Analysis and Modelling

Permeability measurements on tests on specimens CE4, CE6, and UA5 demonstrates that isotropic and anisotropic stress changes create complex permeability changes that should be considered in dynamic permeability model development. In this section, a coupled geomechanical strain dependent permeability model is developed which includes GSI. The model is then used to predict the stress dependent permeability results for specimens CE4, CE6, and UA5 as well as results reported by Somerton et al (1975). The section starts by summarizing the development of the permeability model, then modelling the laboratory results, and concludes with discussing shortcomings of the approach.

9.2.1 Dynamic Permeability

Numerous researchers have demonstrated that isotropic effective stress increases caused by changes in total stress create a permeability decrease due to fracture/cleat closure. Based on these findings, several analytical and coupled geomechanical models, which often include sorption induced strains, have been developed to predict changes in permeability. Analytical models create a simplified geomechanical relationship, which reduces to a change in pore pressure resulting in a change in stress or strain. This change in stress or strain is then related to a change in porosity or permeability. The coupled reservoir geomechanical model relates a change in stress or strain from a geomechanical simulation to a change in porosity or permeability. Extensive reviews of analytical models (Palmer, 2009) and coupled models (Gu, 2009) are available.

Liu et al. (1999) developed a formulation relating Rock Quality Designation (RQD) and the Rock Mass Rating (RMR) system to permeability and changes in permeability. The derivation to the model developed here is similar for normal deformation; however, it is extended to include the effects of shear deformation and joint persistence. The full derivation of the new dynamic permeability (termed Deisman dynamic permeability - DDP) model, starting from the Navier-Stokes equation derived for fracture flow, is provided in Appendix A along with:

- Comparison versus the Gu (2009);
- Parametric analysis for: initial σ, E_i, ν, GSI, h, k_{ii}, d_i;
- Modelling the permeability data from GH3, GH7, GH10, E8, E10, CR tests;
- Modelling the Somerton et al (1975) data sets;

Permeability

An idealized coalseam is shown with orthogonal and persistent bedding planes, face and butt cleats (or fracture sets) is shown in Figure 130. The permeability in the "*i*" direction (k_{ii}) is due to the summation of flow through fractures existing in the "*ij*" and "*ik*" planes (46). These fracture have spacings s_k, s_j and apertures b_k, b_j respectively, where the permeability of a single joint is expressed as 47.

$$k_{ii} = k_j + k_k \tag{46}$$

$$k_i = \frac{1}{12 s_i} b_i^3 \tag{47}$$

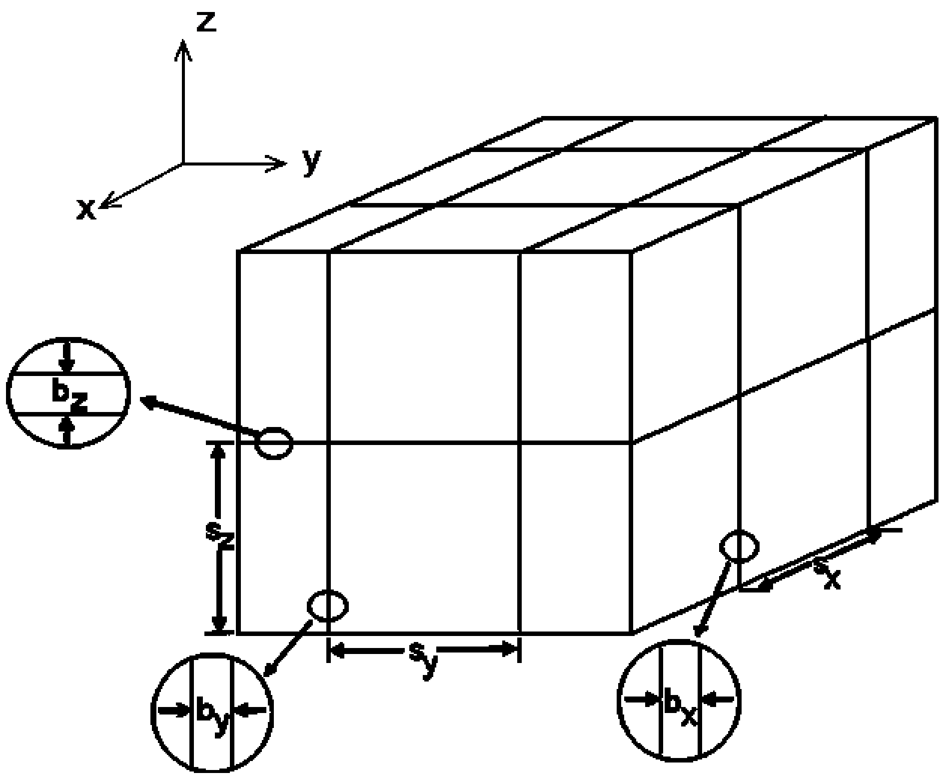

Figure 130. Idealized coal mass with three joint sets (bedding plane, face and butt cleats) and joint set spacings, s_x, s_y, s_z along with the associated hydraulic apertures (b_x, b_y, b_z).

A more practical idealization of the coalseam is where the fracture sets (cleats) are not persistent (Figure 131). In reality, fractures are not through going, but terminate on each other (butt cleat terminate on face cleats, and face and butt cleats terminate on bedding planes). Therefore, if the persistence (p_i), which is a value between 0 and 1 (Cai et al, 2004), is included, the permeability for each fracture becomes (48):

$$k_i = \frac{p_i}{12 s_i} b_i^3 \tag{48}$$

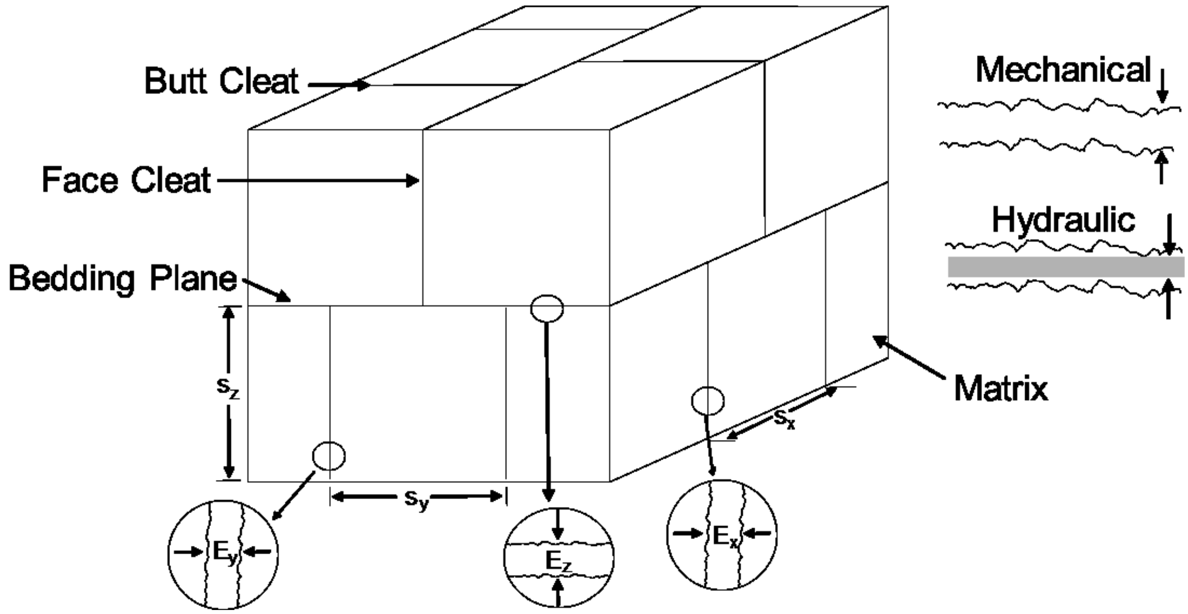

Figure 131. Idealized coal block showing orthogonal, impersistent fractures as well as the mechanical and hydraulic apertures.

Substituting (48) into (46) and rearranging gives an expression for the hydraulic aperture of each fracture set (49), which is similar to Liu et al 1999, but includes p_i:

$$b_i = \left[\frac{6s_i}{p_i} (k_{kk} + k_{jj} - k_{ii}) \right]^{1/3} \qquad 49$$

Strain Dependent Permeability Model

In this work, no differentiation is made between the change in hydraulic aperture and the change in mechanical aperture. Gu (2009) uses a relationship developed for large apertures in hard rock to relate hydraulic to mechanical aperture; however, for coal data does not exist to support this relationship. Therefore, the principle permeability (k'_{ii}) of the reservoir changes with time due to changes in individual joint set permeability (k'_i) (50) caused by changes in fracture aperture (Δb_i) and/or fracture spacing (Δs_i) is (51):

$$k'_{ii} = k'_j + k'_k \qquad 50$$

$$k_i' = \frac{p_i}{12}\frac{\left(b_i + \Delta b_i\right)^3}{(s_i + \Delta s_i)} \quad (51)$$

The final expression for a k'_i as a function of normal strain ($\varepsilon_{RM,ii}$), shear strain ($\varepsilon_{RM,ij}$), shear modulus reduction ratio (G_{RR}) and joint dilation angle (d_i) in a coal mass is (52):

$$k_i' = \frac{p_i}{12(s_i + \Delta s_i)}\begin{bmatrix} b_i + (s_i + \Delta s_i)\varepsilon_{RM,ii}\left(1 - E_{RR}\right) + \\ (s_i + \Delta s_i)\left(1 - G_{RR}\right)\left(\varepsilon_{RM,ij}\tan d_i + \varepsilon_{RM,ik}\tan d_i\right) \end{bmatrix}^3 \quad (52)$$

The $\varepsilon_{RM,ij}$ should be taken at the absolute value to ensure that as shear displacement occurs, the resultant dilation contributes to a positive change in aperture. Gu and Chalaturnyk (2010) also note, and is illustrated by the volumetric strain data from Medhurst (1996), that dilation only occurs after a certain minimum amount of shear strain has occurred ($\varepsilon_{RM,ij\ min}$). Therefore, (52) is partitioned into two equations where (53) is relevant for strain below the strain dilation threshold, and (54) should be used above the threshold:

$$k_i' = \frac{p_i}{12(s_i + \Delta s_i)}\left[b_i + (s_i + \Delta s_i)\varepsilon_{RM,ii}\left(1 - E_{RR}\right)\right]^3 \ when\ \varepsilon_{RM,ij} \le \varepsilon_{RM,ij\min} \quad (53)$$

$$k_i' = \frac{p_i}{12(s_i + \Delta s_i)}\begin{bmatrix} b_i + (s_i + \Delta s_i)\varepsilon_{RM,ii}\left(1 - E_{RR}\right) \\ + (s_i + \Delta s_i)\left(1 - G_{RR}\right)\left(\left|\varepsilon_{RM,ij} - \varepsilon_{RM,ij\min}\right|\tan d_i\right) \\ (s_i + \Delta s_i)\left(1 - G_{RR}\right)\left(\left|\varepsilon_{RM,ik} - \varepsilon_{RM,ik\min}\right|\tan d_i\right) \end{bmatrix}^3 \ when\ \ \varepsilon_{RM,ij} > \varepsilon_{RM,ij\min} \quad (54)$$

Porosity Model

Once the hydraulic apertures are calculated, the hydraulic porosity of the facture sets can be calculated. The hydraulic porosity differs from the actual pore volume existing in the fracture as it is based on flow measurements. If the mechanical aperture can be determined by taking into account the physical roughness or tortuosity of the fracture, then the actual porosity could be calculated (Gu and Chalaturnyk, 2006). The total joint porosity ($\eta_{f,T}$) can be calculated as a summation of each individual joint set ($\eta_{f,i}$) through (55).

$$\eta_{f,T} = \sum \eta_{f,i} = \sum \frac{p_i b_i}{s_i} \quad (55)$$

The equations developed for Δb_i can also be used to create an expression for change in porosity due to deformation and added to the initial aperture (b_i). The new fracture porosity can then be calculated through (56):

$$\eta'_{f,T} = \sum \eta'_{f,i} = \sum \frac{p_i(b_i + \Delta b_i)}{(s_i + \Delta s_i)} \quad (56)$$

Dynamic Permeability Data

The permeability measurements on CE4, CE6 and UA5 specimens from the "Unconventional Triaxial with Permeability and Particle Size" laboratory program were best fit with the DDP model. Several model variables were assumed and kept constant for all of the model fits, including: persistence ($p_1 = 0.5$, $p_2 = 0.7$, $p_3 = 0.99$), dilation angle ($d_i = 10$), and shear strain cut off ($\varepsilon_{RM,ij\ min} = 0.001$). The Young's modulus and 'h' values from the "Conventional Triaxial Compression with Velocity and Permeability" program on the Cardinal River coal specimen were selected at the starting point to fit the measured permeability data. The three coal specimens were also considered mechanically isotropic.

The DDP model was best fit by using the initial stress and corresponding permeability. This initial permeability value was used to estimate *GSI* and corresponding fracture spacing (based on Figure 132). The stress path was then used to calculate the strain path and the corresponding permeability. The DDP model was fit to the data by adjusting E_i, v, h, and *GSI*, and adjusted until a reasonable match, ensuring the inputs were within the bounds of the laboratory testing results. The model inputs for CE4, CE6 and UA5 are listed in Table 34 along with the final R^2 value and the stress path and corresponding permeability is shown Figure 133, Figure 134, and Figure 135.

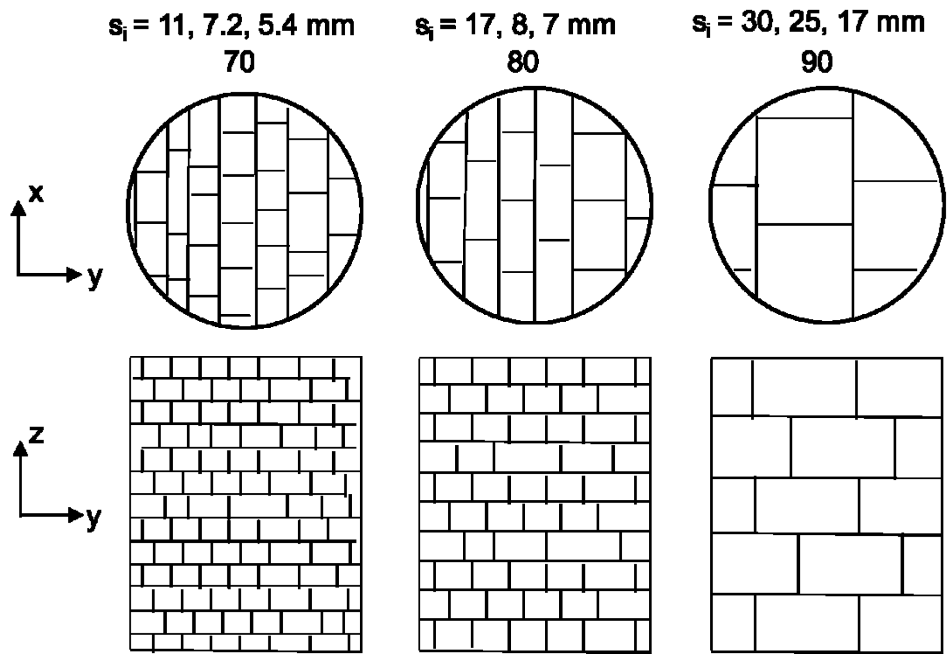

Figure 132. Illustration of fracture spacings in the x, y, and z direction and GSI for synthetic coal specimens with constant fracture persistence.

Table 34. DDP model inputs for CE4, CE6 and UA5 laboratory permeability results.

Test ID	E_i	ν	GSI	h	s_1	s_2	s_3	R^2
	GPa			MPa	mm	mm	mm	
CE4	3.6	0.30	85	5.0	20	17	13	0.999
CE6	3.5	0.25	90	3.2	30	25	17	-0.111
UA5	3.9	0.27	90	2.3	30	25	17	0.944

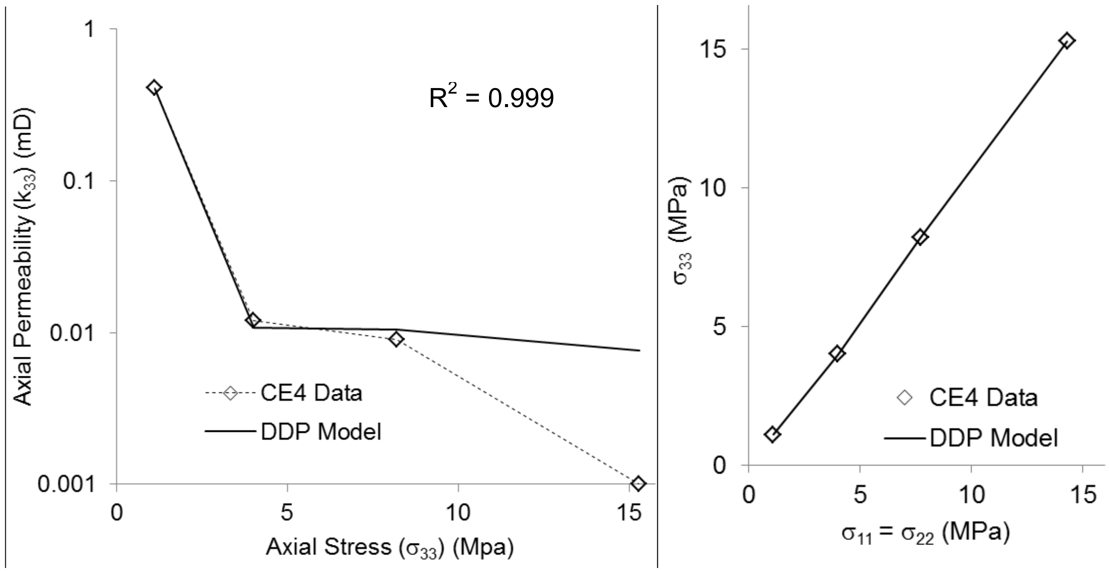

Figure 133. Best fit of the DDP model and stress path against laboratory measurements of permeability on the CE4 specimen ($R^2 = 0.999$).

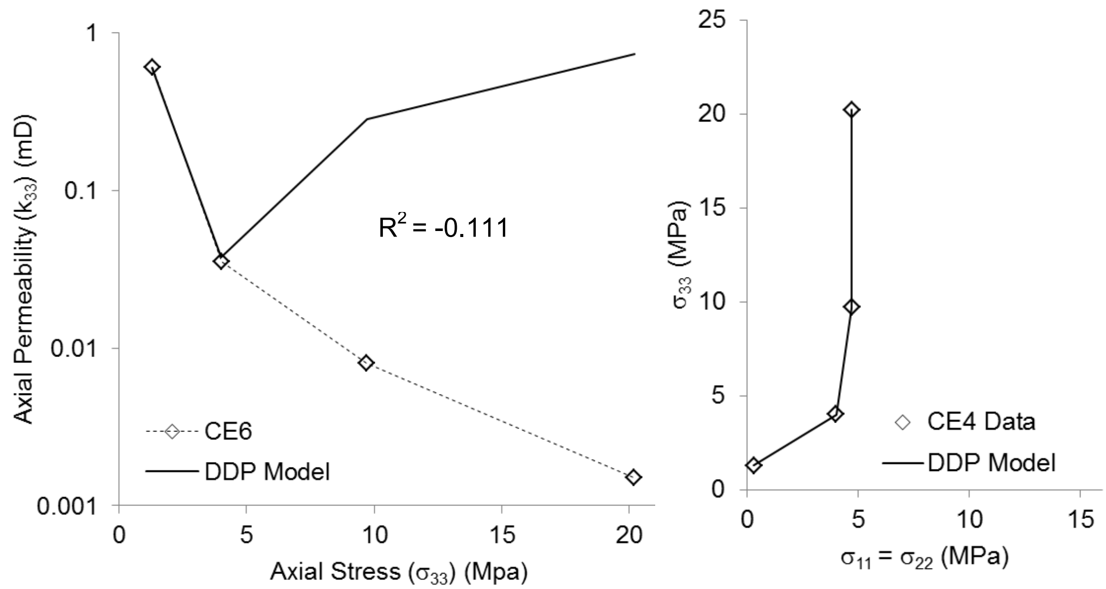

Figure 134. Best fit of the DDP model and stress path against laboratory measurements of permeability on the CE6 specimen.

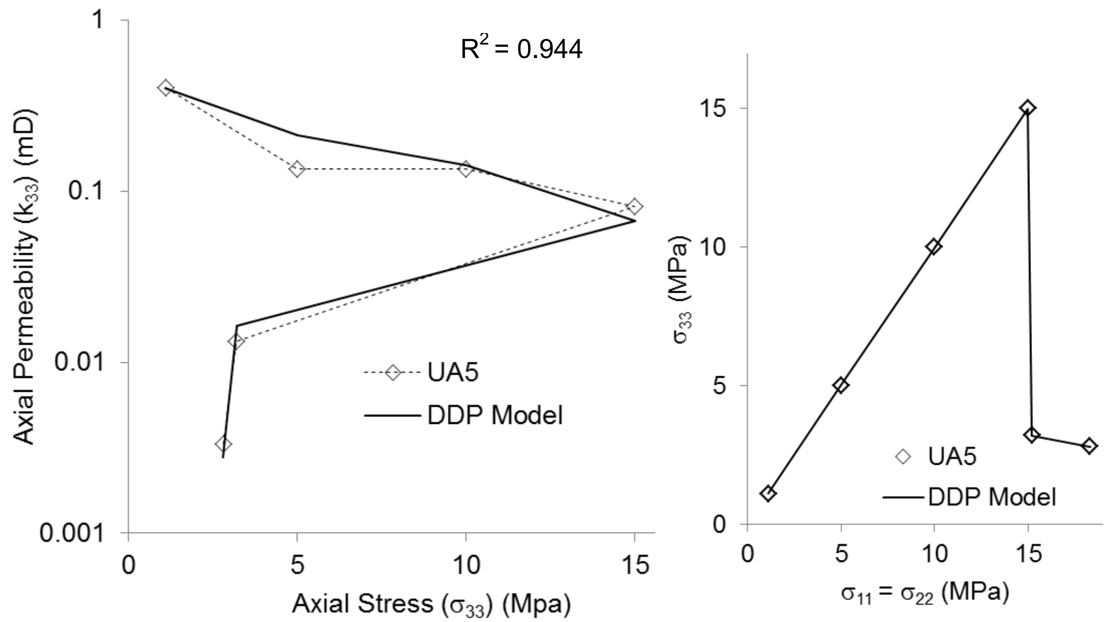

Figure 135. Best fit of the DDP model and stress path against laboratory measurements of permeability on the UA5 specimen.

Dynamic Permeability Discussion

The DDP model is able to capture the change in vertical permeability due to isotropic (CE4) and horizontal stress changes (UA5), but the model is not capable of capture vertical permeability changes due to large changes in vertical stress (CE6). Therefore, the model should be used with caution if large vertical stress anisotropy is expected and accurate vertical flow is required in coal.

Specimen CE4 Results

In the CE4 specimen test, isotropic loading resulted in a decrease in permeability until a minimum permeability was reached at 4 MPa. A slight stress anisotropy (0.5 MPa) was applied to the specimen (σ_{11} = 8.2 MPa, $\sigma_{22} = \sigma_{33}$ = 7.7 MPa) at the next stage which created an overall decrease in vertical flow apertures and associated permeability. The final stress state also had 1 MPa anisotropy, but overall an overall stress increase (σ_{11} = 15.3 MPa, $\sigma_{22} = \sigma_{33}$ = 14.3 MPa), causing a vertical permeability decrease. The mechanical input for the DDP model was all reasonable and agrees well with measured laboratory results (E_i = 3.5 GPa, ν = 0.3, h = 3.9 MPa) and the predicted permeability did follow the overall measured permeability well (0.999), except for the final data point.

Specimen CE6 Results

In the CE6 specimen test, the DDP model matched the measured results when moving from stress state 1 ($\sigma_{11} = 1.3$ MPa, $\sigma_{22} = \sigma_{33} = 0.3$ MPa) to stress state 2 ($\sigma_{11} = 4$ MPa, $\sigma_{22} = \sigma_{33} = 4$ MPa) using reasonable geomechanical data. However, after this point, the DDP models ability to match the change in axial permeability due to applied axial stress was very poor.

Initially the stress field was isotropic, and then the axial stress increased in compression ($+\Delta\sigma_{33}$) (Figure 136). This resulted in a compressive axial strain ($+\Delta\varepsilon_{33}$) and a corresponding dilative radial strain due to Poisson's effect ($-\Delta\varepsilon_{11}$,$-\Delta\varepsilon_{11}$). The axial strain caused the horizontal fractures to close ($-\Delta b_3$), while the radial strain caused the vertically orientated fractures apertures open ($+\Delta b_1$, $+\Delta b_2$) (see equation 50). The fluid travels vertically through the vertical fractures (k_1, k_2), which terminate on the horizontal fractures (k_3). Fluid then must flow horizontally, through a reduced aperture, until a vertical fracture is reached. Therefore, the decrease in horizontal aperture caused the vertical permeability of the specimen to decrease. In the DDP model, there is no reasonable method to account for the influence of the flow path on the directional permeability, and thus the model was unable to predict the change in vertical permeability due to the applied axial stress.

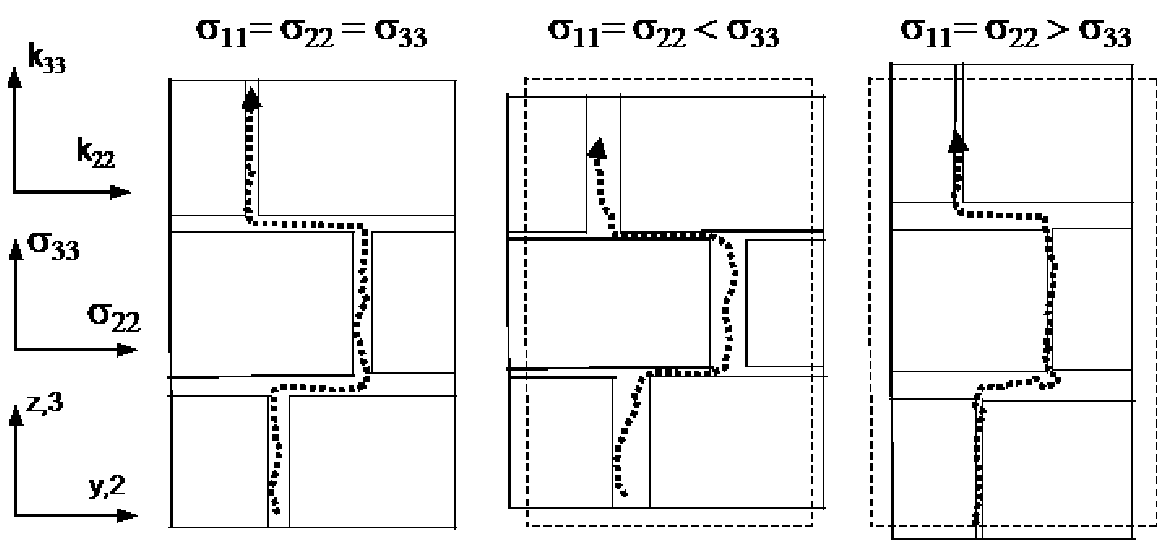

Figure 136. Cross sectional representation of fluid flow path (dotted path with arrow) through deformed fractures/cleats and in a "real" coal under different stress states with original specimen size/shape is shown by the dashed rectangle

Specimen UA5 Results

In the UA5 specimen test, the DDP model matched the measured the complex stress path and resulting axial permeability very well (R^2=0.994). The input parameters for the model were all reasonable: E_i = 3.9 GPa, ν = 0.27, h = 2.7 MPa, and GSI = 90.

Again, the stress field was initially isotropic and loaded incrementally to 15 MPa ($\sigma_{11} = \sigma_{22} = \sigma_{33}$ = 1, 5, 10, 15 MPa) causing the all fractures to close. The axial stress was held constant and the radial stress was decreased ($-\Delta\sigma_{11}$,$-\Delta\sigma_{22}$) which resulted in dilative radial strain change ($-\Delta\varepsilon_{11}$,$-\Delta\varepsilon_{22}$) causing the vertical apertures to increase ($+\Delta b_1$, $+\Delta b_2$). The radial stress decrease also created compressive axial strain change ($-\Delta\varepsilon_{33}$), which lead to horizontal aperture closure ($-\Delta b_3$) (Figure 136). As in the previous loading case, the flow path through the horizontal fractures is not considered in the calculation of vertical permeability. In the UA5 permeability test modeling, the DDP model better predicts the overall behaviour and captures the general shape of the permeability changes.

9.3 Conclusions

The strength, Young's modulus, methane sorption, methane strain and dynamic permeability of coal have been modelled with the discussion of model fits and short comings of laboratory results presented. In general, the strength and Young's modulus measured in the laboratory were well fit using Hoek-Brown and Hoek and Diederichs respectively, using GSI and D as a function of h. The equation relating modulus to *GSI* was developed using hard rock experiments and may be refined for coal; however, it does predict coal behaviour reasonably well. The strength and modulus results from scaled SRM testing do not display acceptable behaviour, and much improvement is required to better represent the intact matrix and joints. The sorption of methane onto coal with changes in isotropic effective stress was modelled using a simple equation which may be suitable for engineering applications, however, the associated induced linear strains were not definitive enough to warrant modeling. A strain based three dimensional dynamic permeability model, which includes mechanical properties (*GSI*, E_i, ν, and dilation angle) was developed. The model showed good agreement for observed laboratory measurements of permeability results for several non-isotropic unconventional stress paths as well as several isotropic results from the literature.

10 Applications: Characterizatoin and reservoir geomechanical simulation of CNOOC-Nexen's CBM field for coal stability and production

This section applies the hydrogeomechanical characterization for coal seam reservoirs to CNOOC-Nexens CBM field. Three hydro mechanical earth models are built using real data obtained from the field and supplemented with data from Chapter 9. The hMEM's are then used to create:

- static 3D wellbore model to assess wellbore drilling azimuths;
- uncoupled reservoir simulations to investigate coal failure in the near well area; and
- coupled flow model to assess the impacts of geomechanics on production.

The study on the Nexen's CBM field was completed as a research service contract between the 2007 and 2010. The work was released for publication in 2014 and 2015 as two conference papers. An assumption of reducing the dynamic Young's modulus by 10% to scale to the static Young's modulus was made prior to the analysis of the data in Chapter 7.6. This assumption was shown to be incorrect based on the limited testing and results may have to be reduced by 30-40%, although more work is required. This study fits into the overall workflow as shown in Figure 137, demonstrating the full application of the characterization workflow and applications to borehole stability and coupled reservoir geomechanical simulation.

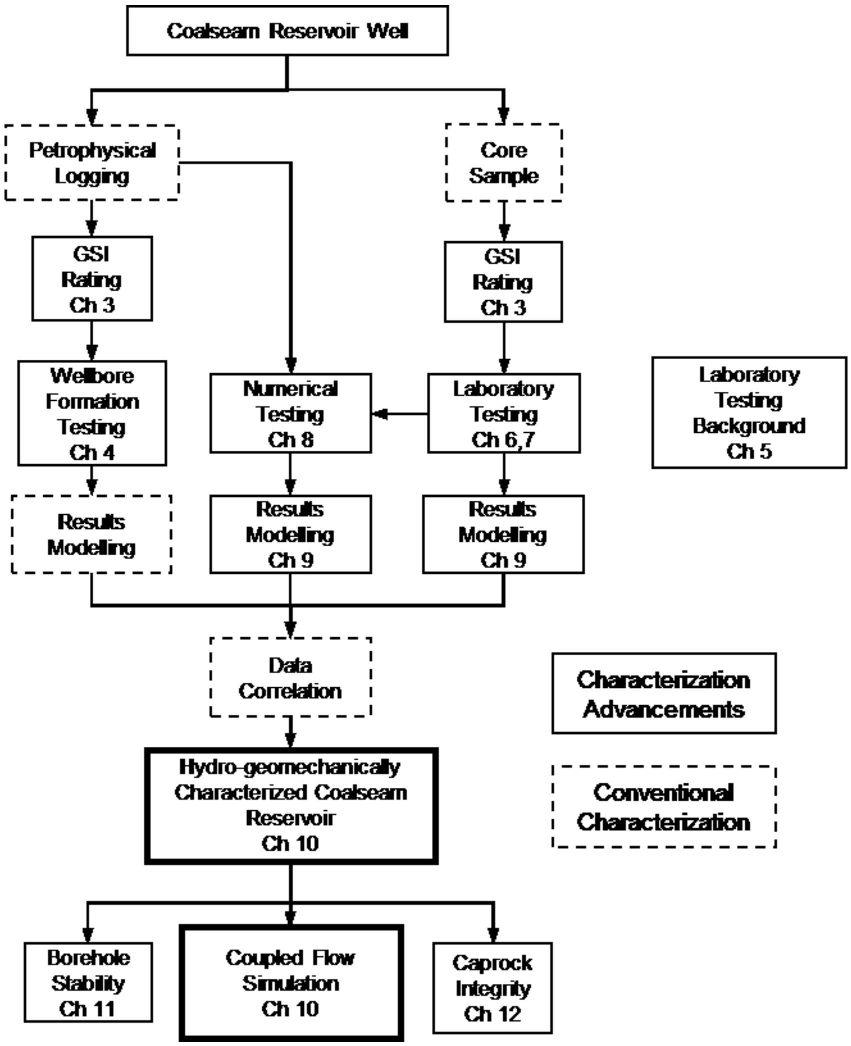

Figure 137. Coalseam reservoir hydro-geomechanical workflow showing where the hydrogeomechanical characterization and coupled flow simulations fits into the overall characterization approach.

10.1 Introduction

In Alberta, the Mannville coal formation between 900m and 1300m has two or, in some places three, seams between 1 and 3 meters thick. The thickest of these seams is generally targeted with horizontal wells for CBM production. Horizontal wells have been used extensively in the USA, but the transfer of the technology to Alberta has had limited successes. This is manifested in production rates from the Mannville usually being less that 3000 m^3/day. Several reasons for the differences in success rates between Alberta and the USA have been postulated, and of the reasons are misunderstood geomechanical effects on production.

Several reasons for the limited success of horizontal wells production have been postulated, with geomechanical effects being included. The list of geomechanical effects includes: high stress fields, high stress anisotropy, weak coal, and coal natural fracture (cleat) closure. For flow the geomechanical effects are cleat closure due to high stress and lack of cleat opening due to low coal shrinkage from gas desorption.

10.1.1 Nexen Energy CBM Field Project Study

Nexen has drilled hundreds of horizontal wells since 2003 in the Manville formation at 950-1100m depth with variable success. Some wells have produced well for many years while some wells have had undergone multiple work overs, and production downtime (1-24 weeks of lost production), due to coal fines plugging downhole pumps or other coal fines related issues (Figure 138).

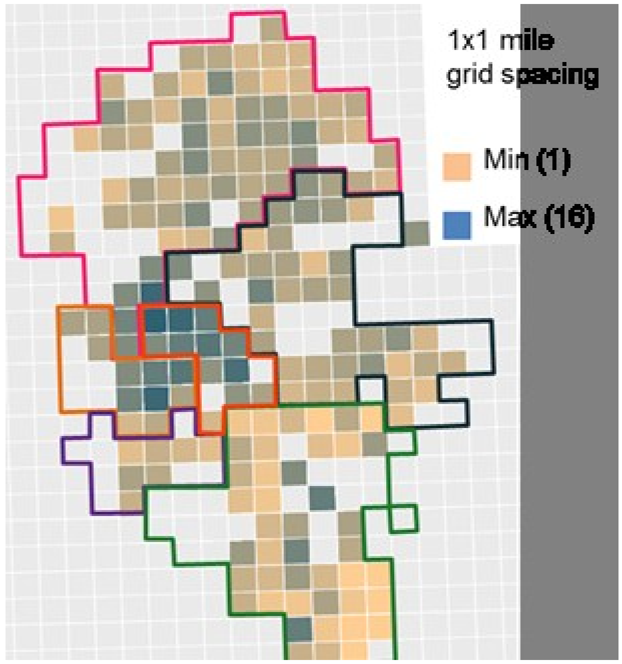

Figure 138. Total well pad work overs from 2002-2014 of the CBM field.

To help understand the geomechanical influences on production, the methodology to characterize the CBM reservoir using the Geological Strength Index (GSI) was applied to Nexen's Manville CBM field. This allowed for consistency across Nexen's CBM field and between the three modeled areas. As well, the use established GSI relationships were possible to help scale the mechanical properties measured in the laboratory to the field.

The methodology used data collected from Nexen's database, third party studies, and Alberta Energy Regulators (AER) core repository. The data was integrated to develop three horizontal well pad hydrogeomechanical (hMEM) earth models. The hMEM models were then used to build three types of models. These were:

- 3D geomechanical wellbore models to analyze initial well orientations for optimal stability during drilling;
- dynamic uncoupled reservoir geomechanical models which were history matched to provide insight into stress field evolution during production. The dynamic stress field was extracted at several locations along the horizontal wells and used to assess wellbore failure during production.

- dynamic iteratively coupled reservoir geomechanical model to help understand the influence of effective stress changes and gas desorption on gas production for three of Nexen's horizontal well pads. One goal was to determine if there will be permeability rebound caused by volumetric strain (shrinkage) due to gas desorption as postulated by many researchers.

Each of these simulations can provide insight into CBM field development issues such as: optimum wellbore azimuth, coal failure during drilling or production creating coal fines, and production increases or decreases due to geomechanical effects. Three locations in the Manville coalseam were examined overall, but only one of the uncoupled simulation well pad models (three lateral wells) is for discussed here for wellbore stability.

10.2 Background and Methodology

10.2.1 Hydrogeomechanical Earth Model

Mechanical Earth models (MEM) (1D/2D/3D) are developed to represent the current geomechanical state of the reservoir and surrounding formations (Desroches et al 2006). In this case, the flow model and the mechanical model were integrated, thus the addition of the 'hydro' in Hydrogeomechanical Earth Model (hMEM). The hMEM's were constructed using Paradigm's Gocad geomodeling package. An hMEM consisted of the reservoir hydromechanical units extending above and below the reservoir, the well paths and wellbore geometries, and all the mechanical and flow properties listed above.

10.2.2 2D Geomechanical model

To help analyze the stability of horizontal wellbore at different azimuths, a simple 3D geomechanical plastic model was built in using Itasca's FLAC3D. A single horizontal wellbore was used and the stress field rotated to analyze different drilling azimuths. The inputs from the hMEM were used and all inputs were kept constant (ie pore pressure and stress were not changed to simulate changes with time).

10.2.3 Reservoir Geomechanical Simulation

Coupled reservoir simulations have been used extensively to include the effects of stress/strain on the flow properties of a CBM reservoir (Gu 2009), (Connell 2009). Uncoupled reservoir geomechanical simulations can be used to analyze the influence of production on the reservoir stress field, without updating flow properties (Deisman and Chalaturnyk 2012). For this study, the flow history matched to Nexen's field data then uncoupled and sequentially coupled simulations were completed.

The general coupling process for CBM using two simulators was developed by Gu (2005a) and uses CMG's GEM for flow simulation and Itasca's FLAC3D geomechanical simulation. A Visual Basic code was developed to control each program, format data, and update permeability maps. The uncoupled simulation runs GEM until completion, then extracts pressures and gas contents and passes them to FLAC3D. The explicitly coupled simulation was set up to run GEM for a time step then extract pressure and gas content at the end of the step. The updated pore pressure creates a change in effective stress. The change in gas content leads to a change in strain. Once the mechanical model has come to equilibrium with the new pore pressures and gas content, the total strain is extracted and used to create a new permeability map based on the equations from chapter 9.2.1. The new updated permeability map is then sent back to GEM, and the process repeated until the end of the total simulation time.

Coupled reservoir geomechanical modeling by Gu and Chalaturnyk (2010) showed that updating porosity is a secondary effect when considering geomechanical in coal seam reservoir. Therefore, dynamic porosity changes in the coupling modeling were not included.

10.3 Data Input

The characterization methods above were applied Nexen's Mannville CBM projects and three of the wellpads in the area were extracted for simulation. The simulation models were each built to cover a 9km by 9km area where the average coalseam thickness was 3 m. The models were labeled A, B and C where A is a trilateral well, and B and C are dual lateral wells and the depths, total vertical stress, and pore pressures varied for each area.

The model well configuration, axes directions, stress directions, and monitoring points (A, B, C) are shown in Figure 139. The reservoir and geomechanical models all contained 57 600 and 576 000 grid block respectively. The geomechanical model was 10 layers thick, with 6 above and 3 below the coal seam. The wells were drilled for the main lateral leg orientation to intersect the maximum permeability while the two drain holes are orientated to intersect the minimum permeability.

To drill horizontal multilateral wells, first a main 'mother bore' well is vertically drilled, in these cases using water as the circulating fluid, then the horizontals are side tracked off the mother bore. Over Nexen's CBM field, several (not all) of the mother bores were cored, geophysically logged (FMI, Dipole sonic, Density logs, etc.), and had fluid loss rates while drilling recorded. Some of the collected data was used to establish relationships to aid in areas were data did not exist.

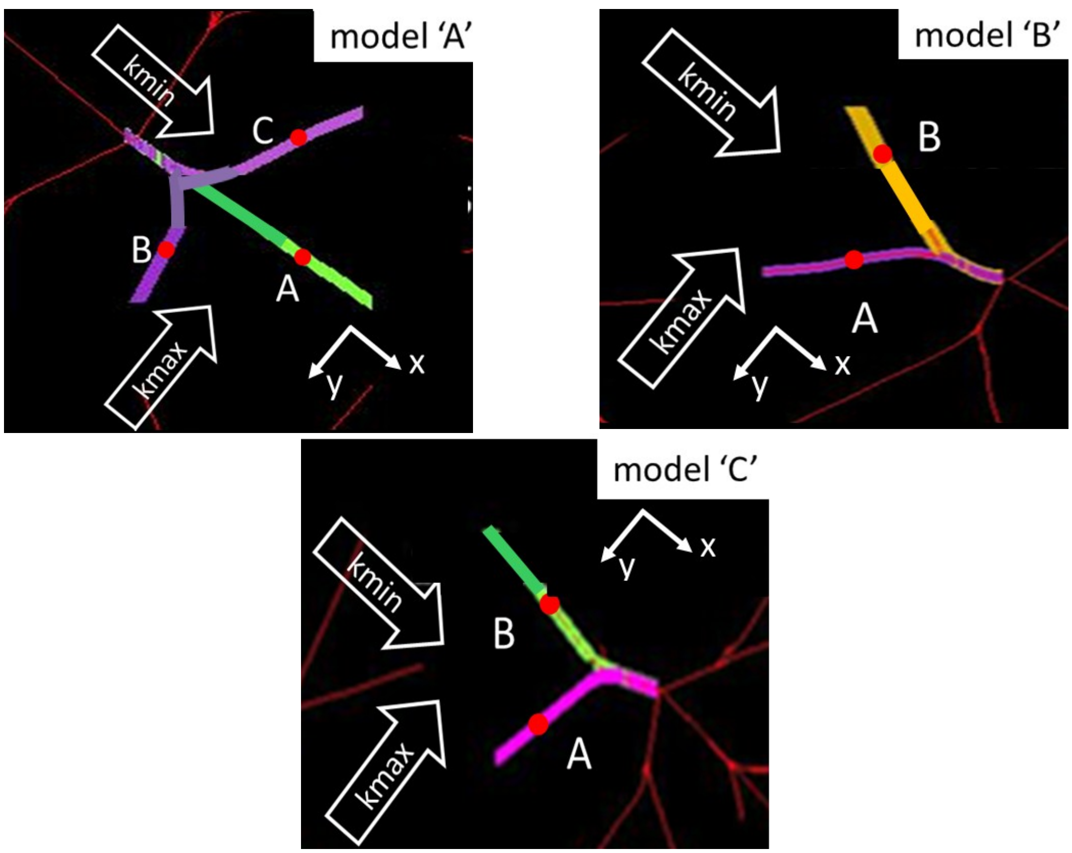

Figure 139. Plan view of the model well configurations, axes directions, stress directions and monitoring points.

10.3.1 GSI – Permeability Correlations

A main component of the study was to consistently characterize the geomechanical characteristics of the coal across Nexen's Manville formation for local well comparisons. GSI was used to accomplish this characterization by assigning values to coal core specimens examined at the AER core repository.

The coal core stored at the AER core repository was slabbed (cut lengthwise at 1/3 the diameter) and left exposed to air, thereby making any laboratory flow or mechanical tests difficult and results unrepresentative of in situ values. However, the slabbing did allow the cleating of the coal to be visible and GSI easily assigned. Several cores from multiples wells inside and outside of the study areas were logged and GSI distribution maps across the entire field possible. In wells where GSI and FMI logs or GSI and fluid loss while drilling logs were available (Figure 140), the data was plotted and correlations developed for use where limited data existed.

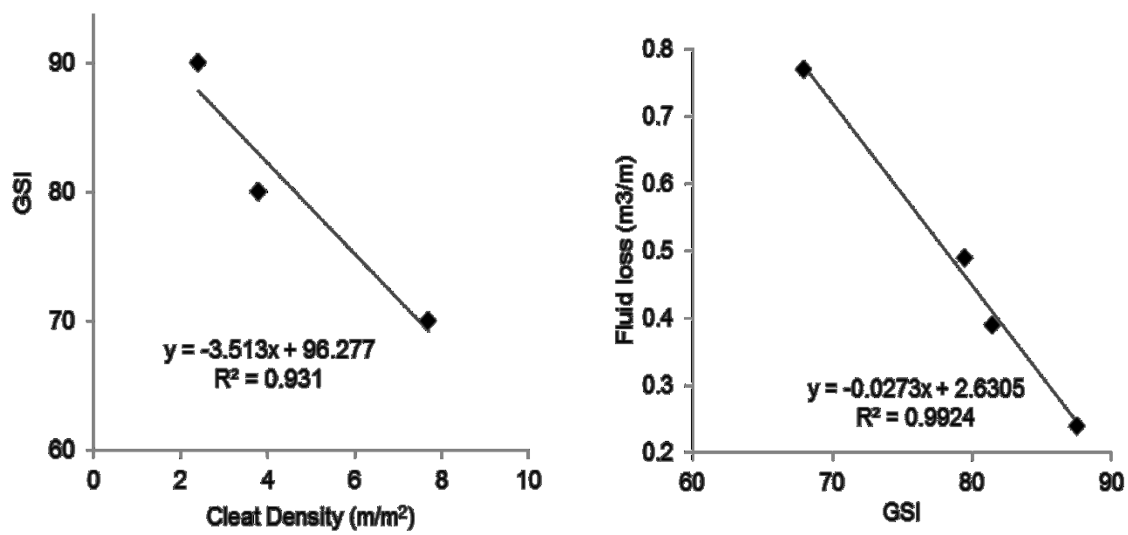

Figure 140. Interpreted GSI values plotted against FMI logged coal cleat density and fluid loss while drilling from the same wellbores

10.3.2 Mechanical Inputs

Stress Field

Measuring all three principal stresses at depth is very difficult, and therefore the stress field presents the largest uncertainty almost any geomechanics project. The stresses were determined by first using the density logs from each of the model mother bore wells were used to create a vertical stress profile. The minimum effective stress profile was created measured during a large regional scale study which analyzed minifrac and hydraulic fracturing data, and pore pressures. A well 22 km away from the project area had several mini fracs completed. This vertical profile was used as a control point to create a minimum horizontal effective stress profile and an S_o profile using:

$$S_0 = \frac{Minimum\ Horizontal\ Effective\ Stress}{Vertical\ Effective\ Stress} \qquad 57$$

This S_o profile was applied to the vertical effective stress profile to calculate a minimum effective stress profile for model A. The maximum horizontal stress was estimated to be slightly greater than the vertical stress as the CBM field is in a strike-slip basin, based on results from Bell et al., (1994). This maximum horizontal stress value is always debatable if it is not directly measured. The reservoir pore pressure was measured across the CBM field and it was assumed the matrix and cleat pressures were in equilibrium (Figure 141) where the orientation of stress field was taken from Bell and Babcock (1986) (Figure 142). A complete list of the maximum and minimum stress field and pore pressures values used at the reservoir depth for each of the models is provided in Table 35.

$$K_0 = \frac{Maximum\ Horizontal\ Effective\ Stress}{Vertical\ Effective\ Stress} \qquad 58$$

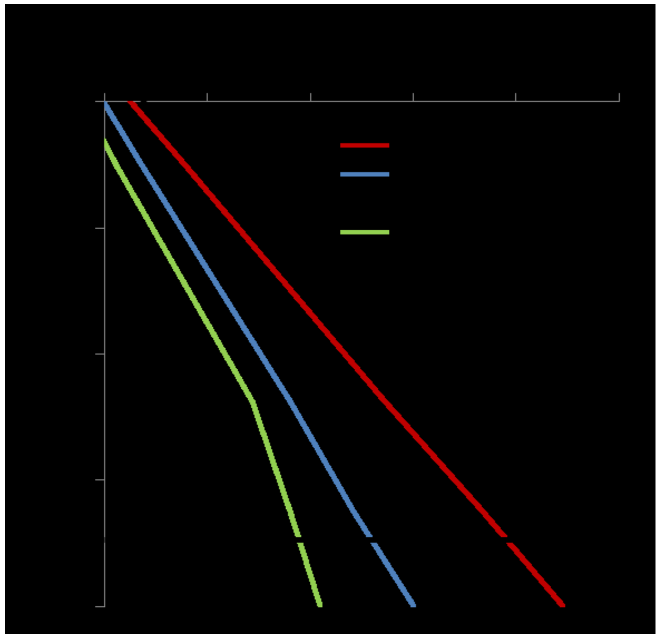

Figure 141. Effective vertical, maximum and minimum effective stress, and pore pressure profiles for model A.

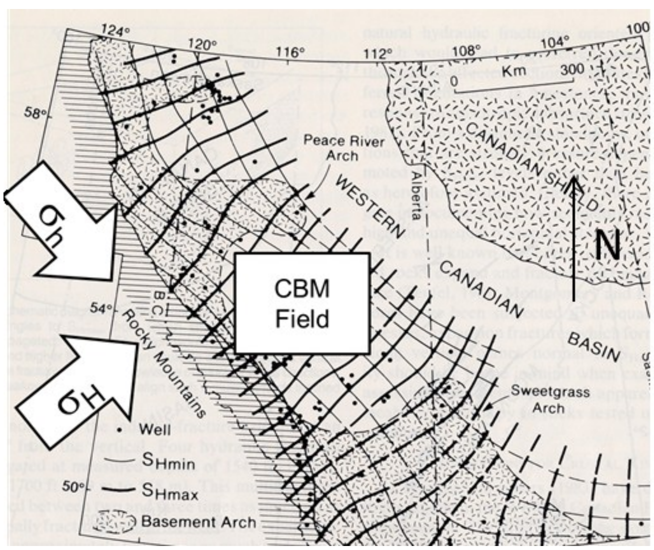

Figure 142. Stress trajectories in Western Canadian Basin and Nexen's CBM field location (modified from Bell and Babcock, 1986).

Table 35. Summary of the total and effective stress fields and the pore pressures.

Property	Units	A		B		C	
		Min	Max	Min	Max	Min	Max
Min Total Stress, i	MPa	17	17	13	14	13	13
Max Total Stress, j	MPa	23	23	26	27	21	21
Vertical Total Stress, k	MPa	21	21	24	25	23	23
Min Eff. Total Stress, i	MPa	7.8	7.8	5	5	4.3	4.3
Max Eff.Total Stress, j	MPa	13.8	13.8	18	18	12.3	12.3
Vertical Eff. Total Stress, k	MPa	11.8	11.8	16	16	14.3	14.3
Fracture Pressure	MPa	9.2	9.2	8	9.2	8.7	8.7
Matrix Pressure	MPa	9.2	9.2	8	9.2	8.7	8.7

Constitutive Properties

Several density (ρ) logs and dipole sonic logs measuring normal (V_p) and shear (V_s) wave velocity were available for analysis, which allowed for the calculation of the dynamic Young's modulus (E_D) and Poisson's ratio (ν_D). However, correlations between static and dynamic properties were not available for this CBM field, therefore the dynamic values were reduced by 10% to represent intact static values (NOTE: after further review and results from laboratory testing above, 30-40% is a more realistic reduction). Additionally, core was collected and an average GSI of 70 (GSI = 65, 65, 80) was assigned for to the 2 m coalseam, therefore the Young's modulus was scaled to the field using GSI. The generalize workflow to estimate the mechanical properties was:

1. Select the wells which have dipole sonic logs;
2. Calculate the dynamic modulus from the measure formation velocity;
3. If only a single P wave (compression wave) was run, correlate the compression wave to the S wave (shear wave) through density (this relationship is generally poor).
4. Use this log to calculate dynamic Young's modulus and dynamic Poisson's Ratio.
5. Reduce the measured dynamic Young's modulus and Poisson's Ratio by 10% (Note: after recent laboratory testing on analogous core, this reduction value should be closer to 35%).

The dipole sonic logs probe the coal cleats and matrix, but the simulation requires the intact Young's modulus, which was back calculated. The minimum effective stress was measured and it was assumed that the volume of coal probed by the dipole sonic log was not disturbed (D = 0) and the only disturbance which would occur in the coalseam would be from production. Therefore, it was possible to back calculate a dynamic, intact Young's modulus for the coalseam based on the Young's modulus reduction ratio equation. From the approach, a vertical profile for each of the models was created, and the profile for model C is shown in Figure 143.

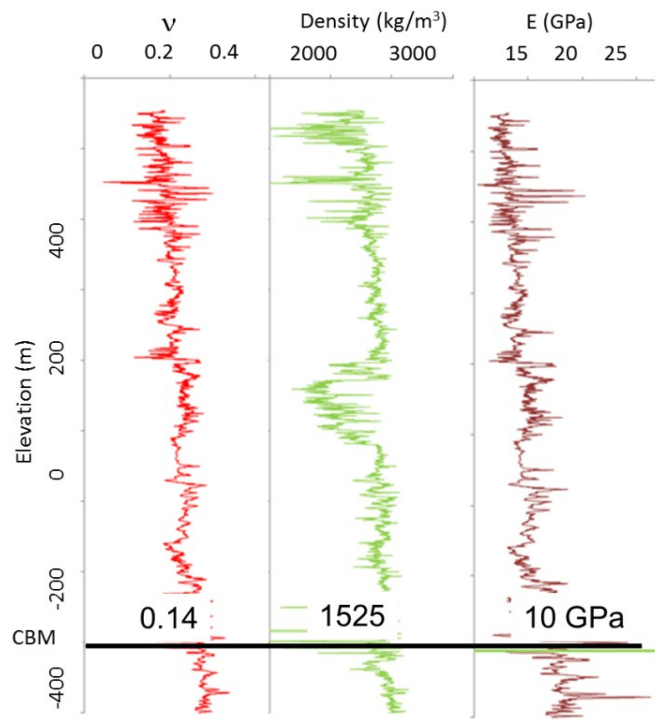

Figure 143. Static elastic mechanical property profile.

After data review for each of the models, the calculated dynamic Poisson's ratio was considered to be too large (>0.4). Also, the h parameter from (2) was not measured. Therefore, laboratory values from 9.1 were used for Poisson's ratio (ν) and h. Due to the lack of geomechanical data, it was not possible to create property distribution maps, therefore only single values were used each CBM model. All mechanical properties used in the modeling are listed . The elastic properties outside of the CBM zone were the same for each model, but varied with depth (Figure 144).

Table 36. Summary of the mechanical properties in each of the hMEM models.

Zone	Property	Units	A	B	C
CBM Reservoir	Intact Young's Modulus	GPa	8.5	6.4	10
	Poisson's Ratio		0.14	0.14	0.14
	h factor	GPa	0.4	0.4	0.4
	GSI		72.5	70	70
	Lang Sorp Strain Press.	MPa	6.0	6.0	6.0
	Max Lang. Sorp. Strain		0.0025	0.0025	0.0025
Over/Underburden	Intact Young's Modulus (GSI=100)	GPa	See Figure 143		
	Poisson's Ratio		0.3	0.3	0.3

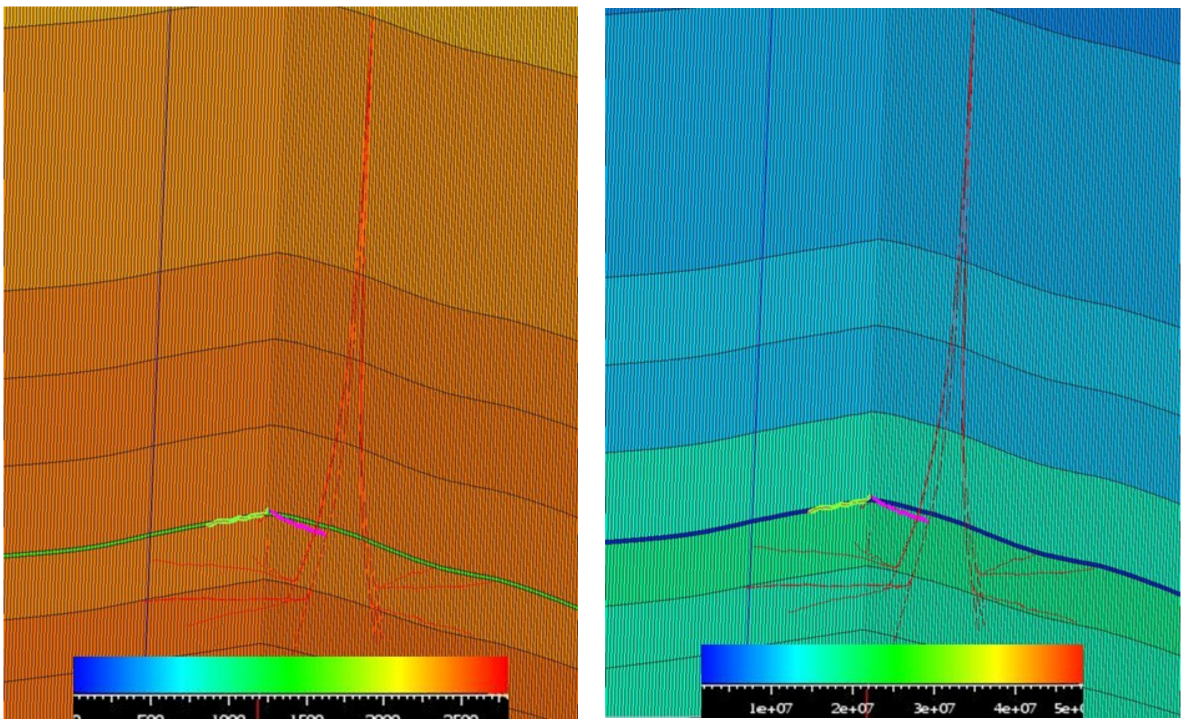

Figure 144. The density (kg/m^3) (right) and Young's modulus (Pa) (left) are shown for model 'B'. The density and Young's modulus profile was held constant for model 'A', 'B', and 'C' outside of the CBM reservoir.

Strength Data

Strength data was unavailable, therefore strength results from analogous coal strength studies were used from data provided in 9.1.1 and summarized in Table 37.

Table 37. Geomechanical input parameters for 2D wellbore stability model.

Property	Coal
Intact Young's Modulus (MPa)	10
Poisson's Ratio	0.14
GSI	70
σ_{ci} (MPa)	20
m_i	6.0
h (MPa^{-1})	4.0

Swelling and Shrinkage

Coal is an organic material, where the surface area of the pores interacts with the contained fluid (CH_4, CO_2, etc) and this interaction causes volumetric changes within the coal (Mitra et al., 2008). Patching (1965) found that different gas pore pressures caused coals samples to change in volume. Mazumder et al., (2006) provides a summary of previously measured linear volumetric strain coefficients with changes in gas pressure. St. George and Barakat (2001) stated that volumetric shrinkage associated with gas desorption has a large influence on the stress field. These changes in stress result in strain changes, which are important for changes in permeability. In this study, the model used by Gu and Chalaturnyk (2010) for strain (ε_{GC}) to due to gas pore pressure (P) was used to capture these volumetric strain effects and is expressed as:

$$\varepsilon_{GC} = \varepsilon_{Lmax} P / (P_{LS}+P) \qquad 59$$

where ε_{Lmax} is the total linear strain at maximum gas pressure and P_{LS} is the Langmuir strain pressure.

The linear desorption strain properties measured on a single coal sample from the CBM field. This was the only sorption strain test completed and was used for all of the modeling. The data does not fit a perfect Langmuir isotherm model however the traditional form of the model is reasonable (Figure 145). The data was fit to equation (3), resulting in ε_{Lmax} = 0.0025 and P_{LS} = 6000 kPa, which are low when compared to published values (Robertson and Christiansen 2007).

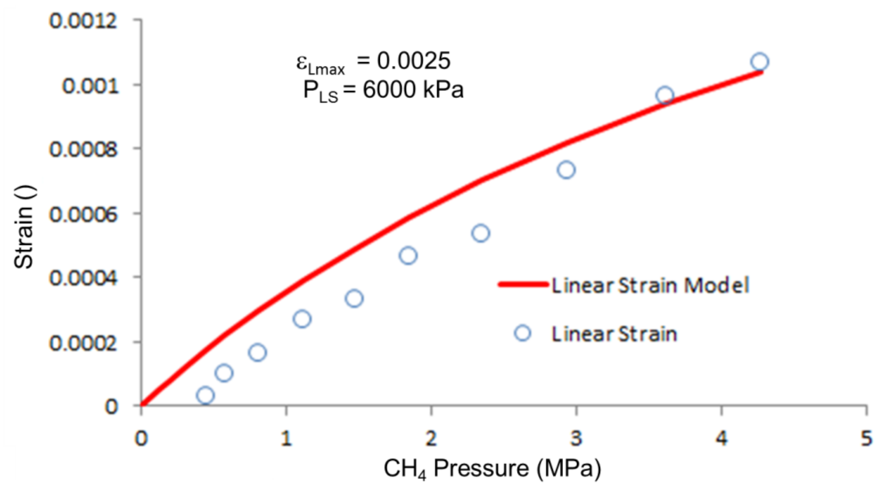

Figure 145. Linear strain experimental data modeled using 59.

10.3.3 Flow Inputs

The flow properties used to populate the hMEM came from extensive petrophysical work completed by the Nexen's CBM team. This data included: density, gas content, desorption isotherm, gas diffusion coefficient, fracture permeability, fracture spacing, and porosity, gas saturations, and relative permeability.

The permeability was measured in the field for each of the main wells through injection testing. This measured permeability is bulk radial flow permeability, which would include flow in three directions. To estimate the directional permeability, the maximum horizontal to minimum horizontal to vertical permeability was assumed to be 4:1:1. Using equations developed by (Liu et al 1999), the fracture spacings, permeability and fracture apertures were iterated until the average cleat density calculated from GSI was roughly equal and all the fracture apertures assumed equal at 60μm. This calculation process was essentially an optimization problem until reasonable values were determined. The fracture porosity was unknown and was estimated at 5%. The matrix porosity was not measured and does not affect simulation results, but is required and was set to 0.001 is given. A summary of the flow data is provided in Table 38.

Table 38. Summary of the minimum and maximum fracture spacings, fracture permeability, and fracture aperture for each model.

Property	Units	A		B		C	
		Min	Max	Min	Max	Min	Max
Frac Perm, x	mD	4.7	4.7	3	6	1	10
Frac Perm, y	mD	1.2	1.2	0.5	1.5	0.5	2
Frac Perm, z	mD	0.4	1	0.2	0.6	0.2	1
Frac Spacing, x	mm	200	200	200	900	150	200
Frac Spacing, y	mm	400	400	10	400	50	50
Frac Spacing, z	mm	100	100	500	2000	300	300
Frac Aperture	μm	60	60	20	50	25	25

To model the reservoir section and remain consistent with the geomechanical simulation, the reservoir model was one vertical block thick. Each of the models had several measurements for gas content and Langmuir desorption isotherms. Property distribution maps and averages for each of the models were created for each required model property. The average methane gas content had a minimum average value equal to 0.288 mol/kg in model B and a maximum average value equal to 0.450 mol/kg in Model A. The desorption coefficient used in modeling was only measured on a few samples throughout the field therefore it was averaged and set to 50 days. The remaining average CBM properties required for modeling methane desorption (Langmuir pressure, Langmuir volume, fracture saturations) are listed in Table 39.

Table 39. Summary of the averaged flow properties in each of the hMEM models.

Property	Units	A	B	C
Frac Porosity	%	5	5	5
Langmuir Pressure	MPa	4.158	6.4	4.74
Langmuir Max CH_4	mol/kg	0.662	0.491	0.51
CH_4 Content	mol/kg	0.455	0.288	0.333
Desorption Coeff (t)	Days	50	50	50
Fracture CH_4 Sat.	%	5	5	5
Fracture Water Sat.	%	95	95	95

10.4 Modeling Results

The ‘model A’ hMEM model was used to create five orientated 3D wellbore models and an uncoupled reservoir geomechanics simulation. The wellbore modeled sections were used to analyze initial wellbore stability and were then used to help assess the dynamic wellbore stability extracted from the uncoupled reservoir geomechanical simulations. Each of the models A, B, and C were also run in iteratively coupled mode to assess the influence of geomechanics on changes in flow and production. An analytical approach was also used to assess the value of sorption strain inclusion in the coupled modeling.

10.4.1 Initial Borehole Stability Analysis

There are several horizontal well drilling direction options in the coalseam and analysis of five horizontal wellbore azimuths was completed. The five directions were selected representing wells drilled aligned with the major or minor maximum horizontal stress and three directions in between (Figure 146).

The vertical stress acting on the wellbore model remains unchanged for each azimuth, but as the wellbore azimuth direction changes between the maximum and minimum stress, the stress horizontal stress acting on the wellbore will change. The horizontal stress was calculated with the tensor rotation matrix and results shown in Table 40 and applied as initial boundary conditions to the FLAC3D model (gravity was neglected). The FLAC3D model (Figure 147) and mechanical properties (Table 37) remained constant.

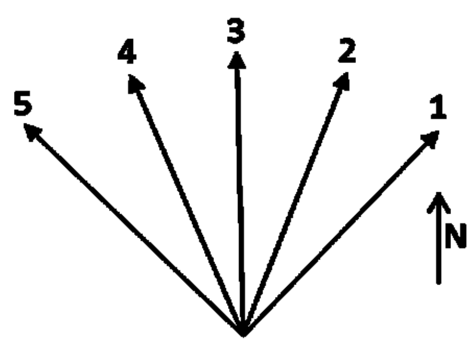

Figure 146. Horizontal well directions for 2D for initial wellbore stability.

Table 40. Horizontal wellbore directions (Figure 146) and resulting stress applied to the cross section of the wellbore.

	Counter Clockwise Angle from East Degrees	σ_{zz} MPa	σ_{zz} MPa	σ_{yy} MPa	σ_{xy} MPa
1	45	20	15	5.0	0.0
2	67	20	15.8	4.2	2.2
3	90	20	18.0	2.0	3.0
4	112	20	20.1	0.1	2.2
5	135	20	21	1.0	0.0

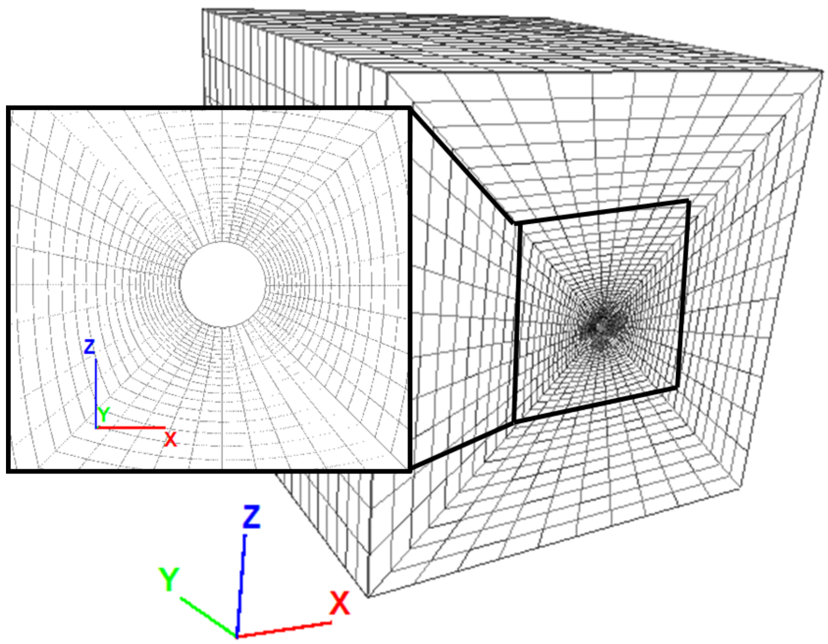

Figure 147. FLAC3D wellbore stability model with fixed bottom and stress boundary conditions.

Results from each of the simulations show that as the wellbore become more aligned with the minimum horizontal stress trajectory, the horizontal failure distance decreases and becomes more uniform. Although failure diameter is still large, results indicate that the preferred drilling direction to minimize the failure zone is in direction 5, which is also the optimum flow alignment (Figure 150). The order of preferred drilling direction for maximum stability, based on the initial stress field and estimated coal properties, is: 5 (135 degrees), 4 (112 degrees), 1 (45 degrees), 3 (90 degrees) and 2 (67 degrees).

Table 41. Results from finite element analyses for horizontal wellbores orientated in multiple directions in the coalseam.

No	Plastic Volumetric Strain	
1 (45°)		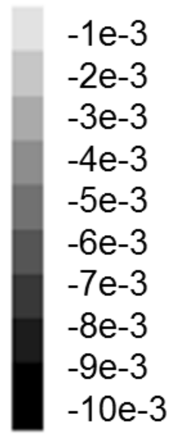
2 (67°)		
3 (90°)	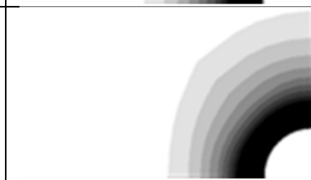	
4 (112°)		
5 (135°)		

10.4.2 Analytical modeling of permeability changes due to pressure depletion

In Nexen's case, the sorption strain measurement was low when compared to published data. Therefore, an analytical assessment of the influence of sorption strain on change in permeability was done prior to the inclusion of the model into the coupled simulations. Through superposition, and assuming the coal remains elastic, the total coal strain (ε_{RM}) is the sum of strain resulting from sorption (3) and strain due to changes in effective stress (ε_E).

$$\varepsilon_{RM} = \varepsilon_{GC} + \varepsilon_E \qquad (60)$$

The elastic strain due to changes in effective stress is calculated through Hooke's law. In this case, for a single element analytical model, where changes are only due to changes in pore pressure, shear stress is not generated, and Hooke's law (using effective stress notation and Biot's coefficient is 1) reduces to:

$$\varepsilon_{Ex} = E_{RM}^{-1}\,[\sigma'_{xx} - \nu\sigma'_{yy} - \nu\sigma'_{zz}]$$
$$\varepsilon_{Ey} = E_{RM}^{-1}\,[\sigma'_{yy} - \nu\sigma'_{zz} - \nu\sigma'_{xx}] \qquad 61$$
$$\varepsilon_{Ez} = E_{RM}^{-1}\,[\sigma'_{zz} - \nu\sigma'_{xx} - \nu\sigma'_{yy}]$$

Using (4), the resulting permeability due to changes in individual strain components from (6) were calculated for gas pressures ranging from 9000 to 0 kPa. Figure 148 shows the changes in permeability due to shrinkage for each model. In model 'A', GSI is slightly higher (72.5) than 'B' and 'C' (70), which results in a larger value of E_{RR} for 'A'. The larger value results in less strain being partitioned to the fracture aperture change defined by (4), thus less permeability reduction.

Figure 149 shows the change in permeability due to changes in effective stress. The reduction of reservoir pressure causes mechanical compressive strain, and the compressive strain is related directly to Young's modulus. Additionally, the GSI values for each model are similar enough, that the strain partitioning to the apertures does not dominate the permeability changes. Therefore, the changes in permeability follow the Young's modulus of the coal in these cases, with the highest change in permeability being related to the lowest Young's modulus (model 'B').

If the change in permeability was due solely to the shrinkage of the coal, the change in permeability would be minor (< 0.5% at 50% of initial reservoir pressure), and there would be a minimal corresponding production increase. In these simply modeled cases, the change in permeability due to compression from pore pressure reduction dominates the changes in permeability. Therefore, it is expected that there is no long term enhancement of permeability due to gas production and coal shrinkage and the inclusion of sorption strain in the coupled simulations is not required.

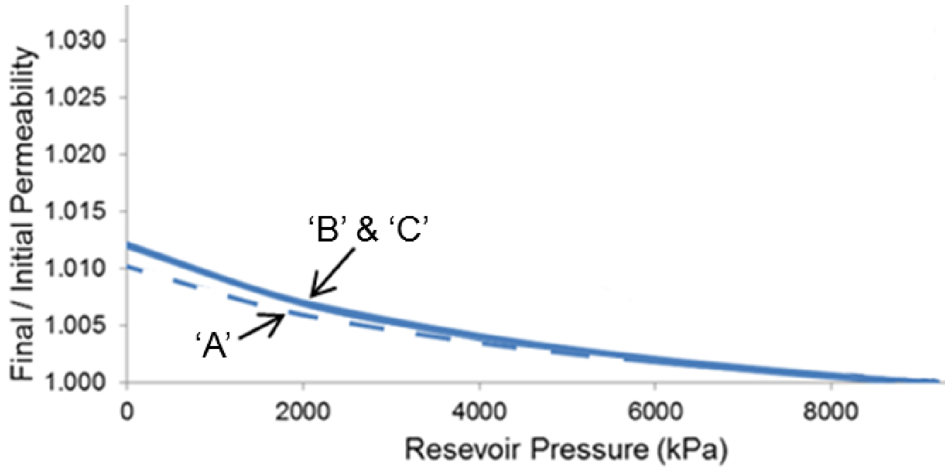

Figure 148. Changes reservoir permeability due only to changes in gas pressure causing coal shrinkage.

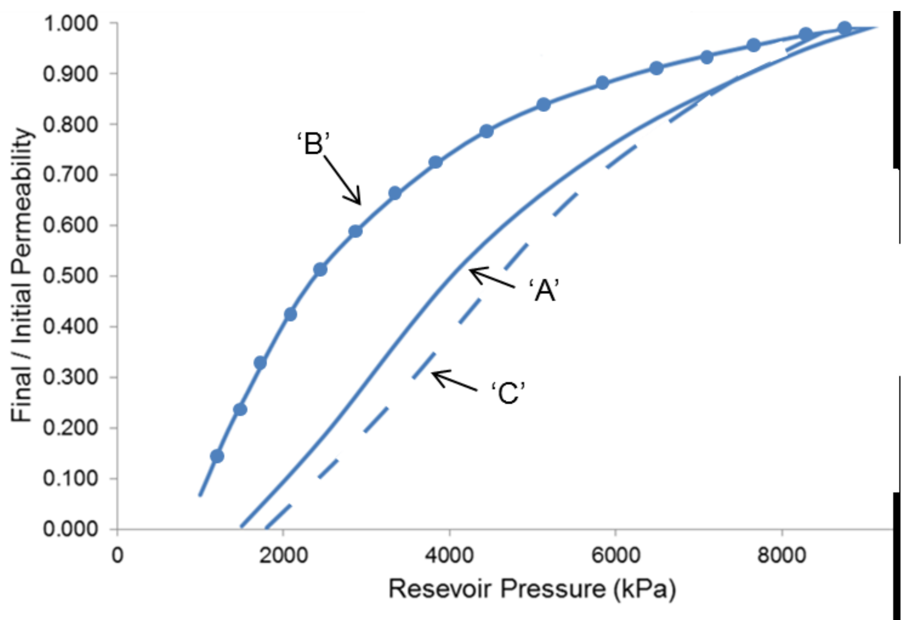

Figure 149. Changes reservoir permeability in *i* direction due only to changes in mechanical compression caused by reservoir pressure decrease.

10.4.3 Uncoupled Simulation

The 'model A' hMEM model was used to construct the reservoir model containing one main horizontal well and two side tracked horizontal. The model was 9 km x 9 km wide and 2 m thick, using a single layer and 57,000 total grid blocks. The main horizontal and the two sidetracked horizontal wells and three monitoring points (A, B, and C) are shown in Figure 150. The main lateral leg was drilled to intersect the maximum permeability and the two side tracked wells intersecting a combination of the maximum and minimum permeability.

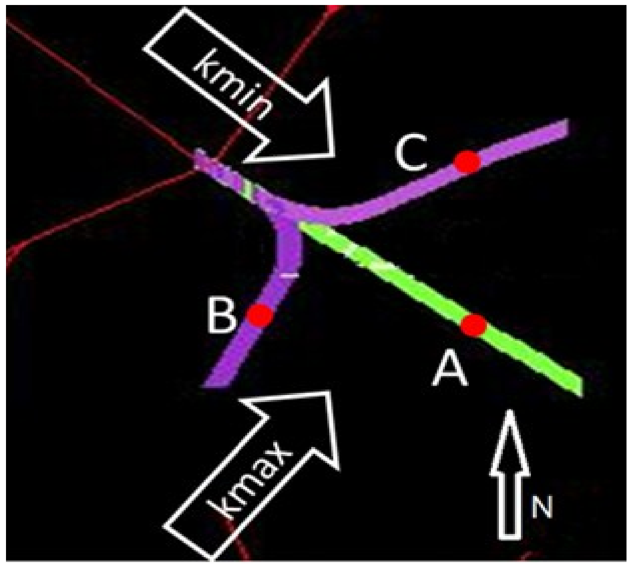

Figure 150. Model A horizontal wellbore configuration with the main horizontal in green and two sidetracked wells in purple. The maximum (kmax) and minimum permeability (kmin) directions and analysis points A,B, and C are shown.

Flow simulation production constraints were: a maximum bottom hole water rate of 80 m^3/day, minimum bottom hole pressure of 1 MPa, and unconstrained gas flow. The model was history matched to field data by adjusting the initial fracture water saturation to 0.75 and the skin factor to 160 (Figure 151). The pressure results from the history matched model were then fed, sequentially, into the geomechanical model at 20 selected time steps spaced over 10 years in 6 month increments.

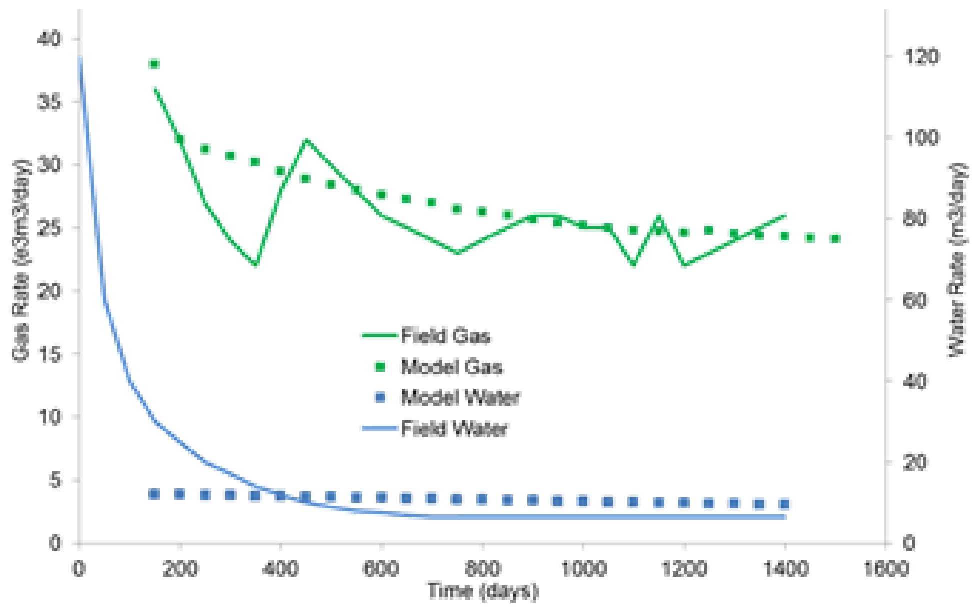

Figure 151. Reservoir simulation model showing history matched gas and water rates.

The model A hMEM model was also used to construct the geomechanical model which exactly matched the reservoir model grid dimensions. The geomechanical model also extended 500m above and 300m below the reservoir and contained a total 576,000 grid blocks and 10 total layers. The model boundary conditions were: stress profile conditions on the top and side boundaries, and a roller boundary on the bottom.

Wellbore Stability during Production

The elastic stress field and pore pressure evolution at points A (Figure 152), B (Figure 153), and C (Figure 154) were extracted from the uncoupled simulations at the uncoupled time steps. The effective stress paths and pore pressure were then plotted with two super imposed Hoek-Brown envelopes (σ_{ci}=20,40; m_i =6, GSI=70) for these three points to assess bulk coal failure and not wellbore specific failure. If the grid block reaches the failure envelope, the coal could fail, resulting in large amounts of coal fines being generated, plugging cleats (Deisman et al 2008) or plugging wellbores or pumps, which would require the wells work overs. Bulk failure of the reservoir does not occur in the grid block at A, however does occur for the grid blocks at B and C after 8.5 and 10 years, respectively. The stress and pore pressure field evolution is not shown, but because the two sidetracked horizontal wells are drilled in the directions which intersect low permeability, the pore pressure gradient was much higher near the well. This higher pore pressure gradient contributed to higher stress changes in the near well area, moving the stress path closer to the failure envelope.

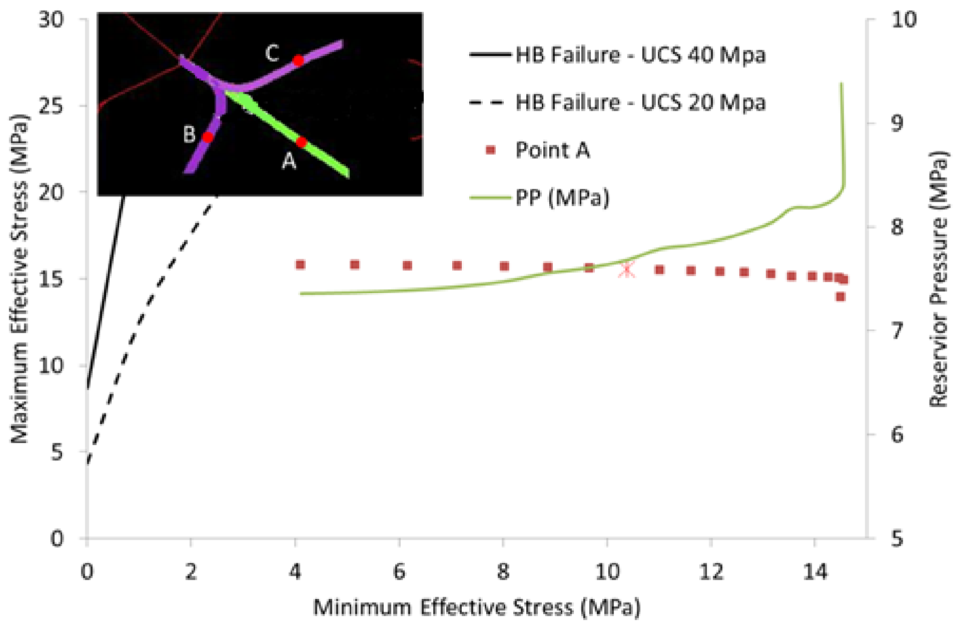

Figure 152. Wellbore analyses for Point A in direction 5 along the multilateral wellbore. The differential stress of 5 MPa is noted with a red star data point along the square point stress path.

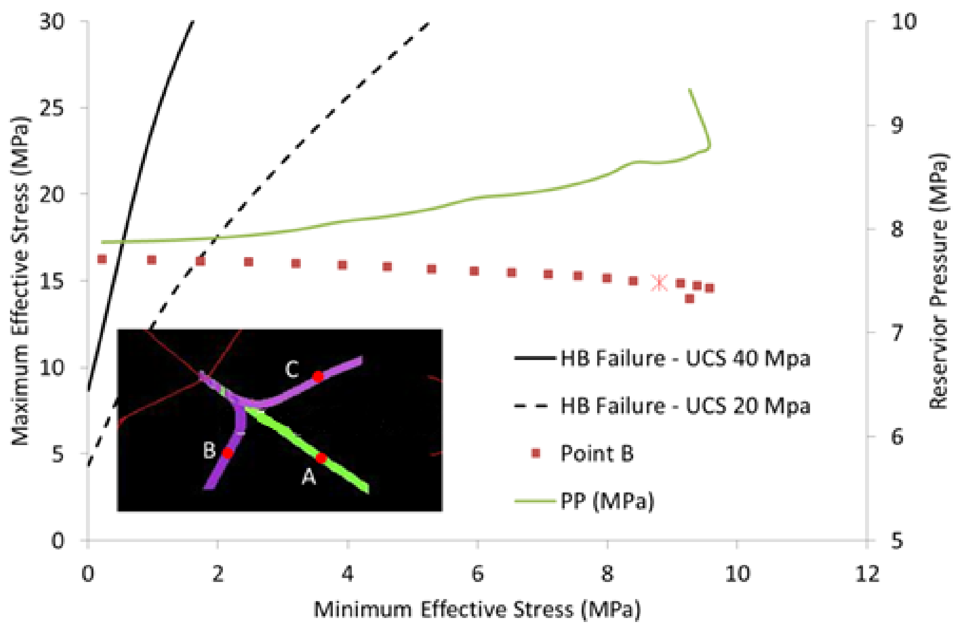

Figure 153. Wellbore analyses for Point B in direction 2 along the multilateral wellbore. The differential stress of 5 MPa is noted with a red star data point along the square point stress path.

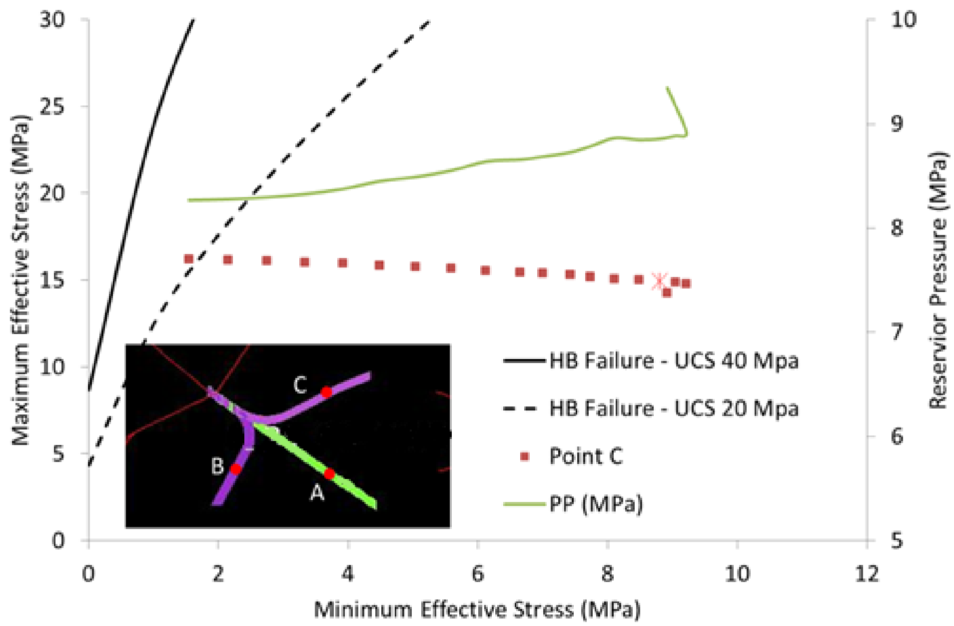

Figure 154. Wellbore analyses for Point C in direction 2 along the multilateral wellbore. The differential stress of 5 MPa is noted with a red star data point along the square point stress path.

Each wellbore was also analyzed for failure at points A, B, and C using the results from Table 41. The main wellbore was orientated in an optimum direction (direction 5) for initial virgin wellbore stability and the two sidetrack horizontal wells and are oriented in directions that would have stability issues (direction 2). For each location, once the differential stress reached 5 MPa, a point was marked on the stress path in each figure and corresponding pore pressure noted. This differential stress of 5 MPa, according to Table 41 creates the worst case scenario for coal failure and potential for coal fines generation. Additionally, the analysis was non-conservative as the reduction in effective stress related to pore pressure was not taken into account. The main wellbore reaches a 5 MPa differential stress after 2 MPa near well reservoir pressure decrease. The horizontal sidetracked wells at points B and C reached 5 MPa differential stress at a near wellbore reservoir pressure reduction of 0.8 MPa and 0.5 MPa respectively.

It is difficult to assess the influence of a failed zone on overall production and the development of a failed zone around the wellbore does not indicate complete loss of the horizontal well. In these cases, a wellbore liner placed prior to production should be used to keep the wellbore open, however it is the generation of small coal fines during failure which cause the greatest issues creating production down time due to work over operations.

10.4.4 Coupled Simulation Results

Initial flow only simulations were completed using GEM to history match water and gas flow for each model. The maximum bottom hole water rates and minimum bottom hole pressures were set for each of the simulations and the gas was allowed to flow with a bottom hole pressure of 1000 kPa. The water and gas rates were adjusted by only altering the initial fracture saturation with the remainder of the simulation inputs unaltered. Only in one case did the gas and water rates matched reasonably well. Once the models were history matched, the coupled simulation was turned on to determine the difference between production with and without geomechanical coupling.

History Matching and Coupled Results for ‘A’

The match of the gas rates was important for this coupled simulation analysis. One of the goals was to determine permeability rebound caused by volumetric strain (shrinkage) due to gas desorption would be present. Once the flow model was set, the coupled simulation was executed. The results showed no permeability rebound and that the geomechanical effects only caused a very slight to no decrease in both gas and water rates.

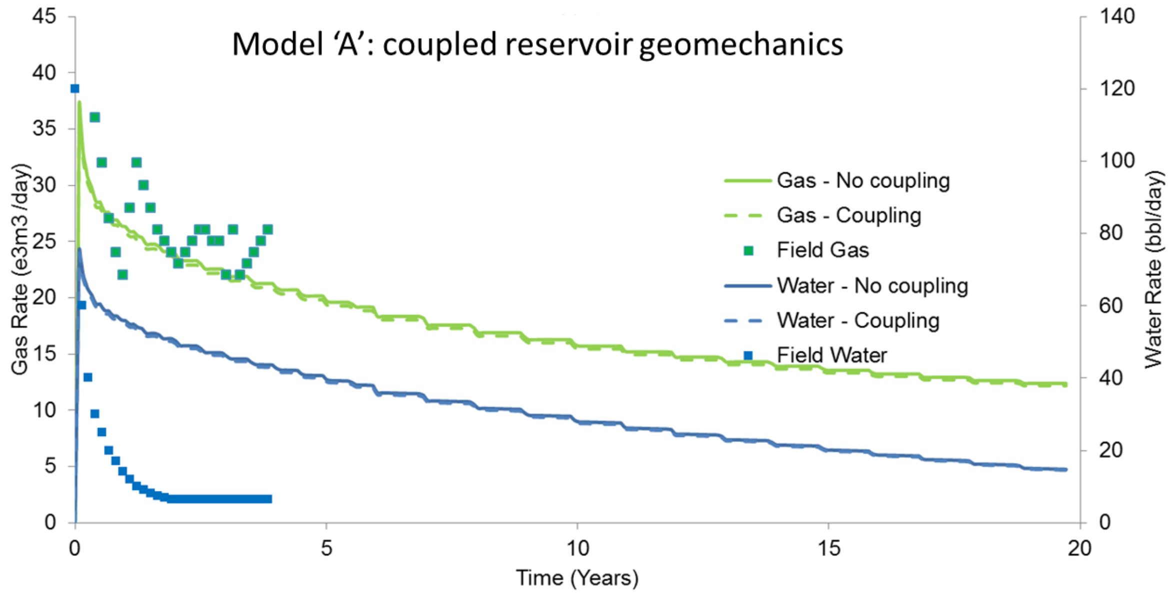

Figure 155. Results for coupled and uncoupled CBM simulation model with field measured gas and water results the 'A' well pad.

The permeability multipliers for three points in the reservoir along the multilateral were tracked (Figure 139) and plotted with reservoir simulation time (Figure 156). The results show that at each point there were slight decreases in the vertical permeability (no contribution to flow in a 1 vertical block model). The permeability in x (i) and y (j) direction remained essentially constant, with only a slight decrease.

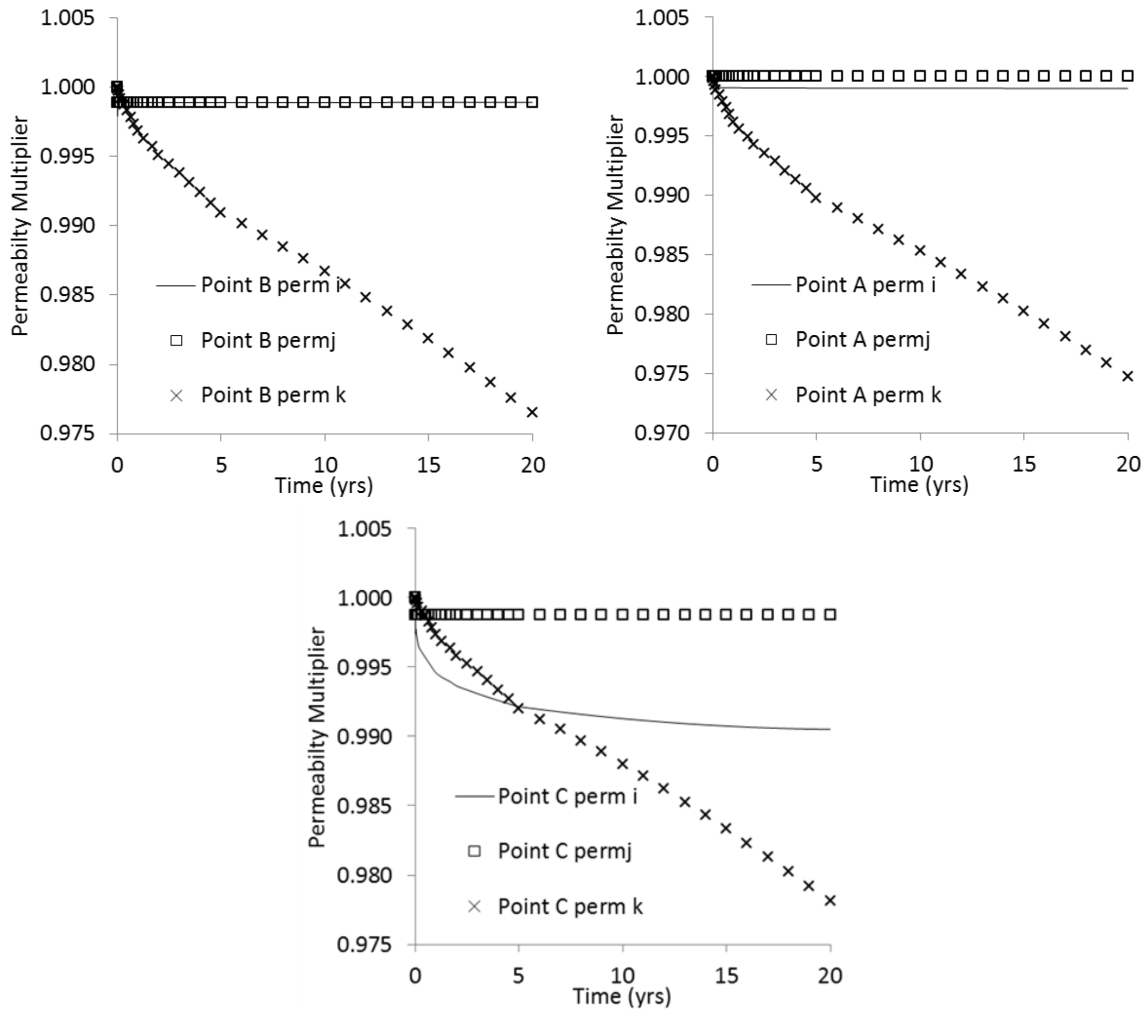

Figure 156. Dynamic permeability multipliers at points A, B, and C on the lateral sections of the well pad 'A'.

History Matching and Coupled Results for 'B'

The same procedure used in 'A' to history match was also used in 'B'. The water and gas field rates proved to be very difficult to match due to the low production rates of gas and higher water rates. The final fracture saturations were set to 0.8, the bottom hole wellbore pressure was set constant to 1000 kPa and the maximum daily water rate was fixed at 100 cubic meters per day. A reasonable match in the first 2 years of the wells life was made, but it was not possible to match the sharp decline (Figure 157). The results from the history matching of the flow model were fed into the coupled reservoir geomechanical. Again, the results in Figure 158 show there was no permeability rebound and that the geomechanical effects do not create any changes in production.

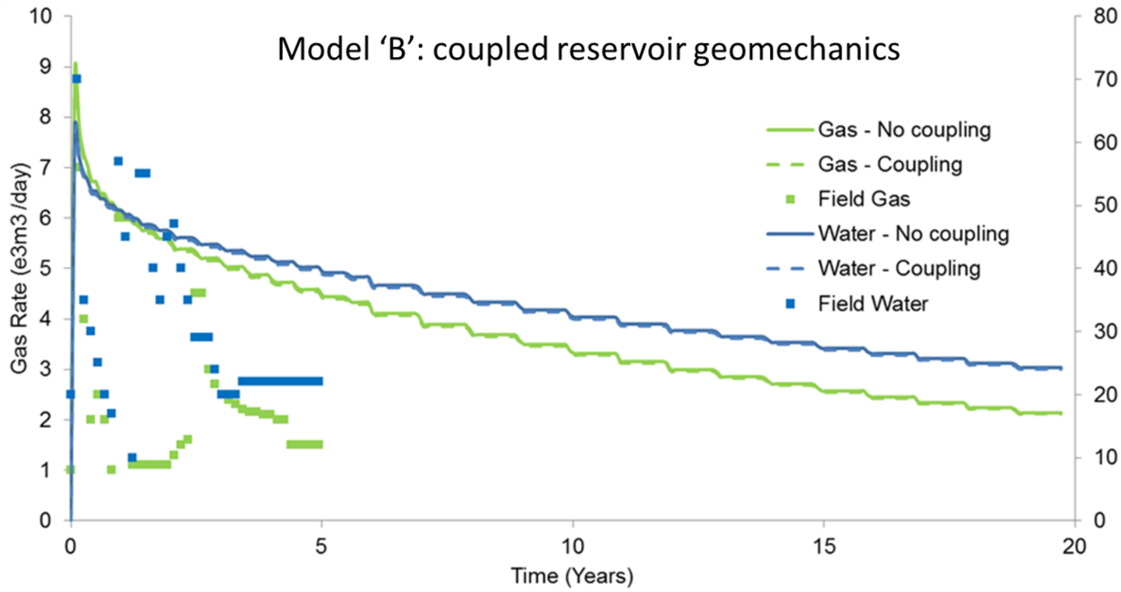

Figure 157. Results for coupled and uncoupled CBM simulation model with field measured gas and water results the 'B'.

The permeability multipliers for two points in the reservoir along the multilateral were tracked (Figure 139) and plotted with reservoir simulation time (Figure 158). The results show that at each point there is slight decrease in the vertical permeability down to 98.5 % of the original value with the remainder of the permeability in *x* (*i*) and *y* (*j*) directions dropping an even smaller amount at point A (99% of original value). This further shows no permeability rebound in the forward modeling and only a slight decrease in each of the directional permeabilities.

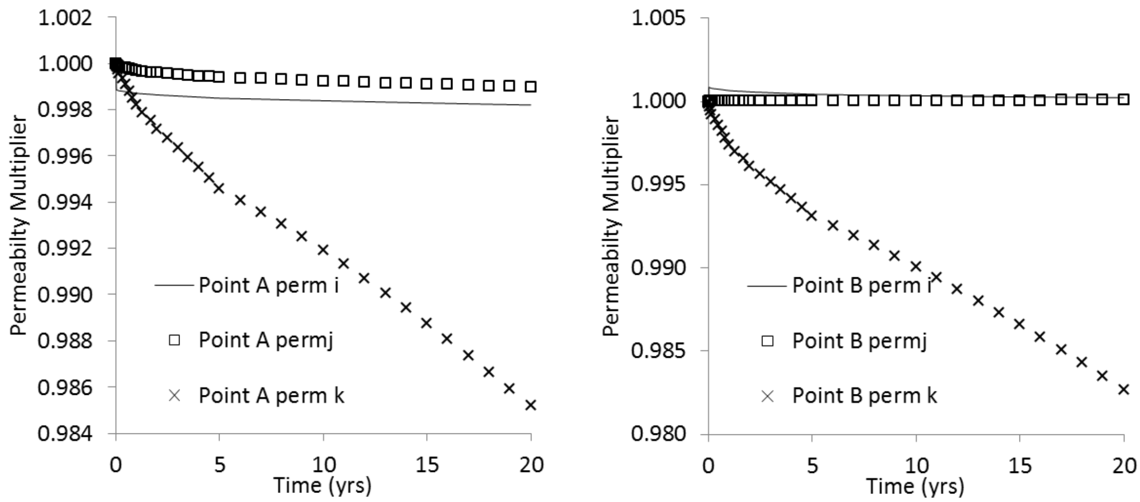

Figure 158. Dynamic permeability multipliers at points A and B on the lateral sections of the well pad ‘B’.

History Matching and Coupled Results for ‘C’

As in ‘A’ and ‘B’, only the fracture saturation was changed try to history match the production data. The bottom hole wellbore pressure was set constant at 1000 kPa, the maximum daily water rate was fixed at 150 cubic meters per day, and the fracture water saturations were set to 0.7. The flow model showed a reasonable match to the gas rate in Figure 159 however the water rate was not matched.

The coupled model was turned on with the resulting flow model. The results show that there is no permeability rebound and that the geomechanical effect does not influence the permeability and resulting flow into the reservoir.

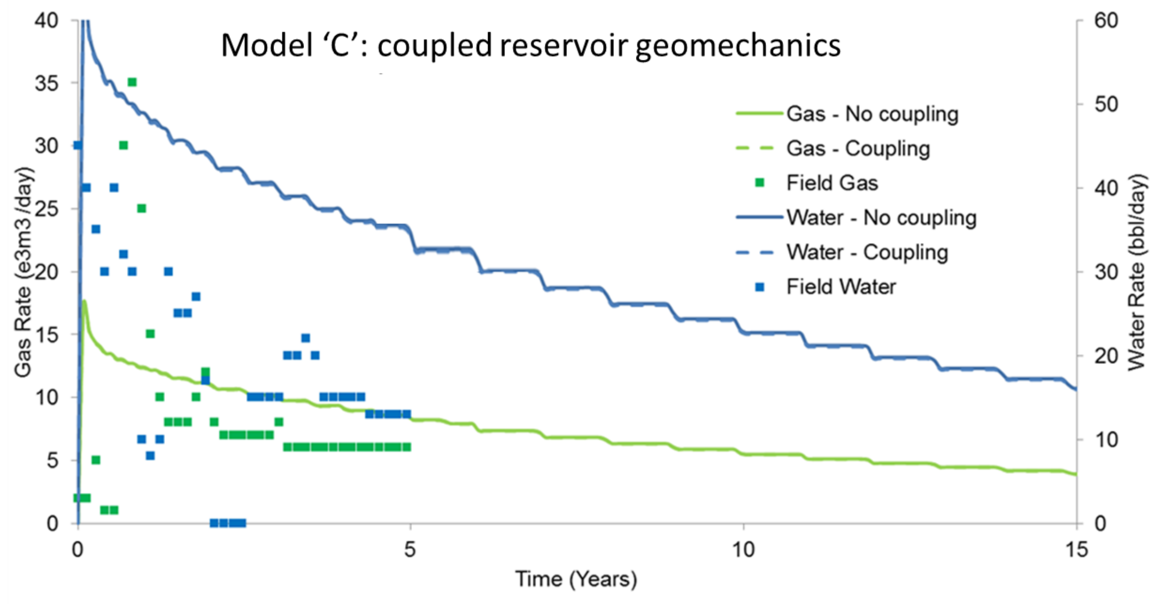

Figure 159. Results for coupled and uncoupled CBM simulation model with field measured gas and water results the 'C'.

The permeability multipliers for two points in the reservoir along the multilateral were tracked (Figure 139) and plotted with reservoir simulation time (Figure 160). The results show that at each point there is slight decrease in the vertical permeability with the permeability in x (i) and y (j) directions dropping a minimal amount.

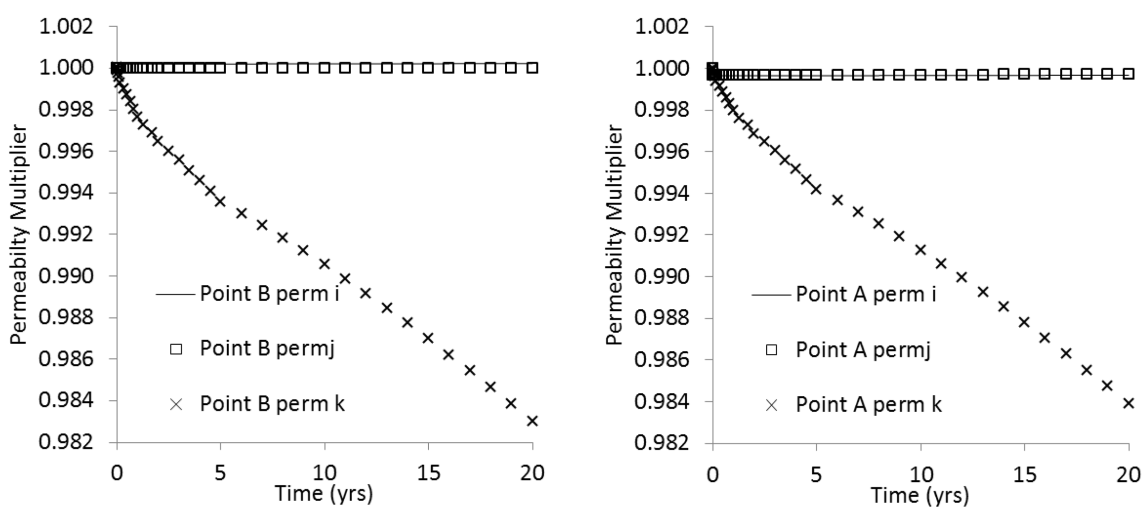

Figure 160. Dynamic permeability multipliers at points A and B on the lateral sections of the well pad 'C'.

10.5 Conclusions

The Geological Strength Index and developed workflow was used to characterize the Nexen's CBM field. Three areas were selected for coupled simulation modeling to investigate the influence of geomechanics on wellbore stability and long term production.

The hMEM model included both the mechanical and flow properties derived from:

- core investigation to determine GSI and formation micro imaging logs to measure coal cleat density;
- density and dipole sonic logs to calculate dynamic Young's Modulus and Poisson's Ratio, reduced 10% to approximate static values, and further reduced using GSI;
- assumed strength properties taken from the literature reduced using local GSI;
- third party testing to measure vertical and minimum horizontal stress and pore pressure and stress directions;
- in situ testing to measure bulk permeability; and
- core collection to measure gas content, Langmuir Isotherms, and diffusion coefficients.

The data was fed into two models: a simple 3D wellbore stability model built using FLAC3D, and uncoupled and coupled reservoir geomechanics simulator using CMG's GEM and Itasca's FLAC3D. The 3D wellbore model was used to assess initial horizontal wellbore drilling azimuths. The uncoupled model was used to assess the influence of stress evolution on stability during production over a ten year period for a multi-lateral horizontal wellbore configuration. The coupled simulation was used to determine long term influences of strain changes on production.

Analytical models were used to first analyze the impact of sorption strain and elastic strain from changes in pore pressure and the resulting impact on permeability. Data from a laboratory sorption strain test completed by Nexen showed small strain changes due to changes gas content (shrinkage/swelling). Due to this limited shrinkage of the coal, the elastic changes dominated the changes in permeability. This indicated there would be no long term permeability increases therefore sorption strain was not included in the coupled simulations.

The initial wellbore stability study found that drilling 135 degree counter clockwise from the East was optimal, but the wellbore would reach a failure state at 2 MPa of near well pressure decrease. The near wellbore coal failure does not mean the well will be lost completely, but it does indicate that a wellbore liner should be used to keep the wellbore open, and fines may be generated and need to be account for in well planning.

The uncoupled simulation results showed that further production pressure decrease over 8-10 years may cause large scale coal failure outside of the near well region. The large scale failure could lead to coal fines plugging coal cleats (gas/water flow paths) in the aperture and at cleat intersections.

Coupled reservoir geomechanical flow simulations were then used to more closely investigate the potential for permeability/production changes. In each of the three cases, it was shown that geomechanical factors have a negligible impact on production and that permeability rebound will not occur in this field.

11 Applications: Borehole Modeling

The characteristics of near wellbore stability are important to the production of the entire reservoir. Understanding the changes in permeability of the coal in response to the drilling of a wellbore are critical when evaluating CBM resource potential. Identifying the material properties that control the reservoirs response to the introduction of a production well is the first step to understanding the permeability changes. The second step is to evaluate the controlling hydro-mechanical properties by measuring in the laboratory or in the field. The third step is to simulate the actual wellbore drilling and subsequent near well production response. This can be accomplished through complex testing methods (physical models) or through numerical simulation (computer codes). Complex testing methods may offer insight into the controlling processes, but may be offset by the higher associated costs. Numerical simulations are appealing because of lower costs, but may be offset by the usually simplified approach to the solution of the controlling equations (thermo-hydro-mechanical equations).

This section uses the hydromechanical characterization workflow described in previous chapters (Figure 161) to numerically investigate the coalseam engineering issues of:

1. Horizontal wellbore stability;
2. Drilling mud infiltration; and
3. Drilling induced permeability changes.

These studies focus on the effects of drilling and production on the stability of a single horizontal wellbore drilled in the target seam as a function of wellbore diameter in the Medicine River seam, Norris CBM field. An example of the workflow to measure the effects of wellbore displacement on the mechanical properties and permeability (no flow) was first conducted. Then, two wellbore diameters were modeled, 150 mm and 50 mm to investigate the scale effects on wellbore stability and fluid inflow. The two wellbores were simulated: underbalanced and overbalanced with no mud cake, and overbalanced with a mud cake. The coal's strength envelope was constructed using the Geological Strength Index estimated from retrieved core and Hoek-Brown strength and deformation properties were taken from laboratory testing results (presented in Chapters 7 and 9). The first models were completed using flow and mechanics independently, and the final study simulated if coupled effects were important to consider for drilling fluid infiltration.

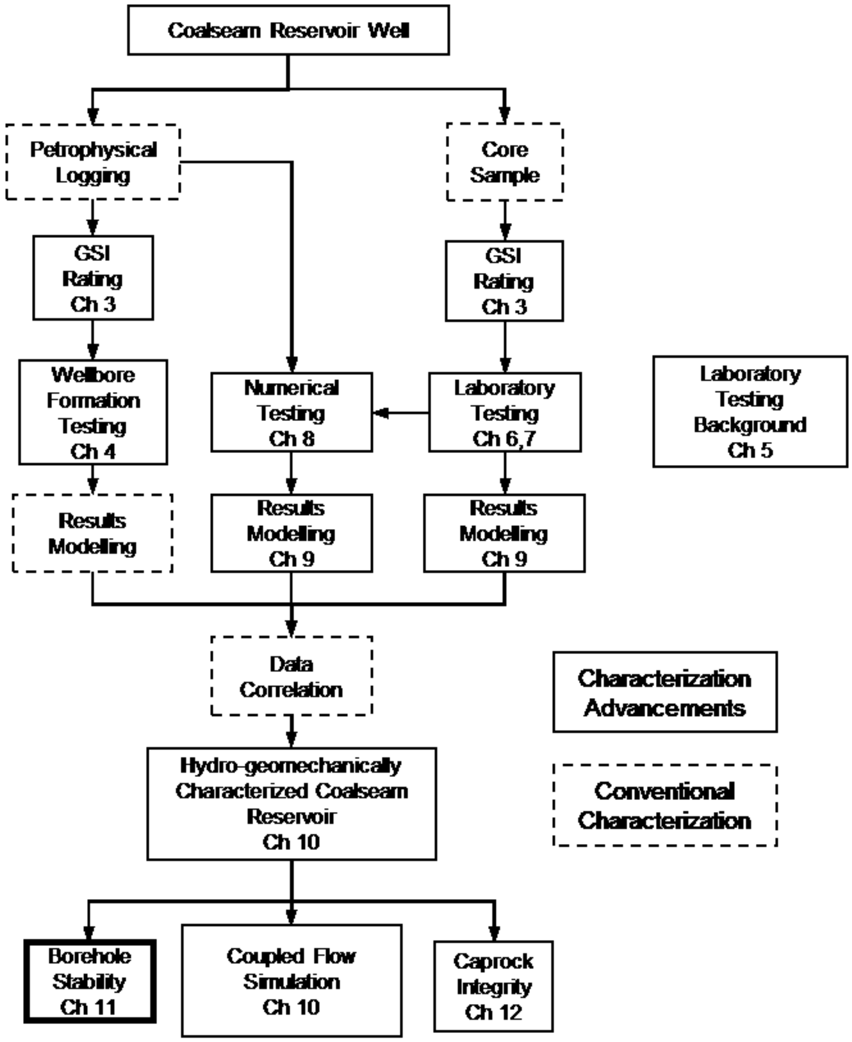

Figure 161. Coalseam reservoir hydro-geomechanical workflow showing where the borehole stability modelling fits into the overall characterization approach.

The study on the Norris area CBM 5 spot pilot was completed while working for CDX Canada as part of an NSERC Industrial Postgraduate Scholarship (IPS) in 2003-04. The results of the study were not made public until after the coupled modelling work was completed, and therefore could not be used for the coupled modeling. Ideally, the results from the Norris MR study should have been fed directly into the coupled modelling study, however this was not possible.

11.1 Field Case: Borehole Stability Analysis during Drilling and Production

Coalbed methane development in the Norris area was initially intended to be achieved through hydraulically fractured vertical 5 spot pattern wells. However, the initial production values were very low and alternative production methods using horizontal wells were required. This section describes the initial horizontal wellbore stability assessment during simulated drilling and production investigation on two wellbore diameters: 150 mm and 50 mm. The major concerns to be addressed include

- Is it possible to drill the horizontal wells underbalanced?
- Should a mud filter cake be used?
- If a filter cake is not used, could coal fines plug the formation?
- Should a slotted wellbore liner be used to prevent collapse? and,
- What wellbore diameter should be drilled for maximum stability?

To address these issues, a two dimensional numerical model was constructed using FLAC4.0 and mechanical and flow simulations were conducted.

11.1.1 Background

The Norris study area is located east of Edmonton, in the central Plains of Alberta, 14-53-18-W4. The target coal seams belong to the Lower Cretaceous Mannville Group with an estimated bulk permeability of 6 mD (Gentzis et al., 2008). The coal seams were drilled as vertical 5 spot pattern; however the initial production rates of 7887 m^3/d from 5 verticals pilot was low for commercial development. Therefore, drilling horizontal wells in the thickest of the four Mannville coal seams, the Medicine River seam, was considered as an option.

11.1.2 Initial Coring and Vertical 5 Spot Pilot Production

Four coal seams exist in the Mannville Formation in the 14-53-18W4 Legal Subdivision, and are, in order from most shallow to deepest: the Upper Mannville, the Sparky, the Medicine River (MR), and the Ostracod seam. The Upper Mannville coal seam has a thickness of 1.1 to 1.5 m, at an average depth of 763.5 m, and a gas content of

0.220 mol/kg. The Sparky Seam has net thickness of 1.7 to 2.2 m, at an average depth of 776.5 m, and a gas content of 0.179 mol/kg. The MR Seam is the thickest (1.8 to 2.7 m), at an average depth of 791.5 m, and a gas content of 0.204 mol/kg. The Ostracod Seam was not cored because of its close proximity to a water bearing sandstone. As a result, this seam is deemed unsuitable for vertical fracture stimulation or even for horizontal drilling. Coal rank is high volatile C bituminous based on vitrinite reflectance for all seams ($\%R_{oMax}$= 0.53–0.57). The MR Seam is overlain and underlain by shale, and is divided in two distinct sections based on core description and interpretation of digital core photos taken during coring.

Production History

The first CBM vertical well in the Norris area 07-14 was drilled in February 2002 and was put on production July 2002. In May 2003, four additional wells were drilled to complete the five-spot pilot (Figure 162) and were put on production in July 2003. Although cumulative gas production volume from the pilot's five wells reached a peak of almost 7887 m^3/d, within a year the cumulative production volume from all five wells had declined to 4366 m^3/d. There was considerable variation in the gas production rates and volumes among the pilot wells. The 13-14 well had performed better than the others. Initially, it was anticipated that the central well would produce at higher rates than the others because of the pressure interference from outer wells and initiating greater desorption at the inner well; however, this was not the case. This indicated that the coal in the well region of 13-14 likely had greater permeability, which resulted in greater depressurization of the reservoir. An injection-falloff test conducted in the MR Seam at 13-14, in combination with an evaluation of water production of the entire 5-spot pilot over three years, resulted in an estimated absolute permeability of about 6 mD for the coals in the pilot location (Gentzis et al., 2008). Due to the low production rates, horizontal well drilling was investigated as a means to increase production by accessing more of the coal seam. The MR seam was selected for horizontal drilling due its thickness, upper and lower shale boundaries (prevent water inflow), and sufficient gas content.

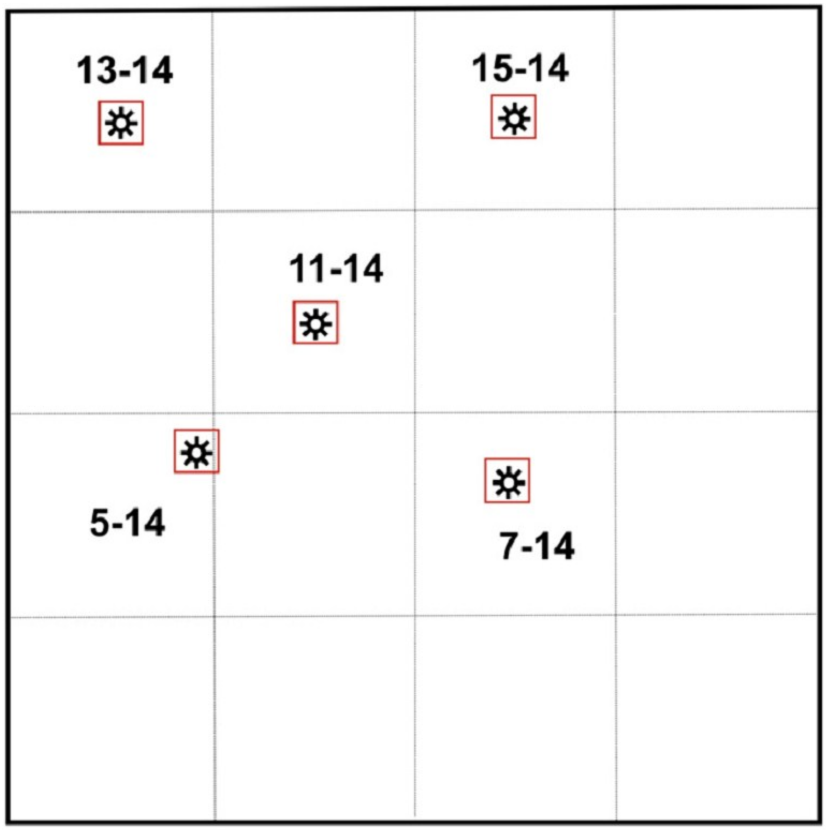

Figure 162. An outline of the 5-spot vertical coalbed methane pilot at Norris in 14-53-18W4 legal subdivision.

11.1.3 Mechanical Properties of the MR Seam

Core collected for geological and petrophysical interpretation during vertical well drilling was not preserved for geomechanical testing as this area was initially intended to become a vertical CBM pilot. Thus, the mechanical properties of the MR seam and surrounding coal were based on laboratory testing on coal from the Alberta foothills/mountains regions and not from the Norris area (completed outside of this thesis and listed below). Because the strength was estimated for the Norris project, the lowest failure envelope which fit the data was used for the Hoek-Brown (HB) parameters. The GSI of the laboratory tested specimens was set to 85 and the intact HB properties were calculated as: $\sigma_{ci} = 23$ MPa, $m_i = 13$, $E = 4.0$ GPa and $\nu = 0.32$. All of these values are reasonable when compared to results obtained from testing in Chapter 7 and Chapter 9.

Mechanical and flow properties for the shale above and below the coal were also estimated. The reservoir pore pressure was measured during the fall off testing, the vertical stress was calculated from geophysical density logging, and the horizontal stresses field were assumed to be less than the vertical stress. The complete mechanical and flow properties, along with a schematic of the MR seam are illustrated in Figure 163.

The coal was split into two distinct upper and lower zones labeled: Coal 1 (upper) and Coal 2 (lower). Coal 1 was 0.6 m thick and Coal 2 was 1.6 m thick. The assigned horizontal and vertical permeabilities in the upper coal interval were 1 mD and 0.25 mD respectively, whereas for the lower coal interval the values were 4 mD and 1 mD, respectively. These are lower values when considering the numbers obtained from long-term production testing (6 mD). Vertical permeability between coal and shale was estimated to be 0.001 mD.

After drilling, the MR Seam cores were described and photographed. Description of the coal included rock lithotypes (coal, shale, partings, shaley coal, carbonaceous shale, mudstone, etc.), coal lithotypes (bright, banded, dull), cleat development (face/butt), cleat spacing and cleat mineralization and presence of shear surfaces (slickensides). GSI was estimated based on the reassembled photographs of the 90 mm core diameter. A GSI of 85-90 was assigned to the Coal 1 interval based examination of the 90 mm core which indicated a slightly cleated coal. In Coal 2, there were missing core intervals which could be associated with lower GSI values and therefore a GSI of 75 to 80 was assigned, indicating a more friable coal. This lower GSI value may be useful in identifying highly fractured/cleated zones within a seam that may cause problems during horizontal drilling.

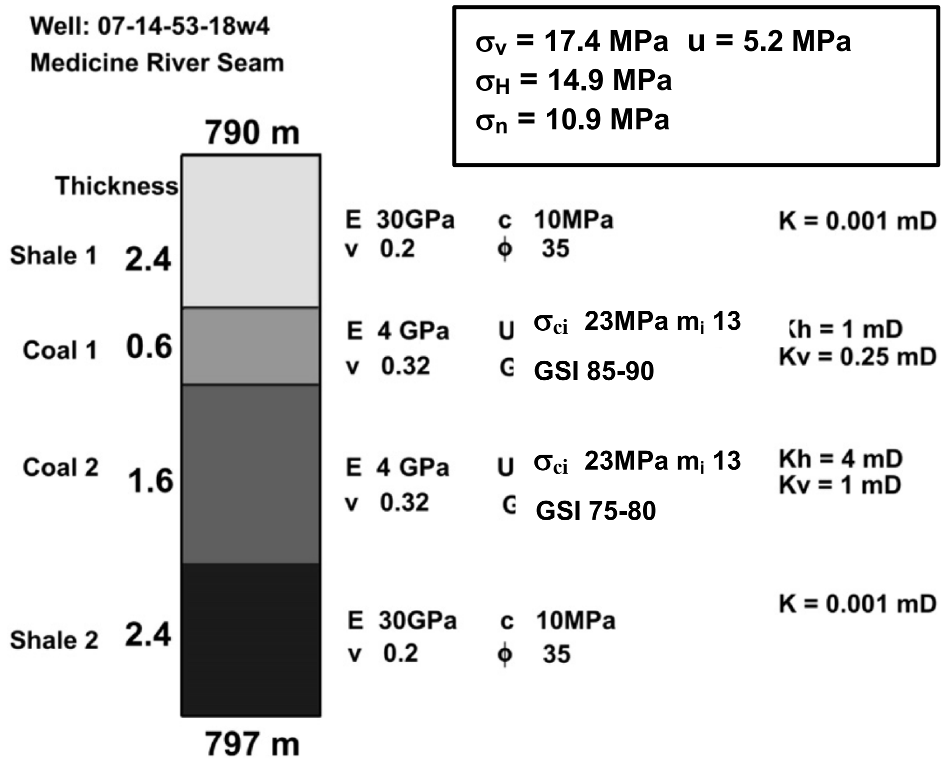

Figure 163. Basic lithologic breakdown of the target Medicine River Seam, along with assigned geomechanical properties and vertical/horizontal permeabilities.

Strength Envelope for 150 mm and 50 mm Wellbore

The GSI assigned to the Coal 1 and Coal 2 intervals was based on the examination of 90 mm core, but because the borehole sizes being considered are 150 mm diameter and 50 mm, GSI must be revised to reflect these borehole diameter changes. For the 150 mm diameter borehole, GSI was reduced to a range of 70 to 80 for Coal 1, and 55 to 65 for Coal 2. For the 50 mm diameter borehole, GSI was increased to a range of 94 to 98 for Coal 1, and 85 to 90 for Coal 2.

The resulting HB strength envelopes for the 150 mm and 50 mm horizontal boreholes are shown in Figure 164 and Figure 165 respectively. The laboratory data points show that coal peak strengths are variable, which also agrees with results presented in Chapter 7.

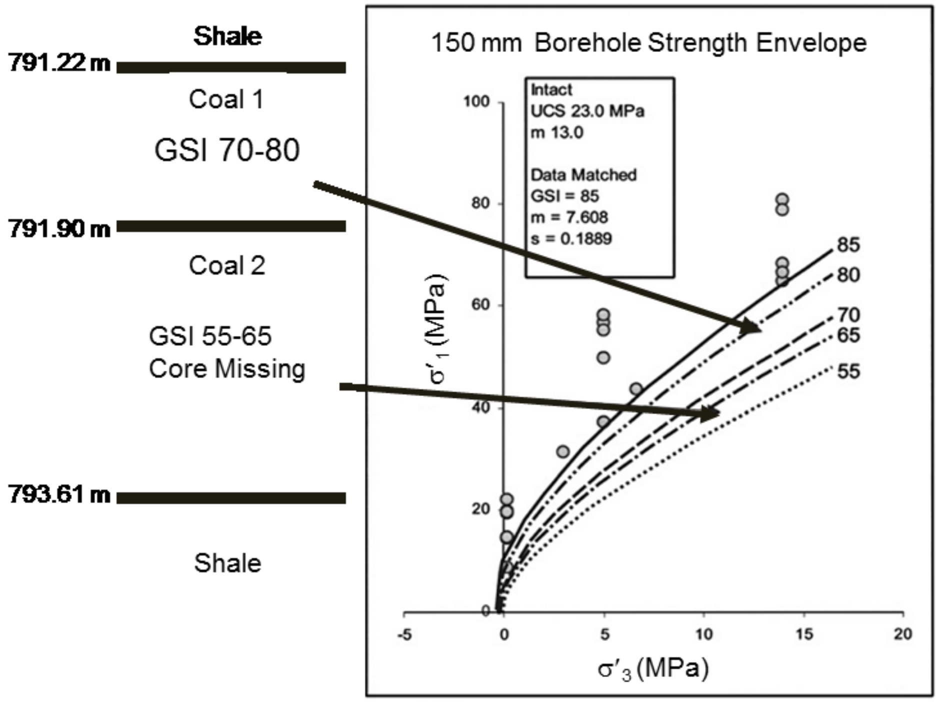

Figure 164. The Medicine River Seam interval showing the assigned *GSI* values and the corresponding strength envelope for a 150 mm wellbore drilled into the coal seam.

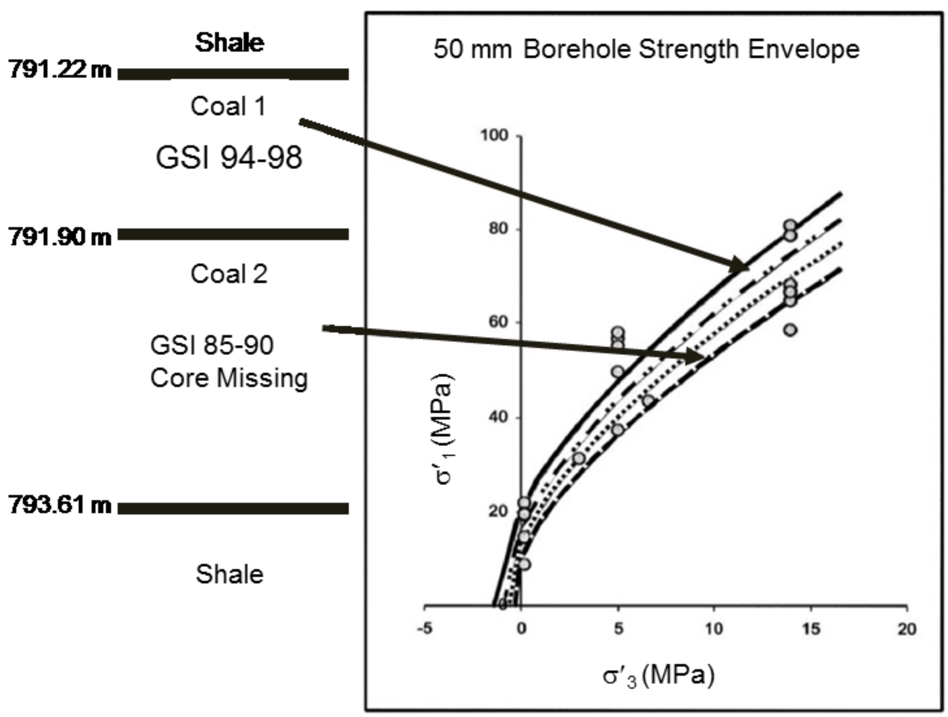

Figure 165. The Medicine River Seam interval showing the assigned *GSI* values and the corresponding strength envelope for a 50 mm wellbore drilled into the coal seam.

11.1.4 Drilling and Production Scenarios

A model cross section of horizontal wellbore drilling is used to demonstrate the application of the proposed integration of deformation, strength, and permeability change. The borehole model used is vertically half symmetric with an anisotropic effective stress field. The geomechanical numerical modelling software used in this study was FLAC 4.0, which simulates in the 2D, and in this case, the x and z direction. The well was simulated to be drilled in the direction of the minimum horizontal stress to intersect the face cleats (or major fracture set), therefore the horizontal total stress was 14.95 MPa and the vertical total stress was 17.38 MPa.

Two scenarios were investigated:

- Drilling; and
- Production

The simulations served to answer the following:

- how far can coal fines be pushed into the formation when drilling 3 MPa overbalanced into Coal 1;
- how stable are the 50 mm and 150 mm wells once production begins and wellbore pressure is 1.0 MPa; and,
- do the 50 mm and/or the 150 mm wells need slotted liners.

For these initial simulations, the coal permeability and deformation was static and not updated due to effective stress changes.

11.1.5 Drilling and Production Scenario Results

The first scenario investigated the potential for pushing coal fines, generated during drilling, into the formation with and without a filter cake with 3 MPa pressure in the 150 mm borehole. The filter cake was simulated by decreasing the permeability in the first row of elements 3 orders of magnitude less than the coal permeability to 1 μD.

Figure 166 (a-d) shows the pressure changes due to drilling into the coal in the middle of the seam after 0.25 s, 2 s, 10 s, and 600 s without a filter cake. After 600 seconds of simulation time, the distance into the formation 2200 mm away from the borehole wall.

If the borehole were to be drilled with a filter cake, very little pore pressure penetration (70 mm) was expected even at t = 650 s (Figure 167a-c).

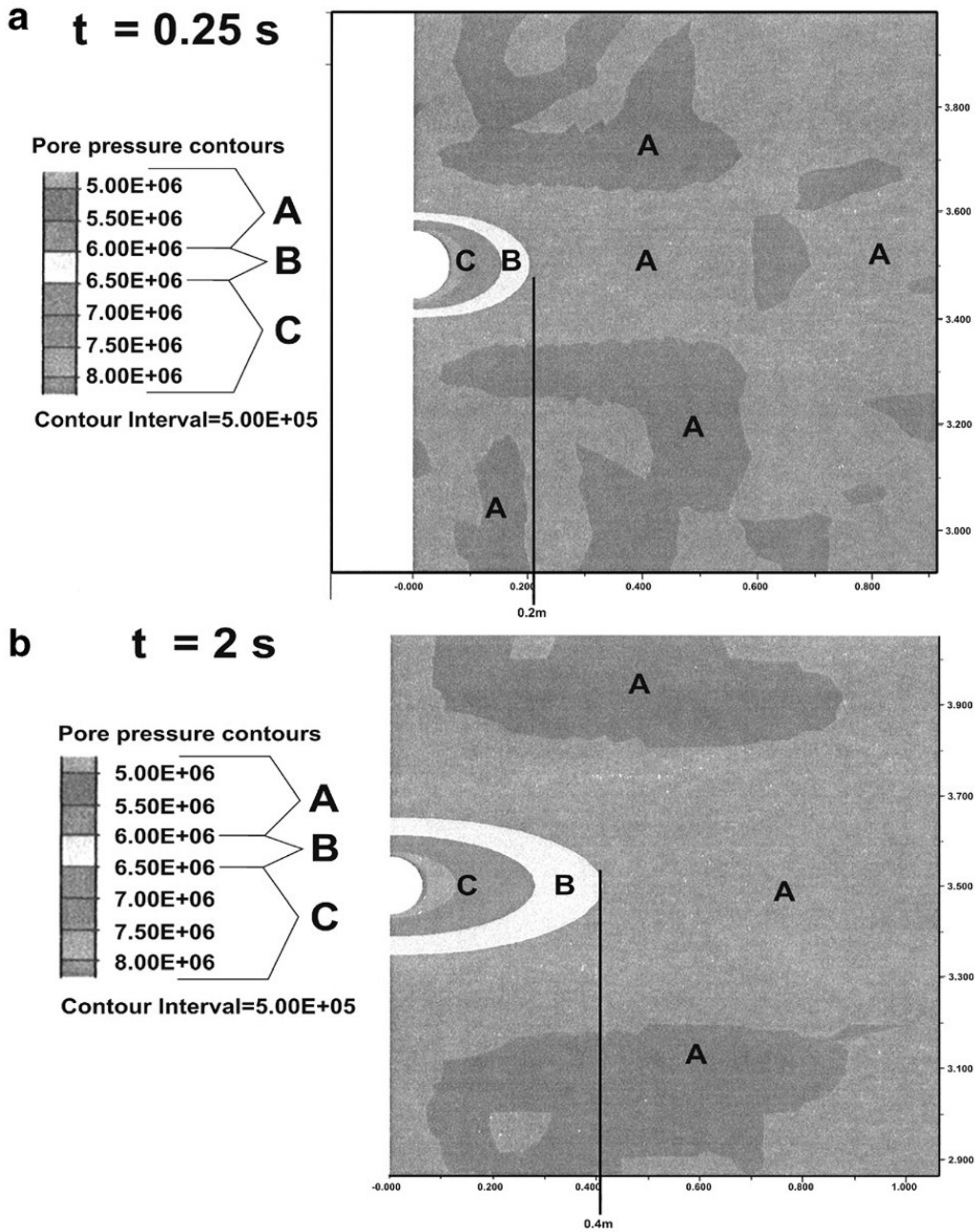

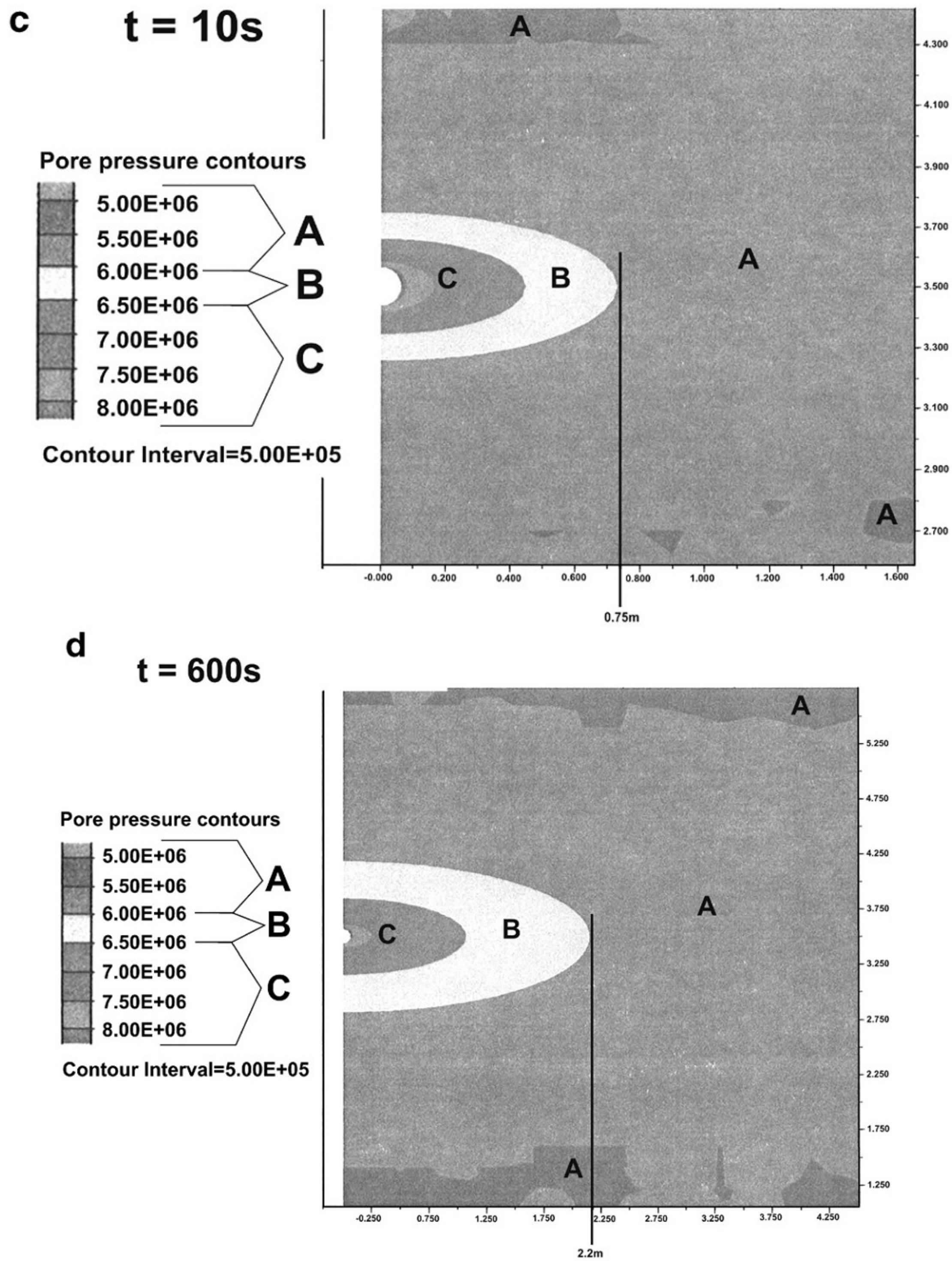

Figure 166. Transient fluid flow in a horizontal wellbore drilled into the MR seam with no filter cake formation. The bar scale to the left shows variations in pore pressure in the coal seam. (a) shows drilling fluid penetration for *t* = 0.25 *s*, (b) shows the same for *t* = 2 *s*, (c) is for *t* = 10 *s*, and (d) is for *t* = 600 *s*.

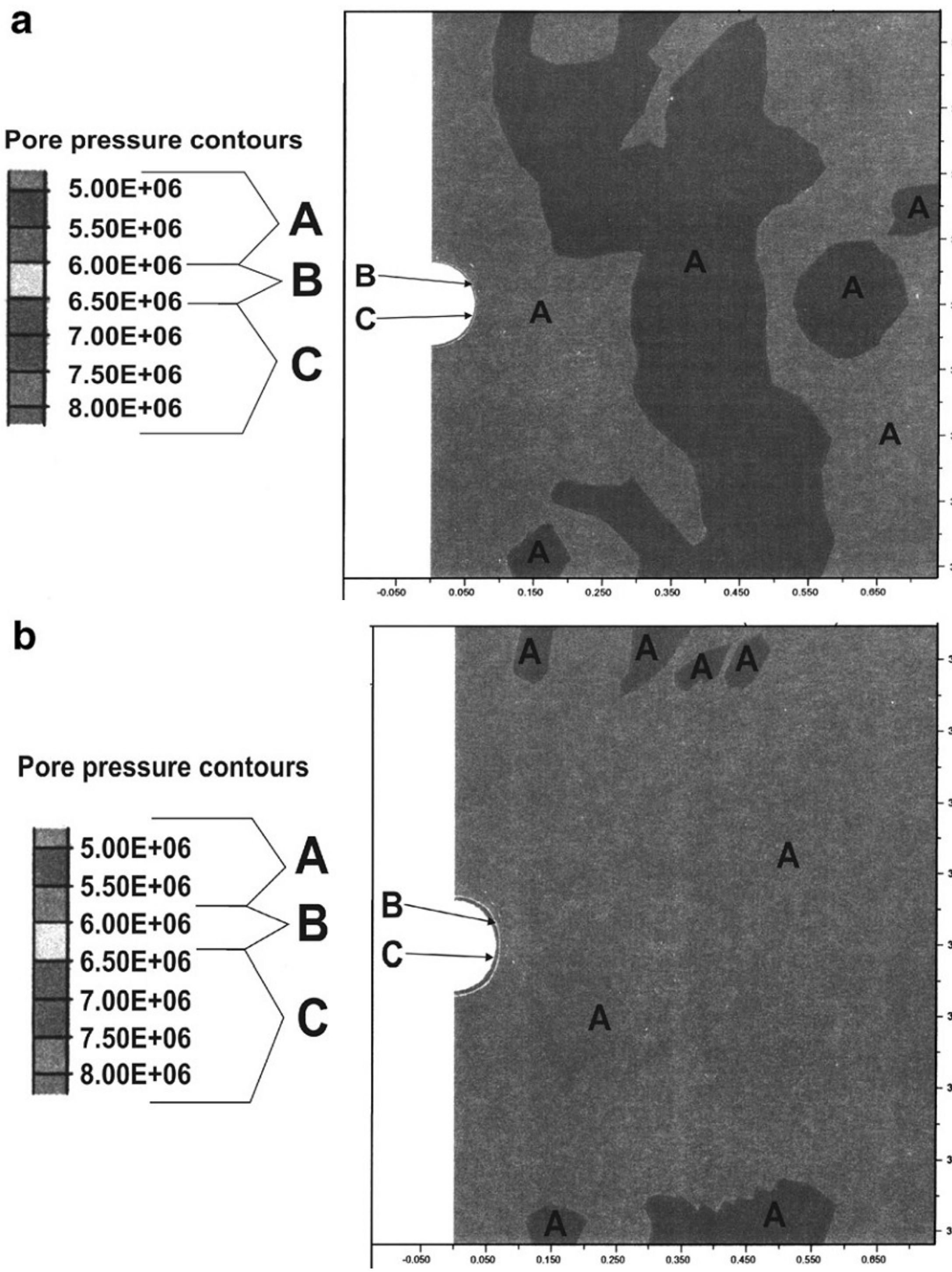
a
Pore pressure contours
5.00E+06
5.50E+06
6.00E+06
6.50E+06
7.00E+06
7.50E+06
8.00E+06
A
B
C
b
Pore pressure contours
5.00E+06
5.50E+06
6.00E+06
6.50E+06
7.00E+06
7.50E+06
8.00E+06
A
B
C

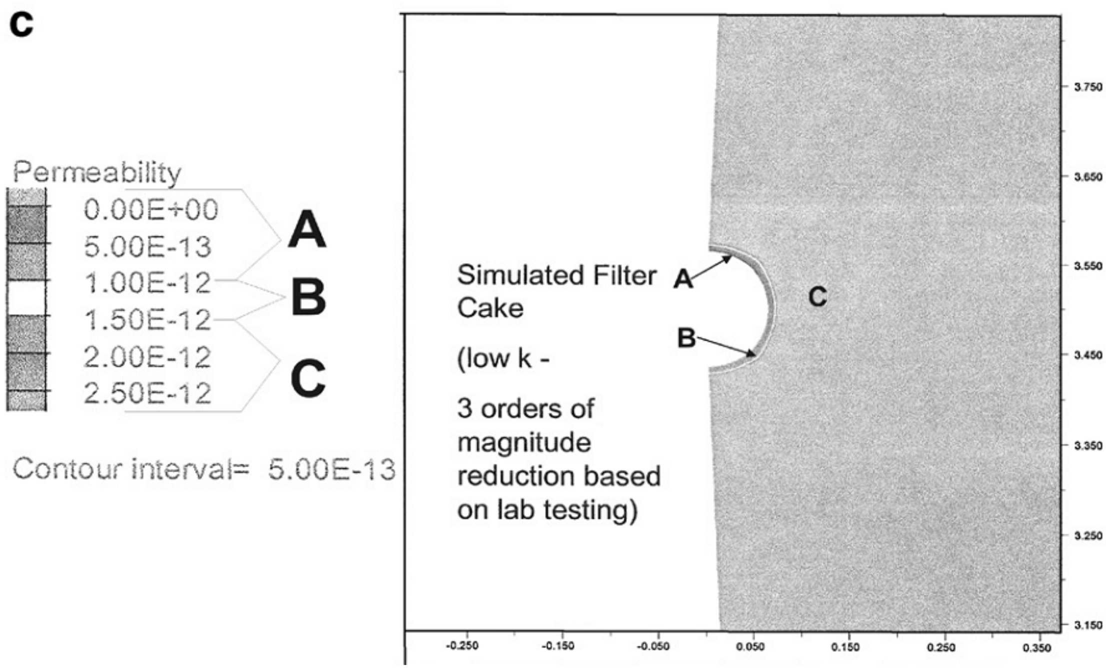

Figure 167. Transient fluid flow in a horizontal wellbore drilled into the MR seam with filter cake formation. The bar scale to the left shows variations in pore pressure in the coal seam. (A) shows drilling fluid penetration for $t = 0.25\ s$, and (B) shows the same for $t = 650$ s; (C) shows the permeability of the simulated filter cake formed against the coal face when drilling overbalanced.

The results for the 150 mm diameter hole show the pore pressure contours distribution in the near wellbore region (Figure 167). The pore pressure gradient near the wellbore is a function of coal permeability. The lower the permeability of the coal, the steeper the pore pressure gradient in the near wellbore vicinity becomes, increasing the seepage forces and decreasing the effective stresses (Vaziri and Xiao, 2003). This could result in unstable conditions and increase the failure of the coal. The increase in pore pressure with time from the drilling fluid causes the cleats to open and drilling fluid to penetrate the coal seam. The model predicts an increase in pore pressure up to 2.2 m away from the wellbore. This increase, however, does not account for competing coupled geomechanical effects of total stress increases due to wellbore creation and fluid pressure increases due to overbalanced drilling.

With the use of this simple simulation for this Norris section shows that an effective filter cake prevents drilling fluid penetration. The drilling fluid could carry coal fines into the coal cleat system, potentially clogging the flow fractures. Therefore, an efficient filter cake, which does not clog coal fractures and shut down coalseam permeability, should be selected and used in the Norris area.

Production Conditions

The wellbore stability and coal failure of both the 150 mm and 50 mm diameter borehole were investigated when the near wellbore area is at 1.0 MPa pressure was also investigated. The HB strength/stress ratio increases from the contact between the wellbore with the coal into the area of virgin coal reservoir.

At GSI values of 80 and 65, the 150 mm diameter wellbore was not stable (Figure 168). For the coal to remain stable at these *GSI* values, an equivalent σ_{ci} would be 42.0 MPa. However, the σ_{ci} of the coal in the middle section was estimated to be 23 MPa. At these low *GSI* values, the 150 mm diameter hole is very unstable. It would require an 85% increase above the estimated strength, which is at the upper end of laboratory testing results (Chapter 9) to have a stable 150 mm diameter hole. In the case of the 50 mm diameter hole, following the same sequence of events as the 150 mm borehole above, the wellbore remains stable in the Coal 1 (GSI 95) and Coal 2 (GSI 85) (Figure 169).

A

B

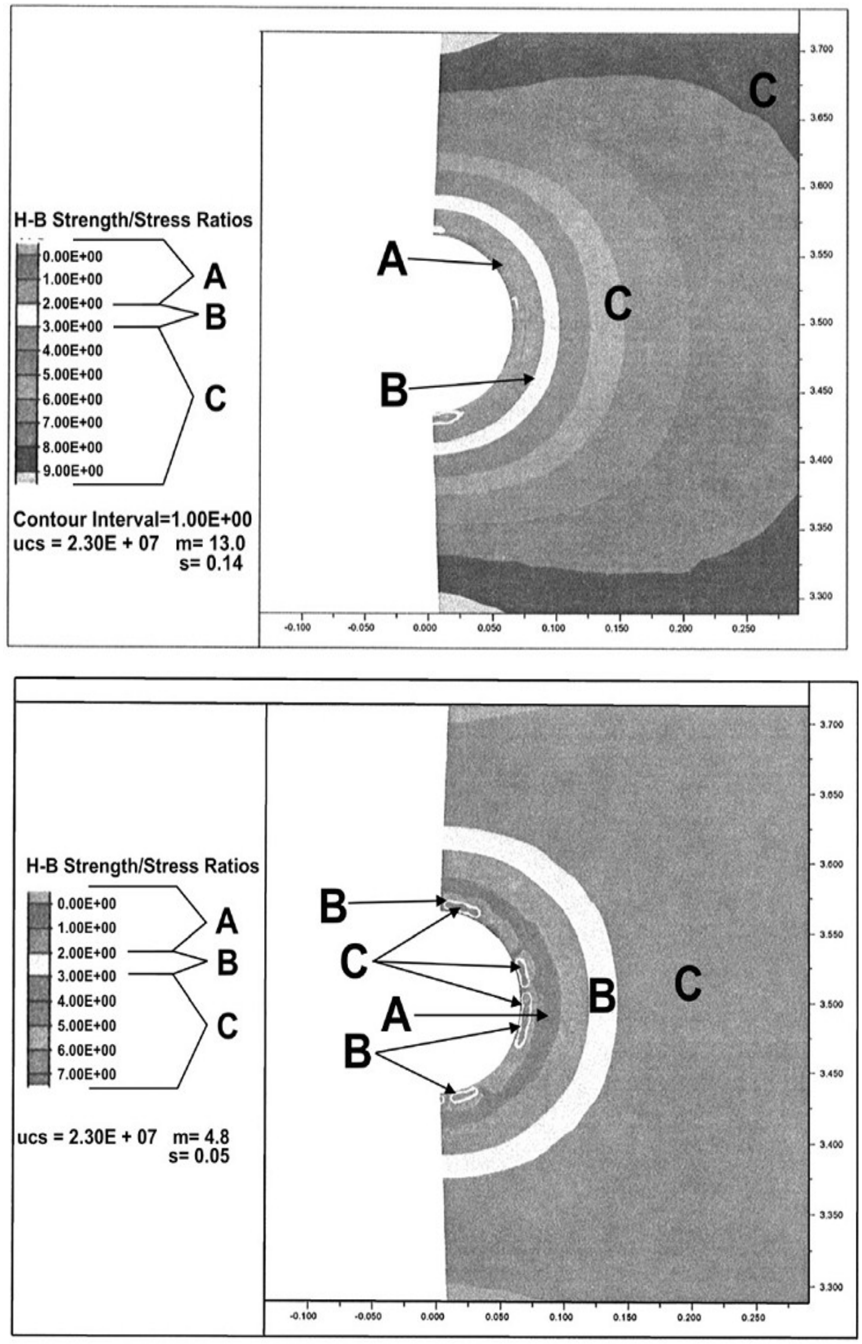

Figure 168. Stability of a 150 mm horizontal wellbore drilled in the Medicine River seam during production and as a function of *GSI*. (A) is for *GSI* = 80 and shows an unstable hole; (B) is for *GSI* = 65 and also shows an unstable hole. The bar scale to the left shows the HB strength/stress variations expected around the wellbore.

C

D

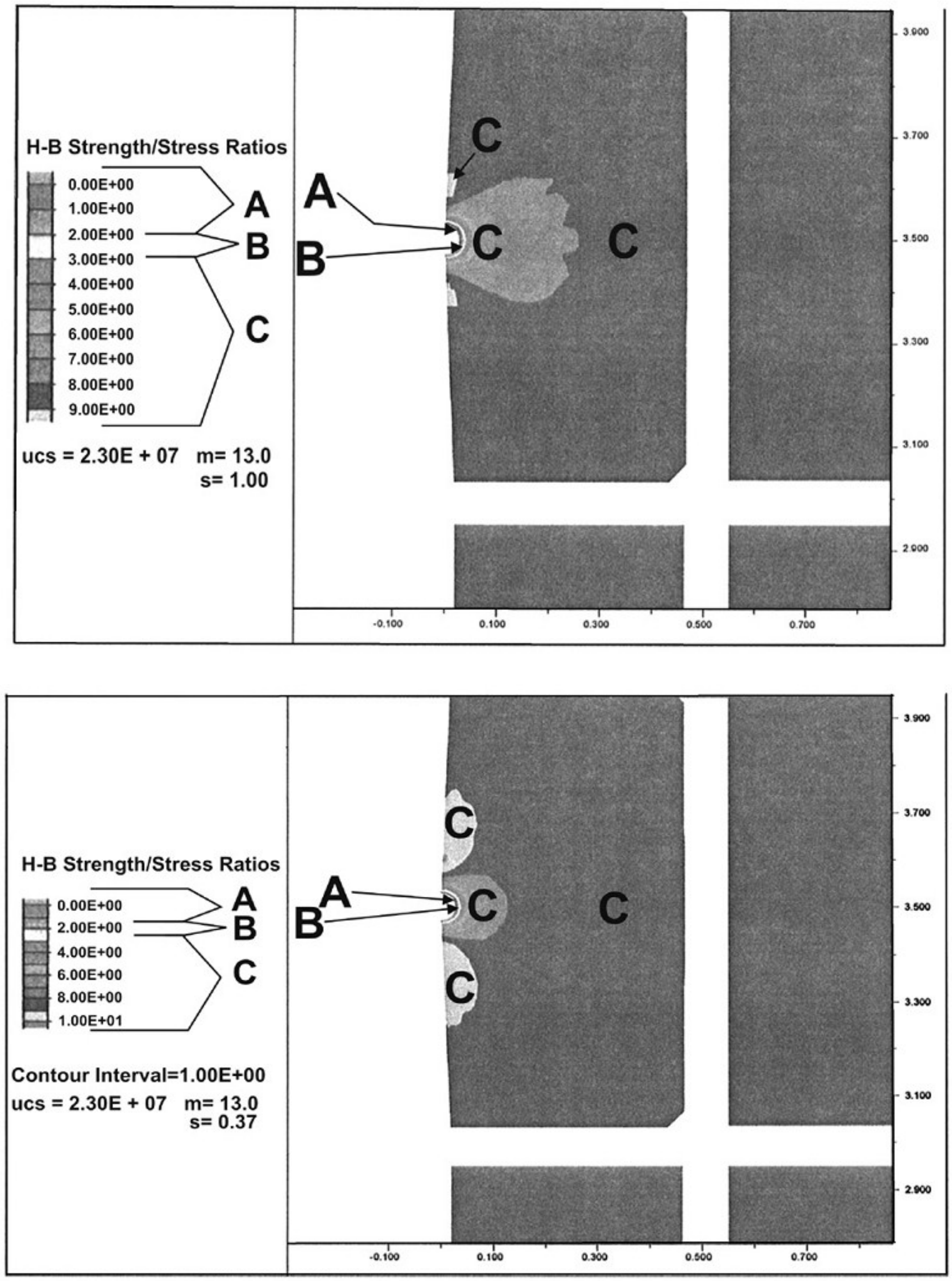

Figure 169. Stability of a 50 mm horizontal wellbore drilled in the Medicine River Seam during production and as a function of *GSI*. (C) is for *GSI* = 95 and shows a stable hole; (D) is for *GSI* = 85 and shows a stable hole. The bar scale to the left shows the HB strength/stress variations expected around the wellbore.

The 50 mm diameter hole was the only borehole which remained stable in Coal 1 and Coal 2, whereas the 150 mm diameter borehole required a slotted liner to be installed after drilling. The preferred location for the wellbore was in Coal 1, where GSI was higher, however permeability is lower. The preferred option should be the 50 mm diameter borehole for the Norris MR coal seam evaluated in this study location. An advantage, other than stability of smaller diameter horizontal wellbores, is that smaller diameter wells have been shown to perform better for carrying water and can produce higher gas flow rates (Wilson et al., 2002). The above authors observed that at 1380 kPa reservoir pressure, a 75 mm wellbore produced more gas than a 150 mm wellbore for both 600 m and 1800 m long horizontals, for all well trajectories.

Theoretical stability models based on classic poroelastic stress solutions predict that borehole stability does not depend on hole diameter (Wilson et al., 2002). However, Cameron et al. (2007) stated that a 150 mm horizontal wellbore was predicted to collapse earlier than a 75 mm wellbore when drilling in a high-volatile A bituminous coal at almost 900 m depth. The result from this borehole study on the 50 mm and 150 mm borehole study using the on high volatile C bituminous coals in the central Alberta Plains at 750–800 m depth are in agreement with those of Cameron et al. (2007). Using the HB and GSI based system allows for the direct inclusion of the coal fracture and cleating system, and takes into account the influence of the borehole size on stability.

11.2 Coupled Mechanical and Flow Effects

The second phase of the borehole stability modelling was to investigate the effects of coupling on strength and flow, where the previous section dealt only with flow and strength in an uncoupled manner. In this section, a horizontal well model was developed to intersect the maximum permeability in an anisotropic stress field (Figure 170). The model was constructed such that the borehole was drilled in the direction of the minimum effective stress, intersecting the maximum permeability. The borehole was modelled in two dimensions using half symmetry with a borehole diameter of 140 mm. The geomechanical numerical modelling software used here was FLAC 4.0, which simulates in 2D, and in this case, the x and z direction. The boundaries of the model were ten times the diameter of the borehole. The vertical effective stress (σ'_v) was 10.0 MPa, the maximum horizontal effective stress (σ'_H) was 13.0 MPa, the minimum effective horizontal stress was 5.0 MPa where the coal seam reservoir pressure was 10.0 MPa. This stress field has the horizontal stress being the maximum, where in the Norris study, the vertical stress was the maximum.

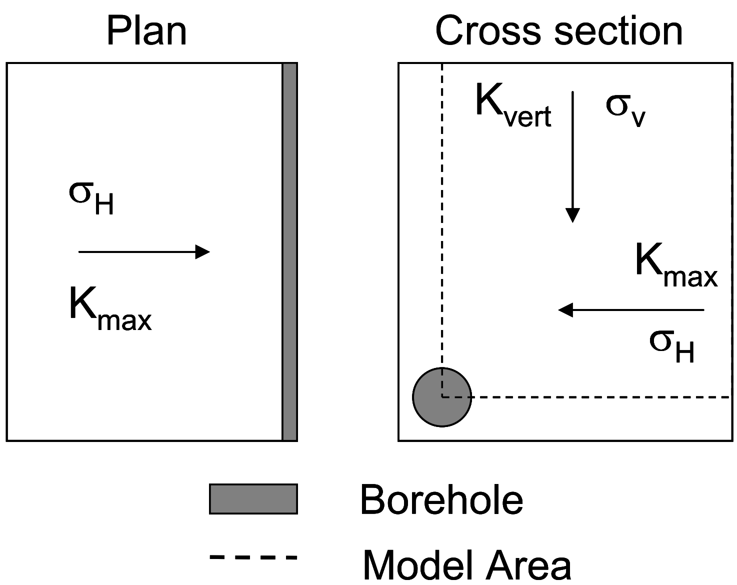

Figure 170. Geometry of a quarter horizontal borehole model showing the maximum and vertical permeability (k) and maximum horizontal (σ_H) and vertical stress (σ_v) directions.

The intact mechanical properties are selected from the GH7 seam from Alberta, Canada (Table 42). Initially, the GH7 coal was assigned a GSI of 90 and the intact HB properties determined, and used in this study. After further analysis, GSI was adjusted to 85, and the HB intact properties calculated again. This is the reason that the current GH7 values do not agree with those presented in Table 42. The intact HB properties were adjusted to fit the borehole size by reducing GSI from the original 90 for the 64 mm diameter core to 80 for the 140 mm diameter borehole, where 80 may still be optimistic. The cleat and bedding plane dilation angles were assumed to be equal with both at 5 degrees.

Table 42. Summary of the geomechanical properties used in the horizontal borehole model.

Mechanical Property	Symbol	Units	Value
GSI	GSI		80
Young's Modulus	E_i	GPa	3.4
Poisson's Ratio	ν		0.3
Dilation Angle	d_i	deg	5
Joint Stiffness Factor	h	MPa	3.7
Intact UCS	σ_{ci}	MPa	45.5
HB coefficient m	m_i		6.2
HB coefficient s	s_i		1.0
Tensile Strength	σ_T	MPa	0.8

The initial vertical and horizontal permeability used in the coal seam were 5 mD and 10 mD respectively. The cleat spacing was 8 mm and the bedding plane spacing was 17 mm. The porosity and porosity changes were not calculated. The borehole was drilled to intersect the maximum permeability and the fracture apertures in the x and z directions were required calculated as 20 μm and 14 μm respectively.

Horizontal Well Drilling

The horizontal wellbore creation was simulated in 10 stages, where the stresses were reduced to 10% of the initial stress field in ten equal stages. This final 10% stress state was meant to mimic a mud cake, however, flow was not simulated and only the mechanical effects on permeability change were captured.

11.2.1 Strength, Deformation, and Permeability Discussion

The HB parameters were degraded from their initial intact values provided in Table 42 through GSI and were calculated with a FLAC FISH routine and used in the modelled simulation of horizontal wellbore advancement. Figure 171 shows the stress state of all of the modelled zones in principal stress space as well as a plot of the HB failure envelope. The failed or plastic zones in the model were only present at the top and bottom of the wellbore in this case. This was expected as the maximum stress will 'flow' around the borehole, creating zones of high compression, while the minimum stress is reduced due to the presence of the borehole wall. The interior of the borehole was held at 10% of the initial stress. The simulation of a small filter cake contributed to a small plastic zone at the top and bottom of the borehole.

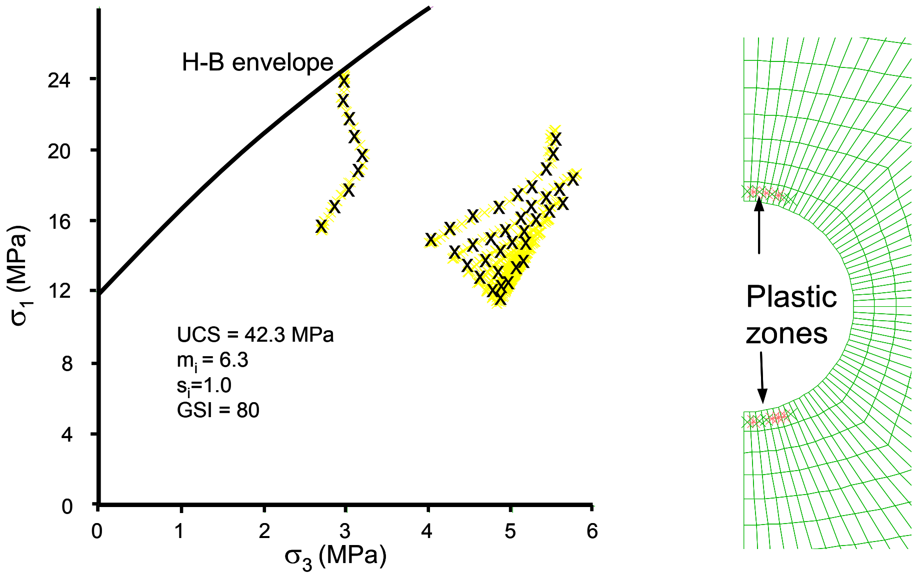

Figure 171. Plot of stress state of all the zones in the model and the HB failure envelope and the plastic zones around the borehole.

The Young's modulus was calculated as a function of the minimum effective stress using the Hoek and Deideriechs Modulus reduction ratio function with GSI and the D function. In the near well region, the minimum effective stress was influenced by the presence of the borehole, and increases with increasing distance from the borehole. Figure 172 shows the results from the borehole model at the final stage of drilling, where the interior of the borehole was held at 10% of the initial stress levels. In the horizontal direction, the modulus is reduced near the well bore, whereas in the vertical directions above and below the wellbore, the modulus increased slightly. These changes in modulus in the near borehole region will create larger or smaller deformations at the same stress levels than further from the borehole region, and will thus spatially influence the changes in permeability.

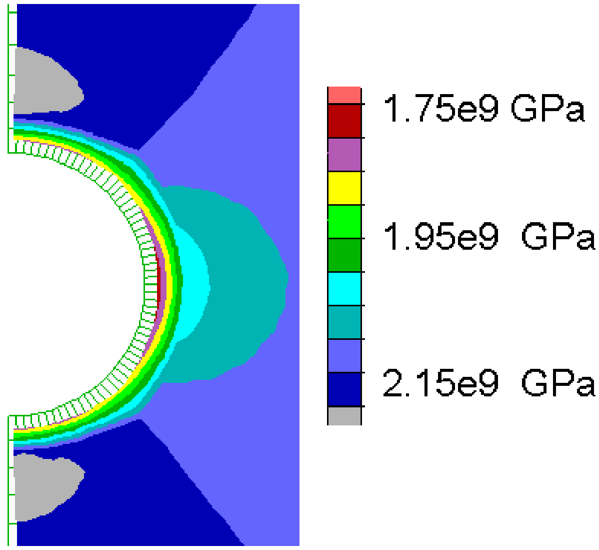

Figure 172. The Young's modulus in the near borehole region at the final stage of simulation.

The progression of changes in the horizontal, vertical, and shear stress, deformation in the horizontal and vertical directions, and the horizontal and vertical permeability at three stages of the simulation are presented in Figure 173. In this simulation, the deformation of the fracture set parallel to the page was not simulated and therefore, the change in horizontal permeability is due only to deformation of the bedding planes.

The horizontal permeability k_{xx} is a contribution of the joint set flow in k_y and k_z, where the vertical permeability k_{zz} is a contribution of the joint set flow in k_x and k_y. In this simulation case, the 2D nature does not allow for changes in the aperture in the k_y direction. Therefore, the horizontal permeability k_{xx} is due to changes in the k_z fracture permeability and the k_{zz} permeability is due to changes in the k_x fracture permeability aperture.

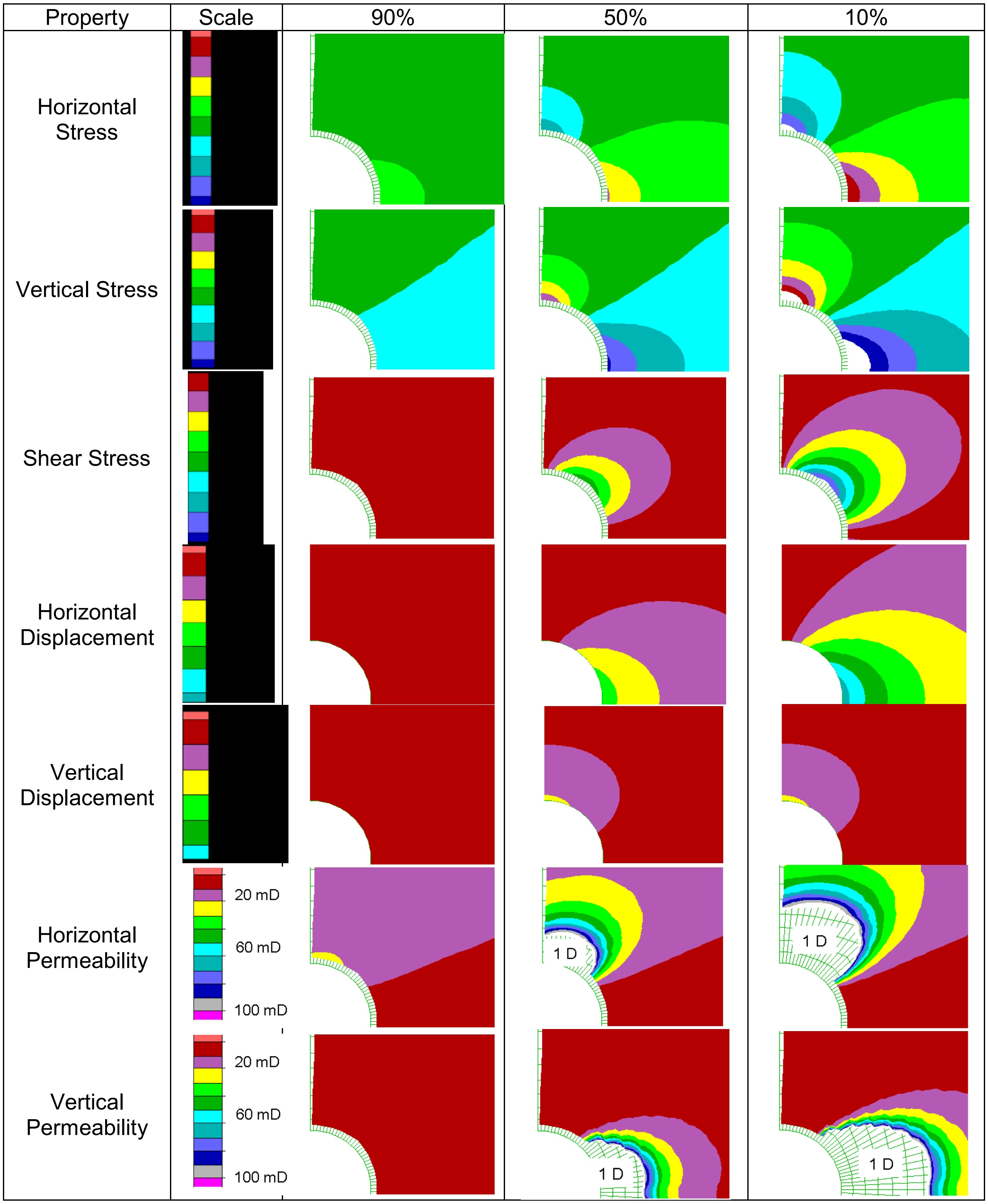

Figure 173. Figures of progression of horizontal, vertical, and shear stress, x and y displacement towards the borehole, and changes in horizontal and vertical permeability at 90%, 50% and 10% of simulated borehole construction. The model size shown is only 1/5 of the actual model size.

Figure 173 shows the evolution of the vertical stress due to the creation of the borehole and how those stress changes influence the vertical and horizontal permeability. Horizontally adjacent to the borehole, the vertical stress field is near the in situ value, however, above the borehole, the stress is unloaded as the borehole is created. The stress unloading creates deformation in the vertical direction towards the borehole, and thus increases the bedding plane aperture, creating an increase in horizontal permeability above the borehole. The borehole wall is displaced 0.5 mm as the vertical stress at that location approaches zero. A similar logic can be used to explain the changes in permeability shown in the vertical direction horizontally adjacent to the borehole.

The results show that in the near well region, the reduction of stress due to the drilling of the wellbore create a more disturbed area (represented by a decrease in the Rock Mass Young's modulus calculated through D). This causes the permeability to change; however, not in the direction of flow perpendicular (towards) the wellbore, but in the direction of flow parallel to the wellbore. Therefore, the increase in permeability due to deformation towards the wellbore will not create increases in flow out of the wellbore, unless the wellbore is directly connected through a fracture or highly conductive plan. Although permeability changes, these changes will most likely not influence the flow of wellbore drilling fluids into the formation, and as a conclusion, coupled reservoir geomechanical effects do not need to be considered when studying drilling infiltration into coal.

11.3 Conclusions

This study used the Geological Strength Index concept and the FLAC finite area software to simulate the uncoupled (flow and mechanics only) and coupled (geomechanics on flow) conditions associated with the drilling of a horizontal well into coal. The first investigation applied the GSI characterization approach, to the Medicine River, Norris area coal seam, to study horizontal wellbore infiltration and the effects of diameter on stability, however no site specific field data were available. The flow and mechanical studies were initially run separately (flow did not feed into mechanics), and then a secondary study was conducted using the DDP model for a similar horizontal wellbore simulation.

Results showed that no significant fluid invasion into the coal seam was observed when drilling in such a manner that leads to the formation of an effective filter cake. Without the formation of a filter cake however, the minimum depth of pore pressure invasion was modelled to be 2200 mm. Not using filter cake could result in an impediment to gas flow from the reservoir into the wellbore as a result of plugging of the permeability pathways by coal fines generated during the drilling process.

A 150 mm and 50 mm diameter horizontal borehole were modelled to simulate production with a bottom-hole pressure of 1 MPa. The GSI characterization system was used to adjust the strength of the material based on the borehole diameter. The 150 mm diameter hole was predicted to fail and a production liner would be required. The 50 mm diameter hole would remain stable during drilling and production and the wellbore should not require a liner. Thus, the smaller diameter hole would be the safer option from a wellbore stability viewpoint.

The second half of this near wellbore study used the DDP model to investigate changes in permeability which may lead to increased flow into the formation. The DDP model was run in and uncoupled where the permeability was adjusted only based on the mechanical deformation due to the borehole creation. The results of the study concluded that the permeability around the wellbore model does change; however, this permeability changes does not influence the flow towards the borehole. The stress changes only influence the permeability parallel to the borehole. Therefore, for this study, when investigating drilling fluid penetration into the formation, coupled geomechanical effects on flow/permeability do not need to be considered.

12 Applications: Coupled Flow Modelling for Caprock Integrity during CBM and CO_2 storage

This section applies the hydrogeomechanical characterization for coal seam reservoirs to a coupled flow model for caprock integrity during CBM and CO_2 storage activities. The previous work is required to partially obtain the required inputs for coupled reservoir geomechanical modelling work. The coupled modelling application and the process to gather the required characterization data is shown in Figure 174.

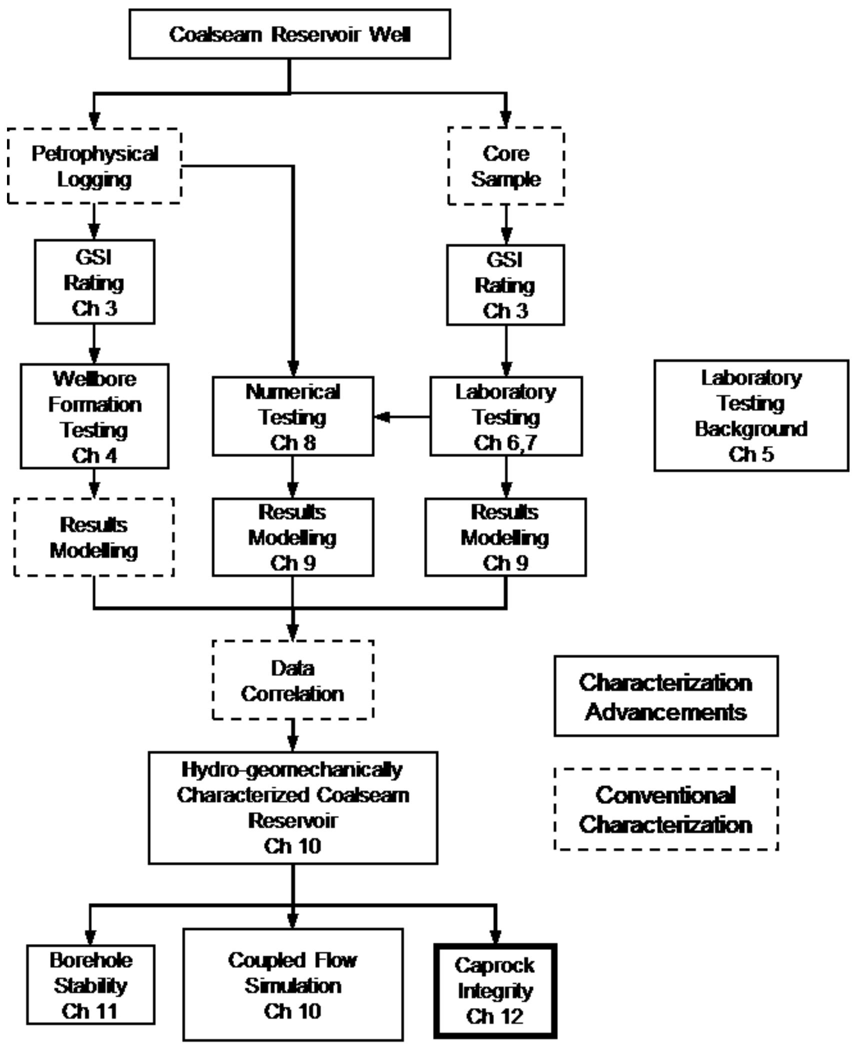

Figure 174. Coalseam reservoir hydro-geomechanical workflow showing what is required to conduct caprock integrity assessments for CBM and ECBM operations.

12.1 Introduction

The CO_2 sequestration life cycle is dependent on a number of operational considerations including the production life of the reservoir, the production performance (good/bad), and if a well is present in the coalseam. If the reservoir was past pressure depletion (primary) recovery and large amounts of gas remained, an ECBM infill pattern may be used to recover more gas. If primary recovery was not economical, then ECBM may be started immediately, and if storage was the only concern, then CO_2 may be injected without production. Each of these scenarios would lead to CO_2 storage; however, the effective stress path and flow behavior of the reservoir would not be unique (Gu and Chalaturnyk, 2005).

One approach to increase production in the Upper Manville formation may be to use enhanced coalbed methane (ECBM) recovery techniques. ECBM involves injecting a secondary gas, such as CO_2 or a gas mixture (flue gas), into the formation to displace the methane (Mavor et al, 2004). CO_2 is preferentially sorbed to coal over methane by a ratio of approximately 2:1, therefore potentially creating a value added option to any CO_2 storage operation in coal (Gunter et al., 2005).

However, changing the gas content and composition, as well as fluid pressures leads to changes in effective stress, creating deformation inside the reservoir as well as surrounding formations (Gu and Chalaturnyk 2006, Connell, 2009). This deformation leads to changes in permeability in the reservoir, and potential damage to surrounding sealing formations for storage (Jimenez 2006). Surface seismic is one approach to monitor and verify the location of CO_2 in a formation or if it has leaked to surrounding formations (McCrank and Lawton, 2008).

12.2 Background

The reservoir geomechanical processes in coal seam reservoirs can be conceptualized as an interaction of multiphase flow behavior (matrix and fracture pressure, gas volume and gas composition) and mechanical behavior (deformation and mechanical properties). While these interactions can be captured in fully coupled formulations describing all the relevant physics of the process, most simulators have been developed by neglecting or simplifying some component of the physics. When considering reservoir flow simulation, the calculation of deformation of the reservoir is generally neglected and to this end, commercial flow simulators are developed to only handle flow. Thus, some form of coupled simulation approaches are required to re-include the physics for the flow-deformation process (Deisman et al., 2009; Jing et al., 1995; Tran et al., 2004; Settari and Walters, 2001).

In this work, the sequentially coupled approach is applied, where two separate simulators (flow and mechanics) are used. The codes are linked at selected time steps by passing coupling variables (pressure, gas content, stress and strain). This approach has been previously applied for coalseam reservoirs (Connell, 2009; Connell and Detournay, 2009; Gu and Chalaturnyk, 2005a, 2005b; Gu and Chalaturnyk, 2010).

12.3 Modelling

A coupled reservoir geomechanical simulation was designed to show the influence of *GSI* on the overall performance of a coal seam reservoir system. The modelling scenario used a nine spot pattern, with a single well for primary CBM production and then CO_2 injection (Figure 175).

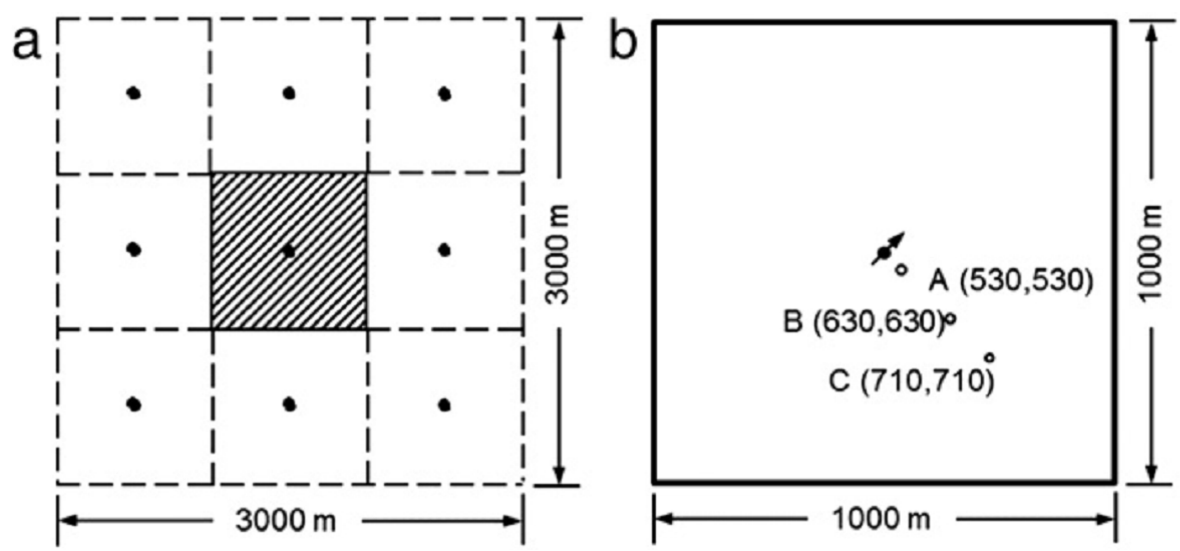

Figure 175. .a) Nine spot production and injection pattern with only the center section being simulated to create roller and gradient pressure boundary conditions. b) A, B, and C are the monitoring points used for stress path analysis.

The simulation codes used were CMG's GEM (Computer Modelling Group Limited, 2010) for flow and Itasca's FLAC3D (Itasca, 2012) for geomechanics. The codes were coupled through a Visual Basic for Applications module. The module passed pressure from the flow simulator to the mechanical code. The mechanical code passed back strain that was translated into permeability changes based on the equations in Section 2.3.2. The mechanical code also included the equations from Section 2.3.2 for deformation. The mechanical code was run in orthotropic elastic mode with the input properties shown in Table 43 with only changes in pore pressure modelled (a shrinkage model was not included). The reservoir stress paths were analyzed for exceeding the material strength.

Table 43. Basic Geomechanical Properties.

Parameters	Units	Over/underburden	Shale Caprock	Coal
Bulk Unit Weight	kN/m^3	2300	2300	1500
Young's Modulus	GPa	30	20	3.44
Poisson's Ratio		0.3	0.3	0.3

12.3.1 Geostatistical Distribution

A total of 12 simulations were set up: a baseline simulation using *GSI* equal to 80 (80*GSI*) and the remaining 11 simulations used a distributed *GSI* with a minimum of 70, maximum of 90, and mean of 80. The initial *GSI* based modulus properties for simulation of the distributed properties was calculated using equations from Section 2.3.1 and Section 2.3.2. *GSI* fundamentally represents the number of joints in a given volume, or the joint spacing. Therefore, permeability is also a function of *GSI* and an appropriate technique to determine this function would be through core logging, downhole permeability testing, and petrophysical logging (Formation Micro Imager).

GSI **to permeability, joint spacing, and modulus**

The focus of this work was to demonstrate the use of geostatistical distributions of *GSI* to assess reservoir performance, therefore simple relationships between *GSI*, fracture spacing and constant fracture apertures were developed based on reasonable assumptions. Table 44 provides the initial fracture spacing and aperture for 80*GSI*. Fracture spacing for *GSI* equal to 90 and *GSI* equal to 70 were then estimated and plotted to create relationships for *GSI* versus joint spacing (Figure 176). A quadratic function was selected to simply fit through all of the data points, although other functions may fit equally as well. However, if more cleat spacing to *GSI* research were undertaken for coal, a natural log function based on the cleat condition and cleat block volume, similar to Cai and Kaiser (2006) which was developed for tunneling, may be created.

Table 44. Basic properties of reservoir system model.

Property	Units	Value
Top depth of coal seam	m	1000
Coal seam thickness	m	4
Shale caprock thickness	m	20
Well Radius	m	0.1
Vertical total stress	kPa	22,000
Minimum horizontal stress	kPa	17,000
Maximum horizontal stress	kPa	24,700
Seam pressure	kPa	9,000
Seam temperature	(°C)	30
Fracture spacing (i,j,k)	(m)	0.1, 0.05, 0.025
Fracture aperture (i,j,k)	(μm)	15,20,7.5
Fracture porosity	(%)	1
Permeability (GSI=80): i,j,k	(mD)	8,2,6
Matrix porosity	(%)	0.001
Water density	(kg/m^3)	990
Water viscosity	(cp)	0.644
Fracture water saturation	(%)	100
Langmuir volume	(mol/kg)	0.4
Langmuir pressure	(kPa)	6900
Sorption time: CH_4,CO_2	days	10,10

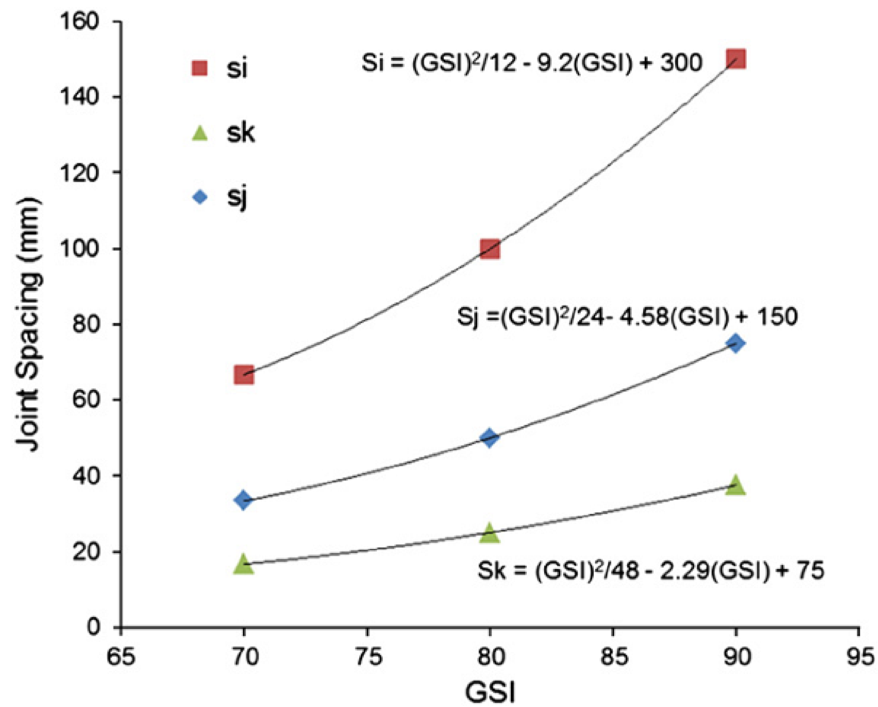

Figure 176. Estimated relationship between *GSI* and joint spacing.

The fracture aperture was assumed to be the same for each value of *GSI* (*i,j,k*=15, 20, 7.5 µm), and using the initial permeability equations, continuous functions for permeability as a function of *GSI* were created (Eq 62, Eq 63, and Eq 64). This allows the initial geomechanical and flow models to be reasonably consistent, where a higher or lower *GSI* value indicates a lower or higher value of permeability, respectively.

$$k_{ii} = (GSI)^2 / 80 - 2.61(GSI) + 144 \tag{62}$$

$$k_{jj} = (GSI)^2 / 278 - 0.748(GSI) + 41 \tag{63}$$

$$k_{kk} = (GSI)^2 / 74 - 2.86(GSI) + 158 \tag{64}$$

To create a consistent property to account for the changes in joint spacing (Section 2.2.1), a fictional directional *GSI* was used to adjust Young's modulus (*E*) which honours the observations of Szwilski (1985) (Eq 65, Eq 66, Eq 67, and Eq 68) (see Section 2.1.1). The Young's modulus is initialized and updated using:

$$E_x > E_y > E_z \tag{65}$$

$$GSI_x = GSI + 5 \tag{66}$$

$$GSI_y = GSI \tag{67}$$

$$GSI_z = GSI - 5 \tag{68}$$

Geostatistical simulation

Unconditional sequential Gaussian simulation geostatistical technique was used to generate 11 realizations for coupled reservoir geomechanical simulation. An essential aspect of the geostatistical modelling was to establish quantitative measures of spatial correlation to be used for the realization simulations. Spatial variability is different for each variable such as facies indicator or rock properties (*GSI*). The variogram is the most commonly used measure of spatial correlation for facies and property modeling.

Experimentally, a semivariogram for lag distance (*h*) is defined as the average squared difference of values separated approximately by *h* as shown in Eq 69 (Deutsch, 2002):

$$\gamma(h) = \frac{1}{2N(h)} \sum_{N(h)} \left[z(u) - z(u+h) \right]^2 \tag{69}$$

N(h) is the number of pairs separated by distance *h*, *z(u)* is random variable at location u and *γ(h)* is the experimentally calculated semivariogram for lag distance.

The experimental variogram points are not directly used in subsequent geostatistical modelling steps such as kriging and simulation; a parametric variogram model is fitted to the experimental points. Nugget effect, spherical, exponential, Gaussian, and hole effect model are common variogram models used to fit experimental variogram.

Frequently there is a need to model joint distribution of multiple variables and variables should be simulated dependent on each other, i.e. co-kriging and co-simulation and not independent kriging and simulation for each individual variable. In that case, cross variogram which determines spatial continuity of each two different variables should be established and considered in addition to variogram generated for each individual random variable (Deutsch, 2002). In the case presented here, it would be ideal to have a relationship between *GSI* and permeability, or *GSI* and joint spacing. This relationship can be developed based on field testing (well tests, etc.) and observations (formation micro image logging, core logging, etc.).

A spherical variogram was selected (Table 45) and unconditional sequential Gaussian simulations were completed using “sgsim” program from “GSLIB” package (Deutsch and Journel, 1998) to generate the synthetic realizations shown in Figure 177 which have means and standard deviations shown in Table 46.

Table 45. Spherical variogram simulation parameters.

Nugget Effect	Max Horizontal Range (m)	Minimum Horizontal Range (m)	Vertical Range (m)
0	700	700	3

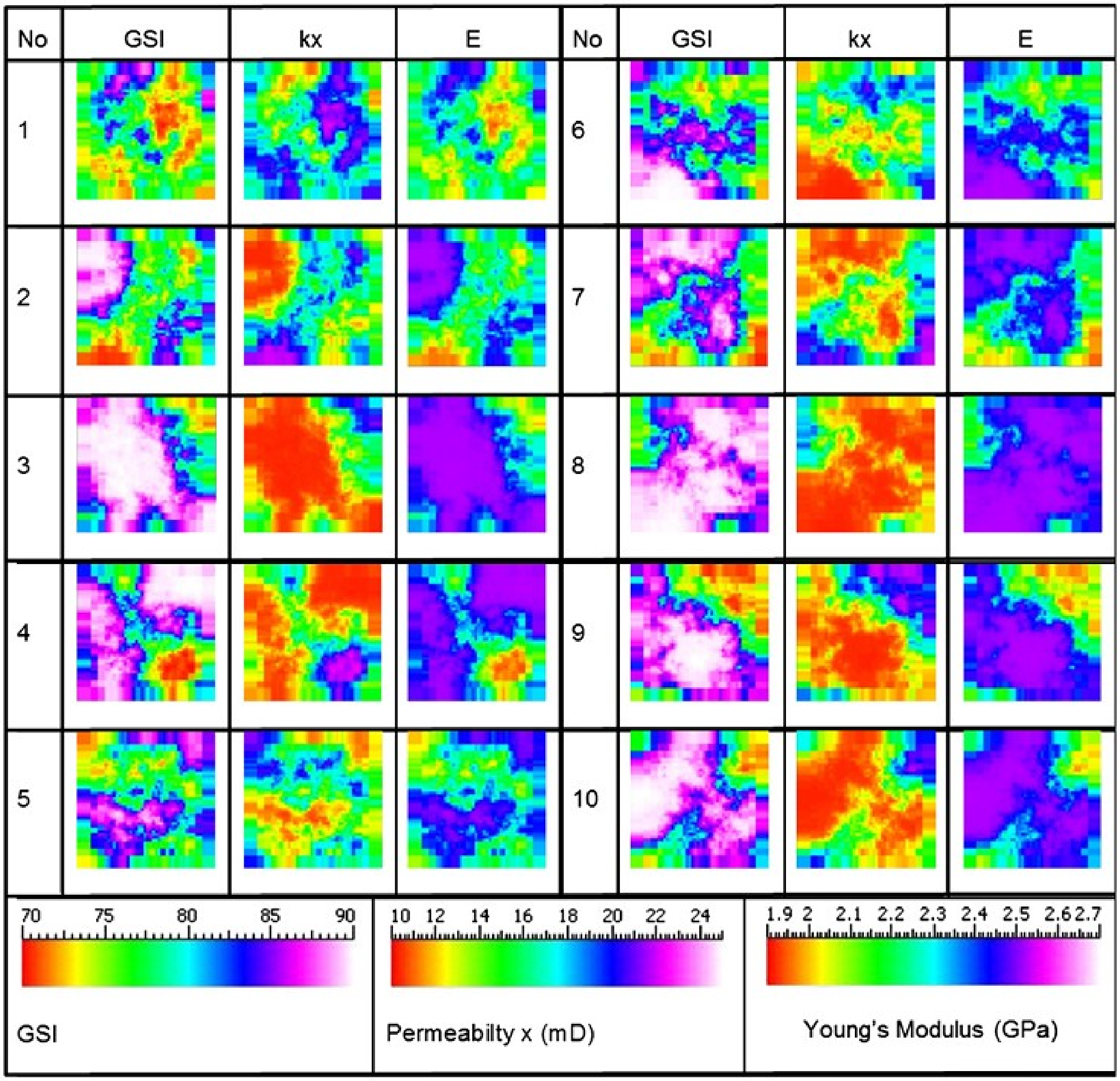

Figure 177. 10 of the 11 realizations of *GSI* and associated permeability and Young's modulus values for the synthetic simulation case. The area matches Figure 175 and is 1000 m by 1000 m.

Table 46. Mean and standard deviation for each of the *GSI* realizations.

Realization Number	Mean	Standard Deviation
1	78.6	5.7
2	79.9	5.8
3	83.4	6.2
4	82.6	6.2
5	79.8	5.5
6	81.8	5.2
7	80.9	5.8
8	85.2	4.8
9	81.2	6.0
10	81.5	6.1
11	78.0	5.6

12.4 Results and Discussion

The study aimed to investigate the variable influence that fracture density throughout the reservoir had on primary production and CO_2 storage through the use of *GSI*. The performance of the reservoir system (reservoir and caprock) is interpreted in the context of production, injection and reservoir and caprock integrity. Production and injection profiles, plus methane and CO_2 adsorption profiles are investigated. Six stress path monitoring points in the reservoir and cap rock are selected for presentation.

12.4.1 CH_4 and CO_2 Rates and Cumulative Production

The well was operated in primary methane production mode for 2 years, then shut in and CO_2 injection started. The uncoupled (flow only) and coupled case were both conducted for 80*GSI*. As expected, the coupled case showed a lower production rate and lower total production than the flow only case. During primary production, where volumetric strain due to changes in gas content is not represented, the decrease in pressure leads to an increase in effective stress, which in turns leads to a reduction in permeability. The peak gas rate was also higher for the uncoupled (370 MSft^3/day) versus the coupled modelling approach (310 MSft^3/day) (Figure 178). The uncoupled model had 210 MMS ft^3 whereas the coupled model had 180 MMSft^3 of cumulative gas production after 2 years.

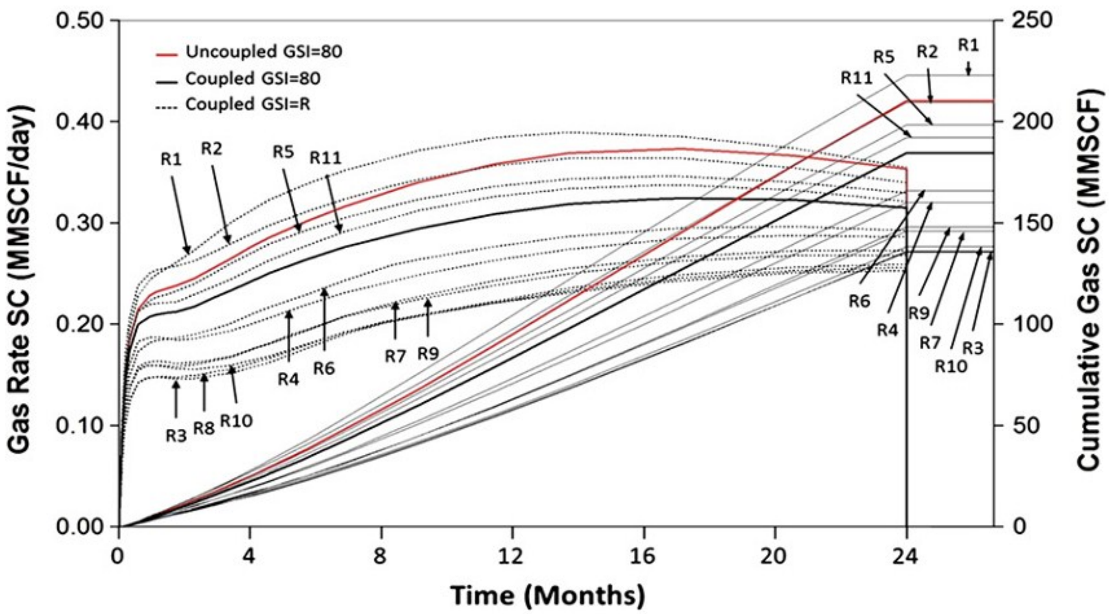

Figure 178. Two years of primary methane production simulation results for uncoupled and coupled reservoir geomechanics using constant *GSI* variable *GSI* (R) with a BHP of 1 MPa.

After the well was operated in primary methane production mode for 2 years, CO_2 injection with a BHP of 13 MPa was started. The peak injection gas rate was higher for the uncoupled (2.7 MMS ft^3/day) versus the coupled modelling approach (2.3 MMS ft^3/day) (Figure 179). The cumulative injected CO_2 for the uncoupled case was 310 MMSft^3, while the coupled case was 270 MMSft^3 after the 3 months of injection.

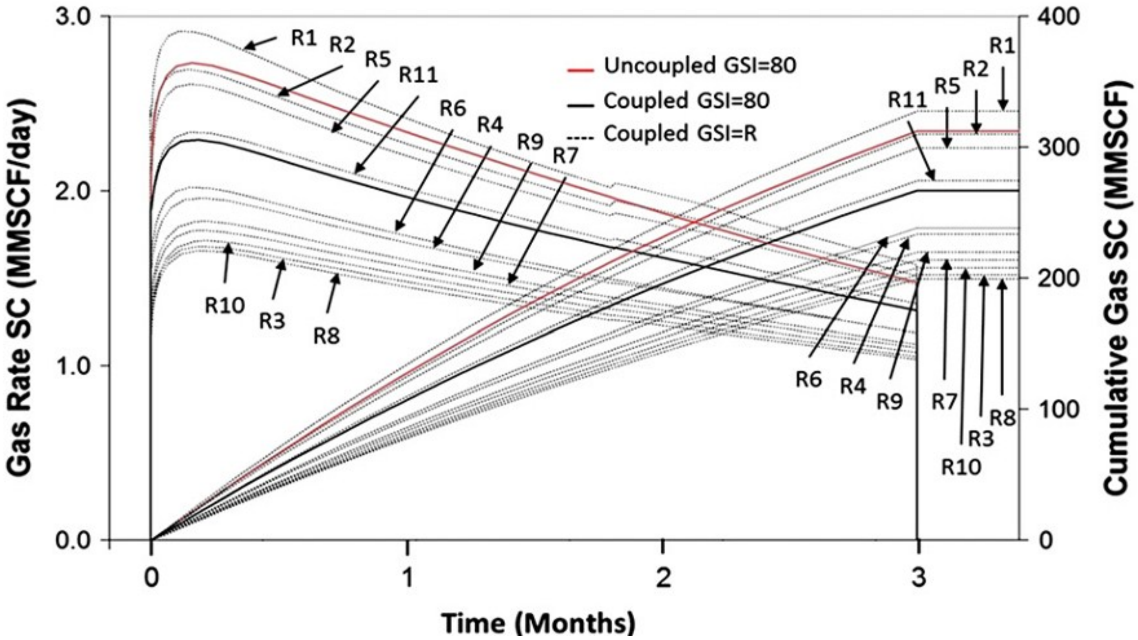

Figure 179. Results for 3 months of CO_2 injection at 13 MPa after 2 years of methane production for the uncoupled and coupled reservoir geomechanics simulations.

The distributed *GSI* models gave peak gas rates and cumulative gas results, all equally probable, ranging above (385 $MSft^3$/day, 220 $MMSft^3$) and below (220 $MSft^3$/day, 135 $MMSft^3$) the 80*GSI*. A similar result was shown for peak CO_2 injection rates and cumulative injected gas results ranging above (2.95 $MMSft^3$/day, 320 $MMSft^3$) and below (1.6 $MMSft^3$/day, 200 $MMSft^3$) coupled constant *GSI* case. The injection rates of CO_2 for the coupled case, if started with no primary production, would be higher than the coupled case, as increases in reservoir pressure would correspond to increases in permeability and thus injectivity. However, due to primary production operations, the reservoir had started at a lower permeability due to pressure depletion (or increased effective stress). The injection rates for the coupled case show a slower decrease in injectivity due to decreases in effective stress.

Geostatistical GSI

Realizations R1, R2, R5, and R11, with means of 78.6, 79.9, 79.8 and 78.0 respectively, all showed higher production rates and cumulative gas production than the simulation using 80*GSI* (which has an initial k_x of 15 mD) (Table 46). The remaining realizations, with *GSI* means above 80, all displayed much lower production rates and cumulative production than the 80*GSI*. The variability between the *GSI* values above and below 80 was expected and the trends are rational, however the variability in production rates and cumulative production shows a much larger than anticipated spread from the constant *GSI* simulation.

Investigation of the distribution of *GSI* and permeability for realizations R1, R2, and R5 (R11 is not shown) reveals high permeability areas or trends in the center of the model which is where the producer/injector is located. These higher permeability zones or 'fairways' can account for the displayed higher cumulative and production rates. The opposite also holds true, when the producer/injector is situated in a low permeability zone, the cumulative production and rates are much lower (R3, R8, and R10).

12.4.2 Desorption and Adsorption

Figure 180 shows the distribution of adsorbed methane after 2 years of production and Figure 181 shows the adsorption of CO_2 after 3 months of injection. Results indicated that during constant injection for the injection period of time, the distribution of *GSI* has little influence on the areas of gas desorption or adsorption. However, it should be noted that each of the simulations was completed to the end of 2 years, and not based on cumulative production. To investigate the influence of a distributed *GSI* on desorbed gas, it would be more appropriate to compare each case at a time where equal cumulative gas production volume has occurred. This comparative approach is not possible in the selected set of coupled simulations. Comparing realizations R2 and R5, which have means of 79.9 and 79.8 respectively, with 80*GSI* results show that desorbed gas distribution is different at the end of the production, but not injection. The cumulative produced gas for R2, R5 and 80GSI was 210, 199, and 185 $MMSft^3$, respectively. The 80*GSI* case shows a moderately uniform desorption zone, whereas the other two realizations present different evolving patterns. Comparing R2 to R5 *GSI* distribution maps (Figure 177), there is a zone of high *GSI* (low permeability) in the North West of R2, where in R5, there are two high *GSI* zones, one in the North East and one in the South West. In the R2 desorption profile, the high *GSI* areas appear to only moderately affect the desorption profile, while in R5, the desorption zone is more constrained by these high *GSI* areas.

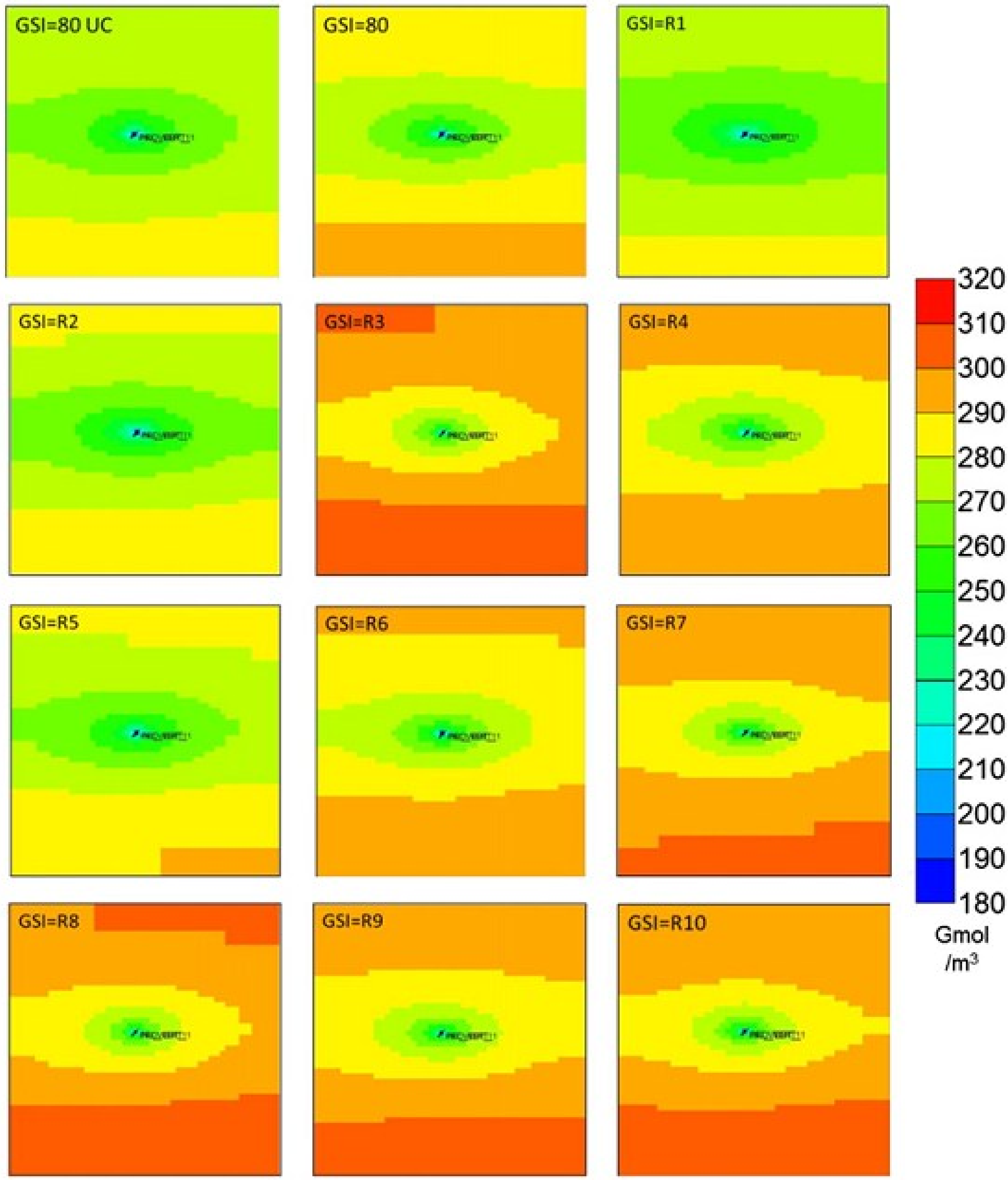

Figure 180. The distribution of sorbed methane after 2 years of production at 1 MPa BHP. The area matches Figure 177 and is 1000 m by 1000 m.

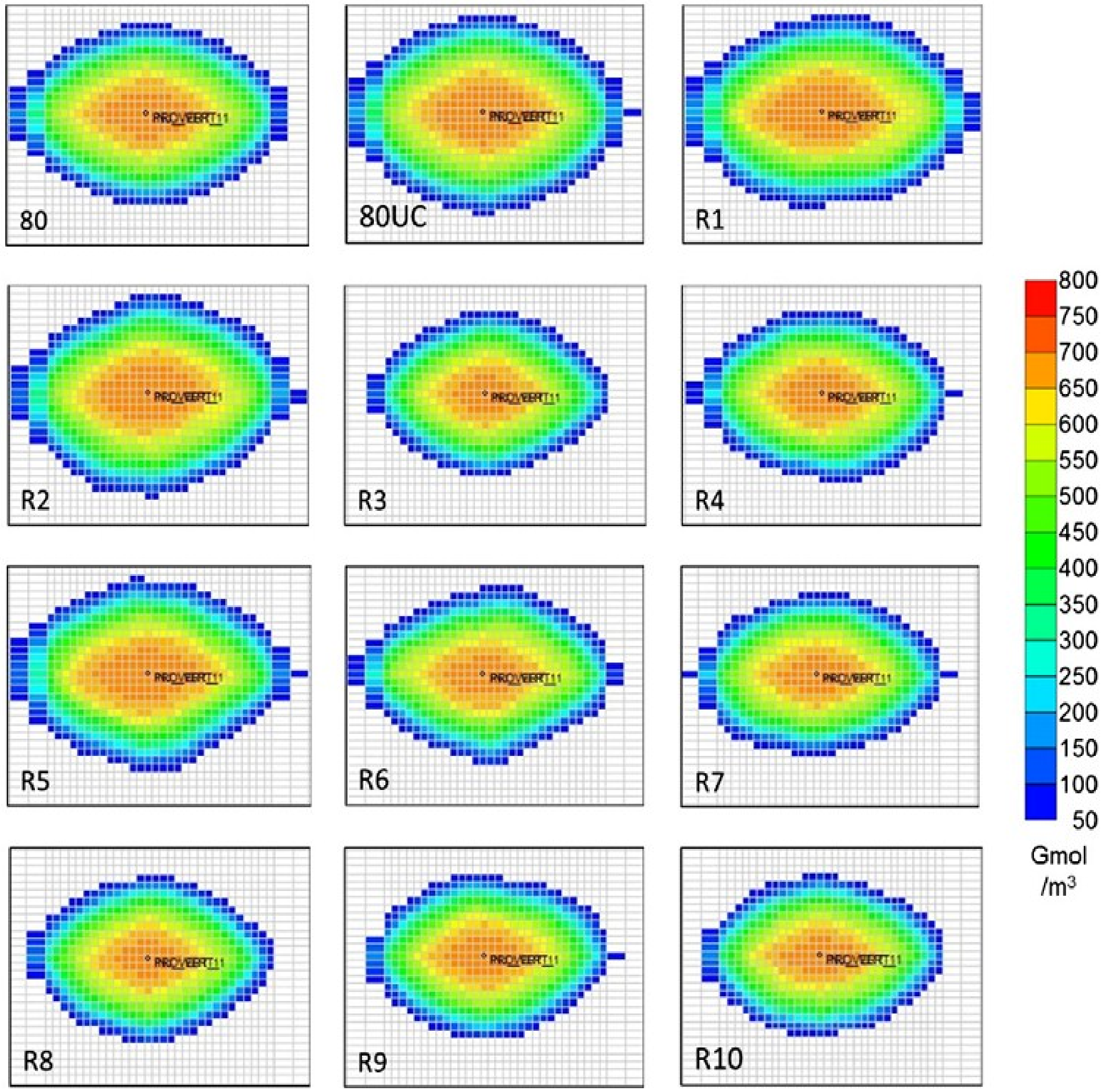

Figure 181. The distribution of adsorbed CO_2in the reservoir at the end of 3 months of injection at 13 MPa BHP. The area matches Figure 177 and is 1000 m by 1000 m.

12.4.3 Stress Path

The principal stresses paths for each of the monitoring points in the reservoir and directly above in the caprock (see Figure 175b) were plotted for the each of the coupled cases (Figure 182). The 80*GSI* stress path is represented with a solid line where the distributed *GSI* realizations are shown with dashed lines. The plotting of the stress path for the elastic simulations allows the investigation into the behavior of the system and the potential for failure in the reservoir and more importantly for CO_2 storage, the overlying caprock (Jimenez, 2006).

Reservoir Stress Path

The major (σ'_1) and minor (σ'_3) principal stresses decrease initially with the initial production and then the minor stress decreases significantly once the depletion pressure front reaches that point in the reservoir. At the end of production, the reservoir pressure is increased due to the injection of CO_2, which lowers the principal stresses. After the initial decrease due to injection, both principal stresses at each monitoring point rebound. In each of the cases, the distribution of *GSI* shows a similar stress path trend and none of them deviate from the general behavior of the constant *GSI* simulation case.

The response of each of the monitoring points is a function of the overall response of the reservoir and caprock system as well as the individual value of *GSI* for that grid block, since *GSI* is linked to Young's modulus. Therefore, labeling the stress paths and linking those to the realizations would not provide enough information to make reasonable decisions.

The Hoek–Brown failure criteria for a *GSI* value of 80 is plotted, however this is only a reference since each of the envelopes at each location would vary depending on the *GSI* for that cell in the simulation. However, it is likely that Pt. A would have failed where Pt. B and Pt. C would be very close to failure based on strength values, for example, from Gentzis et al. (2007). The approach, when conducted for each of the cells in the reservoir, does provide an initial estimation of the behavior, and helps to determine if failure may occur and changes to operating procedures are required for CO_2 storage.

Caprock Stress Path

The stress paths show the major (σ'_1) and minor (σ'_3) principal stresses decrease initially with the initial production for points A and B and then rebound to be above the initial stress state (Figure 182). The stress path for point C only proceeds upwards. At each of the cases, the change in stress is not large, with the stress changes at point A being the largest (σ'_1 and σ'_3 each are approximately 1.5 MPa).

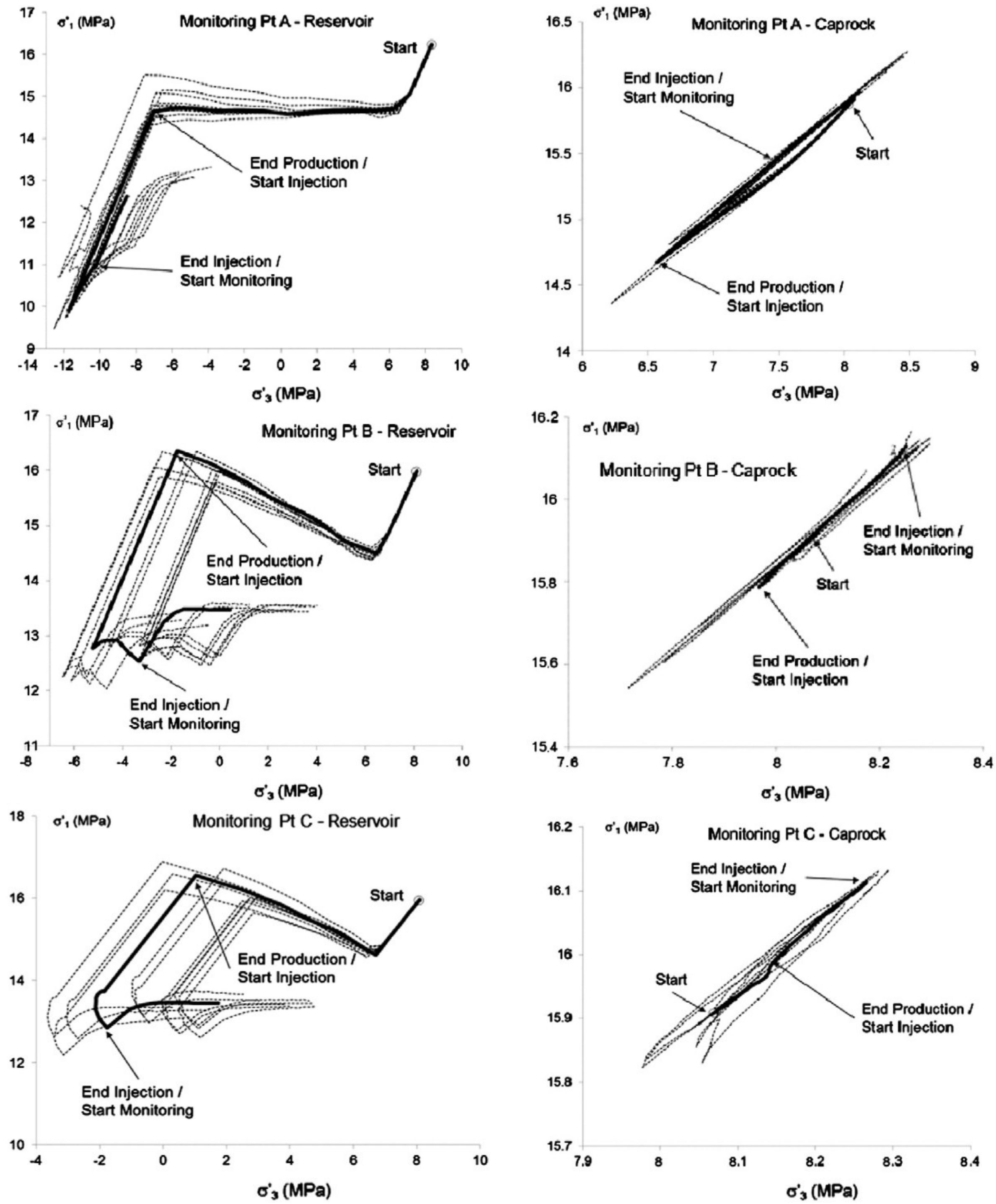

Figure 182. .The stress paths at the reservoir monitoring points shown in Figure 175. a) and b) are monitoring point A for the reservoir and caprock, respectively. c) and d) are monitoring point B for the reservoir and caprock, respectively. e) and f) are monitoring point C for the reservoir and caprock, respectively. The solid line represents the 80 *GSI* model where the dashed lines are the realization

This small change in relation to the larger changes in the reservoir may be explained by both the boundary conditions and the stiffness contrast and thickness differences between the reservoir and caprock. The reservoir is allowed to compress freely due to the roller boundary conditions, moreover the caprock is an order of magnitude stiffer and much thicker than the reservoir and therefore will not deform as much due to surrounding activities.

If failure envelopes where plotted for each of the monitoring points in the caprock, the minimal stress changes in the caprock would show that the three monitoring locations would likely not be at failure. Even though low permeability shale may be an ideal caprock, testing on strength properties is still desirable.

12.5 Conclusions

A spherical geostatistical model was used to populate 11 realizations with the Geological Strength Index for a coalseam coupled reservoir geomechanics simulation study. *GSI* was linked to initial reservoir permeability and was used in coupled reservoir geomechanical simulations to dynamically update permeability and Young's modulus. The results of the simulation work showed that the introduction of a geostatiscally distributed geomechanical indicator (*GSI*) linked to dynamic permeability and Young's modulus greatly influenced the cumulative and production rate of methane as well as the cumulative and rate of CO_2 injection. Additionally, it was demonstrated that the distribution of *GSI* throughout the reservoir had little influence on the distribution of desorbed gas during production or adsorbed gas during injection. The stress paths at three monitoring points showed the changes due to production and injection were variable and deviated from the magnitude of stress changes however the basic shape of the stress path was not altered significantly throughout the realizations.

Conversion of Gas Production Units

$1MMSft^3 = 28.3x10^3\ m^3 = 1.2x10^6$ Gmol

13 Conclusions and Recommendations

A new systematic hydro-geomechanical characterization workflow for coalseam reservoirs was developed and its utility demonstrated using two example applications. Several new observations based on laboratory testing were made including the influence of stress on the adsorption isotherm and the suppression of the volumetric strain associated with gas sorption. A new dynamic permeability model, which included the new disturbance factor function, was developed and shown to fit laboratory observed permeability results very well when using acceptable measured laboratory mechanical properties. The Synthetic Rock Mass modelling approach was investigated in this work, and found to be lacking sufficient capabilities to capture the observed rock mass strength.

13.1 Summary

Rice and Paul stated in 1995, that the primary factors constraining coalseam reservoir development are cost and level of technology available to access the reservoir and a poor understanding of the reservoir behaviour. Since that period, several developments have been made in understanding coal as a reservoir, particularly the influence of geomechanics on the well stability and reservoir performance. This thesis has provided a systematic hydro-geomechanical characterization workflow for the inclusion of geomechanics into the development of a coalseam reservoir by modifying an already established conventional coalseam reservoir workflow. This is particularly important as deeper coalseams have been identified as targets for the disposal and long term storage of CO_2 as a means to mitigate the release of anthropogenic greenhouse gases to the atmosphere, and therefore require geomechanically assessment.

Conventional coalseam reservoir workflow includes field planning and procedures, desorption testing for gas content and sorption isotherms, coal compositional analysis to determine coal rank, and characterization of the fractures and coal macerals. As well, standard oil field injection fall off tests to determine formation permeability and geophysical well logs to determine coal seam locations and thickness would be run.

The hydro-geomechanical characterization workflow was built from a conventional workflow, which includes in situ formation testing, core logging, and laboratory testing

(Figure 183). Characterization of the core using the Geological Strength Index (*GSI*), a new tool for small interval vertical permeability testing, and specific laboratory and numerical testing supplemented the current reservoir characterization procedures. By integrating these additions, the effects of geomechanics on the behaviour of the coalseam reservoir can be systematically assessed for mechanical stability and reservoir flow.

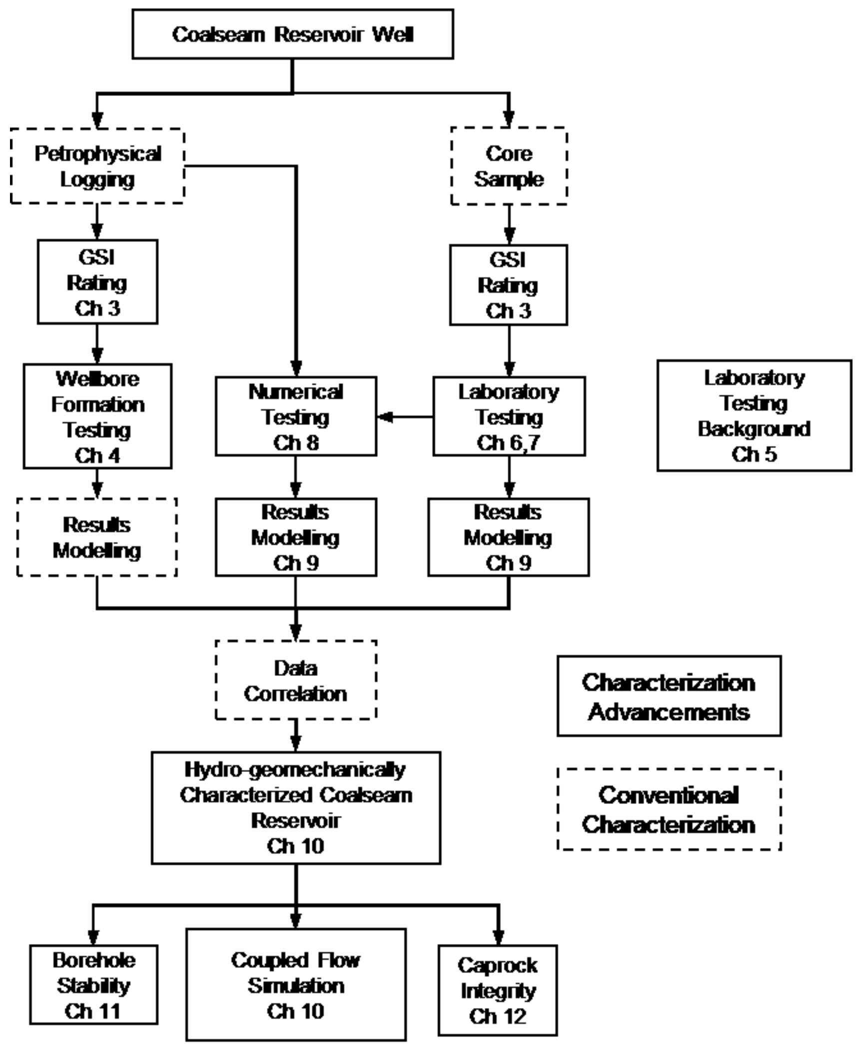

Figure 183. Coalseam reservoir hydro-geomechanical workflow with the dashed boxes representing areas where additions outside of standard characterization are included.

The hydrogeomechanical characterization workflow started with the drilling of a coalseam well and the collection of core samples. The core samples natural cleating/fracturing were analyzed and assigned a GSI value, and then stored for laboratory testing and portioned for determination of gas content. The core hole was then geophysically logged, where the three critical geomechanical logs to run include: dipole sonic, density and formation micro imager (FMI). Next, the formation was tested using a traditional injection/falloff test to obtain bulk permeability. Then the newly developed PTT tool was deployed to measure the formation over a small vertical interval. The collected core samples were then used for canister desorption to determine coalseam gas content, while maintaining the integrity of the specimen for geomechanical testing or using only recovered rubblized core. The remaining coal core was then tested under geomechanical conditions to assess: strength, deformation, dynamic permeability, sonic velocity, and stress dependent desorption. Once this workflow was completed, the coalseam was sufficiently hydro-geomechanically characterized and studies on wellbore stability, permeability changes around the wellbore, and reservoir performance including geomechanics were conducted. As well, the workflow does not eliminate elements of the conventional characterization approach, therefore any conventional reservoir engineering correlations and studies can be completed.

A critical component of the workflow is the use of the GSI and the ability to scale from the laboratory to the field. Hoek's original GSI figures were designed as a non-dimensional technique to apply an index to a fractured rock structure versus an excavation opening. This non-dimensional approach was applied to collected coal specimens, typically containing fractures at the laboratory scale, to scale the measured Hoek Brown (HB) strength parameters to intact HB parameters and measured Young's modulus values to intact values through the Hoek and Diederichs Young's modulus reduction ratio function. The Hoek and Deideriechs Young's modulus reduction ratio function is sensitive to the disturbance factor, D, however it is not well defined. Therefore, a function which relates the D to the effective confining stress was developed and includes a pseudo joint stiffness factor, h. This function is relatively simple to determine based on laboratory data, and fits the laboratory data reasonably well.

The wellbore deployed Pressure Transient Testing (PTT) tool was developed as a part of a secondary research program to assess the sealing capabilities of annular cement behind a cased wellbore. The PTT tool was deployed in the Weyburn field to assess the integrity of wellbore cements placed in the 1950s and their ability to seal against vertical migration of formation fluids. The tool has a four packer design capable of being run in a

115 mm diameter wellbore (open or cased) and transmits a fluid pulse down a coiled tubing while measuring the pressure at four locations (3 between packers, 1 below bottom packer). In a newly cemented coalseam wellbore with competent cement, or in an open hole, the PTT tool is capable of measuring the coalseams vertical permeability, supplementing the data acquired by a conventional pressure falloff test.

The strength and deformation behaviour of coal has been shown to be variable, depending on stress state, orientation, gas content, gas type, and scale of investigation. The flow behaviour and, very recently, adsorption capacity of coal is shown to be dependent on orientation and stress/strain state. Therefore, to test these behaviours in the context of the hydro-geomechanical workflow, a two laboratory testing apparatus were designed and constructed capable of testing these observed behaviours. The first testing system included a triaxial cell capable of measuring coal fines and permeability during strength testing. The second system included a triaxial cell capable of measuring sonic normal and shear wave velocities and deformation due to changes in axial and radial stress, gas content, and gas type. As well, the triaxial cell and flow system was able to measure gas volumes flowing through the sample for permeability measurements as well as sorption on the coal, all at isothermal temperatures. The construction of these laboratory apparatus allowed for three separate testing programs to be conducted: one at a commercial laboratory and two at the University of Alberta.

The first testing program was comprised of several conventional triaxial tests with measurement of compressional and shear wave velocities and flow to calculate the dynamic Young's modulus and permeability, respectively. The testing was completed by a consulting company (TerraTek) with the processed data provided for analysis. The second program used unconventional stress paths with permeability measurements at various stress states along the stress path. During permeability testing, a production cell was used to collect coal fragments during sample failure for fragmentation measurements. The third testing program used a triaxial stress path that remained in the elastic range and measured sonic velocity, deformation, and gas sorption at several effective stress states. This program was completed utilized the LPG apparatus with the newly developed Deisman Triaxial (TDS) cell. All of the coal specimens tested were prepared from large block coal samples collected and preserved from three different open pit mine sites: Greenhills, Elkview, and Cardinal River located in the Rocky Mountains in Canada.

The results from the testing program (and previous researchers work) demonstrated that the strength, deformation, sonic velocity, permeability, and gas content of the coal are all dependent on the effective stress. Additionally, dilation during gas sorption was measured, showing that the application of an effective stress did suppress the increase in volume of the specimen however, further research is required. In general, the specific testing outlined in this laboratory testing program should be used for the hydro-geomechanical characterization of the coalseam. The testing program also showed that there is a relationship between the static and dynamic Young's modulus. The testing program also showed that the gas content of the coal did not influence the static or dynamic Young's modulus however, further long term testing is required to be definitive.

After the laboratory testing program had been completed, the results were scaled up to reservoir size for further reservoir engineering analysis. The empirical approach discussed so far is the use of GSI, but the hydro-geomechanical characterization workflow also considered the use of the Synthetic Rock Mass (SRM) approach. The SRM is a numerical technique that uses laboratory calibrated Bonded Particle Models to simulate the intact coal matrix, where the fractures are explicitly accounted for through a sliding joint model. The SRM was then tested, numerically at several scales using conventional geomechanical tests to determine geomechanical properties at several scales. Initially, it was attempted to validate the SRM in 2D against smaller laboratory specimens of simulated rock with 1, 2 and 3 fractures. The SRM matched the observed fracturing reasonably well; however it was unable to match the measured strength. The SRM was then used in 3D for a coal seam, simulating 140, 200, 300, and 500 mm diameter coal specimens at multiple confining stresses. The results were extracted to supplement the GSI approach of scaling from the laboratory to the field.

Once the laboratory and SRM results were collected, the data was modelled to provide relationships between the laboratory and field for engineering applications, where the field applications could include borehole stability or the influence of geomechanics on flow. The results for strength modelling were fit using the HB strength parameters and GSI.

HB with GSI provided a consistent approach for scaling from the laboratory to the field for investigations into borehole stability across several borehole sizes. Additionally, the modelling of the coal strength results using the HB parameters showed that using a_{RM} of 0.4 provided the best fit. The Young's modulus reduction ratio, along with the disturbance factor function using the h parameter, fit the laboratory results very well and should be adopted for hydro-geomechanical characterization workflow. A function to relate the influence of stress on the sorption isotherm was developed for engineering applications, but caution should be used when applying it to the field.

Several permeability measurements were made at multiple unconventional stress paths/states (not only constant confining stress and applied deviator). To capture these behaviours and to link the mechanical testing to the changes in permeability, the Young's modulus reduction ratio function was used as an input to a strain-based dynamic permeability (DDP) model. The dynamic permeability model accounts for fracture persistence, change in aperture, anisotropic Young's modulus, and anisotropic strain changes, in addition to being linked directly to GSI, allowing for direct and consistent inclusion into the hydro-geomechanical characterization workflow. The DDP model was applied against observed laboratory results from this work, and from other researchers and showed excellent agreement for conventional isotropic and unconventional anisotropic changes in permeability.

After the development of the hydro-geomechanical characterization workflow, the approach was applied to a data set from CNOOC Nexen and the Norris coalseam reservoir area in Alberta. Core was initially collected and/or photographed and GSI was assigned to intervals based on those photographs. In-situ testing was used to determine the bulk permeability of the formation. The characterized coalseam was then analyzed under drilling and the production for stability, fluid flow, fluid flow changes and coal fines inflow causing plugging of formation. For CNOOC Nexen, wellbore azimuths were assessed using simulation and the long term stability of the coal was assessed using uncoupled simulation. Additionally, coupled simulation was used to assess long term changes in permeability due to geomechanical effects.

In the case of the Norris coalseam, two sizes of boreholes were studied for stability, 50 and 150 mm. The use of characterization workflow allowed for the HB strength envelopes to easily be scaled to either borehole application. The dynamic permeability model was then used to investigate changes in permeability which may influence the near wellbore behaviour during drilling.

The final application of the workflow investigated the behavior of the overlying shales/caprocks in a full coalseam reservoir field where primary production occurred for 2 years and then CO_2 injection began. A simulated coalseam was used and the properties were input based on laboratory testing completed here. The study used the dynamic permeability model and geostatisical realizations of GSI showing the influence of a variable GSI and the inclusion of geomechanics on flow.

13.2 Conclusions

Conclusions have been drawn and presented at the end of each chapter throughout this thesis, therefore only a short summary of those conclusions is presented here.

A methodology to characterize the mechanical and hydro-geomechanical properties of a coalseam reservoir has been presented. The importance of testing for reservoir properties at reservoir conditions is discussed, particularly when testing for behaviours which may be stress sensitive. The Geological Strength Index is applied to coal and provides a consistent approach to scale the strength and deformation properties from a laboratory and borehole scale to required coalseam engineering application scales. The original GSI chart has been redrawn and adapted for application to circular boreholes, rather than the original horseshoe tunnels, This was a minor but required development for the application to coalseam reservoir characterization.

Techniques to determine intact Hoek-Brown parameters and Young's modulus values from fractured coal samples through laboratory testing have been introduced. Approaches using a specimen scale GSI and back calculating the intact compressive strength and m_i parameters using the Levenberg-Marquardt regression approach are shown. Additionally the Young's modulus reduction ratio function developed by Hoek and Diederichs with the inclusion of GSI and *D* has been reviewed. A relationship for *D* as a function of the minimum effective stress has been developed and the function works reasonably well for coal.

A vertical permeability wellbore tool deployable on coiled tubing has been developed and successfully deployed in a CO_2 wellbore integrity project in the IEAGHG Weyburn–Midale CO_2 Monitoring and Storage Project. The PTT tool was designed to measure wellbore cement permeability for deployment inside a 139.7 mm diameter wellbore. The tool was built with sufficient flexibility to be deployed in any type of reservoir material to conduct injection testing over a short interval (0.5m to 3.8m), which is ideal for the thin seams typically encountered in coalseam reservoirs.

Obtaining core for a sampling program can be capital intensive and collecting intact is difficult. Therefore, a non-destructive testing program on a single coal specimen should be used to acquire: static and dynamic anisotropic deformation, the effects of stress on permeability, effects of gas pressure/composition on strain. The strength of the coal may also be determined, after the previous sequence and destructive tests should be planned carefully. These tests can all be conducted using the experimental capabilities developed at the University of Alberta to carry out hydromechanical characterization of coal. The apparatus met several of the design criteria goals including: pore fluid saturation, minimized specimen disturbance, production/injection capabilities, representative stress conditions, internal measurements, and failure analysis and resulting coal fines distribution.

The coal fines collection apparatus was design with slotted platens to produce coal fines generated during failure of the coal specimen. The coal fines could be collected in a downstream production accumulator for further analysis. The low permeability gas apparatus contains a 45 MPa pressure, 60 °C temperature triaxial cell for hydromechanical testing capable of measuring diffusive properties, absolute and relative permeability, strength, deformation and compressional and shear wave velocities under independent axial and confining stresses and fluid saturation conditions.

The testing program in this thesis investigated the influence of effective stress and gas content on the mechanical, flow, velocity and sorption properties of coal. The coal was obtained from three different coal mines: Cardinal River, Greenhills, and Elkview. Three separate coal testing programs were used to measure properties for hydrogeomechanical characterization:

1. Conventional Triaxial Stress path with Velocity and Permeability;
2. Unconventional Triaxial Stress path with Permeability and Particle Size; and
3. Elastic Triaxial Stress path with Velocity and Methane Sorption.

These testing programs specifically investigated the influence of effective stress on the following, and found several key behaviours:

- Deformation: Increasing effective stress created a concave downward non-linear relationship between confining stress and Young's modulus.
- P and S wave velocity: Increasing effective stress created a concave downward non-linear relationship. Increasing gas content did not significantly influence the P or S wave velocity.
- Strength: Increasing the confining stress created a concave down non-linear relationship strength envelope.
- Coal fines generation: During permeability testing during unconventional stress path testing, coal fines were not produced and collected in the accumulator however, fines may have been created but were not able to flow through the cleats.
- Permeability: Several permeability tests were completed, showing that as the isotropic effective stress increased, the permeability decreased, however if an unconventional stress path was used, the permeability increased relative to the isotropic value.
- Gas Content: The application of effective stress reduced the sorbed methane of the coal at equivalent gas pressures for increasing effective stress states.
- Swelling Strain: The application of effective stress reduced the swelling strain experienced by the coal at equivalent gas pressures for increasing effective stress states.

The SRM was used in attempts to supplement the existing laboratory testing. The SJ model was shown to reasonably reproduce (within 74%) observed laboratory internal flaw behaviours of crack initiation, propagation and coalescence behaviours. However, there is great concern that the strength values reproduced in the experiments do not match laboratory observations. Calibrating the BPM only to the *UCS*, *E* and ν may not be sufficient to capture observed material behaviours and the 2D version of the SRM should be used with caution and not for design purposes at this point.

The SRM in three dimensions was used to estimate the strength and deformation of a simulated coal seam. Two cases were demonstrated, incorporating different levels of input data and simulation procedures. Scale effects, anisotropy, and confining stress influences were captured for the coal seam. The output from the SRM was intended to complement existing empirical techniques and to add information were data is lacking. The SRM output can be used to help scale the strength and deformation properties of the coal seam to the desired size for the intended application, including bore stability analysis or reservoir geomechanics simulations. The strength and modulus results from scaled SRM testing do not display acceptable behaviour, and much improvement is required to better represent the intact matrix and joints.

The strength, Young's modulus, methane sorption, methane strain and dynamic permeability of coal testing results have been modeled. The laboratory determined strength and Young's modulus were well fit using Hoek-Brown and Hoek and Diederichs respectively, using *GSI* and *D* as a function of *h*. The Hoek and Diederichs equation relating modulus to *GSI*, developed using hard rock experiment data, does predict coal behaviour reasonably well. The sorption of methane onto coal with changes in isotropic effective stress was modelled using a simple equation which may be suitable for engineering applications. A strain based three dimensional dynamic permeability model, which includes *GSI*, E_i, ν, and dilation angle was developed and applied to observed laboratory measurements of permeability results for several non-isotropic unconventional stress paths as well as several isotropic results from the literature.

The hydrogeomechanical characterization approach was used in three applications: full CBM characterization and simulation, borehole stability and fluid infiltration investigation, and a coupled reservoir geomechanical simulation for CBM and CO_2 storage and caprock integrity.

The CBM characterization and simulation application showed the limitations of company collected field data when a specific geomechanical study is not planned. Limited data from CNOOC-Nexen made it difficult to determine inputs for simulation and several assumptions had to be made. Three areas were studied in this example, showing the initial horizontal borehole azimuths required for maximum production and stability. Uncoupled simulation was used to assess the long term wellbore stability and how the stress field in the coal surrounding the wellbores changes and approaches failure. This failure would create coal fines which will plug the flow paths of the coal, reducing production and possibly plugging downhole pumps. Coupled simulation was used to determine the long term influence of geomechanical effects on production. It was shown that these effects for this field were minimal. Additionally, the influence of sorption strain was investigated, and it was determined that for this field, sorption strain does not play a role in increase production.

The borehole and fluid infiltration study used *GSI* and the FLAC finite area software to simulate the uncoupled (flow and mechanics only) and coupled (geomechanics on flow) conditions associated with the drilling of a horizontal well into coal. The investigation applied parts of the hydrogeomechanical characterization approach to study horizontal wellbore infiltration and the effects of borehole diameter on stability. Both 150 mm and 50 mm diameter horizontal boreholes were modelled to simulate production with a bottom-hole pressure of 1 MPa. The 150 mm diameter hole was predicted to fail, whereas the 50 mm diameter hole would remain stable during drilling and production and the wellbore should not require a liner. Next, the DDP model was used in an uncoupled method where the permeability changes were monitored but not used for flow simulation. The results of the study concluded that the permeability around the wellbore model does change; however, this permeability change does not influence the flow towards the borehole.

For the coupled reservoir geomechanical simulation, a geostatistical model was used to populate 11 realizations with the *GSI*, where *GSI* was linked to initial reservoir permeability and then used with the DDP model to update permeability and Young's modulus. The simulation results demonstrated that the introduction of a geostatiscally distributed geomechanical indicator (*GSI*) linked to dynamic permeability and Young's modulus greatly influenced the production rate and cumulative volume of methane as well as the production rate and cumulative volume of CO_2 injection. Additionally, it was evident that that the distribution of *GSI* throughout the reservoir had little influence on the distribution of desorbed gas during production or adsorbed gas during injection. Stress path monitoring points were used in the reservoir and in the overlying caprock, showed that changes from simulation to simulation occurred, but the basic shape of the stress path was not altered significantly throughout the realizations. The results also indicated that caprock did not reach a stress state where fracturing may occur, but further detailed analysis with plastic behaviour should be conducted.

13.3 Recommendations and Future Work

The hydro-geomechanical characterization workflow for coalseam reservoirs was the first attempt to integrate a well-known geological index: GSI. The use of GSI presented here was outside of its traditional area of application and was shown to integrate well into the characterization of coal. The GSI concept, along with several other observations require more investigation to prove their worth as tools for use in characterization of not only coalseam reservoirs, but new unconventional reservoirs, which are naturally fractured or have fractures networks engineered. This section will work through each chapter, providing areas for improvements and future research.

- Chapter 2 provided an overview of the hydrogeomechanical characterization workflow, building off of Levine’s (2006) sorbed gas reservoir characterization approach. The energy industry has looked to shale gas reservoirs as an abundant source of natural gas. Applying the GSI based characterization to the naturally fractured state or to the hydraulically fractured system may provide a means to systematically evaluate and rank the shale gas reservoirs.
- Chapter 3 investigated and focused GSI for coalseam reservoir applications by using Hoek’s original concept of a non-dimensional value adjust to the excavation size. The original concept for GSI was to be used in a non-structured fracture network, however coal (and most rock) does have a structured fracture network. The concept of assigning

GSI to a fractured laboratory specimen needs more detailed and focused work for scaling to intact properties. It is recommended that focused studies be completed on coal or any rock that is fractured at the laboratory scale. However, as noted, obtaining real samples with these characteristics is extremely difficult, and therefore synthetic samples are most likely required.

- Chapter 3 also introduced the disturbance factor function, where D is a function of the effective stress and a joint stiffness factor h. This function worked very well in the Hoek and Diederichs Young's modulus reduction ratio when applied to coal at the laboratory scale. However, the disturbance factor function was not applied to the Hoek Brown failure envelope and was not applied to other rock types. Future work should be completed to investigate the applicability of this function to other rock types and to the Hoek Brown failure envelope calculations. If this function holds true, a more thorough approach for the determination of the property h may then be required.
- Chapter 4 showed the development of a downhole tool which could be applied in an open or cased wellbore with a minimum diameter of approximately 120 mm. The tool worked very well when set up properly, however there were several packers which were damaged during deployment. Detailed investigation into the packer issues is required can be completed in the laboratory.
- Chapter 6 discussed the development of two triaxial testing systems. The coal fines production system worked as desired. The Low Permeability Gas (LPG) flow system and TDS triaxial cell could be improved. The LPG system uses large accumulators to control the flow on one side of the sample and on the other side uses a high precision pump. The system was plumbed to include an additional high precision pump and it would be beneficial to include this for better control for flow through experiments. The TDS triaxial cell was designed to have a radial LVDT chain measure radial displacements however, these displacements were not recorded with sufficient accuracy during the deformation of the coal. Therefore improving the system with point contact LVDTs spaced around the specimen may be a better option for measurement. Additionally, a lead membrane wrap was used to prevent gas migration out of the specimen into the confining fluid. A continuous lead membrane may be an option for future testing.

- Chapter 7 presented results from several laboratory testing programs on coal samples from open pit mines which were analogues for reservoir coalseam samples. Obtaining samples from a deep coalseam reservoir is a priority for testing the theories and verifying the laboratory results presented here. Several of the tests completed used methane and examined the sorption onto the coal and the effects on the mechanical behaviours. These tests were not allowed to come to complete equilibrium, however were very close to equilibrium. It would be recommended to repeat a majority of the coal tests with methane over extended periods (5-10 days per step, instead of 2-3 days) on similar full scale 2.5 inch by 5 inch specimens. The behavior of the sorption isotherms under stress is a critical observation. Recent studies by Hol et al (2011) have used an oedometer cell and applied CO_2 to a crushed coal specimen. The tests presented here used an intact specimen and methane, but the results were similar: applied effective stress influences sorption behaviour. In the tests executed in this work, the coal was initially methane free then methane was sorbed onto the coal. This is not exactly the process which would occur in situ and therefore requires additional work to determine an appropriate procedure to investigate this sorption and sorption strain phenomena.
- Chapter 8 used the SRM in attempts to include better representation of the coal fracture network. Currently, the coal fracture network is represented as through going disks and not rectangular planes. This problem was addressed by Doug Stead at Simon Fraser University (in press) after the work was completed here. Additional numerical work should progress to match laboratory test results for strength and deformation in 2D and in 3D. The 2D fracture coalescence matches the observations well, but the strength and deformation does not match sufficiently. Investigation and improvements in the poor representation of friction angles observed here should be completed.
- Chapter 9 deals with modelling the results of the laboratory and numerical tests. The strength and deformation recommendations have been discussed and the Hoek Brown failure criterion appears to be a much improved method for modelling coal. Further investigation into the a_{RM} exponent should be completed and a more robust function of geological identifier should be determined instead of the current published function. Shortcomings from the sorption testing results have been discussed above, however, an

improved function to capture the changes in Langmuir volume and Langmuir pressure are required rather than the simplistic empirical formulations shown here.

- Chapter 9 also developed a dynamic strain based permeability model and showed the applicability of the model matching some permeability data, and not matching other data. Flow through a fracture network is a complex process and capturing all of the behaviours is overly optimistic and over the past 10-20 years there have been several relationships developed by many researchers. The method developed here may be advantageous over some other models due to the inclusion of GSI, but may be lacking a complete representation of the physics of the problem when compared to others. The investigation into these types of stress/strain based analytical models may have reached their end and with the large capacity of computing power, numerical approaches should be considered for future work.
- Chapters 10, 11 and 12 were applications of the hydro-geomechanical characterization approach for coalseam reservoirs. The borehole stability modelling section did not use real field data for the calibration of the HB failure criterion. Therefore, to truly determine the applicability of the workflow, real data from an active CBM site is required. Also, the coupled reservoir modelling approach for caprock integrity only estimated the geomechanical inputs. A real field case with sufficient data (the CNOOC Nexen study did not have enough field data) would be required to determine the shortcomings of the coupled reservoir geomechanics simulation and the adjustments of the hydro-geomechanical characterization of coal for coalseam reservoirs.

14 References

Alberta Environment, 2013. doa. Dec 10, 2013. http://environment.alberta.ca/02888.html

Ask, D., Cornet, F.H., Fontbonne, F., Nilsson, T., Jönsson, L., Ask, M.V.S. 2009. A quadruple packer tool for conducting hydraulic stress measurements in mines and other high stress settings. International Journal of Rock Mechanics and Mining Sciences. 46, 1097–1102.

Azmi, A.S., Yusup, S., Muhamad, S. 2005. The influence of temperature on adsorption capacity of Malaysian coal. Chemical Engineering and Processing. 45 (5) 392-396.

Arri, L.E., Yee, D., Morgan, W.D., Jeansonne, M.W. 1992. Modeling coalbed methane production with binary gas sorption. Presented at SPE Rocky Mountain Meeting in Casper Wyoming, May 15-21, 1992. 730989

Bachu, S. 2007. Carbon dioxide storage capacity in uneconomic coal beds in Alberta, Canada: Methodology, potential and site identification. International Journal of Greenhouse Gas Control. 1(3): 374-385.

Barton, N., Bandis, S., Bakhtar, K. 1985. Strength, deformation, and conductivity coupling of rock joints. International Journal of Rock Mechanics and Mining Science & Geomechanics Abstracts. 22 (3), 121–140.

Beaton, A., Langenberg, W., Pană, C. 2006. Coalbed methane resources and reservoir characteristics from the Alberta Plains, Canada. International Journal of Coal Geology. 65, 93–113.

Bell, J.S., Price, P.R., and McLellan, P.J. 1994. In situ stresses in the Western Canada Sedimentary Basin. In Geological Atlas of the Western Canada Sedimentary Basin. Mossop, G. & Shetsen I. Canadian Soceity of Petroleum Geologist and Alberta Research Council. 439-446.

Bell, J. S. and Babcock, E. A. 1986. The stress regime of the Western Canadian Basin and implications for hydrocarbon production. *Bul.Can.Pet.Geol.*. 34: 364-378.

Bell, J.S., Bachu, S., 2003. In situ stress magnitude and orientation estimates for Cretaceous coal-bearing strata beneath the plains area of central and southern Alberta. Bulletin of Canadian Petroleum Geology 51 (1), 1–38.

Bell, G.J., Rakop, K.C. 1986. Hysteresis of methane/coal sorption istotherms. Presented at the 61st Annual Technical Conference and Exhibition of the SPE held in New Orleans, LA, USA. Oct5-8, 1986.

Bieniawski, Z.T., 1968. The effect of specimen size on compressive strength of coal. International Journal of Rock Mechanics and Mining Sciences. 5, 325–335.

Bieniawski, Z.T., van Heerden, W.L., 1975. The significance of in situ tests on large rock specimens. International Journal of Rock Mechanics and Mining Science & Geomechanics Abstracts. 12, 101–113.

Brace, W.F., Walsh, J.B., Frangos, W.T. 1968, Permeability of granite under high pressure. Journal of Geophysical Research. 73(6): 2225-2236.

Brown, A.M. 2001. “A step-by-step guide to non-linear regression analysis of experimental data using a Microsoft Excel spreadsheet.” Computer Methods and Programs in Biomedicine. 65 (2001) 191-200.

Busch, A., Gensterblum, Y., Krooss, B.M., Siemons, N., 2005. Investigation of high-pressure selective adsorption/desorption behaviour of CO_2 and CH_4 on coals: an experimental study. International Journal of Coal Geology. 66 (1–2), 53–68.

Bustin, M. 1999. Geology and some engineering aspects of coalbed methane. Canadian Coalbed Methane Forum Technical Conference, Calgary, Canada, September 21-23.

Bustin, R.M., Clarkson, C.R. 1998. Geological controls on coalbed methane reservoir capacity and gas content. International Journal Coal Geology. 38 3-36.

Bustin, R.M. 1997. The importance of fabric and composition on stress sensitivity of -permeability in some coals of the northern Sydney Basin, Australia: relevance to coalbed methane exploitation. American Association of Petroleum Geologists. Bull. 81, 1894–1908.

Butt, S.D. 1999. Development of an apparatus to study the gas permeability and acoustic emission characteristics of an outburst-prone sandstone as a function of stress. International Journal of Rock Mechanics and Mining Sciences. 36(8): 1079-1085.

Butt, S.D. 2006. Characterization of the permeability and acoustic properties of an outburst-prone sandstone. Journal of Applied Geophysics. 58: 1-12.

Berkowitz, N. 1993. An introduction to coal technology. 2nd Edition, Academic Press.

Cai, Y., Liua, D., Mathews, J., Pan, Z., Elsworth, D., Yaoa, Y., Li, J., Guoa, X. 2014. Permeability evolution in fracture coal – combining triaxial confinement with x-ray computed tomography, acoustic emission and ultrasonic techniques. International Journal of Coal Geology. 122 91-104.

Cai, M., Kaiser, P.K., Tasaka, Y., Maejima, T., Morioka, H. 2004. Estimation of rock mass deformation modulus and strength of jointed hard rock masses using the GSI system. International Journal of Rock Mechanics and Mining Sciences. 41, 3–19.

Cameron, J.R., Palmer, I.D., Moschovidis, Z.A. 2007. Effectiveness of horizontal wells in CBM. Paper 0716, 2007 International Coalbed Methane Symposium, Tuscaloosa, AL. 18 pp.

Cho, N., Martin, C.D., Sego, D.C. 2007. A clumped particle model for rock. International Journal of Rock Mechanics and Mining Science. 44, 997–1010.

Clarkson, C.R. Bustin, R.M. 1997. Variation in permeability with lithotype and maceral composition of Cretaceous coals of the Canadian Cordillera International Journal Coal Geology. 33, 135-151.

Computer Modelling Group Limited, 2010. GEM - Generalized Equation of State Model Compositional Reservoir Simulator. Calgary, Alberta, Canada.

Comsol Inc., 2006. Comsol Multiphysics Version 3.2., User's Manual. Burlington, MA, USA.

Comsol Inc., 2008. Comsol Multiphysics Version 3.5., User's Manual. Burlington, MA, USA.

Connell, L.D., 2009. Coupled flow and geomechanical processes during gas production from coal seams. International Journal of Coal Geology. 79, 18–28.

Connell, L.D., Detournay, C., 2009. Coupled flow and geomechanical processes during enhanced coal seam methane recovery through CO_2 sequestration. International Journal of Coal Geology. 77 222–233.

Corkum, A.G., Martin, C.D. 2007. The mechanical behaviour of weak mudstone (Opalinus Clay) at low stress levels. International Journal of Rock Mechanics and Mining Sciences. 44 196–209.

Crow, W., Carey, J.W., Casada, S.E., Williams, D.B., Celia, M.A. 2010. Wellbore integrity of a natural CO_2 producer. International Journal of Greenhouse Gas Control. 4 186–197.

Cosdale, P.J., Beamish, B.B., Valix, M. 1998. Coalbed methane sorption related to coal composition. International Journal of Coal Geology. 35 147-158.

Cui, X., and Bustin, R.M. 2005. Volumetric strain associated with methane desorption and its impact on coalbed gas production from deep coal seams. AAPG Bulletin V89 N9 1181-1202.

Dabbous, M.K., Reznik, A.A., Mody, B.G., Fulton, P.F., and Taber, J.J. 1976. Gas water capillary pressure in coal at various overburden pressures. Soc. Pet. Eng. J. 16, 261-268.

Deisman, N. and Chalaturnyk, RJ. 2012. Comparative stress distribution in coupled and uncoupled SAGD reservoir simulation. In *Proceeding of CIM – 21st Canadian Rock Mechanics Symposium. Edmonton, Canada. 7-9th, 2012.*

Deisman, N., Mas Ivars, D., Chalaturnyk, R.J. 2009. An Adaptive Continuum/Discontinuum Coupled Reservoir Geomechanics Simulation Approach for Fractured Reservoirs. SPE Reservoir Simulation Symposium, 2-4 February 2009, The Woodlands, Texas, 2009. SPE 119254-MS.

Desroches, J, James, L., Berard, T. 2006. Building a mechanical earth model for storage integrity. In *Proceedings, CO2SC Symposium 2006. LBNL, Berkely, California, March 20-22/ 2006.*

Deutsch, C.V. 2002. Geostatistical Reservoir Modeling. New York, Oxford.

Deutsch, C.V. 2002. Work Flow in Geostatistical Reservoir Modeling., ed. Journal, A.G. Chap. 1.6, 21-29. Oxford: Applied Geostatistical Series.

Deutsch, C.V., Journel, A.G., 1998. GSLIB: Geostatistical Software Library and User's Guide, Second edition. New York, Oxford.

Douglas, K.J. 2002. The Shear Strength of Rock Masses. M.Sc Thesis. University of New South Whales.

Detournay, E. 1998. Hydraulic conductivity of closed rock fracture: an experimental and analytical study. Underground Rock Engineering. 168-173.

Environment Canada. 2013. Canada's Emissions Trends. Cat. No.: En81-18/2013E-PDF. ISSN 2291-9392.

Flores, R.M. 1997. Coalbed methane: from hazard to resource. Int. J. Coal Geol. 35 3-26.

Gas Research Institute. 1992. Gas Research Institute Topical Report, GRI-92/0460.1, 62.

Gamson, P.D., Beamish, B., and Johnson, D.P. 1993. Coal microstructure and micropermeability and their effects on natural gas recovery. Fuel. 73, 87-99.

Gentzis, T., 2009. Stability analysis of a horizontal coalbed methane well in the Rocky Mountain Front Ranges of SE British Columbia, Canada. International Journal of Coal Geology. 77, 328–337.

Green Tweed Oilfield Operations, 1930 Rankin Road, Houston, TX 77073 USA.

Gu, F., Chalaturnyk, R.J. 2005a, Analysis of coalbed methane production by reservoir and geomechanical coupling. Journal of Canadian Petroleum Technology. 44(10): 33-42.

Gu, F., Chalaturnyk, R.J. 2005b. Sensitivity study of coalbed methane production with reservoir geomechanic coupling simulation. Journal of Canadian Petroleum Technology. 44 (10). 23-32.

Gu, F., Chalaturnyk, R.J. 2006. Numerical simulation of stress and strain due to gas sorption/desorption and their effects on in-situ permeability of coal beds. Journal of Canadian Petroleum Technology. 45 (10), 52–62.

Gu, F. 2009. Reservoir and geomechanical coupled simulation of CO_2 sequestration and enhanced coalbed methane recovery. Ph D Thesis, University of Alberta, Edmonton, Alberta, Canada.

Gu, F., Chalaturnyk, R.J. 2010. Permeability and porosity models considering anisotropy and discontinuity of coalbeds and application in coupled simulations. Journal of Petroleum Science and Engineering. 74 (3–4), 113–131.

Gunter, W.D., Mavor, M.J., Robinson, J.R. 2005. CO_2 storage and enhanced methane production: Field testing at Fenn-Big Valley, Alberta, Canada, with application, In Greenhouse Gas Control Technologies. 7. 413-421.

Gunter, W.D., Gentzis, T., Rottenfusser, B.A., Richardson, R.J.H., 1997. Deep coalbed methane in Alberta, Canada: a fuel resource with the potential of zero greenhouse gas emissions. Energy Conversion and Management. 38, S217–S222.

Harpalani, S. 2006. Flow behavior of deep coal-gas reservoirs. Golden Rocks 2006, The 41st U.S. Symposium on Rock Mechanics, Golden, Colorado, USA, June 17-21.ARMA/USRMS 06-918.

Harpalani, S. and Chen, G. 1993. Gas slippage and matrix shrinkage effects on coal permeability.

Harpalani, S and Chen, G. 1997. Influence of gas production induced volumetric strain on permeability of coal. Journal of Geotechnical and Geological Engineering. 15 303–325.

Harpalani, S., Singh, K., and Zutshi, A. 2006. CO_2/N_2 flow behavior of deep coal-gas reservoirs. Proceedings of Golden Rocks 2006, the 41st US symposium on rock mechanics (USRMS), Paper 06-918, Golden, Colorado, USA.

Harrison, S., 2002. Hydrogeological characterization of the Weary Creek exploration area, southeastern British Columbia. Proceedings, 4th Annual Unconventional Gas and Coalbed Methane Conference, Calgary, AB, October 2002.

Hawkes, C.D., Gardner, C. 2013. Pressure transient testing for assessment of wellbore integrity in the IEAGHG Weyburn–Midale CO_2 Monitoring and Storage Project. International Journal of Greenhouse Gas Control Technology. 16 (S), S50–S61.

Hawkes, C.D. 2007. Assessing the mechanical stability of horizontal boreholes in coal. Canadian Geotechnical Journal 44, 797–813.

Hazzard, J.F., Young, R.P. 2000. Simulating acoustic emissions in bonded-particle models of rock. International Journal of Rock Mechanics and Mining Science. 37,867–872.

Hazzard, J.F., Young, R.P. 2002. Moment tensors and micromechanical models. Tectonophysics 356, 181–197.h

Hazzard, J.F., Young, R.P. 2004. Dynamic modelling of induced seismicity. International Journal of Rock Mechanics and Mining Science. 41, 1365–1376.

Ho, A. 2002. Experimental Methodology Used to Investigate Transport Processes in Cap Rock. M Sc, Civil and Environmental Engineering University of Alberta. p. 135.

Hoek, E., Brown, E.T. 1997. Practical estimates of rock mass strength. International Journal Rock Mechanics and Mining Science. 34, 1165-1186.

Hoek, E. 1994. Strength of rock masses. International Society of Rock Mechanics New Journal. 2 (2), 4–16.

Hoek, E. Brown, E.T. 1997. Practical estimates of rock mass strength. International Journal of Rock Mechanics and Mining Sciences. 34 (8), 1165–1186.

Hoek, E., Corranza-Torres, C., Corkum, B. 2002. Hoek–Brown Criterion—2002 edition. Proceedings of the NARMS-TAC Conference, vol. 1. University of Toronto Press, Toronto, Canada, pp. 267–273.

Hoek, E., Deideriechs, M.S. 2006. Empirical estimation of rock mass modulus. International Journal of Rock Mechanics and Mining Sciences. 43 (2), 203–215.

Hol, S., Peach, C.J., Spiers, C.J. 2011. Applied stress reduces the CO_2 sorption capacity of coal. International Journal of Coal Geology. 85, 128–142.

Hol, S., Spiers C.J. 2012. Competition between adsorption induced swelling and elastic compression of coal at CO_2 pressures up to 100 MPa. Journal of Mechanics and Physics of Solids. 60 1862-1882.

Holt, R.M., Kjolaas, J., Larsen, I., Li, L., Pillitteri, A.G., Sonstebo, E.F. 2005. Comparison between controlled laboratory experiments and discrete particle simulations of the mechanical behaviour of rock. International Journal of Rock Mechanics and Mining Science. 42, 985–995.

Hsieh, P.A., Tracy, J.V., Neuzil, C.E., Bredehoeft, J.D., Silliman, S.E. 1981. A transient laboratory method for determining the hydraulic properties of tight rocks – I. Theory. International Journal of Rock Mechanics Mining Science and Geomechanics Abstracts. 18, 245–252.

Hycal Energy Research Laboratories. Special Core Studies, Coring, Preserving, and Testing, 1999 p. 509.

Itasca Consulting Group Limited, 2011. FLAC3D – Fast Lagrangian Analysis of Continua in 3 Dimensions Version 4.0, User's Manual. Minneapolis.

Itasca Consulting Group Inc. 2008. PFC2D - Particle Flow Code in 2 Dimensions, Version 4.0 Minneapolis, ICG.

Itasca Consulting Group, 2007. PFC 3D —Particle flow code in 3 dimensions. Ver. 4.0 PreRelease. Minneapolis, USA.

Itasca, 2012. Fast Lagrangian Analysis of Continua in 3 Dimensions (FLAC3D). Ver. 5.0 Itasca Consulting Group, Minneapolis, USA.

Inouye, A. 1951. A modern theory on the structure and caking properties of coal from the rheological viewpoint. Journal of Colloid Science. 6 190.

Jimenez, J. 2006, Geomechanical Performance Assessment of CO_2 - EOR Geological Storage Projects. Ph D, Civil and Environmental Engineering, University of Alberta. p. 327.

Jing, L., Tsang, C.-F., Stephansson, O. 1995. DECOVALEX—an international co-operative research project on mathematical models of coupled THM processes for safety analysis of radioactive waste repositories. International Journal of Rock Mechanics and Mining Science & Geomechanics Abstracts. 32 (5), 389–398.

Jones, C., Smart, B.G.D. 2002. Stress induced changes in two phase permeability. Presented at Rock Mechanics Conference in Irving Texas, October 20-23. SPE/ISRM 78115.

Kaiser, P.K. and Morgenstern, N.R. 1981. Time-dependent deformation of small tunnels –II. Typical test data. International Journal Rock Mechanics and Mining Science & Geomechanical Abstracts. 18, 141-152.

Karacan, CO. 2007. Swelling-induced volumetric strains internal to a stress coal associated with CO_2 sorption. International Journal of Coal Geology. 72. 209-220.

Khandelwal, M., Singh, TN. 2009. Correlating static properties of coal measures rocks with P-wave velocity. International Journal of Coal Geology. 79. 55-60.

Kulatilake, P.H.S.W., Malama, B., Wang, J. 2001. Physical and particle flow modeling of jointed rock block behavior under uniaxial loading. International Journal of Rock Mechanics and Mining Sciences. 38, 641–657.

Karacan, O., and Okandan, E. 2001. Adsorption and gas transport in coal microstructure: investigation and evaluation by quantitative X-ray CT imaging. Fuel. 80. 509-520.

Labauch, S.E., Marrett, R.A., Olson, J.E. and Scott, A.R. 1998. Characteristics and origins of coal cleat: A review. International Journal of Coal Geology. 35, 175-207.

Langenberg, C.W., Beaton, A., Berhane, H. 2006. Regional evaluation of the coalbed-methane potential of the Foothills/Mountains of Alberta, Canada. International Journal of Coal Geology. 65, 114–128.

Laxminarayana, C., Crosdale, PJ. 1999. Role of coal type and rank on methane sorption characteristics of Bowen Basin, Australia coals. International Journal of Coal Geology. 40. 309-325.

Levine, J.R. 1996. Model study of the influence of matrix shrinkage on absolute permeability of coalbed reservoirs. In: Gayer, R., Haris, I. (Eds.), Coalbed Methane and Coal Geology, vol. 109. Geological Society Special Publication, pp. 197–212.

Levine, J.R. 2006. Composition and analysis of sorbed gas reservoirs. May 22, 2006. 2006 International Coalbed Methane Symposium Short Course. Tuscaloosa, Alabama, USA

Liu, J., Elsworth, D., Brady, B.H. 1999. A coupled hydromechanical system defined through rock mass classification schemes. International Journal for Numerical and Analytical Methods in Geomechanics. 23, 1945–1960.

Li, H., Shimada, S., Zhang, M. 2004. Anisotropy of gas permeability associated with cleat pattern in a coal seam of the Kushiro coalfield in Japan. Environmental Geology. 45-50.

Langmuir, I. 1918. The adsorption of gases on plane surfaces of glass, mica and platinum. Journal of the American Chemical Society. 40. 1361-1403.

Marinos, P., Hoek, E., and Marinos, V. 2006. Variability of the engineering properties of rock masses quantified by the geological strength index: the case of ophiolites with special emphasis on tunnelling. Bulletin of Engineering Geology and Environment. 65, 129-142.

Mas Ivars, D. 2010. Bonded-Particle Model for the Deformation, Yield and Failure of Jointed Rock Masses. Ph. D. Thesis, KTH, Stockholm, Sweden. 2010.

Mas Ivars D., Deisman N., Pierce M., and Fairhurst C. 2007. The synthetic rock mass approach – a step forward in the characterization of jointed rock masses. in The Second Half Century of Rock Mechanics (11th Congress of the International Society for Rock Mechanics, Lisbon, July 2007.

Mas Ivars D., Pierce M., DeGagné D. and Darcel C. 2008. Anisotropy and scale dependency in jointed rock mass strength — A synthetic rock mass study. Published in the proceedings of the First International FLAC/DEM Symposium on Numerical Modeling, Minneapolis, U.S.A.

Mas Ivars, D., Pierce, M., Darcel, C., Reyes-Montes, J., Potyondy, D.O., Young, R.P., Cundall, P.A. 2001. The Synthetic rock mass approach for jointed rock mass modelling. International Journal of Rock Mechanics and Mining Science. 48 219-244.

Massarotto, P., Rudolph, V., Golding, S.D., Iyer, R. 2003. The effect of directional net stresses on the directional permeability of coal. in the proceedings of the International Coalbed Methane Symposium Tuscaloosa, Alabama April 2003.

Mavor, M.J. 1999. Coal natural gas reservoir properties and formation evaluation techniques. In Canadian Coalbed Methane Forum Technical Conference, Calgary, Canada, September 21-24. Sproule.

Mavor, M.J., Gunter, W.D., Robinson, J.R. 2004. Alberta Multiwell Micro-Pilot Testing for CBM Properties, Enhanced Methane Recovery and CO_2 Storage Potential SPE Annual Technical Conference and Exhibition, Houston, Texas, 26-29 September 2004.SPE 90256-MS.

Mazumder S., Karni, A., Heinz Wolf, K. 2006. Swelling of coal in response to CO_2 sequestration for ECBM and its effect on fracture permeability. SPE Journal. 390-398.

McCrank, J., Lawton, D.C. 2008. Seismic characterization of a CO_2 flood in Ardley Coals, Alberta, Canada. The Leading Edge. 28. 820-825.

Medhurst, T.P. 1996. Estimation of the in situ strength and deformability of coal for engineering design. Ph D Thesis, Dept. Min. Min. Mat. Eng., University of Queensland, Australia.

Medhurst, T.P., Brown, E.T. 1997. A study of the mechanical behaviour of coal for pillar design. International Journal of Rock Mechanics and Mining Sciences 35, 1087–1105.

Milne, D., Hadjigeorgiou, J., Pakalnis, R. 1998. Rock mass characterization for underground hard rock mines. Tunnelling and Underground Space Technology 13 (4), 383–391.

Min, K.B., Rutqvist, J., Tsang, C.F., Jing, L. 2004. Stress-dependent permeability of fractured rock masses: a numerical study. International Journal of Rock Mechanics and Mining Sciences. 41 1191-1210.

Mitra, A., Harpalani, S., Kumar, A. 2008. CO_2/N_2 injection in deep coals and its impact on coal permeability. San Francisco 2008, the 42nd US Rock Mechanics Symposium and 2nd U.S.-Canada Rock Mechanics Symposium, held in San Francisco, June 29-July 2, 2008. ARMA 08-077.

MacLeod K, Chec R, and Hughes D. 2000. CBM Resource Potential in the Plains Area of Alberta. Presented at the 2000 SPE/CERI Gas Technology Symposium held in Calgary, Alberta, Canada 3-5 April. SPE 59784.

Neuzil, C.E., Cooley, C., Silliman, S.E., Bredehoeft, J.D., Hsieh, P.A. 1981. A transient laboratory method for determining the hydraulic properties of tight rocks – II. Application. International Journal of Rock Mechanics Mining Science and Geomechanics Abstracts. 18, 253–258.

National Energy Board. 2014a. Canada's Energy Future – Reference Case and Scenarios to 2030 – Energy Market Assessment. doa. Dec 8, 2014. https://www.neb-one.gc.ca/nrg/ntgrtd/ftr/archive/2007/nrgyftr2007chptr3-eng.html

National Energy Board. 2007. Coalbed Methane Fact Sheet. Doa: Dec 8, 2014. http://www.neb-one.gc.ca/nrg/sttstc/ntrlgs/rprt/archive/hrsshcnynclbdmthn2007/clbdmthnfctsht-eng.html

Ornes, A., Chalaturnyk, R.J. 2008. Numerical simulations in support of the design of in-well verification testing of well integrity. In: 4th Wellbore Integrity Network Meeting in Paris, France

Palmer, I., Moschovidis, Z.A., Cameron, J. 2005. Coal failure and consequences for coalbed methane wells. SPE No. 96872, Society of Petroleum Engineers Annual Technical Conference and Exhibition. Dallas, TX, U.S.A., Oct. 9–12.

Palmer, I.D., Moschovidis, Z.A., Cameron, J.R. 2005b. Coal failure and consequences for coalbed methane wells. SPE Paper 96872, Presented at the 2005 SPE ATCE, Dallas, TX. 11pp.

Palme, ID. 2009. Permeability changes in coal: analytical modeling. International Journal of Coal Geology. 77 119-126.

Pan, J., Meng, Z., Hou, Q., Ju, Y., Cao, Y. 2013. Coal strength and Young's modulus related to coal rank, compressional velocity and maceral composition. Journal of Structural Geology. 54. 129-135.

Pan, Z., Connell, L.D., Camilleri, M. 2010. Laboratory characterisation of coal reservoir permeability for primary and enhanced coalbed methane recovery. International Journal of Coal Geology. 82 252-261.

Park, E.S., Martin, C.D., and Christiansson, R. 2004. Simulation of the Mechanical Behavior of Discontinuous Rock Masses Using a Bonded-Particle Model. Proceedings of the 6th North American Rock Mechanics Symposium, Houston. Paper No. 04-480.

Patching, T. 1965. Variations in permeability of coal. Rock Mechanics Symposium, Toroton, Canada, Jan 15-16, 1965.

Peng, D.Y., Robinson, D.B. 1976. A new two constant equation of state. Industrial and Engineering Chemistry: Fundamentals 15:59-64.

Pierce M., Cundall P., Darcel, C., Min, K., Potyondy, D., Young, R.P., Reyes-Montes, J. & Pettitt, W. 2005. Six Monthly Technical Report, Caving Mechanics, Sub-Project No. 4.2: Research and Methodology Improvement, & Sub-Project 4.3, Case Study Application. ICG Report to Mass Mining Technology Project, 2004-2007, September.

Pierce, M., Mas Ivars, D., Cundall, P.A. and Potyondy, D.O. 2007. A synthetic rock mass model for jointed rock. Proceedings of the Rock Mechanics: Meeting Society's Challenges and Demands, 1st Canada-U.S. Rock Mechanics Symposium, Vol. 1, 341-349, Vancouver, Canada.

Pomeroy, C.D., Robinson, D.J., 1966. The effect of applied stress on the permeability of a middle rank coal to water. International Journal of Rock Mechanics and Mining Sciences. 4, 329–343.

Pone, J.D.N., Hile, M., Halleck, P.M., Mathews, J.P., 2009. Three dimensional carbon dioxide-induced strain distribution within a confined bituminous coal. International Journal of Coal Geology. 77, 103–108.

Potyondy, D., Cundall, P. 2004. A bonded-particle model for rock. International Journal of Rock Mechanics and Mining Science, 41, 1329-1364.

Potyondy, D.O. 2008. Smooth-Joint Model Version 3 (for PFC2D/3D Manual), Itasca Consulting Group, Inc., Internal Technical Memorandum, March 10.

Press, W.H., Teukolsky, S.A., Vetterling, W.T., Flannery, B.P. 1999. Numerical Recipes in C. Cambridge University Press, Cambridge, United Kingdom, pp. 683–688.

Robertson, E.P., Christiansen, R.L. 2007. Modeling laboratory permeability in coal using sorption induced strain data. Society of Petroleum Engineering: Reservoir Evaluation Engineering. 10, 260-269.

Rodgers, R.E. 1994. Coalbed methane: principles and practice. Englewood Cliffs NJ USA.

Sabir, A. 2004. A comparative study of CO_2 adsorption on intact and crushed coal. M Sc, Civil and Environmental Engineering, University of Alberta, p. 209.

Schweinfurth, SP. 2009. An introduction to coal quality. US Geological Survey Professional Paper 1625-F. Ch C.

Schuyer, J., Dukstra, H., van Krevelen, D.W. 1954. Chemical structure and properties of coal VII-elastic constant. Fuel. 33 409-418.

Seidle, J.P., Kutas, G.M., Krase, L.D. 1991. Pressure falloff tests of new coal wells. Presented at the Rocky Mountain Regional meeting and low permeability reservoir symposium held in Denver, Colorado, April 15-17, 1991. SPE 21809.

Seidle, J.P., L.G. Huitt. 1995. Experimental measurement of coal matrix shrinkage due to gas desorption and implications for cleat permeability increases. International Meeting on Petroleum Engineering, Beijing, PR China, 14-17 November, 1995.SPE 30010.

Settari, A., Walters, D. 2001. Advances in coupled geomechanical and reservoir modeling with application to reservoir compaction. SPE Journal. 334–342.

Siemons, N., Karl-Heinz, A.A., and Bruining, J. 2007. Interpretation of carbon dioxide diffusion behaviour in coals. International Journal of Coal Geology. 72, 315-324.

Smith, G.G. 1989. Coal Resources of Canada. Geol. Surv. Can. Pap. 89-4, 52.

Somerton, W.H., Söylemezoḡlu, I.M., Dudley, R.C. 1975. Effect of stress on permeability of coal. International Journal of Rock Mechanics and Mining Science & Geomechanics Abstracts. 12, 129–145.

St George, J.D., and Bakarat, M.A. 2001. The change in effective stress associated with shrinkage from gas desorption in coal. International Journal of Coal Geology. 45 105-113.

ST98-2010: Alberta's Energy Reserves 2013 and Supply/Demand Outlook 2013-2022. ISSN 1910-4235. Energy Resource Conservation Board. 2013.

ST98-2010: Alberta's Energy Reserves 2009 and Supply/Demand Outlook 2010-2019. ISSN 1910-4235. Energy Resource Conservation Board. 2010.

Szwilski, A.B., 1984. Determination of the anisotropic elastic moduli of coal. International Journal of Rock Mechanics and Mining Science & Geomechanics Abstracts 21 (1), 3–12.

Tran, D., Settari, A., Nghiem, L. 2004. New iterative coupling between a reservoir simulator and a geomechanics module. SPEJ 56 (9), 362–369 (SPE-88989).

Tzamos, S., Sofianos, A.I. 2007. A correlation of four rock mass classification systems through their fabric indices. International Journal of Rock Mechanics and Mining Science. 44, 477–495.

Vaziri, H.H., Xiao, Y. 2003. Numerical evaluation of geomechanical parameters affecting Productivity Index in weak rock formations: Part 2. Field application. Journal of Canadian Petroleum Technology. 42, 33–3

Wilson, S.M., Moschovidis, Z.A., Cameron, J.R., Palmer, I.D. 2002. New model for predicting the rate of sand production. Paper SPE/SSRM 78168, Rock Mechanics Conf., Irving, TX, Oct. 20–23

Wong, L.N.Y., Einstein, H.H. 2006. Fracturing behaviour of prismatic specimens containing single flaws. In ARMA/USRMS 06-899.

Wong, R.H.C., Chau, K.T., Tang, C.A., Lin, P. 2001. Analysis of crack coalescence in rock-like materials containing three flaws – Part 1: Experimental approach. International Journal of Rock Mechanics and Mining Sciences. 38 909-924.

Walsh JB. 1981. Effect of pore pressure and confining pressure on fracture permeability. International Journal of Rock Mechanics and Mining Science. 18 429-435.

Yee, D., Seidle, J.P., Hanson, W.B. (1993) Gas sorption on coal and measurement of gas content. In: B.E. Law and D.D. Rice (Editors), Hydrocarbons from coal. American Association of Petroleum Geologists, Tulsa, Oklahoma, 203-218.

Zheng, Z., Khodaverdian, M., McLennan, J.D. 1991. Static and dynamic testing of coal specimens. Society of Core Analysts Symposium, 1991.

15 Appendix A

This section provides the machine shop drawings required to construct the TDS triaxial cell.

TDS-6500

Triaxial Pressure Cell

Specification Sheet and Operating Overview

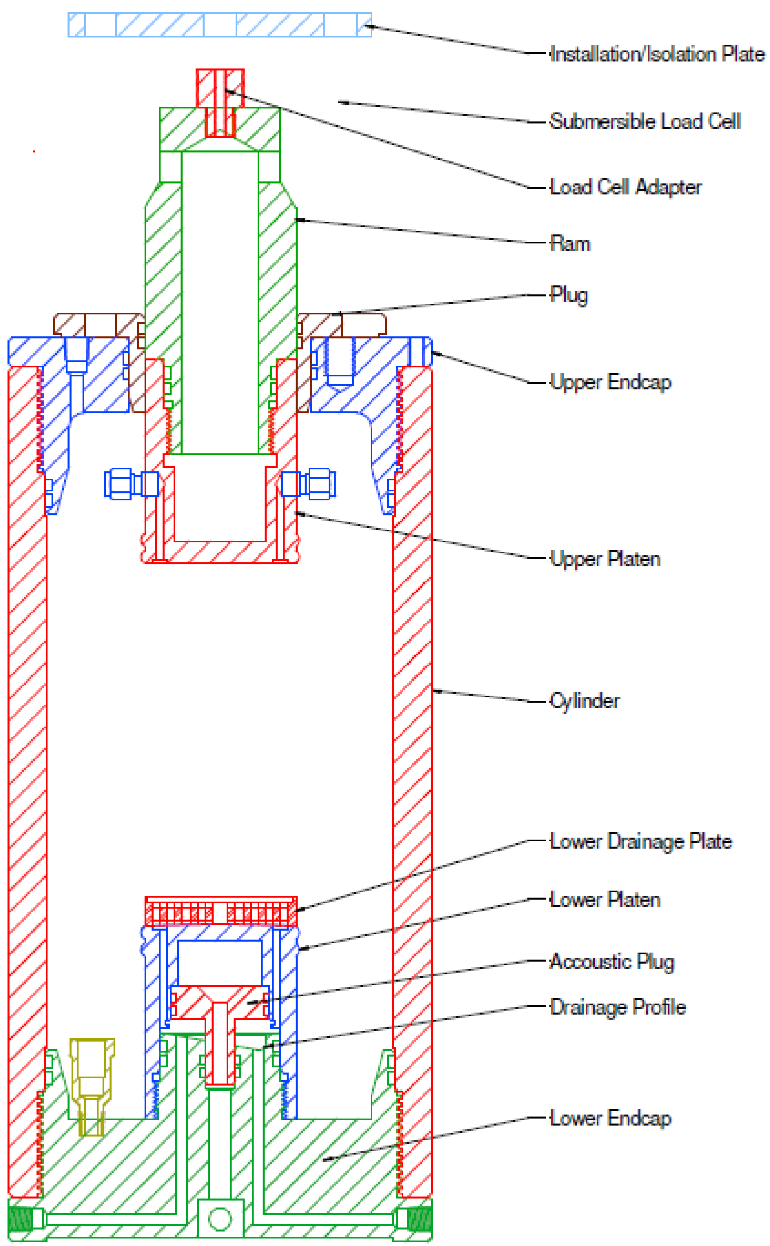

Limits of Operation

> **IMPORTANT**
>
> Failure to operate the triaxial cell within the limits of operation defined below can result in serious injury or death. DO NOT EXCEED ANY ONE OF THE PERFORMANCE SPECIFICATIONS LISTED BELOW AT ANY TIME!

Max. Operating Pressure:	**6500 psi (44.8 MPa)**
Max. Operating Temperature:	**60°C (140°F)**
Confining Fluid:	**Silicon oil or other non-corrosive liquids**
Test Sample Diameter:	**2.5"**
Maximum Sample Height:	**5.0"**

Important Operating Notes

1) **ALWAYS INSTALL A BURST DISK OR A CALIBRATED RELIEF VALVE PARALLEL TO THE CELL CONFINING PRESSURE LINE TO ENSURE THE CELL INTERNAL PRESSURE NEVER EXCEEDS THE RATED CAPACITY LISTED ABOVE.**

   This is an essential safety component that must be in place before commencing any testing. This safety device must always be exposed to the cell pressure, and not isolated from the cell by any sort of isolation valve. Even if your pressure pumps are not capable of reaching the rated pressure, you still must install a safety device to prevent over-pressuring of the cell. For example, heating the cell fluid can cause a dramatic rise in cell pressure, far beyond the maximum delivery of the pumps, due to fluid expansion. Other circumstances may also exist in which the cell pressure could increase unexpectedly.

2) The material of construction for structural members of the cell is AISI 4140 Quenched & Tempered (minimum yield stress of 110,000 psi). This alloy will rust when water wetted or exposed to other corrosive fluids. Therefore, always ensure cell threads are thoroughly coated with a barrier grease / thread compound to minimize contact with water and to prevent thread galling upon make-up.

   If parts come in contact with water or other corrosive liquids, wipe off and coat parts with mineral oil to prevent oxidation.

DO NOT USE THE CELL IF RUST IS PRESENT ANYWHERE ON THE UPPER AND LOWER ENDCAPS, OR ON THE CYLINDER. THESE PARTS WILL NEED TO BE EXAMINED AND RE-COMMISSIONED OR RE-BUILT BEFORE BEING PUT BACK INTO SERVICE.

3) **Hex head bolts for "Plug" (on top endcap): Only use <u>Grade 8 bolts</u>. Use of lower strength grades may result in bolt failure and severe injury or death to personnel in the area. Never use bolts if rust and/or thread damage is visible. Replace with new ones – don't take a chance.**

   Upon assembly, install washers under all bolts, and torque all bolts to 10 ft-lb in a criss-cross pattern as shown below:

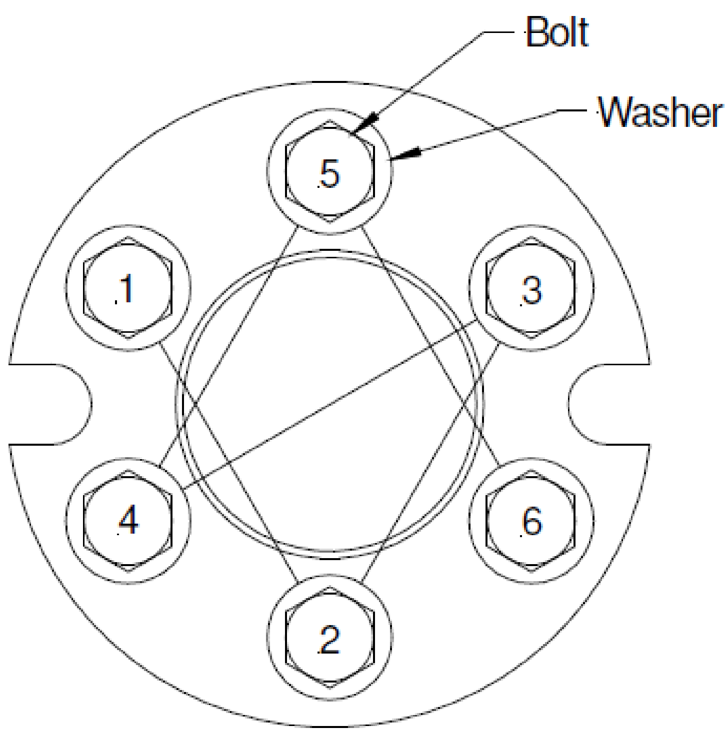

4) When installing the drainage plates against the upper and lower platens, be sure to align a groove in the drainage plate with the hole in the platen (to reduce flow restriction).

5) Before putting the cell into service, ensure ALL components of the cell have "TDS 6500" stamped/engraved/electrochemically etched into them. Upon assembly, ensure that only parts with this labelling are used.

6) Instrumentation feed through fittings: Refer to the manufacturer's specifications on these fittings with regards to recommended torque settings.

7) When assembling the cell components, specifically the cylinder and upper and lower endcaps, ensure threads are fully engaged. Mating parts must "shoulder" against each other (make full contact). There is no minimum make-up torque requirement on these parts – hand tight is acceptable provided that all mating parts are fully engaged.

Cell Commissioning

Although care was taken to ensure stress calculations are accurate, and mill test certificates for the steel provided, it is imperative that the vessel be subjected to a qualification test at 1.5 times the rated operating pressure before it is commissioned for normal testing service. The procedures below are only presented as guidelines, and are not to succeed the standard operating and/or safety procedures of the test laboratory. Use the procedure below as an outline for developing the test procedure based on in-house testing and safety protocols.

1) Assemble the vessel without a test specimen.
2) **Fully saturate with a non-corrosive liquid. All air must be evacuated from the pressure supply lines and most importantly, from within the cell.**
3) Position the cell within a load frame capable of reacting the fluid pressure that will act on the ram. The load frame must be capable of withstanding an axial force of 58,500 lbf (260 kN).
4) Locate the cell behind a blast shield (it is the responsibility of the person(s) conducting the test to ensure the vessel is suitable contained in the event of a rupture or component failure, resulting in a sudden, uncontrolled release of pressurized fluid from within the cell). Consider as well the possibility of bolt failure on the plug which could result in the bolt head becoming a high-velocity projectile as it is "shot-off" from the top of the cell.
5) Complete a safety review/audit of the cell, blast shields, location of personnel, and test procedures. Have a qualified, authorized individual sign off on the procedure.
6) Increase cell pressure slowly (roughly 1000 psi, 6.9 MPa), per minute) until the maximum operating pressure is reached.
7) Stop the pump and hold this pressure for 5 minutes. Monitor the cell pressure to ensure it is stable. A drop in pressure may indicate a leak. If cell pressure is not stable, bleed the pressure, stop the test, and determine the cause of the pressure variance. Do not test again until the problem has been identified and fixed.
8) If no drop in pressure is evident, continue to slowly increase cell pressure to 1.5 times the rated maximum operating pressure.
9) Repeat step #7.
10) Bleed pressure and disassemble the cell.
11) Inspect all components. If any visible signs of damage or yielding are evident, do not use the cell. Further examination into the cause of the damage must occur first.

Bill of Materials for Cell Components

Description	Quantity per cell	Relates to
O-ring: Viton, 70 durometer #230	2	Top ram
O-ring: Viton, 70 durometer #127	2	Accoustic housing
O-ring: Viton, 70 durometer #112	2	Accoustic housing
O-ring: Viton, 70 durometer #224	2	Lower platen
O-ring: Viton, 70 durometer #254	4	Bottom and top endcaps
Backup rings: #254 for above	4	Bottom and top endcaps
O-ring: Viton, 70 durometer #223	2	Ram to top platen
O-ring: Viton, 70 durometer #234	2	Top endcap to plug
O-ring: Viton, 70 durometer #229	10	Apply pre-stress to membrane over stress risers
Lifting eyebolt: ½" UNC x 1" long	1	Ram
½" UNF threaded rod, cut into pieces 7.5" long	2	Installation plate
½" UNF Nuts	4	Installation plate
1/8" tube to 1/8" MNPT bored through male connector (Swagelok)	1	Top cap, for thermocouple feed through
1/8" tube to 1/8" MNPT male connector (Swagelok) – standard	9	All pressure ports in lower endcap and top endcap
1/8" tube to 1/8" Male pipe weld connector (-200-1-2W). NOTE, this part requires machining and welding to platens! See drawing.	3	Upper and lower platens pore pressure
1/8" thermocouple probe, probe length 8" long (not including end junction).	1	Top endcap
½" UNF x 1" Grade 8 hex head bolts. MUST BE GRADE 8.	6	Plug
½" plated washers	6	Plug
Conax wire feedthrough: MHC1-032-A4-V	2	Bottom endcap
24ga, solid conductor copper wire	20'	Instrument feedthrough
1/8" NPT pressure plugs – Hex head, not socket. For plugging unused pressure ports.	4	Bottom endcap
Sintered stone disk, 100 micron, 0.090" thick, 2.4" OD	2	Upper and lower platens
#6-32 x ½" long set screws	2	Locking lower platen in place

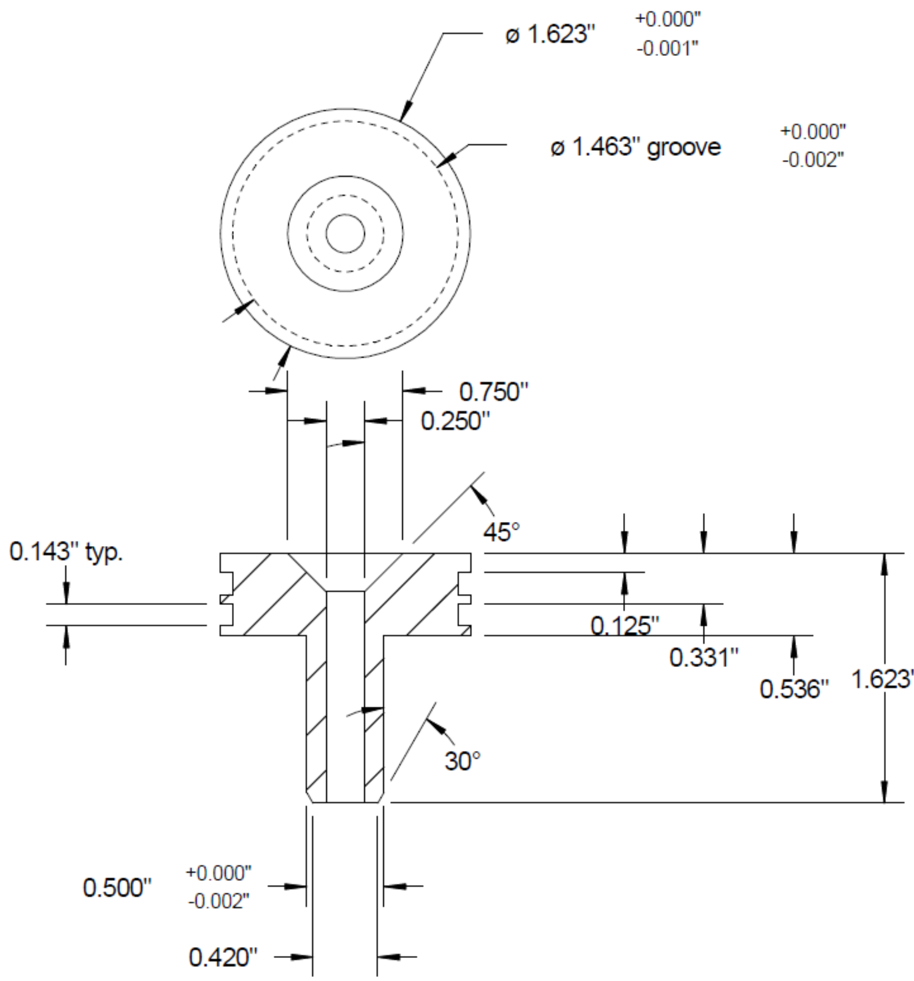

SPECIFICATIONS UNLESS OTHERWISE NOTED:

		TOL.	T.I.R.	FINISH
1) DECIMAL:	x.xxx	±0.005"	0.005"	32µinch Ra
	x.xx	±0.015"	0.015"	64µinch Ra
	x.x	±0.030"	0.030"	125µinch Ra
2) FRACTION:	x/x	±0.030"	0.030"	250µinch Ra
3) ANGULAR:	x.x°	±0.5°		
	x°	±1.0°		

Accoustic Housing Plug (TDS-6500)

Material: 316 SS

Rev	Description	Drawn	Date
0	Original	PML	9-Aug-07

University of Alberta

Sheet: 1 of 1

Scale: NTS

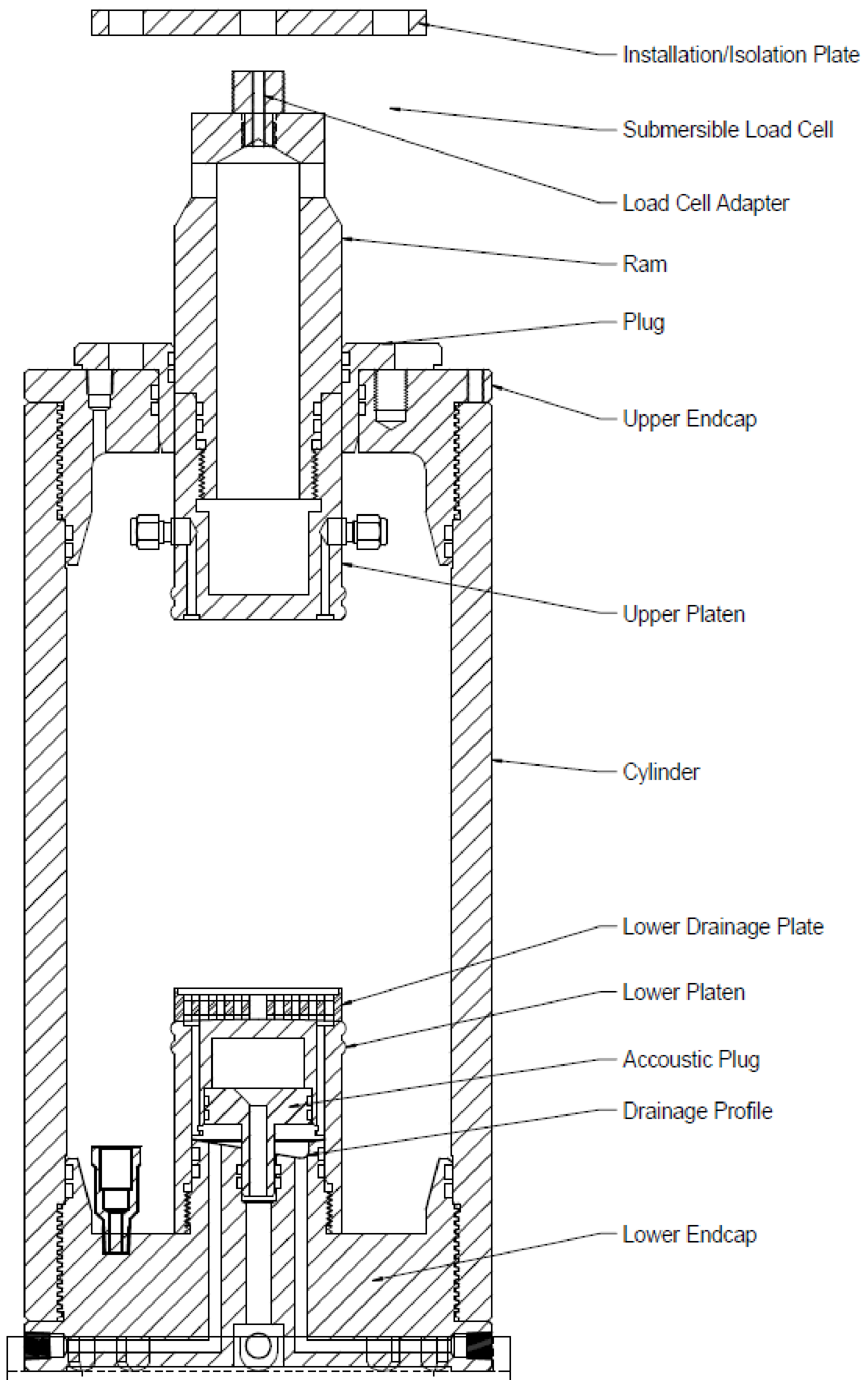

SPECIFICATIONS UNLESS OTHERWISE NOTED:

		TOL	T.I.R.	FINISH
1) DECIMAL:	x.xxx	±0.005"	0.005"	32µinch Ra
	x.xx	±0.015"	0.015"	64µinch Ra
	x.x	±0.030"	0.030"	125µinch Ra
2) FRACTION:	x/x	±0.030"	0.030"	250µinch Ra
3) ANGULAR:	x.x°	±0.5°		
	x°	±1.0°		

TDS-6500 Triaxial Cell - Assembly

University of Alberta

Material:

Sheet: 1 of 1

Rev	Description	Drawn	Date
0	Original	PML	29-May-07

Scale: NTS

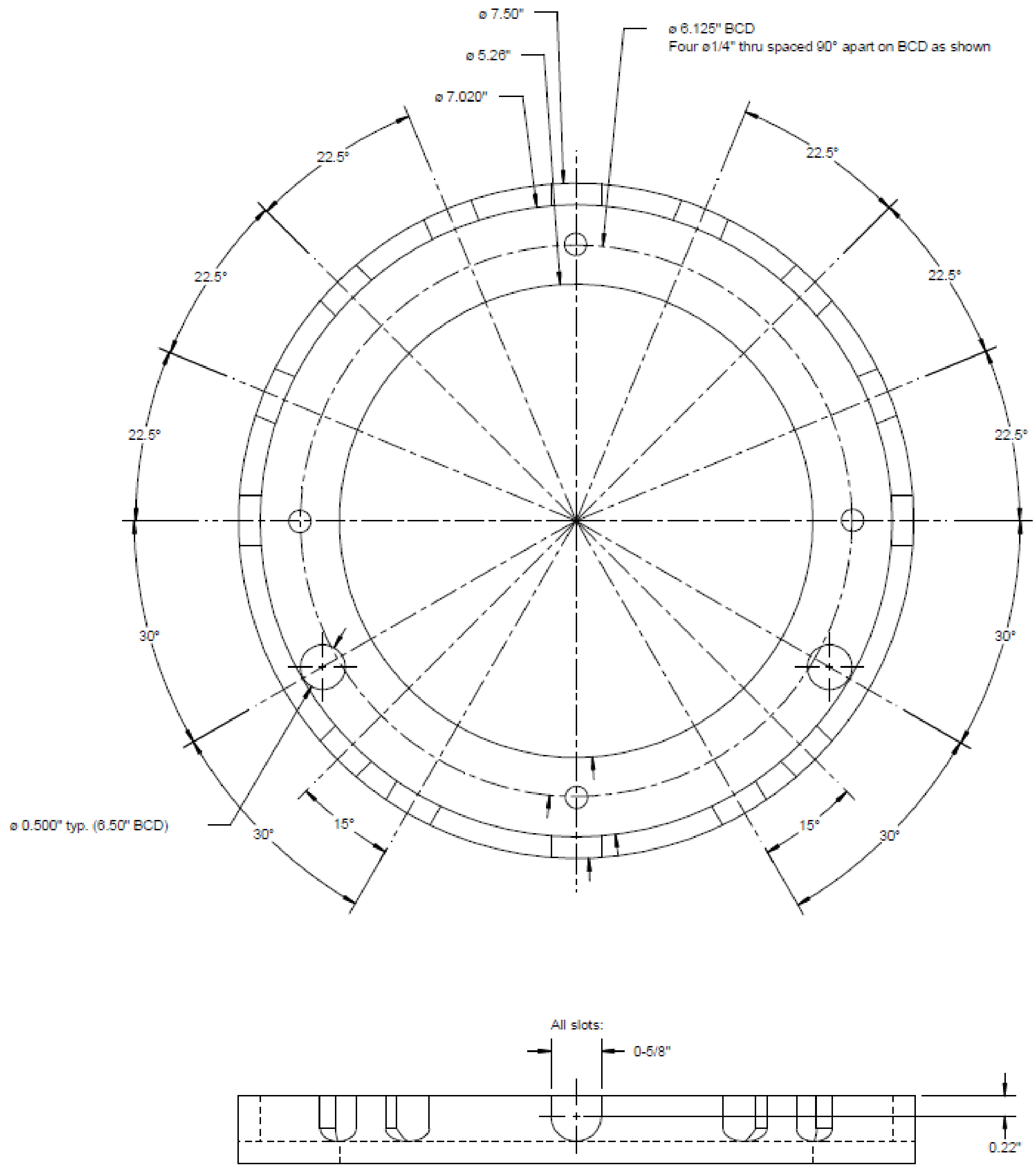

SPECIFICATIONS UNLESS OTHERWISE NOTED:

		TOL.	T.I.R.	FINISH
1) DECIMAL:	x.xxx	±0.005"	0.005"	32µinch Ra
	x.xx	±0.015"	0.015"	64µinch Ra
	x.x	±0.030"	0.030"	125µinch Ra
2) FRACTION:	x/x	±0.030"	0.030"	250µinch Ra
3) ANGULAR:	x.x°	±0.5°		
	x°	±1.0°		

Assembly Ring (TDS-6500)

Material: Carbon Steel

Rev	Description	Drawn	Date
0	Original	PML	9-Aug-07

University of Alberta

Sheet: 1 of 1

Scale: NTS

For all fittings supplied, perform the following modifications:

Fitting, as supplied: Swagelok SS-200-1-2W

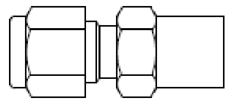

Step 1: machine off hex

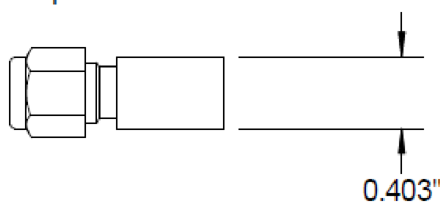

Step 2: shorten length

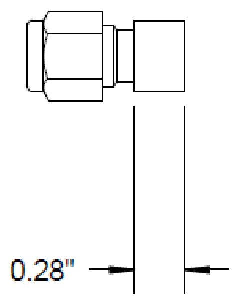

SPECIFICATIONS UNLESS OTHERWISE NOTED:

		TOL.	T.I.R.	FINISH
1) DECIMAL:	x.xxx	±0.005"	0.005"	32µinch Ra
	x.xx	±0.015"	0.015"	64µinch Ra
	x.x	±0.030"	0.030"	125µinch Ra
2) FRACTION:	x/x	±0.030"	0.030"	250µinch Ra
3) ANGULAR:	x.x°	±0.5°		
	x°	±1.0°		

Swagelok Fitting modifications

Material: see above

Rev	Description	Drawn	Date
0	Original	PML	9-Aug-07

University of Alberta

Sheet: 1 of 1

Scale: NTS

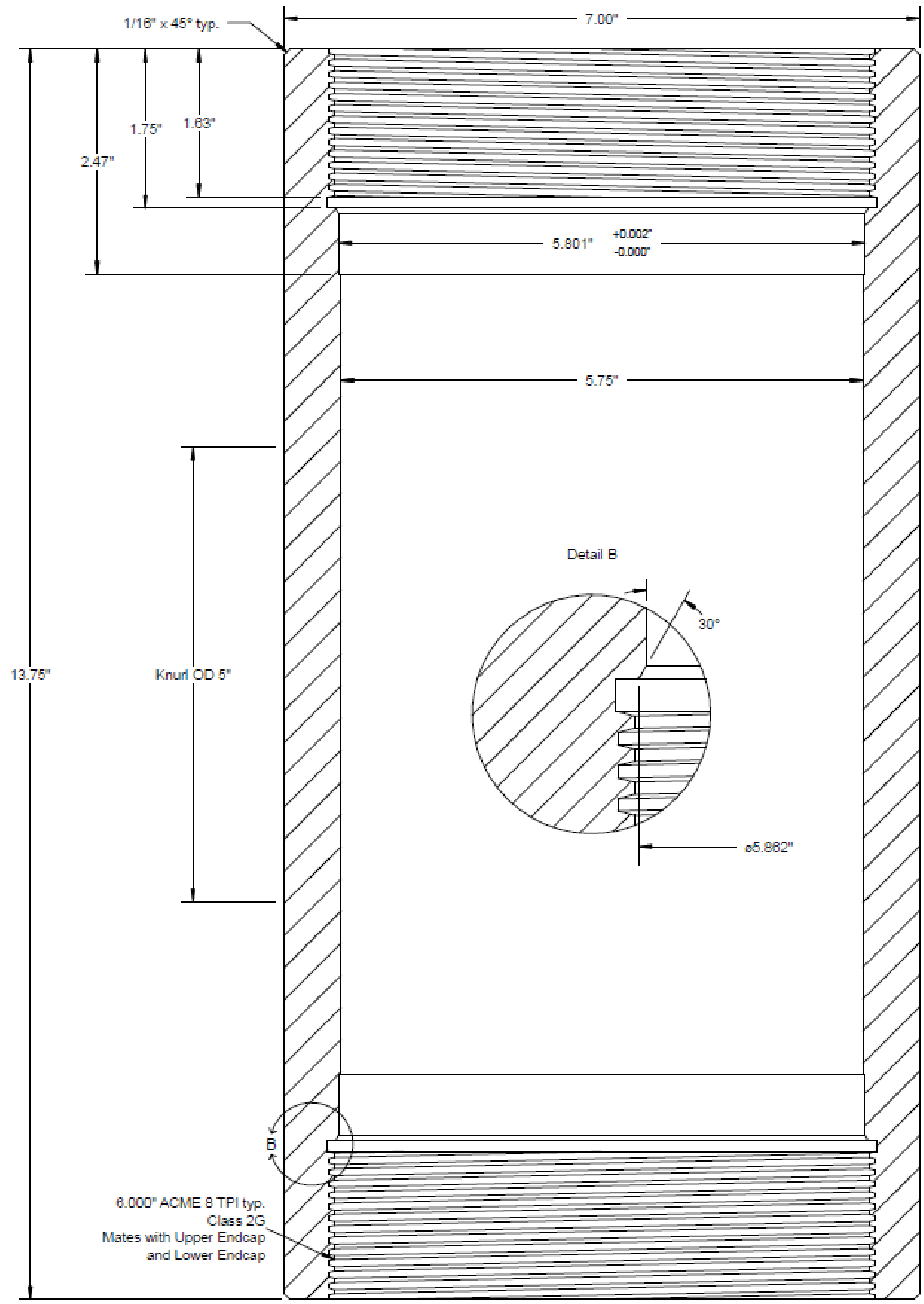

SPECIFICATIONS UNLESS OTHERWISE NOTED:

		TOL.	T.I.R.	FINISH
1) DECIMAL:	x.xxx	±0.005"	0.005"	32µinch Ra
	x.xx	±0.015"	0.015"	64µinch Ra
	x.x	±0.030"	0.030"	125µinch Ra
2) FRACTION:	x/x	±0.030"	0.030"	250µinch Ra
3) ANGULAR:	x.x°	±0.5°		
	x°	±1.0°		

Cylinder (TDS-6500)

Material: AISI 4140 Q&T (min. yield 110,000)

Rev	Description	Drawn	Date
0	Original	PML	28-May-07

University of Alberta

Sheet: 1 of 1

Scale: NTS

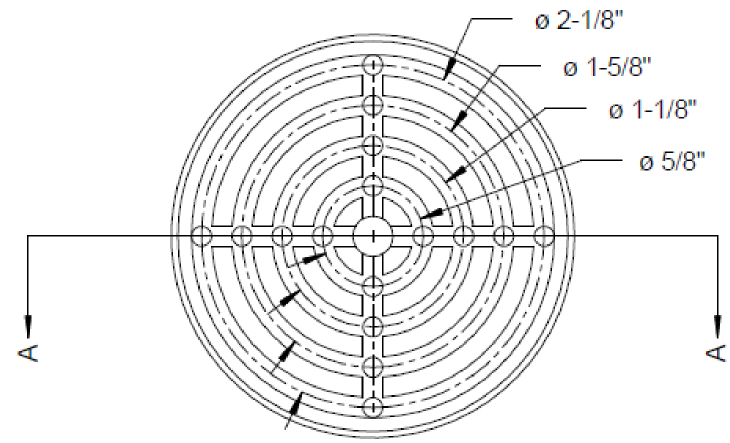

Centre hole ø1/4"
All other holes ø1/8"
All slots 1/8" wide

Section A-A

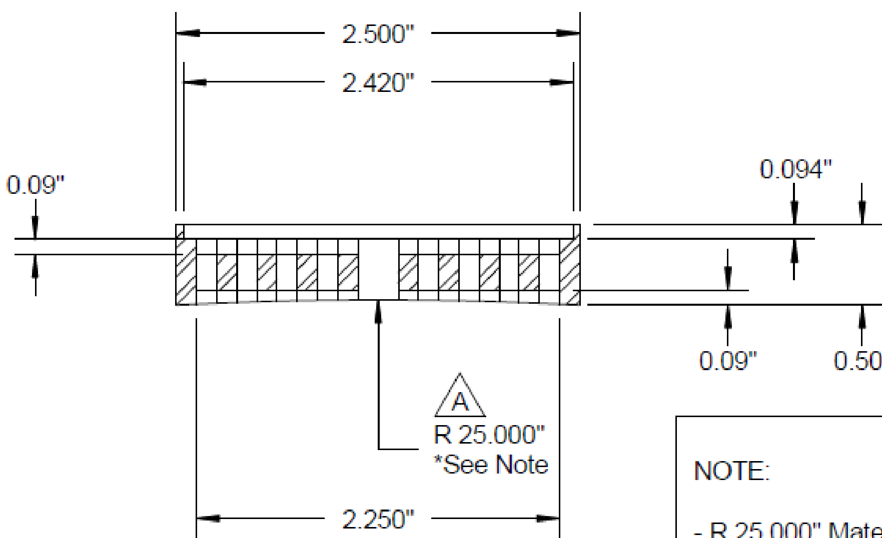

NOTE:

- R 25.000" Mates with Lower Platen.

- Fabricate TWO drainage plates, one WITH R 25.000" and one WITHOUT.

- Sand-blast surface "A" to roughen it.

SPECIFICATIONS UNLESS OTHERWISE NOTED:

		TOL.	T.I.R.	FINISH
1) DECIMAL:	x.xxx	±0.005"	0.005"	32µinch Ra
	x.xx	±0.015"	0.015"	64µinch Ra
	x.x	±0.030"	0.030"	125µinch Ra
2) FRACTION:	x/x	±0.030"	0.030"	250µinch Ra
3) ANGULAR:	x.x°	±0.5°		
	x°	±1.0°		

Drainage Plate (TDS-6500)

Material: 316SS

Rev	Description	Drawn	Date
0	Original	PML	9-Aug-07

University of Alberta

Sheet: 1 of 1

Scale: NTS

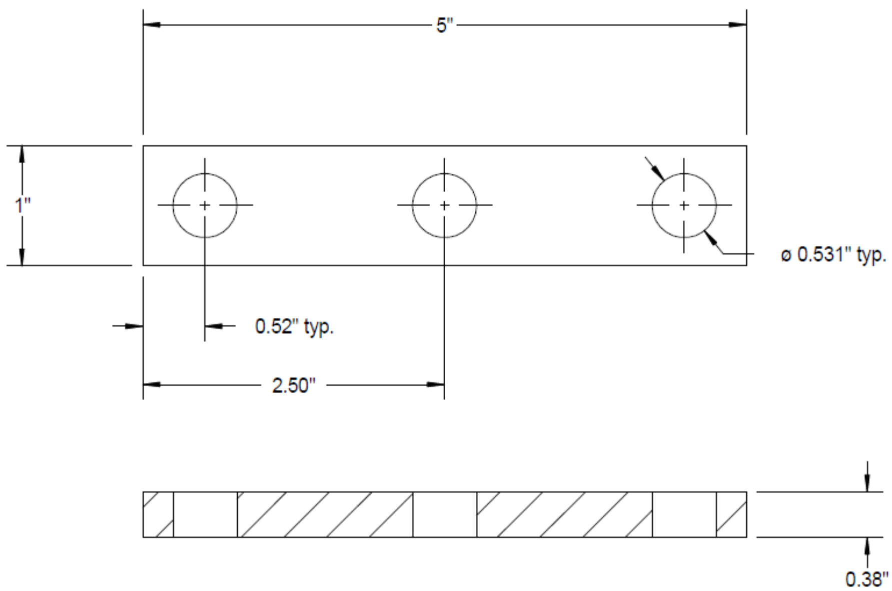

SPECIFICATIONS UNLESS OTHERWISE NOTED:					Installation Plate (TDS-6500)				University of Alberta
		TOL.	T.I.R.	FINISH	Material: 44W carbon steel plate or higher				
1) DECIMAL:	x.xxx	±0.005"	0.005"	32µinch Ra					
	x.xx	±0.015"	0.015"	64µinch Ra					Sheet: 1 of 1
	x.x	±0.030"	0.030"	125µinch Ra					
2) FRACTION:	x/x	±0.030"	0.030"	250µinch Ra	0	Original	PML	28-May-07	
3) ANGULAR:	x.x°	±0.5°			Rev	Description	Drawn	Date	Scale: NTS
	x°	±1.0°							

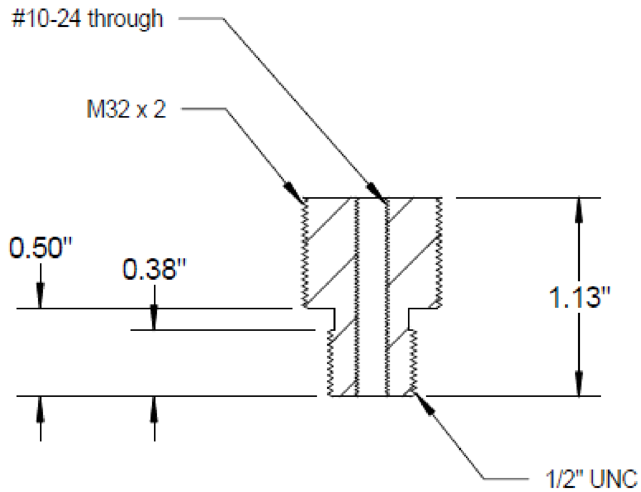

SPECIFICATIONS UNLESS OTHERWISE NOTED:

		TOL.	T.I.R.	FINISH
1) DECIMAL:	x.xxx	±0.005"	0.005"	32µinch Ra
	x.xx	±0.015"	0.015"	64µinch Ra
	x.x	±0.030"	0.030"	125µinch Ra
2) FRACTION:	x/x	±0.030"	0.030"	250µinch Ra
3) ANGULAR:	x.x°	±0.5°		
	x°	±1.0°		

Load cell adapter (TDS-6500)

Material: Carbon steel

Rev	Description	Drawn	Date
0	Original	PML	9-Aug-07

University of Alberta

Sheet: 1 of 1

Scale: NTS

Two Discs:

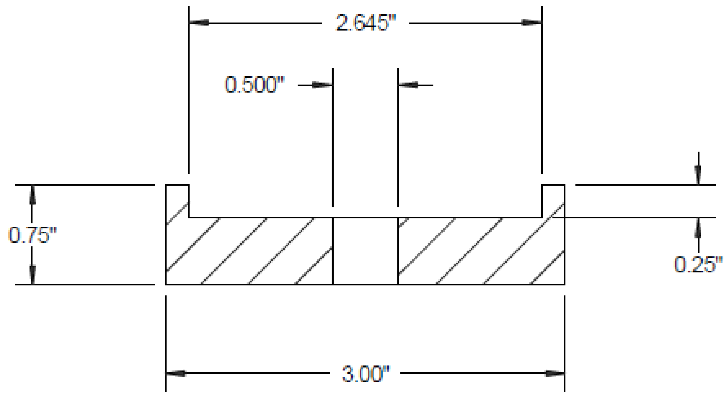

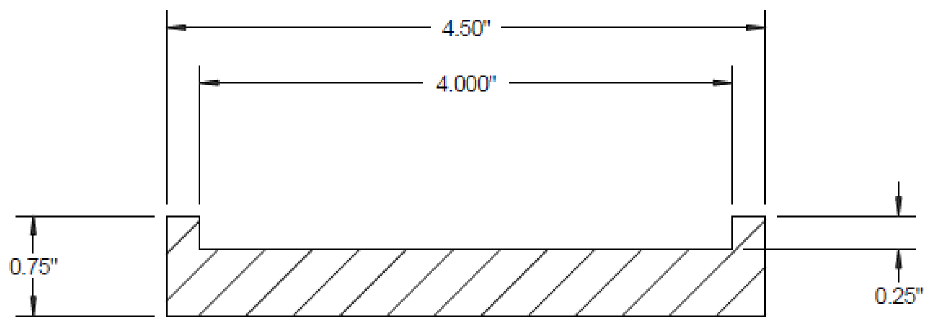

SPECIFICATIONS UNLESS OTHERWISE NOTED:

		TOL.	T.I.R.	FINISH
1) DECIMAL:	x.xxx	±0.005"	0.005"	32µinch Ra
	x.xx	±0.015"	0.015"	64µinch Ra
	x.x	±0.030"	0.030"	125µinch Ra
2) FRACTION:	x/x	±0.030"	0.030"	250µinch Ra
3) ANGULAR:	x.x°	±0.5°		
	x°	±1.0°		

Load Cell Holders (TDS-6500)

Material: Carbon steel

Rev	Description	Drawn	Date
0	Original	PML	9-Aug-07

University of Alberta

Sheet: 1 of 1

Scale: NTS

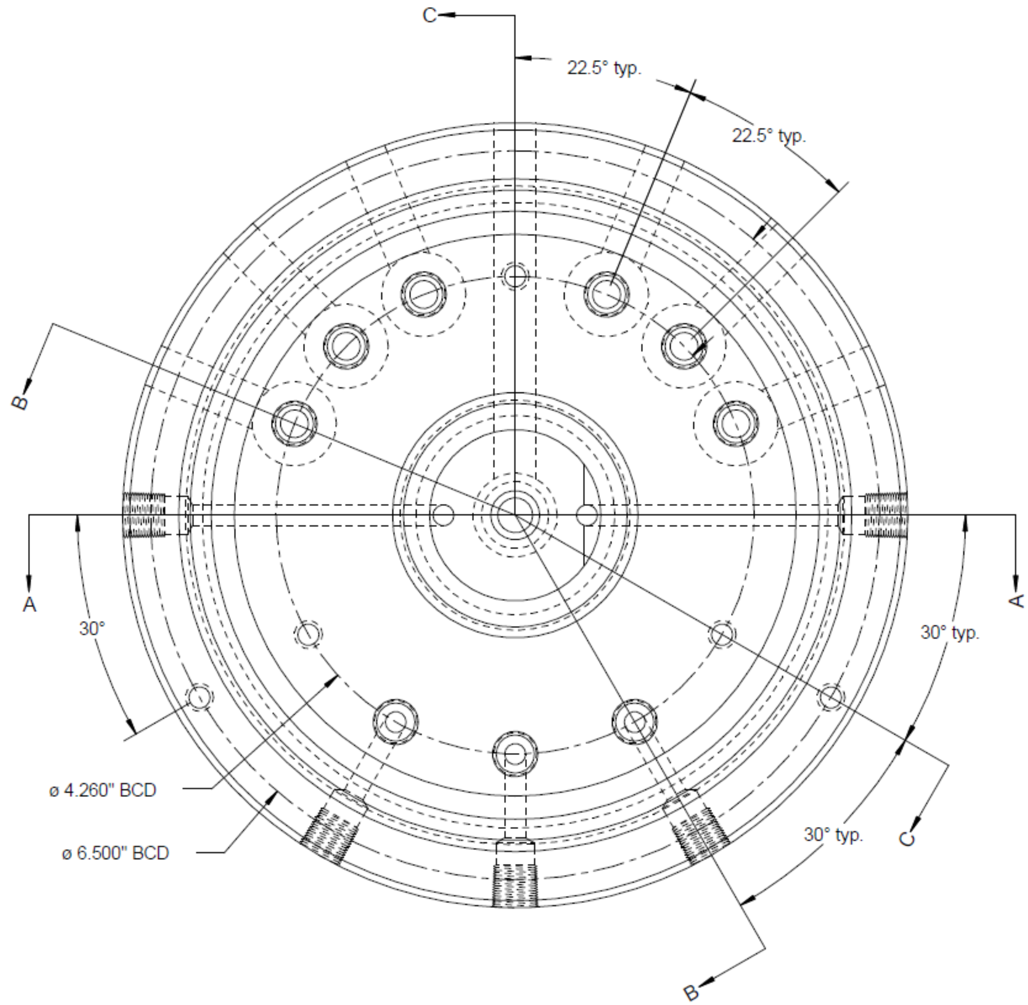

SPECIFICATIONS UNLESS OTHERWISE NOTED:

		TOL.	T.I.R.	FINISH
1) DECIMAL:	x.xxx	±0.005"	0.005"	32μinch Ra
	x.xx	±0.015"	0.015"	64μinch Ra
	x.x	±0.030"	0.030"	125μinch Ra
2) FRACTION:	x/x	±0.030"	0.030"	250μinch Ra
3) ANGULAR:	x.x°	±0.5°		
	x°	±1.0°		

Bottom EndCap (TDS-6500) Top View

Material: AISI 4140 Q&T (min. yield 110,000 psi)

Rev	Description	Drawn	Date
0	Original	PML	28-May-07

University of Alberta

Sheet: 1 of 6

Scale: NTS

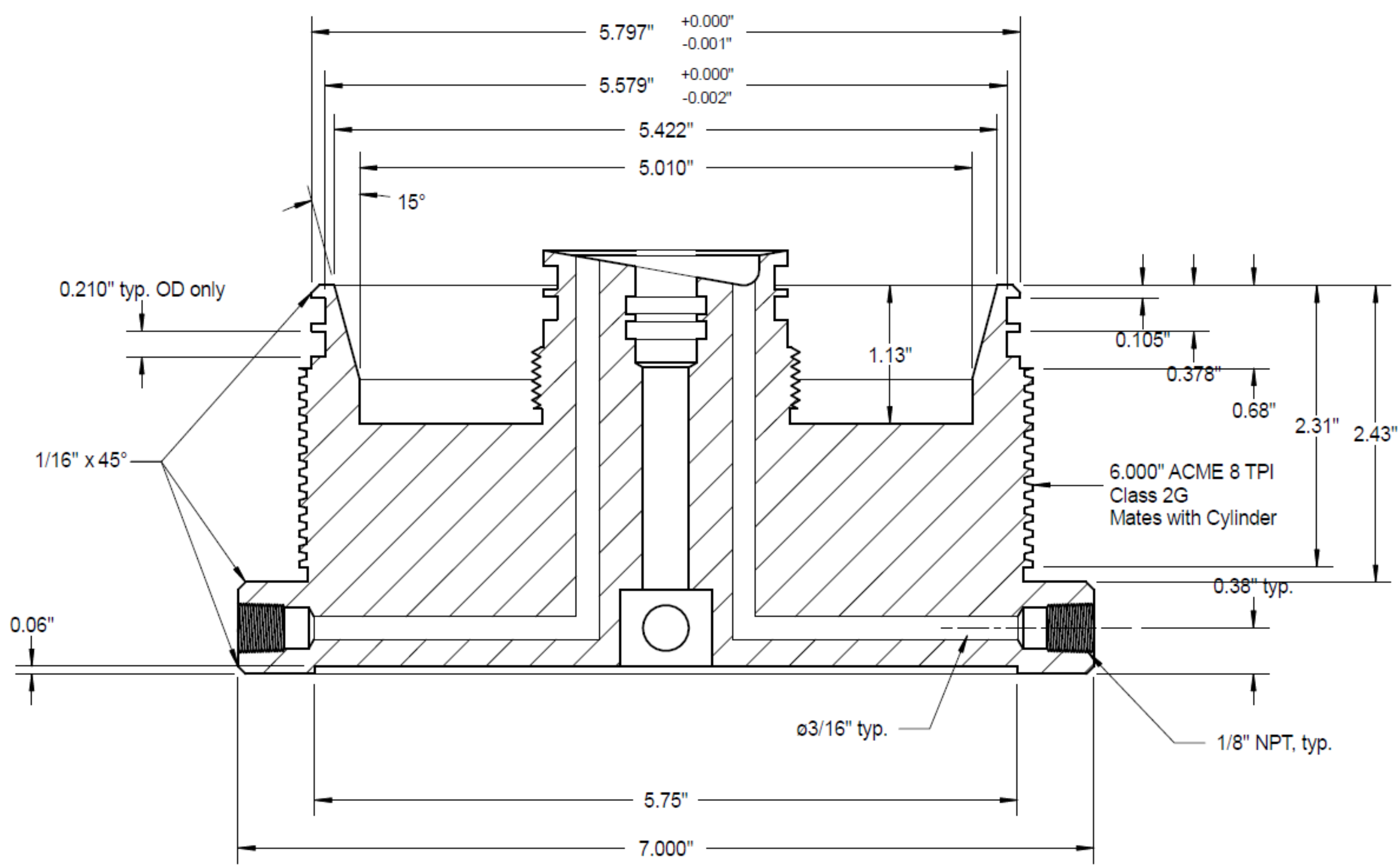

SPECIFICATIONS UNLESS OTHERWISE NOTED:					Bottom EndCap (Section A-A) Outer Features Dim's.			University of Alberta
		TOL.	T.I.R.	FINISH	Material: AISI 4140 Q&T (min. yield 110,000 psi)			
1) DECIMAL:	x.xxx	±0.005"	0.005"	32µinch Ra				Sheet: 2 of 6
	x.xx	±0.015"	0.015"	64µinch Ra				
	x.x	±0.030"	0.030"	125µinch Ra	0 Original	PML	28-May-07	Scale: NTS
2) FRACTION:	x/x	±0.030"	0.030"	250µinch Ra	Rev Description	Drawn	Date	
3) ANGULAR:	x.x°	±0.5°						
	x°	±1.0°						

CONFIDENTIAL INFORMATION NOTICE: This document and the drawings and data it embodies ("Confidential Information") are proprietary to INFLO Solutions Inc. (INFLO) and are provided to the Recipient in confidence. The Recipient accepts this document in confidence and agrees that it will: (1) restrict the use of the Confidential Information to the sole Purpose ("Purpose") for which it was provided; (2) not copy, reproduce or disclose the document or Confidential Information to others in whole or in part; (3) use reasonable care to protect the Confidential Information from unauthorized use, dissemination, or publication; and (4) return the document and all copies upon the completion of the Purpose or upon INFLO's request.

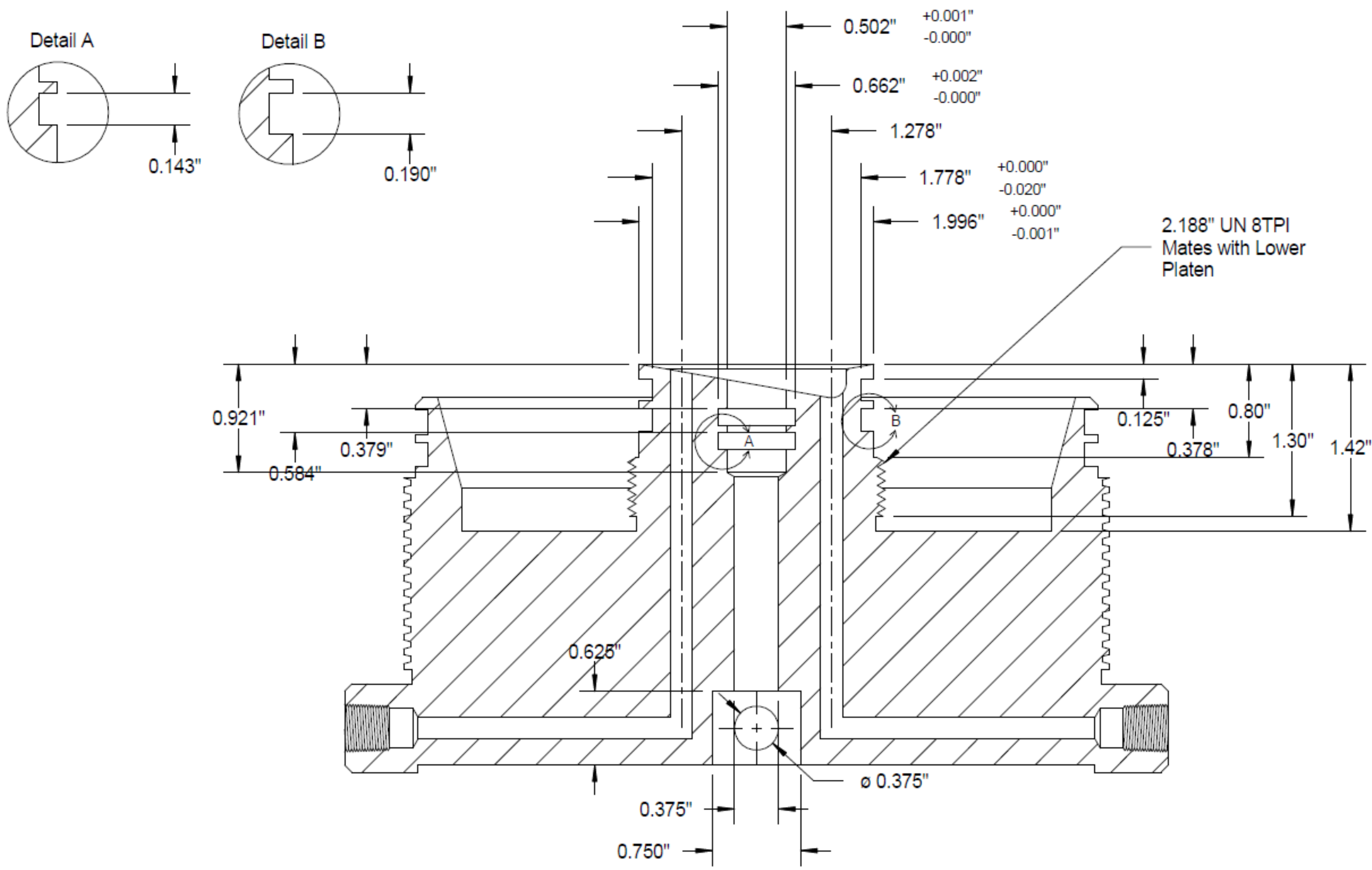

SPECIFICATIONS UNLESS OTHERWISE NOTED:

		TOL.	T.I.R.	FINISH
1) DECIMAL:	x.xxx	±0.005"	0.005"	32µinch Ra
	x.xx	±0.015"	0.015"	64µinch Ra
	x.x	±0.030"	0.030"	125µinch Ra
2) FRACTION:	x/x	±0.030"	0.030"	250µinch Ra
3) ANGULAR:	x.x°	±0.5°		
	x°	±1.0°		

Bottom EndCap (Section A-A) Inner Features Dim's.

Material: AISI 4140 Q&T (min. yield 110,000 psi)

Rev	Description	Drawn	Date
0	Original	PML	28-May-07

University of Alberta

Sheet: 3 of 6

Scale: NTS

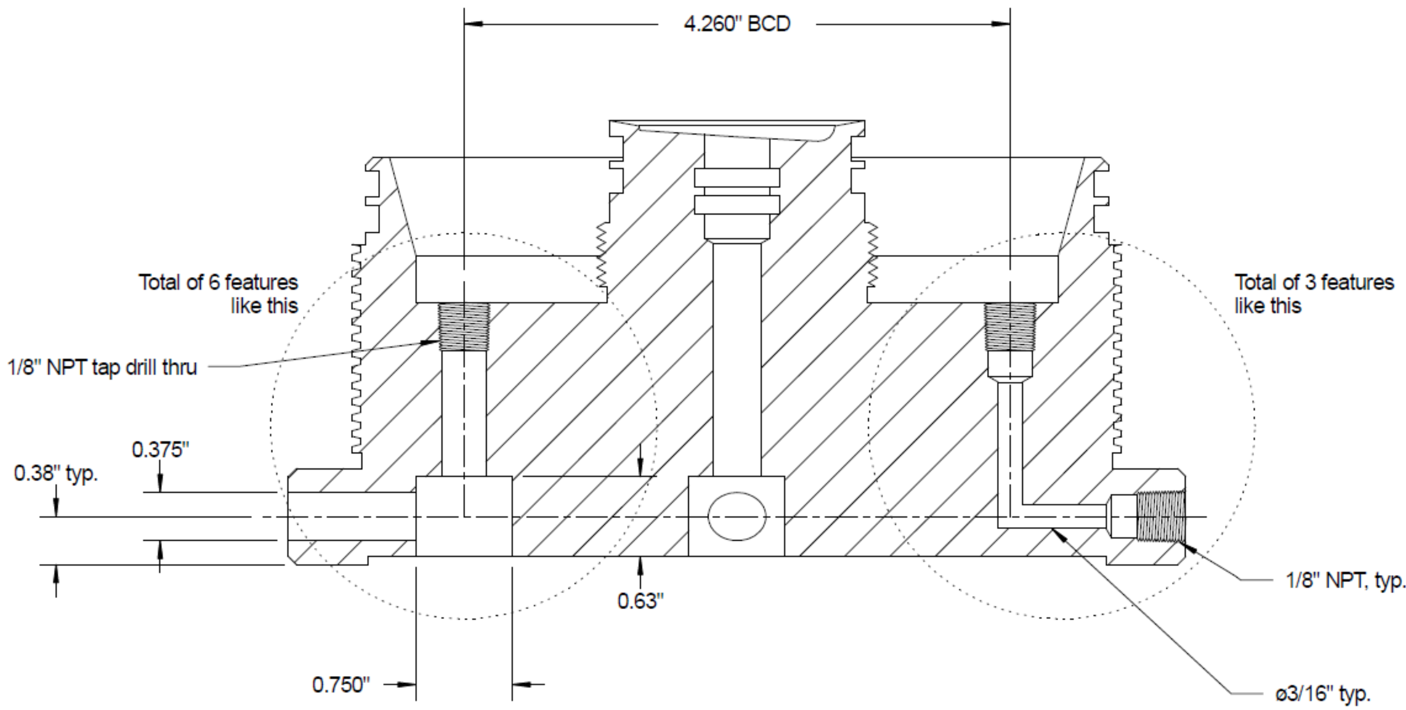

SPECIFICATIONS UNLESS OTHERWISE NOTED:

		TOL.	T.I.R.	FINISH
1) DECIMAL:	x.xxx	±0.005"	0.005"	32µinch Ra
	x.xx	±0.015"	0.015"	64µinch Ra
	x.x	±0.030"	0.030"	125µinch Ra
2) FRACTION:	x/x	±0.030"	0.030"	250µinch Ra
3) ANGULAR:	x.x°	±0.5°		
	x°	±1.0°		

Bottom EndCap (Section B-B)

Material: AISI 4140 Q&T (min. yield 110,000 psi)

Rev	Description	Drawn	Date
0	Original	PML	28-May-07

University of Alberta

Sheet: 4 of 6

Scale: NTS

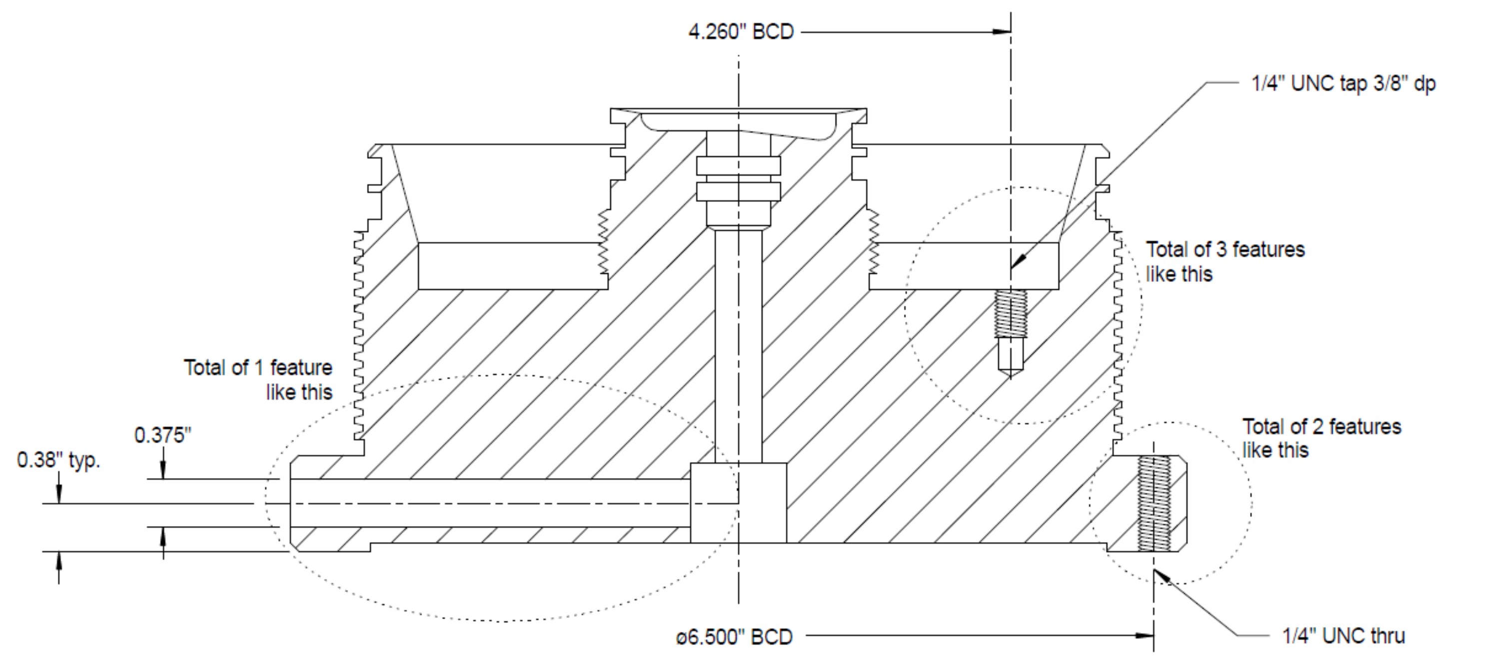

SPECIFICATIONS UNLESS OTHERWISE NOTED:

		TOL.	T.I.R.	FINISH
1) DECIMAL:	x.xxx	±0.005"	0.005"	32μinch Ra
	x.xx	±0.015"	0.015"	64μinch Ra
	x.x	±0.030"	0.030"	125μinch Ra
2) FRACTION:	x/x	±0.030"	0.030"	250μinch Ra
3) ANGULAR:	x.x°	±0.5°		
	x°	±1.0°		

Bottom EndCap (Section C-C)

Material: AISI 4140 Q&T (min. yield 110,000 psi)

Rev	Description	Drawn	Date
0	Original	PML	28-May-07

University of Alberta

Sheet: 5 of 6

Scale: NTS

NOTE: - Drainage profile is created by an intersection of two planes. One at 10° to the horizontal, the other vertical.
- Surface roughness: 1/16" horizontal steps (max) with R1/8" end mill.

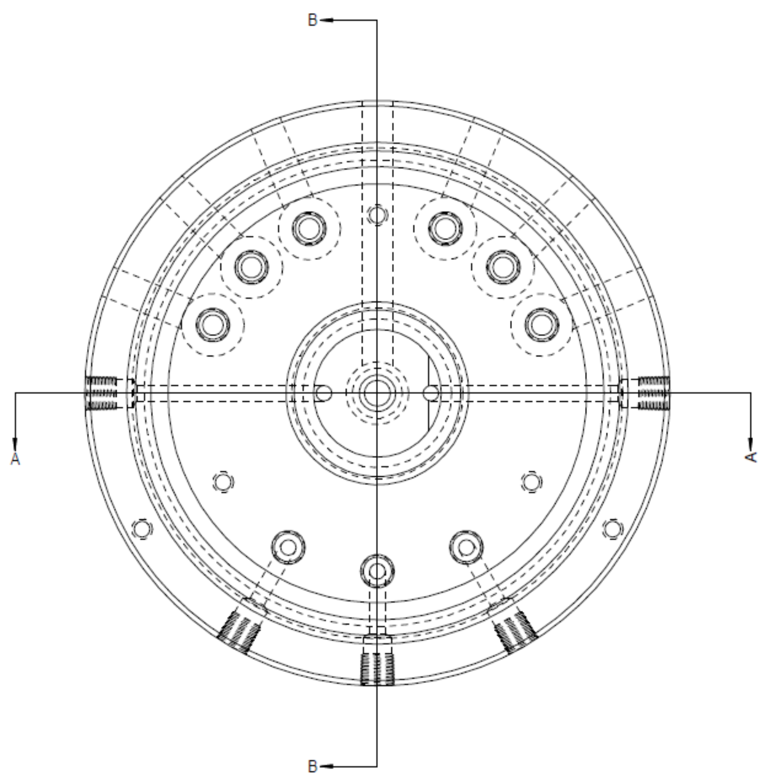

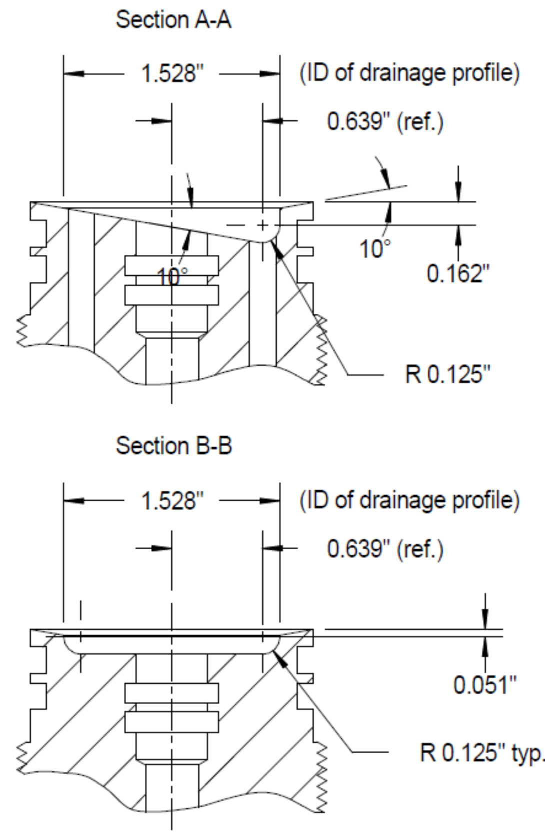

SPECIFICATIONS UNLESS OTHERWISE NOTED:

		TOL.	T.I.R.	FINISH
1) DECIMAL:	x.xxx	±0.005"	0.005"	32µinch Ra
	x.xx	±0.015"	0.015"	64µinch Ra
	x.x	±0.030"	0.030"	125µinch Ra
2) FRACTION:	x/x	±0.030"	0.030"	250µinch Ra
3) ANGULAR:	x.x°	±0.5°		
	x°	±1.0°		

Bottom EndCap Drainage Profile Details

Material: AISI 4140 Q&T (min. yield 110,000 psi)

Rev	Description	Drawn	Date
0	Original	PML	28-May-07

University of Alberta

Sheet: 6 of 6

Scale: NTS

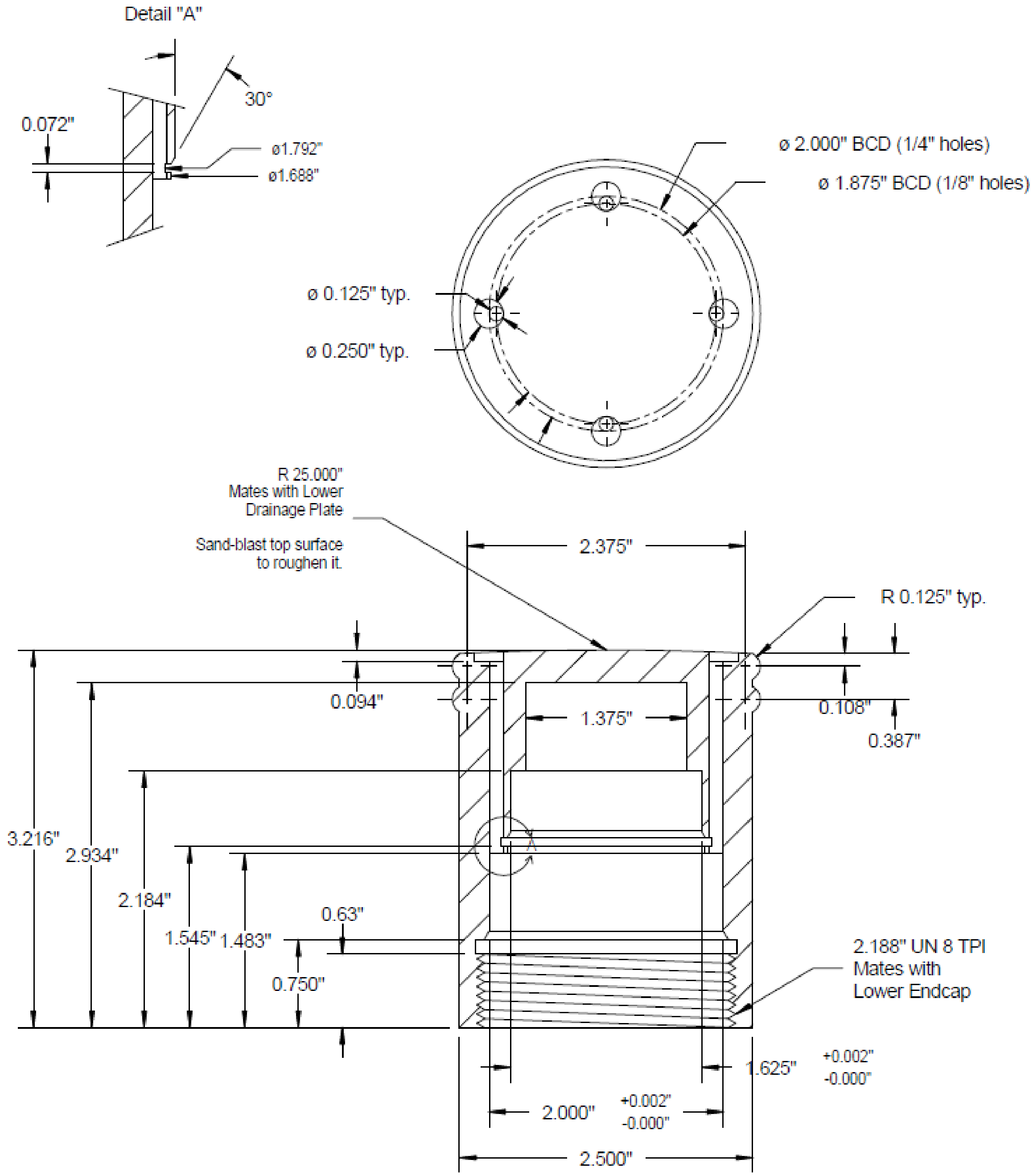

SPECIFICATIONS UNLESS OTHERWISE NOTED:

		TOL	T.I.R.	FINISH
1) DECIMAL:	x.xxx	±0.005"	0.005"	32µinch Ra
	x.xx	±0.015"	0.015"	64µinch Ra
	x.x	±0.030"	0.030"	125µinch Ra
2) FRACTION:	x/x	±0.030"	0.030"	250µinch Ra
3) ANGULAR:	x.x°	±0.5°		
	x°	±1.0°		

Lower Platen (TDS-6500)

Material: 316 SS

Rev	Description	Drawn	Date
0	Original	PML	9-Aug-07

University of Alberta

Sheet: 1 of 1

Scale: NTS

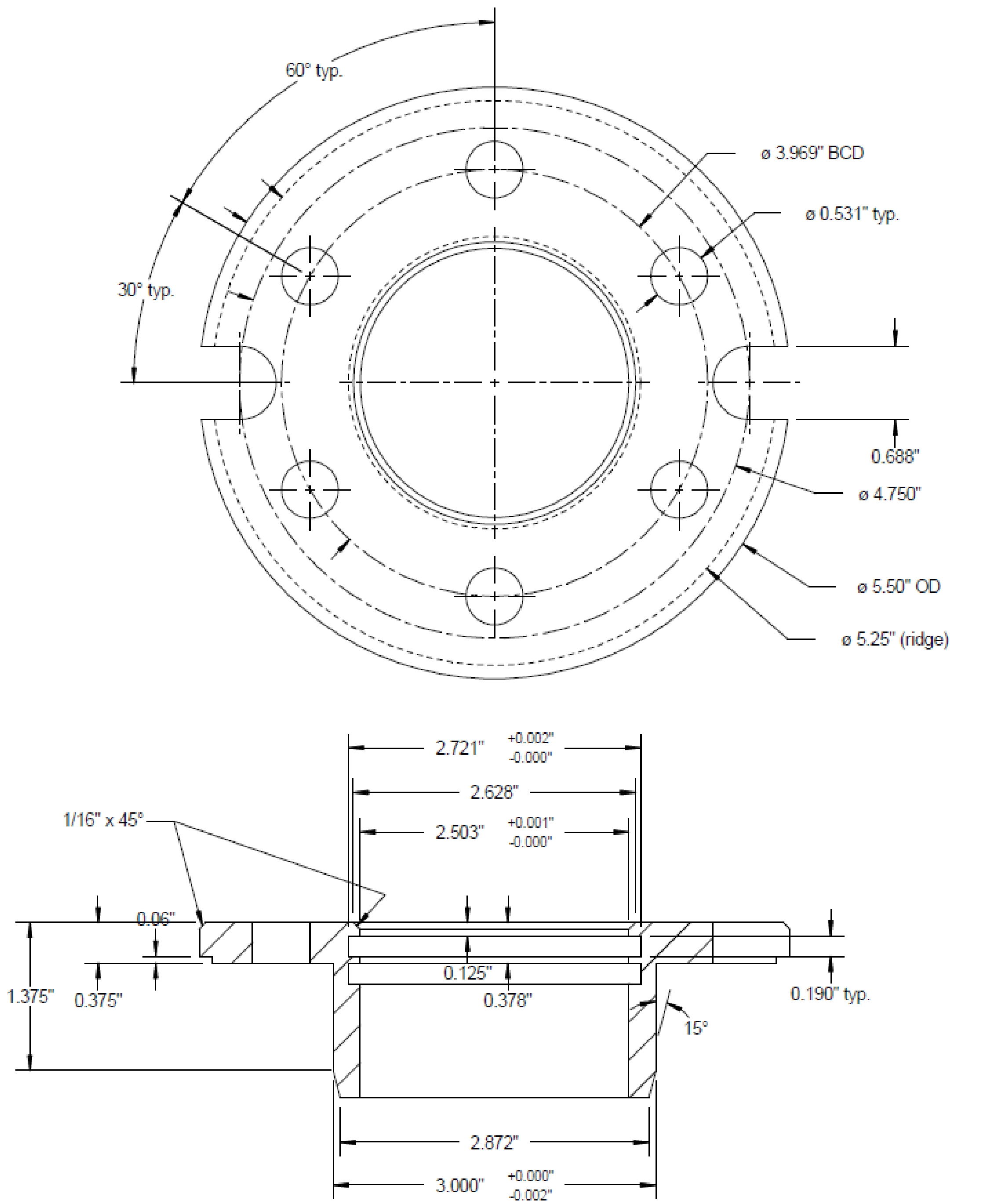

SPECIFICATIONS UNLESS OTHERWISE NOTED:

		TOL.	T.I.R.	FINISH
1) DECIMAL:	x.xxx	±0.005"	0.005"	32µinch Ra
	x.xx	±0.015"	0.015"	64µinch Ra
	x.x	±0.030"	0.030"	125µinch Ra
2) FRACTION:	x/x	±0.030"	0.030"	250µinch Ra
3) ANGULAR:	x.x°	±0.5°		
	x°	±1.0°		

Plug (TDS-6500)

Material: AISI 4140 Q&T (min. 110,000 psi yield)

Rev	Description	Drawn	Date
0	Original	PML	28-May-07

University of Alberta

Sheet: 1 of 1

Scale: NTS

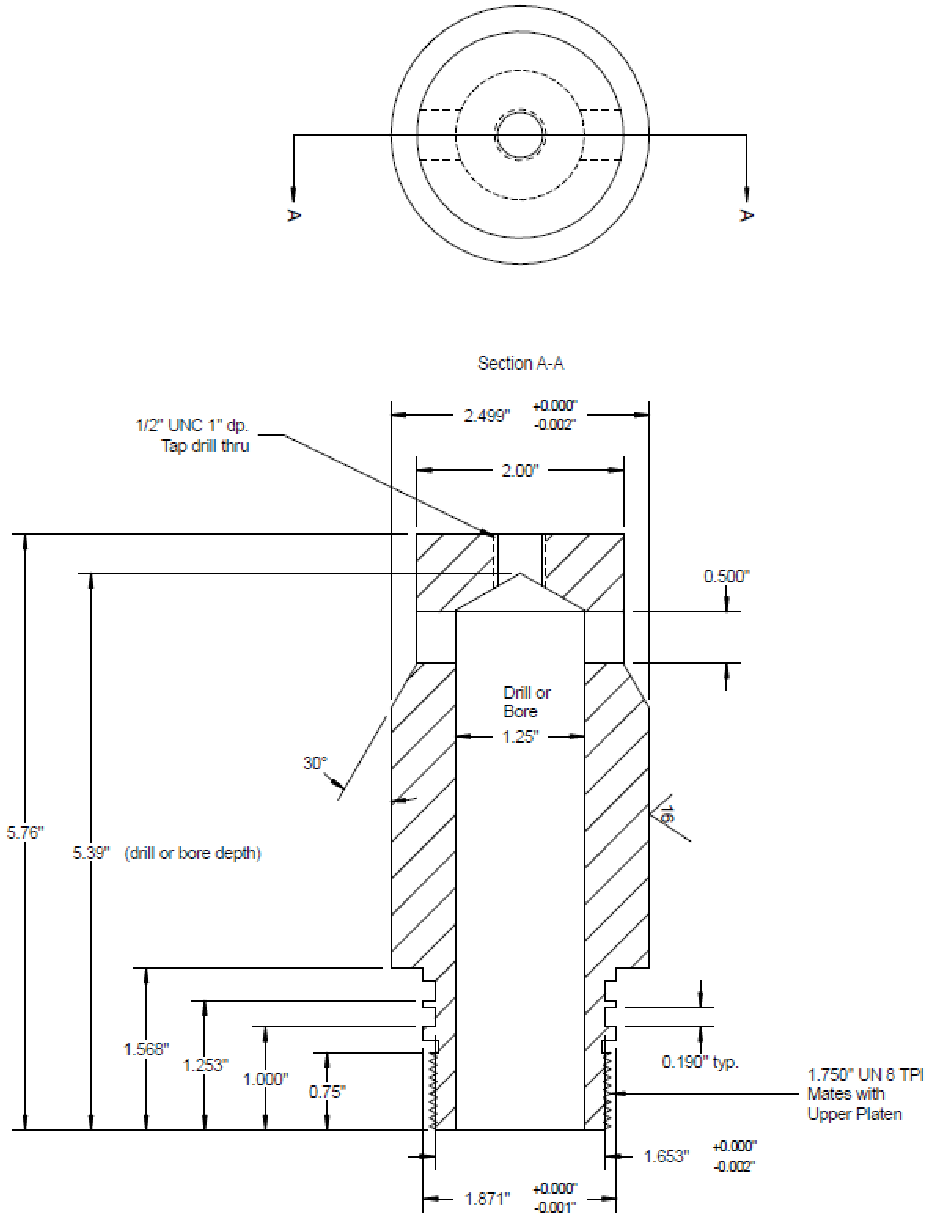

NOTE:

ELECTROLESS NICKEL PLATE ALL SURFACE 0.0010"
MASK OFF ALL THREADS

SPECIFICATIONS UNLESS OTHERWISE NOTED:

		TOL.	T.I.R.	FINISH
1) DECIMAL:	x.xxx	±0.005"	0.005"	32µinch Ra
	x.xx	±0.015"	0.015"	64µinch Ra
	x.x	±0.030"	0.030"	125µinch Ra
2) FRACTION:	x/x	±0.030"	0.030"	250µinch Ra
3) ANGULAR:	x.x°	±0.5°		
	x°	±1.0°		

Ram (TDS-6500)

Material: 4140 Q&T (110ksi minimum yield)

Rev	Description	Drawn	Date
0	Original	PML	28-May-07

University of Alberta

Sheet: 1 of 1

Scale: NTS

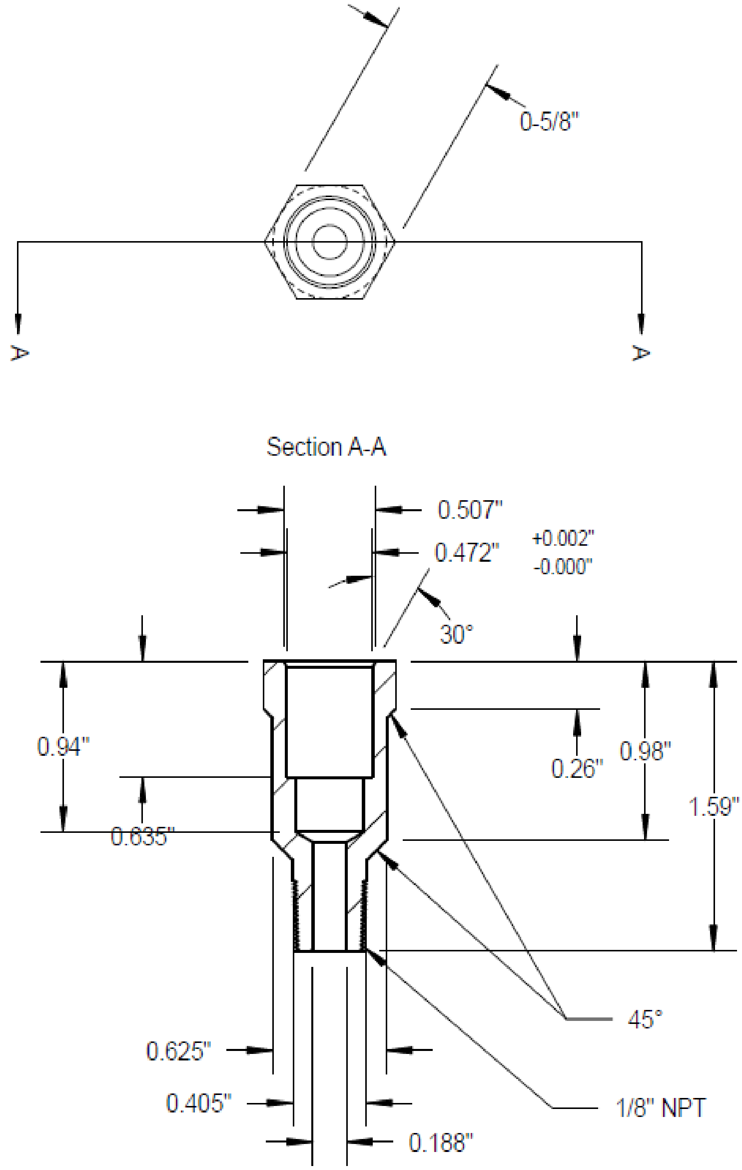

Designed for Seal Connect p/n: 5672-2233 (8 pin connector)

SPECIFICATIONS UNLESS OTHERWISE NOTED:

		TOL.	T.I.R.	FINISH
1) DECIMAL:	x.xxx	±0.005"	0.005"	32µinch Ra
	x.xx	±0.015"	0.015"	64µinch Ra
	x.x	±0.030"	0.030"	125µinch Ra
2) FRACTION:	x/x	±0.030"	0.030"	250µinch Ra
3) ANGULAR:	x.x°	±0.5°		
	x°	±1.0°		

Greene Tweed Seal Connect Housing

Material: 316 SS

University of Alberta

Sheet: 1 of 1

Rev	Description	Drawn	Date
0	Original	PML	9-Aug-07

Scale: NTS

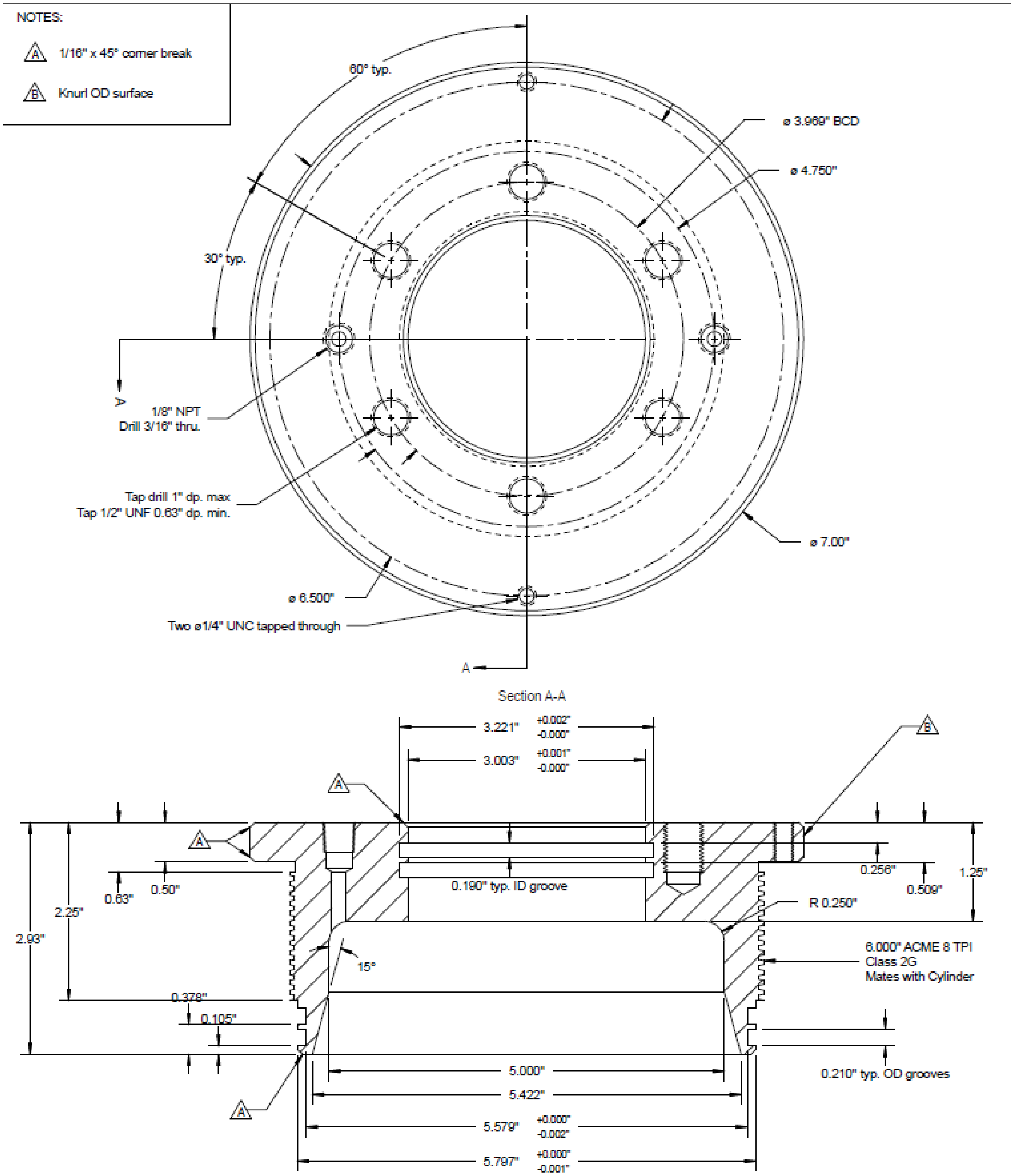

SPECIFICATIONS UNLESS OTHERWISE NOTED:

		TOL.	T.I.R.	FINISH
1) DECIMAL:	x.xxx	±0.005"	0.005"	32µinch Ra
	x.xx	±0.015"	0.015"	64µinch Ra
	x.x	±0.030"	0.030"	125µinch Ra
2) FRACTION:	x/x	±0.030"	0.030"	250µinch Ra
3) ANGULAR:	x.x°	±0.5°		
	x°	±1.0°		

Upper Endcap (TDS-6500)

Material: AISI 4140 (min yield 110,000 psi)

Rev	Description	Drawn	Date
0	Original	PML	9-Aug-07

University of Alberta

Sheet: 1 of 1

Scale: NTS

Port Detail

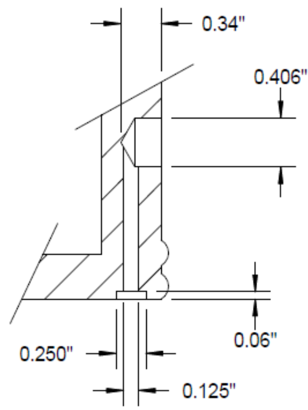

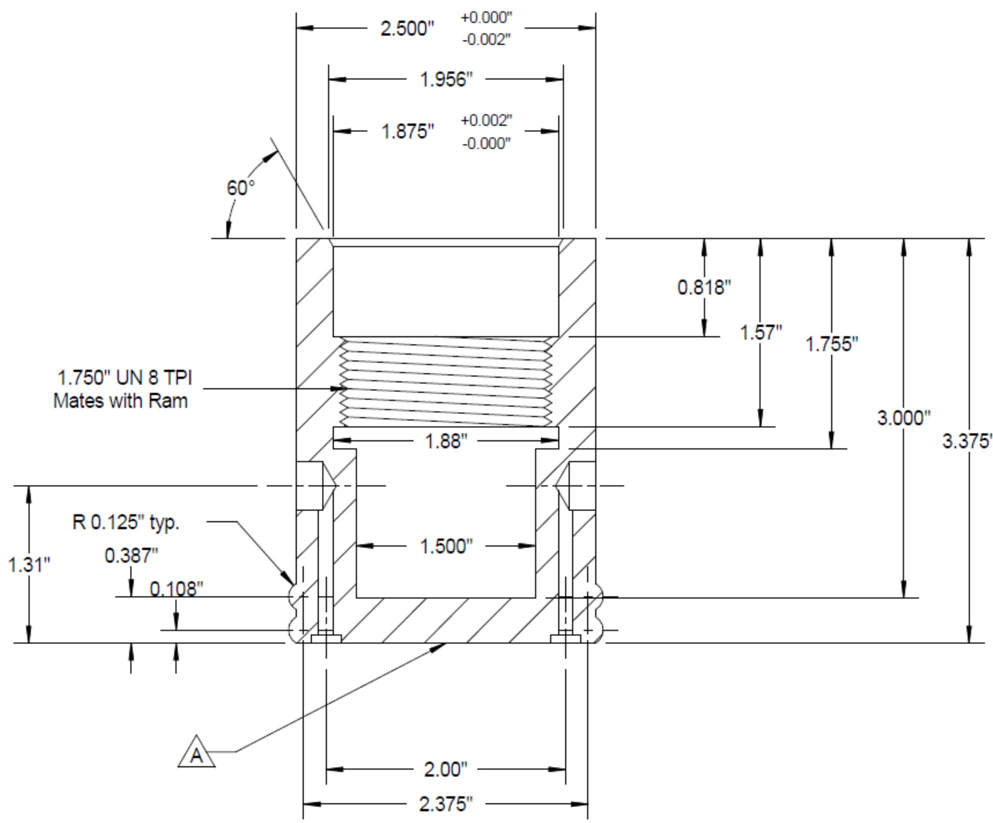

NOTE:

A Sandblast surface "A" to roughen it.

SPECIFICATIONS UNLESS OTHERWISE NOTED:

		TOL.	T.I.R.	FINISH
1) DECIMAL:	x.xxx	±0.005"	0.005"	32µinch Ra
	x.xx	±0.015"	0.015"	64µinch Ra
	x.x	±0.030"	0.030"	125µinch Ra
2) FRACTION:	x/x	±0.030"	0.030"	250µinch Ra
3) ANGULAR:	x.x°	±0.5°		
	x°	±1.0°		

Upper Platen (TDS-6500)

Material: 316 SS

Rev	Description	Drawn	Date
0	Original	PML	28-May-07

University of Alberta

Sheet: 1 of 1

Scale: NTS

16 Appendix B

16.1 Deisman Dynamic Permeability Model

This section outlines the development of a strain based permeability change model. The model uses the full strain tensor calculated from the change in stress, and applies the strain to the hydraulic apertures of the coal mass. The permeability is then updated using an updated hydraulic aperture. The derivation of the model is discussed, a parametric study is provided, and examples of the model applied to literature data.

16.1.1 The "Cubic Law"

Derivation of the 'cubic law' for fracture flow results from a solution to the general Navier-Stokes equation (70):

$$\rho\left(\frac{\partial u}{\partial t}+u\frac{\partial u}{\partial x}+v\frac{\partial u}{\partial y}+w\frac{\partial u}{\partial z}\right)=-\frac{\partial p}{\partial t}+\mu\left(\frac{\partial^2 u}{\partial x^2}+\frac{\partial^2 u}{\partial y^2}+\frac{\partial^2 u}{\partial z^2}\right)-\rho g\frac{\partial h}{\partial x} \qquad 70$$

where ρ is fluid density, p is fluid pressure, μ is dynamic viscosity, and g is gravity. The u vector is the direction of flow, v is opposite the direction of gravity, and w is into the plane. The assumptions of steady state, one dimensional, developed flow (fracture length much greater than fracture width) in a wide channel, and zero flow velocity in other directions are made. Mathematically, these are expressed as:

$$\frac{\partial u}{\partial t}=0 \text{ , steady state,} \qquad 71$$

$$\frac{\partial u}{\partial x}=\frac{\partial^2 u}{\partial x^2}=0 \text{ , developed flow,} \qquad 72$$

$$\frac{\partial^2 u}{\partial z^2}=0 \text{ , wide fracture, and} \qquad 73$$

$v = w = 0$, flow occurs only in one direction. 74

Thus, the Navier-Stokes equation reduces to:

$$\mu\left(\frac{\partial^2 u}{\partial y^2}\right) = \frac{\partial}{\partial x}(p + \rho g h) \qquad 75$$

This relationship is then solved, implementing zero flow velocity at the boundaries of the fracture (where y is any point across the aperture *b*) (76):

$$u = 0 \ @ \ y = 0 \ and \quad y = b; \qquad 76$$

The solution to the velocity of the flow in the aperture is then:

$$u(y) = \frac{1}{2\mu}(p + \rho g h)\left(y^2 - yb\right) \qquad 77$$

The average velocity, u_{avg}, of flow per unit length, *l,* is given by integrating the flow velocity over the entire width of the aperture, *b*, and dividing by the width, *b*:

$$u_{avg} = \frac{1}{b}\int_0^b u(y)dy = -\frac{b^2}{12\mu}\frac{\partial}{\partial x}(p + \rho g h) \qquad 78$$

The permeability, *k*, of a material is defined through Darcy's Law as:

$$u_{avg} = -k_x \frac{1}{\mu}\frac{\partial}{\partial x}(p + \rho g h) \qquad 79$$

Therefore, in determining the permeability of a block which contains parallel fractures, such as coal, the aperture width *b*, aperture spacing, *s*, and fracture length, *l,* must be included. The fracture length is considered to be the length of the unit of the block, therefore the permeability of a material containing parallel fractures may be given as:

$$k_x = \frac{1}{12 s_x} b^3 \tag{80}$$

16.1.2 Strain Based Coupled Flow model

Liu et al. (1999) developed a formulation relating Rock Quality Designation (RQD) and the Rock Mass Rating (RMR) system to permeability and changes in permeability. The approach described here is similar to Liu et al. for the effects of normal deformation; however, it is extended to include the effects of shear deformation on changes in permeability, and developed generally to include isotropic or anisotropic fracture permeability.

Fracture Permeability

The flow in a CBM reservoir is assumed to occur only in the fractures (bedding planes, cleats) with an impermeable matrix. In an idealized coal mass (Figure 184) with the bedding planes, face and butt cleats (or joint sets) orthogonal and persistent, the permeability in the "*i*" direction (k_{ii}) is due to the joints existing in the "*ij*" and "*ik*" planes with spacing and apertures s_k, s_j and b_k, b_j respectively. The total permeability in the "*i*" direction (k_{ii}) can be expressed by summing the contributions from each joint set. The fracture sets as idealized in Figure 184, therefore the persistence (p_i), which is a value between 0 and 1 (Cai et al, 2004), is included for each fracture set. The permeability in direction *ii* is 81 and 82:

$$q_i = -k_j \frac{A_{ik}}{\mu} \frac{\partial}{\partial x}(p + \rho g z) - k_k \frac{A_{ik}}{\mu} \frac{\partial}{\partial x}(p + \rho g z) = -(k_j + k_k) \frac{A_{ik}}{\mu} \frac{\partial}{\partial x}(P + \rho g z) \tag{81}$$

$$k_{ii} = k_j + k_k \tag{82}$$

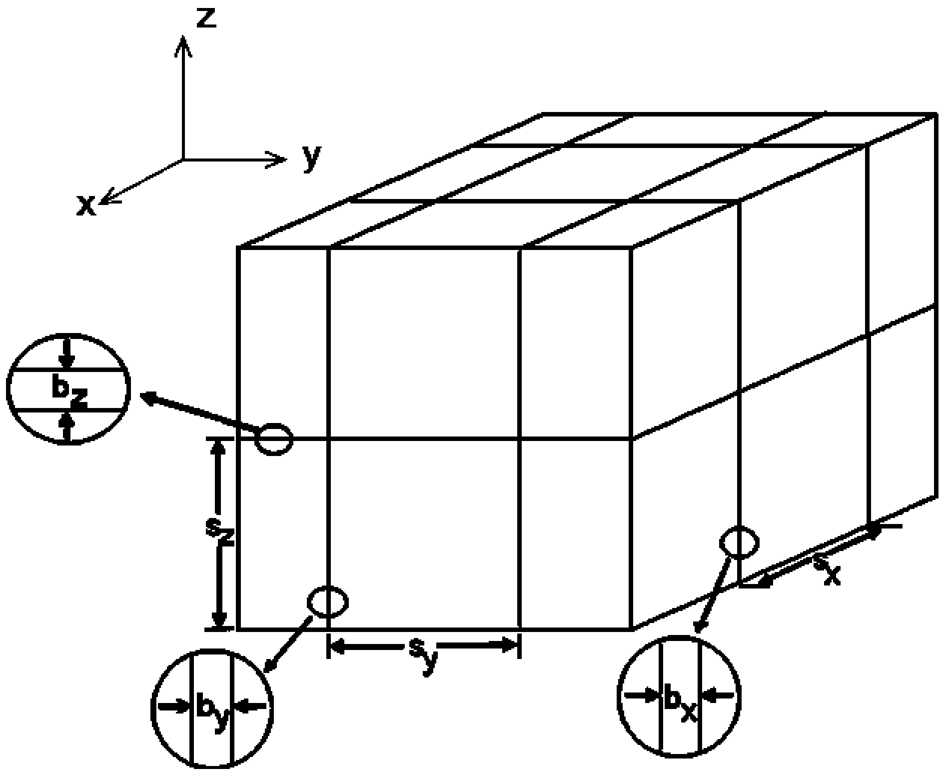

Figure 184. Idealized coal mass with three joint sets (bedding plane, face and butt cleats) and joint set spacings, s_x, s_y, s_z along with the associated hydraulic apertures (b_x, b_y, b_z).

A more realistic idealization of the coalseam is where the fracture sets (cleats) are not persistent (Figure 131). In reality, the fractures are not through going fractures, but terminate on each other (butt cleat terminate on face cleats, and face and butt cleats terminate on bedding planes). Therefore, if the persistence (p_i), which is a value between 0 and 1 (Cai et al, 2004), is included, and the contribution for each fracture set becomes (83)

$$k_i = \frac{p_i}{12 s_i} b_i^3 \qquad 83$$

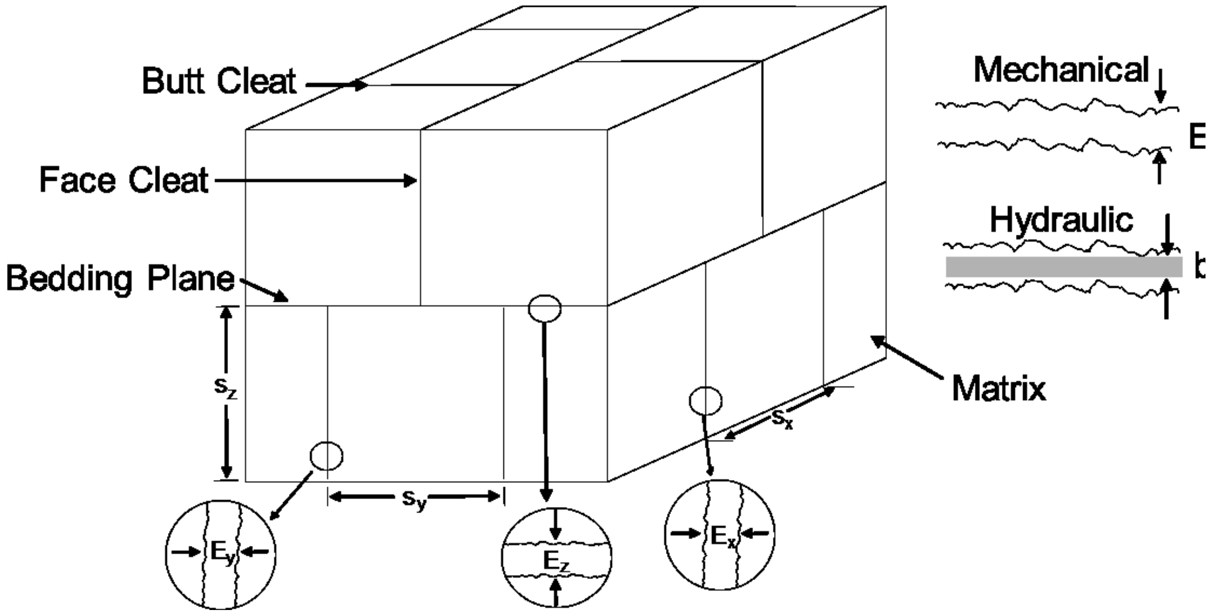

Figure 185. Idealized coal mass showing orthogonal, impersistent fractures as well as the mechanical and hydraulic apertures.

Substituting (48) into (46) and rearranging gives an expression for the hydraulic aperture of each fracture set (49), which is similar to Liu et al 1999, but includes p_i:

$$b_i = \left[\frac{6s_i}{p_i} (k_{kk} + k_{jj} - k_{ii}) \right]^{1/3} \qquad 84$$

Hydraulic Aperture

Assuming that the permeability (k_{ii}) in each direction of the coalseam is known as well as spacing of the joint sets, the average hydraulic apertures (b_i) for each joint set can be calculated. This can be accomplished by substituting (83) into (82), yielding (85):

$$12k_{ii} = \frac{p_j b_j^3}{s_j} + \frac{p_k b_k^3}{s_k} \qquad 85$$

Substitution of the corresponding similar expressions for k_{jj} and k_{kk} into (85) and rearranging gives (86):

$$2\frac{p_i b_i^3}{s_i} = 12k_{kk} + 12k_{jj} - 12k_{ii} \qquad 86$$

By solving for the aperture in (86), a general expression for each hydraulic aperture can be formulated based on initial permeability and fracture spacing (87) (Liu et al, 1999),

$$b_i = \left[6s_i / p_i \, (k_{kk} + k_{jj} - k_{ii})\right]^{1/3} \tag{87}$$

Strain Dependent Permeability

The permeability of a CBM reservoir changes with time (k'_{ii}) due to changes in individual joint set permeability (k'_i) (88) caused by changes in fracture aperture (Δb_i) or fracture spacing (Δs_i) (89):

$$k'_{ii} = k'_j + k'_k \tag{88}$$

$$k'_i = \frac{p_i}{12} \frac{\left(b_i + \Delta b_i\right)^3}{s_i + \Delta s_i} \tag{89}$$

Normal and Shear Strain Contributions

Deformation, either normal (n) or shear (s), created by changes in effective stress ($\Delta\sigma'$) from reservoir production/injection activities leads to Δb_i. From the principle of superposition, Δb_i can be partitioned into changes due to the effects of normal deformation ($\Delta b_{i,n}$) and changes due to shear deformation ($\Delta b_{i,s}$) (dilation/contraction) (90):

$$\Delta b_i = \Delta b_{i,n} + \Delta b_{i,s} \tag{90}$$

The initial length of an idealized coal mass (Figure 130) segment in any direction ($L_{RM,i}$), includes one fracture aperture (b_i), and one matrix length (s_i) (91) (Figure 186):

$$L_{RM,i} = b_i + s_i \tag{91}$$

Changes in length of in direction i ($\Delta L_{RM,i}$) is a summation of change in aperture (Δb_i) and change in length of intact components (Δs_i) (92).

$$\Delta L_{RM,i} = \Delta b_i + \Delta s_i \tag{92}$$

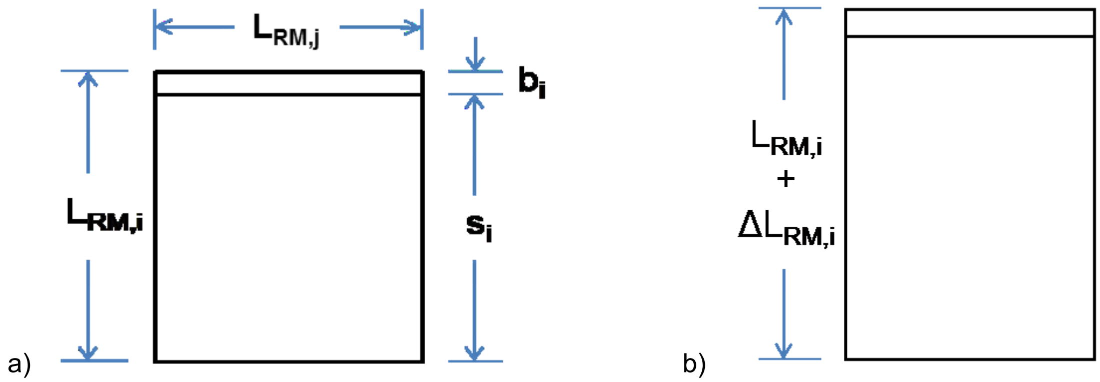

Figure 186. a) Initial rock mass segment length ($L_{RM,i}$) made up one aperture (b_i) and one matrix segment (s_i). b) The change in length of a rock mass segment caused by normal strain.

The of change in axial length of the of a rock mass segment ($\Delta L_{RM,i}$) is a summation of the change aperture due to normal strain ($\Delta b_{i,n}$) and change in intact matrix length (Δs_i) (93):

$$\Delta L_{RM,i} = \Delta b_{i,n} + \Delta s_i \qquad 93$$

Engineering axial strain (or normal strain) of the rock mass ($\varepsilon_{RM,ii}$) is defined as the change in length ($\Delta L_{RM,i}$) divided by the initial length ($L_{RM,i}$) (94):

$$\varepsilon_{RM,ii} = \frac{\Delta L_{RM,i}}{L_{RM,i}} = \frac{\Delta b_{i,n} + \Delta s_i}{b_i + s_i} \qquad 94$$

Using the assumption that b_i is much, much less than s_i, reduces the denominator to (95).

$$\varepsilon_{RM,ii} = \frac{\Delta b_{i,n}}{s_i} + \frac{\Delta s_i}{s_i} = \frac{\Delta b_{i,n}}{s_i} + \varepsilon_{I,ii} \qquad 95$$

Solving the resulting expression for $\Delta b_{i,n}$ then gives (96) (where $\varepsilon_{I,ii}$ is the intact rock strain in the normal direction ii):

$$\Delta b_{i,n} = s_i\left(\varepsilon_{RM,ii} - \varepsilon_{I,ii}\right) \qquad 96$$

Shear deformation of a fracture leads to either fracture dilation or contraction depending on the shear strain and effective normal stress. The effects of changes in length of the fracture "i" in direction "j" on $\Delta b_{s,i}$ is calculate through the corresponding fracture dilation angle (d_i) and expressed as a combination of the shear deformation in each direction orthogonal to the fracture (Δl_{ij}) (97).

$$\Delta b_{i,s} = \Delta l_j \tan(d_i) + \Delta l_k \tan(d_i) \qquad 97$$

Effects of change in aperture due to shear deformation start with the length of a rock mass segment ($L_{RM,i}$) being a summation of the aperture (b_i) and intact matrix length (s_i) (Figure 187). Changes in width of a rock mass segment due to shear deformation ($\Delta L_{RM,j}$) from its original width ($L_{RM,j}$) can be expressed as a summation of the changes of the intact rock component (ΔI_j) and fracture component length (Δl_j) (98):

$$\Delta L_{RM,j} = \Delta I_j + \Delta l_j \qquad 98$$

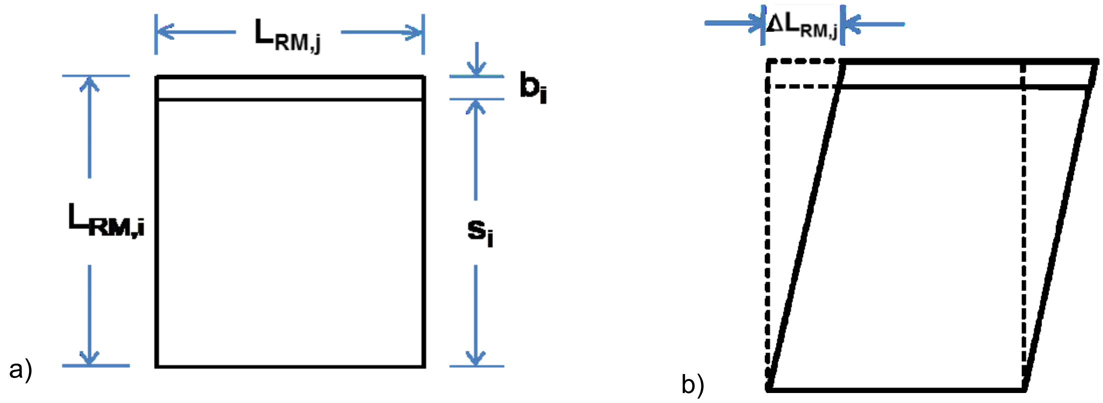

Figure 187. a) Initial rock mass segment width (Lj) where the joint is persistent. b) The change in width of a rock mass segment caused by shear deformation.

Engineering shear strain of the rock mass ($\varepsilon_{RM,ij}$) is defined as the change in width divided by the initial length, which is given by (99):

$$\varepsilon_{RM,ij} = \frac{\Delta L_{RM,j}}{L_{RM,i}} = \frac{\Delta I_j + \Delta l_j}{b_i + s_i} \qquad 99$$

Using the assumption that b_i is much, much less than s_i, reduces the denominator to (100):

$$\varepsilon_{RM,ij} = \frac{\Delta I_j}{s_i} + \frac{\Delta l_j}{s_i} = \varepsilon_{I,ij} + \frac{\Delta l_j}{s_i} \quad 100$$

Solving the resulting expression for Δl_i then gives (where $\varepsilon_{I,ij}$ is the shear strain in the intact rock) (101):

$$\Delta l_j = s_i \left(\varepsilon_{RM,ij} - \varepsilon_{I,ij} \right) \quad 101$$

Intact and Rock Mass Modulus

Hooke's constitutive law relates normal (ε_{ii}) and shear (ε_{ij}) strain to normal (σ_{ii}) and shear (σ_{ij}) stress through E and G in the rock mass and the intact matrix respectively (102 and 103):

$$\varepsilon_{ii} E = \sigma_{ii} \quad 102$$

$$\varepsilon_{ij} G = 2\sigma_{ij} \quad 103$$

A necessary condition for equilibrium is that the forces in the rock mass are equal. Using the assumption that the joint spacing is much, much greater than the apertures, the rock mass area is approximately equal to the intact matrix area. This approximation of equal areas allows for the stress in the intact matrix to be equal to the stress in the rock mass, giving (104 and 105):

$$\varepsilon_{RM,ii} E_{RM} = \varepsilon_{I,ii} E_I \quad 104$$

$$\varepsilon_{RM,ij} G_{RM} = \varepsilon_{I,ij} G_I \quad 105$$

Solving each of these expressions for the intact matrix normal and shear strain and noting that the rock mass modulus divided by the intact modulus is the modulus reduction ratio gives (106) and (107):

$$\varepsilon_{I,ii} = E_{RR} \varepsilon_{RM,ii} \quad 106$$

$$\varepsilon_{I,ij} = G_{RR} \varepsilon_{RM,ij} \quad 107$$

At this point, there is no information on the G_{RR} reduction ratio for coal. A simplified approach could be G_{RR} is equivalent to E_{RR}. Substituting (106) into (96) for aperture change due to normal deformation gives (108) which is the same formulation derived by Liu et al. (1999):

$$\Delta b_{i,n} = s_i \varepsilon_{RM,ii} \left(1 - E_{RR}\right) \tag{108}$$

Substituting (107) into (101) for shear deformation contributing to change in joint length gives (109), which can be substituted into (97) to give an expression relating the shear strain in a rock mass to change in aperture due to shear deformation (110).

$$\Delta l_j = s_i \varepsilon_{RM,ij} \left(1 - G_{RR}\right) \tag{109}$$

$$\Delta b_{i,s} = s_i \varepsilon_{RM,ij} \left(1 - G_{RR}\right) \tan\left(d_i\right) + s_i \varepsilon_{RM,ik} \left(1 - G_{RR}\right) \tan\left(d_i\right) \tag{110}$$

Substituting (108) and (110) into (90) and then into (89) gives a relationship for strain based permeability for a fracture in the coal seam and is labelled the Deisman dynamic permeability (DDP) model for reference. The $\varepsilon_{RM,ij}$ should be taken as the absolute value to ensure that as shear displacement occurs, the resultant dilation contributes to a positive change in aperture. Gu and Chalaturnyk (2010) also note, and is illustrated by the volumetric strain data from Medhurst (1996), that dilation only occurs after a minimum shear strain ($\varepsilon_{RM,ij\ min}$). Therefore, the DDP model is partitioned into two equations where (111) is relevant for strain below the dilation threshold, and (112) should be used above the threshold (contraction due to shear is not modeled):

$$k_i' = \frac{p_i}{12(s_i + \Delta s_i)} \left[b_i + (s_i + \Delta s_i) \varepsilon_{RM,ii} \left(1 - E_{RR}\right)\right]^3 \ when\ \varepsilon_{RM,ij} \le \varepsilon_{RM,ij\min} \tag{111}$$

$$k_i' = \frac{p_i}{12(s_i + \Delta s_i)} \begin{bmatrix} b_i + (s_i + \Delta s_i)\varepsilon_{RM,ii}(1 - E_{RR}) \\ + (s_i + \Delta s_i)(1 - G_{RR})\left(\left|\varepsilon_{RM,ij} - \varepsilon_{RM,ij\min}\right| \tan d_i\right) \\ (s_i + \Delta s_i)(1 - G_{RR})\left(\left|\varepsilon_{RM,ik} - \varepsilon_{RM,ik\min}\right| \tan d_i\right) \end{bmatrix}^3 \quad when \quad \varepsilon_{RM,ij} > \varepsilon_{RM,ij\min} \tag{112}$$

16.1.3 DDP Parametric Study

The DDP model uses the full strain tensor determined after a change in stress to determine an updated permeability. The joint persistence is held constant ($p_1 = 0.5$, $p_2 = 0.7$, $p_3 = 0.95$) and fracture spacing is estimated based on GSI using the GSI chart and bearing in mind that the coal fractures are primarily orthogonal (Figure 188). Using this approach to determine the intact HB strength parameters, a figure of the coal seam can be created and different boreholes constructed to estimate GSI and fracture spacings (Figure 188). This section investigates the influence of adjusting three sets of the input parameters on the behaviour of the model (Table 47): initial stress, E_i, ν, GSI, h, initial k, d_i and $\varepsilon_{\mathrm{RM,ij\ min}}$.

Also investigated is the influence of the loading path on the model`s predicted permeability during: isotropic loading, axial stress change at constant horizontal stress, and horizontal stress change at constant axial stress (Table 48). The initial stress was 10 MPa with the remaining model parameters equal to the constant values provided in (Table 47). The changes in the stress were +/- 4 MPa in each case, which are considered reasonable during for typical CBM field operations.

Table 47. Range of values used to complete parametric analysis on DDP model.

Study ID	Parameter	Symbol	Units	Min.	Constant	Max.
1	Initial Stress	σ	MPa	5	10	15
2	Intact Young`s Modulus	E_i	GPa	1	4	7
3	Poisson’s Ratio	ν		0.15	0.3	0.45
4	GSI			70	80	90
5	h		MPa	1	4	10
6	Initial Permeability	K	mD	1	10	20
7	Dilation Angle	d_i	deg	1	10	20
8	Shear Strain Cut Off	$\varepsilon_{\mathrm{RM,ij\ min}}$		0	0.001	0.002

Table 48. Range of values used to complete parametric effective stress analysis on DDP model.

Study ID	Stress State	σ_{11} (MPa)	σ_{22} (MPa)	σ_{33} (MPa)
9	Isotropic Loading		6,8,10,12,14	
10	Axial Loading	10	10	6,8,10,12,14
11	Horizontal Loading	6,8,10,12,14		10

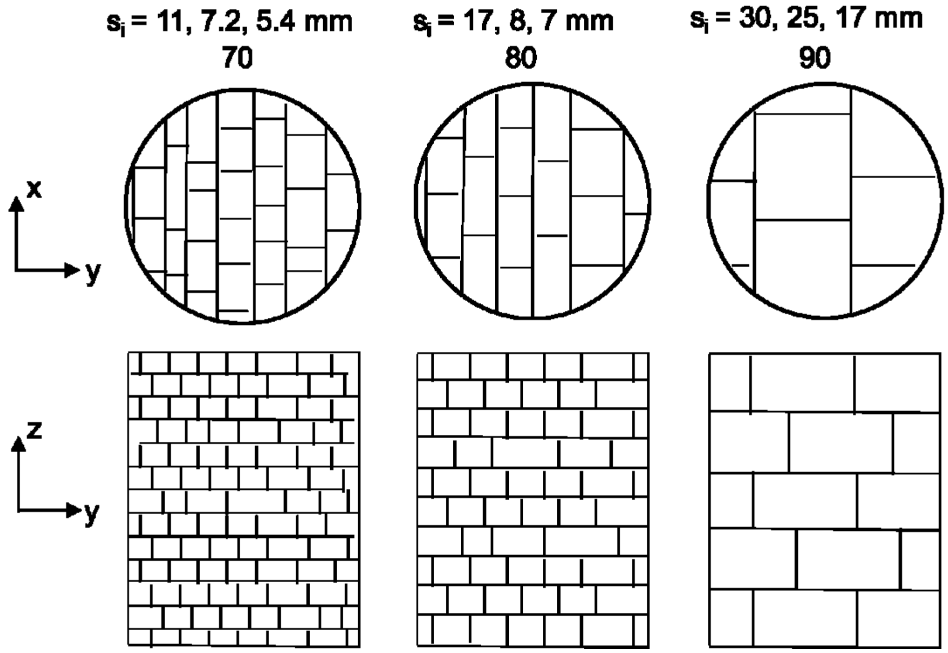

Figure 188. Illustration of fracture spacings in the x, y, and z direction for example coal specimens with GSI = 70, 80, and 90.

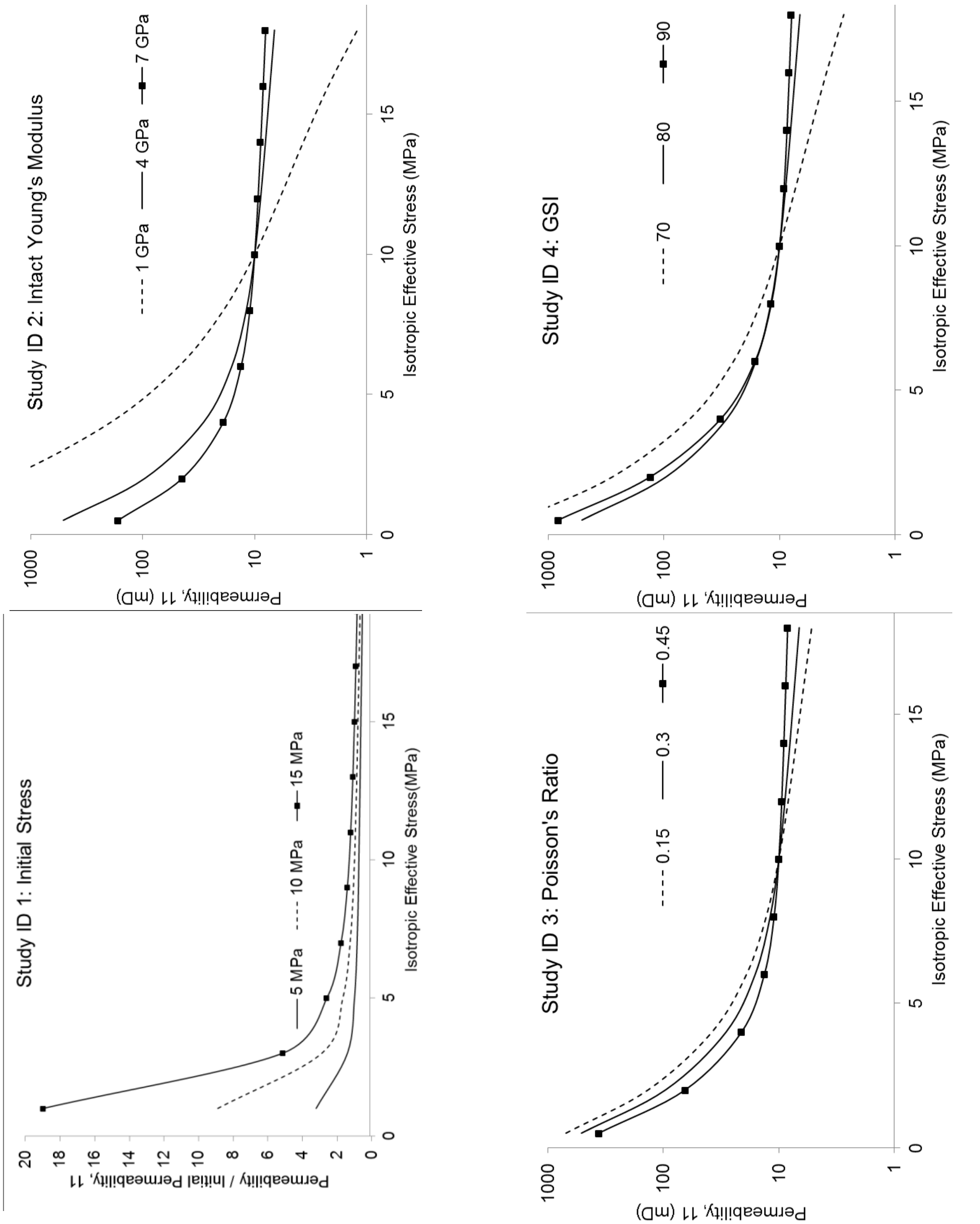

Figure 189. Results for DDP parametric study results 1-4: Initial stress, Intact Young's modulus, Poisson's ratio and GSI.

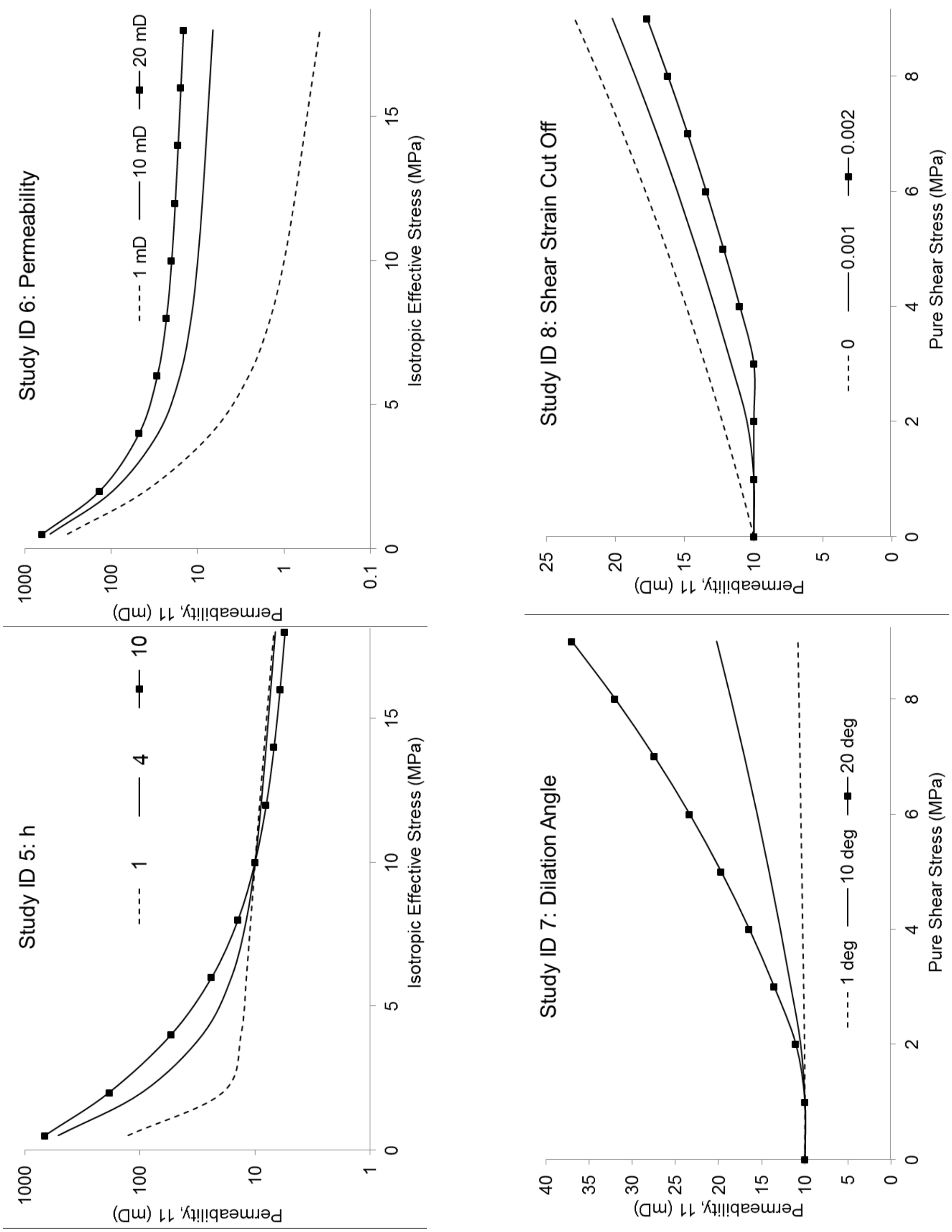

Figure 190. Results for DDP parametric study results 5-8: *h*, initial permeability, dilation angle, and shear strain cut off.

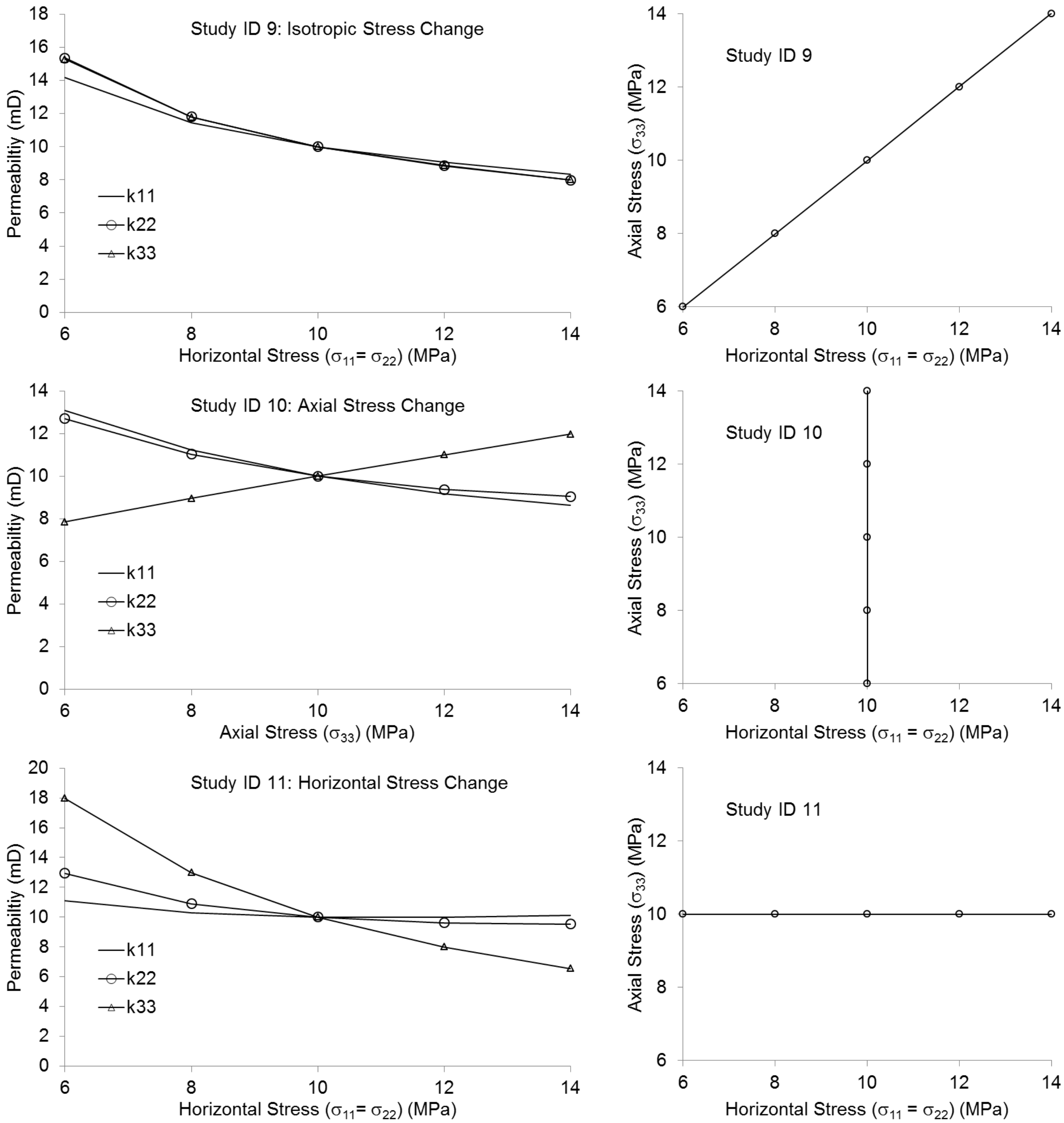

Figure 191. Parametric study results from changes in predicted DDP model due to different stress path loading.

The results of the parametric study on horizontal permeability when simulated against changes in isotropic effective stress are shown in Figure 189, Figure 190, and Figure 191. The parametric study has identified (in order of the test ID):

1. The higher the initial stress, the greater the stress reduction required to achieve an equivalent permeability increase as related to a lower stressed coal;

2. As the Intact Young's modulus decreases, the change in permeability becomes more drastic;
3. Poisson's ratio has limited influence under isotropic stress loading;
4. As GSI decreases, the change in permeability (positive or negative);
5. The h value changes the inflection shape of the change in permeability curve;
6. If the initial permeability is higher, the decrease in permeability with increasing effective stress is reduced;
7. The dilation angle has a limited effective permeability change, and to activate dilative effects, a large pure shear stress is required (4x k11 at 9 MPa pure shear);
8. The shear strain cut off has a large influence on the small changes in permeability;
9. An increase in isotropic effective stress creates a small permeability anisotropy;
10. As σ_{33} increases, k_{11} and k_{22} decrease, while k_{33} increases, and as σ_{33} the opposite permeability change occurs ($\sigma_{11} = \sigma_{22}$ are help constant).
11. As σ_{11} and σ_{22} increase, all permeabilities decrease, and as σ_{11} and σ_{22} decrease all permeabilities increase. The vertical permeability is experiences the greatest change with change in stress.

Laboratory measured properties from laboratory testing principal stress loading (Table 49) were also used as starting points to explore DDP model responses under isotropic stress loading. The stress at which permeability was measured in the laboratory was used as the starting point for the DDP model calculations and the results from testing were used for the required mechanical parameter model inputs.

Table 49. Hydromechanical results on small plug 38 mm diameter specimens (L=19.5 - 50 mm). The average Poisson's ratio from three tests on each coal type was used. The dilation angle, shear strain cut off were set to 10 degrees and 0.001 respectively.

Parameter	Units	GH3	GH7	GH10	8UX	ELK	CR
Ei	GPa	3.3	4.2	5.4	5.1	5.6	4.5
Poisson's Ratio		0.37	0.31	0.36	0.39	0.31	0.32
GSI		85	85	85	85	85	85
h	MPa	4.0	8.1	4.0	2.8	2.0	1.9
Permeability, 33	mD	2.09	0.25	0.02	0.11	0.0009	0.34
Initial Isotropic Stress	MPa	3.4	3.4	3.4	3.4	3.4	3.4

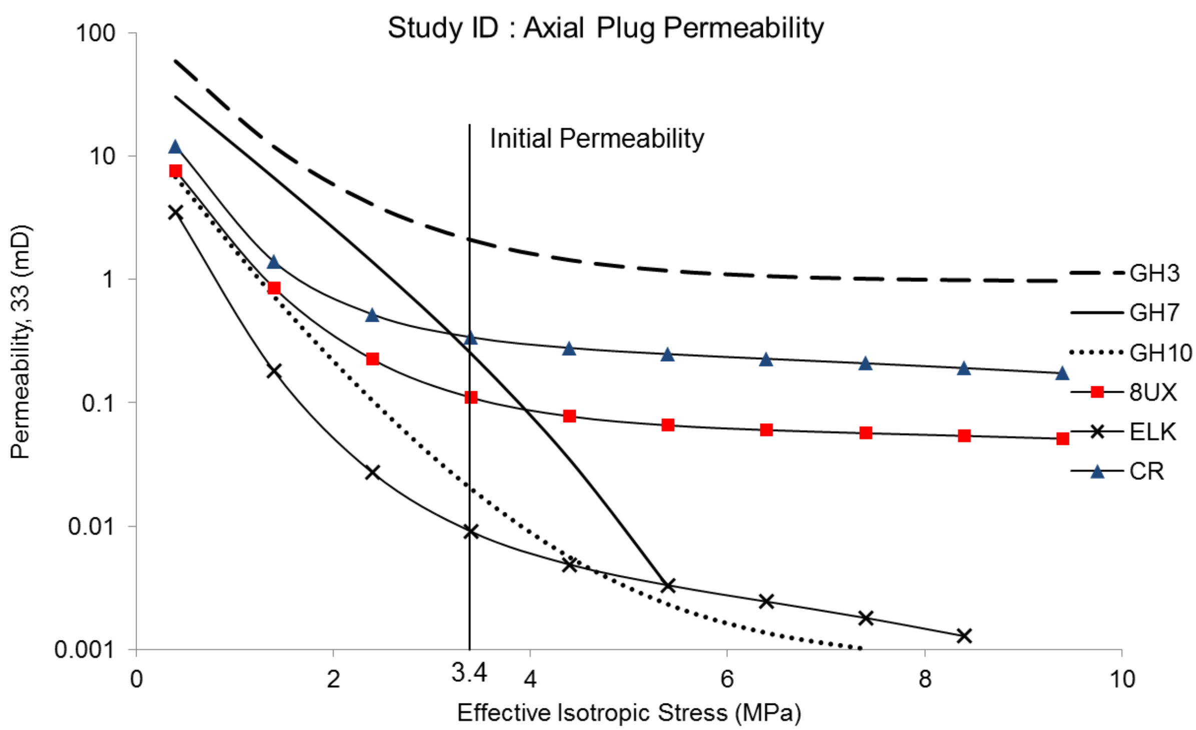

Figure 192. DDP model study on results due to changes in isotropic stress from the Conventional Triaxial with Permeability and Velocity testing program.

The results of the isotropic effective stress loading on the initial parameters from Table 49 are shown in Figure 192. All of the permeability changes with effective stress changes show reasonable results from the DDP model, except for the GH7. The mechanical results from the GH7 testing showed a concave down result which has not been seen in the literature. The most likely result of this trend was the larger value of *h* (8.1) when compared to the other results from mechanical testing.

16.1.4 Model Comparisons

One of the first coupled flow and geomechanics coalseam reservoir dynamic permeability models was derived by Gu and Chalaturnyk (2005). The most recent version of their model (Gu and Chalaturnyk 2010) and inputs (Table 50) were used from comparison against the DDP model. Gu and Chalaturnyk's permeability model is based on stress, where the DDP model is based on strain. In Gu's model, the change in stress can be used to directly calculate permeability changes, where in the DDP mode, the change in stress tensor is used to calculate strain change tensor, which is then used to update permeability.

Table 50. Data used for dynamic permeability model comparisons between the Gu and Chalaturnyk (2010) model and the model developed here.

Parameter	Unit	Value
Initial k (i = 11, 22, 33)	mD	4.0, 4.0, 4.0
Initial Spacing, s (i = 1, 2, 3)	m	0.02, 0.02, 0.02
Persistence (i = 1, 2, 3)		1, 1, 1
Porosity		0.001
Dilation Angle (i = 1, 2, 3)	deg	10, 10, 10
Initial Isotropic Effective Stress	MPa	10
Intact Young's Modulus	MPa	3550
Poisson's Ratio		0.32
GSI		85
h	MPa	5.0

The Gu and Chalaturnyk model is developed for only changes in vertical fractures using the match stick model (k_1, k_2) and does not include bedding plane flow (k_3). Therefore, to calculate the permeability, apertures, and fracture spacing for the DDP model, it was assumed that the permeability and fracture spacings were all equivalent. Several parameters had to be determined from the Gu and Chalaturnyk data for inputs. Based on the uniform fracture spacings, GSI = 85 was used. The fracture persistence was all set to 1, E_i was back calculated to be 3.55 GPa, with $h = 5.0$ MPa. The initial effective stress of the coal was 10 MPa and was the starting point for the permeability measurements. Results of the isotropic effective stress test on a single unit comparison are shown in Figure 193.

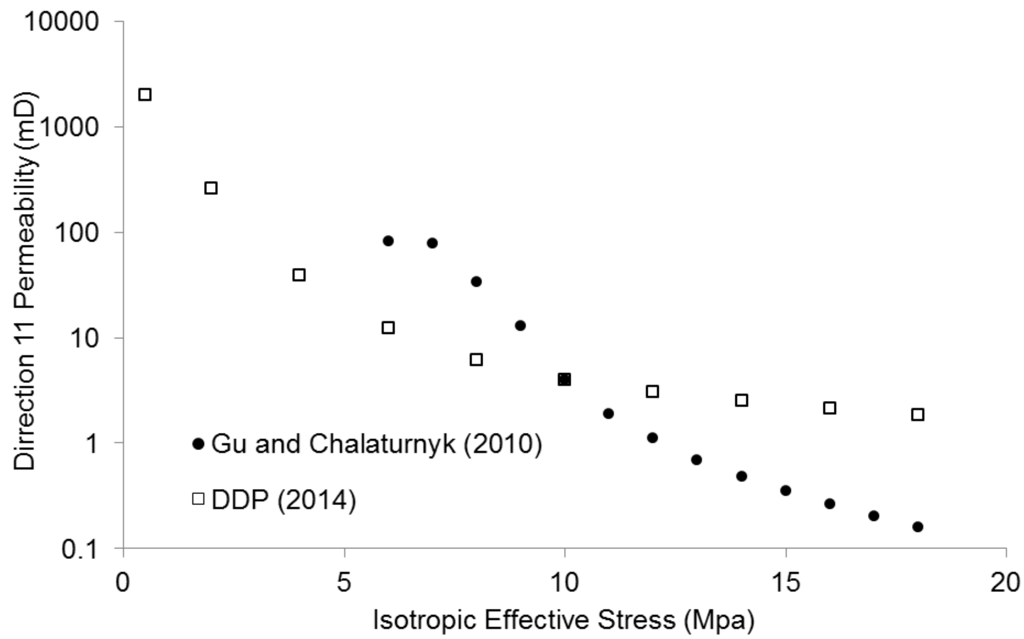

Figure 193. Comparison of the Gu and Chalaturnyk (2010) and DDP models using the input data from Table 50.

The comparison between the two models shows vast differences in model shape and range of permeability prediction. The initial isotropic stress of 10 MPa is the only location where the models are identical and afterwards they diverge at different slopes. The Gu and Chalaturnyk model can only calculate the permeability above 5.5 MPa effective stress, where the DDP model is able to calculate permeability with these input parameters over any stress range.

The range of the Gu and Chalaturnyk model below 10 MPa is limited, and cut off at 5.5 MPa due to the relationship used to calculate the aperture. The fracture aperture is calculated by dividing the normal stress on the aperture by the fracture normal stiffness. The fracture normal stiffness is based on the fracture aperture. The normal stress is calculated based on the fracture normal stiffness through the equivalent continuum model. Therefore, these three calculations require iterations to solve. Additionally, as the fracture aperture approaches the maximum value (the most open), the joint fracture stiffness approaches zero. In this example, at 6.5 MPa the aperture could not be changed due to the relationship to the joint normal stiffness. This lower stress range limit does not exist for the DDP model, because changes in strain, calculated from a constitutive relationship, are partitioned to the matrix and the aperture. However, at very high strains, the DDP model does create a negative aperture, therefore a minimum aperture closure should be employed at very high stress ranges, or very low permeabilities (<0.0001 mD).

16.1.5 Published Permeability Data Matching

Somerton et al. (1975) published extensive results on permeability testing of coal specimens. They also reported two measurements on axial Young's modulus and Poisson's ratio. The coal was taken from a surface mine and the burial history was not included in the publication, therefore, the initial burial stress is unknown.

Several model variables were assumed and kept constant for all of the model fits, including: persistence ($p_1 = 0.5$, $p_2 = 0.7$, $p_3 = 0.99$), dilation angle ($d_i = 10$), and shear strain cut off ($\varepsilon_{RM,ij\ min} = 0.001$). The two reported Young's modulus (4.27 GPa and 8.55 GPa) and two Poisson's ratio measurements (0.16 and 0.34) were averaged (6.4 GPa and 0.25) and used as the geomechanical inputs. The DDP model was best fit by setting the initial stress to the lowest reported value and using the corresponding permeability value. This permeability value was used to estimate GSI and corresponding fracture spacing (based on Figure 188). The compressive isotropic stress path was then followed and the permeability calculated. To better the fit of the model, only GSI (and the corresponding fracture spacing) and *h* were adjusted. The model fitting using the Somerton et al (1975) reported Young's modulus, termed DDP Fit 1 are shown in (Table 51).

The GSI values for DDP Fit 1 are low, and based on specimen preparation for coal it is difficult to prepare specimens below a GSI of 70. Additionally, Somerton et al (1975) indicated that the measured Young's modulus was high when compared to literature data. Therefore, a second fit was fit (DDP Fit 2) was completed using a relatively constant GSI (65-75) and adjusting the E_i to between 3.0 and 4.2 GPa. The DDP Fit 2 results showed better results, which was expected as there is an additional variable to adjust, while keeping the remaining model variables within acceptable literature and measured values. The DDP Fit 1 and Fit 2 results were plotted showing the predicted versus measured values in Figure 194 and Figure 195.

Table 51. Best fit results of DDP model against Somerton et al (1975) permeability measurements under isotropic compression using E_i = 6.4 GPa, ν = 0.25.

Test ID	$\sigma_{o,iso}$ (MPa)	k_{33} @ $\sigma_{o,iso}$ (mD)	GSI	h (MPa)	s_1 (mm)	s_2 (mm)	s_3 (mm)	R^2
1	1.01	1	75	4.0	15	8	6	0.979
2	1.01	20	60	5.0	10	6	4	0.704
3	1.01	8	65	8.0	10	6	4	0.988
4	1.01	18	65	8.0	10	6	5	0.852
5	1.01	4	70	5.5	11	7	5	0.786
6	1.01	5	65	6.0	11	7	5	0.988
7	1.01	9.5	65	8.5	10	7	5	0.931
8	1.01	8	65	8.0	10	7	5	0.949
9	1.01	18	60	10	8	5	3	0.888
10	1.68	30	70	10	11	7	5	0.964
11	1.68	90	55	11	7	4	3	0.997
12	1.01	9	70	11	11	7	5.5	0.998
13	1.68	10	70	8.0	11	7	5.5	0.954
14	1.68	22	60	6.0	10	6	4	0.993

Table 52. Best fit results of DDP model against Somerton et al (1975) permeability measurements under isotropic compression using only ν = 0.25 as constant.

Test ID	$\sigma_{o,iso}$	k_{33} @ $\sigma_{o,iso}$	E_i	GSI	h	s_1	s_2	s_3	R^2
	MPa	mD	GPa		MPa	mm	Mm	mm	
1	1.01	1	4.2	75	3.0	15	8	6	0.9741
2	1.01	20	3.5	70	10	11	7	5	0.936
3	1.01	8	3.8	70	5.5	11	7	5	0.978
4	1.01	18	3.5	70	9.0	11	7	5	0.988
5	1.01	4	3.5	70	9.0	11	7	5	0.904
6	1.01	5	3.7	70	3.6	11	7	5	0.999
7	1.01	9.5	4.0	70	8.0	11	7	5	0.894
8	1.01	8	4.2	70	7.0	11	7	5	0.934
9	1.01	18	3.7	70	10	11	7	5	0.914
10	1.68	30	3.8	70	7.0	11	7	5	0.901
11	1.68	90	3.4	65	10	10	6	4	0.986
12	1.01	9	3.5	70	4.0	11	7	5	0.974
13	1.68	10	3.8	70	3.3	11	7	5	0.996
14	1.68	22	3.0	70	5.0	11	7	5	0.987

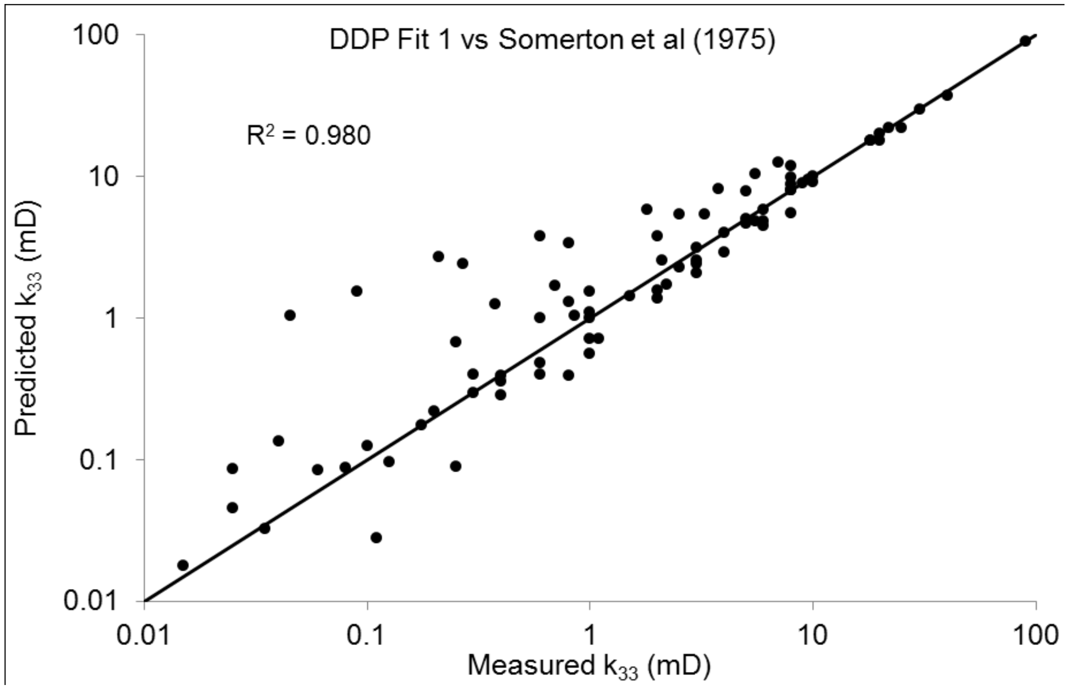

Figure 194. DDP model Fit 1 of Somerton et al (1975) permeability with changes in isotropic stress using reported values: E_i = 6.4 GPa and ν = 0.25.

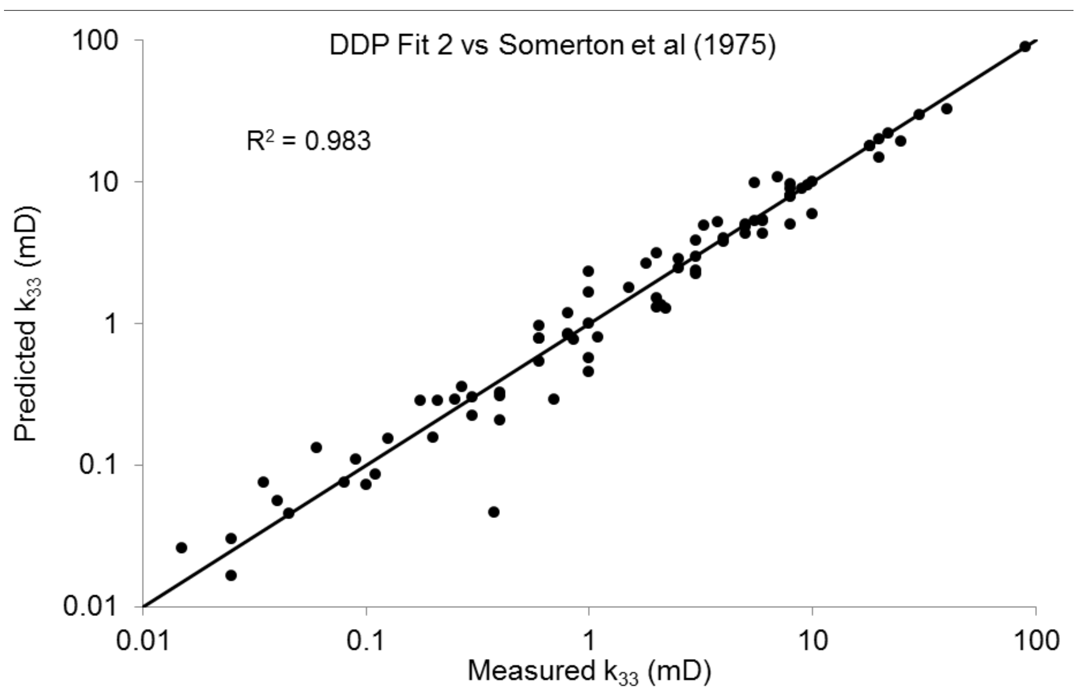

Figure 195. DDP model Fit 2 of Somerton et al (1975) permeability with changes in isotropic stress using only the reported ν = 0.25.